Extragalactic Globular Cluster Systems

Thomas H. Puzia

München 2003

Extragalactic Globular Cluster Systems

Thomas H. Puzia

Dissertation
an der Fakultät für Physik
der Ludwig–Maximilians–Universität
München

vorgelegt von
Thomas H. Puzia
aus Krakau

München, den 12.8.2003

Erstgutachter: Prof. Dr. Ralf Bender
Zweitgutachter: Priv.– Doz. Dr. Achim Weiss
Tag der mündlichen Prüfung: 25.9.2003

"It is encouraging to see how fragile and futile are the majority of astronomical theories and speculations [...], for the futility of speculations emphasizes the importance and durability of observations and indicates the steady progress of the science."

Harlow Shapley, 1930

Für meine Eltern

Contents

List of Figures

List of Tables

Zusammenfassung

Das Ziel dieser Dissertation is die spektroskopische Studie von extragalaktischen Kugelsternhaufensystemen. Ihre Motivation ist das bessere Verständnis der Bildung und Entwicklung dieser Kugelsternhaufensysteme und ihrer Wirtsgalaxien. Zu diesem Zweck werden spektroskopische Linienindices des integrierten Lichts einzelner extragalaktischer Kugelsternhaufen gemessen, aus denen das Alter, die Metallizität und das Häufigkeitsverhältnis von α-Elementen zu Eisen (im folgenden [α/Fe]) abgeleitet werden kann. Dies erlaubt detaillierte Rückschlüsse auf ihre Entstehungsepochen und -mechanismen.

Der entscheidende Vorteil gegenüber Studien des diffusen Galaxienlichts ist die einfachere Natur der stellaren Population in Kugelsternhaufen. Im allgemeinen bestehen Kugelsternhaufen aus Sternen desselben Alters und derselben chemischen Zusammensetzung, was nicht für die stellaren Populationen in den Wirtsgalaxien zutrifft. Da Kugelsternhaufen sich zusammen mit den stellaren Populationen innerhalb des Galaxienkörpers bilden, können jene als Indikatoren für wichtige Sternentstehungepochen in der Galaxienentstehungsgeschichte herangezogen werden. Das Vorhandensein von hochentwickelten Multi-Objekt Spektrographen an heutigen 8–10m-Klasse Teleskopen ermöglicht zum ersten Mal eine umfassende Studie von extragalaktischen Kugelsternhaufensystemen ausserhalb der Lokalen Gruppe.

Nach einem Überblick über den heutigen Wissensstand der Kugelsternhaufenforschung und einer kurzen Einführung in die wesentlichen Analysetechniken in Kapitel 1, befasst sich Kapitel 2 mit der Messung von Linienindices in metallreichen Galaktischen Kugelsternhaufen. Darüberhinaus wird ein Vergleich zwischen den stellaren Populationen im Galaktischen *Bulge* und in Kugelsternhaufen präsentiert. Es wird festgestellt, dass beide stellaren Populationen weitgehend vergleichbare spektroskopische Eigenschafen aufweisen. Insbesondere sind die Verhältnisse zwischen Indices, die sensitiv für α-Element- und Eisenhäufigkeiten sind, sehr ähnlich, was vergleichbare Entstehungsszenarien impliziert. Die einzige Ausnahme bildet die CN Absorption bei 4150 Å, die auf signifikant höhere CN Häufigkeiten in metallreichen galaktischen Kugelsternhaufen deutet.

Da das Alter und die chemische Zusammensetzung dieser Galaktischen Kugelsternhaufen aus Photometrie und hochauflösender Spektroskopie von Einzelsternen sehr genau bekannt ist, werden die gemessenen Linienindices zur Eichung von Populationsentwicklungsmodellen in Kapitel 3 benutzt. Diese Entwicklungsmodelle treffen Vorhersagen für Linienindexstärken des integrierten Lichts von stellaren Populationen als Funktion des Alters, der Metallizität und Elementhäufigkeiten, wie z.B. dem [α/Fe] Verhältnis. Auf der Basis dieser Modelle und des induktiven Erkenntnisgewinns und unter der Benutzung dieser Modelle wird festgestellt, dass sich die [α/Fe] Häufigkeitsverhältnisse in metallreichen Galaktischen Kugelsternhaufen und den stellaren Population im Galaktischen *Bulge* und in Frühtypgalaxien wenig unterscheiden und in allen bei ~ 2.5-fachen der solaren Häufigkeit liegen.

Kapitel 4 widmet sich unter anderem der photometrischen Selektion von Kugelsternhaufenkandidaten in Galaxien ausserhalb der Lokalen Gruppe für die folgende spektroskopische Untersuchung. Spektren von herausragender Qualität, die mit

dem FORS Instrument am *Very Large Telescope* der Europäischen Südsternwarte in Chile aufgenommen wurden, werden benutzt um Radialgeschwindigkeiten und Linienindices zu messen. Es werden extragalaktische Kugelsternhaufensysteme von sieben Frühtypgalaxien, NGC 1380, 2434, 3115, 3379, 3585, 5846 und 7192, untersucht. Dieses Galaxiensample umfasst verschiedene morphologische Typen (elliptische und lentikulare) und verschiedene Umgebungsdichten (Feld und Galaxienhaufen). Durch Radialgeschwindigkeitsmessung bestätigte Kugelsternhaufen erlauben im weiteren die Bestimmung von exzellenten Erfolgsraten der Kandidatenselektion, die basierend auf Mulitbandphotometrie bei 80-100% liegen. Aus dem photometrischen Datensatz werden Farbverteilungen und Flächendichteprofile der einzelnen Kugelsternhaufensysteme abgeleitet. Als ein "Abfallprodukt" der Radialgeschwindigkeitsmessung werden dynamische Massen der Wirtsgalaxien bis zu grossen galaktozentrischen Radien ($\sim 2 - 5$ Effektivradien) gemessen.

Aus diesem Kugelsternhaufensample werden in Kapitel 5 die besten Linienindexmessungen selektiert, um aussagekräftige Resultate über das Alter, die Metallizität und [α/Fe] Elementverhältnis zu garantieren. Zu diesem Zweck werden hier die besten Kombinationen von spektroskopischen Alters- und Metallizitätsindikatoren aus dem sample der gemessenen Linienindices gefiltert. Darüberhinaus wird eine Methode zur quantitativen Bestimmung dieser besten Indikatoren präsentiert. Mit den zuverlässigsten Varianten sogenannter Diagnostischer Diagramme werden globale Trends in der Alters-, Metallizitäts- und [α/Fe]-Struktur von Kugelhaufensystemen in Frühtypgalaxien ermittelt. Zu den wichtigsten Ergebnissen zählt, dass $\sim 34\%$ der Kugelsternhaufen in Frühtypgalaxien jünger sind als $5 \cdot 10^9$ Jahre. Weiterhin erlauben die Analysen den Schluss, dass es eine universelle untere Schranke in der Metallizität für Kugelsternhaufen gibt, die bei einem Wert von $5 \cdot 10^{-3}$ der solaren Häufigkeit liegt. Die Maximalwerte auf der Metallizitätsskala rangieren im Bereich $\sim 2 - 3$-fachen der solaren Häufigkeit. Unterteilt man das sample in metallreiche und metallarme Kugelsternhaufen, findet sich ein interessanter Versatz im mittleren Alter. Während die metallarmen Kugelsternhaufen ein mittleres alter von $(11.3 \pm 0.5) \cdot 10^9$ Jahren aufweisen, habe ihre metallreichen Gegenstücke ein signifikant niedrigeres Alter von $(6.3 \pm 0.8) \cdot 10^9$ Jahren. Darüberhinaus zeigen die metallreichen Kugelsternhaufen eine deutlich höhere Streuung von $\sigma \sim 5.4 \cdot 10^9$ Jahren im Vergleich mit $\sigma \sim 2.7 \cdot 10^9$ für metallarme Kugelsternhaufen. Diese hochinteressanten Resultate implizieren, dass sich überwiegend metallreiche Kugelsternhaufen in sukzessiven Sternentstehungsphasen der jüngeren kosmologischen Historie bilden. Da jedoch auch alte metallreiche Kugelsternhaufen detektiert werden, mussen die Sternentstehungsprozesse, die zur Bildung der Wirtsgalaxien geführt haben, genügend Metalle produziert haben, um das umgebende Gas bis auf solare Metallizität anzureichern.

Es werden [α/Fe] Häufigkeiten im Bereich vom (2.75 ± 0.35)-fachen des solaren Wertes gemessen. Kombiniert mit den vorigen Ergebnissen deutet dies auf Sternentstehungszeitskalen von weniger als 10^9 Jahren hin, in denen das Gas, aus dem sich die Kugelhaufen bildeten, noch nicht wesentlich durch Supernovae des Typs Ia verunreinigt wurde. Dieser Supernovatyp reichert das umgebende Gas vorwiegend mit Eisen an und detoniert ungefähr 10^9 Jahre nach dem Beginn der Sternentstehungsprozesse. Da Kugelsternhaufen aufgrund ihrer geringen Masse keiner signifikanten Selbstanreicherung unterworfen sind, reflektieren diese Resultate die *globalen* chemischen Bedingungen in der Gasphase während der Bildung dieser Kugelsternhaufen. Im Einklang mit einer *globalen* Anreicherungshistorie der Wirtsgalaxies, in der die Chemie jüngerer Objekte immer mehr durch Ejekta von Supernovae des Typs Ia beeinflusst werden, wird festgestellt, dass jüngere Kugelsternhaufen niedrigere [α/Fe] Häufigkeiten aufweisen, mit der formalen Relation 0.02 ± 0.008 dex pro 10^9 Jahren.

Im folgenden Kapitel 6 werden die Alters-, Metallizitäts- und [α/Fe]-Strukturen

in Kugelsternhaufensystemen in Abhängigkeit von Eigenschaften der Wirtsgalaxie untersucht. Dabei wird das Sample durch Linienmessungen aus der Literatur vergrössert, um die statistische Signifikanz der Resultate zu erhöhen. Die Unterteilung des Sample nach Galaxienmorphologie, in Spiral-, Lentikular- und Elliptische Galaxien, erbringt einige interessante Ergebnisse. Zum einen findet sich ein Unterschied im mittleren Alter zwischen Kugelsternhaufen zum einen in Spiralgalaxien und zum anderen in Lentikular- und Elliptischen Galaxien. Während die ersten ein mittleres Alter von $(9.3 \pm 0.8) \cdot 10^9$ Jahren ermittelt wird, weisen die letzteren ein mittleres Alter von $(7.7 \pm 0.7) \cdot 10^9$ Jahren auf. Darüberhinaus findet sich ein monotoner Anstieg in der Altersdispersion mit niedrigsten Werten in Spiralgalaxien $(3.5 \cdot 10^9$ Jahre), über Lentikulargalaxien $(3.7 \cdot 10^9$ Jahre) bis hin zu Elliptischen Galaxien $(4.4 \cdot 10^9$ Jahre). In Übereinstimmung mit Ergebnissen aus vorigen Kapiteln sind diese Zahlen das Resultat einer jungen und metallreichen Kugelsternhaufenpopulation, die zu früheren Galaxietypen immer mehr dominiert. Dies belegen auch die Anteile an Kugelsternhaufen mit Altern jünger als $5 \cdot 10^9$ Jahren. Während $13 \pm 7\%$ der Kugelsternhaufen in Spiralgalaxien solch junge Alter aufzeigen, befinden sich bereits $20 \pm 6\%$ der Kugelhaufen in Lentikulargalaxien unter dieser Altersgrenze. Den grössten Anteil an jungen Kugelsternhaufen mit $42 \pm 8\%$ beheimaten jedoch Elliptische Galaxien. Diese Resultate sind Obergrenzen und beziehen sich rein formell auf die hellsten Kugelsternhaufen in Galaxies. Unter der Annahme, dass alle weniger hellen Kugelsternhaufen in Galaxien älter sind als $5 \cdot 10^9$ Jahre schrumpfen die oberen Anteile auf wenige Prozent.

Wie zuvor findet sich eine untere Metallizitätsgrenze für Kugelsternhaufen in allen Galaxientypen. Das obere Limit variiert jedoch von solaren Werten in Spiralgalaxien über leicht super-solare Metallizitäten in Lentikulargalaxien bis hin zu stark angereicherten Kugelsternhaufen mit Häufigkeiten um den Faktor $\sim 2-3$ der solaren Metallizität. Im allgemeinen, bilden die Alters- und Metallizitätsstrukturen der Kugelsternhaufensysteme in verschiedenen Galaxientypen einen relative monotonen Übergang von Spiral- über Lentikular- bis hin zu Elliptischen Galaxien.

Eine starke Nebenbedingung für Galaxienentwicklungsmodelle ergibt sich aus den $[\alpha/\text{Fe}]$ Häufigkeiten für Kugelsternhaufensysteme in Spiral- und Elliptischen Galaxien. Überhäufigkeiten in $[\alpha/\text{Fe}]$ mit Werten ~ 2.5-fachen der solaren Werte für Kugelsternhaufen in Elliptischen Galaxien können nur in kurzen, intensiven, und frühen Sternentstehungepochen erreicht werden. Die heutigen Kugelsternhaufensysteme von Spiralgalaxien weisen jedoch signifikant niedrigere, in etwa solare Werte auf. Da die *globale* chemische Entwicklung in einer Galaxie $[\alpha/\text{Fe}]$ Häufigkeiten monoton sinkt, können Elliptische Galaxien und ihre Kugelsternhaufensysteme nicht durch die Verschmelzung von heutigen Spiralgalaxien entstehen. Vielmehr implizieren die Daten, dass ein Aufbau von Kugelsternhaufensystemen in Elliptischen Galaxien sehr früh in der kosmischen Entwicklung, vor einer signifikanten Anreicherung durch Supernovae des Typs Ia, abgeschlossen sein muss. Die Entstehungsprozesse, die zu den heute beobachteten Kugelsternhaufensystemen in Elliptischen Galaxien führen, müssen in den ersten Jahrmilliarden nach dem Urknall grösstenteils abgeschlossen sein. Im allgemeinen stehen diese Ergebnisse im Widerspruch zum hierarchischen Galaxienentwicklungsmodell, das längere Zeitskalen, die bis in die jüngere Vergangenheit vor wenigen 10^9 Jahren hineinreichen, für den Aufbau von elliptischen Galaxien vorsieht.

Chapter 1

Introduction

Ever since men observe their ambient world, our knowledge and comprehension of the physics, which represents the deep foundation for the structures in the universe, is steadily growing. The archetypal motivation for each quest of apperception is our curiosity for the origin of all. Observational astrophysics puts this endeavour in a quantifiable context which facilitates our understanding of Nature and brings us closer to the hub of the world.

1.1 Cosmological Framework

The insight that the Universe is expanding (Hubble 1929) opened the door to a whole new field of studies: the formation *and* evolution of the Universe and its ingredients. Direct evidence for the beginning of this dynamical state was missing until Penzias & Wilson (1965) detected a microwave background radiation which is consistent with the afterglow of the Hot Big Bang. In this scenario, spacetime and all matter are created in a singular event a finite amount of time in the past. The early universe was hot, dense, extremely close to homogeneous, and since then adiabatically expanding according to the laws of general relativity. In the standard cosmological picture of the inflationary Hot Big Bang, based on the Cosmological Principle by which the universe is thought to be uniform and isotropic on all scales, the starting point of structure formation is an *almost perfectly* uniform distribution of Hydrogen, Helium, and smidgens of Lithium and Beryllium, just after the time of recombination. The *nearly* perfectness of this distribution is the key to our existence, as the density fluctuations were seeds to objects we observe today as galaxies and galaxy clusters. These density fluctuations, which are thought to be the result of quantum fluctuation in the very early universe before the inflationary phase, can be observed as temperature fluctuations in the cosmic microwave background (e.g. by the COBE and WMAP satellites). Based on such measurements the currently best estimate for the age of the Universe is 13.7 ± 0.2 Gyr (Spergel et al. 2003).

1.1.1 Structure Formation

The principle questions of structure formation are *when and how did the objects we observe today form, and how do they evolve throughout the history of the universe.* By objects we mean astrophysical entities, such as gas, stars, and galaxies, on small scales, and galaxy clusters and super-clusters, on large scales, which can be directly observed with today's telescopes and detectors. Particularly interesting is the beginning and the rate of evolution on different scales, or in different words, the question on which scales structure formation is initiated and how it proceeds.

Do larger objects form first (the top-down scenario) or are they simply assembled by smaller sub-units (the bottom-up scenario), or is a combination of both at work? Observationally, the above questions can be addressed in two different ways: (1) in the deductive way: studying objects directly at the early, intermediate, and late stages of their evolution. (2) in the inductive way: using local, easy to observe, and well-understood tracers of an object's evolution, which survived since their formation the entire cosmic history until today. Both ways are problematic in practice. The direct observation of objects in their early stages of evolution is restricted by our ability to probe large solid angles *and* distances simultaneously which is necessary to obtain statistically significant samples. Our observation techniques are limited to either deep pencil-beam fields or relatively shallow large-field surveys. This combination makes stars in our local neighbourhood, at distances $\lesssim 5$ Mpc[1], and galaxies out to distances of several Gpc, the best studied astrophysical entities so far. Yet, their complexity proves to be overwhelming and needs to be explained in the context of the grand-design structure formation. Since the formation of galaxies can be directly observed only in very few local cases, we have to strike out in the direction of inductive insight. Under the assumption that star formation follows the same physics in the early universe as it does in our neighbourhood, we can study the stellar content of distant galaxies, which cannot be resolved into single stars, by comparing their integrated light to stellar populations with a well-defined star-formation history. Since the stellar content of galaxies represents a record of their evolution, such studies can teach us about the formation of galaxies and structure formation itself.

Before cosmic recombination structure formation was damped out by the smoothing radiation field. After recombination the growth of structure is decisively governed by the interplay of cosmic expansion and the gravitational pull of matter. A region of mass overdensity first follows the expansion and becomes gradually denser with respect to the surrounding material. Once the net gravity of the region dominates over the global expansion, the matter within the region decouples from the overall expansion and starts to collapse. Subsequently, the local overdensity grows as a function of time from the infall of adjacent overdensity regions. The power spectrum of these density perturbations changes only in amplitude, but not in shape, if the growth stays in the linear regime, i.e. $\Delta\rho/\langle\rho\rangle \ll 1$. That is, small density perturbations grow independently on all scales. This is true for large scales, but the growth on smaller scales responsible for later galaxies must enter the non-linear regime, as the today observed overdensities on smaller scales are order of magnitudes higher than on large scales. The details of this growth are determined by the origin of such perturbations, the nature and amount of dark matter, and the energy content of spacetime (known as dark energy), which altogether schedule the epoch of matter-radiation equality (see e.g. Peacock 1999, for details).

As structure formation crucially depends on the matter content of the universe one would like to know the cosmic matter density. Probably the strongest argument on the baryonic matter content of the universe comes from primordial nucleosynthesis, which sets the baryonic density somewhere in the ballpark of a few percent of the critical density (e.g. Copi et al. 1995) and is considerably smaller than the total matter content which manifests itself solely by gravity. The evidence for non-baryonic dark matter is given by observations of galaxy rotation curves. Rather than following the Keplerian fall-off, the rotation curves of galaxies remain flat at large galactocentric radii, implying a linearly divergent mass distribution which exceeds the luminous matter by orders of magnitude. Other direct methods, such as galaxy cluster masses from hot X-ray gas (e.g. White et al. 1993), cluster Sunyaev-Zeldovich effect (e.g. Rephaeli 1995), and gravitational lensing (e.g.

---

[1] 1 pc $= 3.086 \cdot 10^{16}$ m

Allen 1998) imply a total matter density of $\Omega_m \gtrsim 0.2$, in units of the critical density. With the assumption that $H_o > 50$ km s^{-1} Mpc^{-1} and a flat Universe, the matter density was recently derived from the cosmic microwave background anisotropies to be $\Omega_m = 0.27 \pm 0.04$, in units of the critical density (Spergel et al. 2003). Moreover, these cosmic microwave background temperature anisotropies and the redshift-distance relation of type-Ia supernovae (Perlmutter et al. 1999) suggest a dark-energy dominated Universe with a presently accelerated cosmic expansion. All in all, the present data suggest that the baryonic matter is outbalanced by dark matter by about an order of magnitude, and that dark energy accelerates the cosmic expansion.

1.1.2 Chemical Evolution

Widely independent of the exact texture of spacetime, stellar generations are born from the cooling of primordial gas which decouples from the ambient expansion and condenses into stars on small scales (see also Sect. 1.2.2). Throughout their lifetimes these stellar populations pollute their surroundings with stellar winds and supernova ejecta, which contain processed material of elements heavier than the primordial mix of H, He, Li, and Be. The rate of cosmic star formation determines how fast these processes are and is usually given as a function of redshift (or look-back time for a given cosmology, also known as the *Madau*-plot, Madau et al. 1996). The global star-formation rate, which is observed to rise as a function of redshift out to $z \approx 1$ (about 50% of the age of the universe) and remain constant out to redshift $z \approx 4$ (about 10% of the age of the universe), determines the pace of cosmic nucleosynthesis which is imprinted in today's stellar generations.

Since different elements are produced in stars of different mass with different lifetimes, the previously mentioned cosmic chemical evolution becomes in principle accessible through the study of chemical abundances in old stars. For instance, type II supernovae enrich the ambient medium predominantly with α-elements, with typical [α/Fe] ratios[2] $\sim +0.4$ dex (Timmes et al. 1995) already $\sim 10^7$ yr after formation of their massive progenitor stars. Type Ia supernovae, on the other hand, begin to eject mostly iron-peak elements ([α/Fe] ≈ -0.3, Thielemann et al. 1986) about 1 Gyr later (Woosley & Weaver 1995; Tsujimoto et al. 1995; Thomas et al. 1998). Stellar populations with [α/Fe] $\approx +0.4$, as they are observed in massive elliptical galaxies, are interpreted as the result of very short formation timescales[3].

Detailed knowledge of the evolution of single stars was acquired mainly from the stellar populations in the Local Group galaxies. The evolution of the integrated light of a single-age stellar population with a given chemical mix is well understood today. However, it is very unlikely that distant galaxies are represented by one such simple stellar population (SSP). Already the stellar populations in the Milky Way have a complex age and abundance pattern (Majewski 1993). More reasonable to expect in other galaxies are similarly complex stellar populations with a broad mix of ages and chemical compositions, so called composite stellar populations. The interpretation of the integrated light of a composite stellar population is much more complicated than of a SSP. Nevertheless, Nature is sometimes helpful and organises a small fraction of a galaxy's stellar population in globular star clusters which

---

[2] The standard notation of abundance ratios is $[X/Y] = \log(X/Y) - \log(X_\odot/Y_\odot)$, where X and Y are the masses of two individual elements or element groups, normalised to the solar mass abundances $X_\odot$ and $Y_\odot$. In particular, [α/Fe] is the abundance ratio of α-elements O, Mg, Si, S, Ca, Ti, to iron-peak elements, Cr, Mn, Fe, Co, Ni, Cu, Zn, normalised to the solar abundance.

[3]Other less likely options for increased [α/Fe] ratios are a top-heavy IMF and a reduced binary fraction. The latter is inconsistent with the observed frequency of LMXB sources in galaxies (Trinchieri & Fabbiano 1985). The former is less likely since old metal-poor halo stars in the Milky Way also show similarly high [α/Fe] ratios (e.g. Fulbright 2002), which cannot be accounted for by a flat IMF alone (Thomas et al. 1998).

are agglomerations of coeval stars with the same chemical composition. As there is good evidence that these globular clusters are formed together with the stellar populations which constitute the galaxy body, their study holds the potential of deriving more accurate star and galaxy formation histories than those derived from the galaxy's integrated light.

The goal of this thesis is a spectroscopic study of such extragalactic globular cluster systems. The availability of advanced multi-object spectrographs at 8-10m class telescopes allows, for the first time, a comprehensive spectroscopic study of extragalactic globular cluster systems outside the Local Group. The motivation of the thesis is a better understanding of the formation of globular clusters and their host galaxies. For this purpose, spectroscopic line indices are measured for Milky Way globular clusters with ages and chemical compositions known from other approaches, such as isochrone fitting in colour-magnitude diagrams or high-resolution spectroscopy of single globular cluster stars. These indices are subsequently used to calibrate index predictions of SSP models for a wide range of ages and chemical compositions. Following the inductive line of reasoning, the index measurements of the integrated light of individual extragalactic globular clusters are compared to these locally-calibrated stellar population models to infer ages and chemical compositions of the former. As globular clusters are the oldest structures in the Universe, they are good candidates for being the most primeval, first-forming structures which keep a fossil record of the earliest stages of galaxy formation (e.g. Searle & Zinn 1978). Their ages submit to clocking galaxy formation and their chemical compositions mirror the element mix in the gas clouds out of which the first structures formed. This information holds important clues to global star formation and chemical enrichment, and therefore, to structure formation itself.

This spectroscopic study is the first of its kind and is an independent complement to photometric analyses of globular cluster systems which themselves provide constraints on star formation histories of galaxies (e.g. Ashman & Zepf 1998). With these data in hand we hold the key to a deeper understanding of galaxy formation and evolution. The exact definition of line indices and the methods used to derive ages and chemical compositions of extragalactic globular clusters will be detailed below. In the beginning, however, it is appropriate to focus on the object of interest and summarise our current knowledge of globular clusters and globular cluster systems in the framework of galaxy and structure formation.

1.2   Globular Cluster Systems

Globular clusters are found in virtually every galaxy and their collectivity is termed the globular cluster system. Each single globular cluster is a dense conglomerate of $\sim 10^4 - 10^6$ stars with different masses, concentrated within $\sim 10^3$ pc^3. Globular clusters host in general old stellar populations with ages of at least a few times 10^9 years (Gyr). Perhaps their most outstanding cosmological relevance is their old age, which allows us to put lower limits on the age of the universe (e.g. Gratton et al. 1997). Globular clusters come close to what we define as a simple stellar population. Such a population is composed of stars with exactly the same age and chemical composition and follows a passive, so-called pure luminosity evolution, after an initial, compared to their ages relatively short star-formation burst in which the cluster was formed.

Figure 1.1 shows the roughly spherical distribution of globular clusters around the center of our Milky Way. The figure shows the positions of the ~ 150 known Galactic globular clusters (Harris 1996) marked as black dots on top of the COBE FIRAS 2.2 micron map of the Galaxy. The four enlargements show Digitized Sky

Survey images of four globular clusters, three of which (47 Tuc, NGC 6218, and NGC 6553) have roughly the same distance from the sun ($\sim 5 - 6$ kpc), while one globular cluster (NGC 6981) is located in the outer halo of the Milky Way at a distance of ~ 17 kpc. Basically all galaxies in the Local Group (with the exception of M32) host globular cluster systems, and the same can be expected for virtually all galaxies outside the Local Group.

Before we proceed with the description of some major properties of globular cluster systems, it is instructive to briefly review the historical evolution of the field of globular cluster research.
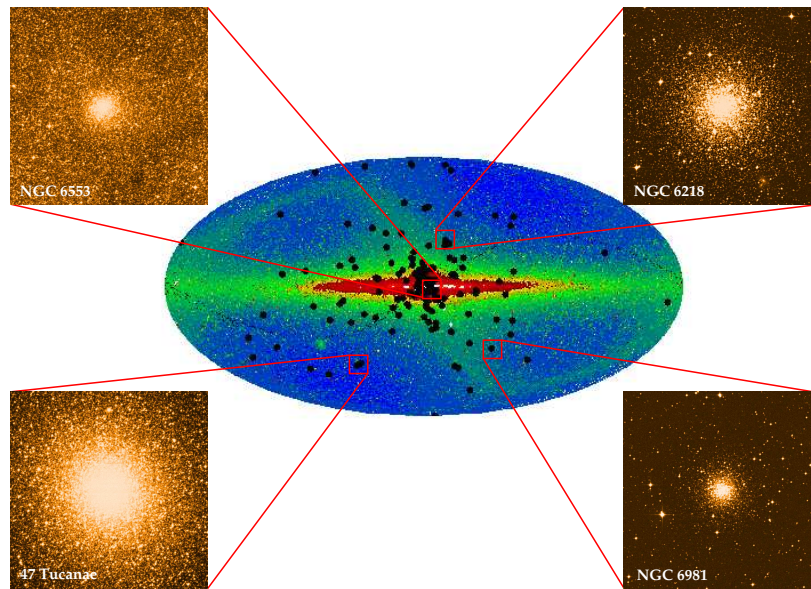
Figure 1.1: The figure illustrates the spherical distribution of globular clusters around the center of the Milky Way. Four individual globular clusters are illustrated as viewed from the Earth. Three globular clusters (47 Tuc, NGC 6218, and NGC 6553) are at similar distance from the sun ($\sim 5 - 6$ kpc), while NGC 6981 is located in the outer Milky Way halo at a distance of ~ 17 kpc from the sun. The zoom-in frames have a 15×15 arcminutes in diameter and were taken from the Digitized Sky Survey. The infrared image of the Galaxy was taken from the COBE FIRAS 2.2 micron map of the Galaxy overplotted with globular cluster data from Harris (1996).

1.2.1   A Historical Overview

The first to use the Galactic globular cluster system to study the structure and size of the known universe, according to which the sun was located at the center of a star cloud, was Karl Bohlin, in the first decade of the 20th century. Motivated by a statement of John Herschel in the 1830s, who remarked that globular star cluster are preferentially found in a relatively small fraction of the sky in the direction of Sagittarius, Bohlin found a rather spherical distribution of these objects and suggested that the sun must be displaced from the center of the Milky Way, if the globular cluster system is a major constituent of our Galaxy.

A quantitative analysis was first performed by Shapley (1918) who determined the distance of the sun to the Galactic center using the apparent brightness of variable stars insinde globular clusters, with known intrinsic luminosities, and the

apparent size and brightness of globular clusters themselves, assuming an average intrinsic size and luminosity. Shapley found that the sun must be offset from the center of the spherical distribution of globular clusters by about 15 kpc, a value which is just around a factor two larger than today's best estimates ($\sim$ 8 kpc, Binney & Merrifield 1998). This result not only shattered Kapteyn's picture, which saw a rather central location of the Solar System in the Galaxy, it also gave a size to the Milky Way one order of magnitude larger than the Kapteyn model. Today we know that the direction of the highest surface density of globular clusters marks the direction of the Galactic center, towards Sagittarius A.

Fourteen years later, Hubble (1932) discovered a spherical distribution of bright objects in the halo of the Andromeda galaxy (M31), with the right systemic radial velocities to be the extragalactic counterparts of local Milky Way globular clusters. Another two decades later, Baum (1955) identified a very rich globular cluster system in M87, the central giant elliptical galaxy in the Virgo galaxy cluster, and determined the distance to Virgo by photometrically comparing globular clusters in M87 and M31. This study initiated other analyses of globular cluster systems in the Fornax (Dawe & Dickens 1976), Hydra (Smith & Weedmann 1976), and the Virgo galaxy cluster (Racine 1968; Hanes 1977). The launch of charged-coupled devices as standard detectors in observational astrophysics set off an avalanche of detailed studies of extragalactic globular cluster systems. An important contribution was a deep study of the globular cluster system in M87 by van den Bergh et al. (1985) who confirmed a turn-over[4] in the globular cluster luminosity function, as it was previously observed for Galactic globular clusters, suggesting similar globular cluster formation *and* destruction mechanisms being at work in both galaxies. Our knowledge until the mid 90s is summarised in the reviews of Harris (1991), Harris (1993), and Richtler (1995).

The globular clusters in our Milky Way range among the oldest stellar structures in the universe and the same was long assumed for their extragalactic analogues. The hypothesis that relatively young globular clusters could form in galaxy-galaxy collisions (Schweizer 1987) revised the picture of ancient stellar systems and lead to a quantitative prediction of the properties of globular cluster systems which formed in galaxy mergers (Ashman & Zepf 1992). The confirmation of some of those predictions, such as bimodal globular cluster colour distributions (see also 1.2.3), by Zepf & Ashman (1993) marks a turning point in globular cluster research. In subsequent years, globular cluster formation was observed in many merging galaxies and merger remnants. Photometric and the still sparse spectroscopic observational evidence until the recent past is described in detail in Ashman & Zepf (1998) and suggests that globular clusters form ubiquitously during star-formation events which build up galaxies. Parallel to the observational efforts the theoretical path to globular cluster formation was followed and shall be sketched in the next section.

1.2.2   Star Cluster Formation

To use globular cluster systems as probes of galaxy formation one needs to understand the formation of globular clusters themselves. Globular clusters are thought to form in giant molecular clouds (Gunn 1980; Fall & Rees 1985; Murray & Lin 1992; Harris & Pudritz 1994; Larson 1996; Elmegreen & Efremov 1997; Cen 2001). When the Jeans mass limit is exceeded, the cloud becomes unstable and begins to collapse. The gas fragments and is subsequently turned into stars in the densest core regions of the cloud. During these condensation processes gas expulsion, driven by radiative feedback of young massive stars, as well as stellar winds and supernova explosions, terminates the star formation in the cloud. The mass loss reduces

---

[4]peak magnitude of the log-normal distribution of globular cluster luminosities

the binding energy of the forming star cluster and can destabilise the system. A forming star cluster which undergoes an instantaneous expulsion of the remaining gas, survives as a dynamically stable system only if more than 50% of the gas is transformed in stars, else the star cluster dissolves on dynamical timescales (Hills 1980). More detailed N-body simulations (e.g. Geyer & Burkert 2001) with gradual gas expulsion, that lasts significantly longer than the crossing time of the cloud, show that somewhat smaller star formation efficiencies are sufficient for a bound star cluster. According to this general picture, globular clusters can form anytime where enough gas can be cooled and/or be compressed. During their stable phase, giant molecular clouds are believed to be supported by supersonic turbulence (Harris & Pudritz 1994; Mac Low & Kleessen 2003) until an outside trigger initiates the collapse. Many trigger mechanisms were suggested in the past, of which cooling represents one way to create a thermal instability in giant molecular clouds (Fall & Rees 1985). However, to cool efficiently the presence of metals is required. Some globular clusters have metallicities which are too low to allow efficient cooling of the parent cloud, and therefore imply different ways to initiate the collapse of metal-poor primordial gas clouds. For instance, gravitational stress can increase the ambient gas pressure and induce the collapse by pressure instabilities (Elmegreen & Efremov 1997; Bekki et al. 2002). Another trigger mechanism can be convergent shocks caused by the external radiation field during the reionization epoch (Cen 2001). A comprehensive discussion of star cluster formation models and a comparison with observations can be found in Harris (2001). Regardless of the discordancy with respect to the trigger mechanism, star clusters are very likely to form in giant molecular clouds, and survive a Hubble time as dynamically stable globular clusters.

1.2.3 Properties of Globular Cluster Systems

Most of our knowledge about globular cluster systems was acquired from broadband photometry. The photometric detection of extragalactic globular clusters is based on the overdensity of objects with colours resembling old stellar populations. In elliptical galaxies a rich globular cluster system has surface densities of some hundreds of clusters per square arcminute close to the galaxy center. This surface density decreases with larger galactocentric radii down to a few objects at several effective radii[5]. Apparent magnitudes of a typical Galactic globular cluster at the distance of the Virgo galaxy cluster are $V \approx 24$ mag. For more distant and/or less rich globular cluster systems background contamination becomes a point of concern. In such cases, ground-based studies profit from multi-colour photometry in weeding out background galaxies. Space-based high-resolution imaging, on the other hand, resolves single globular clusters at the distance of Virgo and can cleanly separate globular clusters from background contaminants. The fewest globular clusters are confirmed by their spectroscopic redshift, since spectroscopic surveys are time consuming and require the use of 8-10m class telescopes to reach even the closest extragalactic globular cluster systems. Consequently, most of their properties presented in the following are based on photometric analyses.

Spatial Distributions

The most we know about spatial distributions of globular clusters around galaxies was derived from rich globular cluster systems in giant elliptical galaxies and the Local Group galaxies. Such studies are limited by the field of view and the very central parts of the globular cluster system which are hidden in the noise of the

---

[5]In a circular aperture one effective radius contains one-half of the total light emitted from an object.

high surface brightness of the host galaxy. In general, radial globular cluster surface density profiles can be parameterized by power laws of the form $\Sigma_{\mathrm{GCS}} \propto r^{-\alpha}$, where the exponent varies between $\alpha \approx 1.0$ and 2.5 (Ashman & Zepf 1998). The exponent is correlated with the luminosity of the host galaxy in the sense that more extended globular cluster surface density profiles are found in brighter galaxies. Very few such studies exist for globular cluster systems in spiral galaxies, but the available ones fit into this relation. The radial profiles of globular cluster systems appear on average more extended than the galaxy light, with no obvious reason for this offset.

Azimuthal distributions are even more difficult to access than radial profiles. However, for a handful of early-type galaxies the position angle of the surface density profile for globular clusters and the galaxy halo light is similar within $\sim 10 - 20^{\mathrm{o}}$ (Kissler-Patig 1997; Ashman & Zepf 1998).

Luminosity Function

The distribution of globular cluster magnitudes (i.e. logarithmic luminosities) is called the globular cluster luminosity function, often abbreviated as the GCLF. The GCLFs of the Milky Way and M31 can be well approximated by a Gaussian (Hanes 1977) with a mean magnitude $M_V = -7.4 \pm 0.2$ and a dispersion $\sigma = 1.2$ mag (Harris 1991; Ashman & Zepf 1998). Usually we have no access to the entire luminosity function for globular cluster systems outside the Local Group, but are limited by photometric completeness typically reaching the turn-over magnitude of the GCLF. From deep Hubble Space Telescope (HST) imaging of globular cluster systems in elliptical galaxies a Gaussian function was comfirmed to be a good representative for all studied systems with a dispersion of $\sigma \approx 1.4$ for elliptical compared to 1.2 for spiral galaxies (Harris 1991, 2001). Moreover, the study of many globular cluster systems in galaxy clusters revealed that the variation of the absolute turn-over magnitude appears to be less than ~ 0.2 magnitudes (Secker & Harris 1993; Ajhar et al. 1994; Blakeslee 1996; Kohle et al. 1996), including Local Group globular cluster systems, which makes the GCLF turn-over magnitude a good standard candle to obtain distances to better than $\sim 20\%$ accuracy (Jacoby et al. 1992).

At first glance, the nearly constant turn-over magnitude is a surprising result, as individual globular cluster are subject to dynamical effects which accelerate their dissolution and/or destruction. For instance, every cluster is subject to evaporation due to the loss of high-velocity stars which is a result of equipartition of kinetic energy due to two-body relaxation. The efficiency of this process is maximized for compact low-mass globular clusters. Another destruction mechanism is dynamical friction which causes globular clusters to spiral into the center of their galaxy where strong tidal fields lead to their disruption. Furthermore, globular clusters in spiral galaxies on strongly inclined orbits which penetrate the disk are subject to disk-shocking. The result of such gravitational shocks is a transfer of kinetic energy to the stars within the cluster and results in increased stellar velocities and consequently an enhanced loss of stars. Numerical simulations have recently shown that the cluster destruction processes shape the GCLF significantly only within the first few Gyr (Fall & Zhang 2001). Starting with a power-law globular cluster mass function, comparable to the mass function of giant molecular clouds, the Gaussian magnitude distribution of old globular cluster systems is reproduced by removing clusters with smallest masses (typically $\lesssim 10^4 M_\odot$). The exact location of the peak depends on the efficiency of cluster destruction and the age of the system. Hence, the variations in the GCLF turn-over magnitude can be at least partly attributed to variations in cluster destruction processes.

Assuming a Gaussian GCLF with the above dispersion for all old globular cluster systems, the total number of globular clusters can be computed by sampling the GCLF down to its turn-over magnitude and integrating over the entire lumi-

nosity function and the surface density profile. The number of globular clusters found in this way correlates with galaxy luminosity and varies from a few in dwarf galaxies to a few ten thousand in giant elliptical galaxies (Kissler-Patig et al. 1997; Ashman & Zepf 1998). To understand the formation efficiency of globular clusters as a function of galaxy luminosity (or mass) their total number is usually normalised to the total luminosity of the galaxy V-band magnitude in units of $M_V = -15$, and is defined as the specific frequency, $S_N = N_{\rm GC}10^{\,0.4(M_V+15)}$ (Harris & van den Bergh 1981). Straightforward application of this measure shows that elliptical galaxies have more globular clusters per luminosity than spiral galaxies. However, since the stellar populations in elliptical and spiral galaxies are not the same (different mass-to-light ratios) it is fairer to normalise the number of globular clusters to the total stellar mass, as it was done by Zepf & Ashman (1993) who introduced the parameter $T = N_{\rm GC}/(M_{\rm gal}/10^9 M_\odot)$. Unfortunately, the access to the total mass requires the knowledge of the dynamical mass or the mass-to-light ratio of a galaxy, which are generally difficult to obtain. Using mean mass-to-light ratios for spiral and elliptical galaxies, Zepf & Ashman (1993) have shown that elliptical galaxies have T values on average a factor 2–3 higher than spiral galaxies. Moreover, there is a general trend for elliptical galaxies between T and galaxy luminosity, indicating higher-luminosity galaxies having higher globular cluster formation efficiencies.

Colour Distribution

Photometric studies are usually performed in more than one filter, so that globular cluster colours become accessible. Having constructed a globular cluster colour distribution, one can analyse the mean, the dispersion, as well as its shape. Probably the most important feature of globular cluster colour distributions is their multimodality. According to the dependence of photometric colours on metallicity and age, the presence of two or more modes in the colour distribution points to several sub-populations of globular clusters which formed in multiple distinct episodes and/or mechanisms. Mean colours and colour dispersions of globular clusters in elliptical galaxies have in general higher values than globular cluster colour distributions in M31 and the Milky Way (e.g. Couture et al. 1991). This result holds at all galactocentric radii. Sophisticated statistical analyses reveal that the shapes of at least half of the colour distributions in elliptical galaxies are at least bi-modal (Gebhardt & Kissler-Patig 1999; Larsen et al. 2001; Kundu & Whitmore 2001a,b). The comparison with globular cluster systems in spiral galaxies is difficult owing to the smaller number of globular clusters in these systems and the differential dust absorption, which complicates the reddening corrections of individual objects within or behind the dusty disks. Thus, our knowledge of globular cluster colour distributions in late-type galaxies, in particular outside the Local Group, is sparse. Yet, we know that the colour distributions in both M31 and the Milky Way are bi-modal and that the few globular cluster systems in spirals outside the Local Group which are observed edge-on are in line with this result.

The interpretation of such colour distributions is difficult since broad-band colours are sensitive to both age and metallicity. This effect is known as the age-metallicity degeneracy (e.g. Worthey 1994); as a rule of thumb, doubling the age or tripling the metallicity will have the same effect on optical colours of a globular cluster's integrated light. Composite optical and near-infrared colours have an increased sensitivity to metallicity relative to purely optical colours. Combining optical/near-infrared colours with optical colours can partly break this age-metallicity degeneracy (Kissler-Patig et al. 2002; Puzia et al. 2002b; Hempel et al. 2003). From such studies we know that the dispersion in colour is mainly driven by metallicity and that the difference in mean colour between globular cluster systems in spiral and elliptical galaxies is also mainly due to a higher mean metallicity of

globular clusters in elliptical galaxies. The metallicity of globular clusters in the Milky Way and other Local Group galaxies can be studied with other techniques (e.g. high-resolution spectroscopy, colour-magnitude diagrams, etc.) and it is found that globular cluster colour distributions are almost entirely driven by metallicity. Age effects cannot be completely neglected in globular cluster systems outside the Local Group, but there are arguments that metallicity effects remain the dominating source of colour differences. For instance, we know that most Galactic globular cluters are older than 10 Gyr with a mean age of 13 Gyr and a dispersion of a 2-3 Gyr (e.g. Krauss & Chaboyer 2003), which makes Galactic globular clusters rank among the oldest stellar structures in the Universe. The change in photometric colours at such old ages is negligible compared to the colour dispersion of globular cluster systems and typical mesurement errors. Therefore it is unlikely that redder mean colours of extragalactic globular clusters are produced by older ages, since this would require older ages, inconsistent with the age of the universe.

The spectroscopic study of globular cluster systems presented in this thesis is the first large attempt to access globular cluster ages and metallicities using the alternative (and more reliable) approach of spectroscopic diagnostics.

Kinematics

Only in the recent years efficient wide-field multi-object spectrographs became available at 8-10m class telescopes, pushing the limits of kinematical studies of globular cluster systems outside the Local Group. One motivation of such studies are radial velocities of many globular clusters which can be used as tracer particles of the galaxy potential. Their more extended distribution relative to the galaxy light makes them particularly interesting as they probe the outer regions of a galaxy's halo. In this way, many giant elliptical galaxies were shown to be inconsistent with constant mass-to-light ratio (M/L) profiles and were required to have extended dark matter halos with M/L ratios increasing with galactocentric radius (e.g. Kissler-Patig et al. 1998a; Kissler-Patig & Gebhardt 1998; Kissler-Patig et al. 1999; Richtler et al. 2002).

Some interesting insights on galaxy formation come from a net rotation discovered in the globular cluster system in the Virgo giant ellipticals M87 (e.g. Cohen 2000; Côté et al. 2001) and NGC 4472 (e.g. Zepf et al. 2000; Côté et al. 2003) beyond $\sim 3r_{\rm eff}$. Such a rotation is consistent with a signature imprinted in a single major merger event which shaped the dynamics of the outer halo. In the central giant elliptical NGC 1399 in the Fornax cluster, only marginal evidence is found for rotation at large radii, but a significantly increased velocity dispersion is measured at large radii, suggesting that the outer globular cluster population traces the entire galaxy cluster potential (Kissler-Patig et al. 1999).

Splitting the globular cluster system by photometric colour into red (metal-rich) and blue (metal-poor) sub-components shows no significant differences in their kinematics for elliptical galaxies. In the Milky Way and other spiral galaxies, on the other hand, the red globular cluster sub-population shows significant rotation similar to the disk and suggests that this globular cluster sub-population is kinematically connected to the disk/bulge component, while the blue sub-population appears to share the kinematics of the halo (Zinn 1985). On average, the red (metal-rich) globular cluster sub-population in spiral galaxies has the tendency to have a smaller velocity dispersion and be supported by rotation as the stellar disk. The blue (metal-poor) sub-component, on the other hand, does not show a significant rotation and is kinematically hotter and shares the kinematics of the halo stellar population. All these kinematic signatures suggest that the globular cluster sub-populations in the Milky Way share kinematic properties of major Galactic sub-components. This fuels the speculation that globular cluster sub-populations

form together with major stellar population sub-components of the galaxy itself.

1.2.4 Globular Clusters as Fossil Records

Although a globular cluster system constitutes a negligible mass fraction of a galaxy ($\sim 0.25\%$, Blakeslee et al. 1997; McLaughlin 1999), the formation of globular clusters is tightly linked to the star-formation history of galaxies. Several arguments support the hypothesis that globular clusters trace star-formation events in galaxies. (1) The formation of massive star clusters, which are going to survive the next Hubble time as globular clusters, is observed in nearby gas-rich merging galaxies (e.g. Whitmore & Schweizer 1995; Schweizer 1997) and starburst galaxies (e.g. Johnson et al. 1999; Homeier et al. 2002). (2) Studies of globular cluster systems in galaxies which show signatures of previous dynamical interaction reveal a star cluster population with ages consistent with the dynamical age of the merger remnant (e.g. Schweizer & Seitzer 1998; Goudfrooij et al. 2001a,b). (3) Young massive star clusters are observed in the disks of spiral galaxies with modest star-formation rates. Their number is correlated with the star formation rate per unit area in these systems (Larsen & Richtler 2000). (4) Normalising the number of globular clusters to the total baryonic mass of the host reveals a surprisingly constant value ($\sim 0.25\%$, McLaughlin 1999), independent of galaxy morphology. (5) There is a relationship between the mean metallicity of globular cluster systems and the host galaxy luminosity, which is independent of galaxy morphology (Brodie & Huchra 1991; Durrell et al. 1996; Forbes et al. 1996). (6) The number of globular clusters is tightly correlated with the total luminosity of galaxies brighter than $\sim M_V \lesssim -18$, in the sense $N_{\mathrm{GC}} \propto L^{\alpha}$, where $1 < \alpha < 2$ (Ashman & Zepf 1998).

This is good evidence that the global star formation in galaxies leaves local imprints in its globular cluster system and that both stellar systems experience similar enrichment histories. Hence, globular cluster systems can be used as probes of galaxy formation.

1.3 Galaxy Formation Scenarios

Ever since Hubble (1926) introduced his epoch-making classification of galaxies (the Hubble Sequence or the so-called tuning-fork diagram), considerable effort was undertaken to understand the nature of this sequence. However, a complete consensus of theoretical insight and empirical evidence on the mechanisms and timescales that lead to the observed variety of galaxy morphologies is still not reached. The wealth of observations over the past four decades has led to two galaxy formation scenarios, i.e. the *monolithic collapse* and the *hierarchical merging*. We are currently in a very confusing state where observations seem to support parts of the qualitative predictions of both scenarios. The situation is far from being clear, as a good quantification of the importance of both these scenarios for the formation of early-type galaxies as a function of redshift, environment, and galaxy morphology is still pending. The main reason for this leeway is that star-formation histories of early-type galaxies cannot be resolved in great detail. The integrated light of galaxies resembles a palimpsest, and we lack the means to read the imprints of *each* major star-formation event in the past. However, this problem can be resolved by the study of extragalactic globular cluster systems. Knowing the formation histories of globular cluster systems can provide an important piece of evidence to the question of whether merging is the dominant mode of early-type galaxy formation or just a perturbation effect on early formed structures.

The two antipodal paradigms of galaxy formation are lively discussed in the literature since several years, and shall be presented in the following.

Monolithic Collapse

In the classical (because historically first) *monolithic-collapse* scenario, galaxies form from individual super-giant gas clumps (Eggen et al. 1962; Larson 1974). The angular momentum of the gas cloud and the timescale of transforming the gas into stars determines the morphology of the forming galaxy. If the gas is turned into stars on timescales longer than the dynamical timescale of the cloud, with high angular momentum, the formation of a disk galaxy is likely. Dissipational processes lead to a settling of the gas in a disk where star formation continues and uses up the remaining enriched gas to form subsequent stellar populations. If the galaxy forms with low angular momentum on timescales considerably shorter than the the dynamical timescale of the parent gas cloud, then the collapse preferentially leads to the formation of a spheroidal galaxy through violent relaxation processes (Lynden-Bell 1967).

In this scenario, the majority of stars in early-type galaxies is expected to form early, at redshifts $z \gtrsim 2$ (e.g. Tinsley 1972; Larson 1975; Silk 1977; Arimoto & Yoshii 1987, etc.), with the most massive structures forming first (top-down scenario). The small dispersion in empirical scaling laws, such as the colour-magnitude relation, the fundamental plane, and the Mg–σ relation seems to support such an early formation in a rapid collapse with subsequent passive evolution (e.g. Faber 1973; Bower et al. 1992; Bender et al. 1992, 1993; Bender 1996; Bender et al. 1996; Treu et al. 1999; Peebles 2003). However, the predictions of the early monolithic collapse scenario on number counts of extremely red galaxies at moderate redshift are clearly too high compared with observations (Zepf 1997). Other evidence can only be reconciled with a slightly modified picture of the monolithic collapse scenario. For instance, the collapse of a single cloud predicts too steep metallicity gradients for early-type galaxies. Allowing an amalgamation of gas sub-clumps and/or a fragmentation of the single super-giant gas cloud (e.g. Larson 1976) leads to shallower gradients which are in better agreement with observations (Davies et al. 1993). The extension of the simplistic monolithic collapse model to a merging of gas clouds leads us naturally to the idea that galaxies can be formed via hierarchical merging of gaseous and/or stellar sub-components.

Hierarchical Merging

The *hierarchical-merging* picture sees early-type galaxies as the result of multiple merging and accretion events of smaller units over an extended period of time, until the very recent past. Gas of the merging sub-units is funneled to the central parts of the merger where it is turned into stars. This process comes to pass many times throughout the lifetime of a galaxy. In this way a significant fraction of stars is formed below a redshift of unity and implies that more massive galaxies have more extended star-formation histories (bottom-up scenario).

The ideas of hierarchical merging are implemented in numerical simulations of gravitational clustering of cold dark matter halos (e.g. White & Frenk 1991; Kauffmann et al. 1993; Baugh et al. 1998; Cole et al. 2000; Somerville et al. 2001, etc.). In these semi-analytic models, the initial distribution of the baryonic matter is similar to the distribution of the dark matter. In contrast to the dark matter, the baryonic matter cools and accumulates at the center of each dark matter halo, where it is turned into stars. These cooling processes are assumed to be truncated when two dark matter halos of similar mass merge (major merger event, $m_1/m_2 \gtrsim 0.1$). The cold gas is transformed into stars in an instantaneous burst, while the remaining baryonic gas is shock-heated to the virial temperature of the new dark matter halo. This hot gas cools and settles in the new dark matter halo until it condenses to stars or another merger occurs. Amalgamation of dark matter halos with a high

mass contrast $(m_1/m_2 \lesssim 0.1)$ can be considered as accretion events rather than mergers. After the merger of these dark matter halos, the infalling small galaxy is stripped of its gas and its star-formation runs dry on timescales which depend on the satellite's reservoir of cold gas. The stripped gas is added to the shock-heated hot halo. The massive central galaxy finally devours the satellite on dynamical friction timescales that can be of the order of a Hubble time depending on the mass of the satellite (Binney & Tremaine 1987; Cole et al. 1994).

In general, the morphology of a galaxy is determined by the number of major merger events of its dark matter halo. A halo which experienced one or more major mergers is likely to host a spheroidal galaxy at its center. Disk-dominated galaxies form in relatively undisturbed dark matter halos where the hot gas has enough time to cool and condense in the disk. The most massive dark matter halos are predicted to host giant elliptical galaxies at their center (Barnes 1988).

There is good observational evidence of ongoing mergers and accretion events (e.g. Arp & Madore 1987; Schweizer 1990; Whitmore & Schweizer 1995; Ibata et al. 1995) supporting the hierarchical merging scenario. The light profiles of the relaxed core regions of some of these merger remnants are consistent with early-type galaxies (Schweizer 1982; Wright et al. 1990). Moreover, we observe disturbed kinematical signatures in at least 50% of early-type galaxies and the existence of kinematically decoupled cores (Franx & Illingworth 1988; Jedrzejewski & Schechter 1988; Bender 1988, 1996; Balcells & González 1999). Such observations are consistent with merger events which perturb the internal kinematics of early-type galaxies. Irrespective of many successful predictions of the semi-analytic models (e.g. Cole et al. 1994; Kauffmann & Charlot 1998), there still remain problems, some of which are the too high predicted angular momentum of spiral galaxies (Cole et al. 2000) and the too low predicted $[\alpha/\text{Fe}]$ of massive early-type galaxies (Thomas & Kauffmann 1999).

1.4   Stellar Population Synthesis

1.4.1   Basics

The purpose of each stellar population model is the understanding of the formation and evolution of galaxies. As we will use such models to derive globular cluster ages, metallicities, and abundance ratios, some words are indicated to describe their basic architecture. Ideally, one would like to know the properties (such as the presence of certain stellar types, stellar ages, chemical composition, spatial distribution, and stellar kinematics) of *each* stellar population which contributes to the integrated light of a stellar system. As we have seen above, a galaxy can be assembled in many different ways opening a wide parameter space of ages and chemical compositions for the contributing stellar populations. Clearly, the integrated light of a galaxy will be the sum of i stellar populations which formed throughout its lifetime. These stellar populations can be fractionised into j units of simple stellar populations (Renzini & Buzzoni 1986). While stellar populations are associated with a specific star formation mechanism and/or epoch, a simple stellar population defines a sample of star with the same age *and* chemical composition. Hence, in a simplified form we can write for the integrated flux F as a function of total mass M, chemical abundances X_n and time

$$F(M, X_n, t)_{\text{Galaxy}} = \sum_i k_i F(M, X_n, t)_{\text{Population,i}} \qquad (1.1)$$

$$F(M, X_n, t)_{\text{Population}} = \sum_j l_j F(\text{IMF}, X_n, t)_{\text{SSP,j}} \qquad (1.2)$$

where k_i and l_j are the mass fractions of the respective sub-units. For galaxies outside the Local Group this task proves to be futile as even $F_{\text{Population,i}}$ is not accessible, because we cannot resolve the systems into single stars. The only way out is to use tracer stellar populations (globular clusters) and reconstruct a rudimentary star formation history with *principle component* simple stellar populations. In this way the integrated flux can be broken down in

$$F(M, X_n, t)_{\text{Galaxy}} = \sum_x m_x F(\text{IMF}, X_n, t)_{\text{SSP,x}}. \tag{1.3}$$

The interpretation of the integrated light is based on the understanding of the systematics of stellar populations in the local neighbourhood, that is in the Milky Way. By means of spectral diagnostics, observed integrated spectra of distant stellar systems can be compared with synthesized spectra for simple stellar populations of known age and chemical composition or with reference spectra of well-studied objects.

In general, such observed spectra can be analysed in three different ways: (1) A library of stellar template spectra for a wide range of surface gravities $\log g$, effective temperatures T_{eff}, and chemical composition, is initially observed. This library is then used in combination with theoretical isochrones to obtain the best-fitting integrated spectrum (*population synthesis technique*). However, the lack of enough stellar spectra with high resolution to cover a wide range in age and chemical composition, and the lack of local stars with extremely high abundances, which are found in extragalactic systems, hampers this approach. (2) Theoretical isochrones are the starting point of the *evolutionary synthesis technique*. Assuming an initial mass function (typically a Salpeter-type power law, Salpeter 1955), and an empirical library of stellar fluxes to convert from $\log g$, T_{eff}, and chemical composition to observational parameters (e.g. Lejeune et al. 1997, 1998; Westera et al. 2002), one can compute the integrated spectrum of a stellar population of a given age and metal content. For predictions of line indices so-called fitting functions can be calculated using an empirical stellar library. These functions define the behaviour of an index I as a function of T_{eff}, $\log g$, and [Fe/H] (Gorgas et al. 1993; Worthey 1994; Worthey & Ottaviani 1997). Another ingredient is the set of response functions which give the fractional change of an index I as the result of an abundance change of a given element under the constraint of constant total metallicity. The only work published so far focused on the α-elements O, N, Mg, Ca, Na, Si, Ti and iron-peak elements Cr and Fe (Tripicco & Bell 1995). These empirical functions are used to predict line strengths for stellar populations which then need to be calibrated on local stellar populations, e.g. Galactic globular clusters, with well-known parameters (e.g. Thomas et al. 2003a). The advantage of this lengthy computation is the ability to extrapolate predictions for SSPs with chemical abundance patterns which are not found in the local neighbourhood. (3) Another widely used method is the comparison of observed spectra with the integrated spectra of well-studied reference objects. This can lead to a deeper understanding of the stellar populations in the observed object by examination of differences between reference and object spectrum (*differential approach*) if the differences in abundance pattern are under control. In a more liberal form (without a reference object), this technique can be used to study differences between similar objects with various properties, such as environmental density, morphology, mass, etc. (e.g. Bower et al. 1990; de Carvalho & Djorgovski 1992; Kuntschner et al. 2002a).

1.4.2 Diagnostics

There are two complementary observational techniques to study integrated spectra. (1) Low-resolution spectroscopy ($R \lesssim 1000$) aims at covering a long wavelength

baseline, ideally from the mid-UV ($\sim$ 2500 Å) to the near-IR ($\sim$ 2.6 μm). The goal is to completely sample the spectral energy distribution (SED) of a stellar system, including the contributions of all types of stars, from the hottest turn-off stars (i.e. hot blue horizontal branch stars) to the coolest stars at the tip of the post-asymptotic giant branch. A major problem of this approach is the uniqueness of the spectrum. It is well known that the integrated spectra are highly degenerate in age and metallicity (e.g. Faber 1972; O'Connell 1976; Worthey 1994). (2) Rather than aiming for the full wavelength coverage, higher-resolution spectra ($R \gtrsim 1000$) can provide more detailed information on individual spectral features. Some absorption features with their different dependencies on stellar atmosphere parameters ($\log g$, T_{eff}, and chemical composition) can better constrain the contribution of specific stellar evolutionary phases to the integrated light. With this information, one then can attempt to solve the non-uniqueness problem of integrated low-resolution spectra. However, this latter approach works only for stellar systems with low velocity dispersion, such as globular clusters, where single spectral features can be resolved.

Throughout this thesis, we follow the path of low-resolution spectroscopy using line indices as diagnostics for age and basic chemical composition. A major difference between the two canonical galaxy-formation scenarios described above are the different predicted star-formation histories of early-type galaxies which stand in marked contrast to each other and allow a differentiation between the models. While in the hierarchical merging picture galaxies are thought to experience longer assembly timescales, the monolithic collapse scenario predicts early and short periods of star formation. We will use two different techniques, direct and chemical clocking, to constrain the ages and formation timescales of extragalactic globular clusters and infer the formation histories of their host galaxies. Both techniques are presented below.

Direct Clocking

As a stellar population grows older, the main sequence temperature decreases, and, to the first order, the integrated light is consistent with a cooler stellar population. There are also higher-order effects which can influence this general trend, such as the horizontal branch morphology, which becomes significant at old ages and low metallicities. Such biases will be discussed in detail in the course of this thesis. In general, observables which trace the mean photospheric temperature can be used as diagnostics to determine the age of a stellar population. The Balmer line series is such a spectroscopic tracer. The strength of the Balmer line series shows a maximum at $T \approx 10^4$ K and decreases towards higher and lower temperatures. Strongest Balmer lines are found in A-type stars with typical main sequence lifetimes of $\sim$ 1 Gyr (Binney & Merrifield 1998). For older stellar populations weaker Balmer lines indicate higher ages. The strength of specific Balmer lines which fall in the optical spectral range of our data will be used to determine the ages of individual extragalactic globular clusters.

Chemical Clocking

Abundance ratios in stellar populations primarily depend on the specific stellar evolutionary phases which contributed to the chemical enrichment of the parent molecular cloud. Stars of different mass contribute with their specific mix of elements in their ejecta to the chemistry of the cloud on different timescales. These abundance patterns are imprinted in the stellar progeny of the cloud. Hence, abundance ratios can be used as clocks for star-formation timescales. The most prominent example is the ratio between α-elements (i.e. O, Mg, Si, S, Ca, Ti) and iron-peak elements (i.e. Cr, Mn, Fe, Co, Ni, Cu, Zn).
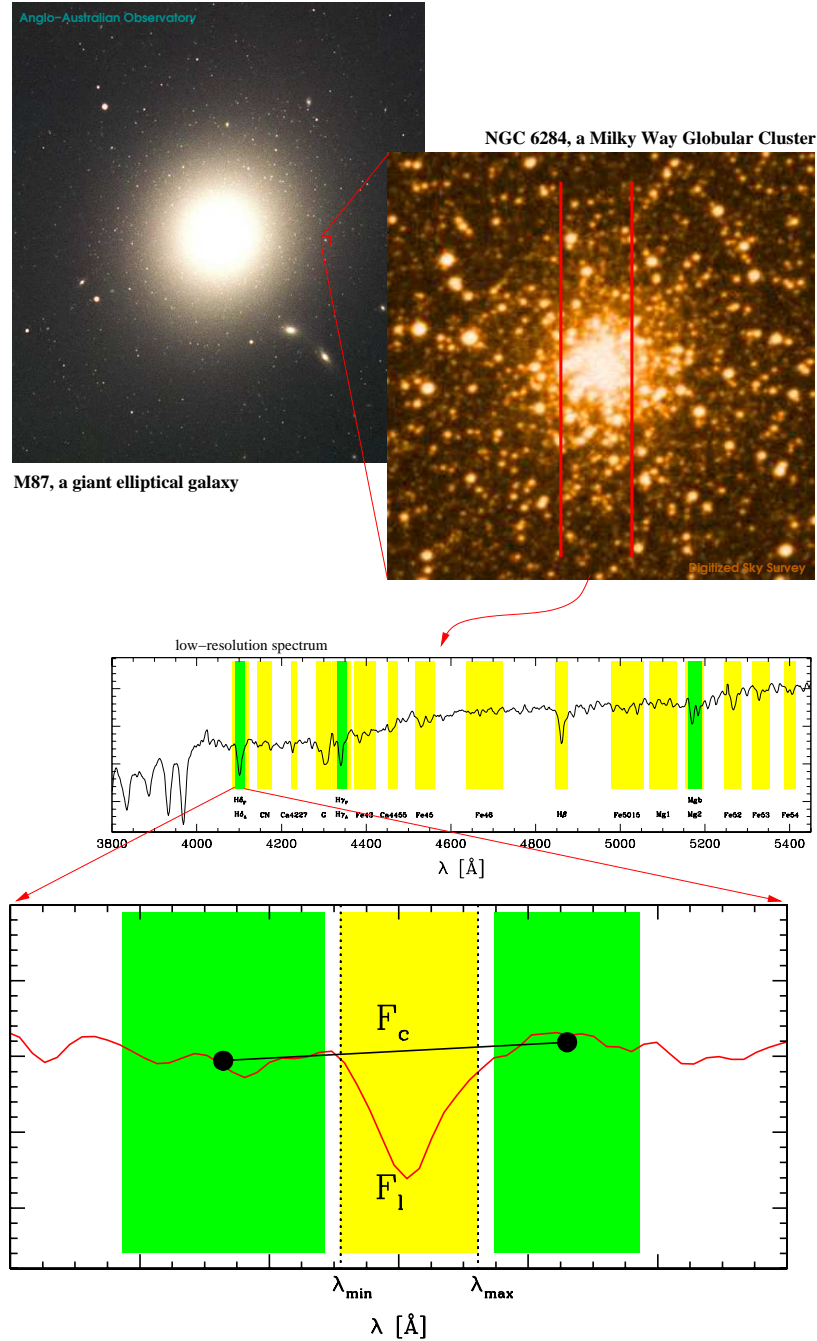
Figure 1.2: The figure illustrates the way to obtain a line-index measurement of the integrated light of an extragalactic globular cluster. Representatively, we show the rich globular cluster system in the giant elliptical galaxy M87, and in the enlargement the Galactic globular cluster, NGC 6284, with the spectrograph slit projected ontop. A low resolution spectrum is obtained from the integrated light falling through the slit. At the very bottom of the plot, the graphical definition of a line index is shown. The feature passband with boundaries λ_{min} and λ_{max} is flanked by two neighbouring continuum passbands. The mean flux in both continuum passband is used to linearly interpolate a *pseudo*-continuum throughout the feature passband. The ratio between the observed flux F_{l} and the flux of the *pseudo*-continuum F_{c} per unit wavelength is used to calculate the line index.

1.5 The Lick Index System

The Lick standard system was initially introduced by Burstein et al. (1984) in order to homogenise the study of low-resolution integrated spectra of extragalactic stellar systems. The Lick index system, based on observations carried out with the image dissector scanner (IDS) at the Lick Observatory, has been continuously updated and refined by several authors (González 1993; Worthey et al. 1994; Worthey & Ottaviani 1997; Trager et al. 1998) and currently defines 25 line indices for specific atomic and molecular absorption features in the optical wavelength range from ~ 4100 Å to ~ 6100 Å. The precise definition of line index passbands allows a uniform measurement and interpretation of spectroscopic data, in particular, of indices sensitive to age and chemical abundances (see also App. A). We will use the Lick index system to derive ages, metallicities, and abundance ratios of individual extragalactic globular clusters in early-type galaxies. This approach is sketched in Figure 1.2.

A general problem in defining the strength of a spectroscopic absorption feature is the accurate determination of the continuum. This is particularly problematic for integrated spectra of galaxies, which show typical velocity dispersions $\sim 200 - 300$ km s^{-1} and smear all spectroscopic features over a range of ~ 5 Å in the optical, making it impossible to define the *true* continuum. The Lick system bypasses the problem by defining a *pseudo*-continuum around strong absorption features. To determine the continuum level inside the feature passband (see Figure 1.2), a linear interpolation of mean fluxes in the two satellite passbands is performed which defines the *pseudo*-continuum $F_{\rm c}$. The flux ratio in the feature passband between the absorption line $F_{\rm l}$ and $F_{\rm c}$ is then used to define the line index

$$I_{\rm a} = \int\limits_{\lambda_{\min}}^{\lambda_{\max}} \left(1 - \frac{F_{\rm l}(\lambda)}{F_{\rm c}(\lambda)} \right) d\lambda \qquad (1.4)$$

in units of Å, where $\lambda_{\min}$ and $\lambda_{\max}$ define the blue and red boundaries of the feature passband, respectively (see Figure 1.2). Note that if $F_{\rm c}$ would be the *true* continuum, $I_{\rm a}$ would closely resemble an equivalent width. The subscript "a" indicates that the definition in equation 1.4 is used for narrow atomic absorption features which are calculated in Ångstrøm. For molecular absorption features[6] the line index is defined as

$$I_{\rm m} = -2.5 \log \left[\frac{1}{\Delta_\lambda} \cdot \int\limits_{\lambda_{\min}}^{\lambda_{\max}} \frac{F_{\rm l}(\lambda)}{F_{\rm c}(\lambda)} d\lambda \right] \qquad (1.5)$$

in units of magnitudes, where $\Delta_\lambda = \lambda_{\max} - \lambda_{\min}$. The transformation between the Ångstrøm and magnitude scale can be performed with the following equations

$$I_{\rm a} = \Delta_\lambda \left(1 - 10^{-0.4 \, I_{\rm m}} \right) \qquad (1.6)$$

$$I_{\rm m} = -2.5 \log \left(1 - \frac{I_{\rm a}}{\Delta_\lambda} \right) \qquad (1.7)$$

1.6 Outline of the Thesis

The thesis is organised in seven chapters, and is divided in two major parts which are closely related. The purpose of the first part (Chapters 2 & 3) is the calibration of SSP model predictions for spectroscopic line indices with well-understood stellar

---

[6]One exception is the G4300 index which is measured in Å, although the strength of the dominant G-band within the feature passband is driven by CH absorption bands.

populations in Galactic globular clusters. These models are later used (Chapter 4–6) to analyse extragalactic globular cluster systems, for which we derive ages, metallicities, and abundance ratios.

A general overview of the field of globular cluster research and a motivation of this work is given in Chapter 1.

In Chapter 2, we present spectroscopic observations for a sample of metal-rich Galactic globular clusters and the Galactic bulge. These observations are used to measure Lick line indices for these two stellar systems. Index measurements of globular clusters and the bulge are compared and empirical index-metallicity relations are calibrated with the new data. The content of this Chapter is published in Puzia et al. (2002b).

The obtained data of Galactic globular clusters are then used in Chapter 3 to calibrate simple stellar population models out to solar metallicities, for the first time. With these models, we compare index ratios of Galactic globular clusters with those of the Galactic bulge and the diffuse light of elliptical galaxies, in order to test the hypothesis of similar abundance ratios in all three stellar populations. The content of this Chapter is published in Maraston et al. (2003).

In Chapter 4, we describe the photometric selection of candidate globular clusters, as well as the sample of spectroscopically confirmed extragalactic globular clusters and the success rates of our candidate selection. The photometric data is used to derive colour distributions of the studied globular cluster systems and the corresponding surface density profiles. As a byproduct dynamical masses of the host galaxies are measured. A compilation of previously published Lick indices for globular clusters in elliptical, lenticular, and late-type galaxies, other than studied here, is also provided. The content of this Chapter is currently in press and will be published in Astronomy & Astrophysics.

Chapter 5 deals with the selection of the best spectroscopic data and the best combination of Lick indices to achieve most reliable age and metallicity estimates. With the previously calibrated SSP models, we focus on global age and metallicity trends in the studied globular cluster systems and on their global $[\alpha/\text{Fe}]$ ratios.

In the following Chapter 6, a comparison of the ages, metallicities, and abundance ratios of globular cluster systems in late-type, lenticular, and early-type galaxies is performed. Moreover, we divide our sample by host galaxy properties, in order to study systematics in globular cluster ages, metallicities, abundance ratios as a function of environmental density, absolute B band magnitude, and central velocity dispersion.

The conclusions of this thesis are given in Chapter 7 along with a short summary of the major results. An outlook to future projects is presented there as well.

Chapter 2

Integrated-Light Spectroscopy of Milky Way Globular Clusters[1]

2.1 Introduction

In this Chapter[1] we describe the spectroscopic observations of globular clusters in the Milky Way as well as stellar fields in the Galactic bulge. Spectroscopic line indices are measured on these spectra and the stellar populations in globular clusters and the bulge are compared.

Stars in globular clusters are essentially coeval and – with very few exceptions – have all the same chemical composition, with only few elements breaking the rule. As such, globular clusters are the best approximation to *simple stellar populations* (SSP), and therefore offer a virtually unique opportunity to relate the integrated spectrum of stellar populations to age and chemical composition, and do it in a fully empirical fashion. Indeed, the chemical composition can be determined via high-resolution spectroscopy of cluster stars, the age via the cluster turnoff luminosity, while integrated spectroscopy of the cluster can also be obtained without major difficulties. In this way, empirical relations can be established between integrated-light line indices (e.g. Lick indices as defined by Faber et al. 1985) of the clusters, on one hand, and their age and chemical composition on the other hand (i.e., [Fe/H], [α/Fe], etc.).

These empirical relations are useful in two major applications: 1) to directly estimate the age and chemical composition of unresolved stellar populations for which integrated spectroscopy is available (e.g. for elliptical galaxies and spiral bulges), and 2) to provide a basic check of population synthesis models.

Today we know of about 150 globular clusters in the Milky Way (Harris 1996), and more clusters might be hidden behind the high-absorption regions of the Galactic disk. Like in the case of many elliptical galaxies (e.g. Harris 2001), the Galactic globular cluster system shows a bimodal metallicity distribution (Freeman & Norris 1981; Zinn 1985; Ashman & Zepf 1998; Harris 2001) and consists of two major sub-populations, the metal-rich bulge and the metal-poor halo sub-populations.

The metal-rich ([Fe/H] > -0.8 dex) component was initially referred to as a "disk" globular cluster system (Zinn 1985), but it is now clear that the metal-rich globular clusters physically reside inside the bulge and share its chemical and

---

kinematical properties (Minniti 1995; Barbuy et al. 1998; Côté 1999). Moreover, the best studied metal-rich clusters (NGC 6528 and NGC 6553) appear to have virtually the same old age as both the halo clusters and the general bulge population (Ortolani et al. 1995a; Feltzing & Gilmore 2000; Ortolani et al. 2001; Zoccali et al. 2001, 2003; Feltzing et al. 2002), hence providing important clues on the formation of the Galactic bulge and of the whole Milky Way galaxy.

Given their relatively high metallicity (up to $\sim Z_\odot$), the bulge globular clusters are especially interesting in the context of stellar population studies, as they allow comparisons of their spectral indices with those of other spheroids, such as elliptical galaxies and spiral bulges. However, while Lick indices have been measured for a representative sample of metal-poor globular clusters (Burstein et al. 1984; Covino et al. 1995; Trager et al. 1998), no such indices had been measured for the more metal-rich clusters of the Galactic bulge. It is the primary aim of this Chapter to present and discuss the results of spectroscopic observations of a set of metal-rich globular clusters that complement and extend the dataset so far available only for metal-poor globulars.

Substantial progress has been made in recent years to gather the complementary data to this empirical approach: i.e. ages and chemical composition of the metal-rich clusters. Concerning ages, HST/WFPC2 observations of the clusters NGC 6528 and NGC 6553 have been critical to reduce to a minimum and eventually to eliminate the contamination of foreground disk stars (see references above), while HST/NICMOS observations have started to extend these studies to other, more heavily obscured clusters of the bulge (Ortolani et al. 2001).

High spectral-resolution studies of individual stars in these clusters is still scanty, but one can expect rapid progress as high multiplex spectrographs become available at 8–10m class telescopes. A few stars in NGC 6528 and NGC 6553 have been observed at high spectral resolution, but with somewhat discrepant results. For NGC 6528, Carretta et al. (2001) and Coelho et al. (2001) report respectively [Fe/H]= +0.07 and −0.5 dex (the latter value coming from low-resolution spectra). For [M/H] the same authors derive +0.17 and −0.25 dex, respectively. For NGC 6553 Barbuy et al. (1999) give [Fe/H]= −0.55 dex and [M/H]= −0.08 dex, while Cohen et al. (1999) report [Fe/H]= −0.16 dex, and Origlia et al. (2002) give [Fe/H]= −0.3 dex, with [α/Fe]= +0.3 dex. Some α-element enhancement has also been found among bulge field stars, yet with apparently different element-to-element ratios (McWilliam & Rich 1994).

Hopefully these discrepancies may soon disappear, as more and better quality high-resolution data are gathered at 8–10m class telescopes. In summary, the overall metallicity of these two clusters (whose color magnitude diagrams are virtually identical, Ortolani et al. 1995a) appears to be close to solar, with an α-element enhancement [α/Fe] $\simeq$ +0.3 dex.

The α-element enhancement plays an especially important role in the present study. It is generally interpreted as the result of most stars having formed rapidly (within less than, say $\sim$ 1 Gyr), thus having had the time to incorporate the α-elements produced predominantly by Type II supernovae, but failing to incorporate most of the iron produced by the longer-living progenitors of Type Ia supernovae. Since quite a long time, an α-element enhancement has been suspected for giant elliptical galaxies, inferred from the a comparison of Mg and Fe indices with theoretical models (Peletier 1989; Worthey et al. 1992; Davies et al. 1993; Greggio 1997). This interpretation has far-reaching implications for the star formation timescale of these galaxies, with a fast star formation being at variance with the slow process, typical of the current hierarchical merging scenario (Thomas & Kauffmann 1999). However, in principle the apparent α-element enhancement may also be an artifact of some flaws in the models of synthetic stellar populations, especially at high metallicity (Maraston et al. 2001b). The observations presented in this paper are

also meant to provide a dataset against which to conduct a direct test of population synthesis models, hence either excluding or straightening the case for an α-element enhancement in elliptical galaxies. This aspect is extensively addressed in Chapter 3.

The main goal of this Chapter is the measurement of the Lick indices for the metal-rich globular clusters of the bulge and of the bulge field itself. Among others, we measure line indices of Fe, Mg, Ca, CN, and the Balmer series which are defined in the Lick standard system (Worthey & Ottaviani 1997; Trager et al. 1998).

2.2   Observations and Data Reduction

2.2.1   Observations

We observed 12 Galactic globular clusters, 9 of which are located close to the Milky-Way bulge (see Fig. 2.1). Four globular clusters belong to the halo sub-population with a mean metallicity [Fe/H]≤ -0.8 dex (Harris 1996). The other globular clusters with higher mean metallicities are associated with the bulge. Our sample includes the well-studied metal-rich clusters NGC 6553 and NGC 6528, which is located in Baade's Window. Several relevant cluster properties are summarized in Table 2.1. Our cluster sample was selected to maximize the number of high-metallicity clusters and to ensure a high enough signal–to–noise ratio (S/N) of the resulting spectra.

Long-slit spectra were taken on three nights in July 5th to 7th 1999 with the Boller & Chivens Spectrograph of ESO's 1.52 m on La Silla. We used grating #23 with 600 grooves per mm yielding a dispersion of 1.89 Å/pix with a spectral range from $\sim$ 3400 Å to $\sim$ 7300 Å. We used the detector CCD #39, a Loral 2048$\times$2048 pix^2 chip, with a pixel size of 15 μm and a scale of 0.82$''$/pix. Its readout noise is 5.4 e^- and the gain was measured with 1.2 e^-/ADU. In order to check the dark current we also obtained dark images which resulted in a negligible average dark current of 0.0024 e^-s^{-1}pix^{-1}. The total slit length of the spectrograph covers 4.5$'$ on the sky. For the benefit of light sampling the slit width was fixed at 3$''$, which guarantees an instrumental resolution ($\sim$ 6.7 Å) which is smaller than the average resolution ($\gtrsim$ 8 Å) of the Lick standard system (Worthey et al. 1994; Trager et al. 1998). The mean seeing during the observing campaign varied between 0.8$''$ and 1.6$''$, resulting in seeing-limited spectra. Consequently, the stellar disks are smeared over 1–2 pixel along the spatial axis.

To ensure a representative sampling of the underlying stellar population we obtained several spectra with slightly offset pointings. In general three long-slit spectra were taken for each of our target clusters (see Table 2.2 for details). The observing pattern was optimized in time (i.e. in airmass) to obtain one spectrum of the nuclear region and spectra of adjacent fields by shifting the telescope a few arc seconds (i.e. $\sim$ 2 slit widths) to the North and South. Exposure times were adjusted according to the surface brightness of each globular cluster to reach an statistically secure luminosity sampling of the underlying stellar population. Before and after each block of science exposures, lamp spectra were taken for accurate wavelength calibration.

In addition to the globular cluster data, we obtained long-slit spectra of three stellar fields near the Galactic center (see Fig. 2.1). Two of them are located in Baade's Window. The exposure time for a single bulge spectrum is 1800 seconds. Five slightly offset pointings have been observed in each field resulting in 15 exposures of 30 minutes each.

During each night Lick and flux standard stars were observed for later index and flux calibrations. Table 2.2 shows the observing log of all three nights. Figure 2.1 gives the positions of all observed globular clusters (filled dots) and bulge fields

GC	R_{gc} [kpc]	[Fe/H]	r_h [arcmin]	$\mathrm{E}^{\mathrm{a}}_{(B-V)}$ [mag]	$(m-M)_V$ [mag]	$v^{\mathrm{b}}_{\mathrm{rad}}$ [km s^{-1}]	v_{rad} [km s^{-1}]	HBR$^{\mathrm{c}}$
NGC 5927	4.5	-0.37	1.15	0.45	15.81	-130 ± 12	-107.5 ± 1.0	-1.00^d
NGC 6218 (M12)	4.5	-1.48	2.16	0.40	14.02	-46 ± 23	-42.2 ± 0.5	0.97^d
NGC 6284	6.9	-1.32	0.78	0.28	16.70	8 ± 16	27.6 ± 1.7	1.00^e
NGC 6356	7.6	-0.50	0.74	0.28	16.77	35 ± 12	27.0 ± 4.3	-1.00^d
NGC 6388	4.4	-0.60	0.67	0.40	16.54	58 ± 10	81.2 ± 1.2	-0.70^e
NGC 6441	3.5	-0.53	0.64	0.44	16.62	-13 ± 10	16.4 ± 1.2	-0.70^f
NGC 6528	1.3	-0.17	0.43	0.56	16.53	180 ± 10	184.9 ± 3.8	-1.00^d
NGC 6553	2.5	-0.34	1.55	0.75	16.05	-25 ± 16	-6.5 ± 2.7	-1.00^d
NGC 6624	1.2	-0.42	0.82	0.28	15.37	27 ± 12	53.9 ± 0.6	-1.00^d
NGC 6626 (M28)	2.6	-1.45	1.56	0.43	15.12	-15 ± 15	17.0 ± 1.0	0.90^d
NGC 6637 (M69)	1.6	-0.71	0.83	0.16	15.16	6 ± 12	39.9 ± 2.8	-1.00^d
NGC 6981 (M72)	12.9	-1.40	0.88	0.05	16.31	-360 ± 18	-345.1 ± 3.7	0.14^d

a   taken from Harris (1996)

b   this work

c   horizontal branch parameter, (B−R)/(B+V+R), for details see e.g. Lee et al. (1994)

d   taken from Harris (1996)

e   taken from Zoccali et al. (2000b)

f   Due to very similar HB morphologies in CMDs of NGC 6388 and NGC 6441 (see Rich et al. 1997), we assume that the HBR parameter is similar for both globular clusters and adopt HBR= −0.70 for NGC 6441.

Table 2.1: General properties of sample Globular Clusters. If not else mentioned, all data were taken from the 1999 update of the McMaster catalog of Milky Way Globular Clusters (Harris 1996). R_{gc} is the globular cluster distance from the Galactic Center. r_h is the half-light radius. $\mathrm{E}_{(B-V)}$ and $(m-M)_V$ are the reddening and the distance modulus. v_{rad} the heliocentric radial velocity. Note, that our radial-velocity errors are simple *internal* errors which result from the fitting of the cross-correlation peak. The real *external* errors are a factor $\sim 3-4$ larger. HBR is the horizontal-branch morphology parameter (Lee et al. 1994).

(open squares) in the galactic coordinate system.
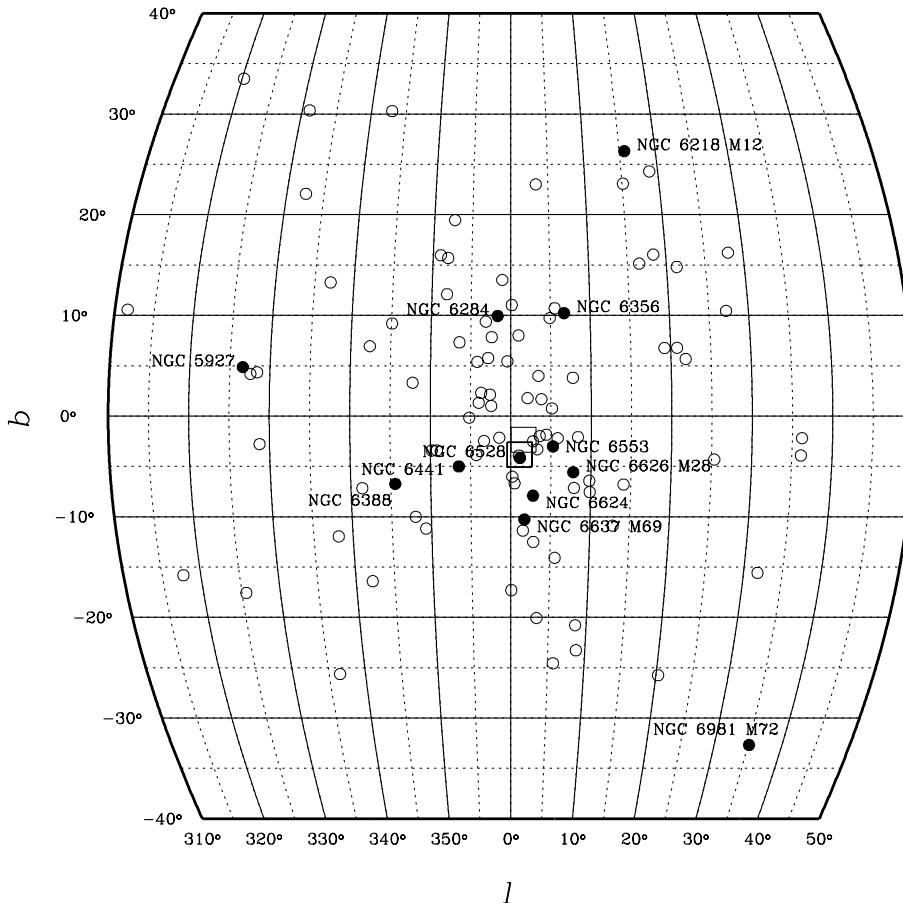
Figure 2.1: Distribution of galactic globular clusters as seen in the galactic coordinate system. The filled circles are the observed sample globular clusters while open circles mark the position of other known Milky Way globular clusters. All observed globular clusters are appropriately labeled. The positions were taken from the Globular Cluster Catalog by Harris (1996). Large squares show the positions of our three bulge fields for which spectroscopy is also available. Note that two of the three fields almost overlap in the plot.

2.2.2   Data Reduction

We homogeneously applied standard reduction techniques to the whole data set using the IRAF[2] platform (Tody 1993). The basic data reduction was performed for each night individually. In brief, a masterbias was subtracted from the science images followed by a division by a normalized masterflat spectrum which has been created from five quarz-lamp exposures. The quality, i.e. the flatness, of the spectra along the spatial axis was checked on the sky spectra after flatfielding. Any gradients along the spatial axis were found to be smaller than $\lesssim 5\%$.

---

[2]IRAF is distributed by the National Optical Astronomy Observatories, which are operated by the Association of Universities for Research in Astronomy, Inc., under cooperative agreement with the National Science Foundation.

Night	Targets	Exptime	RA(J2000)	DEC (J2000)	$l[°]$	$b[°]$
5.7.1999	NGC 5927	3×600s	15h 28m 00.5s	−50° 40' 22"	326.60	4.86
	NGC 6388	3×600s	17h 36m 17.0s	−44° 44' 06"	345.56	−6.74
	NGC 6528	3×600s	18h 04m 49.6s	−30° 03' 21"	1.14	−4.17
	NGC 6624	3×600s	18h 23m 40.5s	−30° 21' 40"	2.79	−7.91
	NGC 6981	1×1320s	20h 53m 27.9s	−12° 32' 13"	35.16	−32.68
	Bulge1	5×1800s	18h 03m 12.1s	−29° 52' 06"	1.13	3.78
6.7.1999	NGC 6218	3×1200s	16h 47m 14.5s	−01° 56' 52"	15.72	26.31
	NGC 6441	3×600s	17h 50m 12.9s	−37° 03' 04"	353.53	−5.01
	NGC 6553	3×720s	18h 09m 15.6s	−25° 54' 28"	5.25	−3.02
	NGC 6626	3×600s	18h 24m 32.9s	−24° 52' 12"	7.80	−5.58
	NGC 6981	1×1800s	20h 53m 27.9s	−12° 32' 13"	35.16	−32.68
	Bulge2	5×1800s	18h 05m 21.3s	−29° 58' 38"	1.26	4.23
7.7.1999	NGC 6284	3×600s	17h 04m 28.8s	−24° 45' 53"	358.35	9.94
	NGC 5927	2×600s	15h 28m 00.5s	−50° 40' 22"	326.60	4.86
	NGC 6356	3×900s	17h 23m 35.0s	−17° 48' 47"	6.72	10.22
	NGC 6637	3×900s	18h 31m 23.2s	−32° 20' 53"	1.72	−10.27
	NGC 6981	1×1800s	20h 53m 27.9s	−12° 32' 13"	35.16	−32.68
	Bulge3	5×1800s	17h 58m 38.3s	−28° 43' 33"	1.63	2.35

Table 2.2: Journal of performed observations of Milky Way globular clusters.

He-Ne-Ar-Fe lines were used to calibrate all spectra to better than 0.13 Å (r.m.s.). Unfortunately, the beam of the calibration lamp covers only the central 3.3′ along the slit's spatial axis (perpendicular to the dispersion direction), which allows no precise wavelength calibration for the outer parts close to the edge of the CCD chip. We tried, however, to extrapolate a 2-dim. λ-calibration to the edges of the long-slit and found a significant increase in the r.m.s. up to an unacceptable 0.7 Å. Hence, to avoid calibration biases we use data only from regions which are covered by the arc lamp beam. Our effective slit length is therefore 3.3′ with a slit width of 3″. For each single pixel row along the dispersion axis an individual wavelength solution was found and subsequently applied to each object, bulge, and sky spectrum. After wavelength calibration the signal along the spatial axis was averaged in λ-space, i.e. the flux of 3.3′ was averaged to obtain the final spectrum of a single pointing.

Finally, spectrophotometric standard stars, Feige 56, Feige 110, and Kopff 27 (Stone & Baldwin 1983; Baldwin & Stone 1984) were used to convert counts into flux units.

2.2.3   Radial velocities

All radial velocity measurements were carried out after the subtraction of a background spectrum (see Sect. 2.3.1) using cross-correlation with high-S/N template spectra of two globular clusters in M31 (i.e. 158–213 and 225–280, see Huchra et al. 1982 for nomenclature). Both globular clusters have metallicities which match the average metallicity of our globular cluster sample. We strictly followed the recipe of the Fourier cross-correlation which is implemented in the FXCOR task of IRAF (see IRAF manual for details). Table 2.1 summarizes the results including the *internal* uncertainties of our measurements resulting from the fitting of the cross-correlation peak.

Following the rule of thumb, by which 1/10 of the instrumental resolution (~ 6.7 Å) transforms into the radial velocity resolution, we estimate for our spectra a resolution of ~ 40 km s^{-1}. In order to estimate the *real* uncertainty we compare the radial velocity measurements of one globular cluster (NGC 6981) which was

observed in all three nights. We find a dispersion in radial velocity $\sigma_v \approx 17$ km s^{-1} and a maximal deviation of 32.4 km s^{-1}. A comparison of measured radial velocities of all our Lick standard stars with values taken from the literature gives a dispersion of $\sigma_v \approx 40$ km s^{-1} which matches the earlier rough estimate. In the case of NGC 6981, the *internal* error estimate ($\Delta_{\rm cc}v_{\rm rad} = 18.4$ km s^{-1}) underestimates the *real* radial velocity uncertainty assumed to be of the order of ~ 40 km s^{-1} by a factor of ~ 2. Note however, that data of lower S/N will produce larger radial velocity uncertainties. Moreover, taking into account the slit width of 3$''$ the maximum possible radial velocity error for a star positioned at the edge of the slit is ~ 200 km s^{-1}. For high surface-brightness fluctuations inside the slit, this would inevitably result in larger radial velocity errors than originally expected from the calibration quality. Since we sum up all the flux along the slit, we most effectively eliminate this surface-brightness fluctuation effect. In fact, after a check of all our single spectra, we find no exceptionally bright star inside the slit aperture, which could produce a systematic deviation from the mean radial velocity.

After all, we estimate that our *real* radial velocity uncertainties are larger by a factor $\sim 2 - 4$ than the values given in Table 2.1.

2.2.4 Transformation to the Lick System

The Lick standard system was initially introduced by Burstein et al. (1984) in order to study element abundances from low-resolution integrated spectra of extragalactic stellar systems. It has recently been updated and refined by several authors (González 1993; Worthey et al. 1994; Worthey & Ottaviani 1997; Trager et al. 1998). The Lick system defines line indices for specific atomic and molecular absorption features, such as Fe, Mg, Ca and CN, CH, TiO, in the optical range from ~ 4100 Å to ~ 6100 Å. The definitions of a line index are given in Appendix A. We implemented the measuring procedure in a software and tested it extensively on original Lick spectra (see App. A for details). This code is used for all further measurements.

The Lick system provides two sets of index passband definitions. One set of 21 passband definitions was published in Worthey et al. (1994) to which we will refer as the *old* set. A *new* and refined set of passband definitions is given in Trager et al. (1998) which is supplemented by the Balmer index definitions of Worthey & Ottaviani (1997). This new set of 25 indices is used throughout the subsequent analysis. However, we also provide Lick indices based on the old passband definitions (see Appendix B) which enables a consistent comparison with predictions from SSP models which make use of fitting functions based on the old set of passband definitions. Note that indices and model predictions which use two different passband definition sets are prone to systematic offsets. This point will be discussed in Chapter 3.

Before measuring indices, one has carefully to degrade spectra with higher resolution to adapt to the resolution of the Lick system. We strictly followed the approach of Worthey & Ottaviani (1997) and degraded our spectra to the wavelength-dependent Lick resolution (~ 11.5 Å at 4000 Å, 8.4 Å at 4900 Å, and 9.8 Å at 6000 Å). The effective resolution (FWHM) of our spectra has been determined from calibration-lamp lines and isolated absorption features in the object spectra. The smoothing of our data is done with a wavelength-dependent Gaussian kernel with the width

$$\sigma_{\rm smooth}(\lambda) = \left(\frac{{\rm FWHM}(\lambda)^2_{\rm Lick} - {\rm FWHM}(\lambda)^2_{\rm data}}{8\ln 2} \right)^{\frac{1}{2}}. \qquad (2.1)$$

We tested the shape of absorption lines in our spectra and found that they are very well represented by a Gaussian. Worthey & Ottaviani tested the shape of the

absorption lines in the Lick spectra and found also no deviation from a Gaussian. Both results justify the use of a Gaussian smoothing kernel.

The smoothing kernel for the bulge stellar fields is generally narrower since one has to account for the non-negligible velocity dispersion of bulge field stars. A typical line-of-sight velocity dispersion $\sigma_{\mathrm{LOS}} \approx 100$ km s^{-1} was assumed for the bulge data (e.g. Spaenhauer et al. 1992). We do not correct for the mean velocity dispersion of the globular clusters ($\sigma_{\mathrm{LOS}} \approx 10$ km s^{-1} Pryor & Meylan 1993).

Another point of concern for low-S/N spectra (S/N$\lesssim$10 per resolution element) is the slope of the underlying continuum (see Beasley et al. 2000, for detailed discussion of this effect) which influences the pseudo-continuum estimate for broad features and biases the index measurement. However, since all our spectra are of high S/N ($\gtrsim 50$ per resolution element), we are not affected by a noisy continuum.

After taking care of the resolution corrections, one has to correct for systematic, higher-order effects. These variations are mainly due to imperfect smoothing and calibration of the spectra. To correct the small deviations 12 index standard stars from the list of Worthey et al. (1994) have been observed throughout the observing run. Figure 2.2 shows the comparison between the Lick data and our index measurements for all passbands. Least-square fits using a κ-σ-clipping (dashed lines) are used to parameterize the deviations from the Lick system as a function of wavelength. The functional form of the fit is

$$\mathrm{EW}_{\mathrm{cal}} = \alpha + (1 + \beta) \cdot \mathrm{EW}_{\mathrm{raw}},$$

where $\mathrm{EW}_{\mathrm{cal}}$ and $\mathrm{EW}_{\mathrm{raw}}$ are the calibrated and raw indices, respectively. Table 2.3 summarizes the individual coefficients α and β. This correction functions are applied to all further measurements. The corresponding coefficients for index measurements using the *old* passband definitions are documented in Table B.2.

index	α	β	r.m.s.	units
CN$_1$	-0.0017	-0.0167	0.0251	mag
CN$_2$	-0.0040	-0.0389	0.0248	mag
Ca4227	-0.2505	-0.0105	0.2582	Å
G4300	0.6695	-0.1184	0.4380	Å
Fe4384	-0.5773	0.0680	0.2933	Å
Ca4455	-0.1648	0.0249	0.4323	Å
Fe4531	-0.3499	0.0223	0.1566	Å
Fe4668	-0.8643	0.0665	0.5917	Å
Hβ	0.0259	0.0018	0.1276	Å
Fe5015	1.3494	-0.2799	0.3608	Å
Mg$_1$	0.0176	-0.0165	0.0160	mag
Mg$_2$	0.0106	0.0444	0.0112	mag
Mgb	0.0398	-0.0392	0.1789	Å
Fe5270	-0.3608	0.0514	0.1735	Å
Fe5335	-0.0446	-0.0725	0.3067	Å
Fe5406	-0.0539	-0.0730	0.2054	Å
Fe5709	-0.5416	0.3493	0.1204	Å
Fe5782	-0.0610	-0.0116	0.2853	Å
NaD	0.3620	-0.0733	0.2304	Å
TiO$_1$	0.0102	0.2723	0.0133	mag
TiO$_2$	-0.0219	0.1747	0.0342	mag
Hδ_A	-0.1525	-0.0465	1.5633	Å
Hγ_A	0.4961	0.0117	0.6288	Å
Hδ_F	-0.1127	-0.0639	0.4402	Å
Hγ_F	-0.0062	-0.0343	0.1480	Å

Table 2.3: Summary of the coefficients α and β for all 1st and 2nd-order index corrections.

Note, that most passbands require only a small linear offset, but no offset as a function of index strength. While the former is simply due to a small variation in the wavelength calibration, the latter is produced by over/under-smoothing of the spectra. Absorption lines for which the smoothing pushes the wings outside narrowly defined feature passbands are mostly affected by this non-linear effect. However, for passbands of major interest (such as CN, Hβ, Fe5270, Fe5335, Mgb, and Mg$_2$) the Lick indices are satisfactorily reproduced by a simple offset (no tilt) in the index value (see Fig. 2.2).
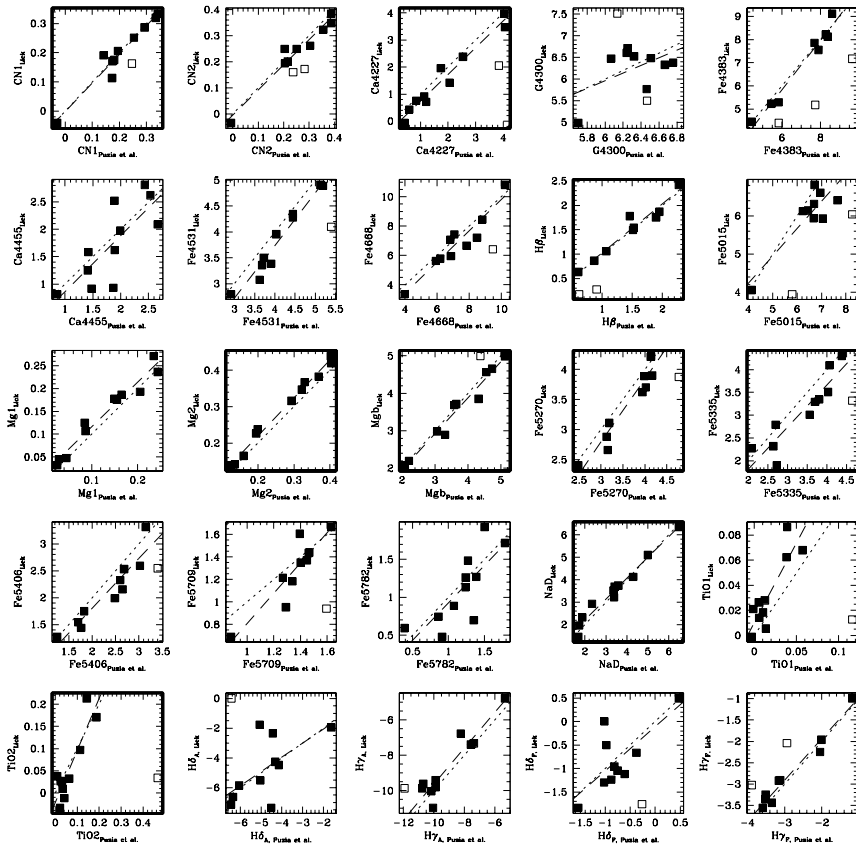
Figure 2.2: Comparison of passband measurements from our spectra and original Lick data for 12 Lick standard stars. The dotted line shows the one-to-one relation, whereas the dashed line is a least-square fit to the filled squares. Data, which have been discarded from the fit because of too large errors or deviations, are shown as open squares. Bold frames indicate some of the widely used Lick indices which are also analysed in this work.

2.3 Analysis of the Spectra

2.3.1 Estimating the background light

Long-slit spectroscopy of extended objects notoriously suffers from difficulties in estimating the contribution of the sky and background light. Since we observe

globular clusters near the Galactic Bulge, their spectra will be contaminated by an unknown fraction of the bulge light, depending on the location on the sky (see Fig. 2.1). In order to estimate the contribution of the background, two different approaches have been applied. The first approach was to estimate the sky and bulge contribution from separately taken sky and bulge spectra (hereafter "background modeling"). The other technique was to extract the total background spectrum from low-intensity regions at the edges of the spatial axis in the object spectrum itself (henceforth "background extraction"). While the first technique suffers from the unknown change of the background spectrum between the position of the globular clusters and the background fields, the second one suffers from lower S/N. However, tests have shown that the "background extraction" allows a more reliable estimate of the background spectrum.

We compare both background subtraction techniques in Table 2.4. We find that the "background modeling" systematically overestimates the background light contribution as one goes to larger galactocentric radii. The index differences increase between spectra which have been cleaned using "background modeling" and "background extraction". This is basically due to an overestimation of the background light from single background spectra which were taken at intermediate galactocentric radii. We, therefore, drop the "background modeling" and proceed for all subsequent analyses with the "background extraction" technique. In summary, the crucial drawback of the "background modeling" is that it requires a prediction of the bulge light fraction from separate spectra which is strongly model-dependent. The bulge light contains changing scale heights for different stellar populations (see Frogel 1988; Wyse et al. 1997, and references therein). The background light at the cluster position includes an unknown mix of bulge and disk stellar populations (Frogel 1988; Frogel et al. 1990; Feltzing & Gilmore 2000), an unknown contribution from the central bar (Unavane & Gilmore 1998; Unavane et al. 1998), and is subject to differential reddening on typical scales of $\sim 90''$ (Frogel et al. 1999) which complicates the modeling. Clearly, with presently available models (e.g. Kent et al. 1991; Freudenreich 1998) it is impossible to reliably predict a spectrum of the galactic bulge as a function of galactic coordinates. The "background extraction" technique naturally omits model predictions and allows to obtain the total background spectrum, including sky *and* bulge light, from the object spectrum itself.

We selected low-luminosity outer sections in the slit's intensity profile (see Fig. 2.3) to derive the background spectrum for each globular cluster. Only those regions which show flat and locally lowest intensities and are located outside the half-light radius r_h (Trager et al. 1995) are selected. We sum the spectra of the background light of all available pointings to create one high-S/N background spectrum for each globular cluster. All globular clusters were corrected using this background spectrum. The background-to-cluster light ratio depends on galactic coordinates, and is $\lesssim 0.1$ for NGC 6388 and ~ 1 for NGC 6528. In order to lower this ratio, only regions inside r_h are used to create the final globular-cluster spectrum. This restriction decreases the background-to-cluster ratio by a factor of $\gtrsim 2$. In the case of NGC 6218, NGC 6553, and NGC 6626 the half-light diameter $2r_h$ is larger or comparable to the spatial dimensions of the slit, so that no distinct background regions can be defined. For these clusters we estimate the background from flat, low-luminosity parts along the spatial axis inside r_h but avoid the central regions (see Fig. 2.3).

2.3.2   Contamination by Bright Objects

To check if bright foreground stars inside the slit contaminate the globular cluster light, we plot the intensity profile along the slit's spatial axis. The profiles of each pointing are documented in Figure 2.3. Since we use the light only inside

GC bkg mode[a]	CN$_1$ mag	CN$_2$ mag	Ca4227 A	G4300 A	Fe4383 A	Ca4455 A	Fe4531 A	Fe4668 A	Hβ A	Fe5015 A
NGC 6624										
BE	0.0497	0.0739	0.4889	4.8910	2.4023	0.5065	2.2739	1.4643	1.6502	4.1850
w/o	0.0635	0.0856	0.6070	5.0023	2.8872	0.5122	2.9936	1.6337	1.5347	4.1861
BM	0.0692	0.0907	0.6064	5.0702	2.7295	0.5335	3.1087	1.0489	1.4807	4.1552
Trager et al. (1998)	...	...	...	...	...	...	...	...	...	...
Covino et al. (1995)	0.02	0.02	...	4.758	...	...	...	...	2.535	...
Cohen et al. (1998)	...	...	...	...	...	...	...	...	1.69	...
NGC 6218										
BE	-0.0763	-0.0596	0.0586	2.7004	-0.1175	-0.0055	0.9504	-0.6060	2.7147	2.7170
w/o	-0.0711	-0.0550	0.0688	2.6871	-0.1207	0.0536	0.8507	-0.7686	2.5817	2.6896
BM	-0.0820	-0.0661	-0.0429	2.4039	-0.8066	0.0178	0.5669	-1.7789	2.8366	2.2599
Trager et al. (1998)	-0.0910	-0.0490	0.6300	1.8700	0.0000	0.1000	1.6900	-1.3200	2.2800	2.1100
Covino et al. (1995)	...	...	...	...	...	...	...	...	1.214	...
Cohen et al. (1998)	...	...	...	...	...	...	...	...	...	...
NGC 6626										
BE	-0.0455	-0.0259	0.1473	3.1433	0.5716	0.0926	1.2946	-0.0206	2.2747	3.1826
w/o	-0.0425	-0.0245	0.1859	3.1207	0.7364	0.1256	1.3939	0.1220	2.1582	3.1877
BM	-0.0459	-0.0277	0.1428	3.0243	0.4942	0.1222	1.3238	-0.2020	2.2132	3.0836
Trager et al. (1998)	...	...	...	...	...	...	...	...	...	...
Covino et al. (1995)	-0.052	-0.052	...	2.713	...	...	...	...	2.443	...
Cohen et al. (1998)	...	...	...	...	...	...	...	...	...	...
NGC 6284										
BE	-0.0417	-0.0227	0.1551	3.1957	0.6659	0.1992	1.4645	-0.1003	2.4274	3.1553
w/o	-0.0347	-0.0155	0.2107	3.3368	0.7969	0.2928	1.4811	0.1469	2.2370	3.2056
BM	-0.0507	-0.0277	0.0278	2.9414	-0.5049	0.0494	1.0449	-2.3533	2.8913	2.2407
Trager et al. (1998)	...	...	...	...	...	...	...	...	...	...
Covino et al. (1995)	-0.082	-0.082	...	1.785	...	...	...	...	2.764	...
Cohen et al. (1998)	...	...	...	...	...	...	...	...	...	...
NGC 6356										
BE	0.0450	0.0648	0.5079	5.0611	2.3472	0.5334	2.2955	1.3231	1.6341	4.0541
w/o	0.0432	0.0626	0.4911	4.8895	2.3269	0.5481	2.1968	1.4871	1.6190	4.1296
BM	0.0561	0.0788	0.4667	5.1272	2.0202	0.5053	2.1965	0.5297	1.7782	3.9587
Trager et al. (1998)	0.0237	0.0726	1.3270	4.8180	3.9220	1.6030	2.6900	2.9720	1.4680	4.2980
Covino et al. (1995)	...	...	...	...	...	...	...	...	1.646	...
Cohen et al. (1998)	...	...	...	...	...	...	...	...	1.62	...
NGC 6637										
BE	0.0248	0.0438	0.4009	5.1912	2.0615	0.4497	2.1725	1.3150	1.6224	3.9535
w/o	0.0223	0.0412	0.3859	5.1082	2.1333	0.3674	2.0921	1.2860	1.5773	3.8951
BM	0.0258	0.0459	0.3493	5.2617	1.9243	0.2976	2.0623	0.7096	1.6590	3.7375
Trager et al. (1998)	-0.0125	0.0048	1.0560	5.0490	0.2010	1.1300	3.4870	1.5220	0.8980	4.6420
Covino et al. (1995)	...	...	...	...	...	...	...	...	1.15	...
Cohen et al. (1998)	...	...	...	...	...	...	...	...	...	...
NGC 6553										
BE	0.1378	0.1619	1.0915	5.4464	4.0079	0.8316	3.0767	3.4849	1.8881	5.7254
w/o	0.0699	0.0842	0.7192	5.0248	4.2101	0.9686	2.5541	3.5774	1.1596	4.9798
BM	0.1107	0.1243	0.7044	5.4233	4.5439	1.3630	2.7317	3.5390	1.0138	5.2232
Trager et al. (1998)	...	...	...	...	...	...	...	...	...	...
Covino et al. (1995)	...	...	...	...	...	...	...	...	...	...
Cohen et al. (1998)	...	...	...	...	...	...	...	...	1.63	...
NGC 6528										
BE	0.0959	0.1174	0.9089	5.2218	4.7754	0.8794	2.7074	4.2181	1.7745	5.1531
w/o	0.0696	0.0877	0.6629	5.1257	4.4139	0.5266	2.7904	4.0300	1.5097	5.0032
BM	0.1229	0.1569	1.3493	6.2741	6.1253	1.4228	3.7042	4.5434	1.0913	6.1269
Trager et al. (1998)	...	...	...	...	...	...	...	...	...	...
Covino et al. (1995)	...	...	...	...	...	...	...	...	...	...
Cohen et al. (1998)	...	...	...	...	...	...	...	...	1.80	...

[a] BE: background extraction; w/o: without background subtraction; BM: background modeling. See Section 2.3.1 for details.

Table 2.4: Comparison of Lick indices CN$_1$ to Fe5015 for our sample globular clusters with data taken from literature. The according errors are given in Table B.1. Our index measurements and the indices of Trager et al. use the *new* passband definitions of Trager et al. (1998). Cohen et al. and Covino et al. use *old* passband definitions of Burstein et al. (1984).

GC bkg mode[a]	Mg$_1$ mag	Mg$_2$ mag	Mgb Å	Fe5270 Å	Fe5335 Å	Fe5406 Å	Fe5709 Å	Fe5782 Å	Na5895 Å	TiO$_1$ mag	TiO$_2$ mag
NGC 6624											
BE	0.0707	0.1721	2.7280	1.8158	1.6403	0.9789	0.5009	0.6411	2.7063	0.0470	0.0628
w/o	0.0696	0.1758	2.6730	1.7832	1.7237	0.9738	0.5322	0.6349	3.8927	0.0542	0.0658
BM	0.0642	0.1669	2.6254	1.6564	1.6780	0.9527	0.4837	0.5945	3.4454	0.0572	0.0719
Trager et al. (1998)	. . .	. . .	. . .	. . .	. . .	. . .	. . .	. . .	. . .	. . .	. . .
Covino et al. (1995)	0.05	0.15	2.486	2.117	1.812	. . .	. . .	. . .	2.881	. . .	. . .
Cohen et al. (1998)	0.048	0.163	2.94	2.09	1.78	. . .	. . .	. . .	2.20	0.035	. . .
NGC 6218											
BE	0.0268	0.0672	1.0628	0.7687	0.8935	0.2246	-0.1909	0.2025	1.2915	0.0182	0.0040
w/o	0.0293	0.0675	1.4179	0.7036	0.7692	0.2148	-0.1939	0.2421	1.2410	0.0059	-0.0067
BM	0.0132	0.0256	1.0507	0.2819	0.4167	-0.1026	-0.5354	0.0523	-0.2041	-0.0222	-0.0679
Trager et al. (1998)	-0.0060	0.0690	1.2800	1.3400	0.5000	0.0600	-0.0600	0.0000	1.6300	0.0020	0.0000
Covino et al. (1995)	0.02	0.07	1.68	1.125	0.8472	. . .	. . .	. . .	. . .	. . .	. . .
Cohen et al. (1998)	. . .	. . .	. . .	. . .	. . .	. . .	. . .	. . .	. . .	. . .	. . .
NGC 6626											
BE	0.0415	0.0919	1.3679	1.0900	0.9747	0.5413	0.1846	0.4735	2.1005	0.0288	0.0382
w/o	0.0424	0.0956	1.3511	1.1049	1.0347	0.5392	0.1824	0.4674	2.2341	0.0299	0.0385
BM	0.0382	0.0841	1.2213	1.0144	0.9603	0.4811	0.1324	0.4479	1.9655	0.0245	0.0274
Trager et al. (1998)	. . .	. . .	. . .	. . .	. . .	. . .	. . .	. . .	. . .	. . .	. . .
Covino et al. (1995)	-0.002	0.063	1.103	1.539	1.229	. . .	. . .	. . .	2.565	. . .	. . .
Cohen et al. (1998)	. . .	. . .	. . .	. . .	. . .	. . .	. . .	. . .	. . .	. . .	. . .
NGC 6284											
BE	0.0427	0.0966	1.4403	0.8563	1.0216	0.5178	0.1110	0.3141	2.3978	0.0159	0.0039
w/o	0.0463	0.1064	1.3460	1.0142	1.0683	0.5497	0.1973	0.3497	2.1540	0.0137	0.0023
BM	0.0063	0.0180	0.0513	-0.3341	0.2294	-0.1227	-0.0984	-0.3166	-2.1392	-0.0380	-0.1080
Trager et al. (1998)	. . .	. . .	. . .	. . .	. . .	. . .	. . .	. . .	. . .	. . .	. . .
Covino et al. (1995)	0.027	0.077	1.075	1.505	1.091	. . .	. . .	. . .	2.433	. . .	. . .
Cohen et al. (1998)	. . .	. . .	. . .	. . .	. . .	. . .	. . .	. . .	. . .	. . .	. . .
NGC 6356											
BE	0.0728	0.1773	2.7863	1.7187	1.6597	0.9557	0.4067	0.5493	3.2660	0.0333	0.0531
w/o	0.0773	0.1851	2.5857	1.9996	1.4993	0.8985	0.3764	0.5451	3.6050	0.0390	0.0579
BM	0.0666	0.1656	2.3420	1.2805	1.7049	0.7273	0.3410	0.3598	2.2064	0.0327	0.0408
Trager et al. (1998)	0.0404	0.1700	2.9800	1.9940	1.4010	1.3970	0.6640	0.6200	3.3290	0.0369	0.0460
Covino et al. (1995)	0.062	0.179	2.776	2.352	1.125	. . .	. . .	. . .	. . .	. . .	. . .
Cohen et al. (1998)	0.070	0.169	3.09	2.00	1.69	. . .	. . .	. . .	3.00	0.029	. . .
NGC 6637											
BE	0.0567	0.1542	2.5420	1.6335	1.3969	0.8222	0.3565	0.4906	2.6053	0.0381	0.0441
w/o	0.0562	0.1541	2.4696	1.5448	1.4297	0.8195	0.3538	0.4789	2.9313	0.0418	0.0464
BM	0.0461	0.1369	2.3096	1.2681	1.2806	0.6971	0.3144	0.3349	1.9320	0.0359	0.0310
Trager et al. (1998)	0.0384	0.1433	2.3720	1.9470	0.9590	0.8580	0.3850	0.1100	3.2550	0.0498	0.0000
Covino et al. (1995)	0.05	. . .	2.671	1.642	1.539	. . .	. . .	. . .	. . .	. . .	. . .
Cohen et al. (1998)	. . .	. . .	. . .	. . .	. . .	. . .	. . .	. . .	. . .	. . .	. . .
NGC 6553											
BE	0.1002	0.2552	3.8961	2.6091	2.2654	1.2371	0.7744	1.0970	3.8792	0.0689	0.1420
w/o	0.0949	0.2513	3.6472	2.4476	2.1073	1.3023	0.7823	1.0423	4.1967	0.0640	0.1245
BM	0.0972	0.2606	3.9386	2.5740	2.2081	1.3565	0.8161	1.1643	3.9533	0.0640	0.1262
Trager et al. (1998)	. . .	. . .	. . .	. . .	. . .	. . .	. . .	. . .	. . .	. . .	. . .
Covino et al. (1995)	. . .	. . .	. . .	. . .	. . .	. . .	. . .	. . .	. . .	. . .	. . .
Cohen et al. (1998)	0.110	0.249	3.88	3.11	2.51	. . .	. . .	. . .	3.40	0.044	. . .
NGC 6528											
BE	0.1149	0.2615	3.7413	2.3673	2.2777	1.5499	0.8223	0.7987	5.1366	0.0750	0.1268
w/o	0.1109	0.2573	3.4276	2.3885	2.0133	1.3893	0.7406	0.6816	5.5471	0.0714	0.1183
BM	0.1248	0.2928	4.1444	2.6491	2.4803	1.7290	0.9335	0.8722	5.4463	0.0939	0.1696
Trager et al. (1998)	. . .	. . .	. . .	. . .	. . .	. . .	. . .	. . .	. . .	. . .	. . .
Covino et al. (1995)	. . .	. . .	. . .	. . .	. . .	. . .	. . .	. . .	. . .	. . .	. . .
Cohen et al. (1998)	0.097	0.247	3.89	2.96	2.45	. . .	. . .	. . .	4.93	0.046	. . .

[a] BE: background extraction; w/o: without background subtraction; BM: background modeling. See Section 2.3.1 for details.

Table 2.4: – continued. Comparison of Lick indices Mg$_1$ – TiO$_2$ for our sample globular clusters with data from literature.

one half-light radius (indicated by the shaded region) and therefore maximize the cluster-to-background ratio, the probability for a significant contamination by bright non-member objects is very low. Even very bright foreground stars will contribute only a small fraction to the total light.
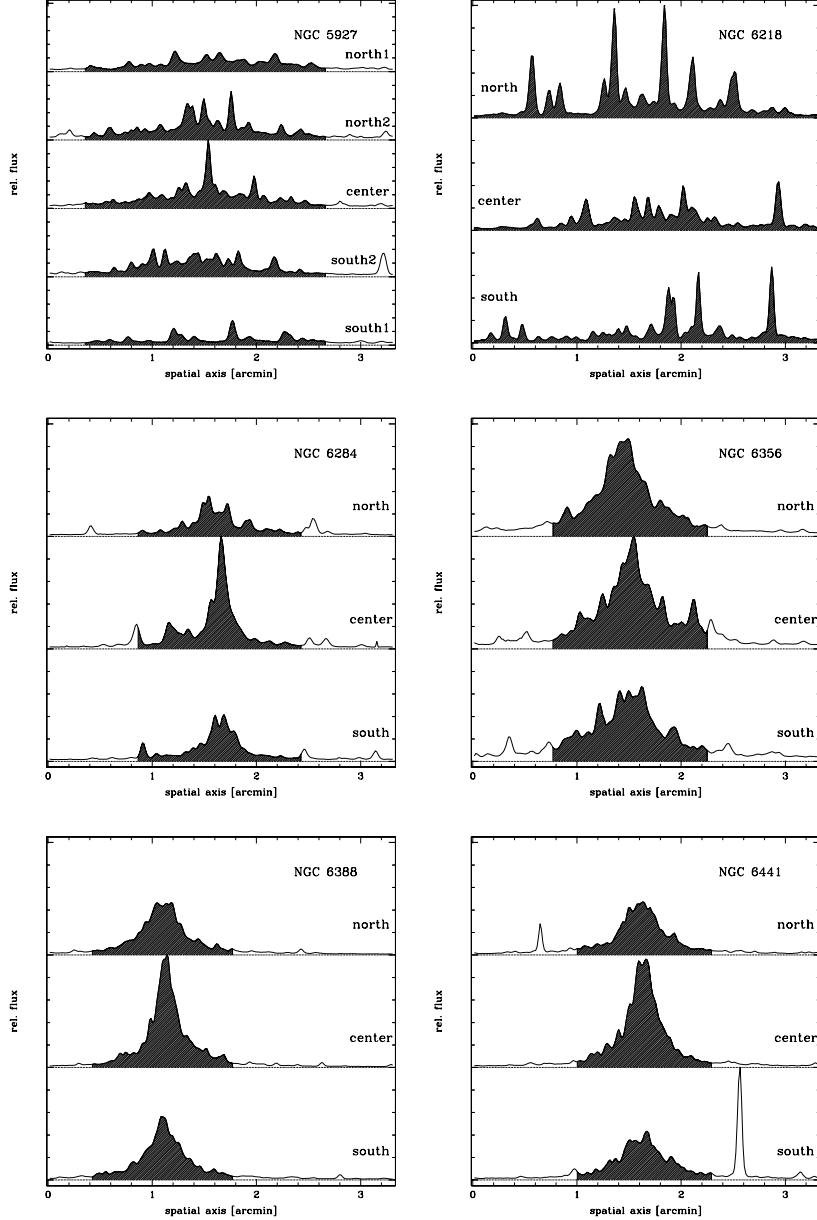
Figure 2.3: Intensity profiles of each pointing for sample globular clusters NGC 5927, NGC 6218, NGC 6284, NGC 6356, NGC 6388, and NGC 6441. The fraction of the profile which was used to create the final globular cluster spectrum is shaded. Each cluster has at least three pointings which are shifted by a few slit widths to the north and south. Note that clusters with a sampled luminosity less than $10^4 L_\odot$ and relatively large half-light radii (i.e. see Sect. 2.3.4 and Tab. 2.1) have strongly fluctuating profiles.

However, three of our sample globular clusters (NGC 6218, NGC 6553, and
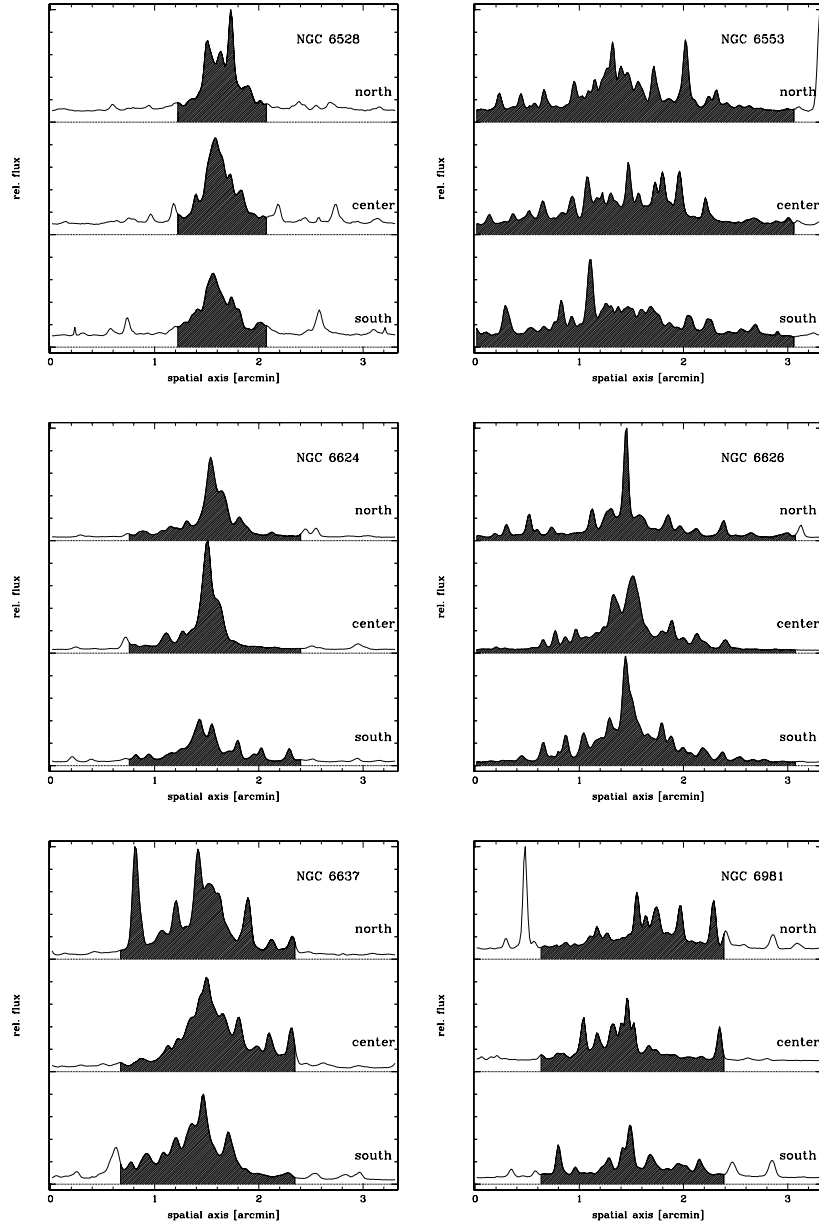
Figure 2.3: – continued. Intensity profiles of each pointing for sample globular clusters NGC 6528, NGC 6553, NGC 6624, NGC 6626, NGC 6637, and NGC 6981.

NGC 6626) are extended and their half-light diameter are just or not entirely covered by the slit. The low radial velocity resolution of our spectra does not allow to distinguish between globular cluster stars and field stars inside the slit. Galactic stellar-population models (e.g. Robin et al. 1996) predict a maximum cumulative amount of 4 stars with magnitudes down to $V = 19.5$ (all stars with $V = 18.5 - 19.5$ mag) towards the Galactic center inside the equivalent of three slits. This maximum estimate applies only to the Baade's Window globular clusters NGC 6528 and NGC 6553. All other fields have effectively zero probability to be contaminated by foreground stars. Nonetheless, even in the worst-case scenario, if 4 stars of 19th magnitude would fall inside one slit, their fractional contribution to the total light would be $\lesssim 1.2 \cdot 10^{-4}$. For globular clusters at larger galactocentric radii this fraction is even lower. Hence, we do not expect a large contamination by foreground disk stars.

One critical case is the northern pointing of NGC 6637 in which a bright star falls inside the half-light radius (see upper panel of the NGC 6637 profile in Fig. 2.3). This star contributes $\lesssim 10\%$ to the total light of the sampled globular cluster and its radial velocity is indistinguishable from the one of NGC 6637. An inspection of DSS images shows that the NGC 6637 field contains more such bright stars which are concentrated around the globular cluster center and are therefore likely to be cluster members. We therefore assume that the star is a member of NGC 6637 and leave it in the spectrum.

2.3.3 Comparison with Previous Measurements

index	offset	dispersion	units
G4300	0.45	0.70	Å
Hβ	0.27	0.57	Å
Mg$_2$	0.009	0.014	mag
Mgb	-0.01	0.27	Å
Fe5270	-0.33	0.44	Å
Fe5335	0.12	0.27	Å

Table 2.5: Offsets and dispersion of the residuals between our data and the literature. Dispersions are $1\,\sigma$ scatter of the residuals.

Lick indices[3] are available in the literature for a few globular clusters in our sample, as we intentionally included these clusters for comparison. The samples of Trager et al. (1998) and Covino et al. (1995) and Cohen et al. (1998) have, respectively, three, six, and four clusters in common with our data. Note that the indices of Covino et al. (1995) and Cohen et al. (1998) were measured with the older passband definitions of Burstein et al. (1984) and are subject to potential systematic offsets. Where necessary we also converted the values of Covino et al. to the commonly used Å-scale for atomic indices and kept the magnitude scale for molecular bands. Table 2.4 summarizes all measurements, including our data. Figure 2.4 shows the comparison of some indices between the previously mentioned data sets and ours. The mean offset in the sense $EW_{data} - EW_{lit.}$ and the dispersion are given in Table 2.5. Most indices agree well with the literature values and have offsets smaller than the dispersion.

Only the Fe5270 index is $0.75\,\sigma$ higher for our data compared with the literature. This is likely to be due to imperfect smoothing of the spectra in the region of ~ 5300

---

[3]We point out the work of Bica & Alloin (1986) who performed a spectroscopic study of 63 LMC, SMC, Galactic globular and compact open clusters. However, the final resolution of their spectra is too low (11 Å) to allow an analysis of standard Lick indices.
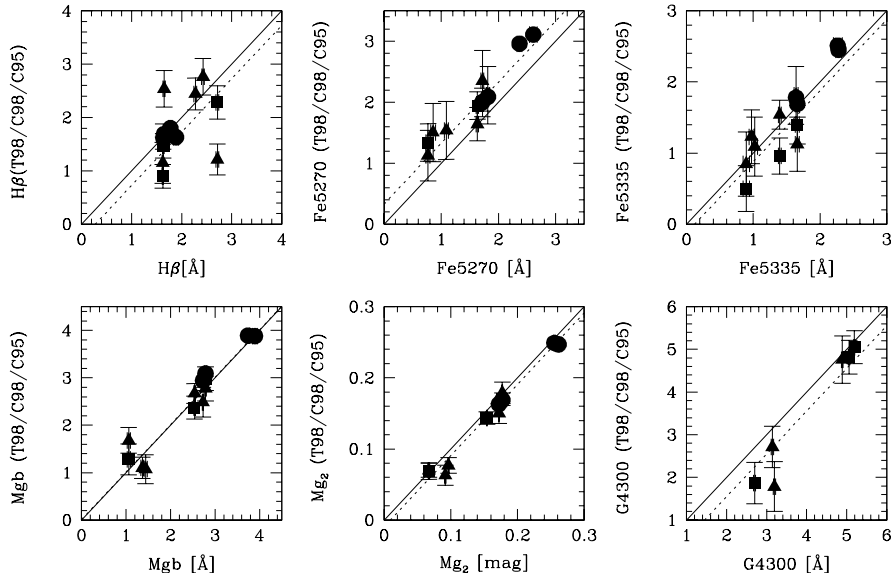
Figure 2.4: Comparison of index measurements of Trager et al. (1998), marked by squares, Cohen et al. (1998), marked by circles (without errors for the Cohen et al. data), and Covino et al. (1995), indicated by triangles, with our data. Solid lines mark the one-to-one relation and dashed lines the mean offsets.

Å. Our smoothing kernel is adjusted according to the Lick resolution given by the linear relations in Worthey & Ottaviani (1997). This relations are fit to individual line resolution data which show a significant increase in scatter in the spectral range around 5300 Å (see Figure 7 in Worthey & Ottaviani 1997). Hence even if our smoothing is correctly applied, the initial fitting of the Lick resolution data by Worthey & Ottaviani might introduce biases which cannot be accounted for a posteriori. However, the offset between the literature and our data is reduced by the use of the synthetic $\langle Fe \rangle$ index which is a combination of the Fe5270 and Fe5335 index. The $\langle Fe \rangle$ index partly cancels out the individual offsets of the former two indices.

2.3.4   Estimating the Sampled Luminosity

The spectrograph slit samples only a fraction of the total light of a globular cluster's stellar population. The less light is sampled the higher the chance that a spectrum is dominated by a few bright stars. In general, globular cluster spectra of less than $10^4 L_\odot$ are prone to be dominated by statistical fluctuations in the number of high-luminosity stars (such as RGB and AGB stars, etc.). For a representative spectrum it is essential to adequately map all evolutionary states in a stellar population, such that no large statistical fluctuations for the short-living phases are expected. We therefore estimate the total sampled luminosity of the underlying stellar population 1) from spectrophotometry of the flux-calibrated spectra and 2) from the integration of globular cluster surface brightness profiles.

As a basic condition of the first method we confirm that all three nights have had photometric conditions using the ESO database for atmospheric conditions at La Silla[4]. We use the flux at 5500 Å in the co-added and background-subtracted

---

[4]http://www.ls.eso.org/lasilla/dimm/

spectra and convert it to an apparent magnitude with the relation

$$m_V = -2.5 \cdot \log(F_\lambda) - (19.79 \pm 0.24) \tag{2.2}$$

where F_λ is the flux in erg cm^{-2}s^{-1}Å^{-1}. The zero point was determined from five flux-standard spectra, which have been observed in every night. Its uncertainty is the 1σ standard deviation of all measurements. After correcting for the distance, the absolute magnitudes were de-reddened using the values given in Harris (1996).[5] The reddening values are given in Table 2.1 along with the distance modulus (Harris 1996). Using the absolute magnitude of the combined globular cluster spectrum, we calculate the total sampled luminosity

$$L_T = BC_V \cdot 10^{-0.4 \cdot (m_V - (m-M)_V - M_\odot - 3.1 \cdot E_{(B-V)})} \tag{2.3}$$

where $M_\odot = 4.82$ mag is the absolute solar magnitude in the V band (Hayes 1985; Neckel 1986a,b). With the bolometric correction BC$_V$ (Renzini 1998; Maraston 1998) we obtain the total bolometric luminosity L_T. The total globular cluster luminosity is compared to the sampled flux and tabulated in Table 2.6 as L_{slit}.

For the integration of the surface brightness profiles we use the data from Trager et al. (1995) who provide the parameters of single-mass, non-rotating, isotropic King profiles (King 1966) for all sample globular clusters. The integrated total V-band luminosities have been transformed to L_T and are included in Table 2.6 as L_{prof}. Note that for most globular clusters the results from both techniques agree well. However, for some globular clusters the integration of the surface brightness profile gives systematically larger values. This is due to the fact that the profiles were calculated from the flux of all stars in a given radial interval whereas the slits sample a small fraction of the flux at a given radius. Hence, the likelihood to sample bright stars which dominate the surface brightness profile falls rapidly with radius. Since bright stars are point sources the slit will most likely sample a smaller total flux than predicted by the surface brightness profile. This effect is most prominent for globular clusters with relatively large half-light radii and waggly intensity profiles (cf. Fig. 2.3).

Among the values reported in Table 2.6, the case of NGC 6528 is somewhat awkward, as the estimated luminosity sampled by the slit is apparently higher than the total luminosity of the cluster, which obviously cannot be. This cluster projects on a very dense bulge field, and therefore the inconsistency probably arises from either an underestimate of the field contribution that we have subtracted from the cluster+field co-added spectrum, or to an underestimate of the total luminosity of the cluster as reported in Harris (1996), or from a combination of these two effects.

From the sampled flux L_{slit} we estimate the number of red giant stars contributing to the total light. Renzini (1998) gives the expected number of stars for each stellar evolutionary phase of a ~ 15 Gyr old, solar-metallicity simple stellar population. In general, in this stellar population the brightest stars which contribute a major fraction of the flux to the integrated light are found on the red giant branch (RGB) which contributes $\sim 40\%$ (Renzini & Fusi Pecci 1988) to the total light. The last two columns of Table 2.6 give the expected number of RGB and upper RGB stars in the sampled light. Upper RGB stars are defined here as those within 2.5 bolometric magnitudes from the RGB tip. The RGB and upper RGB lifetimes are $\sim 6 \cdot 10^8$ and $\sim 1.5 \cdot 10^7$ years, respectively.

Due to the small expected number of RGB and upper RGB stars contributing to the spectra of NGC 6218 and NGC 6637, both spectra are prone to be dominated

---

[5]These reddening values were derived from CMD studies of individual globular cluster and are a reliable estimate of the effective reddening, in contrast to coarse survey reddening maps such as the COBE/DIRBE reddening maps by Schlegel et al. (1998). These maps tend to overestimate the reddening in high-extinction regions.

cluster	F_λ(@5500Å)[a]	$M_V^{\rm b}$	$M_V^{\rm c}$	$BC_V^{\rm d}$	$L_{\rm prof}^{\rm e}$	$L_{\rm slit}^{\rm f}$	$L_{\rm GC}^{\rm g}$	$\frac{L_{\rm slit}}{L_{\rm GC}}$	$N_{\rm RGB}^{\rm h}$	$N_{\rm uRGB}^{\rm i}$
NGC 5927	$(3.6 \pm 0.2) \cdot 10^{-13}$	-5.88	-7.80	1.57	$1.7 \cdot 10^4$	$(3.0 \pm 0.8) \cdot 10^4$	$1.8 \cdot 10^5$	0.171	359	9
NGC 6218	$(2.0 \pm 0.1) \cdot 10^{-13}$	-2.65	-7.32	1.29	$4.0 \cdot 10^3$	$(1.3 \pm 0.3) \cdot 10^3$	$9.3 \cdot 10^4$	0.014	15	0
NGC 6284	$(3.7 \pm 0.1) \cdot 10^{-13}$	-6.27	-7.87	1.32	$1.9 \cdot 10^4$	$(3.6 \pm 0.9) \cdot 10^4$	$1.6 \cdot 10^5$	0.230	435	11
NGC 6356	$(6.4 \pm 0.1) \cdot 10^{-13}$	-6.94	-8.52	1.51	$4.8 \cdot 10^4$	$(7.6 \pm 1.8) \cdot 10^4$	$3.3 \cdot 10^5$	0.233	913	23
NGC 6388	$(2.8 \pm 0.1) \cdot 10^{-12}$	-8.68	-9.82	1.47	$1.6 \cdot 10^5$	$(3.7 \pm 1.0) \cdot 10^5$	$1.1 \cdot 10^6$	0.351	4430	111
NGC 6441	$(2.0 \pm 0.1) \cdot 10^{-12}$	-8.52	-9.47	1.49	$1.3 \cdot 10^5$	$(3.2 \pm 0.9) \cdot 10^5$	$7.8 \cdot 10^5$	0.417	3894	97
NGC 6528	$(4.9 \pm 0.2) \cdot 10^{-13}$	-7.28	-6.93	1.66	$2.3 \cdot 10^4$	$(1.1 \pm 0.3) \cdot 10^5$	$8.3 \cdot 10^4$	$1.376^{\rm j}$	1376	34
NGC 6553	$(2.0 \pm 0.1) \cdot 10^{-13}$	-6.41	-7.99	1.59	$1.5 \cdot 10^4$	$(4.9 \pm 1.4) \cdot 10^4$	$2.1 \cdot 10^5$	0.234	593	15
NGC 6624	$(8.0 \pm 0.7) \cdot 10^{-13}$	-5.78	-7.50	1.54	$1.8 \cdot 10^4$	$(2.7 \pm 0.8) \cdot 10^4$	$1.3 \cdot 10^5$	0.205	322	8
NGC 6626	$(5.6 \pm 0.1) \cdot 10^{-13}$	-5.61	-8.33	1.30	$1.4 \cdot 10^4$	$(1.9 \pm 0.5) \cdot 10^4$	$2.4 \cdot 10^5$	0.082	231	6
NGC 6637	$(8.0 \pm 1.4) \cdot 10^{-14}$	-2.70	-7.52	1.43	$1.5 \cdot 10^4$	$(1.5 \pm 0.6) \cdot 10^3$	$1.2 \cdot 10^5$	0.012	17	0
NGC 6981	$(1.2 \pm 0.1) \cdot 10^{-13}$	-3.95	-7.04	1.31	$7.7 \cdot 10^3$	$(4.2 \pm 1.3) \cdot 10^3$	$7.3 \cdot 10^4$	0.058	50	1
Bulge	$(4.0 \pm 0.3) \cdot 10^{-13}$	-5.14	$\ldots$	1.59	$\ldots$	$(1.5 \pm 0.7) \cdot 10^4$	$\ldots$	$\ldots$	180	5

[a] sampled flux at 5500 Å in erg cm^{-2}s^{-1}Å^{-1}

[b] absolute magnitude of the sampled light

[c] absolute globular cluster magnitude (Harris 1996)

[d] V-band bolometric correction for a 12 Gyr old stellar population calculated for the according cluster metallicity (see Table 2.1). The values were taken from Maraston (1998); Maraston et al. (2003).

[e] sampled bolometric luminosity L_T in $L_\odot$ from the integration of King surface brightness profiles of Trager et al. (1995)

[f] sampled bolometric luminosity L_T in $L_\odot$ calculated from the total light sampled by all slit pointings

[g] globular cluster's total bolometric luminosity L_T in $L_\odot$

[h] expected number of RGB stars contributing to the sampled luminosity

[i] expected number of upper RGB stars ($\Delta M_{\rm Bol} \leq 2.5$ mag down from the tip of the RGB) contributing to the sampled luminosity

[j] see Section 2.3.4

Table 2.6: Sampled and total luminosities of observed globular clusters and bulge. All values have been determined from the co-added spectra of all available pointings. For the co-added bulge spectrum we adopted a mean metallicity of [Fe/H] $\approx$ -0.33 dex (Zoccali et al. 2003).

by a few bright stars. In fact, for both clusters the intensity profiles (see Figure 2.3) show single bright stars. However, the contribution of the brightest single object is $\lesssim 10\%$ (see Sect. 2.3.2) for all spectra. All other spectra contain enough RGB stars to be unaffected by statistical fluctuations in the number of bright stars.

The sampled luminosity of the bulge fields is more difficult to estimate. Uncertain sky subtraction (see problems with "background modeling" in Sect. 2.3.1), and patchy extinction in combination with the bulge's spatial extension along the line of sight make the estimate of the sampled luminosity quite uncertain. Here we simply give upper and lower limits including all available uncertainties. The average extinction in Baade's Window is $\langle A_V \rangle \approx 1.7$ mag and varies between 1.3 and 2.8 mag (Stanek 1996). The more recent reddening maps of Schlegel et al. (1998) confirm the previous measurements and give for our three Bulge fields the extinction in the range $1.6 \lesssim A_V \lesssim 2.1$ mag. We adopt a distance of $8-9$ kpc to the Galactic center and use the faintest and brightest sky spectrum to estimate the flux at 5500 Å. The total sampled luminosity L_T of the final co-added Bulge spectrum is $(1.3-2.6) \cdot 10^4 L_\odot$. Our value is in good agreement with the sampled luminosity derived from surface brightness estimates in Baade's Window and several fields at higher galactic latitudes by Terndrup (1988). According to his V-band surface brightness estimates for Baade's Window and a field at the galactic coordinates $l = 0.1º$ and $b = -6º$, the sampled luminosity in an area equivalent to all our bulge-field pointings in one of the two fields is $(2.6 \pm 0.5) \cdot 10^4 L_\odot$ and $(1.2 \pm 0.3) \cdot 10^4 L_\odot$, respectively.

2.4 Index Ratios in Globular Clusters and Bulge Fields

Figure 2.5 shows two representative spectra of a metal-poor (NGC 6626) and a metal-rich (NGC 6528) globular cluster, together with the co-added spectrum from the 15 bulge pointings.

In the following we focus on the comparison of index ratios between globular clusters and the field stellar population in the Galactic bulge. We include the data of Trager et al. (1998) who measured Lick indices for metal-poor globular clusters and use our index measurements (due to higher S/N) whenever a globular cluster is a member of both data sets.

All Lick indices are measured on the cleaned and co-added globular-cluster and bulge spectra. Statistical uncertainties are determined in bootstrap tests (see App. A.4 for details). We additionally determine the statistical slit-to-slit variations between the different pointings for each globular cluster and estimate the maximum systematic error due to the uncertainty in radial velocity. All line indices and their statistical and systematic uncertainties are documented in Table B.1.

It is worth to mention that the slit-to-slit fluctuations of index values, which are calculated from different pointings (3 and 5 for globular clusters and 15 for the bulge), are generally larger than the Poisson noise of the co-added spectra. Such variations are expected from Poisson fluctuations in the number of bright stars inside the slit and the sampled luminosities of the single spectra correlate well with the slit-to-slit index variations for each globular cluster. More pointings are required to solidify this correlation and to search for other effects such as radial index changes.

2.4.1 The α-element Sensitive Indices vs. $\langle$Fe$\rangle$

α-particle capture elements with even atomic numbers (C, O, Mg, Si, Ca, etc.) are predominantly produced in type II supernovae (Tsujimoto et al. 1995; Woosley & Weaver
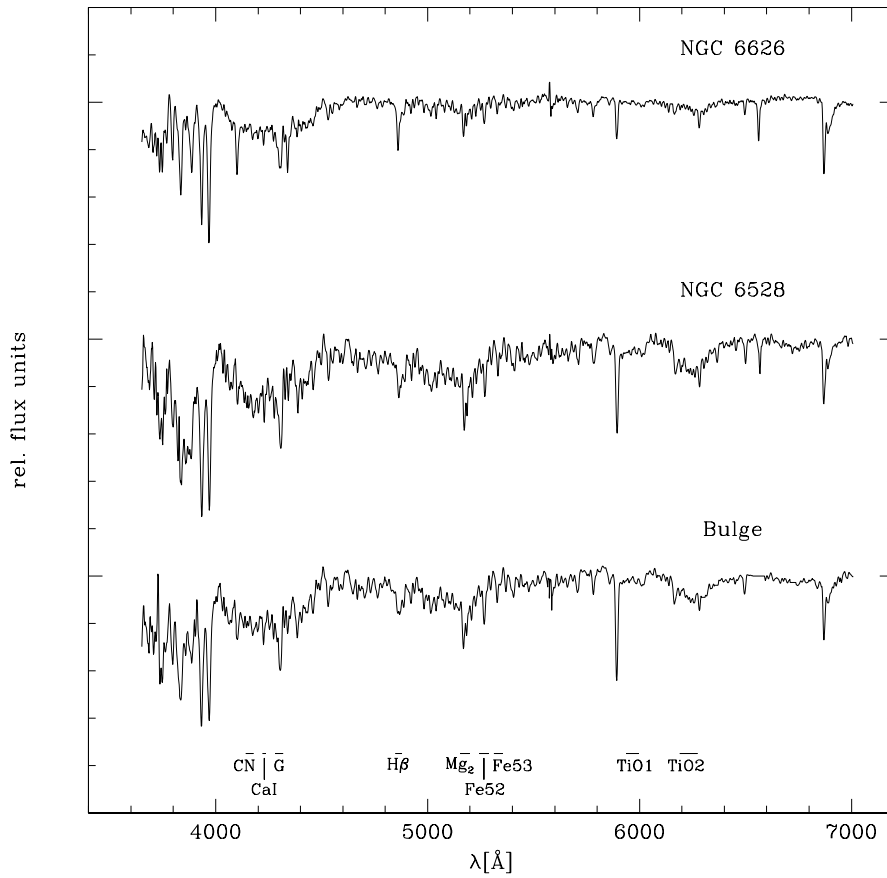
Figure 2.5: Representative spectra of two globular clusters, i.e. NGC 6626 and NGC 6528, and the Galactic bulge. The two clusters represent the limits of the metallicity range which is covered by our sample. NGC 6626 has a mean metallicity [Fe/H]= −1.45 dex. NGC 6528, on the other hand, has a mean metallicity [Fe/H]= −0.17 dex (Harris 1996). Note the similarity between the bulge and the NGC 6528 spectrum. Important Lick-index passbands are indicated at the bottom of the panel.
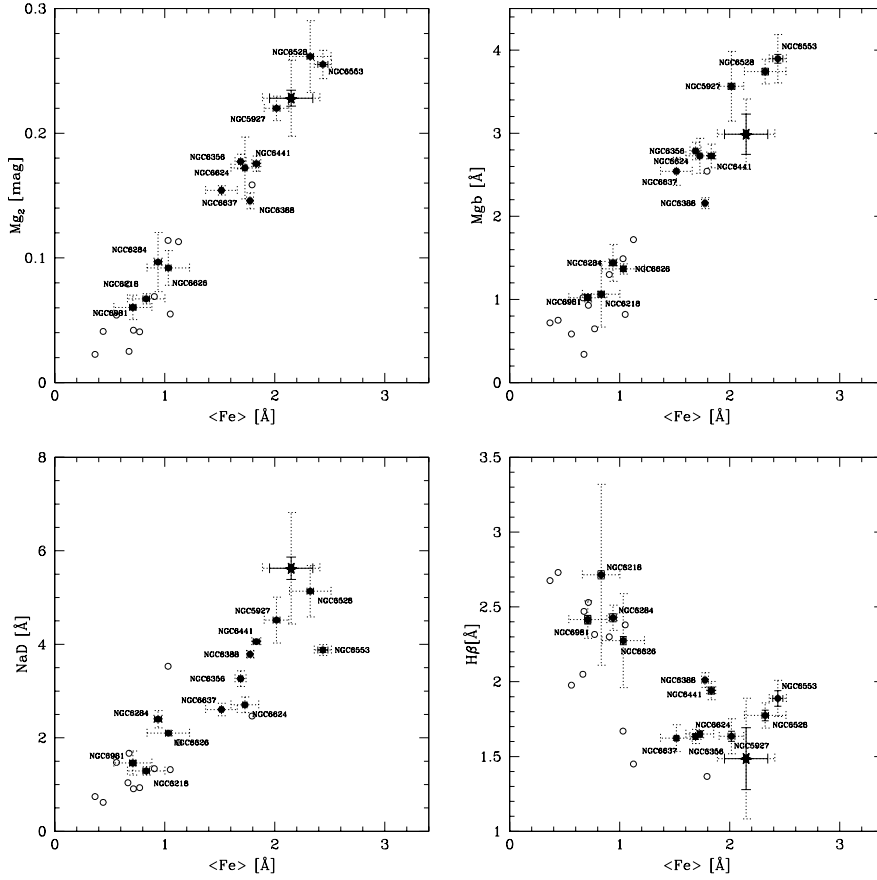
Figure 2.6: Lick-index ratios for Mg_2, Mgb, NaD, $H\beta$ versus the mean iron index $\langle Fe \rangle = (Fe5270 + Fe5335)/2$. Filled dots show the index measurements of our sample globular clusters, whilst open circles show the data of Trager et al. (1998). A solid star indicates the index values derived from the co-added spectrum of the Galactic bulge. Solid error bars show bootstrap errors which represent the total uncertainty due to the intrinsic noise of the co-added spectra. Statistical slit-to-slit fluctuations between different pointings are shown as dotted error bars. Systematic radial velocity errors are not plotted, but given in Table B.1. For clarity reasons no error bars are plotted for the Trager et al. sample which are generally an order of magnitude larger than the intrinsic noise of our spectra. The mean errors of the Trager et al. data are 0.3 Å for the $\langle Fe \rangle$ index, 0.01 mag for Mg_2, and 0.3 Å for Mgb, NaD, and $H\beta$.

Figure 2.6: – continued: G4300, CN_1, TiO_2, and Ca4227 versus $\langle Fe \rangle$. The mean errors of the Trager et al. data are 0.3 Å for the $\langle Fe \rangle$ index, and 0.4 Å, 0.03 mag, 0.01 mag, and 0.4 Å for the G4300, CN_1, TiO_2, and Ca4227 index, respectively.

1995; Thomas et al. 1998). The progenitors of SNe II are massive stars, which explode and pollute the interstellar medium after their short lifetime of some 10^7 years. The ejecta of SNe II have a mean $[\alpha/\text{Fe}] \sim 0.4$ dex. On the other hand, type Ia supernovae eject mainly iron-peak elements ($[\alpha/\text{Fe}] \sim -0.3$ dex) ~ 1 Gyr after the formation of their progenitor stars. Stellar populations which have been created on short timescales are likely to show $[\alpha/\text{Fe}]$ enhancement. The $[\alpha/\text{Fe}]$ ratio is therefore potentially a strong discriminator of star-formation histories. Alternative explanations, however, include a changing IMF slope and/or a changing binary fraction.

Such enhancements have already been suspected and observed in the stellar populations in giant elliptical galaxies (Worthey et al. 1992), the Galactic bulge (McWilliam & Rich 1994), and for disk and halo stars in the Milky Way (Edvardsson et al. 1993; Fuhrmann 1998). A detailed discussion of the $[\alpha/\text{Fe}]$ ratio in our sample globular clusters and their assistance to parameterize simple stellar population models for varying $[\alpha/\text{Fe}]$ ratios will be presented in Chapter 3.

To search for any trends in the index(α)/index(Fe) ratio in the globular cluster population and the bulge we plot supposedly α-element sensitive indices against the mean iron index $\langle \text{Fe} \rangle$. Figure 2.6 shows some representative index measurements for globular clusters and bulge fields. Generally, all the correlations between α-sensitive indices and the mean iron index are relatively tight. For our sample globular clusters a Spearman rank test yields values between 0.87 and 0.97 (1 indicates perfect correlation, -1 anti-correlation) for the indices CN_1, TiO_2, Ca4227, Mgb, Mg_2. The CN_1 and TiO_2 indices show the tightest correlation with $\langle \text{Fe} \rangle$, followed by Mg_2 and Ca4227. All correlations are linear (no higher-order terms are necessary) and hold to very high metallicities of the order of the mean bulge metallicity (filled star in Figure 2.6). The three most metal-rich globular clusters in our sample, i.e. NGC 5927, NGC 6528, and NGC 6553, have roughly the same mean iron index as the stellar populations in the Galactic bulge indicating similar [Fe/H]. This was also found in recent photometric CMD studies of the two latter globular clusters and the bulge (Ortolani et al. 1995b; Zoccali et al. 2003). Ranking by the $\langle \text{Fe} \rangle$ and Mg indices, which are among the best metallicity indicators in the Lick sample of indices (see Sect. 2.5), the most metal-rich globular cluster in our sample is NGC 6553, followed by NGC 6528 and NGC 5927.

The comparison of some α-sensitive indices of globular clusters and the bulge requires some further words. The Ca4227, Mgb, and Mg_2 index of the bulge light is in good agreement with the sequence formed by globular clusters. All deviations from this sequence are of the order of $\lesssim 1\sigma$ according to the slit-to-slit variations. One exception is the CN index which is significantly higher in metal-rich globular clusters than in the bulge. We discuss this important point in Section 2.4.2. In general, our data show that the ratio of α-sensitive to iron-sensitive indices is comparable in metal-rich globular clusters and in the stellar population of the Galactic bulge.

Likely super-solar $[\alpha/\text{Fe}]$ ratios in globular clusters and the bulge were shown in numerous high-resolution spectroscopy studies. From a study of 11 giants in Baade's window McWilliam & Rich (1994) report an average $[\text{Mg/Fe}] \approx 0.3$ dex, while Barbuy et al. (1999) and Carretta et al. (2001) find similar $[\text{Mg/Fe}]$ ratios in two red giants in NGC 6553 and in four red horizontal branch stars in NGC 6528. Similarly, McWilliam & Rich find $[\text{Ca/Fe}] \approx 0.2$ dex, which is reflected by the former observations in globular clusters. Although the studied number of stars is still very low, the first high-resolution spectroscopy results point to a similar super-solar α-element abundance in both Milky Way globular clusters and the bulge which is supported by our data.

2.4.2   CN vs. ⟨Fe⟩

The CN index measures the strength of the CN absorption band at 4150 Å. The Lick system defines two CN indices, CN_1 and CN_2 which differ slightly in their continuum passband definitions. The measurements for both indices give very similar results, but we prefer the CN_1 index due to its smaller calibration biases (see Fig. 2.2) and refer in the following to CN_1 as the CN index.

Like for most other indices, the CN index of globular clusters correlates very tightly with the ⟨Fe⟩ index, following a linear relation (see Figure 2.6). A Spearman rank test yields 0.97 as a correlation coefficient. The apparent gap at CN ~ 0 mag is a result of the bimodal distribution of metallicity in our cluster sample, and similar gaps are recognizable in all other index vs. ⟨Fe⟩ diagrams.

Quite striking is the comparison of the bulge value of the CN index with that of globular clusters at the same value of the ⟨Fe⟩ index: the CN index of the bulge is significantly offset to a lower value by ~ 0.05 mag, corresponding to at least a 2σ effect. This is also evident from Figure 2.5, showing that the CN feature is indeed much stronger in the cluster NGC 6528 than in the bulge spectrum. We also note that the CN index of NGC 6528 and NGC 6553 is as strong as in the most metal-rich clusters in M31 studied by Burstein et al. (1984).

It is well known that globular cluster stars often exhibit so-called *CN anomalies*, with stars in a cluster belonging either to a CN-strong or a CN-weak group (see Kraft 1994 for an extended review). Among the various possibilities to account for these anomalies, accretion of AGB ejecta during the early phases of the cluster evolution appears now the most likely explanation (Kraft 1994; Ventura et al. 2001), as originally proposed by D'Antona et al. (1983) and Renzini (1983). In this scenario, some $\sim 30 \times 10^6$ years after cluster formation (corresponding to the lifetime of $\sim 8\,M_\odot$ stars) the last Type II supernovae explode and AGB stars begin to appear in the cluster. Then the low-velocity AGB wind and super-wind materials may accumulate inside the potential well of the cluster, and are highly enriched in carbon and/or nitrogen from the combined effect of the third dredge-up and envelope-burning processes (Renzini & Voli 1981). Conditions are then established for the low-mass stars (now still surviving in globular clusters) having a chance to accrete carbon and/or nitrogen-enriched material, thus preparing the conditions for the CN anomalies we observe in today clusters. One of the arguments in favor of the accretion scenario is that field stars do not share the CN anomalies of their cluster counterparts (Kraft et al. 1982). Indeed, contrary to the case of clusters, in the field no localized, high-density accumulation of AGB ejecta could take place, and low-mass stars would have not much chance to accrete AGB processed materials. In the case of the bulge, its much higher velocity dispersion (~ 100 km s^{-1}) compared to that of clusters (few km s^{-1}) would make accretion even less likely. In conclusion, we regard the lower CN index of the bulge relative to metal-rich globular clusters as consistent with – and actually supporting – the accretion scenario already widely entertained for the origin of CN anomalies in globular-cluster stars.

2.4.3   Hβ vs. ⟨Fe⟩

Figure 2.6 shows a plot of Hβ vs. ⟨Fe⟩. The Spearman rank coefficient for the globular cluster sequence is -0.52 indicating a mild anti-correlation. At high ⟨Fe⟩, the Hβ index of globular clusters is slightly stronger than that of the bulge field. However, the values are consistent with each other within $\sim 1\sigma$, with the large slit-to-slit variations exhibited by the bulge spectra being a result of the lower luminosity sampling due to the lower surface brightness in Baade's Window compared to globular clusters.

The two clusters NGC 6441 and NGC 6388 show somewhat stronger Hβ com-

pared to clusters with similar $\langle\text{Fe}\rangle$ index. This offset is probably caused by the conspicuous blue extension of the HB of these two clusters, a so far unique manifestation of the "second parameter" effect among the metal-rich population of bulge globular clusters (Rich et al. 1997). Contrary to NGC 6441 and NGC 6388, the other globular clusters with comparable $\langle\text{Fe}\rangle$ indices (i.e. NGC 5927, NGC 6356, NGC 6624, and NGC 6637) have without exception purely red horizontal branches (HBR= −1.0).

Also the two most metal-rich clusters in our sample, NGC 6553 and NGC 6528, appear to have a somewhat stronger Hβ compared to a linear extrapolation of the trend from lower values of the $\langle\text{Fe}\rangle$ index. In this case, however, the relatively strong Hβ cannot be ascribed to the HB morphology, since the HB of these two clusters is purely red (Ortolani et al. 1995a; Zoccali et al. 2001). In principle, a younger age would produce a higher Hβ index, but optical and near-infrared HST color-magnitude diagrams of these two clusters indicate they are virtually coeval with halo clusters (Ortolani et al. 1995a, 2001; Zoccali et al. 2001; Feltzing et al. 2002). So, we are left without an obvious interpretation of the relatively strong Hβ feature in the spectra of these clusters. Perhaps the effect is just due to insecure sampling, i.e., to statistical fluctuations in the stars sampled by the slit in either the cluster or in the adjacent bulge field used in the background subtraction. Another reason for the offset might be the increasing dominance of metallic lines inside the Hβ feature passband which could artificially increase the index value.

2.4.4   Other Indices vs. $\langle\text{Fe}\rangle$

NaD – The correlation coefficient for this index pair is 0.94. Globular clusters and bulge compare well within the errors. Both stellar populations follow, within their uncertainties, the same trend. A clear exception from this correlation is NGC 6553, which shows a significantly lower NaD index for its relatively high $\langle\text{Fe}\rangle$ than the sequence of all other globular clusters. The reason for this offset is unclear.

G4300 – The G4300 index predominantly traces the carbon abundance in the G band. For giants, its sensitivity to oxygen is about 1/3 of that to carbon (Tripicco & Bell 1995). The metal-rich globular clusters fall in the same region as the bulge data. In combination with the CN index which mainly traces the CN molecule abundance, this implies that the offset between bulge and globular clusters in the CN vs. $\langle\text{Fe}\rangle$ plot is most likely due to an offset in the nitrogen abundance between bulge and clusters.

TiO – The TiO abundance is measured by the TiO_1 and TiO_2 indices. Both indices do not differ in their correlation with the mean iron index (Spearman rank coefficient 0.96), but we use TiO_2 because of its better calibration. In Figure 2.6 we plot TiO_2 vs. $\langle\text{Fe}\rangle$ which shows the strongest indices for NGC 6553 and NGC 6528, followed by NGC 5927 and the bulge.

The absorption in the TiO band sensitively depends on T_{eff} which is very low for very metal-rich RGB stars. While the strongest TiO bands are observed in metal-rich M-type giants almost no absorption is seen in metal-rich K-type RGB stars. As T_{eff} decreases towards the RGB tip, a large increase in the TiO-band absorption occurs which drives the observed bending of the upper RGB in color-magnitude diagrams, in particular those which use V-band magnitudes (Carretta & Bragaglia 1998; Saviane et al. 2000). In fact, the most metal-rich globular clusters in the Milky Way, e.g. NGC 6553 and NGC 6528, show the strongest bending of the RGBs (e.g. Ortolani et al. 1991; Cohen & Sleeper 1995). Figure 2.6 shows that the slit-to-slit scatter is extremely large for the metal-rich data. This is likely reflecting the sparsely populated upper RGB. In other words, for metal-rich stellar populations the TiO index is prone to be dominated by single bright stars which increase the slit-to-slit scatter due to statistically less significant sampling (see also the high

slit-to-slit scatter of NGC 6218 due to its small luminosity sampling). Another Ti-sensitive index in the Lick system is Fe4531 (Gorgas et al. 1993). It shows similar behaviour as a function of $\langle\text{Fe}\rangle$.

index	a	b	c	r.m.s.
Mg_2	-2.46 ± 0.10	16.24 ± 1.81	-29.88 ± 6.52	0.151
Mgb	-2.53 ± 0.14	1.11 ± 0.16	-0.14 ± 0.04	0.182
$\langle\text{Fe}\rangle$	-2.83 ± 0.21	1.91 ± 0.36	-0.35 ± 0.13	0.199
[MgFe]	-2.76 ± 0.14	1.59 ± 0.20	-0.26 ± 0.06	0.150
Hβ	-1.99 ± 2.26	2.09 ± 2.24	-0.78 ± 0.54	0.384
CN_1	-0.83 ± 0.11	6.84 ± 0.86	-17.12 ± 13.47	0.314

index	d	e	f	r.m.s.
Mg_2	0.29 ± 0.01	0.22 ± 0.02	0.05 ± 0.01	0.016
Mgb	4.46 ± 0.19	3.51 ± 0.35	0.79 ± 0.14	0.254
$\langle\text{Fe}\rangle$	2.68 ± 0.12	1.85 ± 0.23	0.39 ± 0.09	0.167
[MgFe]	3.45 ± 0.13	2.55 ± 0.24	0.55 ± 0.10	0.173
Hβ	1.55 ± 0.20	-0.33 ± 0.37	0.08 ± 0.15	0.271
CN_1	0.16 ± 0.02	0.26 ± 0.04	0.06 ± 0.02	0.032

Table 2.7: Coefficients of the index vs. [Fe/H] relations. The r.m.s. ($\sqrt{\chi^2/n}$) is given in the units of the parameterization (in dex in equation 2.4 and in Å or mag in equation 2.5).

2.5   Index-Metallicity Relations

We use the mean [Fe/H] values from the 1999 update of the McMaster catalog (Harris 1996) to create parabolic relations between line indices and the globular cluster metallicity as expressed by [Fe/H], based on the Zinn-West scale[6] (Zinn & West 1984). Together with the globular cluster data of Trager et al. (1998) the sample comprises 21 Galactic globular cluster with metallicities $-2.29 \leq$[Fe/H]≤ -0.17. Figure 2.7 shows six indices as a function of [Fe/H] most of which show tight correlations. Least-square fitting of second-order polynomials

$$[\text{Fe/H}] = a + b \cdot (\text{EW}) + c \cdot (\text{EW})^2 \tag{2.4}$$
$$\text{EW} = d + e \cdot [\text{Fe/H}] + f \cdot [\text{Fe/H}]^2 \tag{2.5}$$

where EW is the index equivalent width in Lick units, allows a simple parameterization of these sequences as index vs. [Fe/H] and vice versa. The obtained coefficients are summarized in Table 2.7. Higher-order terms improve the fits only marginally and are therefore unnecessary.

These empirical relations represent metallicity calibrations of Lick indices with the widest range in [Fe/H] ever obtained. Note that the best metallicity indicators in Table 2.7 are the [MgFe] and Mg_2 indices both with a r.m.s. of 0.15 dex. Leaving out globular clusters with poor luminosity sampling and relatively uncertain background subtraction (i.e. NGC 6218, NGC 6553, NGC 6626, and NGC 6637) changes the coefficients only little within their error limits. In particular, the high-metallicity part of all relations is not driven by the metal-rich globular cluster NGC 6553.

We point out that all relations could be equally well fit by first-order polynomials if the metal-rich clusters are excluded. Consequently, such linear relations would overestimate the metallicity for a given index value at high metallicities (except for Hβ which would underestimate [Fe/H]; however, Hβ is anyway not a good metallicity indicator). This clearly emphasizes the caution one has to exercise when deriving

---

[6]Note that to derive [Z/H] from [Fe/H], the [α/Fe] of the globular clusters needs to be accounted for.
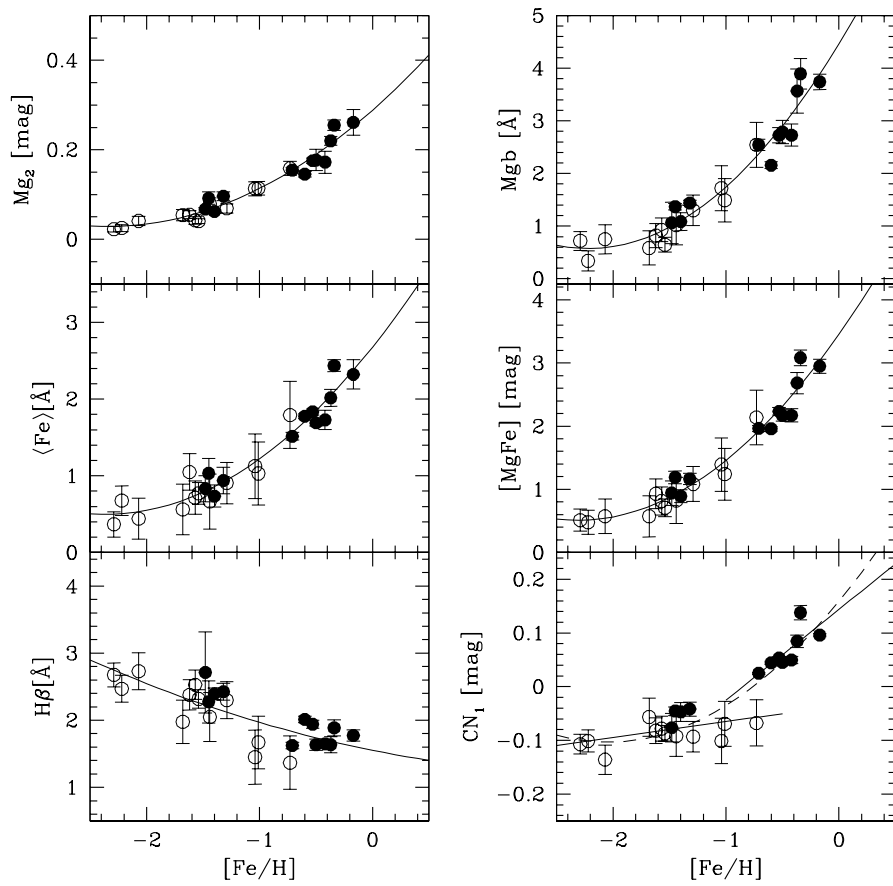
Figure 2.7: Line indices as a function of mean globular cluster metallicity. Our sample globular clusters are shown as filled circles while the open circles denote the globular cluster data of Trager et al. (1998).

mean metallicities from SSP models which have been extrapolated to higher metal-licities. The current sample enables a natural extension of the metallicity range for which Lick indices can now be calibrated. In Chapter 3 we compare the data with the predictions of SSP models.

We also point out that the fitting of the CN index improves when CN> 0 and CN< 0 data are fit separately by first-order polynomials. The lines are indicated in Figure 2.7. Their functional forms are

$$\text{CN} = \quad (0.14 \pm 0.03) + (0.17 \pm 0.06) \cdot [\text{Fe/H}] \quad : \text{CN} > 0$$
$$\text{CN} = \quad (-0.04 \pm 0.02) + (0.03 \pm 0.01) \cdot [\text{Fe/H}] \quad : \text{CN} < 0$$

with reduced χ^2 of 0.025 and 0.023. The inverse relations are

$$[\text{Fe/H}] = \quad (-0.69 \pm 0.09) + (3.54 \pm 1.18) \cdot \text{EW} \quad : \text{CN} > 0$$
$$[\text{Fe/H}] = \quad (-0.86 \pm 0.32) + (8.10 \pm 3.86) \cdot \text{EW} \quad : \text{CN} < 0$$

with a r.m.s. of 0.115 and 0.380. The change in the slope occurs at [Fe/H]~ -1.0 dex and is significant in both parameterizations. The metallicity sensitivity in the metal-poor part is around six times smaller than in the metal-rich part. Only the inclusion of metal-rich bulge globular clusters allows the sampling of the transition region between the shallow and the steep sequence of the CN vs. [Fe/H] relation.

2.6   Galactocentric Index Variations

In Figure 2.8 we plot some Lick indices as a function of galactocentric radius R_{GC}. To increase the range in radius, we again merge our sample with the data for metal-poor halo globular cluster of Trager et al. (1998). The galactocentric radius was taken from the 1999 update of the McMaster catalog of Milky Way globular clusters (Harris 1996). Our compilation includes now both bulge and halo globular clusters and spans a range $\sim 1-40$ kpc in galactocentric distance.

All metal indices show a gradually declining index strength as a function of R_{GC}. The inner globular clusters show a strong decrease in each index out to ~ 10 kpc. The sequence continues at apparently constant low values out to large radii. Furthermore, some indices (CN, Mgb, and $\langle$Fe$\rangle$) show a dichotomy between the bulge and the halo globular cluster system. While the Mgb and $\langle$Fe$\rangle$ indices clearly reflect the bimodality in the metallicity distribution of Milky Way globular clusters, the striking bimodality in the CN index is more difficult to understand. In the context of Section 2.4.2 this may well be explained by evolutionary differences between metal-rich bulge and metal-poor halo globular clusters.

The behavior of Hβ differs from that of the other indices. There is no clear sequence of a decreasing index as a function of R_{GC}, as for the metal-sensitive indices. Instead we measure a mean Hβ index with 2.1 ± 0.5 Å. The strength of the Balmer series is a function of T_{eff}. In old stellar populations, relatively hot stars, which contribute significantly to the Balmer-line strength of the integrated light, are found at the main sequence turn-off and on the horizontal branch. The temperature of the turn-off is a function of age and metallicity while the temperature of the horizontal branch is primarily a function of metallicity and, with exceptions, of the so-called "second parameter".

In the following we focus on the correlation of the horizontal branch morphology on the Hβ index (see also App. F.2). We use the horizontal branch morphology parameter HBR from the McMaster catalog which is defined as

$$\text{HBR} = (B - R)/(B + V + R)$$
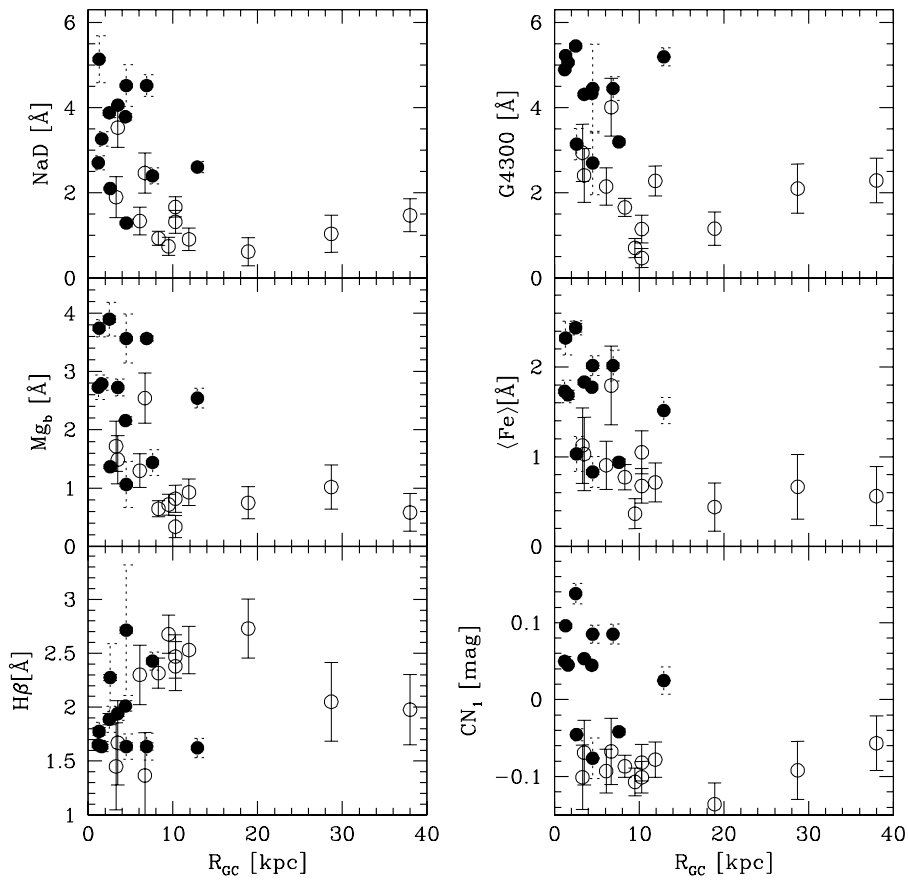
Figure 2.8: Various line indices as a function of galactocentric radius $R_{\rm GC}$. Filled dots show our sample globular clusters. Their error bars are split into the Poisson error (solid error bars which are very small) and slit-to-slit variations (dashed error bars) Open circles mark the globular clusters from Trager et al. (1998).

where B and R are the number of stars bluewards and redwards of the instability strip and V is the number of variable stars inside the instability strip. Figure 2.9 shows that the HBR parameter vs. R_{GC} follows a similar trend as Hβ vs. R_{GC} in Figure 2.8. This supports the idea that the change in Hβ (as a function of R_{GC}) is mainly driven by the change of the horizontal branch morphology as one goes to more distant halo globular clusters with lower metallicities. Indeed, the lower panel in Figure 2.9 shows that HBR is correlated with the Hβ index (Spearman rank coefficient 0.77). The functional form of this correlation is

$$\text{HBR} = (-3.71 \pm 0.41) + (1.75 \pm 0.19) \cdot \text{H}\beta \qquad (2.6)$$

with an r.m.s. of 0.39 which is marginally larger than the mean measurement error (0.36). That is, the scatter found can be fully explained by observational uncertainties. Note that according to this relation the Hβ index can vary by ~ 1 Å when changing the horizontal branch morphology from an entirely red to an entirely blue horizontal branch (see also de Freitas Pacheco & Barbuy 1995). This behaviour is also predicted by previous stellar population models (e.g. Lee et al. 2000; Maraston & Thomas 2000).

Figure 2.9 implies that the change of Hβ is mainly driven by the horizontal branch morphology which itself is influenced by the mean globular cluster metallicity. However, we know of globular cluster pairs – so-called "second parameter" pairs –, such as the metal-poor halo globular clusters NGC 288 and NGC 362 ([Fe/H]≈ -1.2, Catelan et al. 2001) and the metal-rich bulge clusters NGC 6388 and NGC 6624 ([Fe/H]≈ -0.5, Rich et al. 1997; Zoccali et al. 2000b), with very similar metallicities and different horizontal branch morphologies. In fact, NGC 6388 (and NGC 6441, another metal-rich cluster in our sample also featuring a blue horizontal branch) shows a stronger Hβ index than other sample globular clusters at similar metallicities (see Section 2.4.3). Clearly, metallicity cannot be the only parameter which governs the horizontal branch morphology. In the context of the "second-parameter effect" other global and non-global cluster properties (Freeman & Norris 1981) impinging on the horizontal branch morphology have been discussed of which the cluster age and/or several other structural and dynamical cluster properties are suspected to be the best candidates (e.g. Fusi Pecci et al. 1993; Rich et al. 1997). Our sample does not contain enough "second parameter" pairs to study the systematic effects these "second parameters" might have on Hβ, such as the correlation of the residuals of the HBR-Hβ relation as a function of globular cluster age or internal kinematics. A larger data set would help to solve this issue.

2.7   Conclusions

For the first time the complete set of Lick indices have been measured for a sample of metal-rich globular clusters belonging to the Galactic bulge. In combination with data for metal-poor globular clusters this data set has allowed us to establish an empirical calibration of the Lick indices of old stellar populations from very low metallicities all the way to near solar metallicity. On the one hand, these empirical relations can be directly used to get age and chemical composition information for the stellar populations of unresolved galaxies. On the other hand, they can be used to submit to most stringent tests of population synthesis models, an aspect which is the subject of Chapter 3.

The comparison of the Lick indices for the Galactic bulge with those of globular clusters shows that the bulge and the most metal-rich globular clusters have quite similar stellar populations, with the slightly deviating values of some of the bulge indices being the likely result of the metallicity distribution of bulge stars, which extends down to [Fe/H]$\simeq -1.0$ (McWilliam & Rich 1994; Zoccali et al. 2003). Within
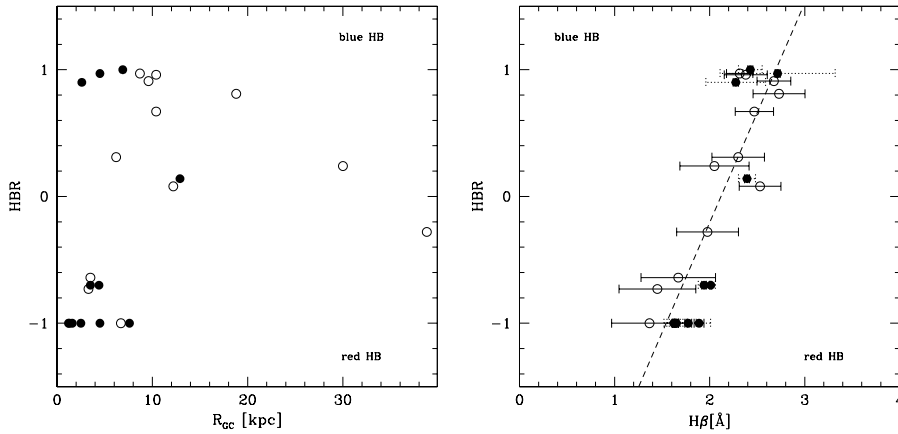
Figure 2.9: Horizontal branch morphology in terms of the HBR parameter as a function of galactocentric radius R_{GC} (upper panel) and $H\beta$ (lower panel). Filled and open circles show our globular cluster data and the data of Trager et al. (1998), respectively.

the uncertainties, both the metal-rich clusters and the bulge appear to have also the same index ratios, in particular those sensitive to [α/Fe]. This implies similar enhancements for individual α-elements in clusters as in the field. Existing spectroscopic determinations of the α-element enhancement in clusters and bulge field stars are still scanty, but extensive high-resolution spectroscopy at 8–10m class telescopes will soon provide data for a fully empirical calibration of the Lick indices at the [α/Fe] values of the bulge and bulge globular clusters.

Some other line index ratios, such as $CN/\langle Fe \rangle$, show clear exceptions. In these cases the bulge indices are definitely below the values for the metal-rich clusters. Several possibilities have been discussed for the mechanism responsible for the CN index offset between the bulge and the clusters, the environmental-pollution being active in clusters (but not in the field) appearing as the most likely explanation. In this scenario, globular cluster stars would have experienced accretion of materials lost by cluster AGB stars, early in the history of the clusters (i.e., when clusters were $\sim 10^8 - 10^9$ years old).

Chapter 3

Calibration of Stellar Population Models[1]

3.1 Introduction

In this Chapter[1] we analyse the data of Chapter 2 by means of SSP model predictions. The data is used to calibrate model predictions up to solar metallicity. With these model predictions, we compare index measurements of Galactic globular clusters, the Galactic bulge, and the diffuse light of early-type galaxies to test the hypothesis of similar chemical composition of the three stellar systems.

Galactic spheroids, i.e., elliptical galaxies and the bulges of spirals, include a major fraction (perhaps the majority) of the stellar mass in the nearby universe (e.g., Fukugita et al. 1998). From the uniformity of their fundamental properties at low as well as high redshift ($z \lesssim 1$) it has been inferred that the bulk of stars in spheroids must be very old, likely to have formed at $z > 2 - 3$ (see Renzini 1999 for a comprehensive review; see also Peebles 2002). Moreover, the space density of passively evolving galaxies at $z \sim 1$ is consistent with the bulk of massive spheroids being already in place and 2-3 Gyr old at this early epoch (Cimatti et al. 2002a,b). Current renditions of hierarchical galaxy formation in CDM dominated universes have so far failed to predict these empirical findings, favoring instead a late formation with major activity even below $z \sim 1$. The culprit is probably in the ways in which star formation and feedback processes have been parameterized and implemented in the so-called semi-analytic models of galaxy formation and evolution (e.g., Kauffmann & Charlot 1998; Cole et al. 2001; Somerville et al. 2001; Menci et al. 2002).

Given our poor understanding of the star formation and feedback processes, the detailed study of the stellar populations in nearby galaxies (the *fossil* records) can provide important clues on their early formation phases, complementary to the direct observation of very high-z galaxies. Indeed, the ages and metallicities of the stellar populations of a galaxy are useful constraints to its formation mechanism. However, the determination of absolute ages and metallicities of composite stellar populations from their integrated spectra is hampered by well known degeneracy effects (Faber 1972; O'Connell 1976; Renzini 1986; Worthey 1994; Maraston & Thomas 2000), and a further complication arises when the abundances of major chemical elements (iron, magnesium, oxygen, etc.) are considered, as traced by narrow-band spectroscopic indices such as the so-called Lick indices, Mg_2, $\langle Fe \rangle$, $H\beta$, etc. (Burstein et al. 1984; Faber et al. 1985; Worthey et al. 1994).

---

[1]The content of this Chapter was published in Maraston, C., Greggio, L., Renzini, A., Ortolani, S., Saglia, R. P., Puzia, T. H., & Kissler-Patig, M. 2003, A&A 400, 823.

The application of this technique to ellipticals revealed that the observed relation between magnesium and iron indices (Mg_2 or $Mg\,b$ vs. $\langle Fe \rangle$) disagrees with the predictions of population synthesis models where the Mg/Fe ratio is assumed to be solar. Observed magnesium indices at given iron are significantly *stronger* than in the models (see Fig. 2 in Worthey et al. 1992). This finding was confirmed by several subsequent studies for other samples of ellipticals (Davies et al. 1993; Carollo & Danziger 1994; Fisher et al. 1995; Jørgensen 1997, Kuntschner & Davies 1998; Mehlert et al. 1998; Longhetti et al. 2000; Thomas et al. 2002a.)

If Lick indices of magnesium and iron trace the corresponding element abundances, *and* the models that are meant for solar ratios of these elements are correct, then the observed indices imply a supersolar Mg/Fe ratio in ellipticals. In turn, according to common wisdom this implies short ($t \lesssim 1$ Gyr) star formation timescales for the stellar populations of ellipticals (e.g., Matteucci 1994; Thomas et al. 1999). In fact, the so-called α-elements (i.e., O, Mg, Ca, Ti, and Si) are promptly released by massive, short-living ($\lesssim 3 \times 10^7$ yrs) progenitors exploding as Type II supernovae, while most iron comes from Type Ia supernovae, whose progenitors span evolutionary timescales from over $\sim 3 \times 10^7$ yrs to many Gyrs (e.g., Greggio & Renzini 1983; Matteucci & Greggio 1986; Pagel 2001)). Therefore, a high α-over-iron ratio ($[\alpha/Fe]$) implies that star formation ceased before the bulk of Type Ia supernovae had the time to enrich with iron the interstellar medium while this was still actively forming stars. Such a short star formation timescale appears to be at variance with the predictions of current hierarchical models for the formation of elliptical galaxies (Thomas 1999; Thomas & Kauffmann 1999), which predict star formation to continue for several Gyrs. In conclusion, the Lick indices of magnesium and iron appear to offer a unique opportunity to estimate the timescale of star formation in galactic spheroids, hence to help for a better understanding of the early formation phases of galaxies.

However, a caveat is in order over the above chain of arguments: how well do Lick indices trace element abundances? Are we sure that population synthesis models correctly predict the values of these indices? (for early discussions of these issues see Tripicco & Bell 1995; Greggio 1997; Tantalo et al. 1998). Indeed, the population synthesis models on the basis of which the magnesium overabundance has been inferred were *not calibrated*, especially in the metallicity range (solar and above) which is relevant to elliptical galaxies. Hence, it could not be excluded that the population synthesis models would underpredict the strength of the magnesium indices, while the Mg/Fe ratio of ellipticals would actually be solar. By calibration of the indices we mean the comparison of their synthetic values with the corresponding quantities measured on objects for which the age and the detailed chemical composition - total metallicity and element abundance ratios - are independently known. For this comparison the best *stellar population templates* are the Galactic globular clusters. However, existing databases of Lick indices of globular clusters (Burstein et al. 1984; Covino et al. 1995) are restricted to the metal-poor objects of the Halo. The most metal rich cluster in the Covino et al. sample is 47 Tuc ($[Fe/H] \sim -0.7$) whose Mg_2 is ~ 0.18 mag, much less than found among ellipticals, which span from $Mg_2 \sim 0.2$ to ~ 0.4 mag.

Globular clusters that are more metal rich than 47 Tuc do actually exist in the Galactic bulge, reaching $Z \sim Z_\odot$ for NGC 6553 and NGC 6528 (Barbuy et al. 1999; Cohen et al. 1999). Cohen et al. (1998) have measured some of the Lick indices for these two clusters, but did so using the Burstein et al. (1984) passbands to define the indices. This does not allow a direct comparison with the theoretical models, which are based on the passbands defined by Worthey et al. (1994). Gregg (1994) measures and analyses spectral indices for several Milky Way GCs including metal-rich objects, among which NGC 6528. Though similar, these spectral indices are not in the Lick system. In Section 3.3 we show that in a model calibration it is

crucial that data and models are set up on the same system, because there are sizable differences in the value of some of the indices, depending on the adopted passbands. Therefore, we obtained optical spectra for a sample of Bulge globular clusters with metallicities [Fe/H] $\gtrsim -0.5$ (including NGC 6528 and NGC 6553), plus some metal-poor globular clusters in order to check the models on a wide metallicity range. In fact, existing Lick indices of metal poor globular clusters (e.g. Covino et al. 1995: Cohen et al. 1998) were also measured in the Burstein et al. (1984) system. The results of the measurement of the indices in the Lick/IDS system are reported in Chapter 2 of this thesis (see also Puzia et al. 2002b).

For at least some of the program clusters the abundance ratios of α-elements to iron are known from high resolution spectroscopy of individual stars in these clusters (Barbuy et al. 1999; Cohen et al. 1999, Carretta et al. 2001; Coelho et al. 2001). While there is certainly room for further improvements in the abundance determinations, these studies indicate an overabundance [α/Fe] $\sim 0.2 - 0.3$ for these clusters. Moreover, their age, determined from color-magnitude diagrams, is virtually identical to the age of Halo globular clusters, i.e., 12–13 Gyr (Ortolani et al. 1995; Rosenberg et al. 1999; Feltzing & Gilmore 2000, Zoccali et al. 2001). Having fairly accurate estimates for their basic parameters (age, [Fe/H], [α/Fe], the measured Lick indices of Bulge globular clusters are used to calibrate the population synthesis models and to test the "magnesium overabundance" solution for ellipticals.

3.2 The Globular Cluster Data

Optical spectra ($3400 < \lambda < 7500$ Å) have been obtained with the Boller & Chivens spectrograph at the ESO 1.5m telescope for a sample of 12 globular clusters (GCs) mostly located in the Galactic bulge and for several (15) positions in the bulge field known as Baade's Window. The data acquisition, reduction and the resulting indices in the Lick system are fully described in Chapter 2. Here we summarize some key features of the data, which are useful to the present discussion.

The target GCs have been selected on the basis of two requirements. First, a high metallicity in order to extend the model calibration towards the range most relevant to ellipticals. Among the 12 clusters in the sample, 7 clusters have metallicities [Fe/H] $\gtrsim -0.5$ (on the scale of Zinn & West, 1984), the most metal-rich ones being NGC 6528 and NGC 6553. The remaining 5 clusters are more metal-poor, and were included in the sample to check consistency with previous studies (e.g. Trager et al. 1998). Second, the availability of independent estimates of element abundances, total metallicities and ages, in order to allow for the empirical calibration of the synthetic indices. As already mentioned, estimates of the metallicity and [α/Fe] ratios are available for the two well-studied clusters NGC 6553 and NGC 6528, which ensures a meaningful model calibration around solar metallicity. For the remaining clusters estimates of the metallicity in the Zinn & West scale and in the Carretta & Gratton (1997) scale are available. This allows us to use the clusters to calibrate the metallicity scale of the models in a relative sense. Nevertheless, it would clearly be useful to extend the detailed elemental abundance determinations to all the clusters in the sample.

Special care has been paid to subtract the foreground/background light from the cluster's light. Indeed, the field and clusters stellar population components in the Bulge appear to be virtually coeval, and to span similar metallicity ranges (Ortolani et al. 1995; Zoccali et al. 2002). The very similar, though not identical, spectral energy distribution of the bulge light could therefore introduce spurious effects on the measurement of the cluster indices, if not adequately subtracted.

The luminosities sampled in the GCs and the bulge fields by the slit of the spectrograph have been carefully evaluated in order to assess the dependence of the

indices on stochastic effects. The number of stars that are expected to be detected in the various evolutionary phases is proportional to the total sampled luminosity and can be easily evaluated (Renzini & Buzzoni 1986, Maraston 1998, Renzini 1998). Therefore, for every cluster it has been checked whether the sampled luminosity is dominated by few, very bright stars, like RGB-tip or E-AGB stars (Table 2.6, Chapter 2). This is important for metallic Lick indices like Mg_2, TiO, NaD, which are very strong in these stars. The uncertainties on the indices associated with the stocastic fluctuation in the number of stars which contribute the light in the relevant wavelength ranges, are included in the error budget (see Chapter 2).

3.3   A Note on the Metallicity Calibration of SSP Models

Some of the Lick indices were designed as metallicity indicators for unresolved stellar populations, therefore to calibrate a model Lick index means to check whether the model gives the observed value of the index for a SSP whose age and composition are independently known. In practice, GCs offer the best proxy to a SSP. However, some ambiguities make such calibration not so straightforward.

3.3.1   Ambiguities in the Definition of Metallicity

From the model side, the total metallicity of model Lick indices is not well defined because of the rôle of the so-called "fitting functions" (see Sect. 3.5.1). The fitting functions are best fits of the Lick indices as measured in stars, as functions of the stellar parameters $T_{\rm eff}$, g and chemical composition. According to the standard procedure (e.g. Buzzoni et al. 1992, 1994; Worthey 1994), the fitting functions are plugged on the isochrones to compute the Lick indices of SSP models (Sect. 3.5, Eqs. 3.4–3.5). Therefore, it is necessary to specify the metallicity parameter(s) for the fitting functions and for the isochrones, and of course they should be the same. While the latter is well-defined by construction (stellar evolutionary models are constructed for well defined sets of abundances), the former is somewhat ambiguous. Indeed, the estimates of the chemical composition of the stars used for the fitting functions come from a variety of sources, both spectroscopic and photometric. These, quite inhomogeneous, metallicities are collected under a parameter referred to as [Fe/H] in the fitting functions available in the literature (Worthey et al. 1994; Buzzoni et al. 1992; 1994). An additional source of complication comes from the fact that a certain total metallicity might be achieved with different proportions of the major elements, the so-called α-elements, with respect to iron. The fact that the fitting functions are derived from observed stars implies that the element abundance ratios are not constant in the fitting. In fact, as well known, the [α/Fe] ratios vary systematically among Milky Way stars (e.g. Mc William 1997), including those in the samples used to construct the fitting functions themselves. On the other hand the specific abundances of magnesium and iron, beside the total metallicity likely affect the strength of Mg and Fe absorption lines (see Sect. 3.4).

From the GC data side, the empirical metallicity scale of GCs is not rigorously defined either. The reference values for the chemical composition of the sample GCs used in this work are taken from the revised compilation by Harris (1996), which is largely based on the Zinn & West (1984) scale. Thomas et al. (2002b) show that the Zinn & West (1984) scale, which is named as [Fe/H], is likely to be closer to the total metallicity rather than to the sole iron abundance. In fact, the Zinn & West scale is tied to the scale set up by Cohen (1983), in which the metallicities which are called [Fe/H] are indeed obtained by averaging [Mg/H] and [Fe/H] (Thomas et al. 2002b). This fact was anticipated by the evidence that the integrated colours of SSP models

as function of the model total metallicity match well with those of Milky Way GCs, when the metallicities of the latter are on the Zinn & West scale (Maraston 2000, Fig. 1). Moreover, the values reported in the Harris (1996) catalogue are *not* just the metallicity in the Zinn & West scale in all cases. When various estimates of metallicity from other sources are available, either from spectroscopy or from colour magnitude diagrams, these are used together with the Zinn & West-based value, and the straight average of the values is published as [Fe/H].

3.3.2 The Effect of the Adopted Lick System

A quantitative model calibration requires that data and models refer to the same spectro-photometric system (see Maraston et al. 2001a). The definition of the Lick system (index passbands, resolution, etc.) has been slightly changed from Burstein et al. (1984), through Worthey et al. (1994, hereafter W94) to Trager et al. (1998). The different index definitions may introduce offsets, which could affect the model calibration. We adopt here the data as measured in the W94 version of the Lick system, since the models are locked to this version via the index fitting functions. The effect of this choice has been tested by computing the W94-like indices for the GC spectra obtained by Covino et al. (1995), then comparing them to the Covino et al. values of the indices that are measured in the Burstein et al. (1984) system. The comparison for the case of 47 Tuc is shown in Table 3.1.

Lick System	Mg_2 (mag)	$Mg\,b$ (Å)	Fe5270 (Å)	Fe5335 (Å)	Hβ (Å)
W94	0.15	2.19	1.64	1.40	1.48
B84	0.18	3.02	2.18	1.88	1.62

Table 3.1: Lick indices of 47 Tuc (spectra of Covino et al. 1995) measured in the Worthey et al. 1994 (W94) system for this work. The corresponding values in the Burstein et al. 1984 (B84) system by Covino et al. (1995) are given in second line.

The differences among the indices are not negligible. The values on the W94 system are systematically lower than those on the Burstein et al. (84). In Sect. 3.6 we demonstrate the impact of the index definitions on the model calibration.

3.4 Results

Figure 3.1 shows the $Mg\,b$ vs. the average iron index $\langle Fe \rangle$ [2] of the GCs of our sample (large filled symbols). The large open circle refers to the coaddition of the spectra of 15 Bulge fields located in Baade's Window. The blue lines are models of Simple Stellar Populations (SSPs), i.e. coeval and chemically homogeneous stellar populations, with total metallicities ([Z/H]) [3] ranging from -2.25 to $+0.67$, and ages between 3 and 15 Gyr. The models are computed with the evolutionary population synthesis code of Maraston (1998), as described in Maraston & Thomas (2000; see also Maraston et al. 2001b and Maraston 2002), and are based on stellar tracks, implemented with the Worthey et al. (1994) fitting functions, to describe the stellar

---

[2] $\langle Fe \rangle = (Fe5270 + Fe5335)/2$

[3] The notation [Z/H] is used to indicate total metallicities, i.e. the total abundance of heavy elements with respect to hydrogen normalized to the solar values, i.e. $[Z/H] = \log(Z/Z_\odot) - \log(H/H_\odot)$. By [Fe/H] we mean the abundance of iron with respect to hydrogen normalized to the solar values, i.e. $[Fe/H] = \log(Fe/Fe_\odot) - \log(H/H_\odot)$. If elements have solar proportions then $[Fe/H] = [Z/H]$. In case of α-element enhancement, the relation between [Fe/H] and [Z/H] is: $[Fe/H] = [Z/H] - 0.94 \cdot ([\alpha/Fe])$ (Thomas et al. 2002b; see also Trager et al. 2000).

indices as functions of effective temperature, gravity and metallicity. The stellar evolutionary tracks are from Bono et al. (1997) and Cassisi et al. (1999) for metallicities up to $Z = 0.04$, from Salasnich et al. (2000) for $Z = 0.07$, and adopt solar abundance ratios. In the following, we refer to these models as standard SSPs. [4]

The GCs indices define a nice sequence to which the Bulge field appears to belong as well. The sequence runs with a shallower slope compared to the standard models, i.e. at a given $\langle \text{Fe} \rangle$ index the data have a stronger $\text{Mg}\,b$ than the models. Several observational evidences show that all galactic GCs have α enhanced abundance ratios, with typical values around $[\alpha/\text{Fe}] \sim +0.3$ (e.g. Pilachowski et al. 1983; Gratton, 1987; Gratton & Ortolani 1989, Carney 1996, Salaris & Cassisi 1996). In particular, for the two most metal rich clusters (NGC 6553 and NGC 6228 with $\text{Mg}\,b \sim 3.8$) Barbuy et al. (1999) find $[\alpha/\text{Fe}] \sim +0.3$ from individual star spectroscopy. The Bulge field stars are also known to be overabundant in Mg with respect to the solar ratio (McWilliam and Rich 1994). Therefore the GC sequence traces the locus of α-enhanced SSPs.

Fig. 3.1 also shows the central values (i.e. those obtained with apertures $R \sim 1/8 \div 1/10\ R_e$) of the indices of field and cluster ellipticals taken from various sources in the literature (see caption). The indices of ellipticals occupy a relatively narrow range in $\langle \text{Fe} \rangle$ and a large range in $\text{Mg}\,b$, stretching from the standard models to the high metallicity extension of the GCs sequence, and beyond. With very few exceptions, both $\text{Mg}\,b$ and $\langle \text{Fe} \rangle$ indices are measured stronger in the nuclei of ellipticals than in the most metal rich GCs in our sample. The stellar populations in the centers of ellipticals seem to be characterized by:

(i) a supersolar total metallicity;

(ii) a range in abundance ratios, from almost solar, to $[\alpha/\text{Fe}]$ values as large as those of the most metal rich bulge clusters, or even more.

Similar conclusions have been proposed in the literature (Worthey et al. 1992; references in Introduction). Yet, these were based on the assumptions that standard models reproduce the indices of solar abundance ratios SSPs (at least at solar metallicity and above), that $\text{Mg}\,b$ and $\langle \text{Fe} \rangle$ trace the Mg and Fe abundance, and that an α- element overabundance affects the indices in the appropriate direction.

Our comparison of the GCs data with the ellipticals, and especially the inclusion of the indices of the metal rich clusters in the galactic Bulge and the bulge field, confirm the validity of these assumptions, the clusters being used as empirical SSPs.

This empirical evidence motivates the construction of new SSP models with various, well-defined $[\alpha/\text{Fe}]$ ratios which are shown in Fig. 3.1 as thick black lines (Thomas et al. 2003, hereafter TMB03). The GCs are now very well represented by a coeval (12 Gyr old) sequence of models with various metallicities and $[\alpha/\text{Fe}] = +0.3$, in agreement with the results from stellar spectroscopy. Note that at low metallicities ($\text{Mg}\,b < 2$) the standard models (blue lines) match with the enhanced models. This is due to the standard calibrations by Worthey et al. (1994) being α-enhanced at sub-solar metallicities (Sect. 3.5; see also TMB03).

In the next Section we conduct a thorough analysis of the standard SSP models, with the aim of assessing whether effects other than an enhanced $[\alpha/\text{Fe}]$ ratio can explain the deviation of the data from the standard models. In other words, we investigate the uniqueness of the "magnesium overabundance" solution.

---

[4]We want to emphasise that what we call standard SSPs, i.e. those based on the Worthey et al. or on the Buzzoni et al. fitting functions *are not* solar-scaled SSPs at every metallicity. Indeed this type of models are constructed by adopting the stellar indices of Milky Way stars, which have a variety of abundance ratios, see Sect. 3.4.
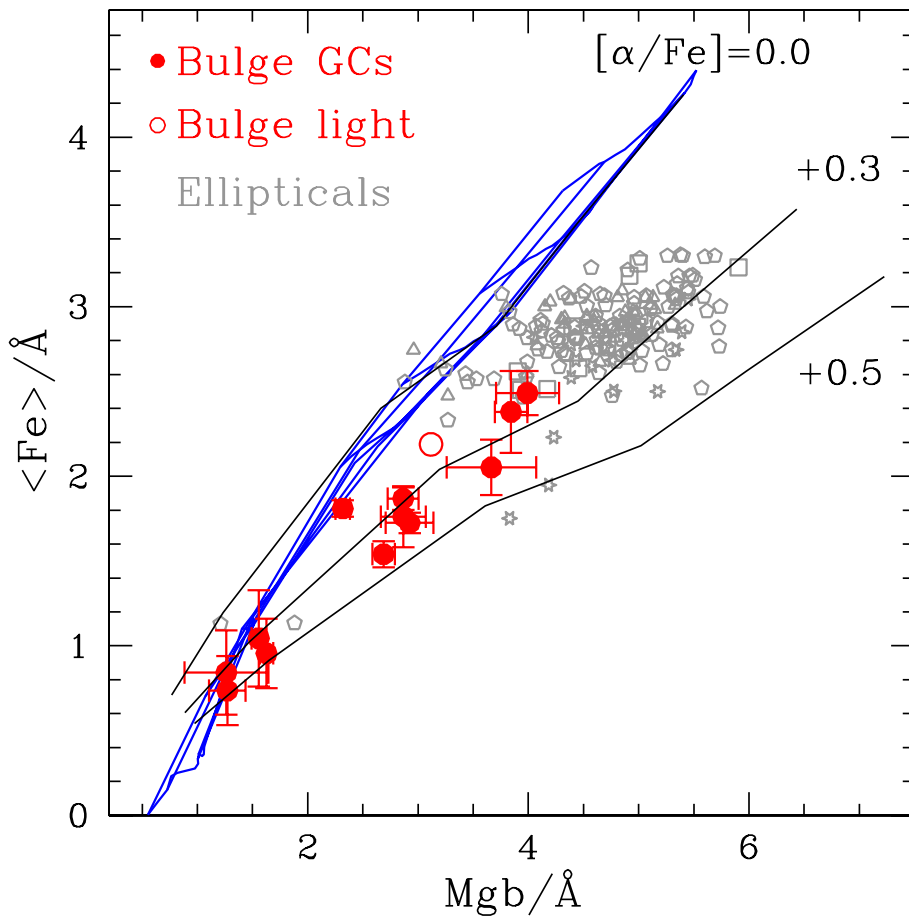
Figure 3.1: Mg b indices vs. average iron $\langle$Fe$\rangle$ indices of galactic and Bulge GCs of our sample (large red filled symbols). The open circle shows the average value of 15 Bulge fields located in Baade's window. Small open grey symbols show the central values of the indices for ellipticals taken from the literature: the field and cluster ellipticals from Beuing et al. (2002, pentagons); the Coma ellipticals from Mehlert et al. (2000, stars); the Fornax ellipticals of Kuntschner & Davies (1998, squares); the field and Virgo ellipticals of González (1993, triangles). Standard SSP models with metallicities [Z/H] = (−2.25, −1.35, −0.55, −0.33; 0.00; +0.35; +0.67), from bottom to top, and ages 3, 5, 10, 12 and 15 Gyr, from left to right, are shown as blue lines. The thick black lines show 12-Gyr SSP models with same total metallicities, and various [α/Fe] = 0, +0.3, +0.5 (Thomas et al. 2002b).

3.5 Model Lick Indices: Key Ingredients and Ambiguities

In the model SSPs, the line-strength of an absorption line with bandpass Δ I^{SSP} is given by

$$I = \Delta \cdot (1 - F_{\text{l}}/F_{\text{c}}), \tag{3.1}$$

where F_{l} and F_{c} are the fluxes in the absorption line and in the continuum, respectively.

In case of Lick indices this formula cannot be applied straightforwardly because of the different spectral resolution of the Lick system (~ 8 Å) and of the model atmospheres (Kurucz-based stellar atmospheres have resolutions of 20 Å in the optical region where the Lick indices are defined). Basically, the problematic quantity is the flux in the absorption line F_{l} , because it depends on the spectral resolution. To overcome this problem, the Lick group has measured the Lick indices on observed stellar spectra having the required resolution (Burstein et al. 1984; Faber et al. 1985). Assigning to each star of their sample the values for the stellar parameters surface gravity (g), effective temperature (T_{eff}) and chemical composition, they have constructed polynomial best-fitting functions which describe the various Lick indices measured on the stars, I^*, as a function of these parameters, i.e. $I^* = \text{f}(T_{\text{eff}}; g; [\text{Fe/H}])$. These polynomial fittings following Gorgas et al. (1993) are called fitting functions (hereafter FFs).

The integrated Lick index of an SSP model is then evaluated as it follows.

The flux in the absorption line of the generic i-th star of the SSP, $F_{\text{l,i}}^*$, can be expressed with Eq. 3.1 as:

$$F_{\text{l,i}}^* = F_{\text{c,i}}^* \cdot (1 - I_{\text{i}}^*/\Delta) \tag{3.2}$$

where I_{i}^* that is the index of the i-th star is computed by inserting in the FFs the values of (T_{eff};g; chemical composition) of the i-th star, and $F_{\text{c,i}}^*$ is its continuum flux. The latter is computed by linearly interpolating to the central wavelength of the absorption line, the fluxes at the midpoints of the red and blue pseudocontinua flanked to the line (Table 1 in Worthey et al. 1994). Eq. 3.1 can be re-written as:

$$I^{\text{SSP}} = \Delta \cdot (1 - \sum_{\text{i}} F_{\text{l,i}}^* / \sum_{\text{i}} F_{\text{c,i}}^*) = \sum_{\text{i}} I_{\text{i}}^* \cdot f_{c,i}^* \tag{3.3}$$

where $f_{\text{c,i}}^*$ are the contribution of each individual star to the total continuum flux of the SSP. Thus, the SSP integrated index I^{SSP} is the weighted average of the stellar indices I^* with the weigths being $f_{\text{c,i}}^*$. When computing actual models, the isochrone representing the SSP is binned in T_{eff} subphases, small enough to ensure that I_i^* is the same for the stars belonging to the given subphase. A good binning is $\Delta T_{\text{eff}} \sim 100$ K (Maraston 1998). Equation 3.3 can re-expressed for the subphases j

$$I^{\text{SSP}} = \sum_{\text{j}} I_{\text{j}}^* \cdot f_{c,j}^* \tag{3.4}$$

where $f_{\text{c,j}}^* = \sum_{\text{i} \in j} f_{\text{c,i}}^*$.

It should be noted that since the rôle of the stellar continua is that of a weight, it is not crucial that they are evaluated on Kurucz-type spectra. A relation similar to equation 3.4 holds for indices measured in magnitudes (e.g. Mg_2):

$$10^{-0.4 \cdot \text{Mg}_2^{\text{SSP}}} = \sum_{\text{j}} 10^{-0.4 \cdot \text{Mg}_{2\text{j}}^*} \cdot f_{c,j}^* \tag{3.5}$$

The two ingredients (I_{j}^* and $f_{c,j}^*$) are discussed comprehensively in the following subsections.

3.5.1   Interplay between Fitting Functions $I^*$and Continua

To explore the systematic effects introduced in SSP models by the use of different sets of FFs, and following Maraston et al. (2001b), we compute the same SSP models with three formulations for the FFs from the literature, i.e. by Worthey et al. (1994, hereafter Worthey et al. FFs), Buzzoni et al. (1992, 1994, hereafter Buzzoni et al. FFs), and Borges et al. (1995, hereafter Borges et al. FFs).

Worthey et al. FFs[5], the most widely used in the SSP models in the literature, are based on the Lick sample of ~ 400 nearby stars. Buzzoni et al. FFs are based on a smaller sample of stars (~ 87), also located in the solar vicinity. As is well known, the α to Fe abundance ratios in nearby stars vary with metallicity, ranging from the super-solar values in the Halo stars ($[\alpha/\text{Fe}] \sim +0.3$) to the solar proportions in the metal-rich disk stars ($[\alpha/\text{Fe}] = 0.0$) (e.g. Wheeler et al. 1989; Edwardsson et al. 1993; Fuhrmann et al. 1995; Fuhrmann, 1998; see the comprehensive review by McWilliam 1997). Thus, likely, these two sets of FFs reflect α enhanced mixtures at low Z, and solar ratios at high metallicity, a trend which is dragged into the SSP models through I_j^* (Eqs. 3.4–3.5). This explains why the standard models in Fig. 3.1 (blue lines) represent well the indices of metal poor GCs.

Borges et al. FFs (see also Idiart & de Freitas Pacheco 1995) have been derived from a sample of roughly 90 stars for which the Mg to Fe ratio has been measured. Thus, they include the [Mg/Fe] ratio as an additional variable besides temperature, gravity and metallicity.

In the following subsections we discuss separately high metallicity and low metallicity model indices.

The Metal-rich Zone

Fig. 3.2 illustrates the interplay between I_j^* and $f_{c,j}^*$ (Equation 4-5) in determining the SSP magnesium and iron indices in the particular case of a 15 Gyr, solar metallicity and solar abundance ratio SSP, with Salpeter IMF. The three sets of FFs considered are color coded as marked in the top-right panel. The x-axis is a monothonic coordinate along the SSP isochrone. The integer values of x (1 to 6) mark the end of the six main evolutionary phases (see the caption and the figure with the isochrone inserted in the top-left panel). Each x-point in Main Sequence ($x \leq 2$) represents the subphase along the Main Sequence isochrone. Each x-point in post-MS ($x > 2$) represents the j subphases of every post-MS major phase, which are equally spaced in effective temperature ($\Delta T_{\text{eff}} \sim 100$ K , Maraston 1998). The top panels show the cumulative $\text{Mg}_2(x)^6$ (left) and $\langle \text{Fe} \rangle(x)$ (right) along the isochrone, which assumes the value of the SSP model at $x = 6$. As in equations 3.4–3.5, each value of $\text{Mg}_2(x)$ and $\langle \text{Fe} \rangle(x)$ is obtained by summing up to point x, the product of I_j^* times $f_{c,j}^*$. These are separately shown in the central and lower panels, respectively. The behavior of I_j^* in the central panels reflects the changing of T_{eff} along the isochrone, both Mg_2 and$\langle \text{Fe} \rangle$ indices being very strong in cool stars.

The three sets of FFs correspond to quite different values for I^* along the isochrone, particularly in the faint dwarf regime ($x \lesssim 1$), at the Tip of the RGB ($x \sim 4$), and at the end of the E-AGB ($x \sim 6$). In spite of that, the SSP indices keep very close along the isochrone, and assume quite similar total values, due to the low contribution to the total continuum flux of these particular phases. Thus, the indices turn out to be quite insensitive to the adopted set of FFs.

---

[5]We notice a typo in Table 3 of Worthey et al. 1994. The fitting functions are mistakenly given as function of $\log \theta$, while they are function of θ, as also stated in the text.

[6]Notice that we plot the Mg_2 index expressed in Å, i.e. $\text{Mg}_2(\text{Å}) = 1 - 10^{(-0.4 \cdot \text{Mg}_2(\text{mag}))}$. We use Mg_2 here instead of $\text{Mg}\,b$ because neither Buzzoni, nor Borges give FFs for $\text{Mg}\,b$. The two indices, however, are very closely related.
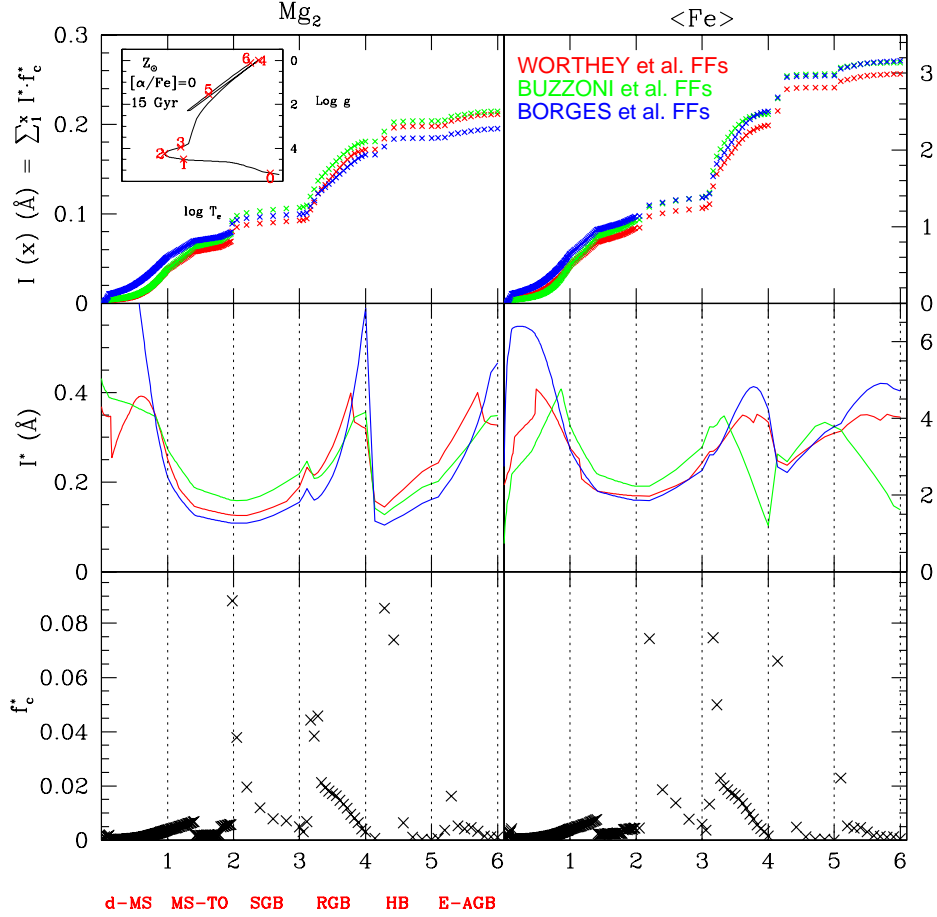
Figure 3.2: Closer look to model Mg_2 (left-hand panels) and $\langle Fe \rangle$ (right-hand panels) indices of a 15 Gyr old SSP with solar metallicity, solar abundance ratios, and Salpeter IMF. The upper panels show the cumulative SSP indices $I^{SSP}(x)$, integrated up to the point x along the isochrone (see text): $x = 1$: lower Main Sequence (d-MS) up to $T_{eff} \leq 5000$ K; $x = 2$: Main Sequence up to Turn Off (TO); $x = 3$: Sub Giant Branch (SGB); $x = 4$: Red Giant Branch (RGB); $x = 5$: Horizontal Branch (HB); $x = 6$: Early Asymptotic Giant Branch (E-AGB). These phases are identified on the corresponding isochrone (small inserted panel), shown in the temperature-gravity plane. Here the label $[\alpha/Fe] = 0$ refers to the composition of the stellar tracks. Colors code the different FFs for I_j^* (Eqs. 3.4–3.5) adopted for the SSP models, by Worthey et al. (red lines), Buzzoni et al. (green lines) and Borges et al. (blue lines). The values I_j^* are shown in the middle panels, with lines connecting the stellar indices of the subphases along the isochrone. Finally the lower panels display the contributions of the various subphases to the total continuum flux, $f_{c,j}^*$ (Eqs. 3.4–3.5). Note that the flux contributions in post-MS ($x > 2$) take into account the fuel consumption, i.e. the product of the stellar lifetimes with the stellar luminosities. For example the contribution of the long lasting RGB bump phase (peak in phase 3-4) is much larger than that of the RGB-tip (end of phase 4), where, in spite of larger stellar luminosities, the evolutionary timescale is much shorter.

As a result of the weighting through $f^*_{c,j}$, the lower MS, RGB and E-AGB bright stars (which have very strong Mg_2) are not important in determining the total SSP index. The most important contributors to the continuum fluxes in the two windows of Mg_2 and $\langle Fe \rangle$ are: the stars around the TO; those on the fainter portion of the RGB (especially at the so-called bump), and the Horizontal Branch stars. Their indices dominate the integrated values. This applies in general to old ($\gtrsim 3$ Gyr) stellar populations, as the relative contribution to the total optical flux of the different phases does not depend much on age in this age range (Renzini & Buzzoni 1986, Maraston 1998).

phase	$Z_\odot$		$10^{-4} Z_\odot$	
	Mg_2	$\langle Fe \rangle$	Mg_2	$\langle Fe \rangle$
d-MS	0.11	0.13	0.10	0.10
MS TO	0.32	0.22	0.26	0.26
SGB	0.05	0.12	0.10	0.10
RGB	0.29	0.30	0.28	0.28
RGB-tip	0.01	0.01	0.10	0.10
HB	0.17	0.17	0.12	0.12
E-AGB	0.05	0.05	0.04	0.04

Table 3.2: Relative contributions of stellar evolutionary phases, to the continuum flux of the Mg_2 index ($\lambda \sim 5175$Å) and $\langle Fe \rangle$ ($\lambda \sim 5300$Å), for 15-Gyr old SSPs with Salpeter IMF, and metallicities: $Z_\odot$ and $Z = 10^{-4}$. RGB tip is the portion within 1 mag from the tip.

The contributions to the total continua of Mg_2 and $\langle Fe \rangle$ of the various evolutionary phases are given in Table 3.2 for 15 Gyr old metal-rich and metal-poor SSPs.

As apparent in Fig. 3.2, Borges et al. FFs provide I_j^* for faint dwarfs which are much larger than those of the other two sets. These result from the exponential increase with decreasing $T_{\rm eff}$ of their FF for Mg_2. In the validity range as specified by the authors ($T_{\rm eff} \gtrsim 3800$ K), the FF for Mg_2 yields values as high as 1.9 mag (corresponding to 0.83 Å in the units of Fig. 3.2), while the coolest dwarf in their observed sample has $Mg_2 = 0.45$ mag (or 0.34 Å). These very strong (extrapolated) Mg_2 indices as obtained with a blind use of the FFs are extremely unrealistic. This example illustrates the importance of checking the behaviour of the algebraic FFs when computing SSP models.

We conclude that the Mg-Fe relation of standard models around solar metallicity (Fig. 3.1) is independent of the fitting functions.

The Metal-poor Zone

As shown in the previous paragraph, the differences in the FFs appear to be unimportant at $\sim Z_\odot$. Actually, the Mg_2 index obtained with the Borges et al. FFs does deviate from the other two values, by an amount which is comparable to the typical observational error affecting the GC data (~ 0.01). This discrepancy becomes more pronounced at very low metallicities, which is relevant for the model calibration with GCs.

Fig. 3.3 is the analogous of Fig. 3.2, but for a very metal-poor SSP with metallicity $Z = 10^{-4}$. We use here the Borges et al. FFs with [Mg/Fe]=0.3 which is appropriate at low metallicities.

At low metallicity the temperature distribution of the isochrone shifts to hotter values (see inserted panels in Fig.s 3.2 and 3.3). The relative contributions to the continuum flux of the different evolutionary phases is very similar to the $Z_\odot$ case (see Table 3.2), but the stellar indices are now very weak, and the strongest Mg_2 are
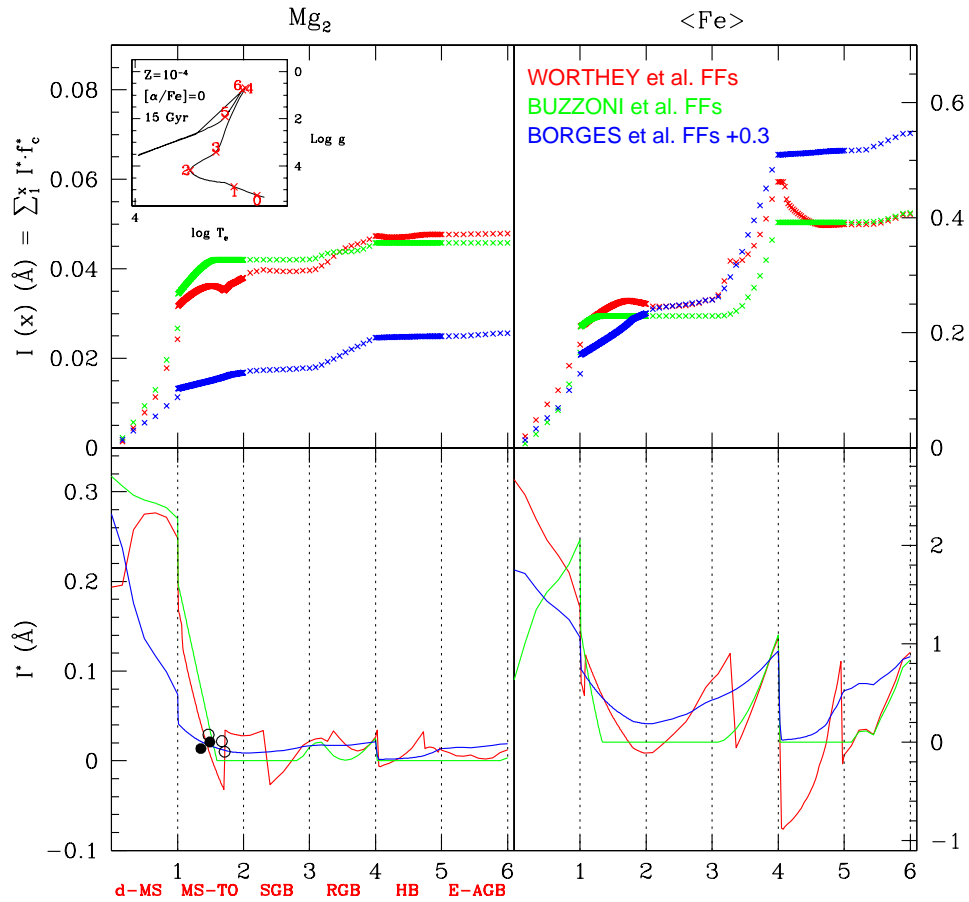
Figure 3.3: Same as Fig. 3.2 but for a very metal-poor SSP with metallicity $Z = 10^{-4}$. Note that the integrated Mg_2 is made up by the lower Main Sequence (d-MS, phase 1). The symbols in the left-hand bottom panel are the values of Mg_2 of the stars in the Lick sample (filled) and in the sample used by Borges (open) with metallicities and gravities appropriate to the MS of these SSP models. As in Fig. 3.2, the label $[\alpha/Fe] = 0$ in the inserted panel refers to the composition of the stellar tracks.

found on the lower MS, which is the coolest portion of the isochrone. As a result, the total Mg_2 of the SSP is very close to the value attained already at the turn-off point. Borges et al. FFs yield much lower stellar indices for the lower MS, compared to the other two FFs, which explains the lower integrated index. Incidentally, this is true also when adopting [Mg/Fe]=0. in the FF formula. It should be noted that the behaviour of the FFs at the low Main Sequence (phase 1) is not constrained by stellar data. Indeed, only 5 main sequence stars (symbols in the lower left panel of Fig. 3.3) are found at [Fe/H] ≈ -1.8 by merging both the Lick and the Borges et al. data base. An improvement of present low-metallicity SSP models can be gained by implementing the stellar libraries with cool, dwarf and low metallicity objects.

The importance of the (lower) main sequence phase on the integrated Mg_2 has the consequence of making this index sensitive to the mass function of the stellar population. This complicates the comparison of the models with the GC data, for which the present day mass function derives from the IMF plus the possible dynamical evolution, which can lead to the evaporation of the low mass stars (e.g. Piotto & Zoccali 1999).

Different from the Mg_2 index, an important contribution to the total $\langle Fe \rangle$ index comes from the RGB portion of the isochrone, where the FFs are very noisy (see right panels in 3.3). Notice that the index computed with Worthey et al. FFs converges to that based on Buzzoni FFs because of negative stellar indices predicted for the hot HB stars. It is very difficult to assess the reliability of the indices as metallicity indicators at such low-Z.

3.5.2   IMF effects

As discussed in the previous sections, Mg_2 indices are very strong in dwarf stars, therefore dwarf-dominated stellar population could in principle allow to reach the very high values of Mg_2 shown by ellipticals. Fig. 3.4 shows the location of such dwarf-dominated SSPs in the Mg_2 vs. $\langle Fe \rangle$ diagram (lower solid lines). Lines connect 12 Gyr old models with metallicities from 3 time to half solar, and IMF's exponents of 4 and 5 (in the notation in which Salpeter is 2.35), from top to bottom, respectively. Worthey et al. FFs have been used for this exercise. Data of ellipticals and GCs are the same as in Fig. 3.1.

Dwarf-dominated stellar populations are able to reproduce the Mg_2 and $\langle Fe \rangle$ indices of ellipticals without invoking abundance effects. It should be noted that in such dwarf-dominated SSPs, $> 70\%$ of the total luminosity is made up by stars close to the H-burning limit. The different slope of these SSP models on the $Mg_2-\langle Fe \rangle$ plane reflects the different dependence of the stellar indices from $T_{\rm eff}$ at the lower end of the MS.

These extreme IMFs are also able to reproduce the low values of the Calcium triplet absorption line at 8600 K observed in ellipticals (Saglia et al. 2002), because its strength decreases with increasing gravity (Jones et al. 1984). However, these models fail at explaining other spectral properties of ellipticals. In fact the corresponding stellar mass-to-light ratios become much larger ($M/L_B > 30$, see Maraston 1998) than the dynamical ones observed in the central portions of ellipticals ($M/L_B \sim 6$, Gerhard et al. 2001). Similarly, a dwarf-dominated elliptical galaxy light was excluded given the strength of the CO absorption (Frogel et al. 1978) and the absence of the Wing Ford bands in absorption (Whitford 1977). The case of such a dwarf-dominated present mass function for GCs, and the Bulge field is ruled out by direct observations of the lower MS (de Marchi & Paresce 1997; Piotto & Zoccali 1999; Zoccali et al. 2000a).

We conclude that an extremely steep IMF is not a viable alternative to explain the high values of the Mg indices in ellipticals.
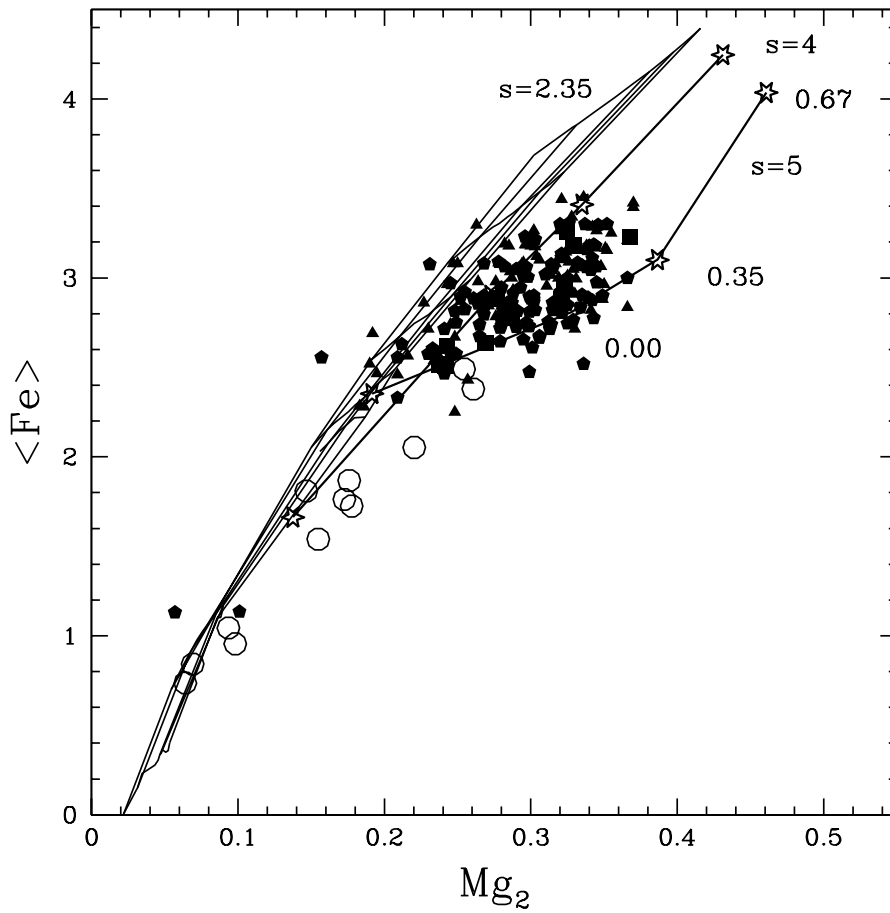
Figure 3.4: Effect of a dwarf-dominated IMF on the Mg_2 and$\langle Fe \rangle$ diagram of SSPs. The model grid for the Salpeter IMF exponent of 2.35 is the same as in Fig. 3.1. The two additional solid lines are dwarf-dominated SSPs with IMF's exponents of 4 and 5, respectively. These SSPs have 12 Gyr and metallicities as indicated by the labels. Data of GCs and ellipticals as in Fig. 3.1.

3.5.3 The Effect of Stellar Evolutionary Tracks

As already stated, our standard SSP models are based on the stellar tracks by Cassisi et al. (1999). Since differences exist among different sets of tracks, it is interesting to check their impact on the model indices. To this aim we have computed SSP models with Worthey et al. FFs, but varying the input tracks. The Padova stellar tracks and isochrones as available on the Web have been used, specifically those by Fagotto et al. (1994) for metallicities [Z/H] $= -1.69$ and -0.69, and those by Salasnich et al. (2000), with solar scaled abundance ratios, for metallicities [Z/H] $= -0.4, 0, 0.35$. The fuel consumption theorem is adopted also for these SSPs, following the method described in Maraston (1998; 2003).
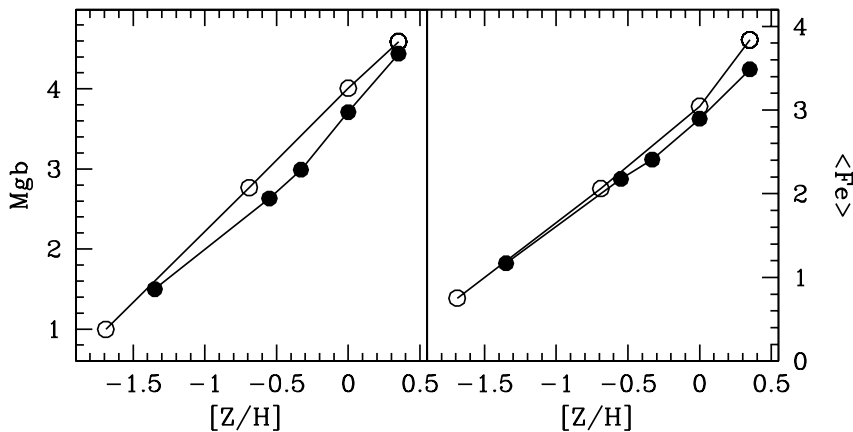
Figure 3.5: Effect of stellar tracks on the Lick indices of 12 Gyr SSPs models with various total metallicities [Z/H]. Filled symbols: SSPs adopting the Cassisi tracks, open symbols: SSPs adopting the Padova tracks.

The results are shown in Fig. 3.5, which compares the Mg b and $\langle$Fe$\rangle$ indices of 12 Gyr SSP models as a function of the total metallicities [Z/H], as obtained with the Cassisi tracks (filled circles) and the Padova tracks (open circles),

The use of the Padova tracks produces slightly stronger Mg b indices, at metallicities [Z/H] between ~ -0.5 and solar. This effect is most likely due to the cooler temperatures of the Padova tracks along the Red Giant Branch with respect to the Cassisi tracks (see also Maraston 2003). A very modest impact is present also for the $\langle$Fe$\rangle$ index. Note that at metallicities above solar the $\langle$Fe$\rangle$ obtained with the Padova tracks is stronger than that obtained with the Cassisi tracks, while the corresponding Mg b indices are consistent. This implies that the discrepancy with ellipticals data is slightly larger when the Padova tracks are used. The differences are however very small, and the conclusions drawn from Fig. 3.1 are not affected by our use of a specific set of stellar tracks.

Recently, isochrones and tracks with super-solar [α/Fe] ratios became available (Salasnich et al. 2000 with [α/Fe] $= +0.3$; see also Bergbusch & VandenBerg 2001; Kim et al. 2002). These improved upon previous calculations that considered only the effect on nuclear reaction rates (e.g. Salaris et al. 1993), while the updated tracks have also included the effect of α-enhancement on the stellar opacities. Here we use the Salasnich's computations in order to check the impact of α-enhanced tracks on the final index values of SSP models. For consistency, we compare the indices based on the two Padova sets, with solar scaled and α-enhanced abundance ratio. This is shown in Fig. 3.6 for the illustrative case of 10 Gyr old SSPs[7].

---

[7]We use here 10 Gyr to avoid interpolation on the Salasnich et al. isochrones
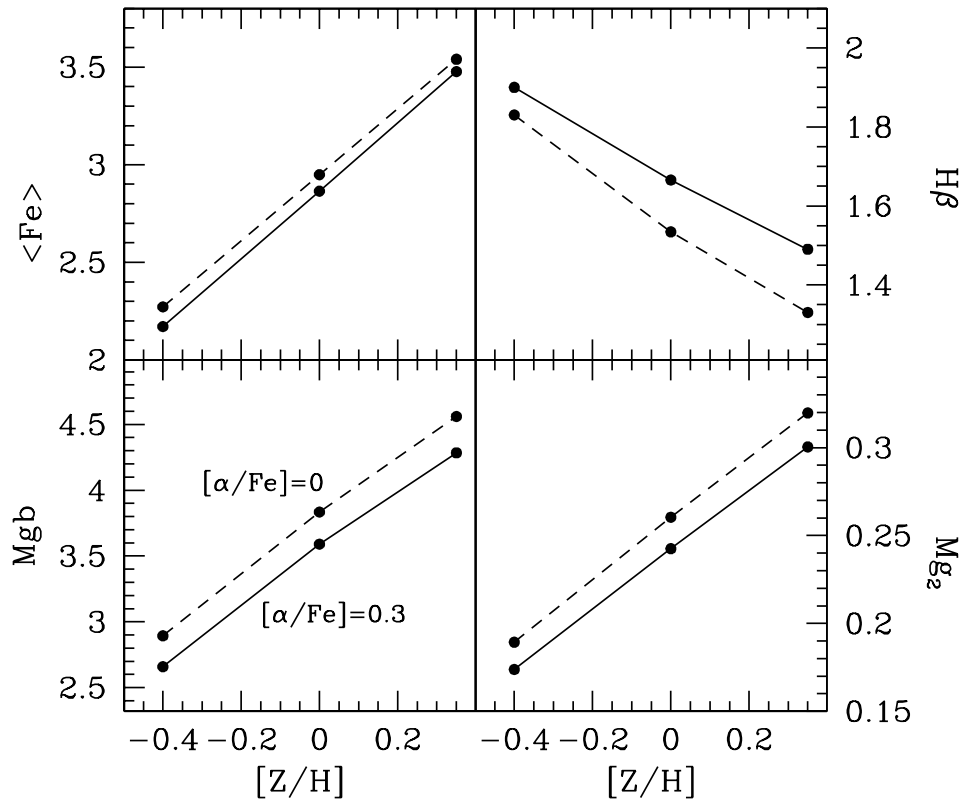
Figure 3.6: Effect of α-enhanced stellar tracks on Mg_2 , $Mg\,b$, $\langle Fe \rangle$ and $H\beta$ of 10 Gyr SSPs (Salpeter IMF) with various total metallicities [Z/H]. Dotted lines: solar-scaled tracks. Solid lines: $[\alpha/Fe] = +0.3$ tracks. Tracks are from Salasnich et al. (2000), the Worthey FFS are adopted.

For the same total metallicity [Z/H], the Mg and Fe indices of SSPs based on α-enhanced stellar tracks (solid lines) are *lower* than those based on solar scaled stellar tracks (dotted lines), This happens because the α-enhanced tracks are bluer than the solar-scaled ones at fixed total metallicity (Salasnich et al. 2000), because of the lower stellar opacities. So, by increasing [α/Fe] *at constant* [Z/H] the Mg indices actually decrease!

This rather counterintuitive behavior is a consequence of the fact that, at given total metallicity, the increase of the [α/Fe] ratio produces only a small increase of the α elements, and instead a large decrease of iron. In fact, in solar proportions the total metallicity is by far dominated by the α-elements ($\sim$ 74% by mass), the iron-peak elements amounting only to $\sim$ 8%, the residual being contributed by elements produced by the p, s, and r processes (Trager et al. 2000; TMB03).For example, compared to solar proportion in a mixture with [α/Fe]=+0.3 the α elements will contribute slightly more than $\sim$ 74%, but the iron peak elements will be reduced by almost a factor of two, down to $\sim$ 4%. Therefore, the main effect is to decrease iron rather than to increase, e.g., magnesium. Since iron is the most effective electron donor (e.g. Salasnich et al. 2000), the lower abundance of iron in enhanced [α/Fe] mixtures has the effect of decreasing their low-temperature opacities, which in turn determine an increase of the temperature of the RGB, and finally a decrease of the Mg indices because these are stronger in cool stars.

The *bluing* of the isochrone also affects the Hβ line indices, which are *stronger* when α-enhanced tracks are adopted (Fig. 3.6, upper right panel). Therefore, in order to reproduce the observed Mg$_2$, $\langle$Fe$\rangle$ and Hβ indices, the α-enhanced tracks require *older* ages.

It should be noted that for the models of Fig. 3.6, the parameter expressing the chemical composition in the Worthey et al. FFs (referred to as [Fe/H] in Worthey et al. 1994) has been considered to represent the total metallicity. As discussed in Sect. 3.3, this might be not entirely correct, since a variety of methods have been used, both photometric and spectroscopic, to determine such parameter for the stars of the Lick sample. If the [Fe/H]'s values are used, the metallic indices shown in Fig. 3.6 decrease even further.

Fig. 3.6 illustrates that accounting *only* for α-enhanced stellar tracks to compute α-enhanced SSP models, while using the same FFs, affects the indices in the wrong direction with respect to the locus occupied by the metal-rich GCs and ellipticals data in Fig. 3.1 (Mg$_2$ is affected more than $\langle$Fe$\rangle$). A fully consistent exploration of the effect of the [α/Fe] ratio requires also the use of fitting functions depending on [α/Fe]. This is done in TMB03.

3.5.4 Summary

The conclusions of the previous paragraphs are the following.

1. Differences in the available sets of FFs do not affect the integrated Mg$_2$ and $\langle$Fe$\rangle$ indices, due to the low contribution to the total continuum flux of those evolutionary phases where the FFs are mostly discrepant.

2. For both Mg$_2$ and $\langle$Fe$\rangle$ (and in general indices measured in the optical) the most important contributors are MS TO, RGB and HB stars. These are the evolutionary phases where the FFs need to be best constrained from stellar data.

3. Results 1 and 2 hold for metallicities [Fe/H] $\gtrsim -1$, and are largely independent of the age and stellar tracks used.

4. At very low metallicities (less than $Z_\odot/10$) the lower MS appears to dominate the value of the SSP Mg_2 index. Uncertainties in the FFs and in the mass function jeopardize the calibration of the theoretical indices with the GC data.

5. At metallicities $\gtrsim Z_\odot/2$, the slope of the *solar scaled* Mg_2 vs $\langle Fe \rangle$ relation for SSP models seems quite robust. One possibility to get strong Mg_2 indices in combination with weak $\langle Fe \rangle$ without invoking a super-solar $[\alpha/Fe]$, is to adopt a very steep exponent for the IMF. However, IMF exponents as large as $4 \div 5$ have to be used in order to encompass the locus occupied by ellipticals. Such values are ruled out by other constraints.

6. When α enhanced tracks are used the Mg_2 and $\langle Fe \rangle$ indices become *weaker*, due to the *blueing* of the isochrone. Therefore, in order to match the observational data of GCs and ellipticals, abundance effects have to be accounted also in the FFs.

3.6   Model Lick Indices: Comparison with the Data

In this section we compare quantitatively the indices for our sample of GCs with the models. Good models have to fulfill two requirements: i) the metallicities obtained using different line-strengths have to be consistent; ii) the metallicities derived from the models have to be in agreement with those determined independently from, e.g. spectroscopy of stars in GCs or CMD fitting. We already know from Fig. 3.1 that condition i) will not be fulfilled at $[Z/H] \gtrsim -0.6$, because the GCs data deviate from the models. It is however important to check quantitatively the discrepancy. For a comparison of the standard SSP models used here with Magellanic Clouds clusters, we refer to Beasley et al. (2002).

In this section we also explore the significance of other Lick indices as metallicity indicators. Finally we calibrate the Balmer lines.

3.6.1   Chemical Compositions from Mg and Fe Indices

Fig. 3.7 compares the metallicities $[Z/H]$ derived from the standard SSP models, with those provided by the revised compilation of Harris (1996), which is largely based on the Zinn & West (1984) scale, for each GC of our sample. The model $[Z/H]$ is obtained by interpolating the Mg_2 index (left-hand panel) and the $\langle Fe \rangle$ index (central panel) on the SSP models (12 Gyr) based on the Cassisi tracks plus the FFs by: Worthey et al. (open circles), Buzzoni et al. (triangles), and Borges et al. (asterisks). The errorbars connect the minimum and maximum model metallicities obtained by subtracting (adding) the observational errors to the measured values. For the empirical metallicities, a conservative error of +0.2 dex has been considered. The right-hand panel refers to a model $\langle Fe \rangle$ index as obtained by using as a metallicity input in the Worthey et al. FFs, the value of the iron abundance $[Fe/H]$ and assuming an $[\alpha/Fe] = +0.3$ (see Sect. 3.3). Also in this case, the interpolation is with the model total metallicity $[Z/H]$.

Fig. 3.7 shows that for standard SSP models:

i) the total metallicities $[Z/H]$ as derived from the Mg_2 index (left-hand panel) are well consistent with the empirical scale of Zinn & West at metallicities lower than ~ -0.5. For NGC 6553 and NGC 6528 the models give $[Z/H]$ values somewhat in excess of the values on the Zinn & West scale, but would agree with the near solar abundance indicated by the spectroscopic observations (Barbuy et al. 1999; Cohen et al. 1999).
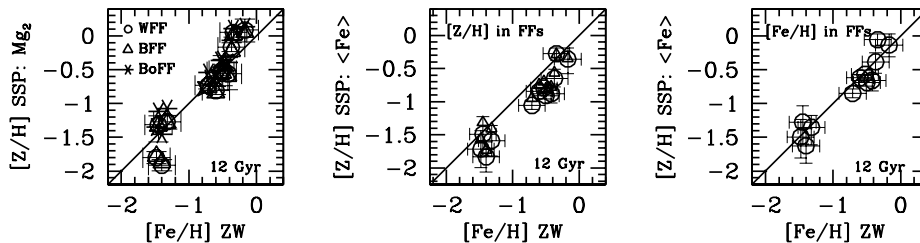
Figure 3.7: Comparison between the SSP-derived total metallicities from Mg_2 (left-hand panel) and $\langle Fe \rangle$ (central panel) for our sample of GCs, with the empirical metallicity scale [Fe/H] as compiled by Harris (1996), which is largely based on the Zinn & West (1984) scale. The standard SSPs, i.e. those based on Milky Way calibrated FFs, used here adopt the Cassisi tracks and: the Worthey et al. FFs (open circles), the Buzzoni et al. FFs (open triangles), the Borges et al. FFs (asterisks). The age of these SSPs is 12 Gyr. The SSP-derived [Z/H] is obtained by interpolating the observed indices on the model grid, separately. Diagonal lines show the 1 to 1 relations. In the right hand-panel the $\langle Fe \rangle$ index of the SSP models is derived by plugging [Fe/H] in the FFs instead of the total metallicity [Z/H](see Sect. 3.3), for the only case of the Worthey et al. FFs.

ii) the total metallicities [Z/H] as derived from the $\langle Fe \rangle$ index, when the latter is computed with [Z/H] as input of the FFs (central panel), are systematically lower than the empirical ones, by roughly 0.3 dex.

iii) the total metallicities [Z/H] as derived from the $\langle Fe \rangle$ index, when the latter is computed by using instead the iron abundance [Fe/H] and assuming a 0.3 dex α-enhancement as input of the FFs (right-hand panel) is consistent with the Zinn & West values.

On the basis of these evidences we conclude that:

i) the standard SSP models, i.e. those based on the Milky Way calibrated FFs, do not underestimate the Mg_2 index; rather they overestimate the $\langle Fe \rangle$ index. The disagreement between the models and the GC (and ellipticals) data would then point towards an *iron deficiency*, as opposed to magnesium enhancement, at virtually all metallicities. Suggestions in this direction can be found in Buzzoni et al. (1994), Trager et al. (2000), MB02;

ii) the model-derived *total* metallicities [Z/H] are in agreement with the metallicities on the Zinn & West scale which are referred as to [Fe/H] (see Sect. 3.3.1).

In the left-hand panel of Fig. 3.7 two of the four clusters at $[Fe/H]_{ZW} \sim -1.4$ (NGC 6218 and NGC 6981) have a too low Mg_2-derived metallicity, when the Worthey et al. or the Buzzoni et al. FFs are used. The SSPs with the Borges et al. FFs, instead reproduce the Mg_2 indices of these two specific clusters, because of the lower Mg_2 indices of these FFs. Since at low Zs the Mg_2 index is dominated by the lower MS component (Sect. 3.5.3), dynamical effects stripping low mass stars could be responsible for the observed low Mg_2 indices of these particular objects. Piotto et al. (2001) show that indeed the mass function of NGC 6981 is consistent with a power-law with a slope flatter than the Salpeter one. We note that NGC 6218 is the object of our sample with the poorest sampled light (Chapter 2).

Fig. 3.8 compares the metallicities of each GCs as obtained from the Mg_2 (left-hand panel) and $\langle Fe \rangle$ (right-hand panel) index using the TMB03 α-enhanced SSP models, with 12 Gyr and $[\alpha/Fe] = +0.3$ (solid black lines in Fig. 3.1). These models
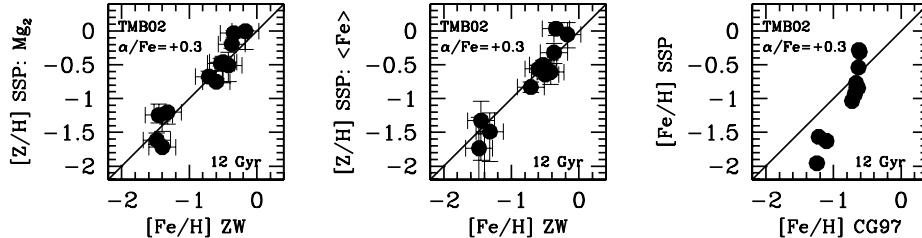
Figure 3.8: The metallicities of the GCs as derived from the α-enhanced SSPs of TMB03, with age of 12 Gyr and $[\alpha/\text{Fe}] = +0.3$. In the left-hand and central panels, the total metallicity [Z/H] as derived with the Mg_2 and the $\langle\text{Fe}\rangle$ index, respectively are compared with the values on the Zinn & West scale. In the right-hand panel the predicted [Fe/H] is compared to the empirical scale of iron abundances by Carretta & Gratton (1997).

include the dependence of the fitting functions for I^* on the $[\alpha/\text{Fe}]$ parameter.

The total metallicities [Z/H] as derived from Mg_2 and $\langle\text{Fe}\rangle$ are in excellent agreement with each other. This results from having taken a super solar $[\alpha/\text{Fe}]$ abundance ratio in the models into account. The metallicities are in excellent agreement with those in the Zinn & West scale, over the whole range covered by our sample. The assumed $[\alpha/\text{Fe}] = +0.3$ for the GCs is in agreement with the $[\alpha/\text{Fe}]$ measured spectroscopically (see e.g. Carney 1996; Salaris & Cassisi 1996). For the Bulge GC NGC 6528 recent spectroscopic abundance determinations give: $Z \sim Z_\odot$, $[\alpha/\text{Fe}] \sim 0.3$, $[\text{Fe/H}] \sim -0.3$ (Barbuy et al. 1999; Origlia et al. 2001). We acknowledge that some controversy exists in the literature: Carretta et al.(2001; see also Cohen et al. 1999) give $[\text{Fe/H}] \sim +0.08$ for 6528 and $[\text{Fe/H}] \sim -0.06$ for NGC 6553, $[\alpha/\text{Fe}] \sim 0.2 \div 0.4$. It would be extremely important to pin down the element abundances for these objects which are the most metal-rich calibrators available.

Carretta & Gratton (1997) provide a metallicity scale for GCs which should reflect the [Fe/H] abundance. The right-hand panel of Fig. 3.8 compares the model-derived [Fe/H] with this scale. The metallicities in the Zinn & West scale are transformed into the Carretta & Gratton scale by adopting the relation provided by the authors. This comparison is rather poor. On this scale the iron abundance of our GC sample appears clustered on two values, while the observed $\langle\text{Fe}\rangle$ indices span a considerable range. It seems difficult to reconcile our index-based [Fe/H] with those in the Carretta & Gratton scale.

We conclude this section discussing the case of 47 Tuc, which allows us to demonstrate the importance of comparing data and models which are set on the same system (see Sect. 3.3.1, Table 3.1). If we use the indices measured in the Burstein et al. (1984) system, 47 Tuc has $[\text{Z/H}] \simeq -0.50$; if we use the indices measured in the Worthey et al. one, we get $[\text{Z/H}] \simeq -0.78$. This last value is in perfect agreement with the metallicity of 47 Tuc in the Zinn & West scale ($[\text{Z/H}] \sim -0.76$, from Harris 1996). In addition we notice that the metallicity derived for 47 Tuc using the indices in the Burstein et al. (1984) is as large as that of NGC 6356, while the comparison of the RGB ridge lines of these two clusters indicates that 47 Tuc is more metal-poor (Bica et al. 1994). For a critical discussion focused on 47 Tuc see Schiavon et al. (2002).

3.6.2 The other Lick Indices as Abundance Indicators

In this section we check the behaviour of the other Lick indices as abundance indicators, by analysing the correlations with $\text{Mg}\,b$ and $\langle\text{Fe}\rangle$, which we have shown

name	$[\text{Fe/H}]_{ZW}$	$[\text{Z/H}]^{SSP}_{WFFs}$		$[\text{Z/H}]^{SSP}_{BFFs}$		$[\text{Z/H}]^{SSP}_{BorFFs}$
		Mg_2	$\langle Fe \rangle$	Mg_2	$\langle Fe \rangle$	Mg_2
NGC 6981	-1.40	-1.91	-1.83	-1.87	-1.73	-1.46
NGC 6637	-0.71	-0.73	-1.05	-0.76	-0.94	-0.54
NGC 6356	-0.50	-0.51	-0.91	-0.55	-0.81	-0.35
NGC 6284	-1.32	-1.27	-1.58	-1.29	-1.41	-1.07
NGC 6626	-1.45	-1.31	-1.48	-1.33	-1.31	-1.12
NGC 6441	-0.53	-0.53	-0.80	-0.57	-0.70	-0.36
NGC 6218	-1.48	-1.80	-1.71	-1.77	-1.57	-1.35
NGC 6624	-0.56	-0.45	-0.88	-0.59	-0.78	-0.39
NGC 6388	-0.60	-0.81	-0.84	-0.84	-0.74	-0.61
NGC 5927	-0.37	-0.17	-0.65	-0.23	-0.56	-0.07
NGC 6553	-0.34	+0.05	-0.27	+0.01	-0.29	+0.11
NGC 6528	-0.17	+0.09	-0.35	+0.06	-0.35	+0.14
47 Tuc(B84)	-0.76	-0.50	-0.66	-0.53	-0.58	-0.33
47 Tuc (W94)	-0.76	-0.78	-1.07	-0.81	-0.96	-0.59

Table 3.3: The metallicities [Z/H] derived with Mg_2 and $\langle Fe \rangle$ of standard SSPs adopting the Worthey et al. FFs (col. 3-4), the Buzzoni et al. FFs (col. 5-6) and the Borges et al. FFs (see left-hand and central panel of Fig. 3.7). The adopted SSP age is 12 Gyr. The last 2 lines report the calibration of 47 Tuc, using the original data by Covino et al. (1995) and those obtained by us on their spectra by adopting the W94 index definition (see 3.2, Table 1). In Col. 2 the empirical metallicities of the GCs as given by Harris (1996) are listed.

(Fig. 3.1) are likely to trace the α elements and the Fe abundances, respectively. To this purpose, we divide the indices into three groups: those which should be predominantly sensitive to α-elements (Mg_1, Mg_2, etc.); those which should trace the Fe abundance (Fe4383; Fe5782; etc.); and the others (CN_1; CN_2; etc.), for which the case is less clear. The correlations are checked with respect to the model predictions. The evolutionary populations synthesis of Maraston (1998, see Sect. 3.3) has been updated for the computations of the whole set of Lick indices given in Worthey et al. (1994), plus the higher-order Balmer lines of Worthey & Ottaviani (1997).

Fig. 3.9 shows the correlation of the first group of indices with $Mg\,b$. The Mg indices: $Mg\,b$, Mg_1 and Mg_2 are very well consistent with each other and can be used as tracers of α-elements. The line-strength Ca4227 still appears to correlate with Mgb, although displaying slightly smaller values, while the other supposed Calcium-sensitive line Ca4455 does not. The reason for such mismatch is not clear to us. We suspect a calibration problem. The titanium-oxide indices TiO_1 and TiO_2 behave consistently with $Mg\,b$ at low metallicities, while at high metallicities these indices would overestimate the α-element abundance with respect to $Mg\,b$. However, TiO is contributed by M-type stars which may be poorly treated in the models and which are present only in the metal-rich clusters. The NaD index scales with $Mg\,b$ although with some scatter. As discussed by TMB03, the reason for the scatter is most probably the absorption by interstellar medium affecting objects close to the galactic plane. Because of this possible source of contamination the NaD index is a problematic metallicity indicator for stellar populations (see also Burstein et al. 1984).

Fig. 3.10 shows the second group of indices that should trace the iron abundance. Indeed, all the plotted indices correlate very well with $\langle Fe \rangle$. The models fit well most of these indices. The only exception is Fe5782, which is underpredicted by the models, suggesting an offset in the FFs. This offset most probably originates from the low signal-to-noise of the Lick/IDS data for Fe5782, which results from the extreme weakness of this line (S. Trager, *private communication*).
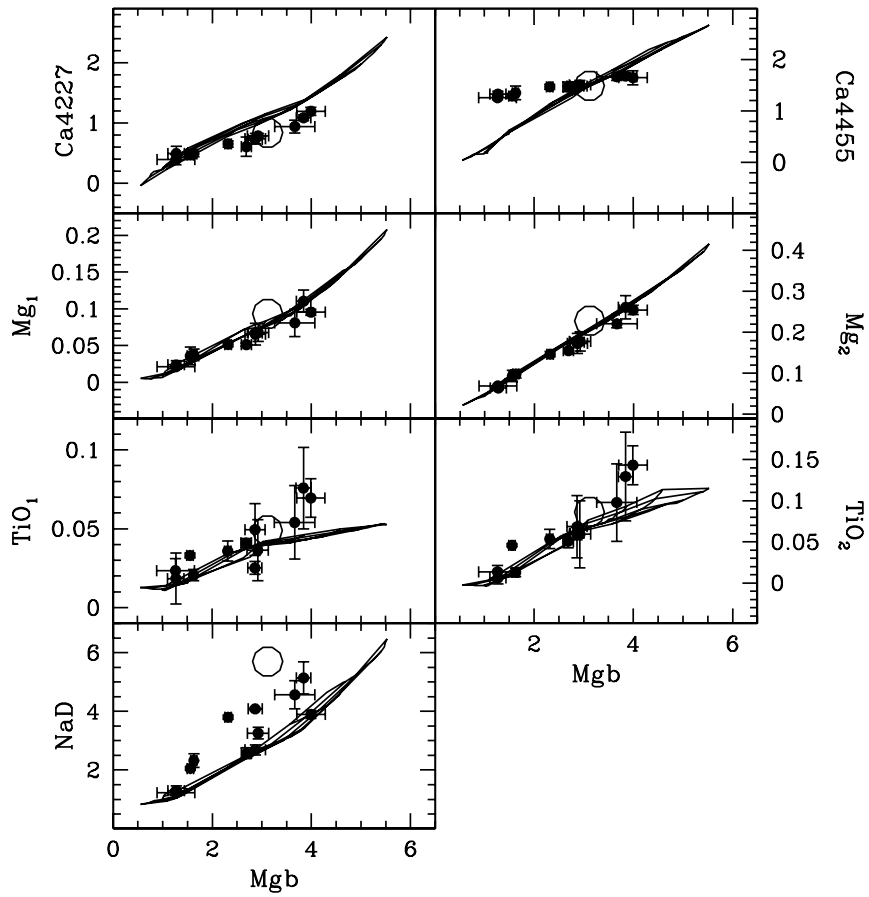
Figure 3.9: Calibration of α-sensitive Lick indices. Standard SSPs like in Figure 3.1. Filled symbols denote our sample GCs, the large open symbol the average value of the Bulge light in the Baade window.
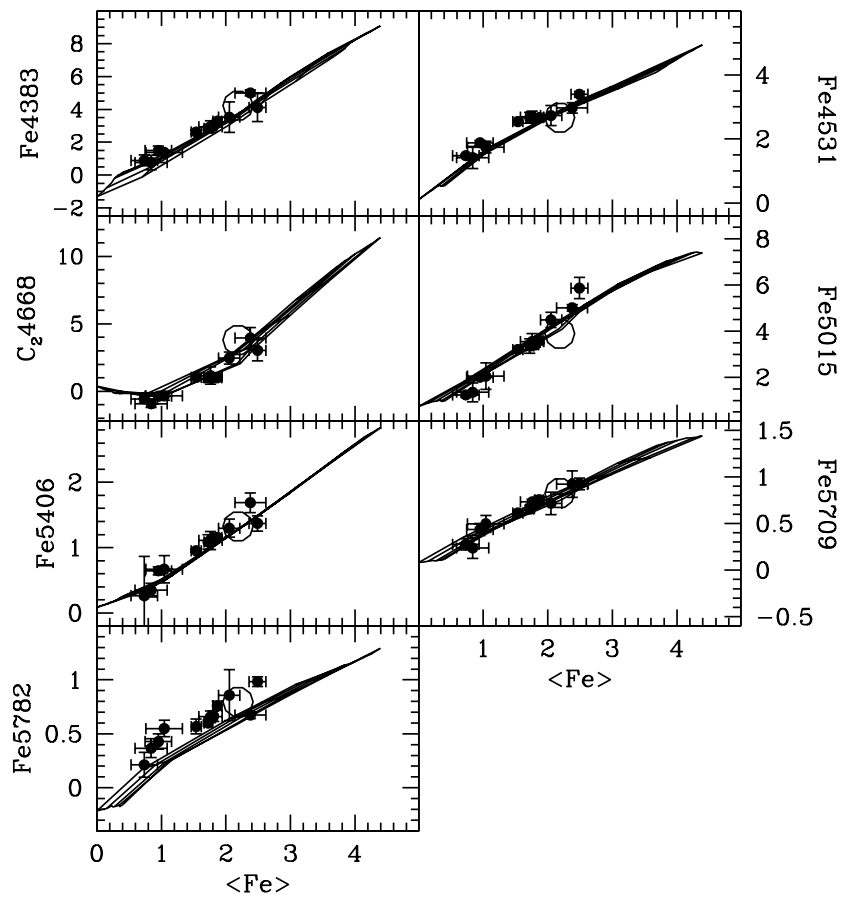
Figure 3.10: Model calibration. Iron-sensitive Lick indices. Model and data like in Fig. 3.9.

It is worth noting that the C_24668 index is tighly correlated to $\langle Fe \rangle$, although is supposed to trace the abundance of Carbon (see Trager et al. 1988). In Fig. 3.11
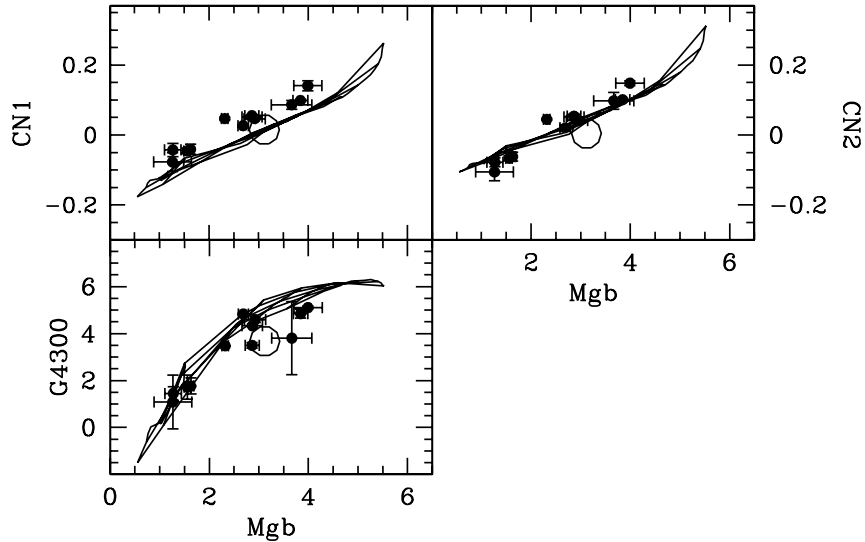
Figure 3.11: Model calibration of remaining Lick indices. Model and data like in Fig. 3.9.

we plot the remaining indices vs Mg b. CN_1 and CN_2 seem to trace the same elements as Mg b, though with an offset, especially at high metallicity and in the CN_1. At least part of the effect could be due to the fitting functions not incorporating stars belonging to high-metallicity GCs. As also discussed in Chapter 2, GCs have stronger CN indices compared to the bulge field (in Baade's Window) at the same value of $\langle Fe \rangle$. This may be caused by GCs stars accreting the CN-rich ejecta of AGB stars. The low-density environment of the field prevents a similar accretion on field stars. Therefore the models at high metallicity are lower than GC data because the fitting functions at high metallicity are contructed with field stars.

Finally also the G-band seems to follow magnesium, but the relation is more scattered.

In Fig.s 3.9 to 3.11, the large open symbol shows the average index values of 15 Bulge fields, located in Baade Window. In all indices, the value of the Bulge field is consistent with an average metallicity close to that of the most metal-rich GCs. This is quantitatively confirmed by the detailed metallicity distribution of the bulge stars from optical-infrared color-magnitude diagrams (Zoccali et al. 2002). The large value of the NaD index for the Bulge average field is again most probably due to contamination by interstellar medium, as discussed above.

3.6.3   Balmer Lines

As well known Balmer lines are strongest in A-type stars, and become pregressively weaker for decreasing temperatures. In synthetic stellar populations their strength is sensitive to the temperature of the main sequence turnoff, hence to the age. Therefore the Balmer line strengths are used to estimate the age of e.g. elliptical galaxies, in an attempt at breaking the age/metallicity degeneracy (e.g. Worthey et al. 1992). However, turnoff stars are not the only potential contributor to the strength of the Balmer lines: Horizontal Branch (HB) stars may be as warm or even warmer than the turnoff. Actually, the Hβ index is perhaps more sensitive to the
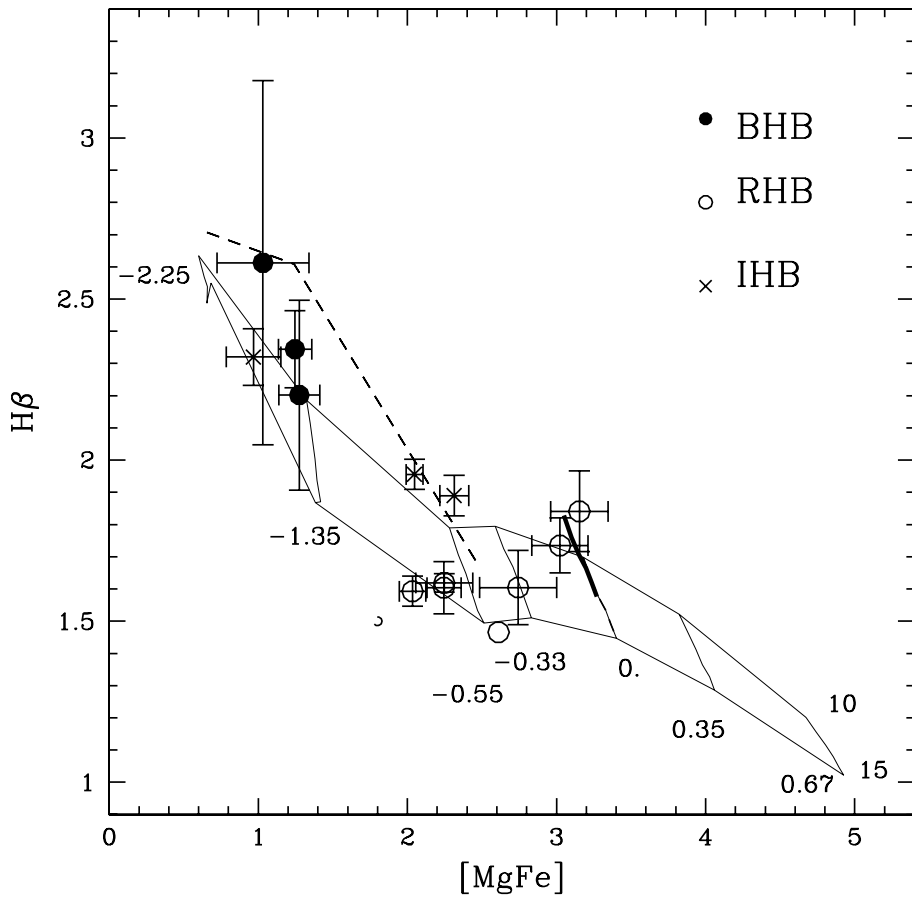
Figure 3.12: Impact of the morphology of the Horizontal Branch on Hβ. Models refer to SSP ages of 10 and 15 Gyr, and [Z/H] from -2.25 to 0.67 as labeled in the Fig.. Solid lines show models in which no mass loss has been accounted along the RGB. The dashed lines are 15 Gyr old models in which mass-loss has been applied at metallicities $\lesssim -0.5$, in order to reproduce the observed Hβ of metal poor GCs (see Maraston & Thomas 2000). The GCs of our sample are plotted according to their observed HB morphology, by means of the HBR parameter (from the Harris 1996 catalogue): pure blue HB (HBR=1, solid symbols); red HB (HBR=0, open symbols); intermediate morphologies (crosses). The open circle without errorbars shows the average value of 15 Bulge fields in Baade window. The very thick line at solar metallicity shows the locus of the solar metallicity models, as corrected to take into account the bluening of the tracks due to α-enhancement (see Fig. 3.6).

temperature distribution of the HB (the HB morphology) than to any other parameter (Worthey 1992; Barbuy & de Freitas Pacheco 1995; Greggio 1997; Maraston & Thomas 2000). Therefore, attempting to break the age/metallicity degeneracy with Balmer lines indices one runs into the age/HB morphology degeneracy. In the modeling the HB morphology cannot be derived from first principles, because of the rôle played by mass-loss on shaping the HB morphology . Additionally, possible dynamical effects (e.g. Fusi Pecci et al. 1993) may determine anomalous HB morphologies at a similar total cluster metallicity (the 2nd parameter problem in Milky Way GCs). Therefore the effect of the HB morphology to be used in SSP models needs to be calibrated on the Balmer indices.

For our models this is done in Maraston & Thomas (2000), to which we refer for more details on the model parameter. In that work the mass-loss to be applied at every SSP metallicity was calibrated in order to reproduce the Hβ line of the GC sample by Burstein et al. (1984), Covino et al. (1995) and Trager et al. (1998). Here we check if those calibrated models are able to reproduce the Balmer lines measured for our sample sample.

Fig. 3.12 shows two sets of SSP models obtained with different prescriptions for the RGB mass loss, various metallicities and two ages (10 and 15 Gyr). Aimimg at calibrating the model Balmer lines with metallicity, we have chosen as x-axis the index [MgFe] [8]. TMB03 show that this index by washing out [α/Fe] effects, is able to trace total metallicity.

The solid lines connect models in which no mass loss is applied to the RGB. In this case the morphology of the HB is red (i.e., all HB lifetime is spent on the red side of the RR-Lyrae location at $\log T_{\rm eff} \sim 3.85$), except at the very low metallicity [Z/H] $= -2.25$, where the HB is spent at $\log T_{\rm eff} \gtrsim 3.85$ even when no mass-loss is applied. The dashed line shows the 15 Gyr SSPs with [Z/H] $\lesssim -0.5$, in which mass-loss has been applied on the RGB according to canonical prescriptions. This leads to extended HBs, with blue morphologies (i.e. the whole HB lifetime is spent the blue side of the RR-Lyrae location) at [Z/H] $= -2.25$, and intermediate HB morphologies at metallicities between [Z/H] $= -1.35$ ($\sim 84\%$ of the HB lifetime is spent blueward the RR-Lyrae) and [Z/H] $= -0.55$ ($\sim 10\%$ of HB lifetime is spent blueward the RR-Lyrae).

The cluster data are plotted according to their observed HB morphologies, (B(lue)HB: filled symbols; R(ed)HB: open symbols; I(ntermediate)HB: asterisks) by means of the HBR parameter (Harris 1996).

The calibrated models by Maraston & Thomas (2000) are able to reproduce the observed Hβ of our sample GCs. In particular they reproduce the relatively strong Hβ (~ 1.9 Å) of NGC 6388 and NGC 6441, which are metal-rich clusters ([Fe/H]$_{\rm ZW} = -0.6; -0.53$) with an extension of the HB to the blue (Rich et al. 1997). The percentage of HB stars that is found blueward the RR Lyrae gap is: $\sim 15\%$ for NGC 6388 (Zoccali et al. 2000b) and $\sim 13\%$ for NGC 6441 (M. Zoccali, *private communication*). This is well consistent with the HB evolutionary timescales of the Maraston & Thomas (2000) models as given above.

Concerning the most metal-rich objects NGC 6528 and NGC 6553, their relatively strong Hβ cannot be ascribed to HB effects since both clusters have a red Horizontal Branch (Ortolani et al. 1995). Part of the effect can be explained in terms of α-enhancement at high metallicities, without invoking young ages which would be in contradictions with CMD determinations (Ortolani et al. 1995). In Sect. 3.5 we have shown (Fig. 3.6) that α-enhanced tracks are bluer than the corresponding solar-scaled ones. As a consequence the Hβ lines are higher by 0.13 Å at solar metallicity. The thick line in Fig. 3.12 connects the SSP models as shifted by this amount. Note however the rather large errorbar on the Hβ of NGC 6553.

---

[8][MgFe]$= \sqrt{{\rm Mg}\,b \cdot \langle {\rm Fe} \rangle}$

The index of the average light of the Bulge is shown as an open symbol without errorbars, and sits on the ~ 15 Gyr model with red HB. The low Hβ line does not leave room for intermediate age stars in our sampled Bulge fields. Finally
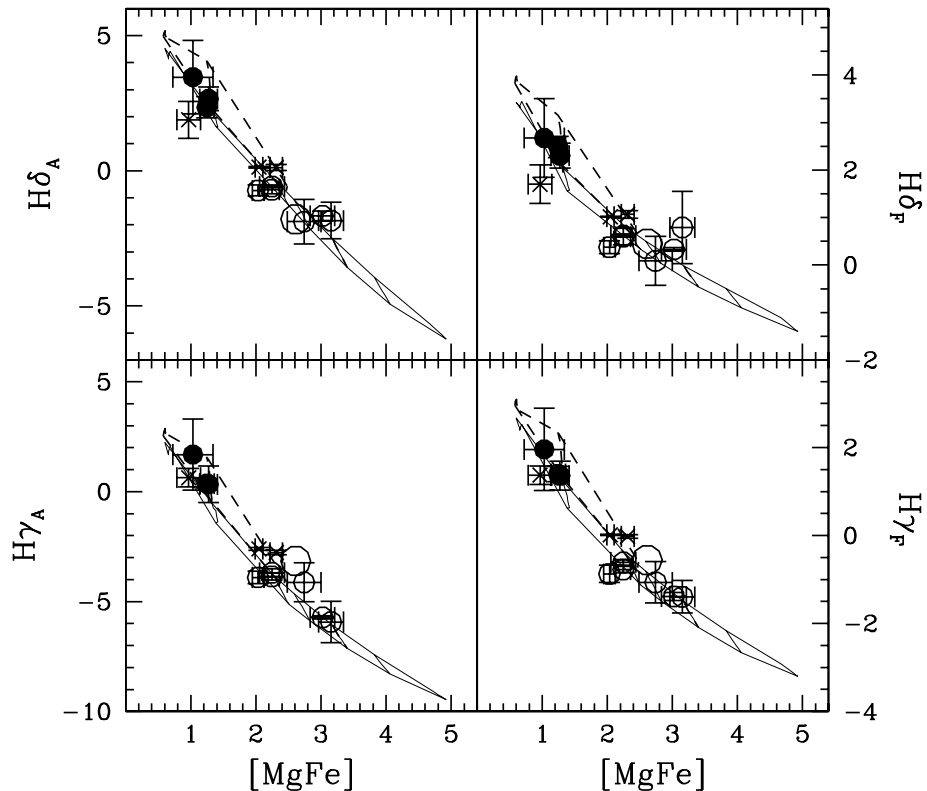
Figure 3.13: Calibration of the higher-order Balmer lines Hδ_A, Hδ_F, Hγ_A and Hγ_F (Worthey & Ottaviani (1997) of the standard SSP models, see Figure 3.12.

we calibrate the higher-order Balmer lines Hδ_A, Hγ_A, Hδ_F and Hγ_F (Worthey & Ottaviani (1997) of the same models, in Fig. 3.13. It can be appreciated a very good consistency between the Hβ and the higher-order Balmer lines.

3.7 Summary and Conclusions

Synthetic Lick indices (e.g., Mg$_2$, ⟨Fe⟩, Hβ, etc.) of stellar population models (SSP) are calibrated over a range of metallicities that extends up to solar metallicity using a sample of galactic globular clusters which includes high-metallicity clusters of the Galactic bulge. These data allow us to investigate *empirically* a well known property of elliptical galaxies, known as "magnesium overabundance" (Worthey et al. 1992), where the observed Mg indices in ellipticals are much stronger at given iron than predicted by *standard* models. By standard models we mean those constructed using stellar templates that are α-enhanced at low metallicity but assume solar elemental proportions at high metallicity. This effect has been generally interpreted in terms

of α-enhancement of elliptical galaxies, even if the bulk of their stellar population is metal rich. However, such conclusion rests on two assumptions: i) the models that are believed to represent solar scaled elemental ratios are correct, and ii) the Lick Mg and Fe indices trace the abundance of the corresponding element.

Using our GC database we have checked *empirically* both assumptions by comparing the Lick indices of the GCs spectra with those of ellipticals. The result is that the magnesium and iron indices of the metal-rich GCs, of the integrated light of the Galactic bulge, and of elliptical galaxies, define a fairly tight correlation in the Mg b-$\langle$Fe$\rangle$diagram, with elliptical galaxies lying on the prolongation of the correlation established by the GCs, i.e., also the metal-rich GCs of the Milky Way bulge exhibit the "magnesium overabundance" syndrome. Since the GCs are indeed known to have enhanced [α/Fe] ratios from stellar spectroscopy ([α/Fe] $\simeq$ +0.3), we conclude that the interpretation of elliptical galaxy spectra in terms of "magnesium overabundance" is indeed correct. The comparison with the GCs further allows us to point out that, rather than "magnesium overabundance", the enhanced [α/Fe] ratio in GCs, and ellipticals is most probably the result of an *iron deficiency with respect to the solar values* (see Sect. 3.6). This agrees with previous suggestions (Buzzoni et al. 1994; Trager et al. 2000b) and with the recent results by TMB03. The enhanced [α/Fe] ratio implies short formation timescales for the bulk stellar population, an important constraint for formation models of elliptical galaxies and bulges (e.g., Matteucci 1994; Thomas et al. 1999), which is difficult to reconcile with current semianalytic models of galaxy formation (Thomas & Kauffmann 1999).

In parallel, the comparison of the SSP model with the GC data has allowed us to shed some light on the models themselves. Around solar metallicity, the standard models are based on the stellar indices of Milky Way *disk* stars (by Worthey et al. 1994 or Buzzoni et al. 1992; 1994), and therefore would reproduce the indices of stellar populations with *solar-scaled* elemental proportions. This explains why they fail to reproduce the Mg b-$\langle$Fe$\rangle$correlation followed by galactic GCs and the Galactic bulge, which are characterized by elemental ratios which are specific to the Galactic *spheroid*. This failure was also noted by Cohen et al. (1998) for both the metal rich globulars of the Milky Way as well as for those of M87, but was not attributed to an abundance effect.

At metallicities [Z/H] $\lesssim -1$. the standard models use metal poor template stars that belong to the galactic halo, hence have supersolar [α/Fe] ratios. This explain why standard models successfully reproduce the Lick indices of the metal poor GCs, which also belong to the halo and are α-element enhanced. The conclusion is that the standard SSP models reflect abundance ratios which vary with metallicity. This clearly complicates their use as abundance indicators for extra-galactic stellar systems.

We have then proceeded to compare the data to a new set of SSP models in which the [α/Fe] ratio is treated as an independent variable (Thomas et al. 2002b). The result is that the Galactic GCs and bulge, as well as most ellipticals, are very well reproduced by coeval, old (12 Gyr) models with [α/Fe] = +0.3, and various metallicities. The uniqueness of this α-enhancement solution for the stellar populations of GCs, the bulge, and ellipticals was checked by thoroughly exploring the parameter space of the SSP models. We find that the Lick indices are little affected by the choice of the specific set of stellar evolutionary tracks or fitting functions. The only viable alternative to abundance effects, which can produce high values of the Mg indices coupled with low values of the Fe indices is a very steep IMF (much steeper than Salpeter). This solution, though formally acceptable, is practically ruled out by many other observational constraints for the clusters, as well as for the bulge and elliptical galaxies.

A closer look to the Mg b-$\langle$Fe$\rangle$diagram reveals that elliptical galaxies, unlike GCs, span a range of [α/Fe] values, from just marginally super-solar, to $\sim$ +0.4. Since the

Mg index correlates with the galaxy luminosity, the trend is in the direction of an increasing α-element overabundance with increasing luminosity (mass). Apparently, the more massive the galaxy, the shorter the duration of the star formation process (Thomas et al. 2002a). The origin of this trend remains to be understood.

Our database of GCs was further used to check in an empirical fashion the effectiveness of the other Lick indices to trace the element abundances. Good indicators of α-elements are found to be all the Mg lines (Mg_2, Mg_1 and $Mg\,b$), and TiO_1 and TiO_2 at subsolar metallicities. Also the index Ca4227 does correlate with the Mg indices, though a small offset between the two might be present. Nearly all iron line indices (Fe4384, Fe4531, Fe5015, Fe5270, Fe5335) are found to display very tight relations against another. The indices CN_1, CN_2 and the G-band G4300 follow Mg. On the contrary, indices such as Ca4455, NaD and Fe5782 appear to be poorly calibrated, and we cannot recommend their use as abundance indicators for extra-galactic systems.

The Balmer Hβ plus the higher-order lines by Worthey & Ottaviani (1997) Hδ_A, Hδ_F, Hγ_A, & Hδ_F are very well reproduced by the standard SSP models considered here (Maraston & Thomas, 2000; Maraston 2003), which indicates that they are only marginally affected by the [α/Fe] ratio (see Tripicco & Bell 1985; TMB03). Much more important for their correct modeling is to account for the Horizontal Branch morphology. In particular the rather high Balmer lines measured for NGC 6388 and NGC 6441 are modelled with a tail of warm Horizontal Branch stars ($\sim$ 10% of the total HB population). These warm stars are indeed observed in the CMD of these two clusters (Rich et al. 1997), in a number ($\sim$ 10%, Zoccali et al. 2000b) which is in perfect agreement with the value required to reproduce the strength of the Balmer lines.

Finally, we point out that the Mg indices of very metal poor stellar populations ([Fe/H] $\sim$ -1.8) are dominated by the contribution of the lower main sequence. Therefore, these indices are prone to be affected by the IMF and in GCs by the subsequent evolution of the mass function due to the dynamical evolution of the clusters themselves. It follows that the Mg indices of very metal-poor stellar populations are not reliable metallicity indicators.

Chapter 4

Integrated-Light Spectroscopy of Extragalactic Globular Clusters[1]

4.1   Introduction

Having understood the globular clusters of the Milky Way, we now turn to extragalactic globular cluster system[1]. Compared to their host galaxies globular clusters are remarkably simple stellar structures. They form throughout the lifetime of the universe and are witnesses of major star-formation episodes (e.g. Ashman & Zepf 1998; Kissler-Patig 2000; Harris 2001). As such, their ages, metallicities, and chemical compositions can provide detailed insights in the formation epochs, processes, and timescales which lead to the assembly of the galaxies we observe in the local universe.

Photometry is one way to assess ages and metallicities of extragalactic globular clusters (among many others Schweizer et al. 1996; Whitmore et al. 1997; Kissler-Patig et al. 1997; Puzia et al. 1999; Maraston et al. 2001b; Jordán et al. 2002; Kissler-Patig et al. 2002; Puzia et al. 2002a; Hempel et al. 2003). However, the age-metallicity degeneracy of photometric colours hampers the detailed reconstruction of star-formation histories (e.g. Faber 1972; O'Connell 1976).

Spectroscopy is an independent alternative to determine star-formation histories and the basic chemistry of globular clusters. The Lick system of absorption line indices (Burstein et al. 1984; Faber et al. 1985; González 1993; Worthey 1994; Worthey & Ottaviani 1997; Trager et al. 1998), although not free from age-metallicity degeneracy, is a way to measure absorption features which are sensitive to age and metallicity. In combination with state-of-the-art simple stellar population (SSP) models that take the effect of element abundance-ratio variations into account (e.g. Maraston et al. 2003; Thomas et al. 2003a) indices can shed light on star-formation timescales and the chemical composition. With today's 8–10m class telescopes the mean Balmer-line index uncertainty for individual extragalactic globular clusters can be reduced to values of the order of the mean isochrone separation in SSP models (~ 0.1 Å between 12 and 13 Gyr). Data of this high-accuracy become available, for the first time, and is in principle capable of resolving star-formation histories even for very old stellar populations.

---

[1]The content of this Chapter is in press and will be published in Puzia, T. H., Kissler-Patig, Thomas, D., Maraston, C., Saglia, R. P., Bender, R., Richtler, T., Goudfrooij, P., & Hempel, M. 2003, A&A.

Previous spectroscopy of globular cluster systems in early-type galaxies aiming at the derivation of ages and metallicities of single clusters was performed for M 87 (Cohen et al. 1998), NGC 1023 (Larsen & Brodie 2002), NGC 1316 (Goudfrooij et al. 2001b), NGC 1399 (Kissler-Patig et al. 1998a; Forbes et al. 2001), NGC 3115 (Kuntschner et al. 2002b), NGC 3610 (Strader et al. 2003a), NGC 4365 (Larsen et al. 2003), NGC 4472 (Beasley et al. 2000), and NGC 4594 (Larsen et al. 2002a). However, the data quality allowed only in a few cases to determine the ages and metallicities of *individual* globular clusters. The data of most studies required summing the spectra of all or at least a given sub-population of clusters to obtain meaningful results. Moreover, the different choices of diagnostic plots (such as Hβ vs. $\langle$Fe$\rangle$ or Hγ vs. Mgb) made the comparison between galaxies difficult. The existence of SSP models with *well-defined* abundance ratios only recently allows to account for varying abundance ratios, such as [α/Fe]. Inconsistent use of index passband definitions between data and models introduced additional uncertainties.

In this Chapter, we present photometry and Lick line-index measurements from our on-going spectroscopic survey of globular cluster systems in early-type galaxies. These high-quality spectroscopic data will be used in subsequent Chapters of this thesis to derive accurate ages, metallicities, and [α/Fe] ratios in a self-consistent fashion. The sample presented here includes photometric and spectroscopic data for 143 extragalactic globular clusters.

4.2 Pre-Imaging Data

The host galaxies (NGC 1380, NGC 2434, NGC 3115, NGC 3379, NGC 3585, NGC 5846, and NGC 7192) were selected to sample a significant range in environmental density at intermediate galaxy luminosity and velocity dispersion in the range $-19.2 \gtrsim M_B \gtrsim -21.2$ and $184 \lesssim \sigma \lesssim 264$ km s^{-1}, respectively. All galaxies are of early type ($T < -2$) according to the RC3 galaxy catalog (de Vaucouleurs et al. 1991). Our sample includes five elliptical and two lenticular galaxies (see Tab. 4.1). We used Tully's ρ_{xyz} parameter (Tully 1988) to parameterize the environmental density per Mpc^3 of galaxies which are brighter than $M_{\mathrm{B}} = -16$ to separate field from group/cluster environment. In this work, we define galaxies with $\rho_{\mathrm{xyz}} < 0.5$ as field objects and galaxies with $\rho_{\mathrm{xyz}} > 0.5$ as group/cluster members. Three galaxies of our sample (NGC 1380, NGC 3379, and NGC 5846) are assigned group/cluster membership, while the remaining four galaxies are considered field members. Among other relevant parameters, ρ_{xyz} and M_B are summarized in Table 4.1 for all our sample galaxies.

The imaging mode of FORS2 at ESO's Very Large Telescope was used to obtain pre-imaging data for each galaxy in multiple filters to select candidate globular clusters for spectroscopic follow-up. Exposure times in each filter are summarized in Table 4.2. Standard calibration routines in IRAF were applied to bias and flatfield the images. Galaxy light was subtracted by, first, removing stellar objects from the image by using SExtractor (v2.1.6 Bertin & Arnouts 1996) and, second, smoothing the residual image with a large median filter. The median filtered image was subsequently subtracted from the original image. This procedure was iterated with a smaller median filter to discard weak haloes around objects on steep galaxy-light slopes near the central regions. SExtractor was used to perform photometry in a 6-pixel-diameter aperture which was found to yield the highest signal to noise of measured magnitudes. The residual flux which falls outside the 6-pixel aperture was measured in a growth-curve analysis for a handful of objects in each filter for each single galaxy. Uncertainties for the aperture correction were found to be of the order ~ 0.01 mag. All instrumental magnitudes were subsequently corrected with these corrections found.

Parameter	NGC 1380	NGC 2434	NGC 3115	NGC 3379	NGC 3585	NGC 5846	NGC 7192	Ref.
type	-2/LA	-5/E0+	-3/L$-$	-5/E1	-5/E6	-5/E0	-4.3/E+	(1)
RA (J2000)	03 36 27	07 34 51	10 05 14	10 47 50	11 13 17	15 06 29	22 06 50	(2)
DEC (J2000)	-34 58 34	-69 17 01	-07 43 07	$+12$ 34 55	-26 45 18	$+01$ 36 21	-64 18 57	(2)
v_{rad}	1841 ± 15	1390 ± 27	670 ± 12	889 ± 12	1399 ± 27	1710 ± 12	2897 ± 32	(1)
E_{B-V}	0.017	0.248	0.047	0.024	0.064	0.055	0.034	(3)
$(B-V)_{eff,o}$	0.92	1.09	0.94	0.98	0.99	1.03	0.97	(1)
$(V-I)_{eff,o}$	1.21	1.42	1.25	1.24	1.26	1.28	1.24	(4)
$(V-K)_{eff,o}$	3.36	3.10	. . .	3.08	. . .	3.12	. . .	(5)
$(m-M)_V$	31.23 ± 0.18	31.67 ± 0.29	29.93 ± 0.09	30.12 ± 0.11	31.51 ± 0.18	31.98 ± 0.20	32.89 ± 0.32	(6)
M_B	-20.04	-19.48	-19.19	-19.39	-20.93	-21.16	-20.55	(7)
a/b^{b}	0.56	0.94	0.49	0.93	0.58	0.89	1.00	(7)
σ^{c}	225	204	264	209	218	252	184	(8)
ρ_{xyz}^{d}	1.54	0.19	0.08	0.52	0.12	0.84	0.28	(7)
N_{GC}^{e}	560 ± 30	. . .	520 ± 120	300 ± 160	. . .	2200 ± 1300	. . .	(9),(10)
S_N^{f}	1.5 ± 0.5	. . .	1.6 ± 0.4	1.2 ± 0.6	. . .	3.5 ± 2.1	. . .	(9),(10)

[a] http://nedwww.ipac.caltech.edu

[b] Ratio of semi-minor/semi-major axis

[c] Central velocity dispersion in km s^{-1}

[d] Environmental density of galaxies brighter than $M_B = -16$ in galaxies/megaparsec^3 (Tully 1988)

[e] Total number of globular clusters

[f] Specific frequency, $S_N = N_{GC} \cdot 10^{\,0.4\cdot(M_V+15)}$ (Harris & van den Bergh 1981)

Table 4.1: Basic information on host galaxies. The references are: (1) de Vaucouleurs et al. (1991); (2) NED[a]; (3) Schlegel et al. (1998); (4) Buta & Williams (1995); (5) Pahre (1999); (6) Tonry et al. (2001); (7) Tully (1988); (8) McElroy (1995); (9) Kissler-Patig et al. (1997); (10) Ashman & Zepf (1998).

Each data set was calibrated using standard-star observations for each night provided by the quality control group of ESO. All observations were performed under photometric conditions and could be calibrated to an average intrinsic accuracy of ~ 0.03 mag.

We augment our optical photometric data with the recently published near-infrared data for NGC 3115 (Puzia et al. 2002a) and for NGC 5846 and NGC 7192 (Hempel et al. 2003).

Galaxy	B	V	R	I	K
NGC 1380	...	700	...	700	...
NGC 2434	...	700	...	700	...
NGC 3115	160	300	160	300	15500[a]
NGC 3379	...	300	...	300	...
NGC 3585	800	...	...	800	...
NGC 5846	900	300	160	300	10000[b]
NGC 7192	900	600	900	600	12000[b]

[a] data were taken from Puzia et al. (2002a).

[b] data were taken from Hempel et al. (2003).

Table 4.2: Journal of photometric observations. Exposure times are given in seconds.

4.2.1 Consistency Check with WFPC2 Photometry

We use WFPC2/HST archive data which were obtained from ST-ECF in Garching to check for consistency of our photometry with that of WFPC2. For the sake of homogeneity, we use the pipeline-processed, co-added (averaged), and cosmic-cleaned image cubes provided as association files by the archive. Photometry was performed in the standard Holtzman et al. (1995a) $0.5''$ radius aperture using SExtractor and corrected for the y-CTE ramp as described in Holtzman et al. (1995b). We transform the WFPC2 filters F450W, F555W, F702W, and F814W to Johnson-Cousins filters B, V, R, and I, respectively, using the prescriptions in Holtzman et al. (1995a).

Galaxy	ΔB	ΔV	ΔR	ΔI	N_{obj}
NGC 1380	...	-0.035 ± 0.018	...	...	142
NGC 2434	...	-0.012 ± 0.021	...	-0.044 ± 0.022	113
NGC 3115	...	$+0.078$ ± 0.017	...	$+0.043$ ± 0.017	79
NGC 3379	...	-0.005 ± 0.020	...	$+0.079$ ± 0.030	46
NGC 3585	...	...	...	-0.080 ± 0.025	89
NGC 5846	...	$+0.011$ ± 0.023	$+0.066$ ± 0.039	-0.055 ± 0.019	89
NGC 7192	-0.049 ± 0.033	$+0.004$ ± 0.025	...	-0.035 ± 0.022	74

Table 4.3: Photometric offsets between FORS2 and WFPC2 data. Offsets are defined in the sense $\Delta m = m_{\mathrm{FORS2}} - m_{\mathrm{WFPC2}}$. The given uncertainties are errors of the mean. The last column shows the number of objects from which the photometric offsets were calculated.

At the distance of the two nearest galaxies in our sample, NGC 3115 and

NGC 3379 (see Tab. 4.1), globular clusters are resolved by HST. Therefore their photometry needs an additional zero-point correction since the standard aperture corrections for stellar profiles (see Holtzman et al. 1995a) do not apply. At the distance of NGC 3115 a globular cluster with a typical half-light radius of 3 pc appears with $\sim 0.06''$ on the chip and will be resolved by the planetary camera (0.0455 $''$/pix). However, such objects on the wide-field chips (0.0996 $''$/pix) are on the edge of being resolved. $\sim 90\%$ of Milky Way globular clusters have half-light radii smaller than 3 pc (Harris 1996) and their counterparts in NGC 3115 and NGC 3379 are expected to have similar size distributions (e.g. Kundu & Whitmore 1998; Larsen et al. 2001). Even if most comparison objects are globular clusters with half-light radii ~ 3 pc, we do *not* expect the aperture corrections to be larger than the total uncertainty of the FORS2 and WFPC2 photometric calibration. For the remaining sample galaxies most globular clusters are not resolved by WFPC2. Hence, we do not apply any aperture corrections to the WFPC2 photometry.

We find good agreement between the two photometric data sets with offsets $\lesssim |0.08|$ mag (see Table 4.3) which were calculated in the sense $\Delta m = m_{\mathrm{FORS2}} - m_{\mathrm{WFPC2}}$. On average, the offsets are small and of the order of their uncertainties showing no systematics with galaxy distance, background level, etc. Hence, we do *not* apply these corrections to our FORS2 data.

4.2.2 Colour-Magnitude Diagrams

In the following two Sections we present the photometric selection of globular cluster candidates for follow-up spectroscopy. For this purpose we use colour-magnitude and colour-colour diagrams.

Figure 4.1 shows colour-magnitude diagrams (CMDs) for our sample globular cluster systems using the FORS2 pre-imaging data. Small dots indicate the entire data extracted from our pre-imaging fields. Asterisks, squares, and 4-prong stars show magnitudes and colours of spectroscopically confirmed globular clusters (see Sect. 4.4.1), background galaxies, and foreground stars, respectively.

Globular cluster candidates were pre-selected by their photometric error ($\Delta m \leq$ 0.2 mag), FWHM ($\leq 1.5 \langle \mathrm{FWHM} \rangle$), PSF ellipticity ($\epsilon \leq 0.6$), and the SExtractor star/galaxy classifier (> 0.0, i.e. only clearly extended sources were rejected). Due to the good spatial coverage of the FORS2 field of view, each sample is the most comprehensive compilation of candidate globular cluster colours so far. We find clear bimodalities in NGC 1380, NGC 3115, and NGC 3585 (note that we lack V band photometry for NGC 3585 and use B magnitudes instead). Weak indications for possible multi-modality are found in each of the former three colour distributions. To test these distributions for *bi*-modality, we apply the KMM algorithm (Ashman et al. 1994) to the constrained samples with a colour range $0.8 < V - I < 1.4$ for NGC 1380, $0.9 < V - I < 1.4$ for NGC 3115, and $1.2 < B - I < 2.4$ for NGC 3585. The code yields peaks at $V - I = 0.94 \pm 0.01$ and 1.20 ± 0.01 mag for NGC 1380 (with a number ratio blue/red= 0.46), $V - I = 1.01 \pm 0.01$ and 1.21 ± 0.01 mag for NGC 3115 (blue/red= 0.87), and $B - I = 1.56 \pm 0.01$ and 2.05 ± 0.01 for NGC 3585 (blue/red= 1.02).

The colour histograms for NGC 2434, NGC 3379, NGC 5846, and NGC 7192 are consistent with single-peak distributions. However, it is interesting to note that these peaks are systematically broader than colour peaks of sub-groups in clearly multi-modal distributions. One reason for a broad single-peak colour distribution (in the optical) might be that the gap between two old metal-poor and metal-rich globular cluster populations is filled by metal-rich intermediate-age clusters. A large spread in age and metallicity in the underlying globular cluster system would naturally produce a sequence in colours rather than multiple distinct peaks. In the context of the hierarchical galaxy formation scenario, *clearly* bi-modal globular
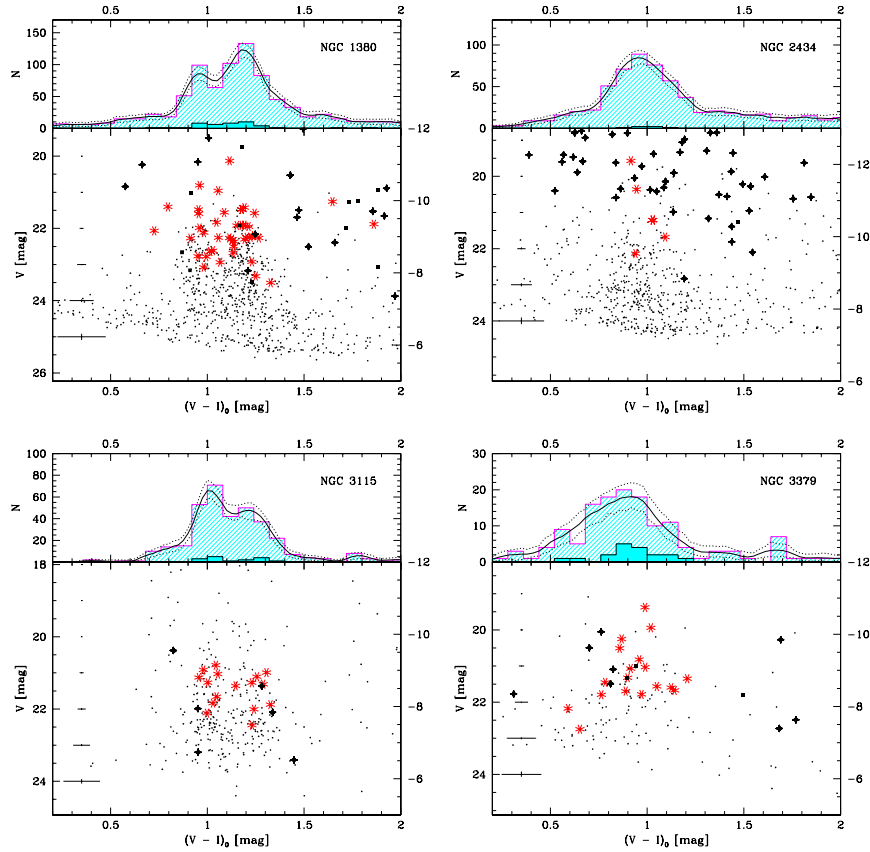
Figure 4.1: V vs. $V-I$ CMDs for globular cluster systems of NGC 1380, NGC 2434, NGC 3115, and NGC 3379. Asterisks indicate spectroscopically confirmed globular clusters; 4-prong stars and filled squares show objects whose redshifts are consistent with foreground stars and background galaxies, respectively. Left ordinates show apparent magnitudes, right ordinates indicate absolute magnitudes calculated using distance moduli from Table 4.1. Each panel shows average photometric error bars near the left ordinate. The upper sub-panels show histograms of the colour distributions. Hatched histograms were created from the entire photometric data, solid histograms show colour distributions of spectroscopically confirmed globular clusters. The solid and dotted lines are probability density estimates with their bootstraped 90% confidence limits (for details see Silverman 1986). The bin size of the histograms was adjusted to 0.08 mag which roughly corresponds to the mean photometric error.
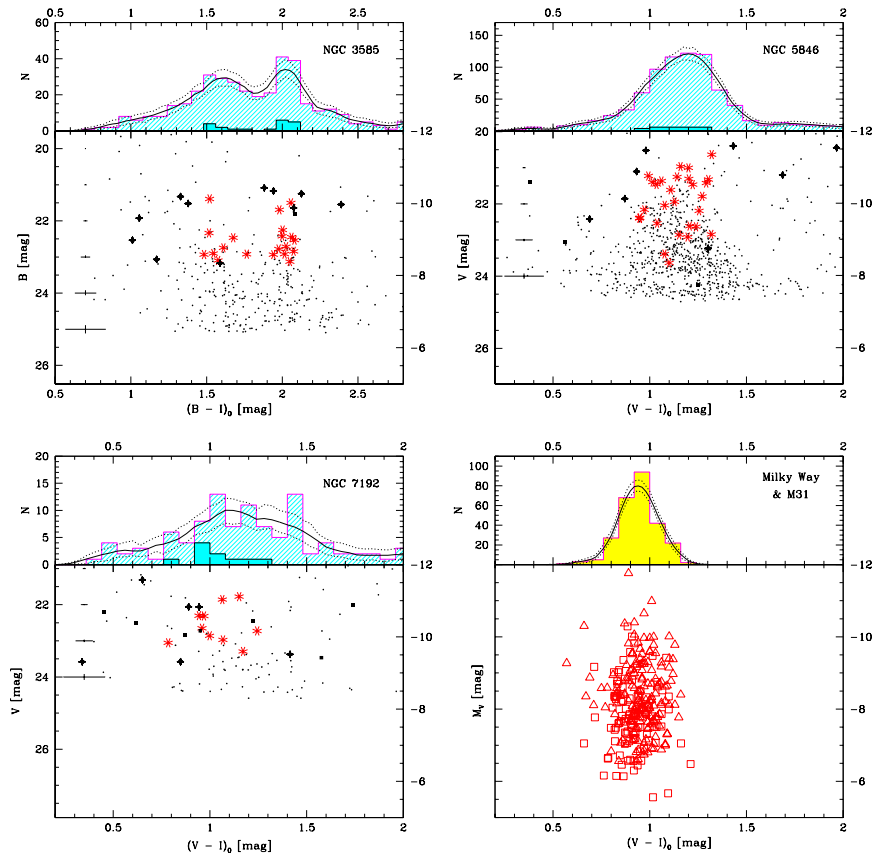
Figure 4.1: – *continued.* CMDs for NGC 3585, NGC 5846 and NGC 7192. Please, note that due to the lack of V-band data, we plot B vs. $B - I$ for NGC 3585. For comparison, the CMD for globular clusters in the Milky Way (*squares*) and M31 (*triangles*) is plotted in the lower right panel. The Milky Way data were taken from the 1999 update of the McMaster catalog (Harris 1996), while M31 data are from Barmby et al. (2000).

cluster colour distributions may have to be considered as special cases of a wide range of colour distribution morphologies.

Indeed, using a combination of optical and near-infrared photometry it was recently shown that NGC 4365 hosts an intermediate-age globular cluster sub-population which produces a single-peak $V - I$ colour distribution (Puzia et al. 2002a). Hempel et al. (2003) find intermediate-age globular clusters in NGC 5846 and NGC 7192, although the case of NGC 7192 is less conclusive. For details on near-infrared-optical colours of globular clusters in NGC 3115, NGC 5846, NGC 7192 we refer the reader to Puzia et al. (2002a) and Hempel et al. (2003).

Most of the colour distributions are consistent with previous colour-distribution studies (Gebhardt & Kissler-Patig 1999; Larsen et al. 2001; Kundu & Whitmore 2001a,b), but only where the latter had large enough sample size. Our photometry goes deep (reaching the GCLF turn-over in most cases, see Fig. 4.6) and our field sampling ($6.7' \times 6.7'$) is large enough to cover a representative fraction ($\geq 51\%$[2]) of the observed globular cluster system. For instance, the $V - I$ colour distribution of NGC 3379 gained a substantial amount of blue globular clusters ($\sim 15\%$ of the entire population down to $V = 23.5$) which have not been included in previous HST/WFPC2 studies (e.g. Larsen et al. 2001). This is likely to be due to a significant difference in spatial distribution of red and blue globular clusters in this galaxy. There is evidence that red clusters are more concentrated towards the center than the blue globular cluster sub-population which rather resides in the halo (see Sect. 4.2.4). This illustrates that colour distributions which were created from photometric data of limited field size (e.g. HST/WFPC2) might be misleading if significant differences in spatial distributions of globular cluster sub-populations are present.

4.2.3 Optical/Near-Infrared Colour-Colour Diagrams

We combine now our optical FORS2 photometric data with recently published near-infrared data for NGC 3115 (Puzia et al. 2002a), NGC 5846, and NGC 7192 (Hempel et al. 2003) and construct optical/near-infrared two-colour diagrams of candidate and confirmed globular clusters. All near-infrared data were obtained with the ISAAC instrument attached to ESO's VLT with a $2.5' \times 2.5'$ field of view. Figure 4.2 shows $I - K$ vs. $B - K$ diagrams with spectroscopically confirmed globular clusters marked as asterisks. Due to the smaller field of view of the near-IR data, these two-colour diagrams are restricted to the central regions of each galaxy and do not cover a representative of the entire globular cluster system (see discussion in §4.2.2). Although optical/near-infrared colours are powerful metallicity discriminators (e.g. Puzia et al. 2002b), they are of limited use for the slit mask design due to the very constrained field of view.

However, *a posteriori* it is worthwhile to compare optical/near-infrared colours of globular clusters, background galaxies and foreground stars in order to minimise contamination of the candidate selection. Based on our set of photometric passbands (B, V, R, I, K), we find that the combination of $I - K$ and $B - K$ separates globular clusters from stars and galaxies most reliably. In the following we describe how to reduce the contamination of globular cluster candidate samples by foreground stars and background galaxies.

Eliminating Foreground Stars

Globular clusters fall on a rather narrow sequence in the $I - K$ vs. $B - K$ diagram (hatched region in Figure 4.3). In general, at similar $I - K$ colours, cool giant stars lack B band flux compared to the integrated light of globular clusters and

---

[2]The fraction was determined with the surface density profiles found in Sect. 4.2.4.
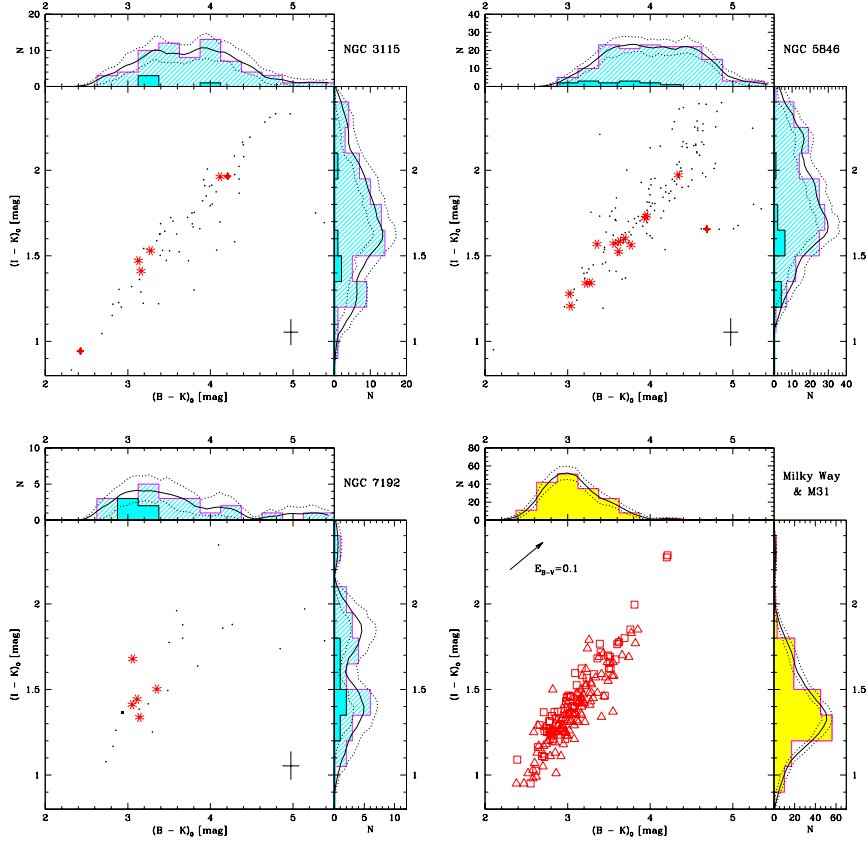
Figure 4.2: Optical/near-infrared $I - K$ vs. $B - K$ two-colour diagrams for objects in NGC 3115, NGC 5846, and NGC 7192. Near-infrared data for NGC 3115 were taken from Puzia et al. (2002a) while the near-infrared data for NGC 5846 and NGC 7192 were taken from Hempel et al. (2003). Average photometric errors are indicated in the lower right corner of each diagram. Asterisks indicate spectroscopically confirmed globular clusters. 4-prong stars and solid squares show colours of confirmed foreground stars and background galaxies, respectively. Hatched and solid histograms in the sub-panels show the colour distributions of all objects and of spectroscopically confirmed globular clusters. Solid lines within the sub-panels are probability density estimates with their 90% confidence limits (dotted lines). In the lower right panel we show colours of globular clusters in M31 (*triangles*) and the Milky Way (*squares*). Optical colours for Milky Way globular clusters were taken from Harris (1996), near-infrared colours were adopted from Aaronson & Malkan (in preparation). The data for M31 globular clusters are from Barmby et al. (2000).
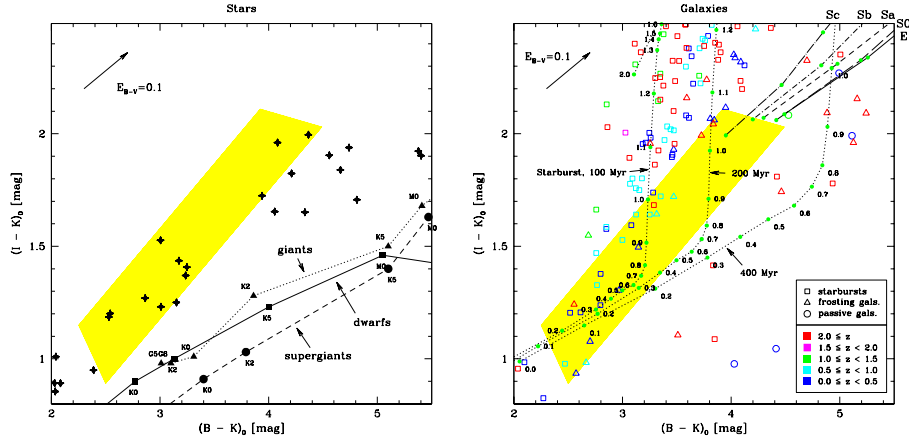
Figure 4.3: This figure compares in the two-colour diagram the position of globular clusters (indicated by a shaded region, see also Fig. 4.2) versus the mean locus of possible contaminating objects, such as foreground stars (left panel) and background galaxies (right panel). **Left panel:** Measured colours of stars were taken from the FORS Deep Field (Heidt et al. 2003; Gabasch et al. 2003) and are indicated by 4-prong stars. Due to their small surface density we use the full set of stars found in the FDF which has a field-of view of ~ 39 square arcminutes. Number counts have to be corrected when contamination estimates are performed for our sample (field of view 6.25 square arcminutes for the K-selected data, ~ 45 square arcminutes for the optical data). Spectral sequences of dwarf, giant, and supergiant stars in the disk are shown as solid, dotted, and dashed lines, respectively, and were taken from Cox (2000). Spectral types are indicated along each sequence. The offset between FDF stars and the spectral sequences is due to a higher metallicity of the latter which were constructed from stars in the solar neighbourhood. **Right panel:** Open squares mark starbursts, open triangles are galaxies in which star-formation ceased a few Gyrs ago (so-called "frosting" galaxies), while open circles show colours of old passively evolving elliptical galaxies. The full data set from the FDF was used ($I_{50\% \, compl.} \approx 26.37$, Heidt et al. 2003) and thinned so that expected number counts in the field-of-view of the K-selected data can be directly read off. Colour coding of the photometrically determined redshift for all galaxies is indicated in the lower right corner. Additionally, we k-correct the colours for E, S0, Sa, Sb, and Sc galaxies using template spectra of Mannucci et al. (2001) and Kinney et al. (1996). The sequences are labeled in the upper right corner of the right panel. Shaded dots along the sequences indicate redshifts which increase from $z = 0.0$ in steps of $\Delta z = 0.1$ towards redder colours. Dotted lines show the evolution of k-corrected colours for starburst galaxies with an age of 100, 200, and 400 Myr using templates from Maraston (2003, in preparation). Redshifts are marked along each sequence.

have therefore redder $B - K$ colours. As the effective temperature of red giants is a sensitive function of metallicity, more metal-poor (warmer) stars will be more likely to resemble mean globular cluster colours. This is shown in the left panel of Figure 4.3. It is important to keep in mind that age and metallicity of contaminating stars depend on the sampled galactic coordinates. In order to illustrate the difference in colour between disk and halo stars in the $I - K$ vs. $B - K$ diagram we plot colours of stars found in the FORS Deep Field (FDF, galactic coordinates $l = 191.40^o$, $b = -86.46^o$; Heidt et al. 2003, Gabasch et al. 2003) and representative colours of disk dwarf, giant, and supergiant stars in the solar neighborhood (Cox 2000). While the former sample is likely to be dominated by old metal-poor halo stars[3], the latter data resemble colours of metal-rich disk stars. To show the metallicity offset between metal-poor and metal-rich stars more clearly we plot all stars found in the FDF field with a field-of view of ~ 39 square arcminutes (indicated by stars in Fig. 4.3). Thus, number counts have to be rescaled as the field of view of our combined optical/near-infrared photometry is only 6.25 square arcminutes. Metal-rich disk stars can be reliably separated from globular cluster candidates as the former are significantly redder in $B - K$. The colours of metal-poor halo stars, on the other hand, are more similar to globular cluster colours. However, the surface density of these stars with metallicities [Fe/H] $\lesssim -1.5$ is relatively low, of the order of one star per field-of-view in our optical data (~ 45 square arcminutes) in the range $18 \leq V \leq 22.5$, with little dependence on galactic coordinates (Robin et al. 1996).

In general, the combination of optical and near-infrared photometry provides a good discriminator to distinguish between globular clusters and metal-rich foreground stars. However, the colours of metal-poor globular clusters can be mimicked by metal-poor halo stars. These stars need to be sorted out by other selection criteria such as magnitude. Based on the FDF data and the Galactic stellar population model (Robin et al. 1996), we expect a total stellar contamination of $\lesssim 1 - 10\%$ (depending on the richness of the globular cluster system) at galactic latitudes $|b| \gtrsim 40^o$. At lower latitudes the foreground contamination is rising.

Eliminating Background Galaxies

Another source of contamination are background galaxies. To estimate their $I - K$ and $B - K$ colours, we use a sub-sample of the FDF data which corresponds to our combined optical/near-infrared data in field-of-view size and photometric completeness (mainly limited by the near-infrared photometry at $K \sim 21.5$). In the right panel of Figure 4.3 we plot $I - K$ vs. $B - K$ colours of galaxies with high star-formation rate (open squares), galaxies in which star formation ceased a few Gyrs ago (so-called "frosting" galaxies, open triangles), and passively evolving ellipticals (open circles) (see Heidt et al. 2003; Gabasch et al. 2003, for a quantitative classification). Judging from the FDF data in Figure 4.3, we find that the blue part of the mean globular clusters locus, indicated by the shaded region, is mainly contaminated by starburst galaxies while the red part is prone to contain "frosting" galaxies. Depending on the boundary definitions, we find $\sim 20 - 30$ starbursts and $\sim 10 - 15$ "frosting" galaxies inside the region where globular clusters are preferentially found. However, most of these galaxies would be resolved in our photometry (typical seeing $\leq 1''$) and rejected by the FWHM (or size) selection.

Potentially problematic objects are distant starburst galaxies which are barely resolved and still bright enough to be classified as globular cluster candidates. At redshift unity, one arcsecond corresponds to ~ 8 kpc in a flat Λ-universe with $\Omega_m = 0.3$ and $H_0 = 70$ km s^{-1} Mpc^{-1} (at $z = 2$, one arcsecond covers ~ 8.4 kpc).

---

[3]The FDF line of sight is almost perpendicular to the Galactic disk.

Typical sizes of distant starburst galaxies range between a few hundred pc to a few kpc (e.g. Guzman et al. 1998; Soifer et al. 2001) and can be reliably resolved with ground-based photometry up to $z \approx 0.1$. At $z \approx 1.0$ even the brightest starbursts with typical absolute magnitudes $M_V \approx -21$ up to -22 mag are already too faint to enter our magnitude selection (cut at $V = 23$ mag). We conclude that provided good photometric quality (seeing $\leq 1''$), starbursts are reliably rejected by the combination of FWHM and magnitude selection below $z \approx 0.1$ and above $z \approx 1.0$. Optical/near-infrared colours can be a good additional discriminator for the remaining intermediate-redshift space as shown in the following.

We simulate the redshift evolution (both k-correction and luminosity corrections) of optical/near-infrared colours of a 100, 200, 400, and 800 Myr old starburst using template spectra taken from Maraston (2003, in preparation). The latter templates include the stellar evolutionary phase of thermally pulsing AGB stars, that dominates the infrared and bolometric flux at these ages (e.g. Maraston et al. 2001b). We use spectra of instantaneous star-formation with a metallicity $[Z/H] = -0.33$. We find that young starbursts between 100 and 200 Myr produce colours which are consistent with globular cluster colours in the redshift range between $z = 0.1$ and $z = 1.0$. As most starbursts are intrinsically located in high-reddening regions, we note that bright unresolved starbursts with ages ≤ 100 Myr and reddening values $E_{B-V} > 0.1$ can show typical globular cluster colours, as well. Those objects could contaminate the blue sub-sample of globular cluster candidates (see reddening vector in the right panel of Fig. 4.3). Starburst older than ~ 300 Myr have colours that are inconsistent with globular cluster colours beyond a redshift $z \approx 0.2$. Indeed, at these ages the AGB-phase transition boosts both colours to $I - K \gtrsim 2.5$ and $B - K \gtrsim 4.0$.

The k-corrected colours for galaxies are simulated with empirical template spectra of Mannucci et al. (2001) and Kinney et al. (1996) for elliptical, lenticular, and spiral galaxies. To account for the luminosity evolution requires to adopt a model for these galaxies and goes far beyond the aim of this exercise. The k-correction paths are shown in the right panel of Figure 4.3 with redshifts indicated by filled dots starting at $z = 0.0$ and increasing in steps of $\Delta z = 0.1$ to redder colours. It is obvious that non-starforming early-type galaxies entirely avoid the mean colour locus of globular clusters at all redshifts. Colours of low-z later-type galaxies are only marginally consistent with the reddest globular clusters. Sc galaxies below $z = 0.1$ intersect the shaded region where red globular clusters are found. However, these galaxies are efficiently rejected by the FWHM selection.

We conclude that the $I - K$ vs. $B - K$ diagram allows one to reliably disentangle globular cluster candidates from foreground disk stars as well as early-type and spiral galaxies with no or little on-going star-formation. Remaining potential contaminants are unresolved starbursts with ages $\lesssim 300$ Myr at intermediate redshifts between $z \approx 0.1$ and ~ 1.0. Based on FDF data we expect $\sim 35 - 45$ background galaxies down to $I = 22.5$ within the FORS field-of-view (~ 45 square arcminutes) with colours resembling those of globular clusters. The majority of these galaxies is resolved and rejected by the PSF selection. Indeed, the only background galaxy found in our K-selected sample with optical/near-infrared colours (4% of the sample; a fill-in object with $V = 22.83$, $B - K = 3.06$, and $I - K = 1.42$) is consistent with a young unresolved starburst galaxy at $z \approx 0.14$. The spectrum has too low S/N to allow a more accurate classification based on spectral features. The corresponding absolute magnitude of the object is $M_V \approx -16.3$ and is consistent with a SMC-type galaxy ($M_V = -16.2$ mag Binney & Merrifield 1998).

The overall surface density of contaminating objects with globular-cluster colours and magnitudes which are bright enough for integrated-light spectroscopy ($V \gtrsim 22 - 23$ at 8–10m-class telescopes with colours as indicated in Fig. 4.3) is negligible ($\lesssim 10\%$) where the surface density of globular clusters is high, that is within

$\sim 1\,R_{\text{eff}}$. Multi-object spectroscopic studies are therefore expected to have a highest success rates in central regions of a globular cluster system. We refer to Section 4.4.2 for an analysis of the success rate of the candidate selection.

4.2.4 Radial Surface Density Profiles of Globular Cluster Systems

Galaxy	blue	red	all
NGC 1380	2.78 ± 0.33	2.56 ± 0.42	2.63 ± 0.37
NGC 2434	(1.08 ± 0.98)	(2.56 ± 0.24)	2.56 ± 0.25
NGC 3115	0.80 ± 0.36	0.79 ± 0.26	0.79 ± 0.28
NGC 3379	(0.64 ± 0.84)	(2.09 ± 0.67)	1.46 ± 0.28
NGC 3585	1.36 ± 0.12	1.09 ± 0.35	1.22 ± 0.20
NGC 5846	(0.67 ± 0.35)	(1.31 ± 0.21)	1.44 ± 0.33
NGC 7192	(0.82 ± 0.48)	(2.15 ± 0.28)	1.67 ± 0.24

Table 4.4: Power-law exponents, Γ, of globular-cluster surface density profiles, $\Sigma(R) \sim R^{-\Gamma}$, of globular cluster systems and sub-populations. The second and third column shows the slopes for the profiles of the blue and red sub-populations, respectively. In the same order, these slopes are indicated as dashed and dot-dashed lines in Figure 4.4. The last column are the slopes of the entire cluster system. All given errors are uncertainties of the fit. Numbers in parentheses indicate a brute-force division of globular cluster systems which show a single-peak colour distribution in a blue and red globular cluster sub-population (see text for details).

In future papers we will study the properties of globular cluster systems as a function of their host's properties. To derive host galaxy masses we use globular clusters as tracer particles of the galaxy potential in Section 4.4.3. The tracer mass estimator requires the knowledge of the surface-density profiles of the tracer-particle population. Our photometric data probe a large enough range in galactocentric radius to reliably sample the globular cluster surface density profile. Moreover, in some globular cluster system formation scenarios the surface density profile of blue and red clusters is expected to change differently as a function of radius (e.g. Ashman & Zepf 1992; Côté et al. 1998). It is therefore important to study the profiles of each globular cluster sub-sample to control radial biases of further analyses.

In order to derive surface-density profiles we use the IRAF task ELLIPSE and the pre-selected FORS2 photometric sample (see Sect. 4.2.2). First, we model the surface-brightness profiles of the galaxy light on images which feature the best seeing and which were cleaned of point sources. The same elliptical isophotes are used for surface-brightness profiles in other passbands and to construct the surface-density profile of globular-cluster candidates. Colour-magnitude diagrams in Figure 4.1 show that photometric completeness as a function of colour does not greatly affect the radial surface-density profiles as the change in completeness level is negligible within the colour region from which globular clusters are selected.

In Figure 4.4 we plot surface density profiles of globular cluster candidates. Prior to creating the profiles, we excluded extremely blue objects (which are likely contaminating fore-/background sources, see Sect. 4.2.3) by applying cuts at $V-I = 0.3$ (NGC 3379), $V-I = 0.7$ (NGC 2434, NGC 7192), $V-I = 0.8$ (NGC 1380, NGC 3115, NGC 5846), and $B-I = 1.3$ (NGC 3585). Objects with colours redder than $V-I = 1.3$ (NGC 2434, NGC 3379), $V-I = 1.4$ (NGC 1380, NGC 3115), $V-I = 1.5$ (NGC 5846), $V-I = 1.6$ (NGC 7192), and $B-I = 2.3$ (NGC 3585) were also rejected. Outermost isophotes were used to subtract the background light and
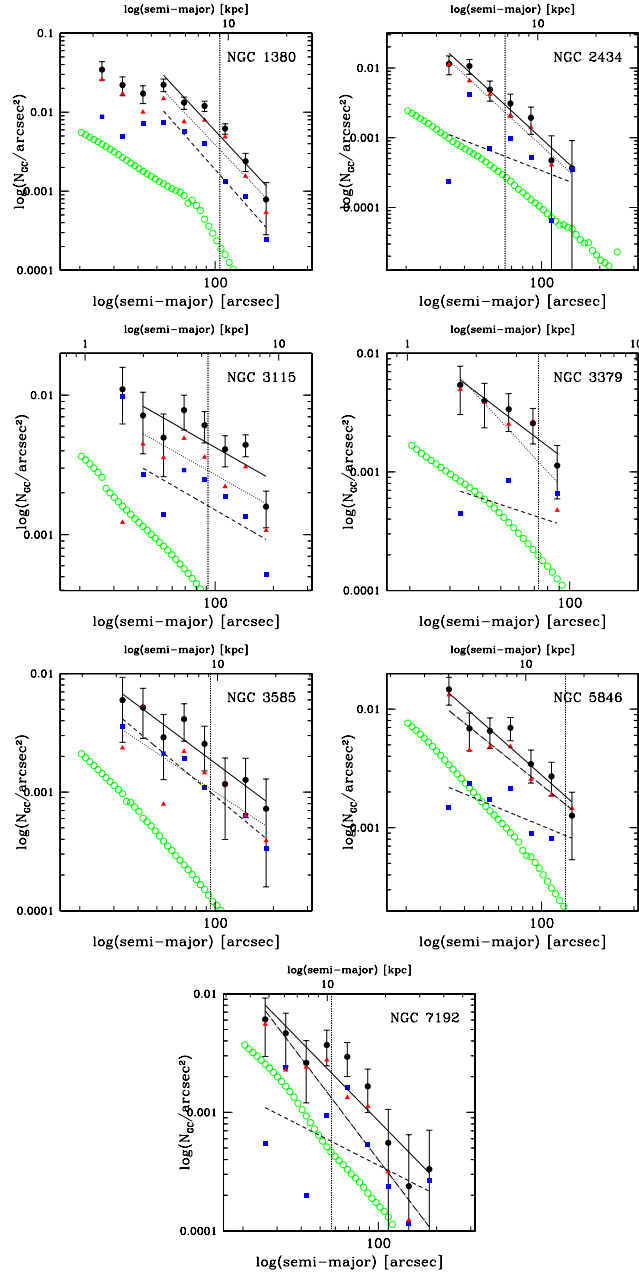
Figure 4.4: Surface density and surface brightness profiles of globular cluster systems and their host galaxies. The surface density of all globular cluster candidates is indicated by black dots with a power-law fit indicated as a solid line. Multi-modal colour distributions were divided at $V - I = 1.1$ or $B - I = 1.8$ into blue and red globular clusters. Power-law fits to the blue and red sub-populations are shown as dashed and dotted lines, respectively. Open circles show the scaled surface brightness profile of the host galaxy derived from I band photometry. Both profiles were calculated using the same isophotes. A vertical line indicates the effective radius of each system taken from de Vaucouleurs et al. (1991). Poisson errors are indicated for the total surface density profiles.

the surface density of background objects. Depending on the distance of the galaxy, the outermost accessible radii vary between ~ 10 and ~ 50 kpc, which corresponds to $R \geq 2\,R_{\mathrm{eff}}$ for all sample galaxies. Henceforth we compare only the slopes of the surface brightness profiles of the galaxy and the surface density profiles of globular cluster systems. Within the range of our globular cluster data colour-index changes of the diffuse light are negligible and we representatively use the I band surface brightness profile, since I-band data is available for all our sample galaxies. In order to have a fair comparison of the slopes we plot $\log(N_{\mathrm{GC}}/\mathrm{arcsec}^2)$ and $\mu_I/2.5$ versus the logarithmic semi-major axis galactocentric distance (Fig. 4.4). However, this procedure compares globular cluster number counts with a luminosity density of the host galaxy and is only valid if the mean M/L ratio of globular clusters remains constant as a function of radius. The mean M/L ratio is subject to change when young globular clusters are concentrated at a given radii. However, we expect that the majority of the globular cluster system is old and that the comparison of the slopes is acceptable to the first order.

The surface-density profile of each globular-cluster system appears generally comparable to or less steep than the galaxy light profile. In the case of the two S0 galaxies, NGC 1380 and NGC 3115, both globular-cluster profiles might be influenced towards the center by the presence of a stellar disk (Bothun & Gregg 1990). Disk shocking and disk instabilities might be responsible for enhanced cluster destruction and could decrease the globular cluster surface density close to the center (Gnedin & Ostriker 1997). Another consequence of the disk is a reduced photometric completeness in the central parts of the galaxy. We exclude central regions inside $\sim 0.5\,R_{\mathrm{eff}}$ from the profile fitting for these two galaxies. In fact, the surface-density profile of globular clusters in NGC 1380 tends to be less steep inside R_{eff} compared to radii larger than one effective radius. Globular cluster systems in elliptical galaxies are less affected by dynamical erosion or by a varying photometric completeness.

We fit power-law profiles of the form $\Sigma(R) \sim R^{-\Gamma}$ to the selected globular cluster data (solid circles in Fig. 4.4). Where colour multi-modality is apparent (see Sect. 4.2.2), we divide each candidate sample into a blue (solid squares) and red (solid triangles) globular clusters with a cut at $V - I = 1.1$ (NGC 1380, NGC 3115) and $B - I = 1.8$ (NGC 3585) and fit power-law profiles to each sub-sample and to the whole globular cluster system. Profiles for blue sub-samples are plotted as dashed lines. Dotted lines indicate profiles for red globular cluster candidates. Table 4.4 summarises the slopes for each galaxy.

The power-law exponents of the globular cluster surface-density profiles cover a wide range from $\Gamma \approx 0.8$ to steep profiles with $\Gamma \approx 2.6$. Blue and red globular cluster sub-populations appear to have similar profiles in all multi-modal galaxies. Although less significant, different power-law exponents are found for blue and red globular clusters (cuts at $V - I = 0.95$ for NGC 2434, $V - I = 0.8$ for NGC 3379, and $V - I = 1.1$ for NGC 5846 and NGC 7192) in galaxies with a single-peak colour distribution. In all cases the metal-poor globular-cluster system is more spatially extended than its metal-rich counterpart. The absolute cluster number densities of blue and red clusters reach comparable values at large radii $\gtrsim 1\,R_{\mathrm{eff}}$. This inevitably leads to the fact that in unimodal galaxies red globular clusters dominate our spectroscopic samples close to the center, while blue clusters are preferentially selected in the halo at large radii. This very interesting result requires a more detailed analysis and must be considered when radial analyses of globular cluster systems are performed.

4.2.5 Selection of Globular Cluster Candidates

For the selection of globular cluster candidates for spectroscopic follow-up we focus on objects with colours representative of high-density regions of a given colour distribution (see Fig. 4.1). Compliant with the restrictions of the slit-mask design (non-uniform spatial coverage of galactocentric radii, minimum slit length for good sky subtraction, limited deviation from the mask meridian for sufficient wavelength coverage, etc.) we representatively sample the underlying colour distributions of each globular cluster system. Furthermore, we focused primarily on objects inside one effective radius where the surface density of clusters is relatively high compared with surface densities of foreground stars and background galaxies.

Another constraint results from the faint magnitudes of the cluster candidates. To increase the likelihood of selecting a globular cluster we assigned a high priority to objects with magnitudes around the expected turn-over of the globular cluster luminosity function (GCLF). This however, has to be traded-off with the minimum S/N of ~ 20 Å^{-1} which is required for reliable index measurements. Overall the limiting magnitude was adjusted to $V = 23$ mag and was exceeded only in a few cases where the slit-mask design forced it.

In particular, our first-choice targets were drawn from the pre-selected sample (see Sect. 4.2.2) in the colour range $0.8 \lesssim V - I \lesssim 1.3$, and where colour information was available, from $1.5 \lesssim B - I \lesssim 2.5$ and $1.0 \lesssim B - R \lesssim 1.7$. According to simple stellar-population models of Maraston et al. (2003) these colour ranges are expected for stellar populations with metallicities $[Z/H] \gtrsim -1.0$ between ~ 1 and ~ 15 Gyr. These cuts exclude clusters with very low metallicities ($\lesssim -1.5$ dex) which have ages less than ~ 5 Gyr. Before the final selection, all colours of cluster candidates were corrected for the respective foreground extinction taken from Schlegel et al. (1998)[4].

In general, the upper selection criteria favour globular clusters which are brighter than the GCLF turn-over. If young ($\lesssim 5$ Gyr) globular clusters are present, they will be preferentially selected compared to old globular clusters due to their brighter magnitudes. In that case, our sample is likely to be biased towards young metal-rich clusters at ages $\lesssim 5$ Gyr.

First-choice candidates are used to create the slit masks. Remaining gaps in-between two slits are filled by objects which suffice slightly relaxed selection criteria. To fill the slit masks most efficiently, we relaxed the magnitude limit and the FWHM cut to include also faint objects. More than 50% of these fill-in objects was found to be genuine globular clusters.

4.3 Spectroscopic Data

We created two slit masks for NGC 1380 and NGC 2434 with 98 and 100 objects in total, respectively. For NGC 3115 we used the MOS unit of FORS2 with the 19 slits aligned to cover 22 objects. For NGC 3379, NGC 3585, NGC 5846, and NGC 7192 we designed one slit mask each to take spectra of 34, 35, 39, and 34 globular cluster candidates, respectively. In total we obtained spectra for 362 globular cluster candidates in seven early-type galaxies.

All data were obtained with the FORS2 instrument at UT2 (unit telescope 2, Kueyen) of ESO's VLT. The data of period 65 (NGC 3115) were taken with the multi-object slit (MOS) unit with 19 movable slits. In period 66 and 67 spectroscopic observations were carried out with the mask-exchange unit (MXU). A MOS

---

[4]Even for the highest-z galaxy in our sample, NGC 7192, the k-corrections of colours used for candidate selection are of the order of a few hundredths mag. Hence, we do not consider these negligible colour corrections.

Galaxy	Program No.	Nights	MOS/MXU Exptime	LSS Exptime
NGC 1380	P66.B-0068	28th − 31st Dec 2000	MXU mask1: 8×1800	4×1800
			MXU mask2: 6×1800	
NGC 2434	P66.B-0068	28th − 31st Dec 2000	MXU mask1: 8×1800	4×1800
			MXU mask2: 6×1800	
NGC 3115	P65.N-0281	5th & 6th May 2000	MOS mask: 6×1800	. . .
NGC 3379	P66.B-0068	28th − 31st Dec 2000	MXU mask: 8×1800+1200	3×1800
NGC 3585	P67.B-0034	26th − 29th May 2001	MXU mask: 15×1800	5×1800
NGC 5846	P67.B-0034	26th − 29th May 2001	MXU mask: 18×1800	5×1800
NGC 7192	P67.B-0034	27th − 29th May 2001	MXU mask: 17×1800+900	6×1800+900

Table 4.5: Journal of spectroscopic observations. Exposure times are given in seconds. Two masks were used for NGC 1380 and NGC 2434. All slit-mask observations were performed with the FORS mask exchange unit (MXU), except for NGC 3115 where we used 19 movable slits of the FORS instrument to create a slit mask (MOS mode). Note that no longslit spectroscopy (LSS) was obtained for NGC 3115.

mask with its 19 movable slits restricts the observations to a limited amount of objects per exposure. The MXU unit, instead, increases the multiplexity by at least a factor of two allowing for simultaneous spectroscopy of up to ~ 40 objects per frame. The total exposure time for each individual mask was adjusted according to the observing conditions and the magnitudes of selected objects. Typical exposure times vary between ~ 3 and ~ 9 hours per mask. The observations were split into sub-integrations of 1800 seconds (see Table 4.5 for details). All exposures used the 600B+22 grism with 600 grooves per mm resulting in a dispersion of 1.2 Å per pixel (R ~ 780) on a 2048× 2048 pix^2 thinned Tektronix CCD chip with 24μm pixels. The readout was done in a single-channel mode. In period 65 this resulted in 5.2 e^- readout noise with a gain 1.85 e^-/ADU. Observations in period 66 and 67 had 5.41 e^- readout noise and a 1.91 e^-/ADU gain. All observations use a slit width of 1″. The mean wavelength coverage of the system is $\sim 3450 - 5900$ Å with a final resolution of ~ 5 Å.

4.3.1   Spectroscopic Data Reduction

All spectra were processed with standard reduction techniques implemented in IRAF[5]. In summary, after subtracting a masterbias all frames were divided by a normalized flat-field image. The residual gradients on the normalized flat were found to be smaller than 0.5%. The resulting images were cleaned off cosmics with the routine by Gössl & Riffeser (2002) employing a 9-σ threshold and a characteristic cosmic-ray FWHM of 1.1 pixel. Optical field distortions in the FORS field-of-view bend spectra which lie away from the optical axis. This effect complicates an accurate sky subtraction as tilted sky lines would be incorrectly subtracted when a central wavelength solution is applied to the object's slit aperture. We have, therefore, calculated a wavelength solution for each pixel row from arclamp spectra and rectified all slit spectra according to this distortion mask. Subsequently, the IRAF task APALL was applied to the rectified MOS/MXU images and used to define object and background apertures. The upper and lower boundaries of an object aperture were adjusted so that the object flux was still higher than the adjacent sky noise level. Limits at $\sim 15\%$ of the peak flux were found to be optimal for all aperture boundaries. The same task was also used to trace the apertures along the dispersion axis and optimally extract the object flux according to Horne (1986).

---

[5]IRAF is distributed by the National Optical Astronomy Observatories, which are operated by the Association of Universities for Research in Astronomy, Inc., under cooperative agreement with the National Science Foundation.

During the extraction procedure the sky is modeled in one dimension perpendicular to the dispersion axis by a linear relation with a κ-σ clipping to remove residual bad pixels. Finally, all spectra are transformed into wavelength space with an accuracy better than 0.1 Å using a low-order spline. Subsequently, we used the flux standards EG21, Feige56, Feige110, LTT377, LTT1020, LTT1788, and LTT3864 to transform raw counts into flux units.

From the different exposures we average all single spectra of each object. Due to varying observing conditions (seeing, atmospheric transparency, alignment of slit masks, etc.), the spectra of each sub-integration series have changing signal-to-noise ratios (S/N). To obtain a final spectrum with the highest possible S/N, we average all single spectra of each given object and weight them by their individual S/N. To determine the weights we calculate the S/N for each spectrum in the range around 5000 Å. The change in S/N between the final spectra with and without weighting is $\sim 10\%$. The following analysis steps make use of the optimally combined spectra.

4.4 Kinematics

4.4.1 Radial Velocities

Radial velocities (v_r) are measured by cross-correlating the combined candidate spectra with high-S/N spectra of two M31 globular clusters, 158-213 and 225-280 (Huchra et al. 1982) using the IRAF task FXCOR. The resulting heliocentric radial-velocity histograms are shown in Figure 4.5 with the numerical values given in Appendix C. The plotted distributions are clearly concentrated around the mean systemic radial velocity measured from the diffuse light (de Vaucouleurs et al. 1991). We define bona-fide globular clusters with radial velocities which are off by maximally ± 400 km s^{-1} of the mean systemic v_r. For most galaxies the distinction between globular clusters and contaminants such as foreground stars and background galaxies is unequivocal since the latter have either much lower or higher v_r. Exceptions are two objects in NGC 3115.

In the case of NGC 3115, objects #10 and #15 have relatively low radial velocities $v_{\rm rad,10} = 344 \pm 48$ and $v_{\rm rad,15} = 285 \pm 19$ km s^{-1}, respectively. Assuming a simple rotation model of the Milky Way the mean streaming velocity of foreground stars in the direction of NGC 3115 ($l = 247.78^o$,$b = 36.78^o$) is $v_{\rm rad} = 220 \cdot \sin(2l) \cos^2(b) \approx 100$ km s^{-1} (van de Kamp 1967). It is therefore unlikely that the two objects are foreground disk stars. Both are, however, not completely inconsistent with high-velocity stars in the galactic halo. Within the colour limits of our selection, 32 stars with magnitudes between $V \approx 21.5$ and ~ 22.5 are expected[6] in the direction of NGC 3115 within the FORS2 field of view (Robin et al. 1996). To decide more conclusively whether the two objects are foreground stars or genuine globular clusters their spectra deserved a detailed investigation. However, the result was inconclusive (see Appendix E).

We conclude that the two objects cannot be assigned confidently to either of the two groups; stars or globular clusters. Both spectra are, therefore, kept in the globular cluster sample but we flag them as problematic.

Using radial velocities we confirm 43 globular clusters in NGC 1380, 6 in NGC 2434, 18 in NGC 3115, 18 in NGC 3379, 20 in NGC 3585, 28 in NGC 5846, and 10 globular clusters in NGC 7192.

---

[6]Model predictions were calculated using the code available at www.obs-besancon.fr/www/modele/modele_ang.html
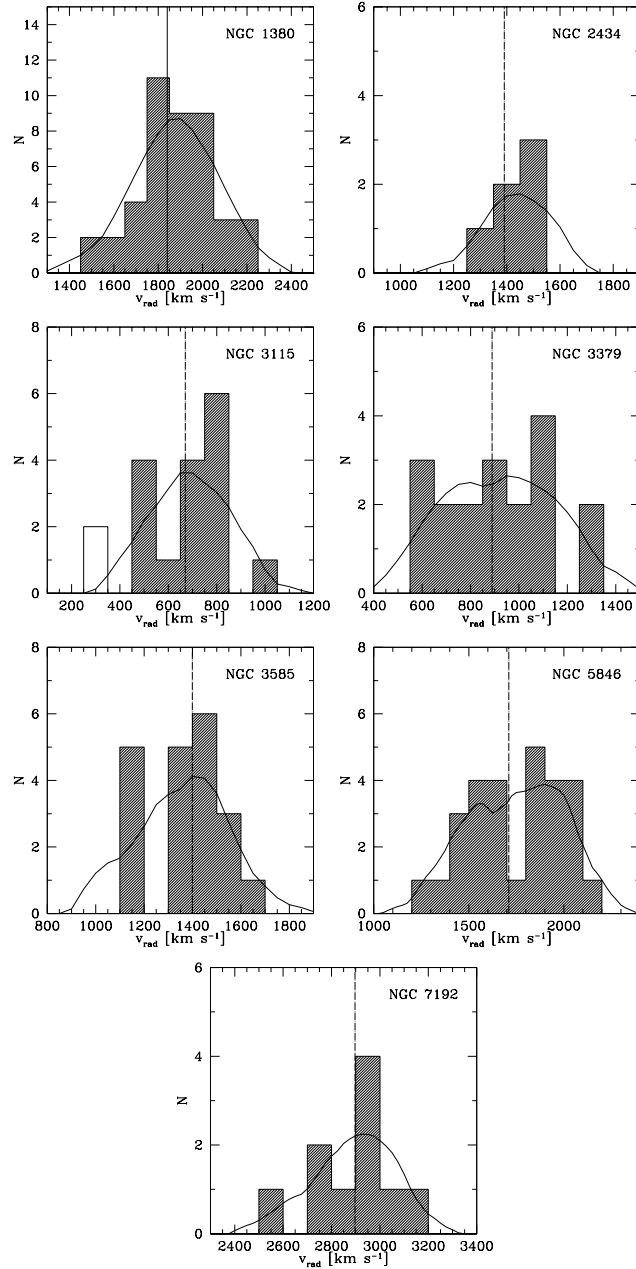
Figure 4.5: Radial velocity histograms for globular clusters in all studied galaxies. The mean heliocentric radial velocity of the host was determined in the optical and is shown as a vertical dot-dashed line taken from the RC3 catalog (de Vaucouleurs et al. 1991). The solid line is a probability density estimate using an Epanechnikov kernel with a fixed width $\delta v_{\mathrm{rad}} = 100$ km s^{-1} (for details see Silverman 1986). Two ambiguous objects in NGC 3115 are indicated by an open histogram (see also Sect. 4.4.1).

4.4.2 Success Rates of Globular-Cluster Candidate Selection

In the following, we calculate the success rate of our candidate selection. For each galaxy, the success rate varies with changing surface density of globular clusters and therefore with galactocentric radius. It is instructive to calculate the success rate for our entire sample and inside one effective radius R_{eff}, *with* and *without* our colour pre-selection. In other words, *with* and *without* fill-in objects. All values are summarised in Table 4.6. In general the success rates drop for larger galactocentric radii.

The major fraction of contaminants are foreground stars, thus it is not surprising that the success rate correlates with galactic latitude. High success rates ($\gtrsim 80\%$) are guaranteed if colour selection is applied and the field of view of the spectrograph covers about one to two effective radii, provided that the host galaxy is located at high galactic latitudes ($|b| \gtrsim 40^o$). Only NGC 2434 suffers from severe foreground contamination. In the case of NGC 1380, a background galaxy cluster is placed right behind the galaxy and contaminates the candidate selection. Unfortunately, the HST photometry does not cover a large enough area to efficiently weed out resolved candidates. All other galaxies have very good success rates inside $1\,R_{\mathrm{eff}}$ typically between ~ 80 and 100% which validates the efficient candidate selection.

Galaxy	total	$< 1\,R_{\mathrm{eff}}$	total$_{\mathrm{sel}}$	$< 1\,R_{\mathrm{eff,sel}}$
NGC 1380	0.44	0.54	0.75	0.80
NGC 2434	0.07	0.06	0.19	0.11
NGC 3115	0.82	1.00	0.88	1.00
NGC 3379	0.53	0.77	0.78	0.90
NGC 3585	0.57	0.90	0.73	0.90
NGC 5846	0.72	0.78	0.86	0.90
NGC 7192	0.29	0.83	0.50	0.80

Table 4.6: Success rates of photometric globular cluster selection as a function of galactocentric radius for the entire sample and inside one effective radius. The numbers give the fraction of confirmed globular clusters with respect to the total number of objects for which spectroscopy was obtained *without* and *including* colour selection of candidates (marked by the index "sel"). The effective radii were taken from the RC3 catalog. Success rates for NGC 3115 were calculated including object #10 and #15.

4.4.3 Host Galaxy Masses

The mass of a galaxy can be probed by its globular cluster system out to large radii ($\gtrsim 2\,R_{\mathrm{eff}}$) including a significant fraction of the halo mass. In the past, several simple mass estimators based on the virial theorem, such as the *projected mass estimator* (Bahcall & Tremaine 1981; Heisler et al. 1985), have been developed to derive masses of galaxy groups. Unfortunately, a key assumption of these mass estimators is that the tracer population follows the mass density of the probed potential. While to zeroth order this is true for galaxy groups, the assumption fails when globular clusters are used as tracers for galaxy potentials (see also Sect. 4.2.4).

Recently, a mass estimator was generalised to cases where the tracer population does not follow the mass profile (Evans et al. 2003). We use this *tracer mass estimator* to derive masses for our sample galaxies using radial velocities and projected radii of our globular cluster samples. For an isothermal potential[7], the general form

---

[7]A basic underlying assumption of all mass estimators is a steady state equilibrium.

of the estimator is

$$M_{\text{press}} = \frac{C}{GN} \sum_i (v_{i,\text{los}} - \langle v \rangle)^2 R_i \tag{4.1}$$

where

$$C = \frac{16(\gamma - 2\beta)}{\pi(4 - 3\beta)} \cdot \frac{4 - \gamma}{3 - \gamma} \cdot \frac{1 - (r_{\text{in}}/r_{\text{out}})^{3-\gamma}}{1 - (r_{\text{in}}/r_{\text{out}})^{4-\gamma}} \tag{4.2}$$

Here, $\langle v \rangle$ is the system's mean radial velocity and β the anisotropy parameter $1 - \sigma_t^2/\sigma_r^2$ which is unity for purely radial orbits and $-\infty$ for a system with solely tangential orbits (Binney 1981). The exponent of the *three-dimensional* density profile of the globular cluster population, defined through $\rho(r) = \rho_0 \cdot r^{-\gamma}$, is not known a priori. However, to a good approximation the power-law rule $\gamma = 1 + d\log\Sigma/d\log R$ (Gebhardt et al. 1996) can be used to derive γ from the surface density profiles in Section 4.2.4 assuming spherical symmetry. The projected radii R_{in} and R_{out} are taken as the 3-dimensional minimal and maximal galactocentric distances r_{in} and r_{out}.

The mass estimator applies only to a pressure-supported tracer population. That is, any net rotation has to be subtracted from the sample before the tracer mass estimator is applied. We eliminate the mean rotational component by fitting a rotation curve to the entire globular cluster sample following Gebhardt et al. (2000). Total masses are calculated by adding the rotational component (assuming a flat rotation curve at large radii) to the pressure component from the tracer mass estimator

$$M_{\text{total}} = \frac{R_{\text{out}} \langle v_{\text{max}} \rangle^2}{G} + M_{\text{press}}, \tag{4.3}$$

Total masses are calculated for isotropic globular cluster orbits ($\beta = 0$). For reasonably extreme anisotropies these mass estimates were found to vary by at most $\sim 30\%$ (Evans et al. 2003). Taking into account the uncertainties in the mean system velocity and the rotational mass component as well as statistical fluctuations due to the limited sample size, we expect a $30 - 50\%$ uncertainty in the total mass estimate. Table 4.7 summarizes the results for all sample galaxies.

Galaxy	R_{in}	R_{out}	$R_{\text{out},<1\,R_{\text{eff}}}$	M_{rot}	M_{press}	M_{total}	$M_{\text{total},<1\,R_{\text{eff}}}$	$N_{\text{GC},<1\,R_{\text{eff}}}$
NGC 1380	1.12	17.13	2.53	0.18	8.44	8.62	1.75	19
NGC 2434	1.40	13.80	2.10	0.09	0.79	0.88	0.31[a]	5
NGC 3115[b]	1.33	14.55	4.82	0.26	2.93	3.19	0.70	18
NGC 3379	0.84	10.41	2.88	0.09	2.76	2.85	0.96	10
NGC 3585	2.26	19.14	2.73	0.21	2.62	2.83	1.41	9
NGC 5846	2.31	24.65	1.63	0.27	11.6	11.9	6.38	18
NGC 7192	3.95	38.02	3.62	1.21	4.47	5.68	0.89	5

[a] No data are available inside $1\,R_{\text{eff}}$; the given mass was calculated inside $2\,R_{\text{eff}}$.

[b] Masses were calculated using globular cluster data from our study and of Kavelaars (1998) and Kuntschner et al. (2002a).

Table 4.7: Host galaxy masses in units of $10^{11} M_\odot$. The total mass was determined from the full set of globular clusters. Inner and outer projected radii which are defined by the projected radial spread of the sample are given in kpc. The rotational and pressure component of the total mass estimate are given separately. The expected uncertainty of the total mass estimate is $\sim 30 - 50\%$. The last two columns show the total mass estimate inside $1\,R_{\text{eff}}$ and the number of test particles. The galactocentric radius (in kpc) of the most distant globular cluster for the mass estimate inside one effective radius is given in column $R_{\text{eff,out}}$.

4.5 Line Indices

4.5.1 Sampled Luminosities

The sampling of the globular cluster luminosity function (GCLF) is illustrated in Figure 4.6. Our spectroscopic samples represent, strictly speaking, only small fractions of the entire globular cluster population and are biased towards high cluster masses. However, from the Milky Way and photometric studies, no large variations of globular cluster properties are expected with mass. Typical values of the sampled fraction of the entire GCLF down to the faintest cluster in the spectroscopic data set vary between 1.5 and 8.5%. All spectroscopic sub-samples are biased towards bright magnitudes and probe the bright end of the GCLF. Taking into account metallicity and age variations inside a globular cluster system our data will be biased towards young globular clusters if present.

Spectra of globular clusters with a total sampled luminosity of less than $\sim 10^5 L_\odot$ are likely to be dominated by stochastic fluctuations of the number of bright stars (see Chapter 2 and Renzini & Fusi Pecci 1988; Renzini 1998). To convince ourselves that enough light is sampled by the slit we estimate the total luminosity L_T of our sample globular clusters from the photometry. We use the distance modulus of Tonry et al. (2001), foreground reddening maps of Schlegel et al. (1998), and bolometric corrections from Maraston (1998) in the equation

$$L_T = BC_I \cdot 10^{-0.4 \cdot (m_I - (m-M) - M_\odot - A_I)} \tag{4.4}$$

As I band photometry is available for all globular cluster systems (see Tab. 4.2) we use I magnitudes for our calculation. The absolute I magnitude of the sun ($M_{I,\odot}$=3.94) was taken from Cox (2000).

The lower right panel in Figure 4.6 shows the distribution of luminosities for the entire globular cluster sample. The mean of the cluster luminosity distribution is $\langle \log L \rangle = 5.85 \pm 0.03$ with a dispersion of $\sigma = 0.37$ dex. Only one globular cluster has a total luminosity lower than $10^5 L_\odot$ (GC#10 in NGC 3379 with $L = 7.2 \cdot 10^4 L_\odot$, see also Tab. C.4). In other words, all clusters are far from the low-luminosity regime where the integrated light can be dominated by a few bright stars. Using the number-counts of Renzini (1998) we find that the total luminosity of each globular cluster is the integral over at least a few thousand stars.

The estimate mentioned above is based on photometry which measures all the light emitted by the cluster. The slits, however, sample less light depending on seeing conditions and mask alignment during the observations. Only four exposures, two NGC 5846 and two NGC 3585 frames, suffered during one night (25./26.5.2001) from bad seeing ($\sim 1.5''$). These exposures were assigned a low weighting factor during the combining process and do not affect the final spectrum.

4.5.2 Calibration of Lick Line Indices

Lick indices (for passband definitions see Worthey 1994; Worthey & Ottaviani 1997) are measured on the fluxed and combined globular-cluster spectra. The wavelength range coverage allows for 17% of our sample to have TiO_1 index measurements. The redder index TiO_2 cannot be measured for all globular clusters. However, both indices are less instructive as they are affected by calibration uncertainties and stochastic fluctuation in the number of mostly contributing cool giant stars (Puzia et al. 2002c; Maraston et al. 2003; Thomas et al. 2003a). Prior to performing the line-index measurements, the spectra were smoothed by a λ-dependent Gaussian kernel to match the Lick/IDS spectral resolution (see Chapter 2). The transformation to the Lick system, the measurement of Lick indices, and the error analysis is performed in the same way as described in Chapter 2.
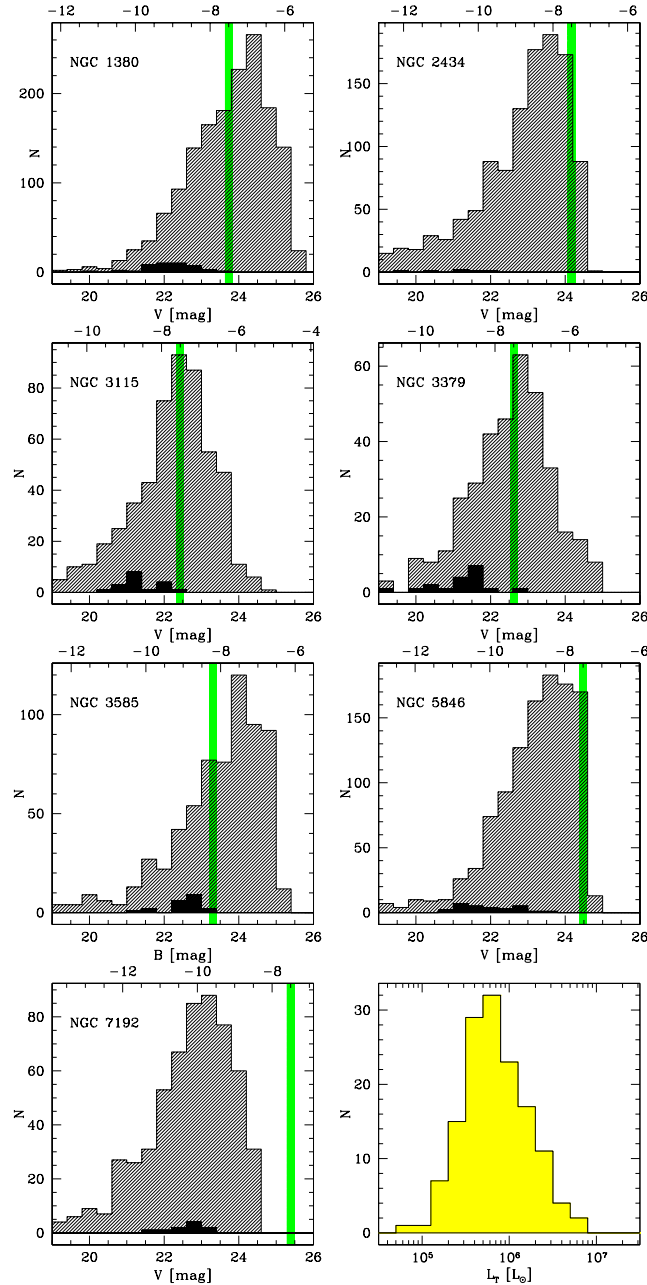
Figure 4.6: Observed globular cluster luminosity functions (GCLFs). Hatched histograms show the magnitude distribution of the entire photometric sample. Solid histograms are spectroscopic samples. A vertical shaded band indicates the location of the GCLF turn over which is found in Local Group globular cluster systems and is expected at $M_V \approx -7.4$ to -7.6 mag (Harris 2001; Richtler 2003). Note that the panel for NGC 3585 refers to B band magnitudes. An absolute magnitude scale is provided at the upper abscissa of each panel. Note that the GCLFs are not corrected for completeness. The lower right panel shows a histogram of globular cluster luminosities, L_T, which are sampled by our spectroscopic data.
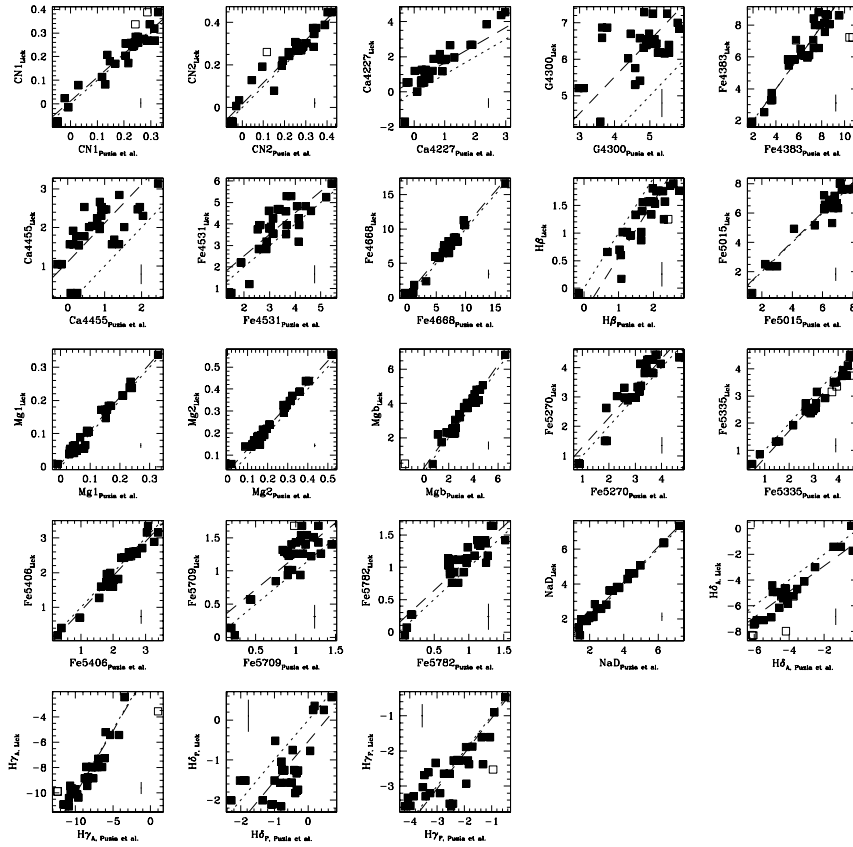
Figure 4.7: Comparison of Lick index measurements on our smoothed standard-star spectra with the published Lick index values for corresponding stars taken from Worthey (1994) and Worthey & Ottaviani (1997). Dashed lines indicate the best least-square fit to the data using κ-σ clipping. Dotted lines show the one-to-one relation. Data with exceptionally large errors or large deviations which were not used in the fitting process are shown as open squares. Note that offsets for TiO_1 and TiO_2 could not be determined due to the lack of wavelength coverage in our standard star spectra. Both these indices remain uncorrected. Typical error bars are indicated in a corner of each panel.
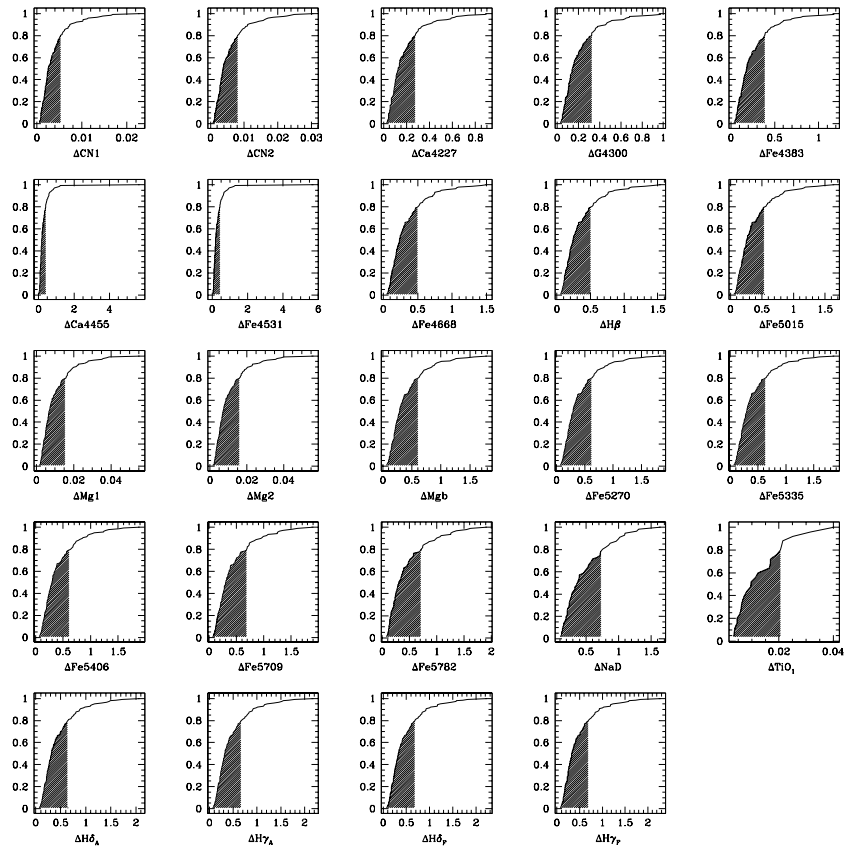
Figure 4.8: Cumulative error distributions of Lick index measurements for the entire globular cluster sample. Index TiO_2 could not be measured due to the limited wavelength coverage of the spectra. Similarly affected is index TiO_1 which could be measured for 17% of our sample. Shaded regions show the best 80% of the entire data set.

In particular, the transformation to the Lick system was performed in the following way. During our observing runs in period 65, 66, and 67 we observed a total of 31 Lick standard stars which are used to accurately tune our spectroscopic system to the Lick/IDS characteristics. All standard-star spectra were observed with the same slit-size $(1.0'')$ and were extracted and smoothed in exactly the same way as the globular cluster spectra. By comparing our standard-star index measurements with published indices measured on original Lick/IDS spectra (Worthey 1994; Worthey & Ottaviani 1997) we calculate correction functions of the form

$$I_{\mathrm{cal}} = I_{\mathrm{raw}} + \alpha \tag{4.5}$$

where I_{cal} and I_{raw} are the calibrated and the measured indices, respectively. These functions allow us to reliably lock each index to the Lick system compensating for minor inaccuracies during the smoothing process and deviant continuum-slopes, compared with original Lick spectra, due to our flux-calibration. The comparison of selected indices between our measurements and the Lick systems is shown in Figure 4.7. A major fraction of the scatter is due to the large errors of the Lick/IDS measurements which are about an order of magnitude larger than our standard-star values. Most indices require only a small correction while the calibration of very noisy indices, such as G4300 and Ca4455, remains uncertain. All globular-cluster indices are corrected with these zero-point offsets. Table 4.8 summarises the correction coefficients α used in Equation 4.5 and the r.m.s. of the calibration.

Calibrated indices and their uncertainties for all globular clusters are presented in the Appendix in Tables D.1 to D.9. A few index measurements are influenced by bad pixels inside the background and/or feature passband due to bad cosmic-ray interpolation. We discard these index measurements from our data. Cumulative error distributions for each index are shown in Figure 4.8. Particularly with regard to future age and metallicity determinations, an age resolution of $\sim 1-2$ Gyr requires Balmer line accuracies $\Delta\mathrm{H}\beta \lesssim 0.05$ Å and $\lesssim 0.1$ Å for the higher-order Balmer line indices, if age is considered as the only parameter which drives Balmer indices. This is not true in general because of the metallicity dependence of horizontal branch and turnoff temperatures (Maraston et al. 2003). We will take these effects into account in future analyses. Very few objects achieve this high index accuracy. A metallicity resolution of 0.1 dex requires $\Delta[\mathrm{MgFe}]' \lesssim 0.15$ Å[8]. About 40% of our data meets this criterion.

Clearly, the age resolution needs to be compromised for a large enough final sample size. Relaxed Balmer-index error cuts at $\Delta\mathrm{H}\beta = 0.4$ Å and 0.6 Å for the higher-order Balmer indices guarantee an age resolution of $\Delta t/t \approx 0.3$. An error cut at $\Delta[\mathrm{MgFe}]' = 0.2$ Å corresponds to a metallicity resolution $\sim 0.25 - 0.4$ dex, depending on absolute metallicity. $\sim 50\%$ of our sample comply with these selection criteria and allow detailed age/metallicity for individual globular clusters.

4.5.3 Representative Spectra

Figure 4.9 shows representative spectra of NGC 5846 globular clusters of increasing Mg*b* index strength. The sequence shows nicely the anti-correlation between the strength of the Balmer line series and Mg and Fe metal lines from low to high metallicities. Note the influence of increasing metallicity on the continuum which lowers the continuum flux in the blue part of the spectrum. In general, most our spectra are of relatively high quality with an average S/N of $\gtrsim 20$ per Å between 5000 and 5100 Å.

---

[8]see Equation 5.3.
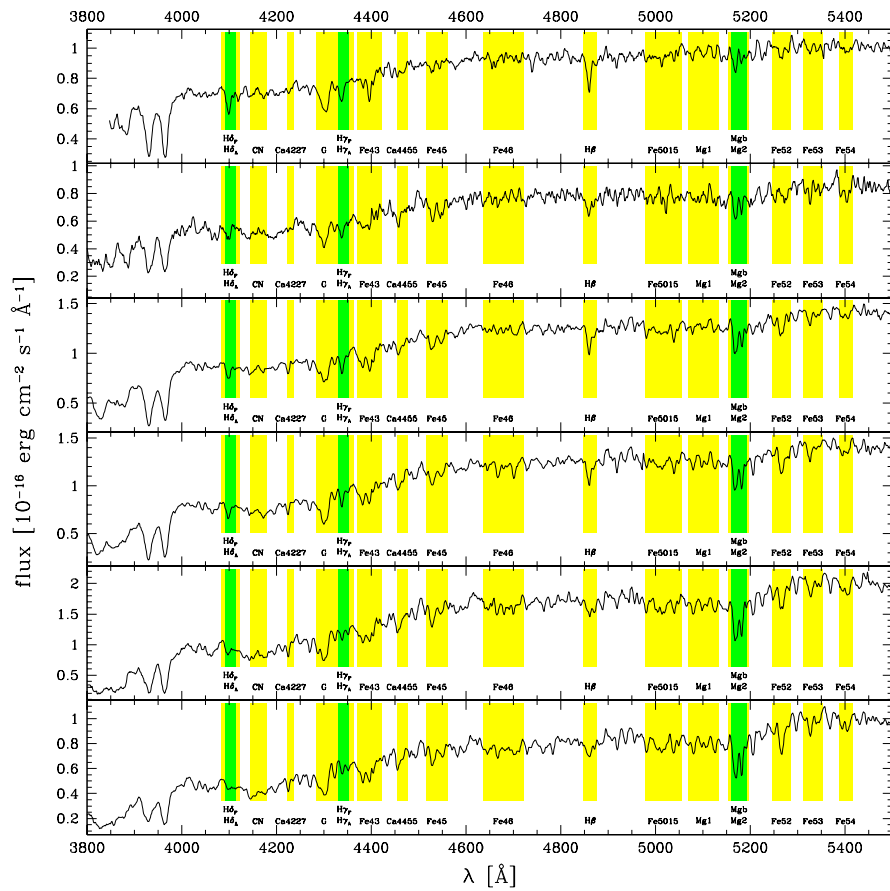
Figure 4.9: Representative spectra from our final globular cluster sample. The relative Mg*b* index strength increases from the upper to the lower panel. Note the anti-correlation in the strength of some prominent spectral features such as Balmer lines and the Mgb feature at ~ 5180 Å. All spectra are taken from the sample of globular clusters in NGC 5846 to demonstrate the influence of increasing metallicity on the continuum flux in the blue (note the changing ordinate scale). Feature passbands of measured Lick indices are shaded and labeled accordingly. Where two index passbands overlap the narrower is shaded darker and the label is elevated.

index	z.p. $- \alpha$	r.m.s.	units
CN_1	0.013	0.032	mag
CN_2	0.017	0.035	mag
Ca4227	0.664	0.587	Å
G4300	1.517	0.745	Å
Fe4384	-0.019	0.637	Å
Ca4455	1.112	0.554	Å
Fe4531	0.521	0.716	Å
Fe4668	0.471	0.594	Å
$H\beta$	-0.435	0.279	Å
Fe5015	0.061	0.515	Å
Mg_1	0.010	0.013	mag
Mg_2	0.028	0.014	mag
Mgb	0.234	0.304	Å
Fe5270	0.295	0.370	Å
Fe5335	-0.281	0.197	Å
Fe5406	-0.101	0.187	Å
Fe5709	0.223	0.208	Å
Fe5782	0.140	0.157	Å
NaD	0.118	0.193	Å
TiO_1	...	...	mag
TiO_2	...	...	mag
$H\delta_A$	-0.899	0.699	Å
$H\gamma_A$	-0.098	0.773	Å
$H\delta_F$	-0.539	0.609	Å
$H\gamma_F$	-0.071	0.575	Å

Table 4.8: Summary of α coefficients and their rms. The corrections for the indices TiO_1 and TiO_2 could not be determined due to the lack of wavelength coverage in our standard-star spectra. Hence, both indices remain uncorrected.

4.6 Globular Cluster Data from the Literature

In the following, we collect published spectroscopic globular-cluster data which will be used in future papers of this series. We focus only on high-quality line indices which were measured with the newer passband definitions of the Lick group (Worthey 1994; Worthey & Ottaviani 1997; Trager et al. 1998) and exclude index data measured with older passband definitions (Burstein et al. 1984).

Some data are measured with the new passband definitions of Trager et al. (1998). However, most Lick-index SSP model predictions are based the fitting functions of Worthey (1994) and Worthey & Ottaviani (1997). Their passband definitions differ for the indices CN_1, CN_2, Ca4227, G4300, Fe4383, Ca4455, Fe4531, C_24668 (former Fe4668), Fe5709, Fe5782, NaD, TiO_1, and TiO_2 from the passband definitions of Trager et al. (1998). To compare data in a homogeneous system, we calculate transformations to the Worthey passband system for indices which were measured with Trager et al. (1998) passband definitions. Table 4.9 summarises offsets for each index which are given in the sense

$$\Delta I = I_{\text{Tr98}} - I_{\text{Wo94}}. \tag{4.6}$$

Note that passband definitions for all Balmer line indices and the widely used Mg and Fe indices Mg_2, Mgb, Fe5270, and Fe5335 do not change between the two systems.

We consider only data which have sufficiently high S/N. A short description of each data set is given below. Age and metallicity estimates for each globular cluster sample are taken from the papers the data were published in.

index	ΔI	r.m.s.	units
CN_1	0.010	0.025	mag
CN_2	0.014	0.020	mag
Ca4227	0.330	0.297	Å
G4300	0.936	0.692	Å
Fe4384	0.166	0.501	Å
Ca4455	0.509	0.225	Å
Fe4531	0.334	0.127	Å
Fe4668	0.211	0.175	Å
Fe5709	0.211	0.251	Å
Fe5782	0.166	0.177	Å
NaD	0.001	0.200	Å
TiO_1	-0.003	0.017	mag

Table 4.9: Summary of index offsets between the Worthey et al. and Trager et al. passband system. Most offsets were calculated using our standard-star spectra and are given in the sense $\Delta I = I_{\mathrm{Tr98}} - I_{\mathrm{Wo94}}$ with the rms of the transformation. Offsets for TiO_1 were calculated using our globular cluster data since the standard star spectra do not cover the full wavelength range. A TiO_2 offset could not be determined due to the lack of wavelength coverage in both our standard-star and globular-cluster spectra.
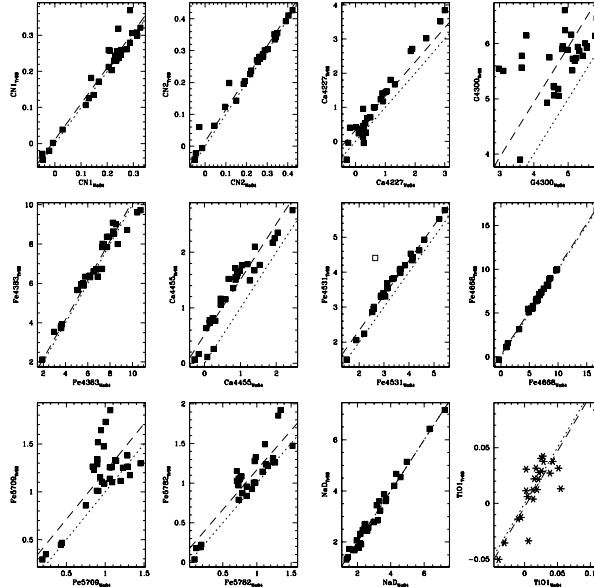
Figure 4.10: Comparison of Lick index measurements performed with Worthey et al. and Trager et al. passband definitions for which passband definitions differ between the two systems. Spectra of Lick standard stars were used, except for TiO_1 where we used globular cluster data. Offsets between the two systems are summarised in Table 4.9.

4.6.1 Elliptical Galaxies

NGC 1023 - Lick indices (CN_2, $H\beta$, G4300, Ca4227, Fe5270, Fe5335, and Mg_2) for 9 globular clusters were measured by Larsen & Brodie (2002) with the passband definitions of Worthey (1994) and Worthey & Ottaviani (1997) on spectra taken with LRIS attached to the Keck I telescope. Some spectra have a S/N on the lower limit to be useful for our future analyses. The sample spans a wide range of cluster ages with two very young globular clusters at ~ 500 Myr to objects at ~ 15 Gyr. Metallicities range from [Fe/H]≈ -2.0 to solar values.

NGC 1399 - Forbes et al. (2001) measure a sub-set of Lick line indices ($H\gamma_A$, $H\beta$, Mg_2, Mgb, and $\langle Fe \rangle$) defined in Trager et al. (1998) and Worthey & Ottaviani (1997) for 10 globular clusters on high-S/N spectra taken with LRIS on Keck I. The majority of the sample are old (~ 11 Gyr) globular clusters. Two clusters are likely to have intermediate ages around 2 Gyr. A broad range in metallicity is covered by the clusters with [Fe/H] from ~ -2.3 to $\sim +0.4$ dex.

NGC 3610 - Eight globular clusters were observed by Strader et al. (2003a) using the LRIS instrument on the Keck I telescope. The relatively faint magnitudes of the clusters and the short exposure time resulted in medium-S/N spectra on which Lick indices ($H\delta_A$, $H\gamma_A$, $H\beta$, CN_2, Ca4227, G4300, Fe5270, Fe5335, Mg_2, and Mgb) were measured using passband definitions of Trager et al. (1998) and Worthey & Ottaviani (1997). Except for one intermediate-age globular cluster (~ 3 Gyr) with a super-solar metallicity the entire sample appears old covering a wide metallicity range from [Fe/H]≈ -2.3 to 0.0 dex.

NGC 4365 - Larsen et al. (2003) measure a subset of Lick indices ($H\beta$, $H\gamma_A$, $H\delta_A$, Fe5270, Fe5335, Mg_2, and Mgb) for 14 globular clusters nine of which are likely to be intermediate-age metal-rich objects ($-0.4 \lesssim$[Z/H]$\lesssim 0.0$, $2-5$ Gyr). The remaining clusters are consistent with old ($10 - 15$ Gyr) stellar populations covering a wide range in metallicity ($-2.5 \lesssim$[Z/H]$\lesssim 0.0$). All indices were measured using passband definitions of Worthey (1994) and Worthey & Ottaviani (1997). The data were taken with LRIS attached to the Keck I telescope.

4.6.2 Lenticular/S0 Galaxies

NGC 3115 - High-quality spectra of 17 globular clusters have been taken by Kuntschner et al. (2002a) with the FORS2 instrument at the VLT. The full set of 25 Lick line indices was measured with passband definitions of Worthey & Ottaviani (1997) and Trager et al. (1998). The authors find a coeval old (~ 12 Gyr) set of globular clusters which covers a wide range in metallicity from -1.5 dex up to solar values.

NGC 4594 - 14 globular cluster spectra of medium S/N have been obtained by Larsen et al. (2002a) with the LRIS on the Keck I telescope. Lick indices ($H\delta_A$, $H\gamma_A$, $H\beta$, Fe5270, Fe5335, Mg_2, and Mgb) using Worthey (1994) and Worthey & Ottaviani (1997) passband definitions were measured. The sample contains globular clusters with ages between 10 and 15 Gyr and a large metallicity spread from very metal-poor to super-solar abundance clusters.

4.6.3 Late-Type Galaxies

Milky Way - The full set of 25 Lick indices was measured on high-quality spectra for 12 galactic globular clusters in Chapter 2 using passband definitions of Worthey (1994), Worthey & Ottaviani (1997), and Trager et al. (1998).

The data were obtained with the Boller & Chivens Spectrograph of ESO's
1.52 m on La Silla. As the Milky Way globular clusters consist of old stellar
populations all sample clusters have ages in the range $10 - 15$ Gyr. Their
metallicities range from [Fe/H]$= -1.48$ to -0.17 dex. This sample is aug-
mented by the data set of Trager et al. (1998) which adds 12 old metal-poor
globular clusters with metallicities from [Fe/H]$= -2.29$ up to -0.73 dex. The
Trager et al. data provide line indices for 21 passbands defined in their own
work. Index measurements for higher-order Balmer line indices which are
defined by Worthey & Ottaviani (1997) are documented in Kuntschner et al.
(2002a) and are added to the Trager et al. data set. Where our and the Trager
et al./Kuntschner et al. data set have objects in common we prefer our data
over the other two because of systematically smaller uncertainties.

M31 - Trager et al. (1998) measure Lick line indices defined in the same work for
18 globular clusters. Index measurements for higher-order Balmer lines are
provided by Kuntschner et al. (2002a) and added to the former data.

M33 - The Lick indices G4300, Hβ, Mg$_2$, Fe5270, and Fe5335 were measured by
Chandar et al. (2002) with the passband definitions of Worthey (1994) for 21
globular clusters. The sample clusters have metallicities from [Fe/H]$= -2.0$
to -0.5 dex and ages from a few Gyr to ~ 15 Gyr. The data were taken with
the HYDRA multifiber spectrograph at WIYN 3.5m telescope (KPNO).

M81 - Schroder et al. (2002) measure Lick indices with passbands defined in Trager et al.
(1998) for 16 globular cluster candidates. Their data were obtained with the
LRIS instrument. Most of the objects are consistent with stellar populations
spanning ages between 8 and 17 Gyr and metallicities between [Fe/H]$= -2.3$
and solar values. One globular cluster candidate appears to be of intermediate
age (~ 3 Gyr) and intermediate metallicity ([Fe/H]≈ -1.0). As M 81 has a
negative systemic radial velocity (-34 ± 4 km s^{-1} de Vaucouleurs et al. 1991)
the selection of globular clusters remains rather uncertain. Schroder et al.
(2002) reduce the ambiguities by restricting the sample to objects with small
projected radii. Furthermore, they compare the strength of Ca I and Hδ ab-
sorption lines with photometric colours and exclude stars using the technique
of Perelmuter et al. (1995).

LMC - Lick indices of 24 globular clusters have been measured on high-S/N spectra
by Beasley et al. (2002). The authors use passband definitions of Trager et al.
(1998) to measure their 16 bluest indices (CN$_1$ to Fe5406) and definitions of
Worthey & Ottaviani (1997) to measure 4 higher-order Balmer line indices.
Their sample spans metallicities from [Fe/H]$= -2.1$ up to solar values with
globular cluster ages of a few million years up to old objects of ~ 15 Gyr.
The observations were performed with the FLAIR instrument at the 1.2 m
UK Schmidt telescope (AAO).

Fornax - Strader et al. (2003b) provide a sub-set of Lick index measurements (CN$_1$,
CN$_2$, Ca4227, G4300, Hβ, Mg$_2$, Mgb, Fe5270, Fe5335, Hγ_A, and Hδ_A) with
passbands defined by Trager et al. (1998) and Worthey & Ottaviani (1997)
for 4 globular clusters in the Fornax dwarf galaxy. The clusters appear to be
metal-poor ([Fe/H]≈ -1.8) and old (~ 15 Gyr) with one cluster being younger
by $\sim 2 - 3$ Gyr. The objects were observed with the LRIS instrument.

4.7 Summary

We present a homogeneous set of Lick indices for 143 extragalactic globular clusters in seven early-type galaxies located in different environments. The indices were measured on high-quality VLT spectra and are currently the largest homogeneous spectroscopic data set of extragalactic globular cluster systems.

The candidate pre-selection for follow-up spectroscopy was confirmed to work very efficiently. Inside one effective radius the success rates are between $\sim 80-100\%$ for galaxies located at high galactic latitudes ($|b| \gtrsim 40^o$).

We provide a method to reduce the number of contaminating fore- and background objects during the candidate selection. A combination of near-infrared and optical colours in a $I - K$ vs. $B - K$ colour-colour diagram allows to disentangle foreground stars and background galaxies from the globular cluster population very efficiently. Fractional contamination can be reduced to $\lesssim 10\%$.

We fit surface brightness and surface density profiles to the galaxy light and the globular cluster system and find that globular cluster systems have in general comparable or more extended profiles than the galaxy light. By dividing the clearly multi-modal globular cluster populations in blue and red sub-samples, we find that both have similar profile slopes. A brute-force division of the remaining single-peak systems reveals that the red globular cluster sub-population is more concentrated than its blue counterpart.

Using the radial velocity information of our globular cluster samples we measure dynamical masses for the seven host galaxies which have total masses between $\sim 8.8 \cdot 10^{10} M_\odot$ and $\sim 1.2 \cdot 10^{12} M_\odot$.

The accuracy of index measurements allows an age resolution $\Delta t/t \approx 0.3$ and a metallicity resolution in the range $\sim 0.25-0.4$ dex depending on the absolute metallicity. Hence, $\sim 50\%$ of our data allows detailed age/metallicity determinations for individual globular clusters.

Chapter 5

Global Ages, Metallicities, and [α/Fe] Ratios

5.1   Introduction

In this Chapter we analyse mean ages, metallicities, and [α/Fe] ratios for our sample of globular clusters in early-type galaxies described in Chapter 4. Diagnostic diagrams, which combine spectroscopic tracers of age, total metallicity, and the abundances of selected species, are used to derive the above parameters. In particular, the choice of a specific age/metallicity diagnostic diagram lacks consistency throughout the literature. In order to homogenise the usage of the optimal combination of Lick indices to construct such a diagram, we provide a method to quantify the relatively best age and metallicity indicator for a given set of SSP model predictions and data quality.

5.2   Selection of Data

Our entire sample contains 143 globular clusters in seven early-type galaxies. Not all spectra satisfy the S/N standards to derive accurate ages, metallicities, and [α/Fe] ratios. It is possible to achieve an age resolution of ~ 1 Gyr (at ages ~ 15 Gyr) only for the brightest globular clusters in our sample. The typical separation between the 15 and 14 Gyr isochrone in current SSP models is of the order $\Delta \mathrm{H}\beta \approx 0.05$ Å, and ~ 0.1 Å for the higher-order Balmer indices. Only 1 object of our sample meets these strict requirements. The final sample has to be built from a compromise between age/metallicity resolution and sample size. We, therefore, relax the selection to clusters with a statistical measurement uncertainty of $\Delta \mathrm{H}\beta \leq 0.4$ Å and ≤ 0.6 Å for higher-order Balmer line indices. This selection corresponds to a minimum age resolution $\Delta t/t \sim 0.3$. We additionally use the composite [MgFe]$'$ index (see below) as a metallicity indicator. An error cut at 0.2 Å for this index guarantees a metallicity resolution between ~ 0.25 dex at high and ~ 0.4 dex at low metallicities. The above selection criteria leave 71 globular cluster spectra in our sample which correspond to $\sim$50% of the initial data.

Our colour selection criteria exclude globular clusters with low metallicities ([Z/H] $\lesssim -1.3$) and relatively young ages ($t \lesssim 5$ Gyr). Figure 5.1 illustrates the age and metallicity ranges imposed by our colour selection of cluster candidates. Although all Milky Way globular clusters are selected by our colour cuts $0.8 \lesssim V - I \lesssim 1.3$, $1.5 \lesssim B - I \lesssim 2.5$, and $1.0 \lesssim B - R \lesssim 1.7$ (we refer to Chapter 3 for details), other galaxies might contain some metal-poor young globular clusters

which were formed from lately accreted primordial gas or accreted from star-forming dwarf irregular galaxies. However, colour-magnitude diagrams in Chapter 4 indicate that, if such young and metal-poor objects exist in our sample galaxies, their number is not significant compared to the remaining globular cluster system (in the worst case $\lesssim 10\%$). Our spectrosopy of some blue objects outside our colour selection (mask fill-in objects) shows that this fraction must be smaller than a few percent.
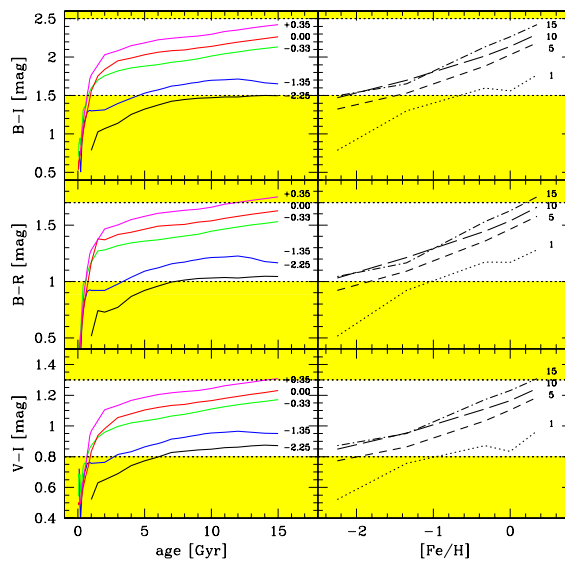
Figure 5.1: Illustrated are colours which were used to select globular cluster candidates as a function of age and metallicity and taken from model predictions of Maraston (2003). Upper and lower colour cuts are indicated as horizontal lines. Curves in left panels are parameterised by metallicity, curves in right panels are parameterised by age and indicated accordingly.

We advise caution with respect to the universality of the derived ages, metallicities and [α/Fe] ratios. These parameters are subject to change, since neither the sampled fraction of each globular cluster system, nor the sampling of colour distributions and luminosity functions is constant from galaxy to galaxy. With the current data set, any such distribution will necessarily be biased towards bright globular clusters. Given the still relatively small numbers of globular clusters per galaxy, a peculiar age and/or metallicity distribution in one galaxy can easily bias any relation between age, metallicity and [α/Fe]. To secure oneself against such biases each single globular cluster system needs to be analysed individually using a statistically representative sample.

5.3 Reducing the Age-Metallicity Degeneracy of Diagnostic Plots

In the following we determine the best combination of indices as diagnostics for age and metallicity. Taking into account the uncertainty of our line index measurements, the mean uncertainties of the Lick system, and the limits on the prediction power of SSP models, we construct the relatively best diagnostic diagram from Lick line

indices. This diagram also maximally reduces the age-metallicity degeneracy of line indices and is least sensitive to variations in $[\alpha/\text{Fe}]$ ratio.

5.3.1 The relatively best Age Indicator

The Balmer line series provides the best spectroscopic age indicator among the set of Lick line indices. The Lick system defines five indices ($\text{H}\beta$, $\text{H}\gamma_\text{A}$, $\text{H}\delta_\text{A}$, $\text{H}\gamma_\text{F}$, and $\text{H}\delta_\text{F}$) for three Balmer lines (Worthey 1994; Worthey & Ottaviani 1997). Figure 5.2 shows the passband definitions for all Balmer indices. In combination with a metallicity diagnostic, these higher-order Balmer line indices are widely used to determine (luminosity-weighted) ages and metallicities of galaxies (e.g. Trager et al. 1998, 2000a,b; Kuntschner 2000; Poggianti et al. 2001; Moore et al. 2002; Kuntschner et al. 2002a; Thomas et al. 2003a).

However, different types of diagnostic plots employing different Balmer-line indices as age indicators are used throughout the literature. Although the age predicting power of an arbitrarily chosen diagnostic plot (most common versions include the $\text{H}\beta$ and Mg_2 or $\langle\text{Fe}\rangle$ indices) might yield accurate-enough results for a specific scientific goal (e.g. the mean age difference between two different galaxy samples), the choice of a specific diagnostic plot is still subject to observational constraints and personal assessment and makes comparisons between studies difficult. As a consequence, most authors use several diagnostic plots with different Balmer line indices and assign equal importance to the results derived from each of those.

In the following we provide a recipe to define a quantity from which the relatively best Balmer-line age indicator can be determined. This quantity takes into account the quality of a given data set and the diagnostic power of theoretical predictions from which one intends to derive the age and metallicity.

In particular, the age sensitivity of an index is a function of the following parameters:

- η: mean error of the data

- ζ: transformation accuracy to the Lick system

- γ: mean error of the original Lick spectra

- δ: accuracy of the Lick fitting functions (Worthey 1994; Worthey & Ottaviani 1997)

- $\mathcal{D}_\text{Z}$: index range covering all ages at a given metallicity, hereafter termed the dynamic range

- $\mathcal{S}_\text{Z,t}$: degeneracy parameter, which quantifies the sensitivity to age and metallicity at a given metallicity and age (i.e. the impact of the age-metallicity degeneracy)

The according numerical values for each parameter are given in Table 5.1 for each Balmer index. It is worth noting that some of these values are only valid for our data quality in combination with the SSP models of Maraston (2003). For different data and SSP models, η, $\mathcal{D}_\text{Z}$, and $\mathcal{S}_\text{Z,t}$ are subject to change. To quantify the most age-sensitive and least metallicity-sensitive Balmer index, we define the quantity

$$\mathcal{R} = \frac{\mathcal{D}_\text{Z} \cdot \mathcal{S}_\text{Z,t}}{\sqrt{\eta^2 + \zeta^2 + \gamma^2 + \delta^2}} \tag{5.1}$$

where the degeneracy parameter, $\mathcal{S}_\text{Z,t}$, is defined as

$$\mathcal{S}_\text{Z,t}(I) = \left.\frac{\partial I}{\partial t}\right|_\text{Z,t} \cdot \left.\left(\frac{\partial I}{\partial Z}\right)^{-1}\right|_{t,Z}. \tag{5.2}$$
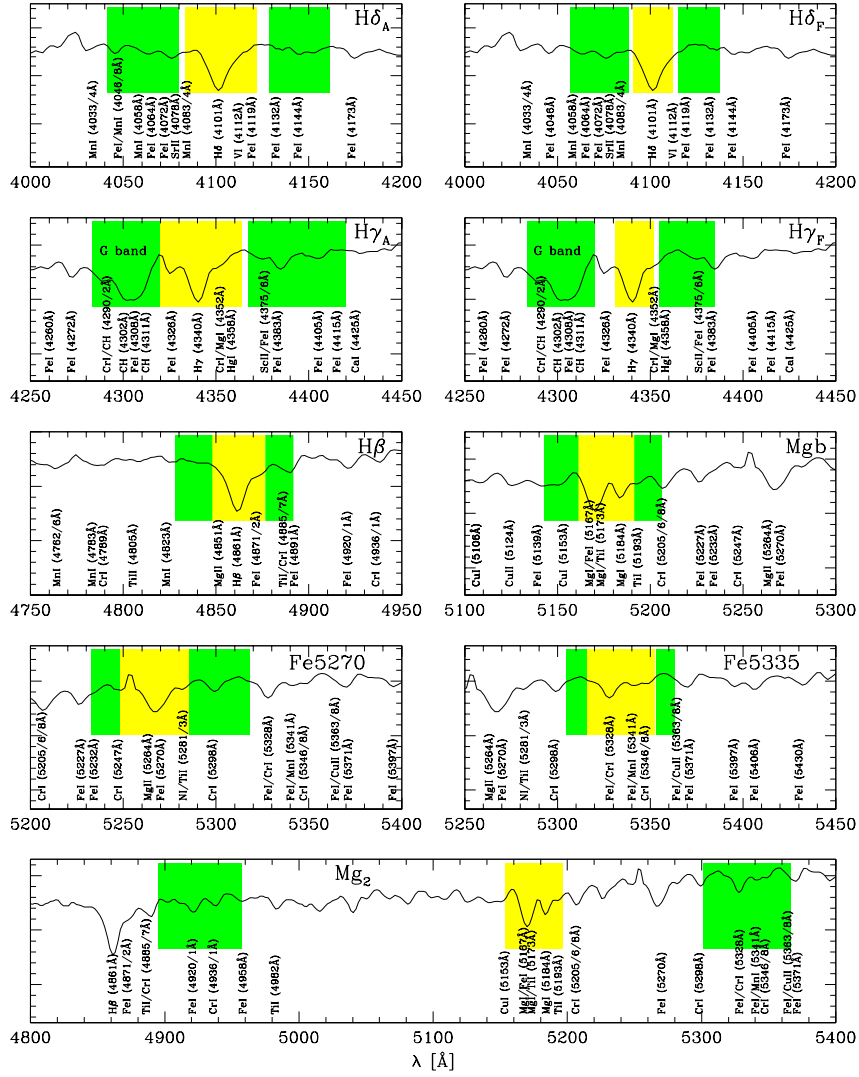
Figure 5.2: Passband definitions for Balmer-line, Mg*b*, Mg₂, Fe5270, and Fe5335 Lick indices with their feature and adjacent continuum passbands. The overplotted spectrum is a high-S/N spectrum of the Galactic globular cluster NGC 6284 (Chapter 2). The resolution is ∼ 7 Å and was left untouched to keep satellite lines visible. Line data were taken from Reader & Corliss (1981). Note the large amount of satellite lines which are included in within the passband definitions.

Table 5.1: Summary of the coefficients relevant to equation 5.1. The coefficients in columns 2-8 are given in units of Å. Columns 9-12 are given in dex/Gyr while the unit of $\mathcal{R}$ in the last column is Å·dex/Gyr.

index	η	ζ	γ	δ	$\mathcal{D}_{-1.35}$	$\mathcal{D}_{0.0}$	$\langle\mathcal{D}_Z\rangle$	$\mathcal{S}_{-1.35,3}$	$\mathcal{S}_{-1.35,13}$	$\mathcal{S}_{0.0,3}$	$\mathcal{S}_{0.0,13}$	$\langle\mathcal{S}_{Z,t}\rangle$	$\mathcal{R}$
1	2	3	4	5	6	7	8	9	10	11	12	13	14
Hβ	0.20	0.232	0.22	1.30	2.55	2.68	2.62	0.389	0.146	0.442	0.120	0.274	0.530
Hγ_A	0.28	0.722	0.48	1.78	7.75	11.01	9.38	0.284	0.068	0.262	0.049	0.166	0.779
Hγ_F	0.28	0.448	0.33	1.34	4.55	5.83	5.19	0.291	0.072	0.123	0.058	0.136	0.478
Hδ_A	0.27	1.043	0.64	1.27	5.73	9.11	7.42	0.262	0.047	0.233	0.047	0.147	0.611
Hδ_F	0.28	0.790	0.40	1.18	3.83	4.47	4.15	0.284	0.054	0.122	0.058	0.130	0.359

$\mathcal{R}$ is essentially the dynamic scale of an index I at a given age and metallicity expressed in units of the total uncertainty. We use the mean dynamic age range $\mathcal{D}_{\mathrm{Z}}$ at two different metallicities [Fe/H]$= -1.35$ and 0.0 between the 1 and 15 Gyr isochrone. Each SSP model provides a well-defined relative age scale which we use here to parameterize $\mathcal{S}_{\mathrm{Z,t}}$ for two different metallicities [Fe/H]$= -1.35$ and 0.0 at two different ages 3 and 13 Gyrs. $\mathcal{S}_{\mathrm{Z,t}}$ is the ratio of age and metallicity partial derivatives at a given metallicity Z and age t (see Eqn. 5.2). In other words, $\mathcal{S}_{\mathrm{Z,t}}$ is a measure of the age-metallicity degeneracy and is maximal for indices which are very sensitive to age and least sensitive to metallicity, at the same time.

The highest $\mathcal{R}$ indicates the best age indicator with least age-metallicity degeneracy. In Table 5.1 we provide values for $\mathcal{D}_{\mathrm{Z}}$ at two different metallicities and for $\mathcal{S}_{\mathrm{Z,t}}$ at four age-metallicity combinations for each Balmer line index. Since SSP models do not provide continuous but discrete predictions the partial derivatives are substituted by difference ratios, i.e. $\partial I/\partial Z \rightarrow \Delta I/\Delta Z$ and $\partial I/\partial t \rightarrow \Delta I/\Delta t$. The quotients are determined by linear interpolation of the SSP models.

We determine the relatively best age indicator from the set of five Lick Balmer indices by combining the mean dynamic range $\langle \mathcal{D}_{\mathrm{Z,t}} \rangle$, the mean age-metallicity sensitivity $\langle \mathcal{S}_{\mathrm{Z,t}} \rangle$, and the total index uncertainty which is the denominator in equation 5.1. The final mean $\mathcal{R}$ is documented in the last column of Table 5.1. We find that the relatively best age diagnostic for our data is the Hγ_A index followed by the indices Hδ_A and Hβ. Hγ_F and Hδ_F have the smallest $\mathcal{R}$ values and are considered as not reliable age indicators.

It is instructive to see that despite the relatively large age-metallicity degeneracy of the Hγ_A index, the most accurate age predictions can be derived with this index. This fact is basically due to the large dynamic range of Hγ_A compared to its mean measurement uncertainty. Hβ, on the other hand, has a relatively large total uncertainty and the measurements will therefore be more scattered over the diagnostic plot's parameter range. In general, the higher-order Balmer lines require less S/N to guarantee a similar total index accuracy as Hβ. If our data set would be infinitely accurate (i.e. $\eta = 0$ in Eq. 5.1), the order of $\mathcal{R}$ from the best to worst Balmer index would remain unchanged. This order is predominantly governed by uncertainties in the fitting functions of the respective index. To vary this order the mean measurement uncertainties have to be very discrepant and the SSP-model predictions have to deviate significantly from the model used here. It is expected that the relative accuracy of Balmer index measurements is comparable between different data sets as they are usually derived from one optical spectrum. The *relative* age scale of SSP models appears to be quite stable from model to model. This scale is used in our above prescription. It can therefore be expected that no large fluctuation in $\mathcal{R}$ will arise from the use of different SSP model predictions[1]. Henceforth, we use the Hγ_A index as our most reliable age-indicator.

5.3.2 Initial Caveat on the Use of Balmer Indices as Age Indicators

As shown by Maraston & Thomas (2000) for Hβ and in Chapter 3 for the higher-order Balmer series, the morphology of the Horizontal Branch (HB), when extended to warm temperatures ($\sim 9000 - 10000$ K), plays a major rôle in increasing the the strength of Balmer indices. This effect is due to metallicity and confuses the use of Balmer lines as pure age indicators (on this topic see also de Freitas Pacheco & Barbuy 1995 and Lee et al. 2000). Since the HB morphology cannot be predicted by first principles of stellar evolution, as it is determined

---

[1]We note that abundance ratio variations are not considered by this exercise and can change the ranking of $\mathcal{R}$.

by mass-loss, the line indices need to be calibrated with globular clusters for which
the HB morphology is known (Chapter 3 and Maraston & Thomas 2000). This
exercise is clearly impossible for extragalactic globular clusters. This is why in
the following we will use models of Chapter 3 which include reddish and bluish
HB morphologies as function of metallicity, and that encompass well the observed
range of Balmer lines in Milky Way globular clusters. As thoroughly explored by
Greggio & Renzini (1990), blue HBs are in principle possible also in metal-rich stel-
lar populations (see also Rich et al. 1997, for two Milky Way globular clusters), that
suffer from enhanced mass-loss or have a high Helium abundance. Models with blue
HBs at high metallicity will be published elsewhere (Maraston 2003), and here we
report on their differential effect.

In the following we use the Balmer indices as age indicators with confidency
at low metallicity, because HB morphology is included in our SSP models and
under control. At high metallicity, we have the warning in mind that ages could be
degenerate with the presence of unresolved blue HBs. For this reason we will refer
to such young ages as "formal". Further potential systematics which can influence
age and metallicity determinations are addressed in Appendix F, among which we
discuss the influence of satellite lines, contamination by ionised gas, model-to-model
variations, and systematics inherent in SSP model.

5.3.3   The Influence of $[\alpha/\mathrm{Fe}]$ Variations on Isochrones
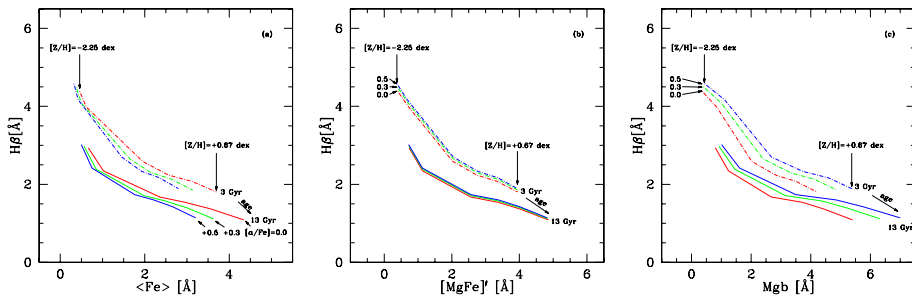
Figure 5.3:   Panel (a): $\mathrm{H}\beta$ vs. $\langle\mathrm{Fe}\rangle$.   Lines show model pre-
dictions (Thomas et al. 2003a) for stellar populations with metallicities
$[\mathrm{Fe/H}]=-2.25, -1.35, -0.55, -0.33, 0.00, 0.35,$ and 0.67 and two ages 13 (solid lines)
and 3 Gyr (dot-dashed lines) parameterized for three different $[\alpha/\mathrm{Fe}]$ ratios 0.0, 0.3,
and 0.5 dex. Panel (b): $\mathrm{H}\beta$ vs. $[\mathrm{MgFe}]'$. Models as in Panel (a). Panel (c): $\mathrm{H}\beta$ vs.
Mgb. Models as in Panel (a).

Recently, Thomas et al. (2003a) calculated new theoretical Lick index predic-
tions which are parameterized for *well-defined* $[\alpha/\mathrm{Fe}]$ ratios for a wide range of ages
and metallicities. These models take into account the effects of changing element
abundance ratios on Lick indices, hence give Lick indices not only as a function
of age and metallicity, but also as a function of the $[\alpha/\mathrm{Fe}]$ ratio. They are based
on the evolutionary population synthesis code of Maraston (1998). The impact
from element ratio changes is computed with the help of the Tripicco & Bell (1995)
response functions, using an extension of the method introduced by Trager et al.
(2000a). Because of the inclusion of element ratio effects, the influence of $[\alpha/\mathrm{Fe}]$
on Balmer indices can be studied, and is illustrated in Figure 5.3. In general, such
variations of $\mathrm{H}\beta$ between isochrones with $[\alpha/\mathrm{Fe}]$ ratios between solar and $+0.5$ dex
are of the order ~ 0.05 Å for low, and ~ 0.2 Å for high metallicities, and corresponds
to an age difference in the range $\Delta t/t \sim 0.2$.

Due to the lack of corresponding response functions in the work of Tripicco & Bell, such predictions are not available for higher-order Balmer indices. Figure 5.2 shows these indices generally include more metal absorption lines in their feature and background passbands than the Hβ index. It is unclear how exactly the higher-order indices change with varying [α/Fe]. However, the empirical calibration of higher-order Balmer lines (see Fig. 3.13 in Chapter 3) shows that the influence of these neighbouring lines cannot be that large, at least for Milky Way globular clusters. Careful modeling of response functions for higher-order Balmer indices is on the way (Korn et al., in preparation) and it is expected these indices behave similarly as Hβ for varying metal abundances.

5.3.4   The relatively best Metallicity Indicator

The index with the highest metallicity sensitivity and minimal age-sensitivity could in principle be found in a comparable way as it was done for the relatively best age diagnostic. The major impact of typical metallicity tracers, such as $\langle$Fe$\rangle$, Mg$_2$, and Mgb, on the absolute metallicity scale is expected to arise from changing abundance ratios. To reduce the influence of [α/Fe] variations on age and metallicity determinations, Thomas et al. (2003a) modify the old [MgFe] index[2] to obtain an entirely [α/Fe]-*insensitive* metallicity index,

$$[\text{MgFe}]' = \sqrt{\text{Mg}b \cdot (0.72\,\text{Fe}5270 + 0.28\,\text{Fe}5335)}. \qquad (5.3)$$

Figure 5.3 shows the behavior of isochrones in three different, frequently used, diagnostic plots. Panel (b) impressively illustrates that [MgFe]$'$, indeed, is essentially independent of [α/Fe]. Henceforth we assume that the [MgFe]$'$ index is the best metallicity indicator and use it in combination with the relatively best age indicator (Hγ_A, see Sect. 5.3.1) to derive ages and metallicities for our selected globular clusters.

5.4   Ages and Metallicities

5.4.1   Hγ_A vs. [MgFe]$'$

Having determined the relatively best age and metallicity diagnostics, we plot Hγ_A vs. [MgFe]$'$ in Figure 5.4 and compare our measurements with theoretical age and metallicity predictions. At this point, we note that all results apply to globular cluster systems of early-type *in general*, and are not biased by a single galaxy in our sample, as far as the sample statistics allows such a statement.

Figure 5.4 reveals that the data are consistent with metallicities in the range $-2.25 \lesssim$ [Z/H] $\lesssim +0.5$. An apparently universal lower metallicity boundary at [Z/H] ≈ -2.3 is found for all sample globular cluster systems. About 25% of our sample globular clusters have formal super-solar metallicities. The average globular cluster at metallicities [Z/H] $\lesssim -0.8$ is consistent with rather old ages between 8 and 15 Gyr. At higher metallicities the mean age of the sample drops significantly. About 34% of globular clusters has formal ages below 5 Gyr. In some extreme cases, individual globular clusters reach formal ages as young as ~ 1 Gyr at solar to super-solar metallicities. Globular cluster with ages below 5 Gyr are not found in the metal-poor sub-population. On the other hand, there are globular clusters with old ages at all metallicities. If the sample is split into formally young and old globular clusters with the 5 Gyr isochrone in the Hγ_A vs. [MgFe]$'$ diagnostic diagram, we find mean metallicities [Z/H] of $+0.27 \pm 0.02$ dex and -0.59 ± 0.12 dex

---

[2] [MgFe] $= \sqrt{\text{Mg}b \cdot \langle\text{Fe}\rangle}$, see González (1993).
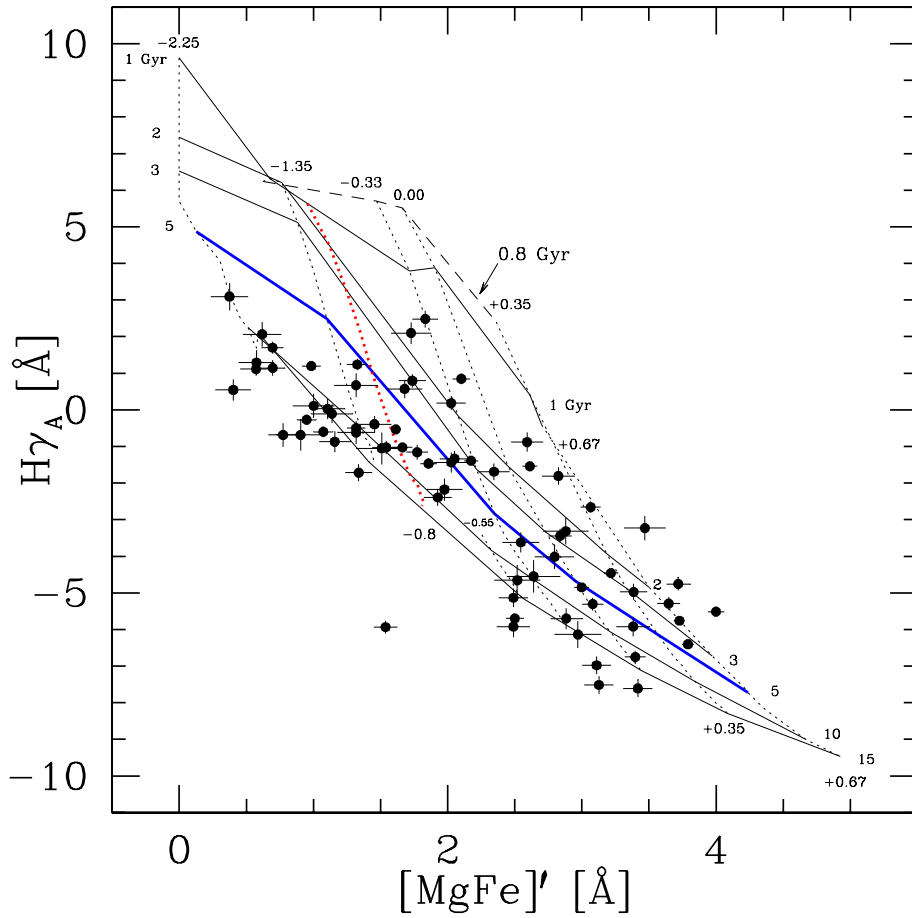
Figure 5.4: Hγ_{A} vs. [MgFe]$'$ diagnostic plot for high-quality globular cluster spectra. SSP models from Chapter 3 have been overplotted for the metallicities [Z/H]$=-2.25, -1.35, -0.55, -0.33, 0.00, 0.35$, and 0.67 dex (dotted lines) and for ages 15, 10, 5, 3, 2, 1 (solid lines), and 0.8 Gyr (dashed line). The thick dotted line is an interpolated iso-metallicity track for [Z/H] $= -0.8$ and is used to split the sample between metal-poor and metal-rich globular clusters. The thick iso-age line is the 5 Gyr isochrone, and is used to split between old and formally young globular clusters.
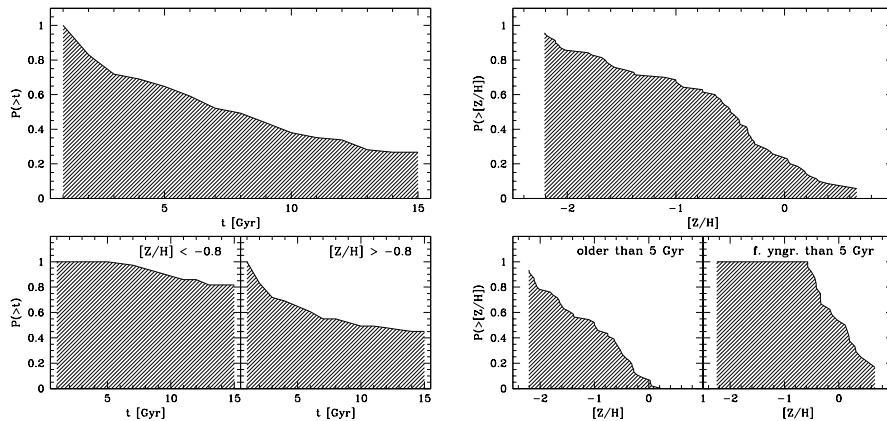
Figure 5.5: Cumulative age and metallicity distributions for globular clusters in early-type galaxies, derived from the Hγ$_A$ vs. [MgFe]′ diagnostic plot. The left panel shows the age distribution for the entire data together with the age distributions for sub-samples split at a metallicity [Z/H] = −0.8. In the right panel the metallicity distributions for the entire sample and sub-sample split by age at 5 Gyr are shown.

for the formally young and old sub-sample, respectively. A linear interpolation of the model grid in the Hγ$_A$ vs. [MgFe]′ diagnostic diagram reveals a mean metallicity [Z/H] −0.08 ± 0.07 dex with a dispersion of 0.89 dex for the entire sample. In Figure 5.5 cumulative metallicity distributions derived from the Hγ$_A$ vs. [MgFe]′ diagnostic plot are shown for the entire sample as well as sub-samples split at a formal age of 5 Gyr. A Kolmogorov-Smirnov (KS) test returns a likelihood of ∼ 70% that the metallicity distributions of the formally young and old sub-samples have the same origin.

We split the sample at [Z/H] ∼ −0.8, corresponding to the dip in the Milky Way globular cluster metallicity distribution (Harris 1996), into metal-poor and metal-rich globular clusters. To determine ages for the two sub-populations, we extrapolate the model tracks linearly to extremely old ages. For metal-poor globular clusters, where isochrones start to overlap at high ages, we use the closest iso-age track to derive an age. With this procedure we find an increase in formal age spread from metal-poor to metal-rich globular clusters. A mean age of 11.3 ± 0.5 Gyr with a dispersion of 2.7 Gyr for metal-poor globular clusters and a mean age of 6.3 ± 0.8 Gyr with a dispersion of 5.4 Gyr for metal-rich clusters is derived from Figure 5.4. The mean age of the entire sample is 8.1 ± 0.5 Gyr with a dispersion of 4.6 Gyr. In the left panel of Figure 5.5 we plot the cumulative age distributions our the entire sample as well as the sub-samples split by metallicity. A KS-test shows that the likelihood that the age distributions for metal-poor and metal-rich globular clusters are drawn from the same parent distributions is only ∼ 10%. Based on a linear weighted least-square fit to the data in the Hγ$_A$ vs. [MgFe]′ diagram and the model of Maraston et al. (2003), we find a significant mean age-metallicity relation −3.5 ± 0.6 Gyr/dex, in the sense that more metal-rich globular clusters appear on average younger.

5.4.2   Other Balmer indices vs. [MgFe]′

In the following, we present mean age and mean metallicity predictions of diagnostic plots using other Balmer-line indices, such as Hβ, Hδ$_A$, Hγ$_F$, and Hδ$_F$, shown in Figure 5.6. All diagnostic diagrams use model predictions of Chapter 3. Accord-
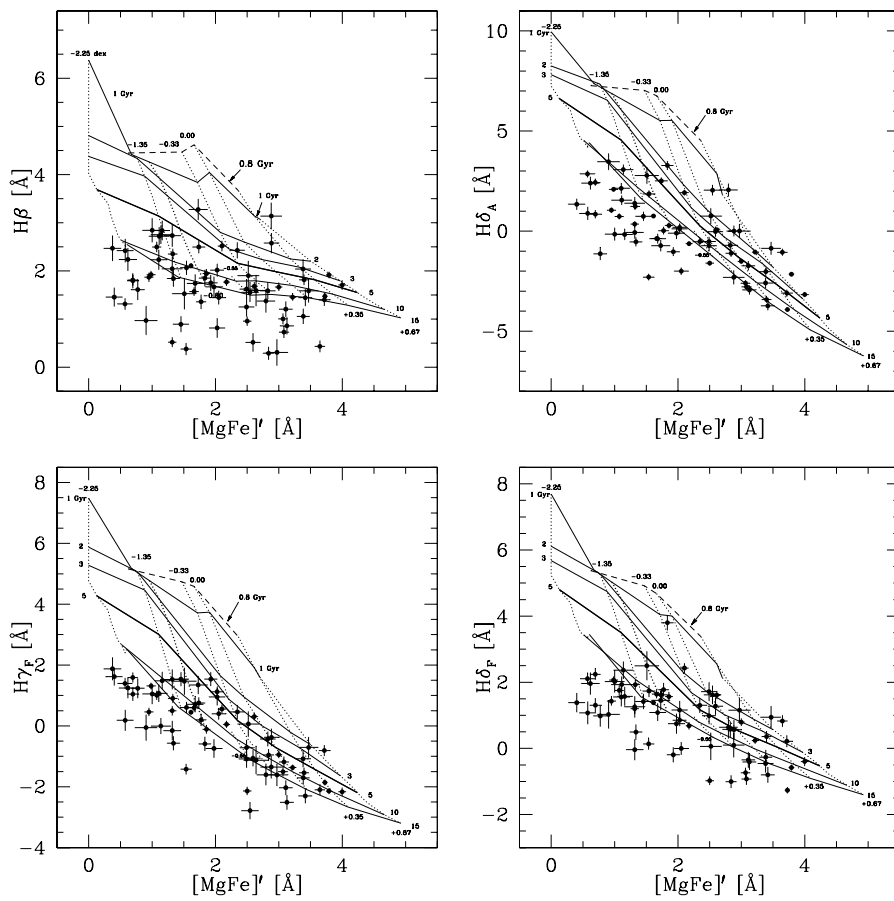
Figure 5.6: Hβ, Hδ_A, Hγ_F, and Hδ_F vs. [MgFe]$'$ diagnostic plots. Model predictions were taken from Chapter 3. As a guide to the eye the 5 Gyr isochrone and the -0.8 dex iso-metallicity track are plotted as thicker lines.

ing to their $\mathcal{R}$ values (Sect. 5.3), these diagnostic diagrams are less reliable. The comparison of derived formal ages and metallicities of individual globular clusters shows that all diagnostic diagrams make *inconsistent age predictions*. Metallicities are on average well reproduced, which is little surprise since all diagrams use the [MgFe]$'$ as metallicity indicator. However, even the *relative* ages differ from diagram to diagram. This is a surprising results as our SSP models are well calibrated and the age predictions for Milky Way globular clusters are consistent (see Chapter 3).

A significant fraction of the data needs large extrapolation of the model grid to derive individual ages and metallicities. We refrain from such very uncertain extrapolations and point out that age and metallicity predictions are strongly dependent on the choice of a specific Balmer index in diagnostic diagrams, even when predictions from one model calculation are used. Instead, we discuss in Section F the systematics which might lead to such inconsistent age/metallicity predictions.

In any case, the conclusions that can be drawn independent of the choice of a specific Balmer index are the following:

- metal-rich globular clusters are on average younger (6.3 ± 0.8 Gyr) compared with metal-poor globular clusters (11.3 ± 0.5 Gyr)

- metal-rich globular clusters exhibit on average a larger age spread (~ 5.4 Gyr) than metal-poor globular clusters (~ 2.7 Gyr)

5.5   [α/Fe] Ratios

In the following Section we derive [α/Fe] ratios for our sample globular clusters using a diagnostic diagram which is least sensitive to age/metallicity variations. Such a diagram can be constructed from the indices $\langle$Fe$\rangle$ and Mg$_2$, which primarily trace the abundances of Iron and the α-element Magnesium (Tripicco & Bell 1995). We note that among the three Mg-sensitive indices, Mg$_1$, Mg$_2$, and Mgb, theoretical index predictions for stellar populations with well-defined abundance ratios (Thomas et al. 2003a) show a relatively large spread in $\langle$Fe$\rangle$ and Mg$_2$ for [α/Fe] ratios between solar and ~ 0.5 dex at high mean metallicities. Given the quality of our data we can expect a good discrimination between α-enhanced and solar-type globular clusters at metallicities [Z/H] $\gtrsim -0.8$.

Figure 5.7 shows that the Mg$_2$ vs. $\langle$Fe$\rangle$ diagnostic diagram is not entirely free from the age/metallicity degeneracy. Iso-[α/Fe] tracks for three different ratios (0.0, 0.3, and 0.5 dex) are plotted for two ages (3 and 13 Gyr, indicated by dotted and solid lines, respectively). It is obvious that one needs age information to use the correct set of tracks. We divide our sample in formally-young and old globular clusters using the 5 Gyr iso-age track in the Hγ_A vs. [MgFe]$'$ diagnostic plot (see Fig. 5.4). For the old sub-sample, we use the 13 Gyr iso-[α/Fe] tracks to derive individual [α/Fe] ratios by linear inter- and extrapolation of the model grid. For formally-young globular clusters, we use iso-[α/Fe] tracks for a 3 Gyr old stellar population. In Figure 5.7, formally-young and old globular clusters are plotted as open and solid circles, respectively.

The majority of globular clusters is consistent with super-solar [α/Fe] ratios. The mean [α/Fe] of the sample is 0.44 ± 0.05 dex. The scatter in [α/Fe] *decreases* as a function of mean metallicity, from ~ 0.5 dex at low metallicities down to ~ 0.3 dex at high metallicities. The scatter of the entire sample is 0.40 dex. *All* globular clusters with [Z/H] $\gtrsim -0.8$ have super-solar [α/Fe] ratios. For globular clusters with smaller metallicities the separation of model tracks is of the order or less than the mean measurement uncertainty and hampers accurate [α/Fe] determinations. However, the model tracks reproduce the mean locus of the data fairly well. We find no evidence for a [α/Fe]–metallicity relation. The successively smaller separation
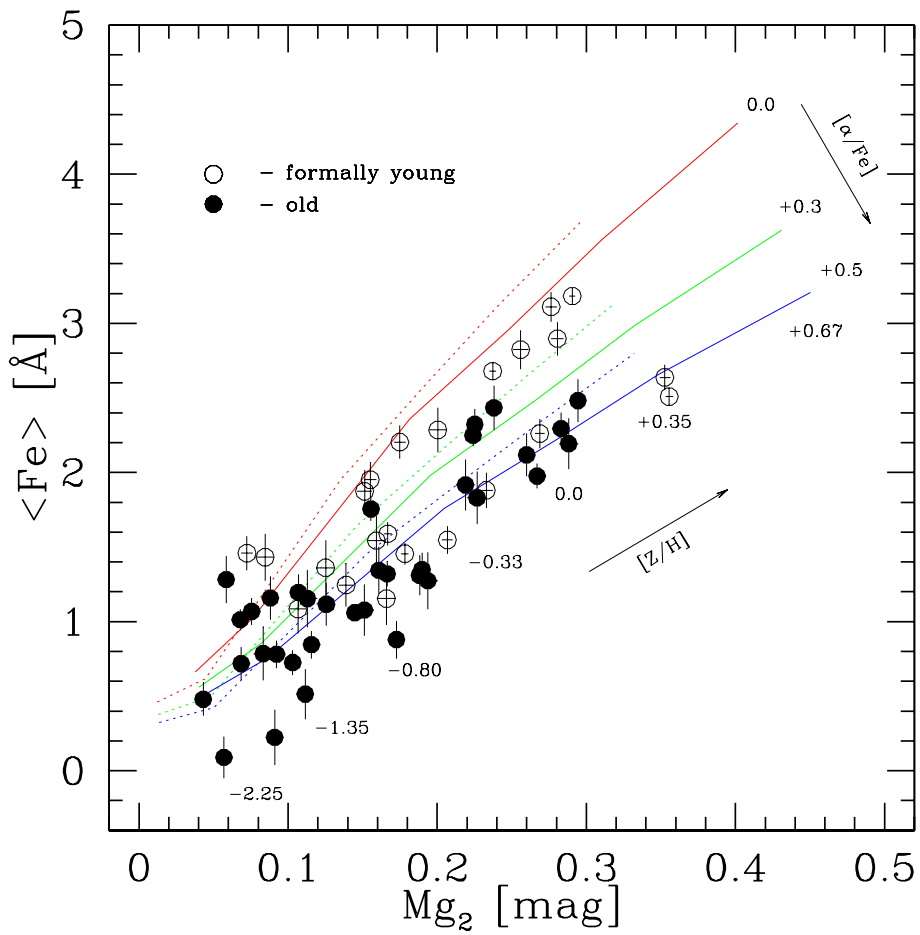
Figure 5.7: The mean iron index ⟨Fe⟩ as a function of Mg₂. The plot shows the sample divided into formally old (*filled circles*) and formally young (*open circles*) globular clusters. SSP models Thomas et al. (2003a) with constant [α/Fe] ratios have been overplotted for [Z/H] between −2.25 and +0.67 dex and two ages 13 (*solid lines*) and 3 Gyr (*dotted lines*) with various [α/Fe] ratios 0.0, +0.3, and +0.5 dex.
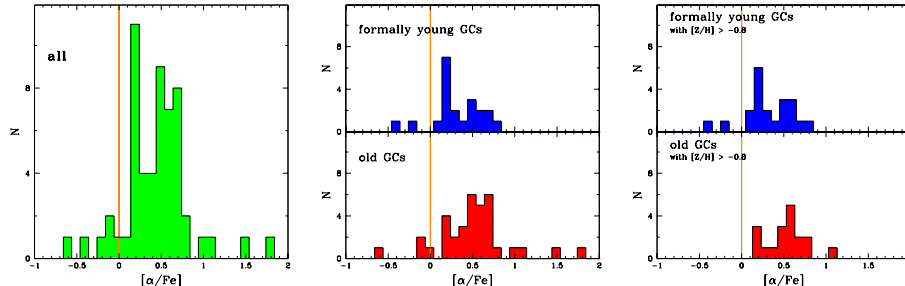
Figure 5.8: Histograms of globular cluster [α/Fe] ratios. A histogram for the entire cluster sample is shown in the *left panel*. The *right panel* shows the distribution of [α/Fe] ratios for old globular clusters (lower sub-panel) and their formally young counterparts (upper sub-panel). [α/Fe] ratios for globular clusters with metallicities [Z/H] > -0.8 are illustrated in the *right panel*. The division in formally young and old objects was performed with the 5 Gyr isochrone in Figure 5.4. In all panels a vertical line indicates solar [α/Fe] ratios.

of the iso-[α/Fe] model tracks at lower metallicities does not allow an accurate determination of this relation anyway. Hence, we refrain from such an uncertain quantification.

Recent measurements of [α/Fe] ratios in globular cluster systems in other early-type galaxies reveal very similar results. For instance, the data of Kuntschner et al. (2002b) for 17 globular clusters in NGC 3115 show that most clusters are consistent with [α/Fe] ≈ 0.3 over the entire range of sampled metallicities. Larsen et al. (2002a) find a super-solar mean [α/Fe] ratio of $+0.4$ dex for globular clusters of all metallicities in NGC 4594 (Sombrero). Using SSP models with non-constant [α/Fe] ratios, Forbes et al. (2001) argue that at least some globular clusters in NGC 1399 exhibit super-solar [α/Fe] ratios.

We find tentative evidence for a [α/Fe]–age relation using the above splitting into formally-young and old objects. The median [α/Fe] for the formally-young globular cluster sample is 0.26 ± 0.06 dex, and 0.54 ± 0.07 dex for old clusters, with a dispersion ~ 0.35 for both sub-samples. We derive a mean [α/Fe]–age relation of 0.02 ± 0.008 dex/Gyr. Histograms of [α/Fe] values for the entire sample and both age sub-samples are shown in Figure 5.8. The difference of ~ 0.3 dex in [α/Fe] between formally-young and old globular clusters is a lower limit, since we choose a rather extreme young age (3 Gyr) for formally-young globular clusters. Using older iso-[α/Fe] tracks for the formally-young sample would increase the [α/Fe] offset between formally-young and old globular clusters.

As can be seen in Figure 5.7 the found [α/Fe]–age relation is most apparent in the metal-rich regime. If only globular clusters with [Z/H] $\gtrsim -0.8$ are considered the median [α/Fe] values for formally-young and old globular clusters are 0.26 ± 0.06 and 0.54 ± 0.05, respectively. A histogram of the corresponding [α/Fe] distributions is shown in the right panel of Figure 5.8. More accurate and especially statistically more significant quantifications of this very interesting result require larger data sets.

In the following we summarize the major findings of this section:

- globular clusters in early-type galaxies have on average super-solar [α/Fe] ratios with a mean ~ 0.4 dex

- formally-young globular clusters have on average lower [α/Fe] ratios than old globular clusters, implying a [α/Fe]–age relation of 0.02 ± 0.008 dex/Gyr

- metal-rich and metal-poor globular clusters exhibit similar $[\alpha/\text{Fe}]$ ratios with no evidence for a $[\alpha/\text{Fe}]$–metallicity relation

5.6 Discussion

5.6.1 Assembly History of Early-Type Galaxies

The hierarchical picture of galaxy formation predicts a more extended period of galaxy assembly for more massive galaxies, leading to a higher fraction of younger stellar populations in these systems. If the dispersion in the Balmer-[MgFe]$'$ diagnostic plots for extragalactic globular clusters is entirely driven by age, we find good indication for a significant fraction of relatively young globular clusters in early-type galaxies. About 34% of our sample globular clusters have formal ages younger than ~ 5 Gyr, implying formation redshifts $z \lesssim 1$. To the first order, this result would be consistent with the predictions of the hierarchical scenario. However, we sample only the bright end of the globular cluster luminosity function, where young clusters preferentially reside. Hence, this fraction has to be considered as an upper limit, also with respect to the fact that formal young ages are not fully secure (see Sect. 5.4). If we consider the fainter globular cluster system being entirely old, that is older than 5 Gyr, then less than a few percent of an average globular cluster system in an average early-type galaxy formed later than redshift of unity. This in turn would be rather inconsistent with the hierarchical merging scenario in which a considerable fraction of an early-type galaxies is predicted to form later than $z_f \sim 1$.

Furthermore, the naive predictions of a younger age of more massive structures in the hierarchical picture holds, only if the fraction of gas-poor to gas-rich mergers, the so-called dry to mixed merger ratio, is constant throughout the entire redshift evolution. Khochfar & Burkert (2003) predict that this ratio depends on galaxy mass, indicating that most massive ellipticals formed early in rather dissipationless mergers of bulge-dominated precursors (see also Kauffmann & Haehnelt 2000). The transition between dry and mixed merger-dominated evolution is predicted to occur between $M_B \approx -20$ and -21 mag[3]. This implies that on average low-luminosity ellipticals should harbour a higher fraction of young globular clusters, while most massive galaxies should preferentially host old globular cluster systems.

Although based on different passband definitions, previous studies find evidence for mostly old globular cluster systems in the massive Fornax galaxy NGC 1399 (Kissler-Patig et al. 1998a), and the two Virgo galaxies M87 (Cohen et al. 1998) and M49 (Cohen et al. 2003) which appears to fit into the framework of selective merging with an early assembly. Future studies with a wider coverage of galaxy masses will have to test the predictions of the selective merging scenario, in particular if the age spread in globular cluster systems increases towards less massive ellipticals.

5.6.2 Formation Timescales

Stellar populations with super-solar $[\alpha/\text{Fe}]$ ratios, as they are observed in massive elliptical galaxies, are interpreted as the result of very short formation timescales, inconsistent with the hierarchical merging scenario (e.g. Thomas & Kauffmann 1999) and favouring an early monolithic collapse (Worthey et al. 1992). Our formal mean $[\alpha/\text{Fe}]$ ratio of ~ 0.4 dex for globular clusters in early-type galaxies is in line with the values measured for the diffuse light (e.g. Davies et al. 1993, 2001; Thomas et al. 2002; Kuntschner et al. 2002a; Eisenstein et al. 2003). The formation timescales of field stars and globular clusters appear to be very similar in elliptical galaxies.

---

[3]Most of our early-type galaxies fall in this transition regime. We find $\langle M_B \rangle_{\text{sample}} = -20.4 \pm 0.6$ with the brightest galaxy being NGC 5846, $M_B \approx -21.2$.

In the light of the hierarchical-merging picture, massive galaxies are predicted to form their stellar populations on extended timescales, and can be expected to host a globular cluster system with a relatively small mean [α/Fe] and a large spread. For globular cluster systems in early-type galaxies, we find a relatively high mean [α/Fe] ratio with a dispersion (~ 0.4 dex) which implies that $\lesssim 10 - 20\%$ of the system has solar or sub-solar [α/Fe] ratios. Within this framework, our data indicates that a large fraction of globular clusters in early/type galaxies are consistent with short formation timescales. At face value, this is in contrast with the predicted formation histories of the hierarchical-merging scenario.

The found indication for a weak [α/Fe]–age relation among globular clusters in early-type galaxies, in the sense that younger objects have lower, but still super-solar [α/Fe] ratios, points to the fact that the high-density regions from which globular clusters were formed barely experienced enrichment from through SN Ia. However, at the moment we cannot test the variations of the mean [α/Fe] and its dispersion, and the [α/Fe]–age relation for globular cluster systems in early-type galaxies as a function of galaxy mass. Clearly, the reason for high [α/Fe] ratios for globular clusters are short formation timescales on small scales, but any [α/Fe]–age relation is driven by the large-scale chemical enrichment history of the parent galaxy. It is important to test whether or not the [α/Fe]–age relation for globular clusters steepens in more massive galaxies as a result of their more extended formation histories, predicted by hierarchical merging. In the same line, predicted smaller mean [α/Fe] with a larger dispersion for globular cluster systems in more massive galaxies need to be verified.

5.6.3   Limitations of the Lick System

It is known that Balmer-line indices can be significantly influenced by unexpected variations in horizontal branch morphology (see App. F.2). Another source of systematic uncertainty are satellite absorption features will fall inside the passband definitions of each index if their variations are not accounted for in SSP models (see App. F.3). In particular, among the Lick Balmer indices, Hβ is most prone to be sensitive to systematic changes of line strengths in Mg, Ti, Cr, Mn, and Fe in its narrowly-defined passbands (see Fig. 5.2). Other Balmer indices are sensitive to Mg, Sc, Ti, V, Cr, and Mn abundances. In principle this should be of no concern as our models are calibrated on Milky Way globular clusters, provide consistent age, metallicity, and [α/Fe] predictions (see Chapter 3), and account for changing chemical compositions which can be adjusted for stellar populations with a different expected mix of elements (Thomas et al. 2003a).

However, some of the abundance ratios in the Milky Way stellar populations, which are hardwired in our models, might not change in lockstep in stellar populations of extragalactic systems as a function of metallicity (e.g. McWilliam 1997; Pettini 2003). Other than in our models the [Mn/Fe] and [Cr/Fe] ratios are clearly not constant and behave differently as a function of metallicity, even in the Solar neighbourhood (e.g. Fulbright 2002). Observational evidence shows that globular clusters in Local Group galaxies exhibit different abundance pattern in different galaxies (e.g. Burstein et al. 1984; Brodie & Huchra 1991). We also know of abundance pattern variations among Galactic globular clusters themselves (e.g. Kraft 1994; Carretta, Gratton, & Sneden 2000). Moreover, there is evidence that the abundance of the α-element Ca does not change in lockstep with other α-elements in early-type galaxies, in contrast to Galactic stellar populations (e.g. Saglia et al. 2002).

A detailed analysis of such effects is clearly beyond the scope of this work. However, consulting the work of Tripicco & Bell (1995), we find that the modelled response functions (for C, N, O, Na, Mg, Si, Ca, Ti, Cr, and Fe) indicate negligible

influence of satellite lines, which fall inside the passband definitions of the Hβ index, on the level of a few percent. Higher-order Balmer indices are expected to be similarly influenced by the same species (Korn et al., in preparation). We conclude that, although the so-far computed response functions indicate little influence of satellite lines on Lick indices, at least part of the scatter in diagnostic diagrams for globular clusters in early-type galaxies might be due to complex abundance variations.

Complex abundance patterns are in principle accessible with higher-resolution spectroscopy of extragalactic globular clusters ($R \gtrsim 7000$, if the velocity dispersions are comparable to Milky Way globular clusters, $\sigma_{\rm los} \lesssim 20$ km s^{-1}, Mandushev et al. 1991). Such studies can even disentangle the contribution of the turn-off and blue horizontal branch stars to the integrated light (Bernstein & McWilliam 2002), and might help to derive reliable ages. For now, we hit the limits of the Lick index system, which was initially devised to study the diffuse light of galaxies with generally high velocity dispersion, and does not allow to assess chemical compositions due to the implemented low-resolution spectroscopy ($R \gtrsim 1000$).

Chapter 6

Ages, Metallicities, and [α/Fe] as a Function of Host Properties

6.1 Introduction

In this Chapter we continue the analysis started in Chapter 5 by comparing the relative age, metallicity, and [α/Fe] distributions of globular clusters in galaxies of different morphological type, environmental density, absolute B magnitude, and central velocity dispersion. Since differences in star-formation history are expected in hierarchical galaxy formation models as a function of environment (Kauffmann 1996), we sample globular cluster systems in isolated galaxies in the field to high density regions within galaxy clusters. Galaxies with bright absolute B magnitudes are massive and/or have experienced recent star formation. Bright galaxies are known to have higher metallicities than their faint counterparts (Faber 1973). Hence, we expect variations in ages, metallicities, and [α/Fe] between globular cluster system in bright and faint hosts. According to the Faber-Jackson relation (Faber & Jackson 1976), where $L \sim \sigma_0^4$, similar results are expected from the division by central velocity dispersion as from the magnitude division. Under the assumption that the system is virialised, systematics in properties of globular cluster systems between high- and low-σ galaxies are based on different masses of the host.

We augment our sample with Lick index measurements collected from the literature. The reader is referred to Section 4.6 for a detailed descriptions of each data set. In summary, we include, in addition to our sample, globular clusters from the early-type galaxies NGC 1023, NGC 1399[1], NGC 3610, and NGC 4365, from the lenticular galaxies NGC 3115 and NGC 4594, and from the Local Group galaxies M31, M33, M81, Milky Way, Fornax, and LMC. For these data, we relax the selection to clusters with Δ[MgFe]$' \leq 0.6$ Å, ΔH$\beta \leq 0.5$ Å, and ΔH$\gamma_{\rm A} \leq 0.7$ Å. Note that most of these samples have only a few indices measured.

For the division by environmental density, absolute B magnitude, and central velocity dispersion we use only early-type galaxies in order to avoid biases of potential environment–morphology, M/L–morphology, and σ–morphology relation. Table 6.1 contains all information which will be used to sub-divide the entire glob-

---

[1]Note that the NGC 1399 data set has no [MgFe]$'$ information available. We use instead the [MgFe] index. The mean offset between the two indices [MgFe]−[MgFe]$'$ is of the order ~ 0.02 Å and 0.05 Å rms with negligible metallicity dependence. Our conclusions are not affected, as this small inconsistency creates a bias which is orders of magnitude smaller than the mean measurement uncertainty.

ular cluster sample in sub-samples of early-type galaxies with different properties. Since we attempt to analyse globular cluster system properties as a function of host galaxy property, it is important to control any correlations between host galaxy parameters which are used to select cluster sub-samples and might potentially be correlated. In the following we test our globular cluster sample for correlations between environmental density, absolute B magnitude, and central velocity dispersion *and* check whether the sample covers these parameter spaces homogeneously. Figure 6.1 shows the distributions of galaxies in the three corresponding correlation plots along with the cuts which are applied to generate sub-samples for later use. We note that the parameter space of M_B for group/cluster galaxies is poorly sampled. Accordingly, our sample lacks low-mass group/cluster galaxies. Sampling deficiencies which might lead to potential biases in age, metallicity, and [α/Fe] distributions are separately discussed in the respective, following Sections.

name	ρ_{xyz} Tully (1988)	M_B RC3[a]	$(m-M)_V$ Tonry et al. (2001)	T Tully (1988)	σ [km/s] McElroy (1995)
NGC 1023	0.57	-19.94	30.29	-2B	216
NGC 1399	1.59	-20.95	31.50	-5	308
NGC 3610	0.30	-19.95	31.65	-5	162
NGC 4365	2.93	-21.03	31.55	-5	261
NGC 4594	0.32	-20.97	29.95	-2AP	249

[a] RC3: (de Vaucouleurs et al. 1991)

Table 6.1: Collection of host galaxy properties for which globular cluster data were collected from the literature. See Sect. 4.6 for a description of the sample.
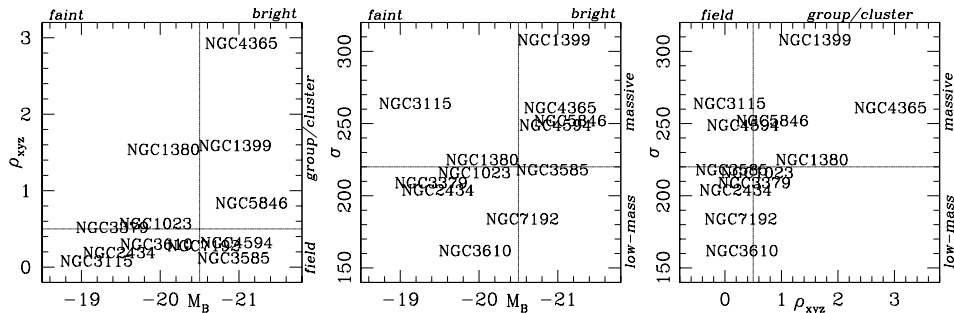
Figure 6.1: **Left panel**: Environmental density, ρ_{xyz} vs. the absolute B magnitude, M_B for the total sample of early-type galaxies. Dotted lines indicate cuts which are applied in later selections. **Middle panel**: Central velocity dispersion, σ vs. M_B. **Right panel**: σ vs. ρ_{xyz}.

6.2   Morphological Type

In the following we compare relative distributions in age/metallicity and [α/Fe] diagnostic diagrams for globular clusters in early-type, lenticular, and late-type galaxies.

6.2.1 Ages and Metallicities

We derive mean ages and metallicities and compare the cumulative age and metallicity distributions of globular clusters derived from the best diagnostic diagram, $H\gamma_A$ vs. $[MgFe]'$ (see also Sect. 5.3). In addition, to illustrate that the choice of a specific Balmer index is crucial for the interpretation of data, we also show the $H\beta$ vs. $[MgFe]'$ diagnostic diagram which exhibits the largest scatter among all age/metallicity diagnostic plots using one of the five Balmer line indices. Both diagrams are components of Figure 6.2 which is sorted from top to bottom by morphological type of the host galaxy for globular clusters in elliptical, lenticular and spiral galaxies, respectively (see Sect. 4.6 for a description of the spiral sample). SSP model predictions in the $H\gamma_A$ and $H\beta$ vs. $[MgFe]'$ age/metallicity diagnostic plots were taken from Chapter 3. We do not plot other higher-order Balmer diagnostic diagrams, as the shown diagrams mark the extremes of all five Balmer diagnostic-plot distributions.

In Figure 6.3 we illustrate the *cumulative* age (left panels) and metallicity distributions (right panels) derived from the $H\gamma_A$ vs. $[MgFe]'$ plot by linear interpolation of the model grid. We do not attempt to extrapolate model grids, but leave the distributions "unfinished", that is at non-unity or non-zero values, indicating that data are located off the grid in the diagnostic diagrams. The cumulative distributions show from left (low ages and metallicities) to right (high ages and metallicities) the fraction of data having values *above* a given age or metallicity. Both the age and metallicity cumulative distributions are also shown parameterised for metallicity and age. In other words, the age distribution is computed for the metal-rich and metal-poor sample, while the metallicity distribution is computed for formally young and old objects. These distributions are shown in corresponding sub-panels. More clearly, the cumulative age distribution is split into two distributions for metal-poor ($[Z/H] < -0.8$ dex) and metal-rich ($[Z/H] > -0.8$ dex) globular clusters. In the case of the cumulative metallicity distribution, we split the sample at a formal age of 5 Gyr into old and formally young globular clusters using the $H\gamma_A$ vs. $[MgFe]'$ diagnostic plot.

Both the $H\gamma_A$ and $H\beta$ diagnostic diagram consistently show that the age dispersion decreases significantly from globular cluster systems in ellipticals over lenticular to spiral galaxies[2]. With the $H\gamma_A$ vs. $[MgFe]'$ diagnostic plot, we find that only $13 \pm 7\%$[3] of the Local Group spiral sample[4] comprising globular clusters in M31, M81, and the Milky Way, have ages formally younger than 5 Gyr. This percentage increases to $20 \pm 6\%$ for globular cluster systems in lenticular galaxies and peaks with $42 \pm 8\%$ in early-type galaxies. For the elliptical, lenticular, and spiral sub-sample we determine mean ages, metallicities and their dispersions from a linear interpolation of the $H\gamma_A$ vs. $[MgFe]'$ model grid. The values are summarised in Table 6.2.

The mean age of globular cluster systems in elliptical and lenticular galaxies is $\sim 7 - 8$ Gyr, with an age dispersion of ~ 4.4 and ~ 3.7 Gyr, respectively. The mean age significantly increases for globular cluster systems in spiral galaxies to $\sim 9.3 \pm 0.8$ Gyr with ~ 3.5 Gyr dispersion. There is tentative evidence that the overall age scatter in globular cluster systems decreases from elliptical to spiral galaxies. Concerning the age structure, globular cluster systems in lenticular galaxies appear to form a transition type between globular cluster systems in spiral and elliptical galaxies. This is illustrated by the cumulative age distributions in the left column

---

[2]Observational errors, which are similar for all three sub-samples, are not taken into account. However, this is irrelevant for the comparison of relative values.

[3]The given error is a statistical error.

[4]Globular clusters in the Large Magellanic Cloud have mostly young to intermediate ages. See Fig. 6.2 and Beasley et al. (2002) for a detailed analysis.

Age in [Gyr]

sample	all mean	σ	[Z/H] < −0.8 mean	σ	[Z/H] > −0.8 mean	σ
E	7.7 ± 0.5	4.4	11.8 ± 0.6	2.7	5.7 ± 0.7	5.1
S0	7.7 ± 0.7	3.7	9.1 ± 0.6	2.1	6.9 ± 1.0	4.5
Sp	9.3 ± 0.8	3.5	10.4 ± 0.7	2.5	8.4 ± 1.0	4.1

[Z/H] in dex

sample	all mean	σ	$t < 5$ Gyr mean	σ	$t > 5$ Gyr mean	σ
E	-0.05 ± 0.07	0.91	$+0.27 \pm 0.02$	0.42	-0.59 ± 0.17	0.81
S0	-0.19 ± 0.11	0.68	$+0.22 \pm 0.03$	0.37	-0.46 ± 0.16	0.62
Sp	-0.40 ± 0.18	0.81	$+0.15 \pm 0.10$	0.61	-0.61 ± 0.21	0.78

Table 6.2: Mean ages and metallicities for globular cluster systems in elliptical, lenticular, and spiral galaxies. The values were derived from the corresponding $H\gamma_A$ vs. $[MgFe]'$ diagnostic diagram and are given in Gyr and dex. The values were calculated *with* very few extremely metal-rich ($[Z/H] \gtrsim +0.7$) outliers, which require an extrapolation of the model metallicity scale. However, only five globular cluster in the elliptical sample and one in the spiral sample are affected.

of Figure 6.3 and the corresponding sub-panels. However, the sample statistics does not allow a clear statement whether the globular cluster systems of lenticular galaxies are more similar to those in either elliptical or spiral galaxies.

Globular clusters in elliptical galaxies reach the highest metallicities, compared to globular clusters in lenticular and spiral galaxies, with $\sim 25\%$ of the entire sub-sample of globular clusters in ellipticals having super-solar metallicities. We find that only $\lesssim 5\%$ of globular clusters in spirals have super-solar metallicities, while $\sim 18\%$ of are found super-solar in lenticular galaxies. We derive, by linear interpolation of the model grid, a mean metallicity $[Z/H] = -0.05 \pm 0.07$ for globular cluster systems in elliptical galaxies, -0.19 ± 0.11 for lenticular galaxies, and -0.40 ± 0.18 in for spiral galaxies. The systematic uncertainty in these values are entirely driven by the metallicity uncertainty in the super metal-rich regime. We estimate the systematic uncertainties to be of the order of ~ 0.2 dex. The lowest-metallicity limit appears to be very similar for all host types. No or very few globular clusters are found below $[Z/H] \approx -2.3$. While this limit is fairly well established for Local Group globular clusters systems, based on high-resolution spectroscopy results, similar lowest-metallicity limits for globular clusters in elliptical galaxies can be inferred from this analysis. These results are in line with previous results based on photometric colours (e.g. Ashman & Zepf 1998; Barmby et al. 2000; Puzia et al. 2002a). However, we note that the fraction of super-solar metallicity globular clusters in the Milky Way is subject to change since Bulge globular clusters with supposedly high metallicities are underrepresented in our spiral sample, as the central regions of the host galaxies were omitted during the observations to avoid complications during background subtraction.

Cumulative age and metallicity distributions in Figure 6.3 illustrate the above results. The outcome of a Kolmogorov-Smirnov (KS) test for the similarity of these distributions is summarised in Table 6.3 and underlines that the distributions of globular clusters in lenticular galaxies are a transition type between those of globular clusters in ellitpicals and spirals. We note that the KS-test suggests that there is
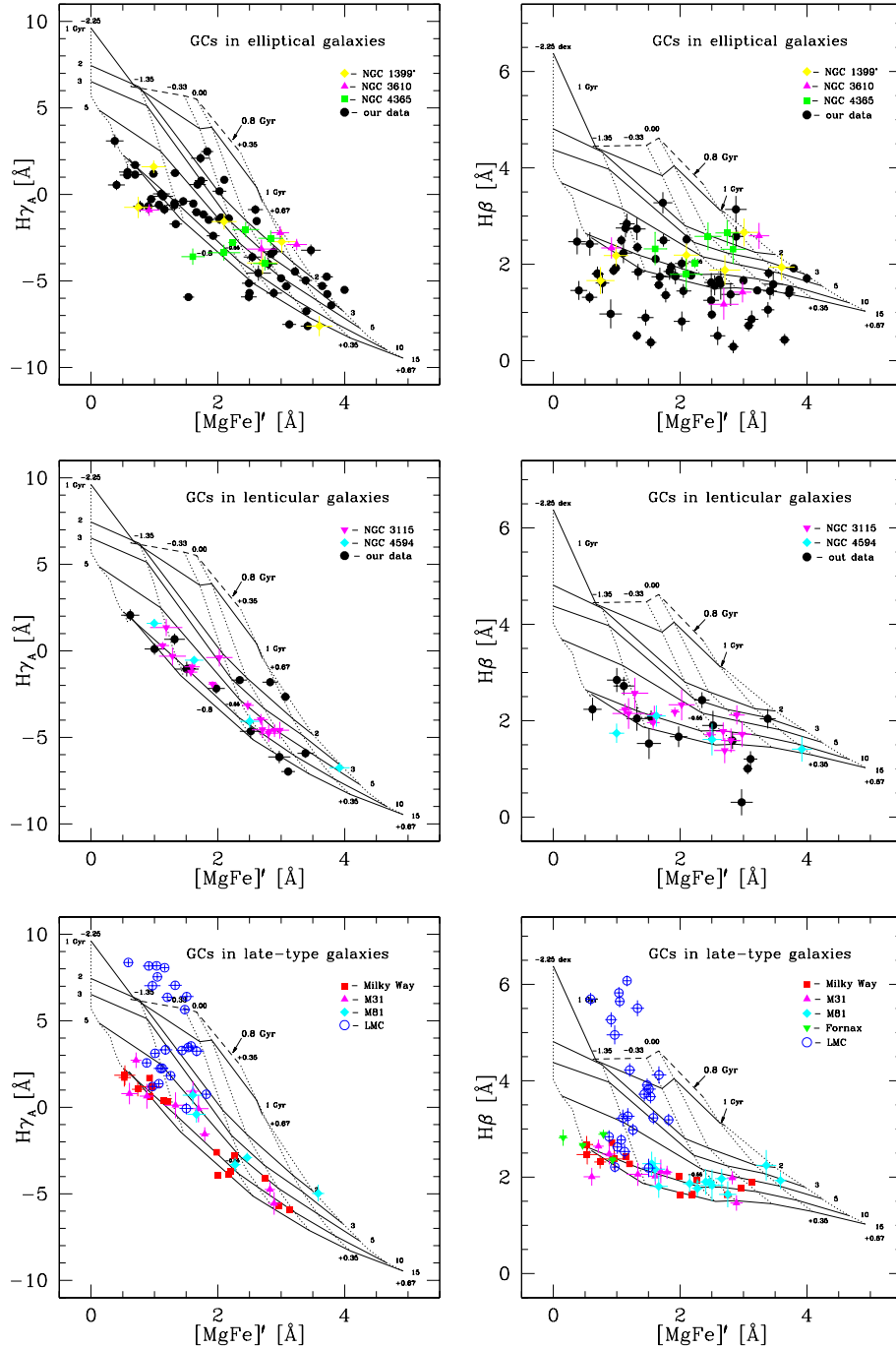
Figure 6.2: **Left panels**: Hγ_A vs. [MgFe]$'$ diagnostic plots for globular cluster systems in elliptical, lenticular, and late-type galaxies (from left to right). SSP models were taken from Chapter 3 for ages 0.8 to 15 Gyr (*solid lines*) and metallicities [Z/H] -2.25 to 0.67 dex (*dotted lines*). Our data are indicated by solid circles, while globular cluster in other galaxies taken from the literature are explained in each individual panel. The data sets are described in detail in Section 4.6. **Right panels**: Hβ vs. [MgFe]$'$ diagnostic plots for globular clusters as in the top row.
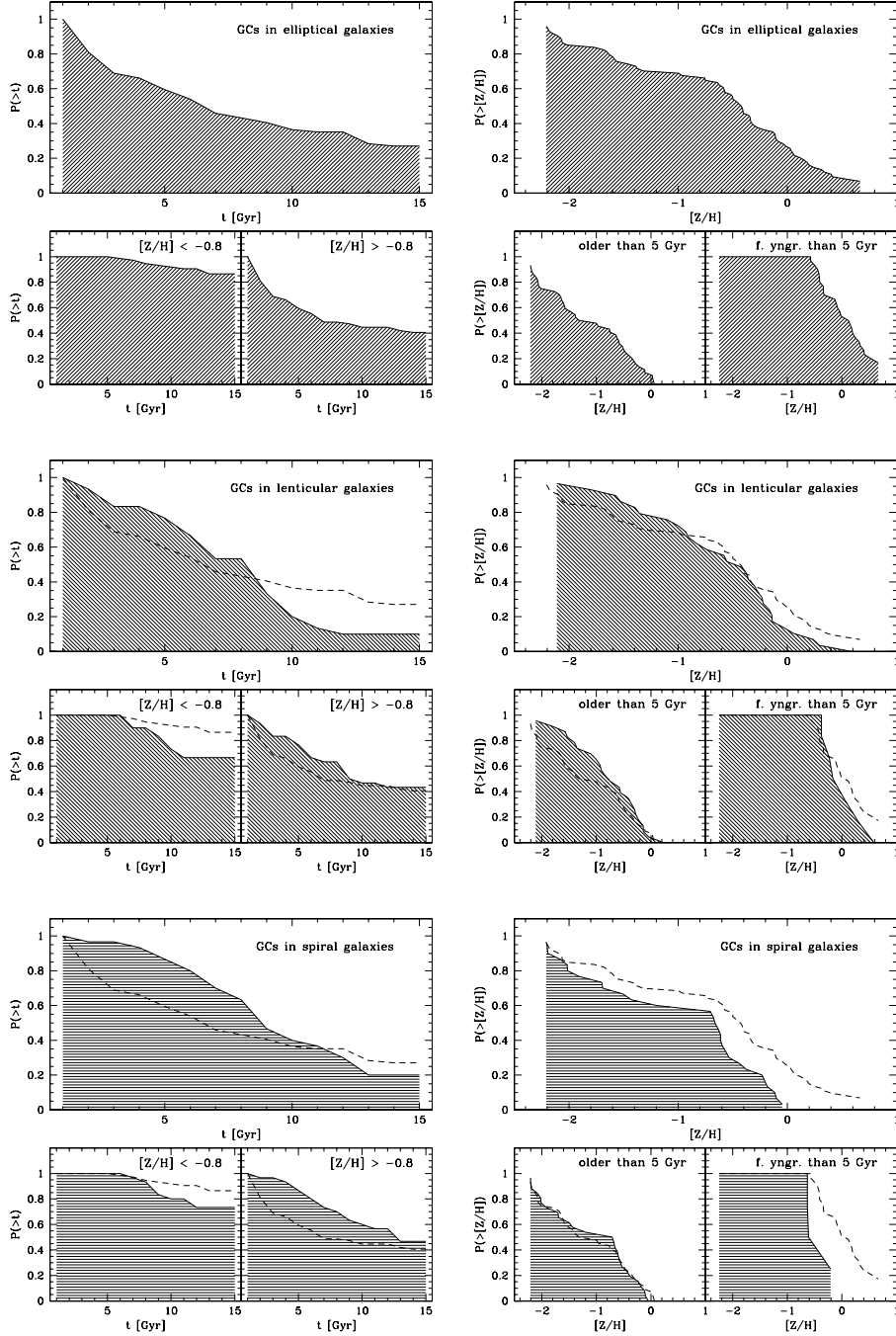
Figure 6.3: **Left panels**: Cumulative age distributions derived from the Hγ$_A$ vs. [MgFe]′ diagnostic diagram for globular clusters in elliptical, lenticular, and spiral galaxies (from left to right). Sub-panels show the corresponding distributions for metal-poor and metal-rich globular clusters. **Right panels**: Corresponding cumulative metallicity distributions derived from the Hγ$_A$ vs. [MgFe]′. Sub-panels show distributions for old and formally young globular clusters. To guide the eye, the cumulative distributions of the elliptical sample are reproduced as dashed lines in the panels for lenticular and spiral galaxies.

a significant difference between the metallicity distributions of globular clusters
in elliptical and spiral galaxies, which is driven by the formally young globular
clusters. On the other hand, we find similarities between old globular cluster systems
in ellipticals and spirals and between young globular cluster systems in ellipticals
and lenticulars. While the age distributions of metal-poor globular clusters are
fairly similar in spiral and lenticular galaxies, the situation is less conclusive for the
metal-rich sub-population. Here, the age distributions of globular cluster systems
in elliptical appears to be dominated by young globular clusters. The fraction
decreases for lenticular galaxies and is minimal in spiral hosts.

[Z/H]	all	$t > 5$ Gyr	$t < 5$ Gyr
E–S0	0.57	0.11	0.96
E–Sp	0.05	0.93	0.24
S0–Sp	0.20	0.33	0.40
Age	all	$[Z/H] < -0.8$	$[Z/H] > -0.8$
E–S0	0.66	0.72	0.96
E–Sp	0.94	0.84	0.87
S0–Sp	0.94	1.00	0.99

Table 6.3: Summary of Kolmogorov-Smirnov significance values for age/metallicity
distributions of globular cluster systems in different galaxy types. Highest prob-
abilities indicate that the samples are likely to be drawn from the same parent
distribution.

Furthermore, we note that the globular cluster system in the Large Magellanic
Cloud (LMC), which is not taken into account in the previous analysis, is signifi-
cantly different from the other globular cluster systems in this study. The compar-
ison with SSP models shows that the LMC globular cluster system is metal-poor
($-1.4 \lesssim [Z/H] \lesssim -0.3$) and relatively young ($\lesssim 8$ Gyr) with only few old objects
(see also Beasley et al. 2002).

6.2.2   [α/Fe] Ratios

The bottom row of Figure 6.4 shows [α/Fe] diagnostic plots for globular clusters
in elliptical, lenticular, and late-type galaxies. SSP model predictions are taken
from Thomas et al. (2003a) for the indices Mg_2 and $\langle Fe \rangle$. Since the iso-[α/Fe] are
degenerate in age, we use the age information derived from the $H\gamma_A$ vs. $[MgFe]'$
diagnostic diagram to pick the model for the correct age. We assign a 3 Gyr old
model to the formally young sub-sample and a 13 Gyr model to the old sub-sample.
We derive $\langle [\alpha/Fe] \rangle_E = 0.38 \pm 0.05$ for globular clusters in elliptical galaxies with
a dispersion of ~ 0.43 dex. For globular clusters in lenticular and spiral galaxies,
we find $\langle [\alpha/Fe] \rangle_{S0} = 0.00 \pm 0.09$ and $\langle [\alpha/Fe] \rangle_{Sp} = 0.03 \pm 0.05$, with correspond-
ing dispersions $\sigma_{S0} = 0.43$ dex and $\sigma_{Sp} = 0.32$ dex. This significant difference
$\Delta[\alpha/Fe] \approx 0.4$ between globular cluster systems in ellitpical galaxies, on the one
hand, and lenticular and spiral galaxies, on the other hand, increases by ~ 0.05 dex
if we use a 10 Gyr model without assigning formal ages to the sample. On average,
globular cluster systems in elliptical galaxies have significantly higher mean formal
[α/Fe] ratios than their counterparts in lenticular and spiral galaxies. However, the
dispersions in [α/Fe] ($\sim 0.43 - 0.45$ dex) are rather high for globular clusters in
elliptical and lenticular galaxies, compared with globular cluster systems of spiral
systems (~ 0.32). The fraction of globular clusters with formally *sub*-solar [α/Fe]
ratios is $\sim 50 \pm 10\%$ for the combined lenticular and spiral sub-sample, and drops
to $\sim 20 \pm 8\%$ for the elliptical sample.
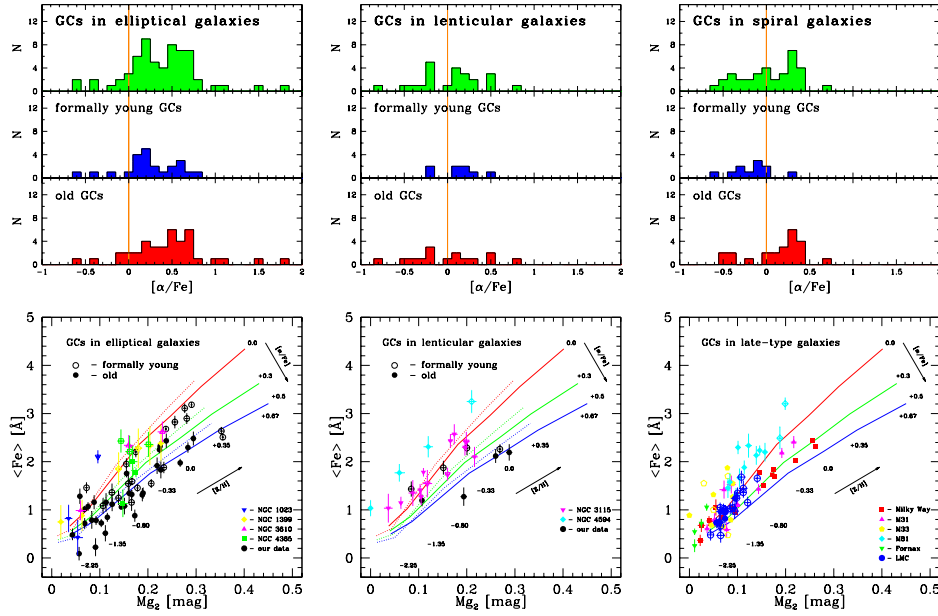
Figure 6.4: **Top row**: [α/Fe] histograms for globular clusters in elliptical, lenticular, and spiral galaxies. The histogram sub-panels are organised as follows: the top sub-panel show the distribution for the entire sample. The middle sub-panel is the distribution for globular clusters with ages formally younger than 5 Gyr. The bottom sub-panel show the [α/Fe] histogram for globular clusters older than 5 Gyr. The division in age was performed with the $H\gamma_A$ vs. [MgFe]' diagnostic diagram. As a guide to the eye, a vertical line indicates solar [α/Fe] ratios. For late-type galaxies only data for the Milky Way, M31, and M81 are considered, since only for these systems $H\gamma_A$ and [MgFe]' indices are available. **Bottom row**: [α/Fe] diagnostic plots, ⟨Fe⟩ vs. Mg_2. Circles indicate our data, other symbols are data from the literature explained in each panel. For elliptical and lenticular galaxies, open symbols denote globular clusters with ages formally younger than 5 Gyr, derived from the $H\gamma_A$ vs. [MgFe]' diagnostic plot. Filled symbol mark globular clusters with ages older than 5 Gyr. Model predictions are from Thomas et al. (2003a) for stellar populations with an age of 13 Gyr (*solid lines*) and 3 Gyr (*dotted lines*) parameterized for three different [α/Fe] ratios, 0.0, 0.3, and 0.5 dex.

[α/**Fe**]

sample	all mean	σ	< 5 Gyr mean	σ	> 5 Gyr mean	σ
E	$+0.38 \pm 0.05$	0.45	$+0.24 \pm 0.07$	0.34	$+0.46 \pm 0.07$	0.45
S0	$+0.00 \pm 0.09$	0.43	$+0.13 \pm 0.09$	0.25	-0.06 ± 0.12	0.49
Sp	$+0.03 \pm 0.05$	0.32	-0.16 ± 0.07	0.23	$+0.13 \pm 0.06$	0.31

Table 6.4: Mean [α/Fe] ratios for globular cluster systems in elliptical, lenticular, and spiral galaxies. The values were derived from the corresponding $\langle$Fe$\rangle$ vs. Mg$_2$ diagnostic diagram and are given in dex. Values are given for entire samples, and sub-samples parameterised by age. The division is made in the Hγ_A vs. [MgFe]$'$ diagnostic diagram at 5 Gyr into old and formally young globular clusters.

It is also interesting to split the samples into formally young and old globular cluster sub-samples and determine their mean [α/Fe] ratios. The distribution of [α/Fe] ratios for globular clusters formally younger than 5 Gyr and older than 5 Gyr is shown in Figure 6.4. Table 6.4 shows that old globular clusters in elliptical and spiral galaxies have significantly higher mean [α/Fe] ratios than their formally young counterparts. The sample statistics for the lenticular sample does not allow a clear statement and we remark that no significant difference in [α/Fe] between the formally young and old globular cluster sub-sample is found. Moreover, we find a significant difference in [α/Fe] between globular clusters in elliptical and spiral galaxies of ~ 0.4 dex for the formally young and ~ 0.2 dex for the old sub-population in the sense that globular clusters in ellipitcal galaxies have higher [α/Fe] ratios. This results indicates that the star-formation timescales for globular cluster in these two different galaxy types differ more for formally younger clusters.

We note *en passant* that indices of Galactic globular clusters at intermediate to $\sim$solar metallicities are consistent with conspicuously higher [α/Fe] ratios compared with clusters in the remaining Local Group spirals. High-resolution spectroscopy established that Milky Way globular clusters have mean [α/Fe] ratios around $+0.3$ dex (Barbuy et al. 1999; Cohen et al. 1999; Carretta et al. 2001; Coelho et al. 2001) and show no significant [α/Fe]–age relation in contrast to the field stellar population (e.g. Fuhrmann 1998). Such measurements for other Local Group globular cluster systems would deliver an invaluable comparison of ages *and* their chemical composition. Systematic offsets in these parameters between the different data sets might be responsible for the exposed role of Milky Way globular clusters in terms of its formal [α/Fe] ratios. On the other hand, at low Mg$_2$ and $\langle$Fe$\rangle$ all samples tend to overlap, indicating consistency at least at low metallicities.

6.3   Environmental Density

In this section we compare age/metallicity and [α/Fe] distributions of globular clusters in galaxies in the field and group/cluster environment. We consider only early-type galaxies (i.e. lenticulars and ellipticals) to avoid any biases connected to the correlation of galaxy morphology and environmental density. The division is performed using the Tully density parameter ρ_{xyz} (Tully 1988, see also Tab. 4.1). We define galaxies with $\rho_{xyz} < 0.5$ as field galaxies and those with $\rho_{xyz} > 0.5$ as

group/cluster galaxies[5]. With this division we have NGC 1023, **1380**[6], 1399, **3379**, 4365, and **5846** in the group/cluster sample and NGC **2434**, **3115**, **3585**, 3610, 4594, and **7192** in the field sample.

6.3.1   Ages and Metallicities

The overall age and metallicity structure of globular cluster systems is not changing significantly with different environmental densities of the host. This is shown in age/metallicity diagnostic plots in Figure 6.5 and Table 6.5 where mean ages and metallicities are summarised. A KS-test for both distributions yields virtually 100% likelihood that each sub-sample is drawn from the same parent distribution. Table 6.6 summarises all likelihood values.

Age in [Gyr]						
	all		[Z/H] < −0.8		[Z/H] > −0.8	
sample	mean	σ	mean	σ	mean	σ
field	7.7 ± 0.6	4.2	11.3 ± 0.6	2.5	5.7 ± 0.9	4.9
group/cluster	7.3 ± 0.6	4.6	12.0 ± 0.7	2.8	5.6 ± 0.8	5.1

[Z/H] in dex						
	all		$t < 5$ Gyr		$t > 5$ Gyr	
sample	mean	σ	mean	σ	mean	σ
field	-0.08 ± 0.09	0.85	$+0.25 \pm 0.03$	0.39	-0.56 ± 0.19	0.77
group/cluster	-0.09 ± 0.08	0.85	$+0.26 \pm 0.02$	0.43	-0.53 ± 0.16	0.77

Table 6.5: Mean ages and metallicities for globular cluster systems in field and group/cluster galaxies. The values were derived from the corresponding Hγ_A vs. [MgFe]$'$ diagnostic diagram and are given in Gyr and dex.

Age	all	[Z/H] < −0.8	[Z/H] > −0.8
field–gr./cl.	0.97	0.99	1.00

[Z/H]	all	$t > 5$ Gyr	$t < 5$ Gyr
field–gr./cl.	0.97	0.98	0.85

Table 6.6: Summary of Kolmogorov-Smirnov significance values for age and metallicity distributions of globular cluster systems in different environments.

The metallicity distributions for the entire set, as well as the distributions for the formally young and old sub-samples are without exception consistent with being drawn from the same parent distribution.

6.3.2   [α/Fe] Ratios

Table 6.7 summarises [α/Fe] for each sample and its sub-samples parameterised by age. There is a significant offset of $\Delta[\alpha/\text{Fe}] \approx 0.2$ dex between the field and

---

[5]A typical field galaxy, e.g. NGC 3115, has ρ_{xyz} values below ~ 0.1, while denser environments reach values ~ 0.5 in the Leo clouds, ~ 1.5 in the Fornax cluster, and $\sim 3-4$ in the Virgo cluster.
[6]Galaxies marked in boldface font are from our study.
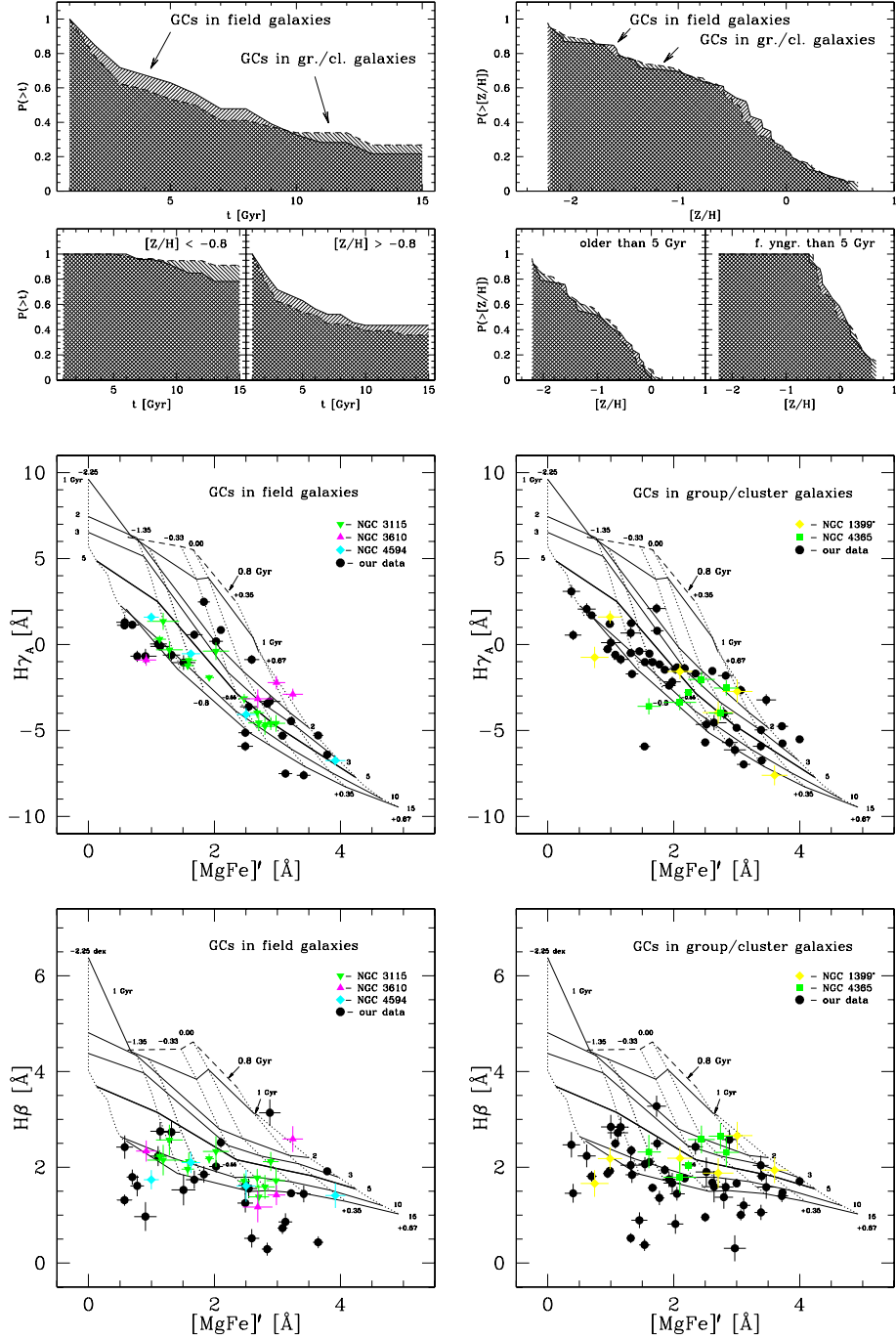
Figure 6.5: **Top row**: Cumulative age and metallicity distributions for globular cluster systems in field (solid line) and group/cluster environment (dashed line), derived from the Hγ$_A$ vs. [MgFe]′ diagnostic diagram. **Middle row**: Hγ$_A$ vs. [MgFe]′ diagnostic plots for globular cluster systems in early-type galaxies in the field (left panel) and group/cluster environment (right panel). SSP models as in Fig. 6.2. **Bottom row**: Corresponding Hβ vs. [MgFe]′ diagnostic plots.
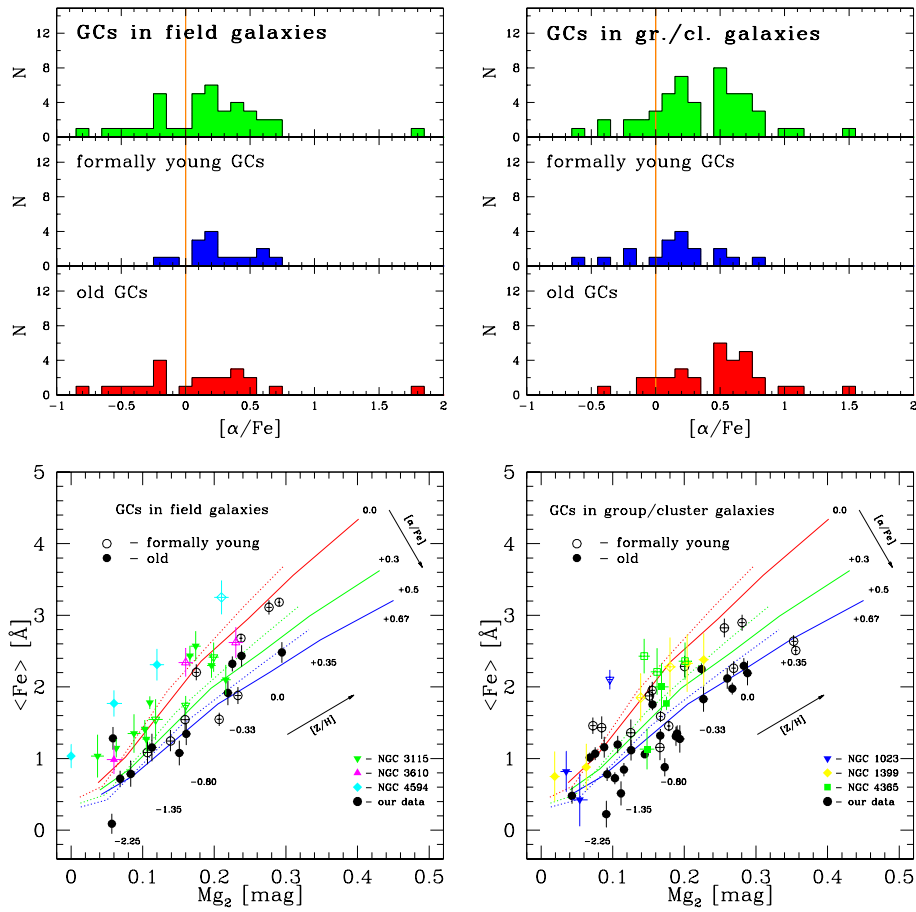
Figure 6.6: **Upper row**: [α/Fe] histograms for globular cluster systems in field and group/cluster environment for the entire sample and the corresponding sub-samples of formally young and old globular clusters with a division at 5 Gyr performed with the Hγ_A vs. [MgFe]′ diagnostic plot. As a guide to the eye, a vertical line indicates solar [α/Fe] ratios. **Lower row**: [α/Fe] diagnostic plots for globular cluster systems in elliptical galaxies in the field (left panel) and group/cluster environment (right panel). Model predictions as in Fig. 6.4.

group/cluster sample, where the group/cluster sample exhibits higher $[\alpha/\text{Fe}]$ ratios.
For the formally young globular cluster sub-samples, we find no difference in $[\alpha/\text{Fe}]$
between field and group/cluster environment. But we determine a significant offset
to higher $[\alpha/\text{Fe}]$ ratios for old globular clusters in group/cluster galaxies. These are
by ~ 0.4 dex more enhanced in α-elements than their counterparts in field galaxies.

	$[\alpha/\textbf{Fe}]$					
	all		< 5 Gyr		> 5 Gyr	
sample	mean	σ	mean	σ	mean	σ
field	$+0.14 \pm 0.08$	0.49	$+0.26 \pm 0.07$	0.26	$+0.07 \pm 0.12$	0.58
group/cluster	$+0.37 \pm 0.06$	0.41	$+0.21 \pm 0.08$	0.37	$+0.48 \pm 0.07$	0.39

Table 6.7: Mean $[\alpha/\text{Fe}]$ ratios for globular cluster systems in field and group/cluster
environment. The values were derived from the corresponding $\langle\text{Fe}\rangle$ vs. Mg_2 diagnostic diagram and are given in dex.

Our sample of globular cluster systems is clearly biased against less-massive
group/cluster galaxies (see Fig. 6.1). Hence, the above findings are subject to
change in case correlations such as mean age, mean metallicity, and mean $[\alpha/\text{Fe}]$
of the globular cluster system and galaxy mass exist. Concerning the prediction of
hierarchical merging (Kauffmann 1996) that more massive structures have younger
mean ages, such biases might in fact be at work and need to be checked with more
comprehensive globular cluster samples.

6.4 Absolute B-Magnitude

We divide the sample into two sub-samples of globular clusters in bright and faint
galaxies using the total B-band magnitude given in Tully (1988). Again we consider
only globular cluster systems in early-type galaxies to avoid a bias in M/L for
different galaxy morphologies. We divide the sample artificially at $M_B = -20.5$ to
guarantee similar numbers of globular clusters in both sub-samples. This division
assigns NGC 1399, **3585**, 4365, 4594, **5846**, and **7192** to the bright sub-sample
and NGC 1023, **1380**, **2434**, **3115**, **3379**, and 3610 to the faint sub-sample.

6.4.1 Ages and Metallicities

As in the sections before, we derive ages and metallicities from the $\text{H}\gamma_{\text{A}}$ vs. $[\text{MgFe}]'$
diagnostic diagram which is shown in the middle row of Figure 6.7. There we also
plot cumulative age and metallicity distributions for both sub-samples and parameterise them by metallicity and age (top panels). We find differing globular cluster
age and metallicity distribution between the bright and faint galaxy sample. There
is marginal evidence ($\sim 2\sigma$) that the mean age of globular cluster systems in bright
galaxies is ~ 1 Gyr younger than the mean age of globular clusters in faint galaxies.
The age spread in globular cluster systems of bright galaxies (~ 4.7 Gyr), however,
is clearly higher than the age dispersion for faint galaxies (~ 3.5 Gyr). The relevant
numbers are summarised in Table 6.8. We find a weak indication ($\sim 2\sigma$) that the
mean metallicity of globular cluster systems in bright galaxies, which reaches solar
values, is ~ 0.25 dex higher than in faint galaxies. This difference is driven by
the younger globular cluster sub-population. The cumulative age distributions in
Figure 6.7 for the metal-poor and metal-rich sub-samples illustrate another interesting difference. While faint galaxies appear to have a relatively younger metal-
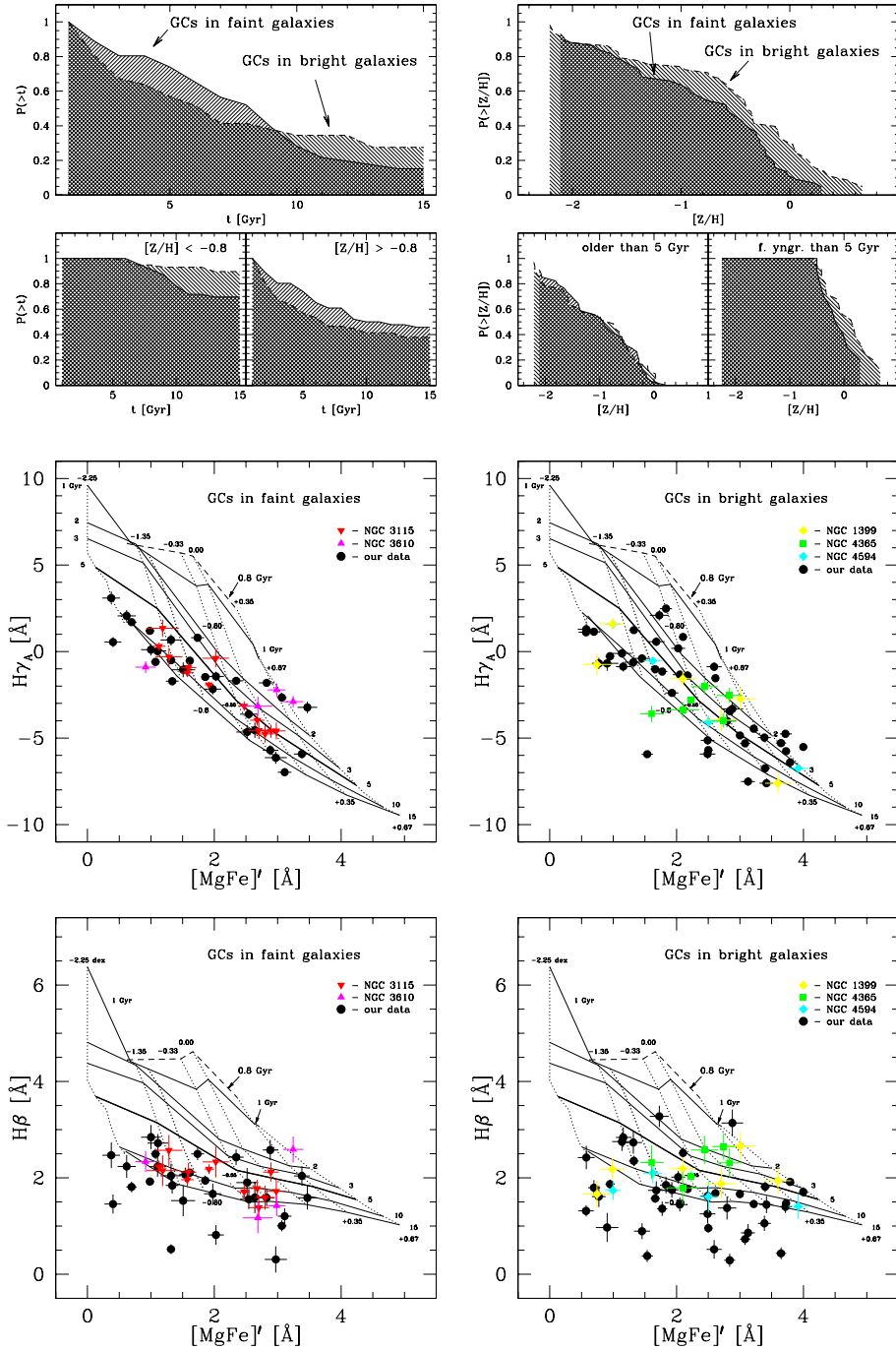
Figure 6.7: **Top row**: Cumulative age (left panel) and metallicity (right panel) distributions for globular clusters in faint ($M_B > -20.5$, solid lines) and bright ($M_B < -20.5$, dashed lines) early-type galaxies. **Middle row**: Hγ$_A$ vs. [MgFe]′ diagnostic plots for globular cluster systems in faint and bright early-type galaxies. SSP models as in Fig. 6.2. **Bottom row**: Hβ vs. [MgFe]′ diagnostic plots as in the top row.
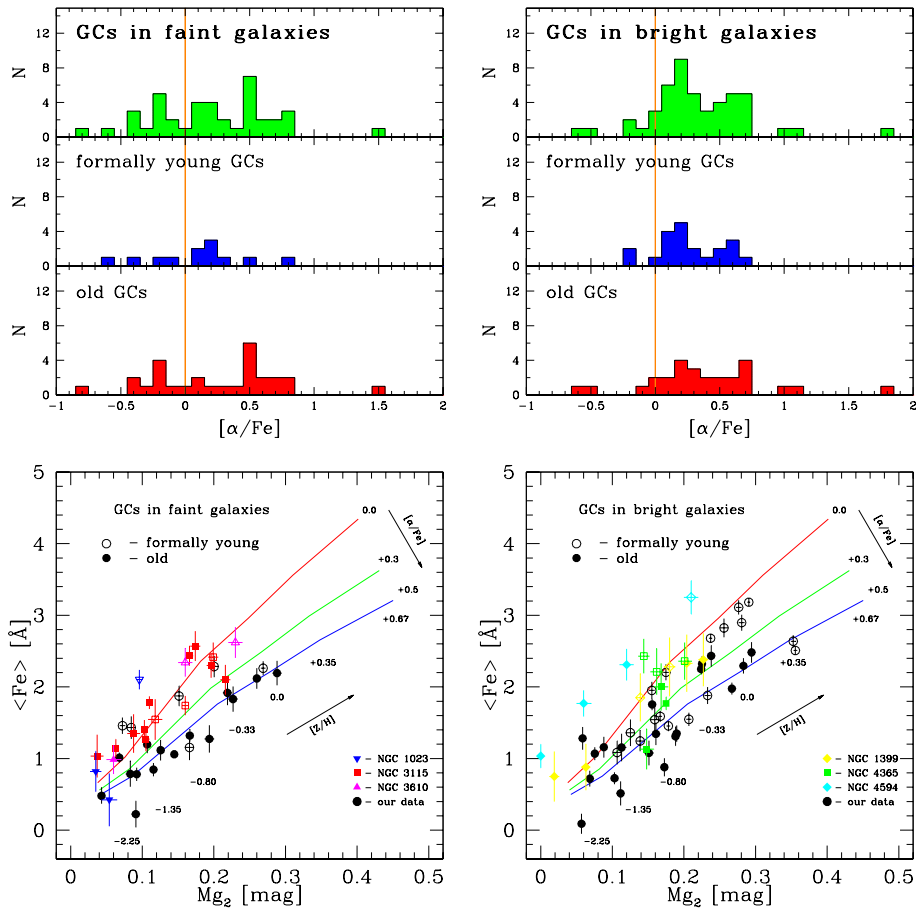
Figure 6.8: **Upper row**: [α/Fe] histograms for globular clusters in bright and faint galaxies with a division at $M_B = -20.5$. Histograms are shown for the entire sample and corresponding sub-samples for formally young and old globular clusters, with a division at 5 Gyr performed with the Hγ_A vs. [MgFe]$'$ diagnostic plot. As a guide to the eye, a vertical line indicates solar [α/Fe] ratios. **Lower row**: [α/Fe] diagnostic plots for globular cluster systems in faint (left panel) and bright galaxies (right panel). Model predictions as in Fig. 6.4.

poor globular cluster system, they host a relatively older metal-rich globular cluster sub-population, compared with globular cluster systems in bright galaxies. This is mirrored by the reduced KS-test likelihoods for the respective sub-samples (see Tab. 6.9).

Age in [Gyr]						
	all		[Z/H] < −0.8		[Z/H] > −0.8	
sample	mean	σ	mean	σ	mean	σ
faint	8.7 ± 0.5	3.5	10.2 ± 0.6	2.5	7.3 ± 0.9	4.2
bright	7.5 ± 0.6	4.7	11.7 ± 0.8	3.0	6.0 ± 0.8	5.2
[Z/H] in dex						
	all		$t < 5$ Gyr		$t > 5$ Gyr	
sample	mean	σ	mean	σ	mean	σ
faint	-0.25 ± 0.12	0.81	$+0.19 \pm 0.01$	0.43	-0.55 ± 0.17	0.76
bright	-0.02 ± 0.07	0.85	$+0.26 \pm 0.02$	0.40	-0.53 ± 0.18	0.78

Table 6.8: Mean ages and metallicities for globular cluster systems in faint ($M_B > -20.5$) and bright ($M_B < -20.5$) galaxies. The values were derived from the corresponding Hγ_A vs. [MgFe]′ diagnostic diagram and are given in Gyr and dex.

[Z/H]	all	$t > 5$ Gyr	$t < 5$ Gyr
faint–bright	0.07	0.95	0.65
Age	all	[Z/H] < −0.8	[Z/H] > −0.8
faint–bright	0.41	0.66	0.75

Table 6.9: Summary of Kolmogorov-Smirnov significance values for age and metallicity distributions of globular cluster systems in faint ($M_B > -20.5$) and bright ($M_B < -20.5$) galaxies.

The found systematics in the sub-samples might be influenced by the lack of magnitude sampling of group/cluster galaxies. While the group/cluster sub-sample spans only ~ 1 mag in M_B, the field sample covers ~ 2 mag. Thus, the results of this section are dominated by the sample of globular cluster systems in field galaxies and need to be confirmed with a larger sample.

6.4.2   [α/Fe] Ratios

In general, all our sub-samples of globular cluster systems in bright galaxies have higher [α/Fe] ratios. Although this is only a $\sim 1.5\sigma$ result, the systematic offset is present for all globular cluster ages. [α/Fe] ratios are summarised in Table 6.10.

6.5   Central Velocity Dispersion

Now we divide our sample into two sub-samples of globular clusters in high and low-σ galaxies. We perform the division at $\sigma = 220$ km/s using the central velocity dispersion compilation of McElroy (1995) to guarantee balanced sample sizes. This

| | [α/**Fe**] | | | | | |
| | all | | < 5 Gyr | | > 5 Gyr | |
sample	mean	σ	mean	σ	mean	σ
faint	$+0.21 \pm 0.07$	0.46	$+0.10 \pm 0.11$	0.39	$+0.26 \pm 0.09$	0.49
bright	$+0.31 \pm 0.06$	0.45	$+0.27 \pm 0.06$	0.26	$+0.34 \pm 0.10$	0.45

Table 6.10: Mean [α/Fe] ratios for globular cluster systems in bright ($M_B < -20.5$) and faint ($M_B > -20.5$) galaxies. The values were derived from the corresponding $\langle$Fe$\rangle$ vs. Mg$_2$ diagnostic diagram and are given in dex.

cut corresponds closely to what is expected ($\sigma \approx 200$ km/s) from the Faber-Jackson relation using the M_B-cut we performed in the previous section. Again we consider only globular cluster systems in early-type galaxies to avoid biases from potential σ galaxy morphology relations. This division leaves NGC **1380**, 1399, **3115**, 4365, 4594, and **5846** in the high-σ sample and NGC 1023, **2434**, **3379**, **3585**, 3610, and **7192** in the low-σ sub-sample.

6.5.1 Ages and Metallicities

We find that high-σ galaxies host globular cluster systems with slightly younger mean ages compared to low-σ galaxies (see Tab. 6.11), as expected from the division by M_B and the Faber-Jackson relation. This marginally significant ($\sim 1.5\sigma$) age difference is driven by the metal-poor globular cluster system which exhibits a significant ($\sim 3\sigma$) age offset of ~ 2 Gyr between globular clusters in low-σ and high-σ galaxies, where the latter host younger clusters. We find no difference in age for the metal-rich sub-samples. The cumulative age distributions in Figure 6.9 show that low-σ galaxies host relatively more old and metal-poor globular clusters. A KS-test of these distributions underlines this result and yields a significantly lower likelihood that the metallicity distributions of older cluster were drawn from the same parent distribution (see Tab. 6.12). However, this result needs to be confirmed with higher number statistics.

| **Age in [Gyr]** | | | | | | |
| | all | | [Z/H] < -0.8 | | [Z/H] > -0.8 | |
sample	mean	σ	mean	σ	mean	σ
low-σ	8.2 ± 0.7	4.5	12.1 ± 0.5	2.2	5.8 ± 1.1	5.5
high-σ	7.3 ± 0.5	4.1	9.9 ± 0.7	2.9	6.2 ± 0.7	4.6

| **[Z/H] in dex** | | | | | | |
| | all | | $t < 5$ Gyr | | $t > 5$ Gyr | |
sample	mean	σ	mean	σ	mean	σ
low-σ	-0.08 ± 0.12	0.98	$+0.27 \pm 0.02$	0.44	-0.69 ± 0.26	0.83
high-σ	-0.08 ± 0.07	0.73	$+0.25 \pm 0.02$	0.39	-0.46 ± 0.12	0.66

Table 6.11: Mean ages and metallicities for globular cluster systems in high and low-σ (division at $\sigma = 220$ km/s) galaxies. The values were derived from the corresponding H$\gamma_{\rm A}$ vs. [MgFe]$'$ diagnostic diagram and are given in Gyr and dex.
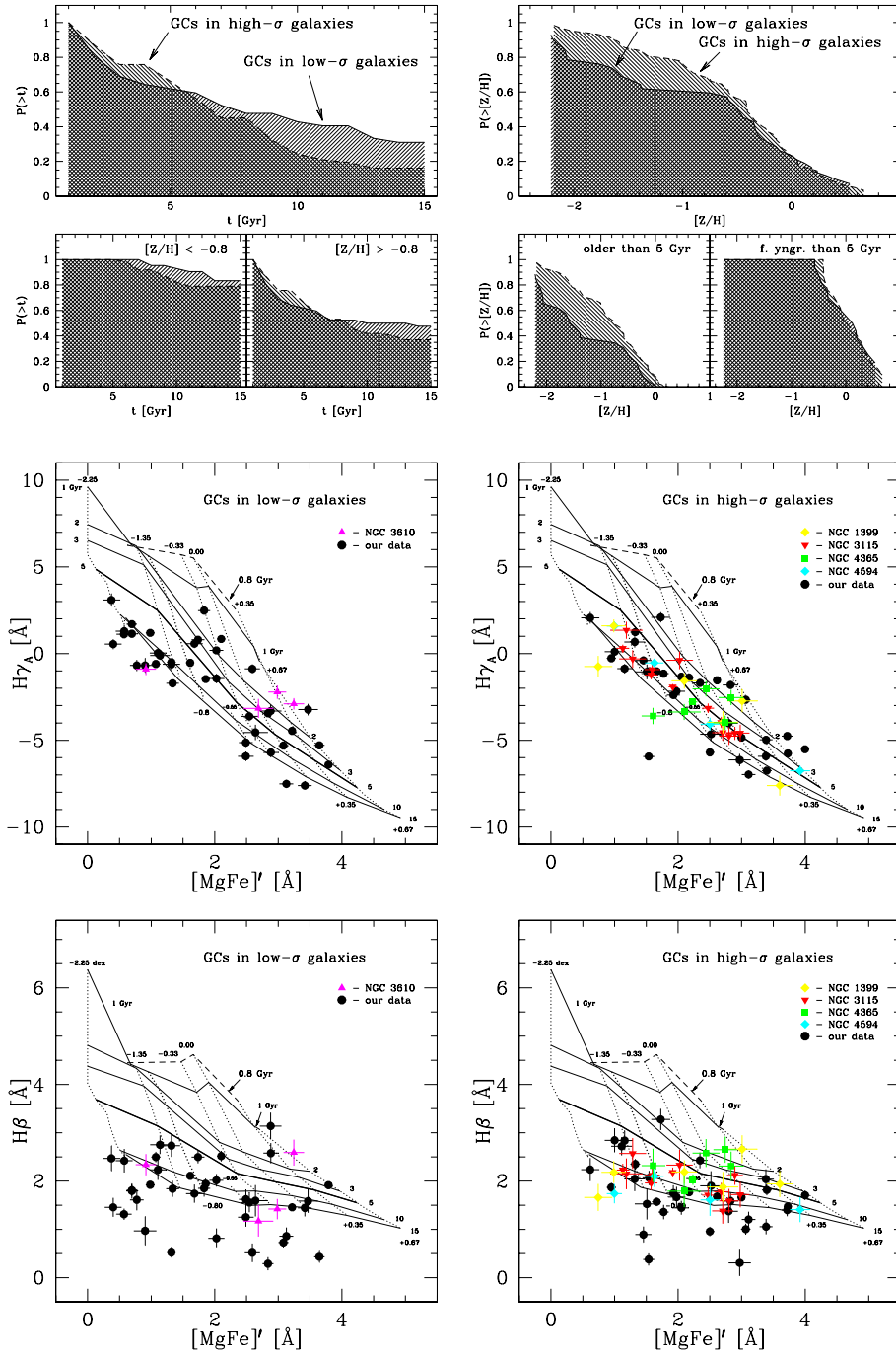
Figure 6.9: **Top row**: Cumulative age and metallicity distributions for globular clusters in galaxies with different central velocity dispersions with a division at σ = 220 km/s. **Middle row**: Hγ_A vs. [MgFe]′ diagnostic plots for globular cluster systems in low-σ (left panel) and high-σ early-type galaxies (right panel). SSP models as in Fig. 6.2. **Bottom row**: Hβ vs. [MgFe]′ diagnostic plots as in the middle row.
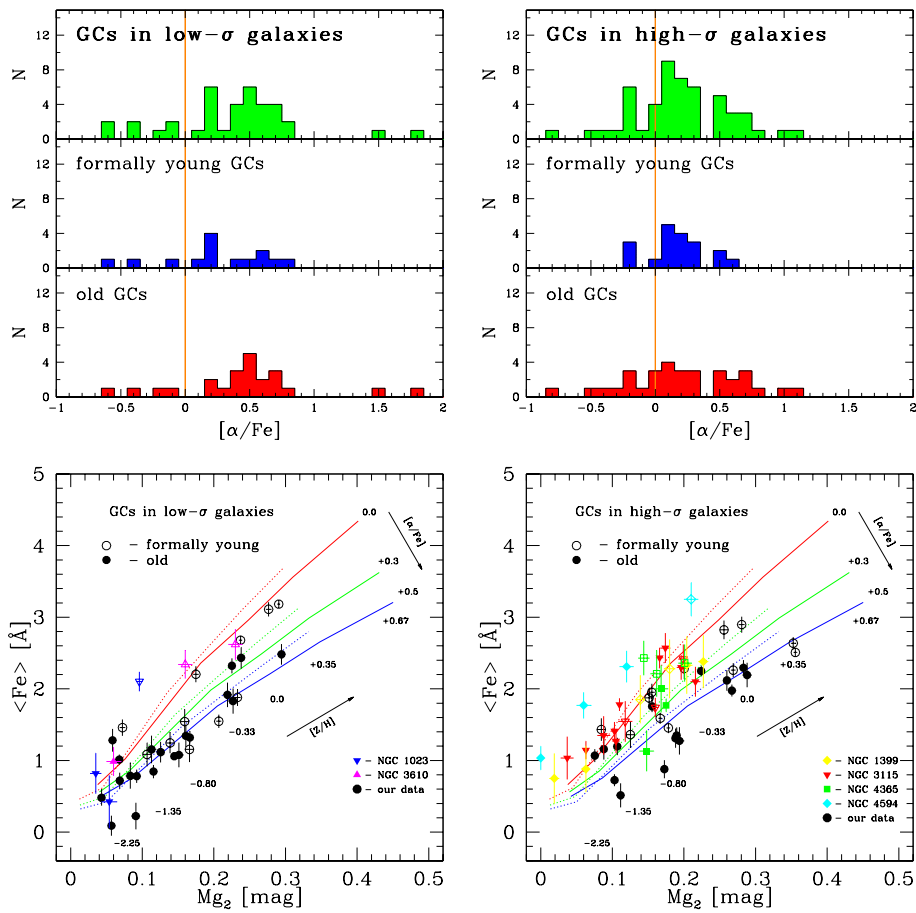
Figure 6.10: **Upper row**: [α/Fe] histograms for globular clusters in bright and faint galaxies with a division at $\sigma = 220$ km/s. Histograms are shown for the entire sample as well as corresponding sub-samples for formally young and old globular clusters. As a guide to the eye, a vertical line indicates solar [α/Fe] ratios. **Lower row**: [α/Fe] diagnostic plots for globular cluster systems in low-σ (left panel) and high-σ galaxies (right panel). Model predictions as in Fig. 6.4.

[**Z/H**]	all	$t > 5$ Gyr	$t < 5$ Gyr
low-σ–high-σ	0.16	0.02	0.87

Age	all	[Z/H] < -0.8	[Z/H] > -0.8
low-σ–high-σ	0.19	0.99	0.96

Table 6.12: Summary of Kolmogorov-Smirnov significance values for age and metallicity distributions of globular cluster systems in galaxies with different central velocity dispersions σ. The division was made at $\sigma = 220$ km/s.

6.5.2   [α/Fe] Ratios

[α/Fe] ratios of globular clusters in low-σ galaxies are on average ~ 0.2 dex higher ($\sim 2.5\sigma$) than of globular clusters in high-σ galaxies, which is mainly driven by the [α/Fe] difference in the old globular cluster sub-population. Sub-dividing the sample into formally young and old globular clusters shows rather similar [α/Fe] ratios for formally young globular clusters in both sub-samples, but a significant ($\sim 2.5\sigma$) offset of ~ 0.27 dex for the old sub-sample in the sense that low-σ galaxies host high-[α/Fe] globular clusters. We note that the dispersion, although only marginally, is higher for all low-σ sub-samples.

	[α/**Fe**]					
	all		< 5 Gyr		> 5 Gyr	
sample	mean	σ	mean	σ	mean	σ
low-σ	$+0.38 \pm 0.08$	0.49	$+0.24 \pm 0.11$	0.40	$+0.46 \pm 0.11$	0.53
high-σ	$+0.18 \pm 0.06$	0.41	$+0.17 \pm 0.05$	0.24	$+0.19 \pm 0.08$	0.49

Table 6.13: Mean [α/Fe] ratios for globular cluster systems in high and low-σ galaxies. The division is performed at $\sigma = 220$ km/s. The values were derived from the corresponding $\langle$Fe$\rangle$ vs. Mg$_2$ diagnostic diagram and are given in dex.

As mentioned in Section 6.3, we are biased towards massive group/cluster galaxies and lack their less-massive group/cluster companions. Moreover, our sample of field galaxies spans a wider range in σ than the group/cluster sample. Therefore, the above results are dominated by globular cluster systems of field galaxies. Better sampling of globular cluster system in low-σ galaxies in a group/cluster environment is needed to remedy this problem.

6.6   Discussion

Globular Cluster Systems in Galaxies of different Morphological Type

We find a wide variety of distributions in age/metallicity and [α/Fe] diagnostic diagrams for globular clusters in elliptical, lenticular, and spiral galaxies. The change in these distributions appears to follow a smooth transition from globular cluster systems in elliptical over lenticular to spiral galaxies. In particular, the formal age dispersion in globular cluster systems decreases from ~ 4.4 Gyr in elliptical over ~ 3.7 Gyr in lenticular to ~ 3.5 Gyr in spiral hosts. The mean ages of globular clusters in elliptical and lenticular galaxies are similar (7.7 ± 0.7 Gyr), while globular cluster systems in Local Group spiral galaxies are significantly older (9.3 ± 0.8

Gyr). This age structure is apparently driven by the increasing impact of a younger metal-rich globular cluster sub-population in early-type galaxies. However, these findings could be partly influenced by a systematic difference in HB morphology at high metallicities and/or of a systematic difference in abundance ratio patterns (see the discussion in Appendix F). While the minimum metallicity of globular clusters appears to be universal for all systems at $[Z/H] \approx -2.3$, the maximum metallicity increases from about solar in spiral galaxies to values reaching $\sim +0.5$ dex in elliptical galaxies. The $[\alpha/Fe]$ distributions of globular clusters in lenticulars are rather similar to globular cluster systems in spiral galaxies with about solar $[\alpha/Fe]$, implying similar formation timescales and allowing for a significant contribution of SN Ia to the chemical enrichment in these galaxies. We find clearly super-solar $[\alpha/Fe]$ ratios for globular clusters in elliptical galaxies, consistent with star-formation timescales shorter than ~ 1 Gyr. In general, it seems that with respect to elliptical galaxies, lenticular galaxies have significantly prolonged star-formation histories on an energetic level comparable to those of spiral galaxies. During their lifetimes lenticular galaxies manage to form globular clusters to higher mean metallicities than spirals, but still not reaching the extreme enrichment of elliptical galaxies.

Similar evidence is found from studies of the diffuse galaxy light (Gunn & Gott 1972; Hogg et al. 1993; Bender & Paquet 1995; Poggianti et al. 2001; Mathieu et al. 2002), which suggest that at least a fraction of lenticular galaxies are gas-deprived descendants of spirals which were formed by tidal and/or ram pressure stripping. Other studies indicate more complex formation histories of lenticular galaxies (van den Bergh 1994; Neistein et al. 1999). However, the stripping scenario poses the question how the outer globular cluster systems of such galaxies could have survived the tidal stress which goes in line with stripping processes.

An interesting implication for the formation of elliptical galaxies can be drawn from the formal $[\alpha/Fe]$ ratios of globular clusters in ellipticals and spirals. If elliptical galaxies are formed from successive mergers of spiral systems (as it is suggested in the hierarchical merging picture), globular clusters which are found in spirals should be also present in the merger remnants, unless the transformation of spirals into ellipticals occurred early, before the majority of globular clusters in today's spirals was formed. Our data indicate that the average globular cluster in a spiral galaxy has solar $[\alpha/Fe]$ ratios which is significantly lower than the formal ~ 0.4 dex for an average globular clusters in elliptical galaxies. Clearly, subsequent merging of gas-rich spirals would rather imply a decrease in the mean $[\alpha/Fe]$ as older stellar populations were given enough time to enrich the ISM with SN Ia ejecta. This is in contrast with our findings and excludes the formation of elliptical galaxies from today's spirals. Our data are rather consistent with the scenario in which the gaseous progenitors of today's spiral galaxies and their globular cluster systems would merge rather early ($z \sim 3 - 4$) to form the globular cluster systems of today's elliptical galaxies, *before* the onset of the enrichment of their ISM through SNe Ia.

Globular Cluster Systems in different Environments

The hierarchical merging picture predicts that the stellar populations in field early-type galaxies are a few Gyr younger than in early-type galaxies in a group/cluster environment (e.g. Kauffmann 1996). Contrary to these predictions, our data show no significant age difference between globular cluster systems in galaxies in a field environment and those located in groups or clusters. We also find no significant offset in mean metallicity.

The only interesting, although weak, indication for a difference is found in young globular cluster systems between field and group/cluster galaxies. Curiously, we find a significant difference in $[\alpha/Fe]$, with globular cluster in field galaxies having around solar ratios, while those in group/cluster galaxies are highly enhanced in α-

elements ([α/Fe] ≈ 0.5). Studies of the diffuse light of early-type galaxies in field and cluster environments find the expected age (and a metallicity) difference together with a relatively constant super-solar mean [α/Fe] (e.g. Kuntschner et al. 2002a). It is therefore possible that our results are only biased by low number statistics and might change if better sampling of both field and group/cluster environment is available.

Globular Cluster Systems in Galaxies with different absolute B-Magnitude

The restframe flux in the B band traces the total galaxy mass and is also sensitive to the presence of young stellar populations. Since the total galaxy mass in our sample changes only within a factor of ~ 10 (see Chapter 4, Sect. 4.4.3) but the absolute B band luminosity varies within a factor of ~ 40, galaxies with bright M_B can be expected, at least to the first order, to host relatively young stellar populations. However, we find that globular cluster systems in galaxies with M_B magnitudes brighter than -20.5 mag are on average only slightly younger by ~ 1 Gyr ($\sim 1.5\sigma$) than globular cluster systems in fainter hosts. This offset appears to be driven by the metal-poor globular cluster system which shows significantly older ages in bright hosts (but see also the caveats in App. F). The behaviour is mirrored in a substantial difference of age structure at low and high metallicities. Bright early-type galaxies host older metal-poor and younger metal-rich globular cluster sub-populations. The latter is a pure consequence of more recent star formation and is expected in the hierarchical scenario where metal-rich globular clusters are formed continuously until the recent past. In turn, this implies that only the metal-rich globular cluster sub-population is augmented in later star formation events. Interestingly, the [α/Fe] for the entire sample and all sub-samples does not change significantly from bright to faint galaxies, but is slightly ($\sim 1.5\sigma$) offset by ~ 0.1 dex to higher values ~ 0.3 dex in bright galaxies. If true this would indicate more vigorous star formation in brighter galaxies. However, in a simple chemical enrichment model younger stellar populations are on average expected to be less enhanced in α-elements. This trend can only be abrogated if local star formation is short and intense enough to significantly pollute the ambient gas with type II supernova ejecta, so that the earlier imprinted abundance pattern are outweighed.

Globular Cluster Systems in Galaxies with different Central Velocity Dispersion

Under the assumption of a relaxed system, the central velocity dispersion traces the central mass of the host galaxy. In the hierarchical galaxy formation scenario, massive structures are predicted to form later than less massive ones. Therefore, more massive galaxies are expected to host younger globular cluster systems.

Our data reveals only tentative evidence ($\sim 2\sigma$) for a younger mean age of globular cluster systems in massive (high-σ) galaxies, which appears to be driven by the ~ 2 Gyr ($\sim 3\sigma$) offset in the metal-poor globular cluster sub-population. At face value, this curious offset would imply that more massive galaxies start to form their metal-poor globular clusters somewhat later than less massive hosts. However, as our spectroscopic age determination is somewhat ambiguous in the metal-poor regime we do not give too much weight to this difference. We find no variation in mean metallicity for globular cluster systems in hosts of different galaxy mass. However, low-mass galaxies tend to host globular clusters with ~ 0.2 dex higher [α/Fe] ratios than their couterparts in massive galaxies. This result is driven by the metal-rich globular cluster sub-population and is again of limited statistical significance ($\sim 2.5\sigma$). If future data verifies such a trend, this would imply that the relatively recent star formation events in massive galaxies are more quiescent

compared with those in less-massive galaxies.

Chapter 7

Conclusions

We have conducted a comprehensive study of ages, metallicities, and $[\alpha/\text{Fe}]$ ratios of extragalactic globular clusters in elliptical, lenticular, and spiral galaxies based on the Lick index system. As a first step, Lick indices were measured for metal-rich Galactic globular clusters which most closely resemble the high-metallicity stellar populations in early-type galaxies. In the following, these Milky Way globular clusters serve as fundamental ingredients of an empirical calibration of synthetic Lick indices (e.g. Mg_2, $\langle\text{Fe}\rangle$, all Balmer indices, etc.) of Simple Stellar Population models that extend up to solar metallicity, for the first time. The model predictions are used to derive ages, metallicities, and $[\alpha/\text{Fe}]$ of extragalactic globular clusters.

As a by-product of the first part of this study, we obtained spectra of the integrated light of the stellar population in the Galactic bulge. Both metal-rich globular clusters and the bulge are similar in most of the indices, except for the CN index. We find a significant enhancement in the $CN/\langle\text{Fe}\rangle$ index ratio in metal-rich globular clusters compared with the Galactic bulge. Index ratios such as $Mgb/\langle\text{Fe}\rangle$, $Mg_2/\langle\text{Fe}\rangle$, $Ca4227/\langle\text{Fe}\rangle$, and $TiO/\langle\text{Fe}\rangle$, are comparable in both stellar population indicating similar enhancements in individual elements which are traced by the indices.

Stellar Populations in the Milky Way and Elliptical Galaxies

It is shown that the spectra of both the globular clusters and the Galactic bulge follow the same correlation between magnesium and iron indices that extends to elliptical galaxies, showing weaker iron indices at given magnesium indices with respect to the predictions of models that assume solar-scaled abundances. This similarity provides robust empirical evidence for enhanced $[\alpha/\text{Fe}]$ ratios in the stellar populations of elliptical galaxies, since the globular clusters are independently known to have enhanced $[\alpha/\text{Fe}]$ ratios from spectroscopy of individual stars. We check the uniqueness of this α-overabundance solution by exploring the whole range of model ingredients and parameters, i.e. fitting functions, stellar tracks, and the initial mass function. We argue that the *standard* models, meant for solar abundance ratios, succeed in reproducing the Mg–Fe correlation at low metallicities ($[\text{Z/H}] \lesssim -0.7$), because the stellar templates used in the synthesis are Galactic halo stars that are α-enhanced. The same models, however, fail to predict the observed Mg–Fe pattern at higher metallicities ($[\text{Z/H}] \gtrsim -0.7$), that is for bulge clusters and ellipticals alike, because the high-metallicity templates are disk stars which are not α-enhanced. We show that the new set of SSP models which incorporates the dependence on the $[\alpha/\text{Fe}]$ ratio (Thomas, Maraston & Bender 2002) is able to reproduce the Mg and Fe indices of Galactic globular clusters at all metallicities, with an α-enhancement $[\alpha/\text{Fe}] = +0.3$, in agreement with high-resolution

spectroscopic determinations.

Extragalactic Globular Cluster Systems

As the next step, high-quality spectra were obtained with the FORS2 instrument at ESO's Very Large Telescope of extragalactic globular clusters in seven early-type galaxies. These are NGC 1380, 2434, 3115, 3379, 3585, 5846, and 7192 which span different morphological types (E–S0) and are located in field and group/cluster environments. Globular cluster candidates were selected from deep B, V, R, I, K FORS2/ISAAC photometry with $80 - 100\%$ success rate inside one effective radius. Using combined optical/near-infrared colour-colour diagrams we present a robust method to efficiently reduce fore-/background contamination of globular cluster candidate selection down to $\lesssim 10\%$.

We find clear signs for bi-modality in the globular cluster colour distributions of NGC 1380, 3115, and 3585, while the colour distributions of globular clusters in NGC 2434, 3379, 5846, and 7192 are consistent with a broad single-peak distribution. For the analysed globular cluster systems the slopes of projected radial surface density profiles, of the form $\Sigma(R) \sim R^{-\Gamma}$, vary between ~ 0.8 and 2.6. Blue and red globular cluster sub-populations show similar slopes in the clearly bi-modal systems. For galaxies with single-peak globular cluster colour distributions, there is a hint that the blue cluster system seems to have a more extended radial distribution than the red one. Using globular clusters as a tracer population we determine total dynamical masses of host galaxies out to large radii ($\sim 1.6 - 4.8\, R_{\rm eff}$). For our sample we find masses in the range $\sim 8.8 \cdot 10^{10} M_\odot$ up to $\sim 1.2 \cdot 10^{12} M_\odot$.

Ages and Metallicities

In the light of calibration and measurement uncertainties, age-metallicity degeneracy, and the relative dynamic range of Lick indices, we find that $H\gamma_A$ is the most reliable age indicator among Lick Balmer-line indices. $[MgFe]'$ is used as the most reliable spectroscopic metallicity indicator which is least affected by $[\alpha/Fe]$ variations. Hence, we find that the most reliable age/metallicity diagnostic diagram which can be constructed from Lick indices is $H\gamma_A$ vs. $[MgFe]'$. From a comparison with our previously calibrated SSP models, we derive that $\sim 34\%$ of globular clusters in early-type galaxies have formal ages $\lesssim 5$ Gyr. Furthermore, we find an universal low-metallicity boundary for globular clusters in all studied galaxies at a formal $[Z/H] \approx -2.3$, while the highest sampled formal metallicities are $\sim 2 - 3\, Z_\odot$ which are derived for globular cluster systems in elliptical galaxies. Globular clusters with metallicities $[Z/H] \gtrsim -0.8$ dex are on average younger with a mean age of 6.3 ± 0.8 Gyr, compared with their metal-poor brethren which show a mean age of 11.3 ± 0.5 Gyr. The metal-rich globular cluster system shows on average a larger age spread of $\sigma \sim 5.4$ Gyr than the metal-poor sub-population, for which we derive $\sigma \sim 2.7$ Gyr. These results imply that metal-rich globular clusters can only be the ones which formed in recent star formation events. However, since we find also metal-rich old globular clusters, the first star-formation epochs which lead to the assembly of the analysed galaxies must have produced enough metals to enrich the ambient medium up to around solar metallicities.

$[\alpha/Fe]$ Ratios

$[\alpha/Fe]$ diagnostic plots show that globular cluster systems in early-type galaxies have formal mean $[\alpha/Fe] = 0.44 \pm 0.05$ with ~ 0.4 dex dispersion. In combination with the former point on formation epochs, this indicates formation timescales considerably shorter than ~ 1 Gyr. In other words, the progenitor clouds out of

which these globular clusters formed, could not have been significantly polluted by type Ia supernovae. Since globular clusters are not massive enough to support significant self-enrichment, the found super-solar $[\alpha/\text{Fe}]$ ratios reflect the *large-scale* chemical conditions during their formation epochs. In addition, we find tentative evidence for an $[\alpha/\text{Fe}]$–age relation for globular clusters in early-type galaxies with the numerical value 0.02 ± 0.008 dex/Gyr. The median $[\alpha/\text{Fe}]$ of globular clusters formally younger than 5 Gyr is 0.26 ± 0.06 dex, while for globular clusters older than 5 Gyr we derive 0.54 ± 0.07 dex. At face value, such a relation is the consequence of the *global* chemical evolution during which younger objects are formed from material significantly enriched by type Ia supernovae.

Extragalactic Globular Clusters as a Function of Host Galaxy Properties

We augment our sample with a compilation of currently available high-quality Lick index measurements for globular clusters in elliptical, lenticular, and late-type galaxies. Among the studied globular cluster systems the mean age was found maximal with $t = 9.3 \pm 0.8$ Gyr and a minimal spread of $\sigma = 3.5$ Gyr in spiral galaxies. Globular cluster systems in early-type galaxies show consistently smaller mean ages 7.7 ± 0.7 Gyr in lenticular and 7.7 ± 0.5 Gyr in elliptical galaxies, with constantly increasing age dispersions $\sigma = 3.7$ and 4.4 Gyr, repsectively. These numbers are basically driven by the metal-rich globular cluster sub-population with metallicities $[\text{Z/H}] \gtrsim -0.8$. The fraction of formally young clusters with ages $t < 5$ Gyr is $13 \pm 7\%$ in the Local Group spiral sample, and increases to $20 \pm 6\%$ for globular cluster systems in lenticular galaxies and culminates with $42 \pm 8\%$ in elliptical galaxies. It cannot be clarified with final confidence whether the formally younger age of globular cluster systems in early-type galaxies is a result of a more recent formation or an unexpected warm horizontal branch morphology at high metallicities. If the younger ages are real, these fractions have to be taken as upper limits, since our data only probe the bright end of the globular cluster luminosity function where relatively young globular clusters are expected to reside. In general, of the brightest $\sim 10\%$ of globular cluster systems in early-type galaxies which we sample, less than $\sim 34\%$ must have formed at redshifts $z_f \lesssim 1$. If the ratio of young to old globular clusters decreases towards fainter cluster luminosity this found fractions are biased towards bright globular cluster magnitudes. As an numerical example, if one assumes that the fainter globular cluster system is entirely old, then the fraction of young globular clusters shrinks to a few percent in early-type galaxies.

Just as for the globular cluster systems in early-type galaxies, the augmented data exhibit an universal low-metallicity boundary for globular clusters in all galaxy types, at a formal $[\text{Z/H}] \approx -2.3$. This suggests a universal process and/or epoch in which the very first globular cluster generation is formed. The highest globular cluster metallicities in spiral galaxies are roughly solar and increase to $\sim 2 - 3\ Z_\odot$ for globular clusters in early-type systems. In general, the age and metallicity distributions of globular clusters in lenticular galaxies appear to form a transition type between elliptical and spiral galaxies, but it is inconclusive from the current data which globular cluster systems are resembled more closely.

Implications for Galaxy Formation Models

A strong constraint on galaxy formation models is put by the $[\alpha/\text{Fe}]$ ratios of globular cluster systems. Globular clusters in elliptical galaxies have formal mean $[\alpha/\text{Fe}] = +0.38 \pm 0.05$, which is clearly enhanced compared to $[\alpha/\text{Fe}] = 0.00 \pm 0.09$ and $+0.03 \pm 0.05$ dex for globular clusters in lenticular and spiral galaxies, respectively. The hierarchical picture sees elliptical galaxies forming in merging events of smaller sub-units. Our data show that these sub-unit cannot be today's lenticular

and spiral galaxies, since their globular cluster systems have by far too low $[\alpha/\text{Fe}]$ to build up the cluster systems of elliptical galaxies with highly super-solar $[\alpha/\text{Fe}]$ ratios. Moreover, subsequent merging of gas-rich spirals would rather lower the mean $[\alpha/\text{Fe}]$ as older stellar populations are given enough time to enrich the ISM with SN Ia ejecta.

Our data suggest a scenario in which gas-rich progenitors of spiral galaxies and their globular cluster systems merge rather early ($z_f \sim 3 - 4$) to form today's elliptical galaxies and their globular cluster systems, *before* the onset of significant enrichment of their ISM by type Ia supernovae.

7.1 Synopsis

For the purpose of a short overview we summarise in the following the major results of this thesis:

- We find good agreement of spectroscopic line index measurements for metal-rich Galactic globular clusters and the diffuse light of the Galactic bulge. One exception is the CN index strength which is enhanced in globular clusters.

- SSP model predictions are calibrated with metal-rich Galactic globular clusters to solar metallicities.

- We show that both the globular clusters and the Galactic bulge follow the same correlation between magnesium and iron indices that extends to elliptical galaxies. This strong empirical evidence that the stellar population in all three systems are enhanced in $[\alpha/\text{Fe}]$ ratios

- In extragalactic globular cluster systems of early-type galaxies we find an increasing formal age dispersion towards higher metallicities.

- Metal-rich ($[\text{Z/H}] > -0.8$ dex) globular clusters in early-type galaxies show lower mean ages $t = 6.3 \pm 0.8$ Gyr than their metal-poor counterparts with a mean age $t = 11.3 \pm 0.5$ Gyr.

- A universal lower bound for globular cluster metallicities is found for all studied galaxies at $[\text{Z/H}] \approx -2.3$ dex.

- Mean $[\alpha/\text{Fe}]$ ratios of globular clusters in early-type galaxies have super-solar values (0.44 ± 0.05)

- There is evidence for an $[\alpha/\text{Fe}]$–age relation in globular cluster systems of early-type galaxies, in the sense that younger objects have lower $[\alpha/\text{Fe}]$ ratios. We find a formal offset of ~ 0.3 dex between globular clusters formally younger than 5 Gyr and the old globular cluster sub-population.

- A comparison of globular cluster systems in galaxies of different morphological type reveals that spiral galaxies host significantly older cluster systems ($t = 9.3 \pm 0.8$ Gyr) than lenticular and elliptical galaxies (both $t = 7.7 \pm 0.7$ Gyr).

- The highest metallicities reached by globular clusters in spiral galaxies are around solar while those for globular clusters in elliptical galaxies reach $\sim 2 - 3 Z_\odot$

- Mean $[\alpha/\text{Fe}]$ ratios for globular clusters in spiral and lenticular galaxies are found around solar, while globular clusters in elliptical galaxies are clearly enhanced in $[\alpha/\text{Fe}]$ reaching ~ 0.4 dex. This indicates different formation timescales/scenarios for globular cluster system in elliptical on the one hand and spiral and lenticular galaxies, on the other hand

- A significant ~ 0.2 dex offset in mean $[\alpha/\mathrm{Fe}]$ between globular cluster systems in field and group/cluster galaxies is found. The latter have higher mean $[\alpha/\mathrm{Fe}]$ ratios around ~ 0.4 dex which seems to be driven by the metal-poor globular cluster sub-population.

7.2 Outlook

This work demonstrates that globular clusters can serve as powerful tools to understand galaxy formation. However, there is still much work to do in this field of research. Hence, some major paths for future activities are sketched in the following:

- *Complex Abundance Pattern*: We find some disturbing evidence that our results might be influenced by unexpected complex abundance pattern (see App. F). At least part of the scatter in age/metallicity diagnostic diagrams (see Fig. 6.2) might be due to complex abundance variations. In particular, we have shown that among the Lick Balmer indices, Hβ is mostly sensitive to systematic changes of line strengths in Mg, Cr, Ti, and Fe in its narrowly-defined passbands (see Fig. 5.2). Other Balmer indices are sensitive to Mg, Sc, Ti, V, Cr, and Mn abundances. As globular clusters probe *local* star-formation events, local variations in abundance patterns appear likely. Such variations are washed out in spectra of the diffuse galaxy light by the *global* mix of stellar populations. In contrast to their host galaxies which exhibit a high velocity dispersion in the integrated light of the diffuse stellar population, higher-resolution spectroscopy of globular clusters ($\sigma_{\mathrm{los}} \lesssim 20$ km s^{-1}, Mandushev et al. 1991) can exhibit a wealth of information on abundance ratios.

- *Controlling the Horizontal Branch Moprhology*: Our SSP models provide accurate understanding of the blue horizontal branch morphology which influence the Balmer line indices and therefore age and metallicity determinations. These systematics are fully under control in the metal-poor regime. However, as the mass-loss for metal-rich stellar populations is not fully understood and difficult to calibrate, our age and metallicity determinations might be affected by unexpected blue horizontal branch morphologies at high metallicities. Clearly, a method for disentangling the influence of age and horizontal branch morphology on Balmer line indices is necessary to bolster such studies. Defining new broad line indices in the near-UV which measure the flux and/or some high-ionization potential spectral features which form in the hot atmospheres of warm blue horizontal branch stars might be the right way to proceed. Another approach might be higher-resolution spectroscopy which allows to determine the contribution of warm blue horizontal branch stars by the shape of the wings of Balmer lines.

- *Extending the Study of Extragalactic Globular Clusters*: If the above problems are under control, an extension of this study to cover a wider parameter space of host galaxy properties is necessary. Increasing the sample statistics would help to scrutinise some tentative results derived in this work. Moreover, a comparison of globular clusters and the diffuse galaxy light out to large radii is a natural continuation of this thesis.

- *Comparison with High-Resolution Galaxy Formation Models*: Still restricted by computational limitations, today's galaxy formation models fail to treat the formation of globular cluster systems *ab initio*, based on fundamental physics. This is a consequence of the limited mass resolution of such models.

The current link of observations of globular cluster system to predictions of galaxy formation models is usually performed over arbitrarily chosen scaling relation for globular cluster formation efficiencies. Higher resolution fully hydrodynamical calculations, which succeed to form a globular cluster system within the modeled galaxy, will become available in the next decade and allow a more quantitative comparison of theoretical predictions to current observations of globular cluster systems.

Many more detailed projects can be envisioned with this type of data, one of which might be the detailed study of the *entire* globular cluster system of selected galaxies, down to faint magnitudes sampling most of the globular cluster luminosity function. Such studies in nearby galaxies, e.g. in the Fornax or Virgo galaxy cluster, are feasible with today's instrumentations at 8-10m class telescopes. At the end of this thesis and in the light of the envisioned projects to come, it seems that globular cluster research holds many golden keys to doors which lead to a deeper understanding of galaxy and structure formation and of our universe as a whole.

Appendix A

The Index Measuring Routine

A.1 Basics

The Lick/IDS standard system is briefly described in Section 1.5. As feature and background passbands include many absorption lines, the index value can sensitively depend on the exact definition of passband boundaries. The Lick system defines 25 line indices (Worthey et al. 1994; Worthey & Ottaviani 1997) for which background and feature passband definitions are given in Table A.1. These passband definitions are used to derive the fitting functions which are used to calculate theoretical model predictions for stellar populations of different age, metallicity, and chemical composition. Needless to say that when measurements are compared to such model calculations, a consistent use of passband definitions is crucial to avoid biased predictions.

A.2 Line Index Response

The different sensitivity of line indices to fundamental stellar parameters allows the definition of a group of age-sensitive indices (Balmer-line indices $H\beta$, $H\gamma_A$, $H\delta_A$, $H\gamma_F$, and $H\delta_F$) and a group of metallicity-sensitive indices (Mg_2, Mgb, Fe5270, Fe5335, etc.).

All indices response in a complex way to changes in age, metallicity, and abundance patterns. Lick indices are insensitive to dust absorption effect as both the flux in the background passbands and in the feature passband is similarly affected. As mentioned above, some Lick indices are rather sensitive to age, such as Balmer-line indices, others are more sensitive to metallicity, such as metal-line indices. Worthey (1994) and Worthey & Ottaviani (1997) quantify this for a solar metallicity 12 Gyr old population by means of the $\mathcal{Z}$ sensitivity parameter, which is defined as the partial derivative

$$\mathcal{Z} = \frac{d\log(\text{age})}{d\log(Z)}\bigg|_I . \tag{A.1}$$

It describes the change in age which is needed to balance a metallicity change so that the index remains constant. Larger numbers indicate stronger metallicity sensitivity and weaker age sensitivity. Table A.1 illustrates that Lick indices fall in three groups with relatively small, intermediate, and high $\mathcal{Z}$ values. Using cuts at $\mathcal{Z} \sim 1.2$ and ~ 2.0 the indices can be classified in groups of good age indicators ($\mathcal{Z} \lesssim 1.2$), good metallicity indicators ($\mathcal{Z} \gtrsim 2.0$), and fully degenerate indices ($\mathcal{Z} \sim 1.6$) which show

index	feature passband	blue continuum	red continuum	units	$\mathcal{Z}$
Hδ_A	4083.500 4122.250	4041.600 4079.750	4128.500 4161.000	Å	1.1
Hδ_F	4091.000 4112.250	4057.250 4088.500	4114.750 4137.250	Å	0.9
CN$_1$	4143.375 4178.375	4081.375 4118.875	4245.375 4285.375	mag	1.9
CN$_2$	4143.375 4178.375	4085.125 4097.625	4245.375 4285.375	mag	2.1
Ca4227	4223.500 4236.000	4212.250 4221.000	4242.250 4252.250	Å	1.5
G4300	4282.625 4317.625	4267.625 4283.875	4320.125 4336.375	Å	1.0
Hγ_A	4319.750 4363.500	4283.500 4319.750	4367.250 4419.750	Å	1.0
Hγ_F	4331.250 4352.250	4283.500 4319.750	4354.750 4384.750	Å	0.8
Fe4383	4370.375 4421.625	4360.375 4371.625	4444.125 4456.625	Å	1.9
Ca4455	4453.375 4475.875	4447.125 4455.875	4478.375 4493.375	Å	2.0
Fe4531	4515.500 4560.500	4505.500 4515.500	4561.750 4580.500	Å	1.9
Fe4668	4635.250 4721.500	4612.750 4631.500	4744.000 4757.750	Å	4.9
Hβ	4847.875 4876.625	4827.875 4847.875	4876.625 4891.625	Å	0.6
Fe5015	4977.750 5054.000	4946.500 4977.750	5054.000 5065.250	Å	4.0
Mg$_1$	5069.125 5134.125	4895.125 4957.625	5301.125 5366.125	mag	1.8
Mg$_2$	5154.125 5196.625	4895.125 4957.625	5301.125 5366.125	mag	1.8
Mgb	5160.125 5192.625	5142.625 5161.375	5191.375 5206.375	Å	1.7
Fe5270	5245.650 5285.650	5233.150 5248.150	5285.650 5318.150	Å	2.3
Fe5335	5312.125 5352.125	5304.625 5315.875	5353.375 5363.375	Å	2.8
Fe5406	5387.500 5415.000	5376.250 5387.500	5415.000 5425.000	Å	2.5
Fe5709	5698.375 5722.125	5674.625 5698.375	5724.625 5738.375	Å	6.5
Fe5782	5778.375 5798.375	5767.125 5777.125	5799.625 5813.375	Å	5.1
NaD	5878.625 5911.125	5862.375 5877.375	5923.875 5949.875	Å	2.1
TiO$_1$	5938.375 5995.875	5818.375 5850.875	6040.375 6105.375	mag	1.5
TiO$_2$	6191.375 6273.875	6068.375 6143.375	6374.375 6416.875	mag	2.5

Table A.1: Passband definitions for the full set of 25 Lick indices which are used in this work. The index definitions were taken from Worthey (1994) and Worthey & Ottaviani (1997).

similar sensitivity to age and metallicity. The group of good age indicators includes all Balmer line indices and the G4300 index, which measures the strength of the G band at ~ 4300 Å. However, the G band is dominated by CH absorption and is subject to systematic effect due to internal mixing and is likely less reliable as age indicator. Superior metallicity indicators appear to be Fe4668, Fe5015, Fe5709, and Fe5782. But none of these absorption features seems ideal for reliable metallicity determinations. Fe4668 was found to be sensitive to C, O, Mg, and Si. Fe5015 is mostly sensitive to iron, but can be affected by [O III] emission. Fe5709 and Fe5782 are weak features which require high S/N ratios and react sensitively to dispersion corrections. More reliable metallicity indicators are Fe5270, Fe5335, and Fe5406 as all measure predominantly strong iron lines. Note that all Mg indices fall in the group of fully degenerate indices.

Emission lines from ionized gas can affect some line indices and bias their interpretation. In particular, all Balmer indices can be affected by Balmer emission. Potential contamination of Fe5015 is likely by [O III] (λ 5007 Å) as well as of the Mgb index by [N I] (λ 5199 Å) (Goudfrooij & Emsellem 1996). As a consequence, ages derived from contaminated Balmer indices would be too old. The emission corrections rapidly decrease from Hβ towards Hγ and Hδ. Osterbrook (1989) showed that the emission line ratios Hγ/Hβ and Hδ/Hβ are of the order 0.5 and 0.25, respectively, for case B recombination. In these premises, higher-order Balmer indices should be preferentially used for age determinations. Emission corrections are important for index measurements of the diffuse galactic light where the ionized gas is embedded within the system and its contribution can only be modeled by means of other emission lines, e.g. [O III]. Provided good background subtraction, globular cluster spectra are free from such emission effects.

The construction of Lick indices entails not only the problem of contamination by emission lines, but also the contamination of satellite absorption lines, which fall within the feature and background passbands. If abundance patterns of local stellar populations, which serve as calibrators for simple stellar population models, do not match those in the observed stellar population, satellite lines can alter index values and bias age and metallicity determinations. To illustrate which absorption lines might affect line index measurements, feature and background passband for all Lick indices are shown in Figure A.1 ontop of a spectrum of a Milky Way globular cluster (NGC 6284). Satellite absorption lines as well as molecular bands are indicated and were taken from Reader & Corliss (1981) and Pearse & Gaydon (1976), respectively. The wealth of "unwanted" contaminants inside the index passbands suggests that narrowly defined indices can suffer from systematic effects due to abundance ratio variations. The contrast between strength of the main absorption line and the strength of all satellite lines defines the reliability of an index in measuring the absorption feature it was designed for.

The passband definitions of line indices which are given in Table A.1 and the index measuring prescriptions were implemented in a code, which performs a full statistical error treatment (see Sect. A.4 for details). In summary, a line index is defined as the missing/additional flux between the spectrum and a pseudo-continuum which is defined by two continuum passbands on either side of the feature passband. Trager et al. (1998) defines a line index as

$$I_{a,o} = \int_{\lambda_{min}}^{\lambda_{max}} \left(1 - \frac{F_l(\lambda)}{F_c(\lambda)} \right) d\lambda, \tag{A.2}$$

where $F_l(\lambda)$ and $F_c(\lambda)$ is the flux of the feature passband and the pseudo-continuum, respectively. However, González (1993) gives another definition of a line index

$$I_{a,t} = \left(1 - \frac{\int_{\lambda_{min}}^{\lambda_{max}} F_l(\lambda)\, d\lambda}{\int_{\lambda_{min}}^{\lambda_{max}} F_c(\lambda)\, d\lambda} \right) \cdot \Delta\lambda. \tag{A.3}$$

While the former is an integral of the flux ratio the latter is the ratio of the flux integrals. We refer to the former as the observer's definition ($I_{a,o}$) and to the latter as the theorist's definition ($I_{a,t}$). For high-S/N spectra the difference between the two definitions is negligible. $I_{a,t}$ is a more global definition and is, therefore, more robust for low-S/N spectra. However, since most literature uses the observer's definition, all the measurements which are given in this paper are $I_{a,o}$ (Eq. A.2). To check for systematic offsets and/or different error patterns, our code performes index measurements with both definitions. Without exception, we find no systematic offset between the measurements and a value-to-value scatter of less than 0.1%. In particular, this causes no problems between theoretical predictions from SSP models, which synthesise line indices using the $I_{a,t}$ definition, and measurements.

A.3   Performance Tests

The whole measurement procedure was tested on original Lick spectra available from the database of Guy Worthey[1]. Applying our code to 6 original Lick spectra (HYA VB 112/sdr310007, HYA VB 111/sdr310010, HYA VB 103 (R)/sdr310017, HYA VB 103 (R+L)/sdr310019, HYA VB 95/sdr320230, and HR 7429/sdr370421) and comparing the results of 150 line index measurements (using the EW_o definition, see

---

[1]The latest passband definitions and FITS files of original Lick calibration spectra have been obtained from http://astro.wsu.edu/worthey/html/index.table.html
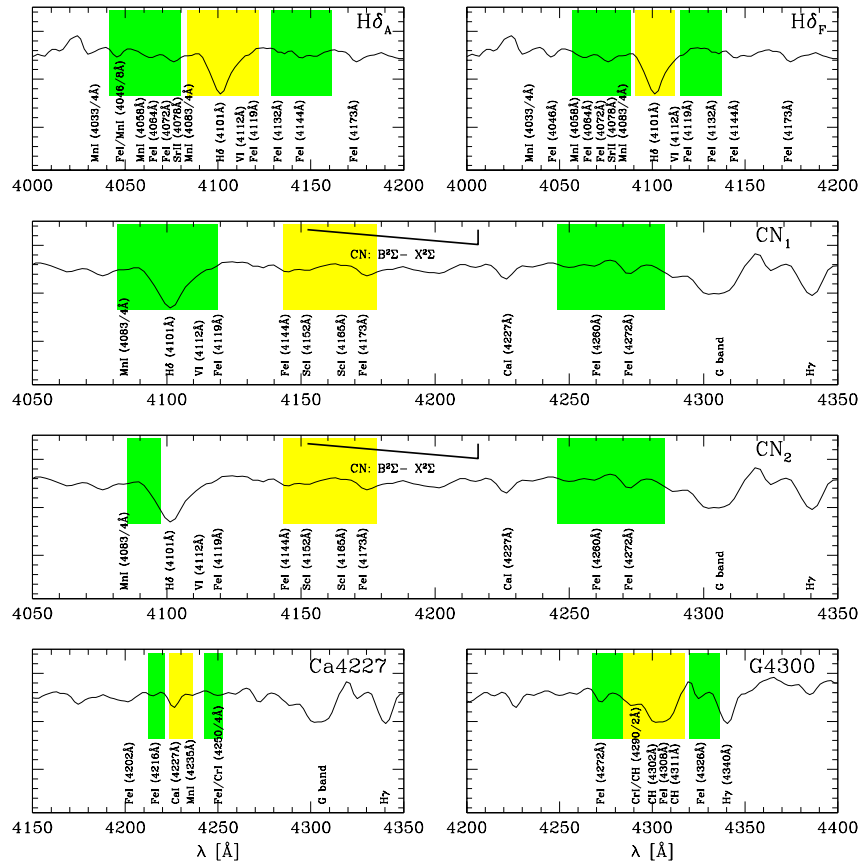
Figure A.1: Passband definitions for Lick indices, $H\delta_A$ to G4300.
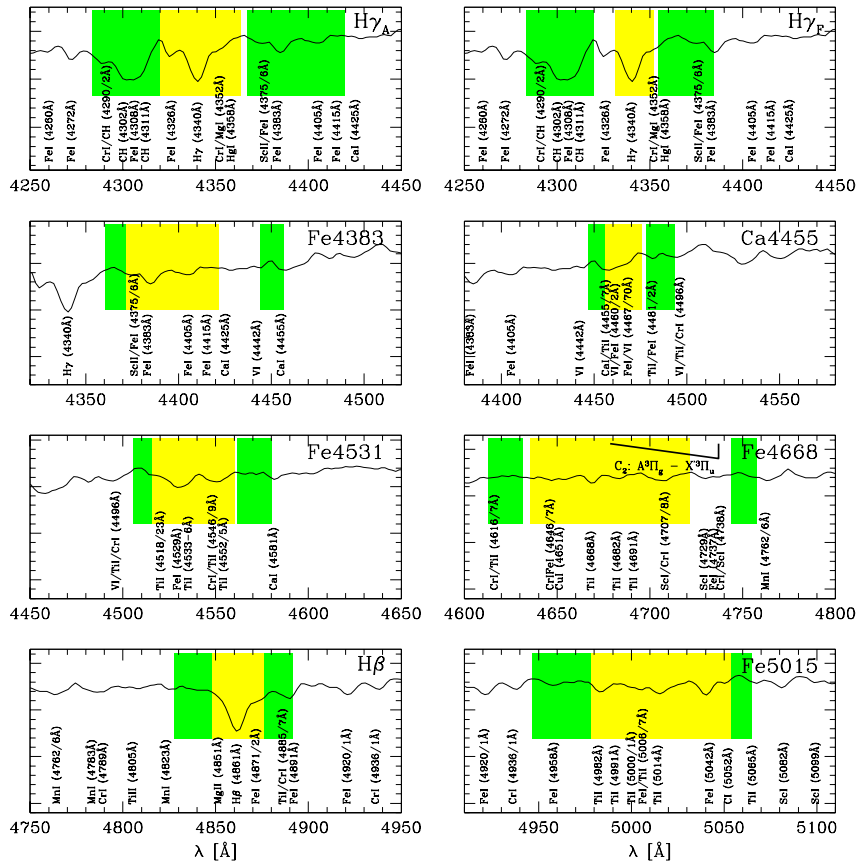
Figure A.1: – continued. Passband definitions of Lick indices, Hγ_A to Fe5015.
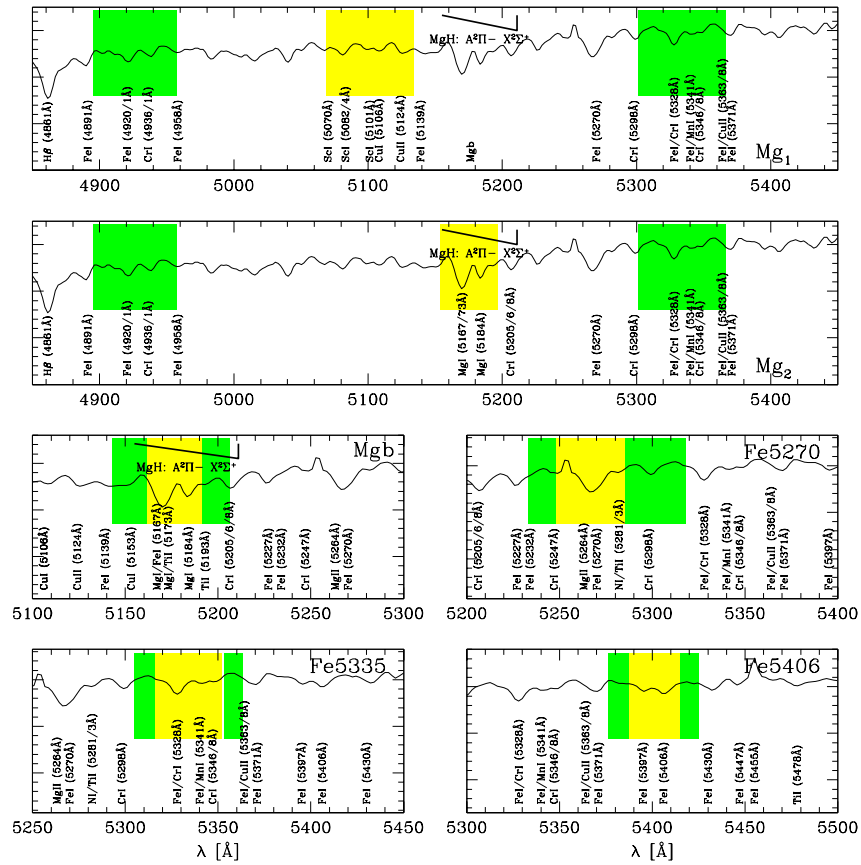
Figure A.1: – continued. Passband definitions of Lick indices, Mg_1 to Fe5406.
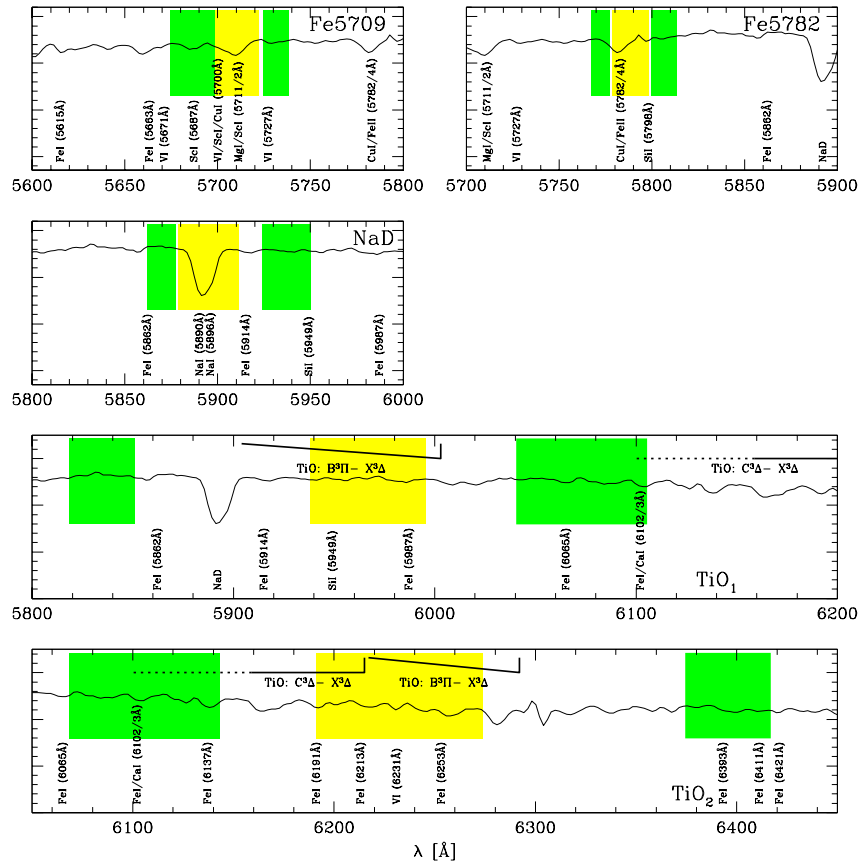
Figure A.1: – continued. Passband definitions of Lick indices, Fe5709 to TiO$_2$.
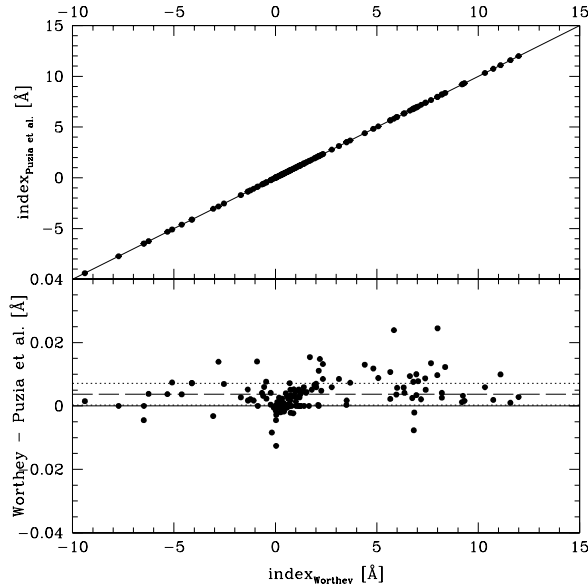
Figure A.2: Comparison of index measurements of Worthey and from our code. The upper panel shows the direct comparison between our and the Worthey data. Each single point gives the measurement for one star in one single passband. Residuals are plotted in the lower panel. The measurements of passbands which are defined in magnitudes have been previously transformed to the Å-scale. From the lower panel we determine the average statistical scatter with 0.0034 Å and a zero offset $0.0037 \pm 2 \cdot 10^{-5}$ Å.

above) with the original data provided by Guy Worthey, we find excellent agreement between the Lick datasets and ours. After transformation of molecular-band indices, which are usually given in magnitudes, to a uniform Å-scale, we determine an average scatter of 0.0034 Å, which is most likely due to the different treatment of sub-pixels at the edges of passbands. The average systematic zero offset between the two datasets was found $0.0037 \pm 2 \cdot 10^{-5}$ Å. Figure A.2 shows a comparison between measurements performed by Worthey and us based on the same data. Since the offset between the two datasets is of the order of the scatter of all index values, we do not consider any correction for all measurements performed in this work. Moreover, the offset is significantly smaller than the errors which result from Poisson noise of the spectra themselves.

A.4   Error Estimation

The main purpose of implementing a new code for index measurements, was the need for a robust error estimate of the indices. Since we deal with CCD data, as opposed to the Lick spectra, which are digitized images of a phosphor screen, we can determine the contribution of the flux Poisson noise of each spectrum to the total error budget. Note that due to the scanning of a spectrum off a phosphor screen the photo-tube suffers from the correlation of photon-noise errors over a wide wavelength range. Moreover, the photo-tube increases the noise due to statistical fluctuations in the amplification process (Robinson & Wampler 1972). The data used in this work is entirely free from these effects.

    Since we need to subtract background spectra from our science spectra it is

necessary to estimate the contribution of errors introduced by the subtraction and any radial velocity uncertainties to the total error budget. Both background and science spectra are included in the estimation of the total index uncertainty. Radial velocity errors are considered as systematic errors and are not included in the statistical error budget, but listed in the paper.

The code determines the total line-index uncertainty in 100 Monte Carlo simulations. Each simulation creates a new object and background spectrum by adding noise according to the Poisson statistics taking into account the detector noise. Line indices are measured on each noise-added spectrum. Since a Monte Carlo test naturally takes into account all possible error correlations in the line-index measurement process (such as the correlation of errors in the background passbands with the errors in the feature passband), the scatter in all simulated line indices is the best estimate for their total uncertainty. We therefore use the $1-\sigma$ standard deviation of all Monte-Carlo line-index measurements as the best guess for the final index uncertainty.

The variations due to uncertain radial velocities are given separately. They are calculated as the deviation of the initial line index by changing the radial velocity within its error limits.

Appendix B

Lick Indices of Galactic Globular Clusters

Table B.1 summarises all our Lick index measurements which were computed with the *new* set of index passband definitions from Trager et al. (1998) and Worthey & Ottaviani (1997). These index measurements are described in Chapter 2.

Table B.2 shows the correction coefficients of the transformation to the Lick system for the *old* set of passband definitions of Worthey et al. (1994).

Table B.3 summarises all our Lick index measurements which were computed with the *old* set of index passband definitions.

Table B.1: Lick indices CN_1 – Mg_1 for all sample globular clusters including statistical and systematic errors. Line one gives the index value. Line two and three document the Poisson error and the statistical slit-to-slit scatter. The systematic deviation of each index due to radial velocity uncertainties is given in line four. This set of indices uses the *new* passband definitions of Trager et al. (1998) and Worthey & Ottaviani (1997).

cluster[a]	CN_1 mag	CN_2 mag	Ca4227 Å	G4300 Å	Fe4383 Å	Ca4455 Å	Fe4531 Å	Fe4668 Å	Hβ Å	Fe5015 Å	Mg_1 mag
NGC 5927	0.0848	0.1146	0.7194	4.4637	3.0248	0.8141	2.3786	2.7464	1.6359	4.8052	0.0848
$\Delta\mathcal{B}$	0.0010	0.0013	0.0183	0.0329	0.0531	0.0261	0.0463	0.0688	0.0335	0.0744	0.0008
$\Delta\mathcal{S}$	0.0116	0.0187	0.1303	1.0389	0.7073	0.1423	0.3439	0.3326	0.1174	0.2154	0.0183
Δv_r	0.0006	0.0033	0.0417	0.0943	0.0529	0.1206	0.0569	0.0367	0.0319	0.1213	0.0000
NGC 6388	0.0446	0.0676	0.3498	4.3312	2.4211	0.4663	2.2645	1.3306	2.0111	4.0880	0.0568
$\Delta\mathcal{B}$	0.0003	0.0004	0.0057	0.0106	0.0171	0.0081	0.0130	0.0224	0.0098	0.0247	0.0002
$\Delta\mathcal{S}$	0.0032	0.0024	0.0496	0.0251	0.0930	0.0595	0.0463	0.0554	0.0489	0.0629	0.0026
Δv_r	0.0002	0.0025	0.0270	0.0761	0.0844	0.0844	0.0482	0.0611	0.0276	0.0853	0.0001
NGC 6528	0.0959	0.1174	0.9089	5.2218	4.7754	0.8794	2.7074	4.2181	1.7745	5.1531	0.1149
$\Delta\mathcal{B}$	0.0012	0.0014	0.0191	0.0393	0.0525	0.0285	0.0498	0.0839	0.0351	0.0850	0.0010
$\Delta\mathcal{S}$	0.0031	0.0028	0.0423	0.1079	0.1826	0.0564	0.1121	0.7903	0.0840	0.0749	0.0147
Δv_r	0.0004	0.0032	0.0402	0.0892	0.1177	0.1250	0.0868	0.1043	0.0314	0.1191	0.0002
NGC 6624	0.0497	0.0739	0.4889	4.8910	2.4023	0.5065	2.2739	1.4643	1.6502	4.1850	0.0707
$\Delta\mathcal{B}$	0.0005	0.0006	0.0102	0.0178	0.0273	0.0154	0.0236	0.0417	0.0199	0.0429	0.0004
$\Delta\mathcal{S}$	0.0064	0.0062	0.1221	0.0299	0.3929	0.1254	0.1314	0.6138	0.0244	0.2230	0.0143
Δv_r	0.0001	0.0030	0.0413	0.0922	0.0981	0.1094	0.0450	0.0735	0.0265	0.1137	0.0003
NGC 6218	-0.0763	-0.0596	0.0586	2.7004	-0.1175	-0.0055	0.9504	-0.6060	2.7147	2.7170	0.0268
$\Delta\mathcal{B}$	0.0007	0.0007	0.0129	0.0258	0.0387	0.0212	0.0340	0.0661	0.0275	0.0665	0.0007
$\Delta\mathcal{S}$	0.0263	0.0200	0.1070	0.7427	0.5029	0.0786	0.3772	0.2757	0.6046	0.2691	0.0019
Δv_r	0.0002	0.0094	0.0527	0.1904	0.0765	0.0615	0.0503	0.0537	0.0049	0.0455	0.0001
NGC 6441	0.0532	0.0760	0.4629	4.3106	2.7542	0.4953	2.3203	1.3379	1.9406	4.2040	0.0721
$\Delta\mathcal{B}$	0.0008	0.0009	0.0169	0.0272	0.0360	0.0190	0.0348	0.0573	0.0240	0.0602	0.0007
$\Delta\mathcal{S}$	0.0025	0.0030	0.0111	0.0749	0.1047	0.0540	0.0446	0.0733	0.0612	0.0430	0.0011
Δv_r	0.0001	0.0027	0.0267	0.0814	0.0717	0.0873	0.0586	0.0992	0.0239	0.0860	0.0001
NGC 6553	0.1378	0.1619	1.0915	5.4464	4.0079	0.8316	3.0767	3.4849	1.8881	5.7254	0.1002
$\Delta\mathcal{B}$	0.0018	0.0023	0.0310	0.0640	0.0820	0.0483	0.0764	0.1223	0.0520	0.1043	0.0012
$\Delta\mathcal{S}$	0.0133	0.0025	0.0622	0.0136	1.1482	0.1425	0.0415	0.7890	0.1208	0.2928	0.0037
Δv_r	0.0007	0.0067	0.1065	0.1527	0.3085	0.1909	0.0892	0.2278	0.0633	0.1827	0.0007
NGC 6626	-0.0455	-0.0259	0.1473	3.1433	0.5716	0.0926	1.2946	-0.0206	2.2747	3.1826	0.0415
$\Delta\mathcal{B}$	0.0006	0.0009	0.0143	0.0272	0.0415	0.0192	0.0356	0.0688	0.0277	0.0656	0.0006
$\Delta\mathcal{S}$	0.0079	0.0067	0.0567	0.3647	0.2003	0.0768	0.2122	0.3109	0.3143	0.3829	0.0118
Δv_r	0.0001	0.0057	0.0386	0.1173	0.0714	0.0639	0.0378	0.0617	0.0204	0.0712	0.0000
NGC 6284	-0.0417	-0.0227	0.1551	3.1957	0.6659	0.1992	1.4645	-0.1003	2.4274	3.1553	0.0427
$\Delta\mathcal{B}$	0.0007	0.0008	0.0162	0.0261	0.0482	0.0231	0.0373	0.0695	0.0270	0.0736	0.0008
$\Delta\mathcal{S}$	0.0130	0.0098	0.0520	0.2768	0.3019	0.1834	0.0797	0.2457	0.1252	0.0646	0.0078
Δv_r	0.0003	0.0053	0.0281	0.1449	0.0564	0.0794	0.0611	0.0369	0.0080	0.0952	0.0002
NGC 6356	0.0450	0.0648	0.5079	5.0611	2.3472	0.5334	2.2955	1.3231	1.6341	4.0541	0.0728
$\Delta\mathcal{B}$	0.0006	0.0007	0.0111	0.0179	0.0295	0.0145	0.0275	0.0503	0.0189	0.0452	0.0005
$\Delta\mathcal{S}$	0.0040	0.0084	0.0586	0.0729	0.1553	0.1408	0.1940	0.3342	0.0839	0.2024	0.0118
Δv_r	0.0002	0.0033	0.0396	0.0897	0.1379	0.1095	0.0544	0.0814	0.0297	0.1106	0.0002
NGC 6637	0.0248	0.0438	0.4009	5.1925	2.0615	0.4497	2.1725	1.3150	1.6224	3.9535	0.0567
$\Delta\mathcal{B}$	0.0004	0.0005	0.0082	0.0135	0.0233	0.0119	0.0216	0.0347	0.0141	0.0368	0.0004
$\Delta\mathcal{S}$	0.0019	0.0073	0.0692	0.0486	0.0989	0.0944	0.0295	0.1497	0.0473	0.0498	0.0021
Δv_r	0.0002	0.0022	0.0643	0.0712	0.1074	0.0958	0.0622	0.0566	0.0267	0.1000	0.0002
NGC 6981	-0.0471	-0.0381	0.1733	2.9404	-0.0202	0.0870	1.0445	-0.3391	2.3928	2.6586	0.0305
$\Delta\mathcal{B}$	0.0006	0.0007	0.0114	0.0216	0.0390	0.0195	0.0331	0.0580	0.0254	0.0594	0.0007
$\Delta\mathcal{S}$	0.0177	0.0101	0.1497	0.2136	0.3709	0.0865	0.0121	0.2190	0.0897	0.0631	0.0058
Δv_r	0.0001	0.0040	0.0268	0.0973	0.0668	0.0383	0.0162	0.0219	0.0027	0.0330	0.0000
Bulge $\sum$	0.0138	0.0314	0.6323	4.4208	3.6806	0.4916	2.3301	4.0002	1.4863	4.4089	0.0979
$\Delta\mathcal{B}$	0.0070	0.0073	0.1302	0.2421	0.3162	0.1589	0.2839	0.4517	0.2069	0.4608	0.0059
$\Delta\mathcal{S}$	0.0440	0.0544	0.2154	0.7785	0.9333	0.7229	0.4293	0.8770	0.4036	0.4365	0.0104
Δv_r	0.0001	0.0010	0.0168	0.0291	0.0208	0.0329	0.0209	0.0316	0.0172	0.0173	0.0000

[a] $\Delta\mathcal{B}$: Bootstraped 1σ Poisson error, $\Delta\mathcal{S}$: slit-to-slit 1σ scatter for index measurements in different pointings, Δv_r: systematic uncertainty due to radial velocity errors.

Table B.1: – continued. Lick indices Mg_2 – TiO_2.

cluster[a]	Mg_2 mag	Mgb Å	Fe5270 Å	Fe5335 Å	Fe5406 Å	Fe5709 Å	Fe5782 Å	NaD Å	TiO_1 mag	TiO_2 mag
NGC 5927	0.2201	3.5692	2.2225	1.8085	1.1667	0.5023	0.8576	4.5095	0.0518	0.0950
$\Delta\mathcal{B}$	0.0010	0.0365	0.0417	0.0465	0.0360	0.0338	0.0268	0.0372	0.0009	0.0008
$\Delta\mathcal{S}$	0.0098	0.4197	0.0979	0.2000	0.1297	0.1372	0.2161	0.4903	0.0246	0.0501
Δv_r	0.0001	0.0193	0.0493	0.0372	0.0294	0.0284	0.0263	0.0218	0.0005	0.0002
NGC 6388	0.1458	2.1580	1.8828	1.6670	1.0154	0.4942	0.6622	3.7854	0.0327	0.0472
$\Delta\mathcal{B}$	0.0003	0.0110	0.0153	0.0131	0.0122	0.0105	0.0087	0.0136	0.0004	0.0003
$\Delta\mathcal{S}$	0.0064	0.0661	0.0407	0.0477	0.0349	0.0553	0.0493	0.0762	0.0069	0.0125
Δv_r	0.0001	0.0210	0.0256	0.0275	0.0225	0.0212	0.0470	0.0188	0.0003	0.0002
NGC 6528	0.2615	3.7413	2.3673	2.2777	1.5499	0.8223	0.7987	5.1366	0.0750	0.1268
$\Delta\mathcal{B}$	0.0010	0.0402	0.0427	0.0417	0.0427	0.0313	0.0312	0.0374	0.0011	0.0009
$\Delta\mathcal{S}$	0.0288	0.1484	0.3639	0.1031	0.1437	0.1773	0.0230	0.5497	0.0274	0.0574
Δv_r	0.0002	0.0081	0.0405	0.0479	0.0372	0.0366	0.0920	0.0069	0.0004	0.0002
NGC 6624	0.1721	2.7280	1.8158	1.6403	0.9789	0.5009	0.6411	2.7063	0.0470	0.0628
$\Delta\mathcal{B}$	0.0005	0.0169	0.0238	0.0307	0.0252	0.0172	0.0196	0.0214	0.0006	0.0005
$\Delta\mathcal{S}$	0.0248	0.2100	0.2131	0.1359	0.1355	0.0276	0.0760	0.1674	0.0178	0.0403
Δv_r	0.0002	0.0222	0.0347	0.0295	0.0406	0.0256	0.0472	0.0210	0.0004	0.0001
NGC 6218	0.0672	1.0628	0.7687	0.8935	0.2246	-0.1909	0.2025	1.2915	0.0182	0.0040
$\Delta\mathcal{B}$	0.0009	0.0355	0.0357	0.0485	0.0390	0.0323	0.0382	0.0397	0.0011	0.0011
$\Delta\mathcal{S}$	0.0041	0.3940	0.1710	0.2960	0.0994	0.1382	0.0971	0.0895	0.0081	0.0078
Δv_r	0.0002	0.0423	0.0150	0.0282	0.0043	0.0064	0.0209	0.0393	0.0002	0.0004
NGC 6441	0.1756	2.7262	1.9505	1.7140	1.0239	0.5481	0.7786	4.0577	0.0215	0.0543
$\Delta\mathcal{B}$	0.0008	0.0275	0.0366	0.0386	0.0246	0.0257	0.0206	0.0251	0.0007	0.0006
$\Delta\mathcal{S}$	0.0061	0.1431	0.0354	0.0728	0.0190	0.0349	0.0331	0.0282	0.0043	0.0081
Δv_r	0.0001	0.0260	0.0268	0.0310	0.0297	0.0257	0.0426	0.0182	0.0004	0.0001
NGC 6553	0.2552	3.8961	2.6091	2.2654	1.2371	0.7744	1.0970	3.8792	0.0689	0.1420
$\Delta\mathcal{B}$	0.0014	0.0524	0.0648	0.0656	0.0486	0.0427	0.0373	0.0535	0.0012	0.0010
$\Delta\mathcal{S}$	0.0114	0.2910	0.1071	0.1125	0.1042	0.0496	0.0138	0.1175	0.0130	0.0254
Δv_r	0.0005	0.0534	0.0706	0.0611	0.0595	0.0388	0.0969	0.0312	0.0009	0.0001
NGC 6626	0.0919	1.3679	1.0900	0.9747	0.5413	0.1846	0.4735	2.1005	0.0288	0.0382
$\Delta\mathcal{B}$	0.0007	0.0308	0.0348	0.0356	0.0311	0.0296	0.0275	0.0321	0.0008	0.0006
$\Delta\mathcal{S}$	0.0139	0.0616	0.2846	0.2615	0.2037	0.1425	0.0976	0.0547	0.0015	0.0017
Δv_r	0.0001	0.0241	0.0212	0.0200	0.0146	0.0198	0.0429	0.0210	0.0001	0.0002
NGC 6284	0.0966	1.4403	0.8563	1.0216	0.5178	0.1110	0.3141	2.3978	0.0159	0.0039
$\Delta\mathcal{B}$	0.0010	0.0333	0.0411	0.0440	0.0378	0.0338	0.0271	0.0414	0.0010	0.0009
$\Delta\mathcal{S}$	0.0098	0.0494	0.3418	0.0506	0.0510	0.0486	0.0908	0.2560	0.0036	0.0051
Δv_r	0.0001	0.0333	0.0029	0.0146	0.0251	0.0244	0.0357	0.0027	0.0002	0.0002
NGC 6356	0.1773	2.7863	1.7187	1.6597	0.9557	0.4067	0.5493	3.2660	0.0333	0.0531
$\Delta\mathcal{B}$	0.0006	0.0218	0.0228	0.0293	0.0208	0.0215	0.0185	0.0252	0.0006	0.0006
$\Delta\mathcal{S}$	0.0237	0.2217	0.0335	0.0657	0.1075	0.0383	0.0426	0.1860	0.0208	0.0434
Δv_r	0.0001	0.0185	0.0318	0.0143	0.0185	0.0201	0.0416	0.0182	0.0004	0.0002
NGC 6637	0.1542	2.5420	1.6335	1.3969	0.8222	0.3565	0.4906	2.6053	0.0381	0.0441
$\Delta\mathcal{B}$	0.0005	0.0167	0.0212	0.0218	0.0175	0.0141	0.0145	0.0221	0.0005	0.0005
$\Delta\mathcal{S}$	0.0059	0.1053	0.0650	0.0750	0.0131	0.0302	0.0585	0.1659	0.0030	0.0084
Δv_r	0.0001	0.0264	0.0335	0.0287	0.0338	0.0257	0.0322	0.0169	0.0004	0.0001
NGC 6981	0.0618	1.0838	0.8710	0.5990	0.1532	-0.1320	0.0108	1.4160	0.0143	-0.0045
$\Delta\mathcal{B}$	0.0008	0.0315	0.0363	0.0413	0.0308	0.0314	0.0313	0.0374	0.0008	0.0009
$\Delta\mathcal{S}$	0.0038	0.1683	0.2496	0.1426	0.5998	0.0718	0.1546	0.1334	0.0153	0.0069
Δv_r	0.0001	0.0121	0.0326	0.0165	0.0046	0.0110	0.0084	0.0074	0.0001	0.0000
Bulge Σ	0.2281	2.9879	2.3942	1.9040	1.1906	0.6347	0.8276	5.6267	0.0466	0.0820
$\Delta\mathcal{B}$	0.0064	0.2415	0.2273	0.3218	0.1953	0.1871	0.1566	0.2401	0.0060	0.0063
$\Delta\mathcal{S}$	0.0305	0.4243	0.4991	0.1580	0.2601	0.2380	0.2212	1.1913	0.0319	0.0570
Δv_r	0.0000	0.0020	0.0041	0.0100	0.0020	0.0098	0.0160	0.0127	0.0001	0.0000

[a] $\Delta\mathcal{B}$: Bootstraped 1σ Poisson error, $\Delta\mathcal{S}$: slit-to-slit 1σ scatter for index measurements in different pointings, Δv_r: systematic uncertainty due to radial velocity errors.

Table B.1: – continued. Lick indices $H\delta_A$ – $H\gamma_F$.

cluster[a]	$H\delta_A$ Å	$H\gamma_A$ Å	$H\delta_F$ Å	$H\gamma_F$ Å
NGC 5927	-1.8817	-4.1268	0.0876	-1.0638
$\Delta\mathcal{B}$	0.0391	0.0429	0.0275	0.0272
$\Delta\mathcal{S}$	0.8170	0.8869	0.5176	0.4666
Δv_r	0.0518	0.0159	0.0458	0.0085
NGC 6388	0.1308	-2.6045	1.0184	0.0148
$\Delta\mathcal{B}$	0.0099	0.0133	0.0060	0.0074
$\Delta\mathcal{S}$	0.0297	0.0570	0.0013	0.0165
Δv_r	0.0206	0.0022	0.0114	0.0065
NGC 6528	-1.6708	-5.7216	0.3290	-1.3866
$\Delta\mathcal{B}$	0.0441	0.0483	0.0296	0.0301
$\Delta\mathcal{S}$	0.1726	0.0633	0.0203	0.0815
Δv_r	0.0437	0.0011	0.0294	0.0037
NGC 6624	-0.5802	-3.6927	0.6196	-0.6094
$\Delta\mathcal{B}$	0.0183	0.0219	0.0134	0.0156
$\Delta\mathcal{S}$	0.0475	0.1873	0.0324	0.0609
Δv_r	0.0324	0.0147	0.0313	0.0043
NGC 6218	3.4626	1.6864	2.6734	1.9579
$\Delta\mathcal{B}$	0.0179	0.0254	0.0112	0.0149
$\Delta\mathcal{S}$	1.3602	1.6168	0.8272	0.9327
Δv_r	0.0026	0.0263	0.0252	0.0235
NGC 6441	0.1216	-2.7734	1.0666	-0.0213
$\Delta\mathcal{B}$	0.0256	0.0282	0.0169	0.0191
$\Delta\mathcal{S}$	0.1103	0.0950	0.0797	0.0350
Δv_r	0.0284	0.0056	0.0178	0.0037
NGC 6553	-1.8415	-5.9315	0.7905	-1.3923
$\Delta\mathcal{B}$	0.0709	0.0685	0.0422	0.0423
$\Delta\mathcal{S}$	0.6727	0.9318	0.7638	0.3674
Δv_r	0.0850	0.0117	0.0201	0.0058
NGC 6626	2.6597	0.3340	2.3038	1.3618
$\Delta\mathcal{B}$	0.0215	0.0285	0.0163	0.0159
$\Delta\mathcal{S}$	0.4341	0.8270	0.2633	0.3315
Δv_r	0.0045	0.0188	0.0070	0.0092
NGC 6284	2.3486	0.3707	2.4889	1.3953
$\Delta\mathcal{B}$	0.0242	0.0295	0.0171	0.0193
$\Delta\mathcal{S}$	0.3979	0.2117	0.2231	0.1705
Δv_r	0.0377	0.0241	0.0137	0.0085
NGC 6356	-0.7045	-3.8585	0.5987	-0.7734
$\Delta\mathcal{B}$	0.0185	0.0225	0.0116	0.0135
$\Delta\mathcal{S}$	0.1400	0.1668	0.1752	0.0702
Δv_r	0.0301	0.0147	0.0147	0.0030
NGC 6637	-0.7261	-3.9037	0.3773	-0.8734
$\Delta\mathcal{B}$	0.0154	0.0184	0.0107	0.0124
$\Delta\mathcal{S}$	0.1956	0.2869	0.1325	0.1962
Δv_r	0.0309	0.0192	0.0160	0.0094
NGC 6981	1.8885	0.6335	1.7022	1.3738
$\Delta\mathcal{B}$	0.0174	0.0225	0.0119	0.0153
$\Delta\mathcal{S}$	0.6826	0.4187	0.4062	0.2100
Δv_r	0.0084	0.0023	0.0109	0.0091
Bulge $\sum$	-0.2080	-3.2443	0.7604	-0.4023
$\Delta\mathcal{B}$	0.2404	0.2509	0.1619	0.1558
$\Delta\mathcal{S}$	1.3701	1.3918	0.6590	0.6703
Δv_r	0.0144	0.0029	0.0098	0.0011

[a] $\Delta\mathcal{B}$: Bootstraped 1σ Poisson error, $\Delta\mathcal{S}$: slit-to-slit 1σ scatter for index measurements in different pointings, Δv_r: systematic uncertainty due to radial velocity errors.

Table B.2: Summary of the coefficients α and β for all 1st and 2nd-order index corrections (see Section 2.2.4). This set of correction coefficients is valid for the *old* passband definitions (see Worthey et al. 1994).

index	z.p. – α	slope – β	r.m.s.	units
CN_1	−0.0003	0.0090	0.0181	mag
CN_2	−0.0271	0.1072	0.0221	mag
Ca4227	0.1738	−0.0696	0.3295	Å
G4300	−1.5890	0.3104	0.4031	Å
Fe4384	0.4658	−0.0057	0.4747	Å
Ca4455	1.1987	−0.2414	0.3443	Å
Fe4531	0.2109	0.0077	0.1986	Å
Fe4668	−1.1136	0.1393	0.6719	Å
Hβ	0.1027	−0.0648	0.1054	Å
Fe5015	−0.7017	0.0811	0.2113	Å
Mg_1	0.0117	−0.0021	0.0107	mag
Mg_2	0.0133	0.0300	0.0117	mag
Mgb	0.2782	−0.0747	0.1400	Å
Fe5270	−0.2250	0.0277	0.2185	Å
Fe5335	−0.2182	0.0126	0.2135	Å
Fe5406	0.0676	−0.0641	0.0330	Å
Fe5709	−0.0406	0.1049	0.0860	Å
Fe5782	0.1770	−0.1260	0.1626	Å
NaD	0.2294	−0.0432	0.1994	Å
TiO_1	0.0156	0.2159	0.0126	mag
TiO_2	−0.0112	0.1047	0.0258	mag

Note: The Lick system provides a library of standard star spectra with published Lick index measurements (Worthey et al. 1994). We were able to reproduce the published values of all Lick indices with the exception of Ca4227 and Ca4455. For these two we find a significant offset and relatively large scatter compared with the published values. Henceforth, we mark both Ca indices as possibly unreliable Ca abundance indicators.

Table B.3: Lick indices CN_1 – Mg_1 for all sample globular clusters including statistical and systematic errors. Lines as in Table B.1. This set of indices uses the *old* passband definitions of Worthey et al. (1994).

cluster[a]	CN_1 mag	CN_2 mag	Ca4227 Å	G4300 Å	Fe4383 Å	Ca4455 Å	Fe4531 Å	Fe4668 Å	Hβ Å	Fe5015 Å	Mg_1 mag
NGC 5927	0.0865	0.0978	0.9411	3.8064	3.5211	1.6646	2.7285	2.4637	1.6045	4.4883	0.0810
$\Delta\mathcal{B}$	0.0010	0.0012	0.0179	0.0386	0.0507	0.0295	0.0459	0.0702	0.0344	0.0722	0.0009
$\Delta\mathcal{S}$	0.0126	0.0241	0.1058	1.5576	0.9231	0.0672	0.3133	0.4348	0.1096	0.3234	0.0186
Δv_r	0.0012	0.0047	0.0702	0.1200	0.0163	0.1565	0.0747	0.0503	0.0318	0.1213	0.0002
NGC 6388	0.0469	0.0447	0.6527	3.4736	2.9890	1.4677	2.6294	1.0270	1.9557	3.4097	0.0515
$\Delta\mathcal{B}$	0.0003	0.0004	0.0057	0.0109	0.0139	0.0088	0.0156	0.0218	0.0112	0.0230	0.0003
$\Delta\mathcal{S}$	0.0033	0.0024	0.0500	0.0257	0.0776	0.0448	0.0532	0.0584	0.0456	0.0944	0.0026
Δv_r	0.0002	0.0034	0.0364	0.1040	0.1054	0.1012	0.0684	0.0729	0.0276	0.0852	0.0001
NGC 6528	0.0985	0.1008	1.0854	4.8485	5.0006	1.6773	2.9677	3.9408	1.7349	5.0086	0.1105
$\Delta\mathcal{B}$	0.0013	0.0015	0.0230	0.0409	0.0569	0.0339	0.0521	0.0846	0.0339	0.0832	0.0008
$\Delta\mathcal{S}$	0.0032	0.0033	0.0418	0.1862	0.1746	0.0540	0.1560	0.7967	0.0784	0.1125	0.0150
Δv_r	0.0006	0.0039	0.0809	0.1036	0.1806	0.1511	0.0951	0.1365	0.0314	0.1191	0.0001
NGC 6624	0.0517	0.0521	0.7426	4.3356	2.9452	1.4807	2.6817	1.1594	1.6189	3.5552	0.0656
$\Delta\mathcal{B}$	0.0005	0.0006	0.0116	0.0181	0.0274	0.0127	0.0250	0.0380	0.0171	0.0414	0.0005
$\Delta\mathcal{S}$	0.0070	0.0082	0.0855	0.0576	0.3535	0.0754	0.1804	0.6350	0.0228	0.3347	0.0146
Δv_r	0.0007	0.0044	0.0604	0.1324	0.1360	0.1319	0.0567	0.0915	0.0264	0.1137	0.0002
NGC 6218	-0.0772	-0.1060	0.3901	1.0869	0.7658	1.2549	1.4226	-0.9178	2.6126	1.3515	0.0211
$\Delta\mathcal{B}$	0.0007	0.0008	0.0123	0.0272	0.0396	0.0201	0.0426	0.0666	0.0274	0.0645	0.0008
$\Delta\mathcal{S}$	0.0267	0.0248	0.0839	1.1431	0.4418	0.0321	0.3419	0.2824	0.5643	0.4039	0.0020
Δv_r	0.0003	0.0108	0.0659	0.2294	0.1154	0.0688	0.0689	0.0654	0.0049	0.0454	0.0000
NGC 6441	0.0553	0.0537	0.7283	3.4935	3.2861	1.4836	2.6659	1.0053	1.8900	3.5838	0.0671
$\Delta\mathcal{B}$	0.0007	0.0009	0.0129	0.0300	0.0404	0.0200	0.0335	0.0541	0.0270	0.0482	0.0006
$\Delta\mathcal{S}$	0.0024	0.0039	0.0065	0.1118	0.1000	0.0440	0.0453	0.0991	0.0571	0.0646	0.0011
Δv_r	0.0004	0.0038	0.0498	0.1094	0.1133	0.1038	0.0668	0.0859	0.0239	0.0860	0.0000
NGC 6553	0.1409	0.1483	1.1934	5.1077	4.1114	1.6442	3.3920	3.0414	1.8410	5.8677	0.0955
$\Delta\mathcal{B}$	0.0020	0.0022	0.0324	0.0627	0.0858	0.0424	0.0781	0.1107	0.0549	0.1332	0.0013
$\Delta\mathcal{S}$	0.0140	0.0064	0.0563	0.0298	0.8549	0.1294	0.0306	0.7740	0.1128	0.4396	0.0038
Δv_r	0.0014	0.0081	0.1601	0.1799	0.3711	0.1395	0.2414	0.2696	0.0632	0.1826	0.0007
NGC 6626	-0.0456	-0.0667	0.4746	1.7188	1.3821	1.2905	1.7474	-0.3440	2.2019	2.0504	0.0360
$\Delta\mathcal{B}$	0.0007	0.0008	0.0135	0.0262	0.0451	0.0226	0.0303	0.0645	0.0276	0.0568	0.0007
$\Delta\mathcal{S}$	0.0074	0.0070	0.0386	0.5166	0.0920	0.0277	0.1797	0.3180	0.2934	0.5749	0.0119
Δv_r	0.0002	0.0065	0.0447	0.1478	0.0980	0.0721	0.0542	0.0687	0.0204	0.0711	0.0000
NGC 6284	-0.0409	-0.0619	0.4875	1.7623	1.4881	1.3502	1.8817	-0.3747	2.3444	2.0094	0.0373
$\Delta\mathcal{B}$	0.0008	0.0010	0.0138	0.0326	0.0473	0.0218	0.0357	0.0604	0.0266	0.0670	0.0007
$\Delta\mathcal{S}$	0.0141	0.0122	0.0468	0.3412	0.2661	0.1297	0.0685	0.2517	0.1168	0.0970	0.0079
Δv_r	0.0000	0.0069	0.0442	0.1951	0.0857	0.0932	0.0438	0.0080	0.0080	0.0952	0.0001
NGC 6356	0.0465	0.0413	0.7848	4.5930	2.8455	1.5022	2.6618	1.0041	1.6038	3.3588	0.0678
$\Delta\mathcal{B}$	0.0006	0.0007	0.0088	0.0195	0.0315	0.0154	0.0252	0.0479	0.0213	0.0440	0.0005
$\Delta\mathcal{S}$	0.0040	0.0096	0.0370	0.1187	0.1224	0.0843	0.1665	0.3278	0.0783	0.3039	0.0119
Δv_r	0.0006	0.0043	0.0568	0.0993	0.1672	0.1287	0.0789	0.0957	0.0297	0.1107	0.0002
NGC 6637	0.0266	0.0201	0.6057	4.8329	2.6127	1.4665	2.5420	1.0281	1.5930	3.2077	0.0514
$\Delta\mathcal{B}$	0.0005	0.0005	0.0084	0.0235	0.0124	0.0205	0.0340	0.0156	0.0370	0.0004	
$\Delta\mathcal{S}$	0.0020	0.0082	0.1589	0.0341	0.1300	0.0900	0.0233	0.1585	0.0442	0.0748	0.0021
Δv_r	0.0004	0.0032	0.0886	0.1077	0.1419	0.1150	0.0743	0.0832	0.0267	0.1000	0.0001
NGC 6981	-0.0429	-0.0781	0.4922	1.4464	0.8959	1.3249	1.4807	-0.5578	2.3203	1.2395	0.0238
$\Delta\mathcal{B}$	0.0006	0.0007	0.0123	0.0218	0.0359	0.0201	0.0331	0.0572	0.0258	0.0652	0.0007
$\Delta\mathcal{S}$	0.0186	0.0127	0.1220	0.2878	0.3189	0.0487	0.0215	0.3210	0.0837	0.0947	0.0059
Δv_r	0.0001	0.0038	0.0345	0.0813	0.0607	0.0336	0.0322	0.0297	0.0023	0.0317	0.0000
Bulge $\sum$	0.0151	0.0041	0.8364	3.6699	4.2236	1.4869	2.6659	3.7960	1.4659	3.8913	0.0932
$\Delta\mathcal{B}$	0.0070	0.0080	0.1300	0.2304	0.3521	0.1761	0.2696	0.4389	0.2203	0.4931	0.0062
$\Delta\mathcal{S}$	0.0447	0.0649	0.2022	1.1400	1.0132	0.3815	0.4590	0.8930	0.3848	0.6334	0.0108
Δv_r	0.0001	0.0014	0.0298	0.0401	0.0366	0.0413	0.0311	0.0450	0.0161	0.0314	0.0000

[a] $\Delta\mathcal{B}$: Bootstraped 1σ Poisson error, $\Delta\mathcal{S}$: slit-to-slit 1σ scatter for index measurements in different pointings, Δv_r: systematic uncertainty due to radial velocity errors.

Table B.3: – continued. Lick indices Mg$_2$ – TiO$_2$.

cluster[a]	Mg$_2$ mag	Mgb Å	Fe5270 Å	Fe5335 Å	Fe5406 Å	Fe5709 Å	Fe5782 Å	NaD Å	TiO$_1$ mag	TiO$_2$ mag
NGC 5927	0.2204	3.6656	2.3001	1.8048	1.2981	0.7175	0.8580	4.5614	0.0540	0.0977
$\Delta\mathcal{B}$	0.0008	0.0363	0.0437	0.0467	0.0420	0.0335	0.0292	0.0395	0.0010	0.0009
$\Delta\mathcal{S}$	0.0096	0.4042	0.0957	0.2183	0.1310	0.1160	0.2358	0.4793	0.0233	0.0470
Δv_r	0.0001	0.0193	0.0492	0.0372	0.0294	0.0380	0.0709	0.0057	0.0005	0.0002
NGC 6388	0.1467	2.3182	1.9680	1.6506	1.1472	0.7119	0.6634	3.7979	0.0359	0.0535
$\Delta\mathcal{B}$	0.0003	0.0125	0.0145	0.0144	0.0118	0.0114	0.0091	0.0136	0.0003	0.0003
$\Delta\mathcal{S}$	0.0063	0.0637	0.0398	0.0521	0.0352	0.0449	0.0461	0.0661	0.0064	0.0117
Δv_r	0.0000	0.0210	0.0256	0.0275	0.0225	0.0308	0.0720	0.0035	0.0004	0.0000
NGC 6528	0.2608	3.8430	2.4415	2.3173	1.6869	0.9225	0.6725	5.1391	0.0758	0.1293
$\Delta\mathcal{B}$	0.0011	0.0368	0.0464	0.0475	0.0333	0.0287	0.0308	0.0361	0.0008	0.0008
$\Delta\mathcal{S}$	0.0284	0.1429	0.3556	0.1126	0.1450	0.1399	0.0070	0.5457	0.0258	0.0538
Δv_r	0.0002	0.0081	0.0406	0.0479	0.0372	0.0533	0.1073	0.0270	0.0005	0.0002
NGC 6624	0.1726	2.8671	1.9025	1.6214	1.1104	0.7311	0.6583	2.6866	0.0495	0.0684
$\Delta\mathcal{B}$	0.0006	0.0197	0.0241	0.0246	0.0207	0.0171	0.0177	0.0234	0.0005	0.0005
$\Delta\mathcal{S}$	0.0245	0.2023	0.2083	0.1484	0.1368	0.0232	0.0519	0.1737	0.0165	0.0378
Δv_r	0.0001	0.0222	0.0347	0.0295	0.0406	0.0353	0.0762	0.0099	0.0004	0.0001
NGC 6218	0.0691	1.2634	0.8790	0.8061	0.3487	0.2373	0.3669	1.2326	0.0234	0.0137
$\Delta\mathcal{B}$	0.0008	0.0311	0.0392	0.0505	0.0345	0.0306	0.0293	0.0429	0.0010	0.0010
$\Delta\mathcal{S}$	0.0040	0.3795	0.1671	0.3232	0.1003	0.1060	0.0832	0.0898	0.0075	0.0075
Δv_r	0.0002	0.0423	0.0150	0.0281	0.0042	0.0086	0.0538	0.0302	0.0001	0.0005
NGC 6441	0.1760	2.8653	2.0341	1.7018	1.1558	0.7563	0.7600	4.0813	0.0251	0.0602
$\Delta\mathcal{B}$	0.0008	0.0300	0.0290	0.0384	0.0285	0.0230	0.0212	0.0281	0.0007	0.0007
$\Delta\mathcal{S}$	0.0060	0.1378	0.0346	0.0794	0.0192	0.0274	0.0350	0.0364	0.0040	0.0076
Δv_r	0.0000	0.0260	0.0268	0.0310	0.0298	0.0346	0.0742	0.0065	0.0004	0.0000
NGC 6553	0.2545	3.9920	2.6779	2.3038	1.3711	0.9255	0.9838	3.8916	0.0695	0.1431
$\Delta\mathcal{B}$	0.0014	0.0533	0.0579	0.0665	0.0492	0.0446	0.0391	0.0488	0.0012	0.0011
$\Delta\mathcal{S}$	0.0112	0.2803	0.1047	0.1228	0.1052	0.0427	0.0216	0.1280	0.0122	0.0237
Δv_r	0.0005	0.0534	0.0705	0.0611	0.0595	0.0624	0.1648	0.0078	0.0010	0.0002
NGC 6626	0.0935	1.5572	1.1931	0.8947	0.6686	0.4963	0.5492	2.0536	0.0330	0.0457
$\Delta\mathcal{B}$	0.0009	0.0295	0.0320	0.0389	0.0298	0.0238	0.0288	0.0360	0.0007	0.0008
$\Delta\mathcal{S}$	0.0137	0.0593	0.2781	0.2855	0.2056	0.0854	0.0715	0.0569	0.0013	0.0015
Δv_r	0.0000	0.0241	0.0212	0.0200	0.0146	0.0282	0.0721	0.0089	0.0002	0.0003
NGC 6284	0.0982	1.6270	0.9647	0.9459	0.6448	0.4366	0.4276	2.3230	0.0206	0.0128
$\Delta\mathcal{B}$	0.0009	0.0371	0.0451	0.0454	0.0349	0.0310	0.0313	0.0374	0.0010	0.0009
$\Delta\mathcal{S}$	0.0096	0.0476	0.3341	0.0552	0.0514	0.0558	0.0631	0.2339	0.0034	0.0049
Δv_r	0.0000	0.0332	0.0029	0.0146	0.0251	0.0282	0.0622	0.0103	0.0002	0.0001
NGC 6356	0.1777	2.9233	1.8075	1.6426	1.0869	0.6549	0.6001	3.2571	0.0364	0.0591
$\Delta\mathcal{B}$	0.0006	0.0258	0.0260	0.0323	0.0266	0.0199	0.0202	0.0254	0.0006	0.0006
$\Delta\mathcal{S}$	0.0234	0.2135	0.0327	0.0717	0.1085	0.0319	0.0157	0.1960	0.0193	0.0408
Δv_r	0.0001	0.0184	0.0318	0.0143	0.0185	0.0315	0.0670	0.0053	0.0004	0.0000
NGC 6637	0.1549	2.6880	1.7243	1.3556	0.9521	0.6132	0.5669	2.5727	0.0409	0.0508
$\Delta\mathcal{B}$	0.0005	0.0171	0.0218	0.0227	0.0182	0.0172	0.0173	0.0195	0.0005	0.0005
$\Delta\mathcal{S}$	0.0058	0.1014	0.0636	0.0819	0.0132	0.0164	0.0664	0.1795	0.0029	0.0080
Δv_r	0.0000	0.0263	0.0334	0.0287	0.0338	0.0341	0.0557	0.0050	0.0005	0.0000
NGC 6981	0.0640	1.2715	1.0125	0.4596	0.2604	0.2753	0.2125	1.3006	0.0184	0.0062
$\Delta\mathcal{B}$	0.0008	0.0298	0.0351	0.0413	0.0334	0.0300	0.0309	0.0415	0.0009	0.0008
$\Delta\mathcal{S}$	0.0037	0.1621	0.2440	0.1557	0.6056	0.0519	0.1117	0.1492	0.0161	0.0075
Δv_r	0.0001	0.0114	0.0297	0.0162	0.0046	0.0081	0.0044	0.0052	0.0003	0.0001
Bulge $\sum$	0.2279	3.1174	2.4678	1.9093	1.3241	0.8255	0.7953	5.6970	0.0489	0.0864
$\Delta\mathcal{B}$	0.0073	0.2229	0.2303	0.2526	0.2251	0.1816	0.1798	0.2335	0.0056	0.0045
$\Delta\mathcal{S}$	0.0315	0.4435	0.4931	0.1720	0.2542	0.1928	0.1954	1.2423	0.0299	0.0538
Δv_r	0.0000	0.0077	0.0108	0.0208	0.0067	0.0159	0.0337	0.0010	0.0002	0.0000

[a] $\Delta\mathcal{B}$: Bootstraped 1σ Poisson error, $\Delta\mathcal{S}$: slit-to-slit 1σ scatter for index measurements in different pointings, Δv_r: systematic uncertainty due to radial velocity errors.

Appendix C

Photometric Measurements of Extragalactic Globular Clusters

The following tables summarise the photometric information for all extragalactic globular clusters confirmed by radial velocity (see Chapter 4). The last column of each table gives the heliocentric radial velocity of each object.

Table C.1: Photometry for **NGC 1380** globular clusters. B band photometry was performed on HST/WFPC2 data. V and I magnitudes were extracted from VLT/FORS2 data.

cluster	RA (J2000)	DEC (J2000)	B	V	I	v_r [km/s]
1380m1GC04	54.10717	−35.03080	. . .	22.84 ± 0.01	21.82 ± 0.01	2021 ± 76
1380m1GC07	54.14715	−35.00487	. . .	21.48 ± 0.01	20.26 ± 0.01	1989 ± 15
1380m1GC08	54.11343	−35.01822	. . .	22.05 ± 0.01	21.06 ± 0.01	2069 ± 54
1380m1GC09	54.12835	−35.00936	. . .	22.33 ± 0.01	21.39 ± 0.01	1992 ± 53
1380m1GC11	54.12429	−35.00638	. . .	22.17 ± 0.01	21.17 ± 0.01	2177 ± 42
1380m1GC12	54.12302	−35.00412	. . .	21.64 ± 0.01	20.37 ± 0.01	1759 ± 19
1380m1GC15	54.11587	−35.00054	. . .	21.54 ± 0.01	20.56 ± 0.01	2011 ± 42
1380m1GC16	54.11230	−34.99823	. . .	23.27 ± 0.02	20.73 ± 0.01	2037 ± 95
1380m1GC19	54.11019	−34.99161	. . .	21.53 ± 0.01	20.33 ± 0.01	1891 ± 27
1380m1GC23	54.13079	−34.97301	. . .	22.32 ± 0.01	21.03 ± 0.01	1911 ± 27
1380m1GC24	54.12244	−34.97604	. . .	22.55 ± 0.01	21.39 ± 0.01	1753 ± 79
1380m1GC25	54.11998	−34.97541	. . .	23.56 ± 0.02	22.21 ± 0.02	1872 ± 54
1380m1GC27	54.11623	−34.97274	. . .	23.13 ± 0.02	22.13 ± 0.02	1845 ± 119
1380m1GC28	54.11594	−34.97202	. . .	21.94 ± 0.01	20.06 ± 0.01	1555 ± 41
1380m1GC30	54.11164	−34.96936	22.60 ± 0.03	21.32 ± 0.01	19.65 ± 0.01	1840 ± 72
1380m1GC33	54.10018	−34.96597	. . .	21.97 ± 0.01	20.77 ± 0.01	2010 ± 24
1380m1GC36	54.11802	−34.94870	22.50 ± 0.02	21.89 ± 0.01	20.82 ± 0.01	1969 ± 28
1380m1GC37	54.10672	−34.94987	23.31 ± 0.08	22.36 ± 0.01	21.15 ± 0.01	1813 ± 44
1380m1GC39	54.10054	−34.94803	23.88 ± 0.14	22.83 ± 0.01	21.85 ± 0.01	1936 ± 57
1380m1GC45	54.10862	−34.93067	23.59 ± 0.05	22.67 ± 0.01	21.62 ± 0.01	1647 ± 67
1380m1GC46	54.10822	−34.92786	23.28 ± 0.04	22.30 ± 0.01	21.05 ± 0.01	1686 ± 31
1380m2GC03	54.11109	−35.01416	. . .	22.32 ± 0.01	21.24 ± 0.01	1798 ± 93
1380m2GC05	54.09937	−35.00162	. . .	23.00 ± 0.01	21.91 ± 0.01	1953 ± 66
1380m2GC11	54.11286	−35.00132	. . .	22.31 ± 0.01	21.08 ± 0.01	1784 ± 46
1380m2GC13	54.10945	−34.99274	. . .	23.38 ± 0.02	22.10 ± 0.02	2031 ± 53
1380m2GC14	54.11019	−34.99161	. . .	21.53 ± 0.01	20.33 ± 0.01	1785 ± 31
1380m2GC15	54.11664	−34.99397	. . .	22.42 ± 0.01	21.26 ± 0.01	1885 ± 46
1380m2GC19	54.11410	−34.98408	. . .	20.19 ± 0.01	19.05 ± 0.01	2140 ± 19
1380m2GC21	54.11310	−34.98104	. . .	21.46 ± 0.01	20.64 ± 0.01	1733 ± 50
1380m2GC22	54.11684	−34.98021	. . .	22.35 ± 0.01	21.20 ± 0.01	1503 ± 87
1380m2GC23	54.11171	−34.97392	. . .	22.12 ± 0.01	21.38 ± 0.01	2194 ± 48
1380m2GC26	54.10950	−34.96517	23.66 ± 0.07	22.98 ± 0.01	21.73 ± 0.01	1663 ± 71
1380m2GC27	54.12712	−34.97306	. . .	21.01 ± 0.01	19.93 ± 0.01	1919 ± 21
1380m2GC30	54.11450	−34.95576	21.55 ± 0.01	20.87 ± 0.01	19.88 ± 0.01	1907 ± 35
1380m2GC33	54.11982	−34.95058	. . .	22.01 ± 0.01	20.77 ± 0.01	1771 ± 48
1380m2GC34	54.11879	−34.94580	23.63 ± 0.05	22.74 ± 0.01	21.58 ± 0.01	1503 ± 68
1380m2GC35	54.12341	−34.94678	22.92 ± 0.03	21.98 ± 0.01	20.80 ± 0.01	1799 ± 35
1380m2GC36	54.12584	−34.94553	23.22 ± 0.04	22.26 ± 0.01	20.99 ± 0.01	1709 ± 35
1380m2GC37	54.12193	−34.94023	23.53 ± 0.05	22.70 ± 0.01	21.66 ± 0.01	1855 ± 57
1380m2GC38	54.13341	−34.94582	22.53 ± 0.02	21.62 ± 0.01	20.51 ± 0.01	2075 ± 22
1380m2GC42	54.12449	−34.92257	. . .	21.96 ± 0.01	20.75 ± 0.01	2163 ± 59
1380m2GC43	54.13475	−34.92701	. . .	22.32 ± 0.01	21.18 ± 0.01	1891 ± 47
1380m2GC45	54.14384	−34.92875	. . .	21.65 ± 0.01	20.67 ± 0.01	1799 ± 40

Table C.2: Photometry for **NGC 2434** globular clusters. B band photometry was performed on HST/WFPC2 data. V and I magnitudes were extracted from VLT/FORS2 data.

cluster	RA (J2000)	DEC (J2000)	B	V	I	v_r [km/s]
2434m1GC11	113.72887	−69.31087	. . .	21.18 ± 0.01	19.89 ± 0.01	1431 ± 45
2434m1GC19	113.73373	−69.28346	23.16 ± 0.03	22.03 ± 0.01	20.66 ± 0.01	1425 ± 30
2434m1GC20	113.69241	−69.31384	. . .	20.39 ± 0.01	19.14 ± 0.01	1288 ± 58
2434m2GC29[a]	113.71639	−69.28687	23.56 ± 0.07	22.50 ± 0.05	21.07 ± 0.04	1507 ± 56
2434m2GC37[b]	113.70513	−69.25395	. . .	22.01 ± 0.01	. . .	1462 ± 54
2434m2GC40	113.73322	−69.26787	23.95 ± 0.06	22.96 ± 0.02	21.68 ± 0.02	1508 ± 71

[a] all passbands from HST/WFPC2 photometry

[b] I band data uncertain due to nearby blooming spike. V band data was calibrated assuming $V - I = 1.0$.

Table C.3: Photometry for **NGC 3115** globular clusters. Optical photometry was performed on VLT/FORS2 data. Near-infrared K band magnitudes were measured on VLT/ISAAC data and taken from Puzia et al. (2002a).

cluster	RA (J2000)	DEC (J2000)	B	V	R	I	K	v_r [km/s]
3115m1GC03	151.28017	-7.75347	23.02 ± 0.04	22.16 ± 0.01	21.51 ± 0.01	20.86 ± 0.01	...	782 ± 46
3115m1GC04	151.29340	-7.75755	22.20 ± 0.02	21.43 ± 0.01	20.90 ± 0.01	20.36 ± 0.01	...	476 ± 25
3115m1GC05	151.29004	-7.74616	22.91 ± 0.03	22.27 ± 0.01	21.78 ± 0.02	21.21 ± 0.02	...	537 ± 38
3115m1GC06	151.29037	-7.74095	22.09 ± 0.02	21.15 ± 0.01	20.50 ± 0.01	19.78 ± 0.01	...	532 ± 19
3115m1GC08	151.29779	-7.73471	22.39 ± 0.02	21.47 ± 0.01	20.72 ± 0.01	20.12 ± 0.01	...	652 ± 22
3115m1GC09	151.29184	-7.72455	21.86 ± 0.01	21.07 ± 0.01	20.52 ± 0.01	20.03 ± 0.01	...	544 ± 36
3115m1GC10	151.31731	-7.73558	21.24 ± 0.01	20.53 ± 0.01	20.09 ± 0.01	19.65 ± 0.01	18.63 ± 0.05	344 ± 48
3115m1GC11	151.31862	-7.73416	22.03 ± 0.02	21.28 ± 0.01	20.76 ± 0.01	20.26 ± 0.01	18.72 ± 0.05	805 ± 30
3115m1GC12	151.31346	-7.72581	21.93 ± 0.01	21.19 ± 0.01	20.62 ± 0.01	20.07 ± 0.01	18.58 ± 0.04	688 ± 22
3115m1GC13	151.32008	-7.71888	21.69 ± 0.01	20.94 ± 0.01	20.38 ± 0.01	19.83 ± 0.01	18.23 ± 0.04	803 ± 25
3115m1GC14	151.31091	-7.70486	22.21 ± 0.02	21.26 ± 0.01	20.62 ± 0.01	19.94 ± 0.01	17.90 ± 0.03	654 ± 29
3115m1GC15	151.32661	-7.71223	22.53 ± 0.02	21.52 ± 0.01	20.87 ± 0.01	20.18 ± 0.01	18.14 ± 0.03	285 ± 19
3115m1GC16	151.33287	-7.70611	23.21 ± 0.04	22.03 ± 0.01	21.38 ± 0.01	20.64 ± 0.01	...	806 ± 24
3115m1GC17	151.32942	-7.69605	22.55 ± 0.02	21.82 ± 0.01	21.28 ± 0.01	20.70 ± 0.01	...	675 ± 34
3115m1GC18	151.33321	-7.69482	22.75 ± 0.03	21.99 ± 0.01	21.45 ± 0.01	20.90 ± 0.01	...	764 ± 37
3115m1GC19	151.33606	-7.69091	22.40 ± 0.02	21.43 ± 0.01	20.80 ± 0.01	20.13 ± 0.01	...	957 ± 24
3115m1GC21	151.33311	-7.68339	23.51 ± 0.05	22.60 ± 0.02	21.99 ± 0.02	21.31 ± 0.02	...	569 ± 50
3115m1GC22	151.34456	-7.68690	22.43 ± 0.02	21.51 ± 0.01	20.89 ± 0.01	20.30 ± 0.01	...	826 ± 24

Table C.4: Photometry for **NGC 3379** globular clusters. All photometric data were obtained with VLT/FORS2 data.

cluster	RA (J2000)	DEC (J2000)	V	I	v_r [km/s]
3379m1GC05	162.00133	12.54659	21.15 ± 0.01	20.20 ± 0.01	632 ± 26
3379m1GC09	161.98579	12.55754	20.59 ± 0.01	19.70 ± 0.01	1130 ± 34
3379m1GC10	161.97459	12.55823	22.83 ± 0.02	22.14 ± 0.07	1037 ± 102
3379m1GC11	161.97401	12.56302	21.53 ± 0.01	20.72 ± 0.02	705 ± 35
3379m1GC12	161.96921	12.56070	21.87 ± 0.01	20.86 ± 0.02	867 ± 35
3379m1GC13	161.97229	12.57023	21.88 ± 0.01	21.08 ± 0.03	941 ± 58
3379m1GC14	161.96004	12.56337	21.40 ± 0.01	20.47 ± 0.02	645 ± 29
3379m1GC15	161.93739	12.55101	21.75 ± 0.01	20.58 ± 0.02	976 ± 58
3379m1GC18	161.95697	12.57579	19.46 ± 0.01	18.43 ± 0.01	1099 ± 21
3379m1GC19	161.96552	12.58456	21.65 ± 0.01	20.56 ± 0.02	1080 ± 32
3379m1GC20[a]	161.95975	12.58526	21.68 ± 0.06	20.52 ± 0.06	1258 ± 38
3379m1GC22	161.96140	12.59146	21.43 ± 0.01	20.19 ± 0.01	586 ± 27
3379m1GC23	161.96083	12.59229	21.11 ± 0.01	20.09 ± 0.01	791 ± 57
3379m1GC24	161.96268	12.59707	20.02 ± 0.01	18.97 ± 0.01	801 ± 14
3379m1GC26	161.94557	12.58963	21.78 ± 0.01	20.86 ± 0.02	747 ± 48
3379m1GC27	161.95096	12.59586	20.90 ± 0.01	19.91 ± 0.01	911 ± 32
3379m1GC30	161.94980	12.60642	22.26 ± 0.01	21.63 ± 0.05	1119 ± 77
3379m1GC33	161.91904	12.59856	20.33 ± 0.01	19.43 ± 0.01	1310 ± 51

[a] all passbands from HST/WFPC2 photometry

Table C.5: Photometry for **NGC 3585** globular clusters. B and I band photometry was obtained with VLT/FORS2 data. The V band measurements were performed on HST/WFPC2 data.

cluster	RA (J2000)	DEC (J2000)	B	V	I	v_r [km/s]
3585m1GC01	168.37447	−26.76739	23.12 ± 0.02	...	20.89 ± 0.01	1329 ± 36
3585m1GC03	168.34747	−26.80268	21.67 ± 0.01	...	20.00 ± 0.01	1355 ± 52
3585m1GC04	168.37122	−26.75289	22.73 ± 0.01	...	20.51 ± 0.01	1416 ± 27
3585m1GC05	168.35960	−26.76735	23.05 ± 0.02	...	20.93 ± 0.01	1569 ± 40
3585m1GC07	168.35529	−26.76541	21.78 ± 0.01	...	19.57 ± 0.01	1338 ± 13
3585m1GC11	168.33916	−26.76138	22.74 ± 0.01	...	20.92 ± 0.01	1126 ± 43
3585m1GC12	168.33437	−26.76063	21.97 ± 0.01	...	19.84 ± 0.01	1540 ± 23
3585m1GC13	168.32205	−26.76943	22.99 ± 0.02	...	20.81 ± 0.01	1358 ± 35
3585m1GC14	168.32941	−26.75135	23.21 ± 0.02	...	21.12 ± 0.01	1107 ± 36
3585m1GC15	168.32906	−26.74574	22.61 ± 0.01	22.38 ± 0.02	20.94 ± 0.01	1411 ± 43
3585m1GC16	168.31792	−26.76046	22.53 ± 0.01	...	20.37 ± 0.01	1103 ± 33
3585m1GC18	168.31964	−26.74491	23.20 ± 0.02	22.94 ± 0.04	21.28 ± 0.01	1477 ± 41
3585m1GC19	168.30736	−26.76420	22.70 ± 0.01	22.15 ± 0.02	20.55 ± 0.01	1401 ± 38
3585m1GC20	168.32455	−26.72389	22.81 ± 0.02	...	20.57 ± 0.01	1697 ± 21
3585m1GC21	168.30592	−26.74966	23.02 ± 0.02	22.68 ± 0.03	21.26 ± 0.01	1513 ± 51
3585m1GC23	168.30353	−26.74171	23.37 ± 0.02	23.13 ± 0.04	21.64 ± 0.02	1412 ± 61
3585m1GC24	168.31082	−26.72189	23.18 ± 0.02	...	21.48 ± 0.02	1419 ± 59
3585m1GC26	168.29779	−26.73590	23.20 ± 0.02	22.52 ± 0.03	21.03 ± 0.01	1137 ± 30
3585m1GC30	168.29041	−26.72560	23.21 ± 0.02	...	21.57 ± 0.02	1113 ± 69
3585m1GC33	168.28152	−26.71842	23.40 ± 0.03	...	21.20 ± 0.01	1326 ± 54

Table C.6: Photometry for **NGC 5846** globular clusters. Optical photometry was performed on VLT/FORS2 data. Near-infrared K band magnitudes were measured on VLT/ISAAC data and taken from Hempel et al. (2003).

cluster	RA (J2000)	DEC (J2000)	B	V	R	I	K	v_r [km/s]
5846m1GC03	226.60867	1.55027	23.50 ± 0.02	22.56 ± 0.02	22.11 ± 0.02	21.54 ± 0.02	...	1264 ± 49
5846m1GC04	226.58614	1.57500	22.66 ± 0.01	21.51 ± 0.01	20.90 ± 0.01	20.13 ± 0.01	...	1848 ± 22
5846m1GC05	226.58652	1.57532	23.97 ± 0.02	23.04 ± 0.03	22.43 ± 0.03	21.81 ± 0.02	...	1691 ± 49
5846m1GC06	226.59790	1.56952	24.07 ± 0.03	23.03 ± 0.03	22.38 ± 0.02	21.63 ± 0.02	...	1923 ± 53
5846m1GC08	226.60419	1.57618	22.17 ± 0.01	21.15 ± 0.01	20.62 ± 0.01	19.92 ± 0.01	...	1602 ± 22
5846m1GC10	226.60513	1.58633	24.61 ± 0.04	23.82 ± 0.05	23.32 ± 0.06	22.64 ± 0.05	...	1880 ± 75
5846m1GC11	226.60857	1.58853	23.23 ± 0.01	22.22 ± 0.01	21.71 ± 0.01	21.07 ± 0.01	...	2166 ± 33
5846m1GC16	226.61493	1.60071	22.71 ± 0.01	21.65 ± 0.01	21.11 ± 0.01	20.35 ± 0.01	...	1921 ± 30
5846m1GC17	226.62686	1.59675	22.79 ± 0.01	21.80 ± 0.01	21.29 ± 0.01	20.61 ± 0.01	18.94 ± 0.02	1918 ± 45
5846m1GC18	226.63960	1.58716	22.50 ± 0.01	21.58 ± 0.01	21.11 ± 0.01	20.49 ± 0.01	19.06 ± 0.02	2090 ± 29
5846m1GC20	226.62782	1.60650	23.43 ± 0.01	22.80 ± 0.02	22.29 ± 0.02	21.52 ± 0.02	19.86 ± 0.04	1688 ± 38
5846m1GC21	226.63219	1.60597	22.46 ± 0.01	21.41 ± 0.01	20.98 ± 0.01	20.34 ± 0.01	18.68 ± 0.01	1391 ± 28
5846m1GC22	226.64700	1.59792	23.15 ± 0.01	22.12 ± 0.01	21.62 ± 0.01	20.92 ± 0.01	19.31 ± 0.02	1849 ± 36
5846m1GC23	226.62381	1.62037	23.26 ± 0.01	22.35 ± 0.01	21.88 ± 0.02	21.30 ± 0.01	20.01 ± 0.05	1576 ± 50
5846m1GC24	226.63728	1.61347	22.26 ± 0.01	21.18 ± 0.01	20.64 ± 0.01	19.91 ± 0.01	18.10 ± 0.01	1459 ± 18
5846m1GC25	226.63792	1.61555	24.16 ± 0.03	23.10 ± 0.03	22.53 ± 0.03	21.83 ± 0.02	20.18 ± 0.06	1401 ± 62
5846m1GC26	226.63879	1.61653	23.44 ± 0.02	22.58 ± 0.02	22.11 ± 0.02	21.56 ± 0.02	20.20 ± 0.06	1858 ± 61
5846m1GC27	226.62816	1.62800	22.74 ± 0.01	21.60 ± 0.01	21.00 ± 0.01	20.24 ± 0.01	18.18 ± 0.01	1932 ± 22
5846m1GC28	226.63023	1.62971	22.56 ± 0.01	21.49 ± 0.01	20.93 ± 0.01	20.21 ± 0.01	18.39 ± 0.01	2018 ± 31
5846m1GC29	226.64372	1.62213	23.67 ± 0.02	22.72 ± 0.02	22.27 ± 0.02	21.60 ± 0.02	20.17 ± 0.05	1600 ± 46
5846m1GC30	226.64409	1.62263	22.44 ± 0.01	21.43 ± 0.01	20.91 ± 0.01	20.22 ± 0.01	18.53 ± 0.01	1732 ± 25
5846m1GC31	226.65656	1.61735	23.44 ± 0.02	22.37 ± 0.01	21.79 ± 0.01	21.04 ± 0.01	...	2009 ± 26
5846m1GC32	226.64847	1.62785	22.52 ± 0.01	21.64 ± 0.01	21.15 ± 0.01	20.53 ± 0.01	...	2073 ± 34
5846m1GC33	226.65421	1.62574	24.35 ± 0.03	23.57 ± 0.04	23.06 ± 0.04	22.42 ± 0.04	...	1543 ± 100
5846m1GC36	226.65306	1.63870	23.06 ± 0.01	21.97 ± 0.01	21.38 ± 0.01	20.63 ± 0.01	...	1838 ± 26
5846m1GC37	226.65140	1.64578	23.82 ± 0.02	22.81 ± 0.02	22.21 ± 0.02	21.50 ± 0.02	...	1644 ± 49
5846m1GC38	226.65915	1.64533	22.47 ± 0.01	21.55 ± 0.01	21.03 ± 0.01	20.41 ± 0.01	...	1537 ± 41
5846m1GC39	226.66132	1.64462	21.99 ± 0.01	20.82 ± 0.01	20.23 ± 0.01	19.42 ± 0.01	...	1426 ± 23

Table C.7: Photometry for **NGC 7192** globular clusters. Optical photometry was performed on VLT/FORS2 data. Near-infrared K band magnitudes were measured on VLT/ISAAC data and taken from Hempel et al. (2003).

cluster	RA (J2000)	DEC (J2000)	B	V	R	I	K	v_r [km/s]
7192m1GC02	331.66461	-64.35384	24.20 ± 0.05	23.17 ± 0.03	22.73 ± 0.02	22.34 ± 0.04	...	3108 ± 96
7192m1GC15	331.70432	-64.33788	23.16 ± 0.02	22.42 ± 0.02	21.85 ± 0.01	21.41 ± 0.02	19.91 ± 0.04	2785 ± 43
7192m1GC16	331.70166	-64.33168	22.79 ± 0.01	21.97 ± 0.01	21.39 ± 0.01	20.86 ± 0.01	19.30 ± 0.02	2956 ± 28
7192m1GC18	331.70337	-64.32433	23.65 ± 0.03	22.97 ± 0.03	22.36 ± 0.01	21.93 ± 0.03	20.46 ± 0.07	2917 ± 60
7192m1GC19	331.70413	-64.32026	23.65 ± 0.03	23.41 ± 0.04	22.96 ± 0.02	22.19 ± 0.03	20.46 ± 0.07	2895 ± 62
7192m1GC20	331.71234	-64.32143	22.69 ± 0.01	21.89 ± 0.01	21.25 ± 0.01	20.69 ± 0.01	...	2713 ± 26
7192m1GC21	331.72278	-64.32507	23.77 ± 0.04	22.84 ± 0.02	22.15 ± 0.01	21.55 ± 0.02	...	2915 ± 31
7192m1GC22	331.70593	-64.30412	23.86 ± 0.04	23.09 ± 0.03	22.44 ± 0.01	21.97 ± 0.03	20.58 ± 0.07	2975 ± 56
7192m1GC23	331.72015	-64.31181	23.15 ± 0.02	22.42 ± 0.02	21.85 ± 0.01	21.43 ± 0.02	...	2599 ± 55
7192m1GC31	331.75983	-64.30913	23.44 ± 0.03	22.76 ± 0.02	22.16 ± 0.01	21.76 ± 0.02	...	3040 ± 55

Appendix D

Lick Indices of Extragalactic Globular Clusters

The following tables contain all line index measurements for extragalactic globular cluster, including statistical and systematic radial velocity errors (see Chapter 4). All tables are arranged by slit-mask observation.

Table D.1: Lick indices CN_1 – Mg_2 for **mask 1** of **NGC 1380** globular cluster observations including statistical and systematic errors.The set of indices uses the passband definitions of Worthey (1994) and for the higher-order Balmer lines the definitions of Worthey & Ottaviani (1997).

cluster[a]	CN_1 mag	CN_2 mag	Ca4227 Å	G4300 Å	Fe4383 Å	Ca4455 Å	Fe4531 Å	Fe4668 Å	$H\beta$ Å	Fe5015 Å	Mg_1 mag	Mg_2 mag
1380m1GC04	0.061	−0.075	0.44	4.00	−4.50	1.60	3.66	−0.54	−0.92	1.37	...	...
$\Delta\mathcal{B}$	0.004	0.006	0.22	0.24	0.30	0.31	0.34	0.42	0.43	0.46	...	...
Δv_r	0.108	0.023	0.15	0.13	0.30	0.16	0.11	0.58	0.08	0.22	...	...
1380m1GC07	0.056	0.063	1.43	6.20	−1.09	2.40	3.25	2.92	1.20	5.54	0.088	0.260
$\Delta\mathcal{B}$	0.002	0.003	0.09	0.10	0.12	0.12	0.13	0.16	0.16	0.18	0.005	0.005
Δv_r	0.011	0.027	0.16	0.20	1.41	0.53	0.91	0.85	0.13	0.71	0.012	0.007
1380m1GC08	−0.038	−0.076	0.82	2.04	−3.17	1.83	2.00	1.36	2.24	0.72	−0.016	0.039
$\Delta\mathcal{B}$	0.002	0.003	0.12	0.14	0.18	0.18	0.20	0.23	0.24	0.26	0.007	0.007
Δv_r	0.007	0.049	0.11	1.06	0.33	0.05	0.47	0.54	0.42	0.20	0.007	0.006
1380m1GC09	−0.022	−0.066	0.53	4.08	−0.99	5.24	3.91	3.76	2.32	3.61	0.004	0.012
$\Delta\mathcal{B}$	0.003	0.004	0.15	0.16	0.20	0.21	0.23	0.28	0.28	0.32	0.008	0.008
Δv_r	0.021	0.013	0.30	0.10	0.63	0.86	0.28	0.60	0.25	0.73	0.006	0.006
1380m1GC11	0.075	−0.008	0.86	4.24	−1.44	0.19	3.79	3.09	2.84	2.96	0.016	0.073
$\Delta\mathcal{B}$	0.002	0.003	0.12	0.14	0.18	0.18	0.20	0.25	0.25	0.27	0.007	0.007
Δv_r	0.067	0.039	0.02	0.17	1.92	0.15	0.87	0.77	0.09	0.30	0.002	0.005
1380m1GC12	0.120	0.136	1.29	4.76	3.54	1.74	3.49	5.46	2.04	5.19	0.116	0.288
$\Delta\mathcal{B}$	0.002	0.003	0.11	0.12	0.15	0.16	0.17	0.20	0.20	0.22	0.006	0.006
Δv_r	0.006	0.007	0.22	0.72	0.62	0.31	0.63	0.97	0.18	1.51	0.005	0.005
1380m1GC15	−0.047	−0.101	0.77	3.18	−3.37	−0.35	2.23	−0.16	2.72	2.70	0.038	0.085
$\Delta\mathcal{B}$	0.002	0.003	0.10	0.11	0.14	0.14	0.15	0.19	0.19	0.20	0.005	0.005
Δv_r	0.026	0.058	0.06	0.62	0.95	0.07	0.63	0.45	0.41	1.39	0.011	0.008
1380m1GC16	...	...	...	...	−6.68	1.69	2.14	−5.46	−0.29	−7.60	...	...
$\Delta\mathcal{B}$	...	...	...	...	0.60	0.62	0.68	0.77	0.78	0.82	...	...
Δv_r	...	...	...	...	0.65	1.34	0.53	1.01	0.21	1.16	...	...
1380m1GC19	0.099	0.121	1.11	5.86	−0.05	1.36	2.60	2.64	1.59	1.55	0.071	0.200
$\Delta\mathcal{B}$	0.002	0.003	0.09	0.10	0.13	0.13	0.14	0.17	0.17	0.19	0.005	0.005
Δv_r	0.048	0.021	0.19	0.07	1.05	0.34	0.42	1.10	0.15	1.97	0.013	0.007
1380m1GC23	0.197	0.167	3.05	6.61	−1.22	2.46	3.44	6.68	0.86	6.60	0.088	0.310
$\Delta\mathcal{B}$	0.004	0.006	0.18	0.20	0.24	0.25	0.27	0.31	0.32	0.35	0.010	0.010
Δv_r	0.096	0.105	0.03	1.49	1.00	0.36	0.49	1.09	0.84	0.13	0.015	0.011
1380m1GC24	0.144	−0.269	4.36	−0.93	3.99	−1.92	4.15	1.07	3.01	6.79	0.082	0.115
$\Delta\mathcal{B}$	0.008	0.014	0.59	0.64	0.70	0.71	0.74	0.83	0.84	0.87	0.022	0.023
Δv_r	0.173	0.096	1.08	1.08	3.14	0.71	0.99	0.46	0.04	1.65	0.049	0.024
1380m1GC25	0.188	0.213	3.06	8.23	0.11	3.62	...	...	...	...	0.165	0.444
$\Delta\mathcal{B}$	0.010	0.016	0.47	0.50	0.60	0.62	...	...	...	...	0.027	0.027
Δv_r	0.026	0.047	0.50	2.88	2.29	0.16	...	...	...	...	0.021	0.026
1380m1GC27	0.042	0.153	1.73	3.56	...	...	...	...	...	...	...	...
$\Delta\mathcal{B}$	0.003	0.005	0.17	0.20	...	...	...	...	...	...	...	...
Δv_r	0.009	0.110	0.45	0.22	...	...	...	...	...	...	...	...
1380m1GC28	0.041	0.060	2.99	4.04	−4.44	1.68	−0.05	6.88	...	...	−0.003	0.046
$\Delta\mathcal{B}$	0.007	0.010	0.35	0.38	0.50	0.51	0.56	0.66	...	...	0.019	0.020
Δv_r	0.095	0.024	0.87	4.21	2.35	0.64	2.10	4.70	...	...	0.045	0.045
1380m1GC30	−0.013	0.112	1.28	4.28	2.61	−0.25	4.24	7.25	...	...	...	...
$\Delta\mathcal{B}$	0.003	0.004	0.14	0.15	0.18	0.18	0.20	0.23	...	...	...	...
Δv_r	0.075	0.016	0.57	0.33	1.92	0.10	0.22	0.13	...	...	...	...
1380m1GC33	0.050	0.030	1.19	4.54	1.54	0.48	3.29	1.47	0.31	5.59	0.062	0.195
$\Delta\mathcal{B}$	0.003	0.004	0.13	0.14	0.17	0.17	0.19	0.27	0.27	0.30	0.007	0.007
Δv_r	0.021	0.023	0.06	0.52	1.91	0.30	0.59	0.52	0.51	0.58	0.025	0.013
1380m1GC36	0.031	0.051	0.98	3.44	−1.76	1.81	2.13	0.81	2.69	3.52	0.022	0.164
$\Delta\mathcal{B}$	0.002	0.004	0.12	0.14	0.19	0.19	0.21	0.25	0.25	0.27	0.007	0.008
Δv_r	0.009	0.024	0.05	0.07	1.02	0.15	0.55	0.48	0.24	1.34	0.010	0.009
1380m1GC37	0.007	0.055	0.38	2.34	−0.77	3.74	3.42	0.26	0.17	6.11	0.092	0.182
$\Delta\mathcal{B}$	0.004	0.006	0.20	0.22	0.29	0.30	0.32	0.41	0.41	0.44	0.011	0.012
Δv_r	0.001	0.009	0.41	0.28	0.29	1.12	0.34	2.78	0.59	2.01	0.003	0.001
1380m1GC39	−0.101	−0.047	−0.38	4.89	−1.85	3.08	1.67	6.44	1.26	5.55	−0.032	0.087
$\Delta\mathcal{B}$	0.006	0.008	0.30	0.34	0.42	0.43	0.48	0.57	0.59	0.63	0.017	0.017
Δv_r	0.111	0.042	0.31	0.31	0.62	1.04	0.95	2.12	0.24	2.39	0.022	0.014
1380m1GC45	0.010	0.128	−0.11	6.81	6.91	4.00	5.98	0.69	3.11	−0.62	−0.007	0.084
$\Delta\mathcal{B}$	0.006	0.009	0.28	0.32	0.39	0.40	0.43	0.53	0.54	0.59	0.016	0.016
Δv_r	0.043	0.042	0.17	1.07	1.29	1.21	0.48	2.34	0.12	0.50	0.047	0.031
1380m1GC46	0.054	0.045	−0.34	5.04	4.33	0.76	2.61	6.60	0.89	6.12	0.112	0.245
$\Delta\mathcal{B}$	0.005	0.007	0.25	0.27	0.32	0.33	0.36	0.42	0.43	0.46	0.013	0.014
Δv_r	0.002	0.003	0.45	0.27	1.56	0.78	0.70	3.67	0.11	0.39	0.012	0.006

[a] $\Delta\mathcal{B}$: Bootstraped 1σ statistical error, Δv_r: systematic uncertainty due to radial velocity errors.

Table D.1: – continued. Lick indices Mgb – Hγ_F for **mask 1** of the **NGC 1380** globular clusters. Note that index TiO$_2$ is missing due to the limited wavelength coverage of the spectra.

cluster[a]	Mgb Å	Fe5270 Å	Fe5335 Å	Fe5406 Å	Fe5709 Å	Fe5782 Å	NaD Å	TiO$_1$ mag	Hδ_A Å	Hγ_A Å	Hδ_F Å	Hγ_F Å
1380m1GC04	...	...	...	...	...	...	...	...	3.22	2.03	3.04	1.54
$\Delta\mathcal{B}$	...	...	...	...	...	...	...	...	0.49	0.50	0.51	0.51
Δv_r	...	...	...	...	...	...	...	...	0.05	0.12	0.47	0.21
1380m1GC07	4.18	2.56	1.68	1.33	1.01	0.90	2.00	0.022	−1.73	−6.98	−0.35	−2.03
$\Delta\mathcal{B}$	0.20	0.20	0.21	0.21	0.21	0.21	0.22	0.006	0.23	0.24	0.24	0.24
Δv_r	0.27	0.16	0.14	0.30	0.12	0.05	0.42	0.012	0.05	1.25	0.51	0.10
1380m1GC08	1.09	0.82	−0.84	1.06	...	...	...	...	2.40	2.06	1.96	1.25
$\Delta\mathcal{B}$	0.29	0.30	0.31	0.32	...	...	...	...	0.32	0.33	0.34	0.34
Δv_r	0.45	0.12	0.99	0.33	...	...	...	...	0.19	0.55	0.06	0.07
1380m1GC09	−0.84	1.28	1.15	0.17	0.58	0.27	...	...	2.87	0.41	2.03	2.07
$\Delta\mathcal{B}$	0.34	0.35	0.35	0.35	0.37	0.37	...	...	0.38	0.39	0.39	0.39
Δv_r	0.82	0.64	0.44	1.08	0.44	0.29	...	...	0.30	0.55	0.07	0.06
1380m1GC11	1.40	1.09	−0.24	0.83	0.65	...	...	...	−0.15	0.11	2.02	1.05
$\Delta\mathcal{B}$	0.29	0.30	0.30	0.31	0.31	...	...	...	0.32	0.33	0.33	0.33
Δv_r	0.15	0.41	0.30	0.06	0.15	...	...	...	0.85	1.47	0.16	0.32
1380m1GC12	4.68	2.76	1.62	1.61	1.45	...	...	...	−2.59	−5.92	−0.46	−1.08
$\Delta\mathcal{B}$	0.23	0.24	0.24	0.25	0.25	...	...	...	0.26	0.27	0.27	0.28
Δv_r	0.64	0.66	0.26	0.35	0.08	...	...	...	0.07	0.32	0.16	0.91
1380m1GC15	0.85	1.47	1.40	0.19	...	...	...	...	1.55	...	1.93	...
$\Delta\mathcal{B}$	0.22	0.22	0.23	0.23	...	...	...	...	0.23	...	0.24	...
Δv_r	0.51	0.32	0.88	0.29	...	...	...	...	0.26	...	0.12	...
1380m1GC16	−1.18	0.26	0.35	...	...	...	...	...	...	...	...	...
$\Delta\mathcal{B}$	0.85	0.86	0.87	...	...	...	...	...	...	...	...	...
Δv_r	1.16	1.76	2.07	...	...	...	...	...	...	...	...	...
1380m1GC19	3.23	2.71	1.86	1.76	...	...	...	...	−0.71	−1.81	0.58	−0.43
$\Delta\mathcal{B}$	0.21	0.21	0.21	0.22	...	...	...	...	0.23	0.24	0.24	0.24
Δv_r	0.26	0.16	0.45	0.10	...	...	...	...	0.04	1.56	0.06	0.29
1380m1GC23	4.77	4.86	3.50	1.79	1.07	−0.44	4.67	0.021	−1.28	−4.79	0.81	−2.28
$\Delta\mathcal{B}$	0.37	0.38	0.38	0.39	0.39	0.39	0.40	0.012	0.43	0.46	0.46	0.47
Δv_r	0.45	0.35	0.70	0.46	0.38	0.32	0.07	0.002	1.13	2.43	0.16	0.55
1380m1GC24	−2.60	0.73	3.15	0.86	6.47	0.40	4.90	...	0.75	3.33	2.21	1.74
$\Delta\mathcal{B}$	0.91	0.92	0.93	0.94	0.95	0.95	0.96	...	0.99	1.01	1.02	1.03
Δv_r	0.51	0.32	1.67	1.38	0.30	1.13	0.91	...	2.22	0.43	0.55	0.71
1380m1GC25	6.93	0.57	5.26	−0.08	−1.21	0.67	1.11	...	−5.05	−12.55	−0.87	−7.83
$\Delta\mathcal{B}$	0.89	0.92	0.94	0.95	0.97	0.97	1.00	...	1.09	1.13	1.16	1.17
Δv_r	0.25	1.66	0.98	1.02	0.86	1.11	0.47	...	5.82	2.86	0.28	0.21
1380m1GC27	...	...	...	...	...	...	...	...	...	...	...	...
$\Delta\mathcal{B}$	...	...	...	...	...	...	...	...	...	...	...	...
Δv_r	...	...	...	...	...	...	...	...	...	...	...	...
1380m1GC28	2.52	−0.54	5.77	2.78	−0.34	−1.18	−0.98	...	5.38	4.83	4.03	3.14
$\Delta\mathcal{B}$	0.78	0.79	0.80	0.81	0.82	0.83	0.84	...	0.87	0.89	0.90	0.91
Δv_r	0.87	2.05	3.43	0.49	0.55	0.73	2.47	...	2.61	0.80	0.20	0.67
1380m1GC30	...	2.04	2.07	1.15	1.43	0.88	...	...	1.12	−4.25	0.29	−0.85
$\Delta\mathcal{B}$	...	0.27	0.27	0.28	0.28	0.28	...	...	0.30	0.31	0.32	0.32
Δv_r	...	0.38	0.24	0.29	0.31	0.15	...	...	1.23	0.38	0.38	0.38
1380m1GC33	3.80	2.41	2.10	1.61	...	...	...	...	0.01	−6.14	1.16	−1.61
$\Delta\mathcal{B}$	0.31	0.32	0.32	0.33	...	...	...	...	0.34	0.36	0.36	0.36
Δv_r	0.39	0.23	0.61	0.07	...	...	...	...	0.31	0.60	0.00	0.36
1380m1GC36	1.78	2.88	1.80	...	0.96	0.12	2.45	0.039	0.72	−2.39	2.23	0.39
$\Delta\mathcal{B}$	0.30	0.31	0.31	...	0.32	0.33	0.33	0.010	0.35	0.36	0.37	0.37
Δv_r	0.55	0.28	0.31	...	0.05	0.17	0.25	0.011	0.30	0.80	0.06	0.29
1380m1GC37	3.27	2.31	1.12	0.98	1.12	−0.44	2.79	...	−0.23	−1.21	0.84	−1.42
$\Delta\mathcal{B}$	0.47	0.48	0.49	0.50	0.50	0.50	0.51	...	0.53	0.55	0.55	0.56
Δv_r	0.30	0.24	0.37	0.26	0.27	0.40	0.44	...	0.19	1.20	0.13	1.10
1380m1GC39	1.83	...	...	0.25	1.02	−0.61	...	...	2.87	2.17	1.16	1.56
$\Delta\mathcal{B}$	0.69	...	...	0.73	0.74	0.74	...	...	0.76	0.79	0.80	0.81
Δv_r	0.76	...	...	0.59	0.22	0.22	...	...	0.64	0.69	0.50	1.26
1380m1GC45	3.90	0.02	2.53	2.15	1.08	1.08	2.99	−0.039	−3.76	−4.32	3.31	−1.76
$\Delta\mathcal{B}$	0.64	0.67	0.68	0.69	0.70	0.70	0.71	0.021	0.80	0.82	0.84	0.84
Δv_r	0.89	0.63	0.18	0.53	0.08	0.43	0.63	0.013	2.74	1.47	0.87	0.92
1380m1GC46	3.76	2.22	3.00	1.60	0.16	0.61	3.08	0.015	−5.36	−4.06	0.42	−0.17
$\Delta\mathcal{B}$	0.50	0.51	0.52	0.52	0.53	0.53	0.54	0.016	0.58	0.60	0.61	0.61
Δv_r	0.57	1.34	0.60	0.43	0.55	0.18	0.57	0.003	0.84	0.73	1.01	0.29

[a] $\Delta\mathcal{B}$: Bootstraped 1σ statistical error, Δv_r: systematic uncertainty due to radial velocity errors.

Table D.2: Lick indices CN_1 – Mg_2 for **mask 2** of **NGC 1380** globular clusters.

cluster[a]	CN_1 mag	CN_2 mag	Ca4227 Å	G4300 Å	Fe4383 Å	Ca4455 Å	Fe4531 Å	Fe4668 Å	$H\beta$ Å	Fe5015 Å	Mg_1 mag	Mg_2 mag
1380m2GC03	0.227	0.232	1.82	3.04	−1.50	0.75	−1.43	−3.26	1.41	6.10	0.054	0.189
$\Delta\mathcal{B}$	0.007	0.011	0.32	0.36	0.45	0.46	0.50	0.59	0.60	0.65	0.018	0.018
Δv_r	0.027	0.028	0.04	0.28	0.79	0.08	0.11	0.94	0.92	0.46	0.002	0.003
1380m2GC05	. . .	. . .	. . .	. . .	. . .	. . .	0.52	3.73	−0.86	9.77	0.136	0.308
$\Delta\mathcal{B}$	. . .	. . .	. . .	. . .	. . .	. . .	0.96	1.06	1.07	1.13	0.036	0.036
Δv_r	. . .	. . .	. . .	. . .	. . .	. . .	5.92	0.87	1.35	0.39	0.001	0.006
1380m2GC11	0.005	0.088	−1.19	7.23	−4.22	1.09	3.32	6.83	2.00	0.62	0.082	0.227
$\Delta\mathcal{B}$	0.005	0.009	0.28	0.30	0.37	0.38	0.40	0.47	0.47	0.50	0.014	0.014
Δv_r	0.072	0.038	0.79	0.74	1.82	0.63	0.92	0.36	0.43	1.41	0.014	0.008
1380m2GC13	−0.218	−0.241	2.51	4.10	−8.04	4.79	4.93	0.42	3.61	9.04	0.146	0.403
$\Delta\mathcal{B}$	0.014	0.023	0.89	0.98	1.18	1.20	1.23	1.42	1.43	1.49	0.039	0.040
Δv_r	0.072	0.165	0.35	0.48	5.15	0.77	2.28	8.39	0.63	2.57	0.093	0.065
1380m2GC14	0.066	0.130	1.23	6.17	0.46	1.43	2.46	3.88	1.90	6.15	0.086	0.257
$\Delta\mathcal{B}$	0.003	0.005	0.17	0.19	0.23	0.24	0.26	0.30	0.30	0.32	0.009	0.010
Δv_r	0.004	0.040	0.15	0.27	1.04	0.21	1.06	0.85	0.16	0.95	0.012	0.009
1380m2GC15	0.031	0.047	2.32	5.49	4.06	1.94	1.70	5.24	2.08	5.38	0.076	0.200
$\Delta\mathcal{B}$	0.007	0.010	0.33	0.38	0.45	0.46	0.51	0.57	0.58	0.62	0.018	0.019
Δv_r	0.003	0.008	0.23	0.39	3.43	0.37	1.96	0.27	0.41	2.42	0.010	0.011
1380m2GC19	0.107	0.117	1.01	3.59	−0.94	1.16	3.18	4.78	1.00	3.97	0.129	0.269
$\Delta\mathcal{B}$	0.001	0.001	0.04	0.05	0.07	0.08	0.08	0.11	0.11	0.12	0.003	0.003
Δv_r	0.004	0.011	0.09	0.26	0.19	0.67	0.12	0.42	0.13	0.16	0.011	0.007
1380m2GC21	−0.066	−0.065	2.02	4.15	−1.86	0.08	2.15	0.99	1.06	3.54	0.061	0.165
$\Delta\mathcal{B}$	0.002	0.004	0.14	0.16	0.20	0.21	0.22	0.27	0.27	0.30	0.007	0.008
Δv_r	0.005	0.027	0.13	0.51	1.62	0.23	0.66	1.59	0.19	0.56	0.002	0.002
1380m2GC22	. . .	. . .	0.25	6.85	2.72	2.98	4.01	6.58	2.19	. . .	0.042	0.234
$\Delta\mathcal{B}$	. . .	. . .	0.42	0.47	0.57	0.59	0.64	0.75	0.76	. . .	0.027	0.028
Δv_r	. . .	. . .	0.59	0.65	1.98	0.04	1.59	1.65	1.36	. . .	0.014	0.011
1380m2GC23	0.052	0.045	0.17	2.65	0.16	1.68	−1.80	4.62	2.37	−1.48	0.054	0.171
$\Delta\mathcal{B}$	0.006	0.008	0.26	0.30	0.39	0.40	0.44	0.51	0.52	0.57	0.016	0.017
Δv_r	0.049	0.060	0.47	1.73	3.74	1.76	1.31	5.15	0.21	1.82	0.012	0.022
1380m2GC26	0.213	0.307	0.01	5.97	−4.95	−2.06	3.51	. . .	−0.25	6.78	0.011	0.135
$\Delta\mathcal{B}$	0.007	0.010	0.28	0.35	0.43	0.45	0.47	. . .	0.55	0.59	0.017	0.018
Δv_r	0.016	0.024	0.18	1.05	0.81	0.68	1.16	. . .	0.39	0.30	0.001	0.003
1380m2GC27	0.073	0.130	0.88	4.48	1.06	1.60	2.55	2.90	2.43	2.72	0.071	0.151
$\Delta\mathcal{B}$	0.002	0.003	0.09	0.10	0.12	0.13	0.13	0.16	0.16	0.18	0.005	0.005
Δv_r	0.032	0.047	0.01	0.13	1.82	0.47	0.31	0.51	0.18	0.10	0.007	0.007
1380m2GC30	0.046	−0.025	1.07	3.47	0.17	0.88	2.25	2.54	2.07	2.18	0.031	0.107
$\Delta\mathcal{B}$	0.001	0.002	0.07	0.08	0.10	0.10	0.11	0.14	0.15	0.16	0.004	0.004
Δv_r	0.045	0.052	0.05	0.53	2.03	0.39	0.51	0.12	0.16	0.46	0.001	0.001
1380m2GC33	0.135	0.101	0.13	4.40	0.69	2.36	3.77	5.62	2.35	6.49	0.093	0.273
$\Delta\mathcal{B}$	0.005	0.008	0.25	0.29	0.32	0.33	0.35	0.42	0.43	0.45	0.013	0.013
Δv_r	0.006	0.004	0.38	1.22	2.02	0.82	0.54	1.10	0.15	0.96	0.008	0.008
1380m2GC34	−0.026	−0.061	1.45	2.67	5.53	0.30	3.94	8.01	2.13	8.41	0.041	0.165
$\Delta\mathcal{B}$	0.009	0.013	0.45	0.51	0.58	0.60	0.64	0.73	0.74	0.79	0.022	0.023
Δv_r	0.019	0.034	0.61	0.19	3.67	0.27	0.93	0.83	0.17	0.37	0.025	0.017
1380m2GC35	0.055	0.046	0.48	4.68	−3.05	1.14	2.50	2.21	1.71	2.60	0.051	0.221
$\Delta\mathcal{B}$	0.004	0.005	0.19	0.21	0.24	0.25	0.27	0.31	0.31	0.33	0.009	0.010
Δv_r	0.022	0.008	0.05	0.55	1.38	0.32	0.27	0.25	0.23	1.21	0.002	0.004
1380m2GC36	0.145	0.176	0.79	6.66	1.48	0.11	3.54	4.49	−0.21	8.73	0.077	0.245
$\Delta\mathcal{B}$	0.005	0.007	0.21	0.24	0.30	0.31	0.34	0.44	0.45	0.48	0.013	0.013
Δv_r	0.028	0.039	0.13	0.47	3.02	0.64	0.32	0.49	1.01	2.49	0.001	0.003
1380m2GC37	−0.005	0.118	0.09	3.21	−6.00	0.46	5.90	. . .	−0.35	5.82	0.085	0.068
$\Delta\mathcal{B}$	0.005	0.008	0.28	0.33	0.40	0.41	0.44	. . .	0.53	0.57	0.016	0.016
Δv_r	0.080	0.067	0.23	0.18	1.07	0.80	0.41	. . .	1.14	0.84	0.004	0.008
1380m2GC38	0.051	0.058	1.47	4.89	−2.25	0.73	3.78	2.95	1.67	4.61	0.064	0.194
$\Delta\mathcal{B}$	0.002	0.003	0.11	0.12	0.15	0.16	0.18	0.21	0.22	0.24	0.007	0.007
Δv_r	0.005	0.018	0.21	0.08	0.34	0.46	0.44	1.23	0.55	0.64	0.015	0.010
1380m2GC42	0.096	0.124	0.96	7.13	−3.09	2.67	2.18	1.34	2.07	6.69	0.051	0.232
$\Delta\mathcal{B}$	0.005	0.007	0.23	0.25	0.31	0.33	0.35	0.42	0.42	0.46	0.013	0.014
Δv_r	0.009	0.009	0.97	0.91	1.75	0.53	0.41	3.26	0.09	1.01	0.011	0.007
1380m2GC43	0.006	0.053	2.58	5.45	−2.14	4.38	6.52	8.96	1.12	5.90	0.053	0.145
$\Delta\mathcal{B}$	0.005	0.008	0.26	0.30	0.37	0.38	0.41	0.46	0.47	0.52	0.014	0.015
Δv_r	0.027	0.023	0.44	1.94	2.92	0.79	1.59	0.46	1.12	0.28	0.005	0.005
1380m2GC45	0.001	−0.007	1.27	3.33	−2.07	0.74	0.27	0.75	2.04	1.82	0.014	0.060
$\Delta\mathcal{B}$	0.002	0.003	0.12	0.14	0.19	0.19	0.21	0.25	0.25	0.27	0.007	0.007
Δv_r	0.003	0.013	0.27	0.11	0.66	0.21	0.31	0.89	0.22	0.52	0.008	0.004

[a] $\Delta\mathcal{B}$: Bootstraped 1σ statistical error, Δv_r: systematic uncertainty due to radial velocity errors.

Table D.2: – continued. Lick indices Mgb – Hγ_F for **mask 1** of the **NGC 1380** globular clusters. Note that index TiO$_2$ is missing due to the limited wavelength coverage of the spectra.

cluster[a]	Mgb Å	Fe5270 Å	Fe5335 Å	Fe5406 Å	Fe5709 Å	Fe5782 Å	NaD Å	TiO$_1$ mag	Hδ_A Å	Hγ_A Å	Hδ_F Å	Hγ_F Å
1380m2GC03	4.13	3.98	−0.23	2.81	0.83	0.67	0.47	0.017	−2.76	1.94	−1.61	0.37
$\Delta\mathcal{B}$	0.68	0.69	0.70	0.71	0.72	0.72	0.73	0.021	0.78	0.81	0.83	0.84
Δv_r	0.23	0.76	0.59	1.10	0.25	0.26	2.79	0.018	0.24	0.78	0.52	0.18
1380m2GC05	5.08	0.42	0.96	−3.45	1.26	−0.51	...	...	...	...	...	...
$\Delta\mathcal{B}$	1.19	1.21	1.22	1.24	1.25	1.26	...	...	...	...	...	...
Δv_r	1.29	0.33	0.65	1.44	0.45	1.30	...	...	...	...	...	...
1380m2GC11	5.45	2.41	3.83	2.87	0.43	2.04	...	0.006	0.23	−5.30	−2.00	−1.90
$\Delta\mathcal{B}$	0.54	0.55	0.56	0.57	0.57	0.57	...	0.017	0.65	0.67	0.69	0.69
Δv_r	0.31	0.90	2.45	1.86	0.25	0.50	...	0.034	1.43	0.60	0.19	0.32
1380m2GC13	4.31	7.69	...	5.98	1.54	1.45	−0.77	...	7.90	−8.89	7.55	−8.16
$\Delta\mathcal{B}$	1.57	1.59	...	1.60	1.61	1.62	1.65	...	1.73	1.79	1.82	1.84
Δv_r	1.37	0.87	...	3.19	1.22	0.31	1.38	...	1.93	2.50	0.39	3.32
1380m2GC14	4.19	2.05	0.13	1.66	1.02	0.53	2.19	...	0.75	−4.65	0.06	0.06
$\Delta\mathcal{B}$	0.34	0.35	0.36	0.36	0.37	0.37	0.37	...	0.39	0.41	0.41	0.41
Δv_r	0.30	0.68	1.24	0.05	0.05	0.25	0.16	...	0.83	0.89	0.25	1.37
1380m2GC15	4.16	1.91	1.19	1.26	1.19	1.33	−0.63	0.025	−2.09	−5.72	0.19	−1.96
$\Delta\mathcal{B}$	0.67	0.68	0.69	0.70	0.70	0.70	0.71	0.021	0.76	0.80	0.81	0.82
Δv_r	0.79	0.07	0.62	0.30	0.34	0.30	0.87	0.005	0.49	0.39	0.12	0.29
1380m2GC19	3.99	2.48	2.04	1.20	0.84	0.66	...	...	−2.60	−2.66	−0.74	−1.51
$\Delta\mathcal{B}$	0.13	0.14	0.14	0.14	0.14	0.15	...	...	0.15	0.15	0.15	0.16
Δv_r	0.11	0.30	0.30	0.27	0.13	0.19	...	...	0.25	1.91	0.11	0.27
1380m2GC21	...	1.10	0.22	0.89	1.60	−0.43	...	...	2.30	−4.56	0.71	−1.82
$\Delta\mathcal{B}$	...	0.33	0.34	0.34	0.34	0.35	...	...	0.36	0.37	0.38	0.38
Δv_r	...	0.39	0.59	0.40	0.57	0.34	...	...	0.35	1.10	0.01	0.28
1380m2GC22	−1.60	−1.32	2.08	1.53	4.47	−0.78	1.26	...	−2.51	−2.34	2.07	−1.26
$\Delta\mathcal{B}$	0.93	0.96	0.97	0.98	0.99	1.00	1.02	...	1.10	1.15	1.17	1.18
Δv_r	4.83	3.38	0.71	1.01	1.84	0.58	3.35	...	0.36	0.46	0.70	0.07
1380m2GC23	−0.84	3.37	4.71	−1.44	0.77	...	...	...	2.96	−1.87	4.55	1.89
$\Delta\mathcal{B}$	0.64	0.65	0.67	0.68	0.68	...	...	...	0.70	0.72	0.72	0.73
Δv_r	0.46	1.30	0.40	0.62	0.43	...	...	...	0.11	2.60	0.58	2.00
1380m2GC26	1.65	0.04	1.92	2.90	...	...	...	...	−6.53	−1.93	0.73	−2.65
$\Delta\mathcal{B}$	0.63	0.65	0.66	0.67	...	...	...	...	0.71	0.74	0.76	0.76
Δv_r	0.74	0.53	0.09	0.08	...	...	...	...	1.52	0.27	1.48	0.01
1380m2GC27	2.65	2.34	1.41	0.97	0.20	0.48	1.85	...	−0.52	−1.69	1.30	0.46
$\Delta\mathcal{B}$	0.19	0.20	0.20	0.20	0.20	0.21	0.21	...	0.22	0.22	0.22	0.23
Δv_r	0.24	0.26	0.04	0.06	0.12	0.07	0.14	...	0.53	1.24	0.02	0.27
1380m2GC30	1.63	1.81	0.59	0.52	...	...	...	...	1.86	−1.03	1.74	0.61
$\Delta\mathcal{B}$	0.17	0.17	0.17	0.17	...	...	...	...	0.18	0.18	0.19	0.19
Δv_r	0.25	0.12	0.19	0.21	...	...	...	...	0.51	0.61	0.15	0.06
1380m2GC33	4.01	3.12	2.54	0.69	...	...	...	...	−6.46	−5.01	−1.02	−2.07
$\Delta\mathcal{B}$	0.47	0.48	0.48	0.49	...	...	...	...	0.53	0.55	0.56	0.56
Δv_r	0.13	0.29	0.34	0.43	...	...	...	...	0.54	2.56	0.81	1.17
1380m2GC34	3.56	3.37	2.02	4.48	...	...	...	...	−0.67	−6.79	1.17	−1.12
$\Delta\mathcal{B}$	0.89	0.90	0.92	0.93	...	...	...	...	0.95	0.98	1.00	1.01
Δv_r	0.14	0.12	0.21	0.13	...	...	...	...	0.45	1.88	0.45	0.67
1380m2GC35	3.18	3.07	1.98	0.72	...	...	...	...	−0.51	−4.26	−0.07	−0.63
$\Delta\mathcal{B}$	0.35	0.35	0.36	0.37	...	...	...	...	0.39	0.41	0.41	0.42
Δv_r	0.25	0.63	0.45	0.73	...	...	...	...	0.40	0.80	0.51	0.20
1380m2GC36	5.38	3.31	2.12	3.17	...	...	...	...	−4.99	−5.94	−1.39	−1.91
$\Delta\mathcal{B}$	0.51	0.52	0.53	0.53	...	...	...	...	0.56	0.58	0.59	0.60
Δv_r	0.12	1.09	0.02	0.25	...	...	...	...	0.64	1.04	0.25	0.94
1380m2GC37	2.38	3.32	−0.13	0.43	...	...	...	...	2.26	−0.55	1.37	−0.55
$\Delta\mathcal{B}$	0.61	0.62	0.63	0.64	...	...	...	...	0.66	0.69	0.70	0.71
Δv_r	1.42	0.34	0.04	0.13	...	...	...	...	0.12	0.33	0.64	0.26
1380m2GC38	3.00	1.34	1.21	1.92	1.37	...	...	...	−0.10	−2.17	0.75	−0.74
$\Delta\mathcal{B}$	0.26	0.27	0.27	0.28	0.28	...	...	...	0.29	0.30	0.30	0.31
Δv_r	0.44	0.45	0.14	0.13	0.53	...	...	...	0.12	0.81	0.17	0.22
1380m2GC42	3.38	3.64	1.54	...	...	...	...	...	−2.70	−0.97	−0.98	0.23
$\Delta\mathcal{B}$	0.50	0.51	0.52	...	...	...	...	...	0.55	0.57	0.57	0.58
Δv_r	0.33	0.10	0.22	...	...	...	...	...	0.61	2.32	0.29	0.81
1380m2GC43	2.47	1.83	0.28	0.17	...	...	...	...	0.74	−3.09	−0.27	−0.62
$\Delta\mathcal{B}$	0.58	0.59	0.60	0.61	...	...	...	...	0.63	0.65	0.66	0.66
Δv_r	0.51	1.59	0.78	0.56	...	...	...	...	0.50	3.36	0.62	1.16
1380m2GC45	1.66	1.29	0.43	1.66	0.81	...	...	...	1.39	0.67	1.26	1.53
$\Delta\mathcal{B}$	0.29	0.30	0.30	0.31	0.31	...	...	...	0.31	0.32	0.33	0.33
Δv_r	0.24	0.19	0.21	0.41	0.18	...	...	...	0.10	1.51	0.37	0.41

[a] $\Delta\mathcal{B}$: Bootstraped 1σ statistical error, Δv_r: systematic uncertainty due to radial velocity errors.

Table D.3: Lick indices CN_1 – Mg_2 for **mask 1** *and* **mask 2** of **NGC 2434** globular clusters.

cluster[a]	CN_1 mag	CN_2 mag	Ca4227 Å	G4300 Å	Fe4383 Å	Ca4455 Å	Fe4531 Å	Fe4668 Å	Hβ Å	Fe5015 Å	Mg_1 mag	Mg_2 mag
2434m1GC11	0.094	0.106	0.15	5.54	1.08	0.60	4.12	0.12	2.23	2.94	0.024	0.083
$\Delta\mathcal{B}$	0.002	0.003	0.11	0.12	0.15	0.15	0.17	0.20	0.21	0.22	0.006	0.006
Δv_r	0.043	0.058	0.15	0.83	0.48	0.15	0.54	0.23	0.10	0.41	0.022	0.028
2434m1GC19	0.026	0.013	1.01	5.25	4.48	2.43	3.10	1.87	1.55	7.75	0.087	0.219
$\Delta\mathcal{B}$	0.002	0.004	0.12	0.14	0.15	0.16	0.17	0.20	0.20	0.22	0.006	0.006
Δv_r	0.009	0.023	0.10	0.15	0.39	0.40	1.00	0.18	0.25	3.36	0.015	0.008
2434m1GC20	−0.066	−0.118	−0.14	4.46	−2.68	1.45	2.59	2.44	1.70	2.52	. . .	. . .
$\Delta\mathcal{B}$	0.001	0.002	0.07	0.08	0.10	0.10	0.11	0.13	0.14	0.15	. . .	. . .
Δv_r	0.041	0.031	0.05	0.37	0.31	0.47	0.46	0.12	0.12	0.52	. . .	. . .
2434m2GC29	0.014	0.025	2.90	2.10	0.94	2.27	2.67	3.47	2.15	2.38	0.081	0.121
$\Delta\mathcal{B}$	0.005	0.007	0.24	0.26	0.31	0.32	0.34	0.39	0.40	0.42	0.012	0.012
Δv_r	0.035	0.062	0.17	1.24	0.70	0.48	0.98	0.65	0.26	1.05	0.006	0.007
2434m2GC37	0.024	−0.034	1.63	7.45	4.89	2.56	4.51	3.93	3.04	0.61	. . .	. . .
$\Delta\mathcal{B}$	0.006	0.009	0.30	0.33	0.39	0.40	0.42	0.49	0.50	0.53	. . .	. . .
Δv_r	0.003	0.031	0.41	0.45	1.92	0.35	0.72	1.43	0.34	0.81	. . .	. . .
2434m2GC40	−0.017	−0.027	−4.20	0.70	−5.69	0.48	−2.04	−4.02	2.36	7.23	0.062	0.083
$\Delta\mathcal{B}$	0.007	0.012	0.41	0.46	0.56	0.58	0.62	0.72	0.72	0.76	0.019	0.020
Δv_r	0.022	0.028	0.88	1.55	1.34	0.18	0.79	3.19	0.07	0.97	0.008	0.004

[a] $\Delta\mathcal{B}$: Bootstraped 1σ statistical error, Δv_r: systematic uncertainty due to radial velocity errors.

Table D.3: – continued. Lick indices Mgb – Hγ_F for **mask 1** *and* **mask 2** of **NGC 2434** globular clusters.

cluster[a]	Mgb Å	Fe5270 Å	Fe5335 Å	Fe5406 Å	Fe5709 Å	Fe5782 Å	NaD Å	TiO$_1$ mag	Hδ_A Å	Hγ_A Å	Hδ_F Å	Hγ_F Å
2434m1GC11	1.61	0.72	0.85	−0.29	0.67	...	...	...	2.14	0.03	1.56	1.07
$\Delta\mathcal{B}$	0.25	0.25	0.26	0.26	0.26	...	...	...	0.27	0.28	0.29	0.29
Δv_r	0.26	0.24	0.75	0.18	0.04	...	...	...	2.02	0.85	0.35	0.22
2434m1GC19	2.94	2.56	1.27	1.14	0.96	0.08	2.09	0.026	2.05	−3.62	1.62	−2.78
$\Delta\mathcal{B}$	0.24	0.24	0.24	0.25	0.25	0.25	0.25	0.007	0.26	0.27	0.28	0.28
Δv_r	0.45	0.10	0.09	0.10	0.12	0.04	0.42	0.003	0.14	1.12	0.08	1.69
2434m1GC20	...	...	...	...	...	...	...	...	7.03	−0.10	2.37	0.69
$\Delta\mathcal{B}$	...	...	...	...	...	...	...	...	0.15	0.16	0.16	0.16
Δv_r	...	...	...	...	...	...	...	...	1.88	0.57	0.19	0.19
2434m2GC29	0.97	0.79	0.25	0.64	−0.73	0.96	...	...	2.89	2.61	3.90	2.48
$\Delta\mathcal{B}$	0.46	0.47	0.47	0.48	0.48	0.49	...	...	0.51	0.53	0.53	0.54
Δv_r	0.40	0.38	1.40	0.36	0.40	0.31	...	...	0.24	0.35	0.18	0.49
2434m2GC37	1.10	0.42	...	...	...	...	...	...	1.69	−5.73	3.50	−1.72
$\Delta\mathcal{B}$	0.54	0.56	...	...	...	...	...	...	0.58	0.60	0.61	0.61
Δv_r	0.06	0.79	...	...	...	...	...	...	0.32	0.86	0.77	0.63
2434m2GC40	2.94	4.66	1.45	0.43	−0.76	0.40	0.06	...	3.75	5.81	3.05	3.52
$\Delta\mathcal{B}$	0.82	0.83	0.84	0.85	0.86	0.86	0.87	...	0.90	0.92	0.93	0.94
Δv_r	0.27	0.53	0.45	0.14	0.46	0.16	0.14	...	2.17	1.23	0.34	0.39

[a] $\Delta\mathcal{B}$: Bootstraped 1σ statistical error, Δv_r: systematic uncertainty due to radial velocity errors.

Table D.4: Lick indices CN_1 – Mg_2 for **mask 1** of **NGC 3115** globular clusters.

cluster[a]	CN_1 mag	CN_2 mag	Ca4227 Å	G4300 Å	Fe4383 Å	Ca4455 Å	Fe4531 Å	Fe4668 Å	Hβ Å	Fe5015 Å	Mg_1 mag	Mg_2 mag
3115m1GC03	0.153	0.218	−1.50	4.32	6.17	2.87	2.85	8.25	2.43	2.65	0.104	0.201
$\Delta\mathcal{B}$	0.017	0.025	0.90	0.97	1.05	1.07	1.13	1.29	1.30	1.37	0.038	0.039
Δv_r	0.012	0.060	0.20	1.27	2.15	1.25	2.57	0.86	1.11	3.32	0.046	0.026
3115m1GC04	−0.071	−0.073	0.62	4.20	2.26	1.84	2.69	1.98	1.80	2.40	0.018	0.111
$\Delta\mathcal{B}$	0.006	0.008	0.29	0.33	0.42	0.43	0.45	0.53	0.54	0.58	0.015	0.016
Δv_r	0.023	0.030	0.16	0.09	2.39	0.28	0.07	0.13	0.52	0.16	0.009	0.007
3115m1GC05	0.059	−0.017	−0.16	1.74	−0.75	−0.79	1.67	4.69	1.82	4.35	0.066	0.029
$\Delta\mathcal{B}$	0.013	0.019	0.63	0.68	0.82	0.85	0.92	1.09	1.11	1.19	0.031	0.031
Δv_r	0.044	0.029	0.63	0.18	1.38	0.76	0.39	2.15	2.25	4.30	0.010	0.020
3115m1GC06	0.143	0.140	1.10	6.78	3.26	1.06	3.44	5.89	1.34	4.44	0.118	0.331
$\Delta\mathcal{B}$	0.006	0.009	0.28	0.33	0.38	0.39	0.41	0.47	0.47	0.52	0.017	0.017
Δv_r	0.030	0.026	0.12	0.53	1.23	0.19	0.37	1.39	0.07	1.89	0.001	0.002
3115m1GC08	0.072	0.013	2.12	6.47	5.49	1.21	1.40	4.35	2.29	6.54	0.085	0.311
$\Delta\mathcal{B}$	0.008	0.011	0.37	0.41	0.49	0.51	0.55	0.61	0.62	0.67	0.020	0.020
Δv_r	0.062	0.011	0.27	0.31	1.25	0.52	0.92	0.06	0.28	1.33	0.002	0.003
3115m1GC09	−0.036	−0.030	0.72	5.12	0.55	1.06	1.35	−4.78	3.38	2.24	0.064	0.109
$\Delta\mathcal{B}$	0.004	0.006	0.21	0.24	0.30	0.31	0.33	0.40	0.40	0.45	0.012	0.012
Δv_r	0.012	0.009	0.20	0.88	0.20	0.38	0.96	1.14	0.03	2.53	0.029	0.035
3115m1GC10	−0.002	0.055	1.79	3.57	3.75	1.64	5.85	. . .	0.89	−0.76	0.023	0.152
$\Delta\mathcal{B}$	0.007	0.011	0.38	0.45	0.54	0.56	0.61	. . .	0.76	0.86	0.022	0.023
Δv_r	0.035	0.006	0.08	0.86	1.41	1.46	0.84	. . .	0.28	0.68	0.063	0.094
3115m1GC11	0.001	0.052	0.86	2.95	−1.40	2.59	0.53	0.39	1.43	1.39	0.045	0.099
$\Delta\mathcal{B}$	0.005	0.007	0.24	0.28	0.34	0.35	0.37	0.44	0.45	0.48	0.013	0.014
Δv_r	0.043	0.067	0.12	0.12	0.34	0.04	0.36	0.75	0.66	1.03	0.031	0.022
3115m1GC12	−0.108	−0.108	−0.03	2.93	−1.48	1.51	2.83	2.38	2.66	2.51	0.056	0.140
$\Delta\mathcal{B}$	0.004	0.007	0.25	0.28	0.34	0.35	0.38	0.45	0.46	0.49	0.013	0.013
Δv_r	0.026	0.045	0.22	0.20	0.76	0.79	0.62	1.34	0.06	1.34	0.008	0.006
3115m1GC13	−0.013	−0.003	0.81	4.42	2.15	1.27	−0.43	3.73	1.61	3.47	0.014	0.148
$\Delta\mathcal{B}$	0.004	0.005	0.19	0.21	0.25	0.27	0.30	0.38	0.38	0.41	0.011	0.011
Δv_r	0.028	0.009	0.11	0.19	0.79	0.27	0.57	0.55	0.14	0.02	0.008	0.009
3115m1GC14	0.112	0.119	0.66	5.56	2.59	0.38	3.53	−0.07	2.09	6.06	0.114	0.270
$\Delta\mathcal{B}$	0.005	0.009	0.30	0.34	0.39	0.41	0.44	0.58	0.58	0.63	0.017	0.017
Δv_r	0.050	0.015	0.19	0.61	0.32	0.36	0.93	2.88	0.31	3.46	0.018	0.013
3115m1GC15	0.065	0.213	1.06	4.34	4.32	2.83	2.88	6.09	2.61	8.69	0.101	0.204
$\Delta\mathcal{B}$	0.010	0.014	0.43	0.47	0.53	0.55	0.58	0.64	0.65	0.70	0.021	0.022
Δv_r	0.022	0.101	0.09	0.22	0.04	2.14	0.53	0.83	0.00	1.96	0.032	0.031
3115m1GC16	−0.044	0.261	0.22	6.58	5.79	1.75	9.30	6.16	−1.58	−2.60	0.095	0.385
$\Delta\mathcal{B}$	0.015	0.022	0.62	0.68	0.80	0.83	0.88	1.06	1.08	1.17	0.035	0.036
Δv_r	0.243	0.091	0.19	0.99	0.66	1.18	2.30	0.90	0.98	2.07	0.003	0.004
3115m1GC17	0.007	−0.054	0.80	0.84	2.53	−0.41	0.76	0.54	3.33	8.27	−0.028	0.077
$\Delta\mathcal{B}$	0.010	0.016	0.55	0.62	0.69	0.70	0.75	0.84	0.86	0.95	0.026	0.026
Δv_r	0.026	0.005	0.14	0.77	1.31	0.53	0.79	0.92	1.12	2.61	0.002	0.001
3115m1GC18	−0.119	−0.040	−1.59	1.00	3.20	−0.65	5.14	6.91	4.74	1.42	−0.081	−0.081
$\Delta\mathcal{B}$	0.011	0.017	0.59	0.65	0.73	0.76	0.83	0.94	0.95	1.04	0.028	0.029
Δv_r	0.021	0.085	0.32	0.18	1.39	0.88	1.45	2.74	5.27	. . .	0.106	0.163
3115m1GC19	0.106	0.116	0.25	2.76	−2.89	−0.74	5.37	1.01	0.04	3.43	0.043	0.131
$\Delta\mathcal{B}$	0.006	0.010	0.30	0.36	0.46	0.48	0.51	0.60	0.61	0.65	0.018	0.019
Δv_r	0.005	0.007	0.51	0.93	1.94	0.54	2.55	2.96	0.70	0.77	0.009	0.019
3115m1GC21	. . .	. . .	. . .	. . .	1.64	3.39	8.42	−1.28	4.37	. . .	0.088	0.107
$\Delta\mathcal{B}$	. . .	. . .	. . .	. . .	1.18	1.23	1.31	1.51	1.54	. . .	0.055	0.056
Δv_r	. . .	. . .	. . .	. . .	4.65	1.48	3.81	2.16	0.44	. . .	0.001	0.003
3115m1GC22	0.047	−0.068	0.88	3.43	2.53	1.07	2.03	−2.59	1.53	2.82	0.023	0.108
$\Delta\mathcal{B}$	0.004	0.005	0.19	0.20	0.24	0.24	0.26	0.32	0.32	0.34	0.009	0.009
Δv_r	0.093	0.044	0.19	0.33	0.41	0.14	0.55	0.50	0.31	1.76	0.003	0.004

[a] $\Delta\mathcal{B}$: Bootstraped 1σ statistical error, Δv_r: systematic uncertainty due to radial velocity errors.

Table D.4: – continued. Lick indices Mgb – Hγ_F for **mask 1** of **NGC 3115** globular clusters.

cluster[a]	Mgb Å	Fe5270 Å	Fe5335 Å	Fe5406 Å	Fe5709 Å	Fe5782 Å	NaD Å	TiO$_1$ mag	Hδ_A Å	Hγ_A Å	Hδ_F Å	Hγ_F Å
3115m1GC03	2.85	4.76	1.87	0.54	1.65	−1.77	. . .	. . .	−1.13	−1.52	−2.99	0.10
Δ$\mathcal{B}$	1.46	1.48	1.50	1.51	1.53	1.54	. . .	. . .	1.60	1.67	1.72	1.73
Δv_r	0.58	0.59	0.91	1.15	0.70	0.68	. . .	. . .	1.36	1.02	1.88	0.50
3115m1GC04	0.97	2.29	−1.33	2.03	0.77	0.28	−0.45	0.029	2.50	0.79	2.45	2.66
Δ$\mathcal{B}$	0.62	0.63	0.65	0.65	0.66	0.66	0.68	0.019	0.72	0.75	0.75	0.76
Δv_r	0.40	0.34	1.17	0.52	0.23	0.17	0.80	0.007	1.49	0.30	0.16	0.42
3115m1GC05	2.51	2.99	3.41	3.06	0.80	0.51	. . .	. . .	−2.28	3.46	−1.31	3.23
Δ$\mathcal{B}$	1.26	1.29	1.32	1.33	1.35	1.36	. . .	. . .	1.42	1.46	1.48	1.49
Δv_r	2.61	1.55	0.48	1.09	0.70	0.17	. . .	. . .	0.37	1.34	0.26	0.75
3115m1GC06	4.53	3.54	2.30	1.77	0.54	1.43	. . .	. . .	−2.67	−7.76	−0.98	−1.87
Δ$\mathcal{B}$	0.54	0.55	0.56	0.56	0.57	0.57	. . .	. . .	0.62	0.66	0.68	0.69
Δv_r	0.53	0.11	0.71	0.45	0.75	0.42	. . .	. . .	1.07	1.29	0.51	0.31
3115m1GC08	2.82	2.68	2.10	2.21	−0.43	0.52	. . .	. . .	−2.61	−2.86	2.17	0.92
Δ$\mathcal{B}$	0.71	0.72	0.73	0.74	0.74	0.75	. . .	. . .	0.81	0.85	0.86	0.87
Δv_r	0.48	0.21	0.79	0.45	0.34	0.56	. . .	. . .	1.15	2.57	0.26	1.79
3115m1GC09	1.29	1.41	2.17	−0.27	. . .	. . .	. . .	. . .	−0.16	−0.33	−0.06	1.19
Δ$\mathcal{B}$	0.50	0.51	0.52	0.53	. . .	. . .	. . .	. . .	0.55	0.57	0.58	0.59
Δv_r	0.12	0.06	0.48	0.03	. . .	. . .	. . .	. . .	0.67	0.05	0.16	0.12
3115m1GC10	1.63	2.66	2.74	1.65	0.08	1.89	4.62	0.110	−0.50	0.83	1.02	1.23
Δ$\mathcal{B}$	0.97	0.99	1.02	1.03	1.05	1.06	1.10	0.032	1.18	1.22	1.23	1.24
Δv_r	1.53	0.25	1.24	0.49	0.79	0.98	0.87	0.025	3.18	0.96	0.34	1.42
3115m1GC11	1.90	1.08	−0.72	0.77	−0.73	0.89	−1.74	0.013	3.65	3.29	3.30	1.16
Δ$\mathcal{B}$	0.53	0.54	0.56	0.56	0.57	0.57	0.59	0.017	0.63	0.64	0.65	0.65
Δv_r	0.12	0.46	0.80	0.34	0.15	0.13	2.08	0.013	0.30	0.81	0.33	0.59
3115m1GC12	1.96	1.83	1.68	1.24	1.06	1.22	0.90	. . .	1.41	−1.24	2.07	−0.60
Δ$\mathcal{B}$	0.52	0.53	0.54	0.55	0.55	0.56	0.56	. . .	0.58	0.60	0.61	0.61
Δv_r	0.32	0.25	0.99	0.06	0.25	0.22	0.30	. . .	0.11	0.64	0.19	0.09
3115m1GC13	1.68	0.77	2.07	0.12	0.28	0.44	2.87	. . .	1.00	−1.13	1.53	0.81
Δ$\mathcal{B}$	0.43	0.44	0.45	0.45	0.45	0.46	0.46	. . .	0.48	0.50	0.51	0.51
Δv_r	1.26	0.67	0.18	0.20	0.44	0.07	2.01	. . .	0.01	0.35	0.14	0.12
3115m1GC14	3.47	3.55	2.85	−0.08	0.37	. . .	. . .	. . .	−5.67	0.29	−0.85	0.20
Δ$\mathcal{B}$	0.66	0.67	0.68	0.68	0.69	. . .	. . .	. . .	0.74	0.77	0.78	0.79
Δv_r	0.46	0.47	0.20	0.65	0.14	. . .	. . .	. . .	0.75	3.25	0.76	0.53
3115m1GC15	5.46	2.92	2.46	2.24	0.77	0.40	2.75	0.019	−1.55	−3.26	0.74	−1.98
Δ$\mathcal{B}$	0.75	0.76	0.77	0.78	0.79	0.79	0.81	0.025	0.86	0.91	0.92	0.93
Δv_r	1.26	1.91	0.07	0.96	0.39	0.15	0.59	0.004	0.24	1.14	0.26	0.38
3115m1GC16	4.24	5.37	2.18	0.46	0.12	−0.20	3.45	0.003	−2.86	−10.39	−1.46	−2.14
Δ$\mathcal{B}$	1.23	1.25	1.27	1.28	1.29	1.29	1.31	0.040	1.46	1.52	1.57	1.58
Δv_r	0.60	0.70	0.41	0.11	0.27	0.20	0.022		0.43	1.27	0.24	1.30
3115m1GC17	0.42	1.25	−0.66	−0.48	1.57	0.21	−1.15	. . .	5.14	−1.26	4.78	1.76
Δ$\mathcal{B}$	1.01	1.03	1.05	1.07	1.07	1.08	1.10	. . .	1.13	1.16	1.17	1.18
Δv_r	0.47	1.57	0.71	0.29	0.82	0.86	0.21	. . .	0.46	0.14	0.72	0.22
3115m1GC18	1.19	3.95	−1.21	1.92	1.06	−3.24	0.62	. . .	1.73	−4.34	2.88	−3.66
Δ$\mathcal{B}$	1.16	1.18	1.23	1.24	1.25	1.26	1.28	. . .	1.32	1.35	1.36	1.38
Δv_r	1.65	0.30	3.31	1.16	0.89	0.06	2.22	. . .	3.52	0.39	1.27	0.39
3115m1GC19	2.29	2.08	2.57	1.58	0.62	0.34	2.54	. . .	0.45	−1.99	0.99	−1.93
Δ$\mathcal{B}$	0.70	0.71	0.72	0.73	0.73	0.74	0.75	. . .	0.80	0.83	0.84	0.85
Δv_r	0.57	0.46	0.84	0.12	0.80	0.20	0.23	. . .	1.23	0.25	0.23	0.59
3115m1GC21	5.03	2.26	4.80	−1.51	2.36	−3.63	. . .	. . .	. . .	−4.66	. . .	−3.61
Δ$\mathcal{B}$	1.79	1.84	1.87	1.89	1.91	1.92	. . .	. . .	. . .	2.18	. . .	2.28
Δv_r	0.55	0.80	1.75	0.82	0.37	0.64	. . .	. . .	. . .	0.29	. . .	1.60
3115m1GC22	2.24	1.29	0.31	−0.58	−0.61	0.50	−0.40	. . .	2.78	−1.05	2.50	1.47
Δ$\mathcal{B}$	0.36	0.37	0.38	0.38	0.39	0.39	0.40	. . .	0.41	0.43	0.43	0.44
Δv_r	0.17	0.19	0.52	0.09	0.04	0.50	0.55	. . .	0.34	0.29	0.08	0.48

[a] Δ$\mathcal{B}$: Bootstraped 1σ statistical error, Δv_r: systematic uncertainty due to radial velocity errors.

Table D.5: Lick indices CN_1 – Mg_2 for **mask 1** of **NGC 3379** globular clusters.

cluster[a]	CN_1 mag	CN_2 mag	Ca4227 Å	G4300 Å	Fe4383 Å	Ca4455 Å	Fe4531 Å	Fe4668 Å	$H\beta$ Å	Fe5015 Å	Mg_1 mag	Mg_2 mag
3379m1GC05	0.022	0.046	0.84	4.26	1.01	1.42	3.15	0.94	2.50	1.65	0.013	0.092
$\Delta\mathcal{B}$	0.001	0.002	0.05	0.06	0.07	0.08	0.09	0.11	0.11	0.12	0.003	0.003
Δv_r	0.026	0.046	0.03	0.22	0.17	0.24	0.57	0.25	0.19	0.49	0.005	0.002
3379m1GC09	−0.023	−0.018	0.97	2.84	0.86	1.24	0.87	1.43	1.92	1.81	0.004	0.068
$\Delta\mathcal{B}$	0.001	0.001	0.03	0.04	0.05	0.05	0.06	0.08	0.08	0.09	0.002	0.002
Δv_r	0.014	0.021	0.05	0.90	0.31	0.13	0.40	0.15	0.17	0.26	0.000	0.000
3379m1GC10	0.011	−0.054	0.89	5.89	−0.37	1.22	2.63	−0.14	−0.81	2.88	0.030	0.126
$\Delta\mathcal{B}$	0.004	0.006	0.21	0.23	0.29	0.30	0.32	0.37	0.37	0.41	0.011	0.011
Δv_r	0.031	0.049	0.32	0.78	1.28	0.50	0.42	0.29	0.70	1.02	0.057	0.036
3379m1GC11	−0.013	−0.039	0.73	3.46	0.34	1.31	1.39	1.47	2.50	1.78	0.023	0.072
$\Delta\mathcal{B}$	0.001	0.002	0.07	0.08	0.09	0.10	0.11	0.13	0.13	0.14	0.004	0.004
Δv_r	0.015	0.016	0.18	0.17	0.23	0.20	0.30	1.77	0.50	0.25	0.005	0.003
3379m1GC12	0.226	0.200	−0.29	7.67	3.72	1.72	1.06	5.51	1.59	4.40	0.111	0.277
$\Delta\mathcal{B}$	0.005	0.006	0.17	0.20	0.24	0.25	0.27	0.32	0.32	0.34	0.010	0.011
Δv_r	0.056	0.023	0.13	0.51	0.11	0.31	0.86	1.39	0.65	0.77	0.032	0.020
3379m1GC13	−0.002	0.008	1.73	4.16	1.59	1.28	3.27	4.18	1.46	3.38	0.017	0.091
$\Delta\mathcal{B}$	0.002	0.003	0.11	0.12	0.14	0.15	0.16	0.19	0.20	0.22	0.006	0.006
Δv_r	0.012	0.024	0.03	0.39	0.32	0.17	1.10	0.06	0.04	0.33	0.016	0.019
3379m1GC14	0.037	0.018	0.85	4.10	2.26	1.46	3.41	−0.60	0.81	4.19	0.047	0.166
$\Delta\mathcal{B}$	0.002	0.003	0.10	0.12	0.15	0.15	0.17	0.20	0.20	0.22	0.006	0.006
Δv_r	0.007	0.021	0.22	0.13	0.09	0.30	0.41	0.71	0.27	0.70	0.004	0.001
3379m1GC15	0.089	0.145	1.72	5.93	6.81	2.20	4.89	7.83	0.59	−5.72	. . .	. . .
$\Delta\mathcal{B}$	0.003	0.004	0.14	0.15	0.20	0.21	0.22	0.26	0.27	0.31	. . .	. . .
Δv_r	0.016	0.015	0.17	0.38	1.49	0.82	0.60	0.38	0.11	2.26	. . .	. . .
3379m1GC18	0.014	0.019	0.87	3.77	1.32	1.66	2.14	1.39	2.11	3.20	0.049	0.145
$\Delta\mathcal{B}$	0.000	0.001	0.02	0.03	0.04	0.04	0.04	0.05	0.05	0.05	0.001	0.001
Δv_r	0.011	0.025	0.10	0.54	0.24	0.23	0.28	0.17	0.36	0.91	0.014	0.010
3379m1GC19	0.023	0.042	2.16	5.86	3.32	0.30	3.69	−0.33	1.51	5.73	0.041	0.156
$\Delta\mathcal{B}$	0.003	0.004	0.15	0.17	0.21	0.22	0.24	0.29	0.30	0.32	0.008	0.009
Δv_r	0.028	0.004	0.31	0.31	0.48	0.38	0.55	3.73	0.08	0.93	0.011	0.008
3379m1GC20	0.214	0.180	1.64	4.04	3.64	1.12	3.34	7.43	2.58	7.81	0.061	0.227
$\Delta\mathcal{B}$	0.003	0.004	0.12	0.13	0.16	0.16	0.18	0.21	0.21	0.22	0.007	0.007
Δv_r	0.014	0.033	0.21	0.95	0.46	0.36	1.52	0.83	0.04	1.69	0.004	0.002
3379m1GC22	0.192	0.116	1.43	4.26	4.13	1.87	4.79	3.82	1.59	6.64	0.090	0.251
$\Delta\mathcal{B}$	0.003	0.005	0.14	0.15	0.17	0.18	0.20	0.24	0.24	0.27	0.008	0.008
Δv_r	0.052	0.034	0.33	0.82	0.49	0.33	0.87	0.45	0.12	2.07	0.001	0.001
3379m1GC23	−0.006	0.020	0.83	4.65	1.60	1.24	2.64	1.06	0.52	−2.09	0.060	0.116
$\Delta\mathcal{B}$	0.001	0.002	0.06	0.06	0.08	0.08	0.08	0.10	0.10	0.12	0.003	0.003
Δv_r	0.019	0.012	0.12	0.30	0.67	0.11	0.15	0.50	0.21	0.25	0.007	0.004
3379m1GC24	0.044	0.063	1.06	3.99	1.86	1.41	2.79	2.03	1.94	3.99	0.057	0.166
$\Delta\mathcal{B}$	0.001	0.001	0.04	0.05	0.06	0.06	0.07	0.09	0.09	0.10	0.003	0.003
Δv_r	0.005	0.015	0.08	0.61	0.43	0.50	0.36	0.25	0.15	0.52	0.010	0.007
3379m1GC26	0.060	0.011	0.21	3.70	−0.10	2.58	3.63	−3.55	2.47	2.06	0.006	0.132
$\Delta\mathcal{B}$	0.003	0.004	0.13	0.15	0.18	0.19	0.20	0.26	0.26	0.29	0.007	0.008
Δv_r	0.028	0.013	0.22	0.52	1.42	0.62	0.85	1.21	0.22	0.16	0.002	0.002
3379m1GC27	0.026	0.014	0.91	4.43	0.57	1.97	3.14	2.96	1.84	3.91	0.046	0.126
$\Delta\mathcal{B}$	0.002	0.003	0.09	0.10	0.13	0.13	0.14	0.16	0.17	0.18	0.005	0.005
Δv_r	0.004	0.006	0.12	0.15	0.39	0.47	0.49	0.04	0.05	0.17	0.012	0.004
3379m1GC30	−0.162	−0.161	0.75	2.12	3.33	0.93	1.88	−3.60	2.84	1.13	0.033	0.035
$\Delta\mathcal{B}$	0.004	0.006	0.21	0.24	0.29	0.30	0.32	0.38	0.38	0.42	0.011	0.011
Δv_r	0.006	0.023	0.25	0.89	0.12	0.05	1.10	0.89	0.08	2.01	0.005	0.006
3379m1GC33	−0.037	−0.017	0.57	2.06	0.20	1.04	0.87	0.51	1.81	1.24	−0.010	0.043
$\Delta\mathcal{B}$	0.001	0.001	0.05	0.06	0.07	0.07	0.08	0.11	0.11	0.12	0.003	0.003
Δv_r	0.032	0.045	0.04	0.92	0.68	0.04	0.80	0.34	0.27	0.14	0.007	0.008

[a] $\Delta\mathcal{B}$: Bootstraped 1σ statistical error, Δv_r: systematic uncertainty due to radial velocity errors.

Table D.5: – continued. Lick indices Mgb – Hγ_F for **mask 1** of **NGC 3379** globular clusters.

cluster[a]	Mgb Å	Fe5270 Å	Fe5335 Å	Fe5406 Å	Fe5709 Å	Fe5782 Å	NaD Å	TiO$_1$ mag	Hδ_A Å	Hγ_A Å	Hδ_F Å	Hγ_F Å
3379m1GC05	1.31	1.00	0.56	0.69	1.20	0.31	0.80	0.004	0.73	−0.60	1.75	1.01
$\Delta\mathcal{B}$	0.13	0.13	0.13	0.13	0.14	0.14	0.14	0.004	0.15	0.15	0.15	0.15
Δv_r	0.08	0.07	0.08	0.15	0.10	0.03	0.06	0.004	0.21	0.16	0.08	0.17
3379m1GC09	0.77	1.55	0.47	0.45	0.28	0.08	0.87	. . .	2.09	1.20	2.07	1.31
$\Delta\mathcal{B}$	0.09	0.10	0.10	0.10	0.10	0.10	0.10	. . .	0.11	0.11	0.11	0.11
Δv_r	0.15	0.05	0.06	0.09	0.08	0.05	0.14	. . .	0.04	0.33	0.15	0.19
3379m1GC10	2.23	3.05	3.77	−1.55	0.55	0.96	. . .	. . .	−0.64	0.53	3.30	−0.75
$\Delta\mathcal{B}$	0.45	0.46	0.46	0.47	0.47	0.48	. . .	. . .	0.49	0.51	0.52	0.53
Δv_r	0.41	0.89	0.74	1.33	0.37	0.17	. . .	. . .	0.23	1.15	0.86	0.60
3379m1GC11	1.66	2.27	0.65	0.63	0.65	0.62	. . .	. . .	2.51	0.80	1.62	0.76
$\Delta\mathcal{B}$	0.16	0.16	0.16	0.17	0.17	0.17	. . .	. . .	0.17	0.18	0.18	0.18
Δv_r	0.74	0.68	0.15	0.05	0.18	0.19	. . .	. . .	0.18	0.72	0.15	0.45
3379m1GC12	3.78	2.14	1.08	2.36	1.53	. . .	. . .	. . .	. . .	−4.55	. . .	−1.13
$\Delta\mathcal{B}$	0.38	0.38	0.39	0.39	0.40	. . .	. . .	. . .	. . .	0.44	. . .	0.46
Δv_r	0.14	0.44	0.26	0.34	0.16	. . .	. . .	. . .	. . .	1.43	. . .	0.59
3379m1GC13	0.57	0.36	0.09	0.27	1.38	0.20	0.79	. . .	1.34	0.55	1.38	1.62
$\Delta\mathcal{B}$	0.25	0.26	0.26	0.26	0.27	0.27	0.27	. . .	0.28	0.29	0.29	0.29
Δv_r	0.09	0.36	0.10	0.24	0.79	0.05	0.08	. . .	0.23	1.35	0.38	0.69
3379m1GC14	2.88	1.77	0.54	0.09	. . .	. . .	. . .	. . .	0.11	−1.44	1.16	0.95
$\Delta\mathcal{B}$	0.24	0.25	0.25	0.25	. . .	. . .	. . .	. . .	0.27	0.27	0.28	0.28
Δv_r	0.17	0.43	0.27	0.10	. . .	. . .	. . .	. . .	0.19	1.09	0.10	0.34
3379m1GC15	. . .	. . .	. . .	. . .	. . .	. . .	. . .	. . .	−2.83	−6.18	−0.29	−3.09
$\Delta\mathcal{B}$	. . .	. . .	. . .	. . .	. . .	. . .	. . .	. . .	0.33	0.35	0.36	0.36
Δv_r	. . .	. . .	. . .	. . .	. . .	. . .	. . .	. . .	0.43	0.56	0.32	0.56
3379m1GC18	2.19	1.35	0.77	0.33	0.63	. . .	. . .	. . .	0.76	−0.53	1.38	0.45
$\Delta\mathcal{B}$	0.06	0.06	0.07	0.07	0.07	. . .	. . .	. . .	0.07	0.07	0.07	0.07
Δv_r	0.19	0.36	0.10	0.47	0.12	. . .	. . .	. . .	0.11	0.26	0.12	0.10
3379m1GC19	2.09	2.15	1.58	1.42	0.62	0.15	1.89	. . .	−1.02	−4.86	0.42	−1.18
$\Delta\mathcal{B}$	0.34	0.35	0.35	0.36	0.36	0.36	0.37	. . .	0.39	0.40	0.41	0.41
Δv_r	0.82	0.66	0.47	0.10	0.62	0.01	0.62	. . .	0.06	0.71	0.26	0.05
3379m1GC20	4.96	1.48	2.18	0.70	0.32	1.22	2.64	. . .	0.01	−5.70	0.57	−0.38
$\Delta\mathcal{B}$	0.24	0.25	0.25	0.25	0.26	0.26	0.26	. . .	0.27	0.28	0.29	0.29
Δv_r	0.45	2.83	0.40	0.25	0.01	0.04	0.50	. . .	0.31	0.17	0.12	0.38
3379m1GC22	4.70	2.60	2.46	0.11	0.55	0.35	4.55	. . .	−0.86	−3.23	0.94	−0.71
$\Delta\mathcal{B}$	0.29	0.29	0.30	0.30	0.30	0.30	0.31	. . .	0.32	0.33	0.34	0.34
Δv_r	0.73	0.93	0.18	0.23	0.09	0.19	0.15	. . .	0.70	0.35	0.53	0.40
3379m1GC23	1.95	0.95	0.74	0.52	2.37	0.68	1.57	. . .	0.35	−0.50	1.20	0.50
$\Delta\mathcal{B}$	0.13	0.13	0.13	0.13	0.14	0.14	0.14	. . .	0.15	0.15	0.15	0.15
Δv_r	0.17	0.13	0.17	0.38	0.10	0.14	0.11	. . .	0.22	1.30	0.03	0.59
3379m1GC24	2.40	1.58	1.06	0.55	0.60	0.60	2.08	0.013	0.28	−1.47	1.57	−0.11
$\Delta\mathcal{B}$	0.11	0.11	0.12	0.12	0.12	0.12	0.12	0.003	0.13	0.14	0.14	0.14
Δv_r	0.18	0.15	0.22	0.11	0.04	0.09	0.16	0.008	0.08	0.34	0.01	0.27
3379m1GC26	0.98	−0.10	0.76	1.61	0.24	. . .	. . .	. . .	. . .	3.09	. . .	1.88
$\Delta\mathcal{B}$	0.31	0.32	0.33	0.34	0.34	. . .	. . .	. . .	. . .	0.36	. . .	0.37
Δv_r	0.30	0.79	0.41	0.22	0.16	. . .	. . .	. . .	. . .	1.33	. . .	0.50
3379m1GC27	2.12	0.50	1.73	0.88	0.47	0.58	. . .	. . .	−0.54	−1.72	0.49	−0.57
$\Delta\mathcal{B}$	0.20	0.20	0.21	0.21	0.21	0.21	. . .	. . .	0.22	0.22	0.23	0.23
Δv_r	1.17	0.61	0.59	0.18	0.08	0.01	. . .	. . .	0.52	0.17	0.47	0.34
3379m1GC30	1.41	−1.61	−0.74	−0.83	0.89	1.06	. . .	. . .	3.22	1.62	3.16	1.19
$\Delta\mathcal{B}$	0.45	0.47	0.49	0.49	0.50	0.50	. . .	. . .	0.55	0.56	0.56	0.57
Δv_r	0.50	0.56	1.79	0.54	0.34	0.35	. . .	. . .	0.70	0.73	0.27	0.43
3379m1GC33	0.89	0.63	0.33	0.11	. . .	. . .	. . .	. . .	2.43	1.70	2.24	1.59
$\Delta\mathcal{B}$	0.15	0.15	0.16	0.16	. . .	. . .	. . .	. . .	0.16	0.17	0.17	0.17
Δv_r	0.16	0.11	0.34	0.09	. . .	. . .	. . .	. . .	0.10	0.45	0.04	0.18

[a] $\Delta\mathcal{B}$: Bootstraped 1σ statistical error, Δv_r: systematic uncertainty due to radial velocity errors.

Table D.6: Lick indices CN_1 – Mg_2 for **mask 1** of **NGC 3585** globular clusters.

cluster[a]	CN_1 mag	CN_2 mag	Ca4227 Å	G4300 Å	Fe4383 Å	Ca4455 Å	Fe4531 Å	Fe4668 Å	$H\beta$ Å	Fe5015 Å	Mg_1 mag	Mg_2 mag
3585m1GC01	0.110	0.133	1.40	7.37	4.43	0.27	3.53	6.07	0.86	5.05	0.132	0.294
$\Delta\mathcal{B}$	0.002	0.003	0.11	0.12	0.15	0.15	0.16	0.18	0.18	0.19	0.006	0.006
Δv_r	0.004	0.015	0.17	0.88	1.47	0.41	0.03	1.57	0.25	0.52	0.013	0.008
3585m1GC03	−0.015	0.015	1.12	3.18	0.24	1.36	2.06	1.45	1.77	. . .	. . .	. . .
$\Delta\mathcal{B}$	0.001	0.001	0.03	0.04	0.04	0.05	0.05	0.06	0.06	. . .	. . .	. . .
Δv_r	0.012	0.030	0.09	0.92	0.36	0.34	0.21	0.32	0.07	. . .	. . .	. . .
3585m1GC04	0.172	0.184	1.50	7.14	2.70	1.94	4.99	7.34	0.43	4.11	0.105	0.276
$\Delta\mathcal{B}$	0.002	0.002	0.07	0.08	0.09	0.10	0.10	0.12	0.12	0.13	0.004	0.004
Δv_r	0.031	0.008	0.10	0.80	0.99	0.74	0.98	0.43	0.15	0.14	0.007	0.006
3585m1GC05	−0.013	0.054	0.70	5.17	3.04	2.00	5.35	8.09	1.25	2.93	0.099	0.151
$\Delta\mathcal{B}$	0.003	0.004	0.13	0.14	0.16	0.16	0.17	0.19	0.20	0.21	0.006	0.006
Δv_r	0.170	0.037	0.15	0.40	0.62	0.34	0.57	1.09	0.34	0.80	0.026	0.034
3585m1GC07	0.161	0.139	1.34	5.67	3.94	2.14	3.03	5.34	1.92	7.71	0.113	0.291
$\Delta\mathcal{B}$	0.001	0.001	0.03	0.04	0.05	0.05	0.05	0.06	0.06	0.07	0.002	0.002
Δv_r	0.010	0.014	0.06	0.40	0.19	0.26	0.61	0.10	0.31	1.31	0.005	0.008
3585m1GC11	−0.021	0.020	0.82	4.24	1.45	0.81	2.85	1.88	1.87	2.58	0.025	0.154
$\Delta\mathcal{B}$	0.001	0.002	0.06	0.07	0.08	0.08	0.09	0.11	0.12	0.13	0.003	0.004
Δv_r	0.018	0.010	0.02	0.12	0.29	0.02	0.54	0.86	0.13	0.89	0.028	0.029
3585m1GC12	0.069	0.066	1.33	5.49	1.25	2.36	3.24	5.13	1.46	4.53	0.085	0.237
$\Delta\mathcal{B}$	0.001	0.001	0.04	0.04	0.06	0.06	0.06	0.07	0.07	0.08	0.002	0.002
Δv_r	0.017	0.032	0.14	0.22	1.33	0.80	0.31	0.40	0.55	0.09	0.009	0.005
3585m1GC13	0.072	0.096	3.26	6.15	5.93	2.15	4.24	3.79	1.44	5.98	0.086	0.238
$\Delta\mathcal{B}$	0.002	0.003	0.09	0.10	0.12	0.13	0.14	0.17	0.18	0.19	0.005	0.005
Δv_r	0.026	0.019	0.24	0.14	0.60	0.57	0.42	0.84	0.46	0.29	0.007	0.005
3585m1GC14	0.152	0.200	1.91	6.16	4.48	1.42	3.02	4.89	1.62	1.78	0.033	0.161
$\Delta\mathcal{B}$	0.002	0.003	0.10	0.12	0.15	0.15	0.17	0.19	0.19	0.21	0.006	0.006
Δv_r	0.016	0.040	0.11	0.25	1.45	0.19	0.37	1.52	0.63	2.67	0.009	0.007
3585m1GC15	0.025	0.053	0.25	3.02	2.15	1.16	2.65	−0.00	1.31	3.23	0.029	0.069
$\Delta\mathcal{B}$	0.001	0.002	0.06	0.06	0.08	0.08	0.09	0.11	0.11	0.12	0.003	0.004
Δv_r	0.036	0.052	0.11	0.46	0.46	0.09	0.66	0.20	0.68	0.23	0.001	0.006
3585m1GC16	0.064	0.113	0.95	5.85	3.79	2.12	2.83	7.93	0.29	3.61	0.114	0.233
$\Delta\mathcal{B}$	0.002	0.002	0.08	0.08	0.10	0.10	0.11	0.13	0.14	0.15	0.004	0.004
Δv_r	0.035	0.018	0.16	0.62	0.80	0.64	0.46	0.51	0.26	0.75	0.011	0.007
3585m1GC18	0.045	0.029	1.29	3.93	−1.85	1.26	2.54	5.65	0.52	2.98	0.045	0.159
$\Delta\mathcal{B}$	0.002	0.003	0.10	0.11	0.14	0.15	0.16	0.19	0.19	0.21	0.005	0.006
Δv_r	0.080	0.009	0.14	0.26	0.49	1.26	1.06	1.41	0.52	0.22	0.006	0.007
3585m1GC19	0.106	0.141	1.76	4.16	0.68	0.46	3.87	5.53	1.32	5.58	0.034	0.200
$\Delta\mathcal{B}$	0.002	0.003	0.09	0.10	0.12	0.13	0.14	0.16	0.16	0.17	0.005	0.005
Δv_r	0.017	0.015	0.18	0.07	0.99	0.29	1.03	1.89	0.03	2.66	0.030	0.045
3585m1GC20	0.102	0.145	1.12	6.17	0.39	3.21	2.74	4.53	0.73	4.60	0.085	0.225
$\Delta\mathcal{B}$	0.001	0.002	0.07	0.07	0.09	0.09	0.10	0.12	0.12	0.13	0.004	0.004
Δv_r	0.032	0.041	0.22	0.17	0.79	0.18	0.28	0.36	0.17	1.42	0.005	0.018
3585m1GC21	−0.005	−0.037	−0.34	2.17	−1.82	1.53	1.26	0.31	1.80	3.03	0.030	0.057
$\Delta\mathcal{B}$	0.002	0.002	0.08	0.09	0.12	0.12	0.13	0.15	0.16	0.17	0.004	0.005
Δv_r	0.035	0.011	0.50	0.13	0.52	0.11	0.63	0.37	0.28	0.26	0.010	0.012
3585m1GC23	−0.089	−0.051	1.10	7.92	−4.54	0.11	0.09	−5.97	0.97	3.49	0.034	0.173
$\Delta\mathcal{B}$	0.002	0.004	0.14	0.15	0.19	0.20	0.23	0.29	0.30	0.31	0.008	0.008
Δv_r	0.013	0.025	0.49	0.62	2.87	1.40	0.89	5.14	0.57	0.36	0.009	0.021
3585m1GC24	0.006	−0.080	0.90	4.94	3.10	0.73	1.86	0.33	2.75	3.34	−0.000	0.058
$\Delta\mathcal{B}$	0.002	0.003	0.11	0.12	0.14	0.14	0.15	0.19	0.19	0.21	0.005	0.005
Δv_r	0.058	0.041	0.24	0.58	0.78	0.03	0.72	0.50	0.23	0.40	0.009	0.013
3585m1GC26	0.089	0.185	1.21	6.25	1.81	1.80	3.32	8.83	1.59	7.19	0.117	0.247
$\Delta\mathcal{B}$	0.002	0.003	0.10	0.11	0.13	0.14	0.15	0.18	0.18	0.20	0.005	0.005
Δv_r	0.009	0.074	0.57	0.92	0.26	0.60	0.60	1.49	0.46	1.62	0.007	0.005
3585m1GC30	−0.086	−0.062	1.03	4.04	−1.03	1.55	−2.13	2.16	1.66	−0.87	0.020	0.061
$\Delta\mathcal{B}$	0.002	0.003	0.10	0.11	0.13	0.14	0.15	0.18	0.18	0.20	0.005	0.005
Δv_r	0.008	0.006	0.29	0.87	0.36	0.19	0.19	2.38	0.40	0.65	0.005	0.006
3585m1GC33	−0.092	−0.016	0.35	3.56	2.60	1.95	2.58	. . .	. . .	. . .	. . .	. . .
$\Delta\mathcal{B}$	0.003	0.004	0.15	0.16	0.18	0.18	0.19	. . .	. . .	. . .	. . .	. . .
Δv_r	0.104	0.015	0.43	0.66	0.35	0.56	1.13	. . .	. . .	. . .	. . .	. . .

[a] $\Delta\mathcal{B}$: Bootstraped 1σ statistical error, Δv_r: systematic uncertainty due to radial velocity errors.

Table D.7: – continued. Lick indices Mgb – Hγ_F for **mask 1** of **NGC 3585** globular clusters.

cluster[a]	Mgb Å	Fe5270 Å	Fe5335 Å	Fe5406 Å	Fe5709 Å	Fe5782 Å	NaD Å	TiO$_1$ mag	Hδ_A Å	Hγ_A Å	Hδ_F Å	Hγ_F Å
3585m1GC01	4.05	2.32	2.64	2.23	0.19	1.66	5.81	...	−2.94	−7.52	−0.41	−2.51
$\Delta\mathcal{B}$	0.20	0.20	0.20	0.21	0.21	0.21	0.21	...	0.23	0.24	0.24	0.25
Δv_r	0.71	0.97	0.10	0.12	0.13	0.13	0.38	...	0.36	0.25	0.59	0.53
3585m1GC03	...	...	...	...	...	...	...	...	1.39	0.12	1.80	0.93
$\Delta\mathcal{B}$	...	...	...	...	...	...	...	...	0.24	0.24	0.25	0.25
Δv_r	...	...	...	...	...	...	...	...	0.23	0.26	0.13	0.07
3585m1GC04	4.06	3.49	2.73	2.17	1.03	1.23	4.61	0.028	−1.06	−5.29	0.83	−2.10
$\Delta\mathcal{B}$	0.14	0.14	0.14	0.14	0.14	0.15	0.15	0.004	0.17	0.17	0.17	0.18
Δv_r	0.14	0.62	0.12	0.07	0.08	0.28	0.44	0.008	0.54	0.95	0.19	0.25
3585m1GC05	3.51	2.64	−0.48	0.95	−0.11	1.27	...	...	−0.73	−5.92	1.72	−1.09
$\Delta\mathcal{B}$	0.24	0.24	0.25	0.25	0.25	0.25	...	...	0.27	0.28	0.28	0.28
Δv_r	0.16	0.53	1.37	0.31	0.17	0.34	...	...	0.35	0.69	0.33	1.95
3585m1GC07	4.32	3.50	2.87	1.57	1.33	1.03	...	...	−2.15	−6.41	−0.58	−2.14
$\Delta\mathcal{B}$	0.07	0.08	0.08	0.08	0.08	0.08	...	...	0.08	0.09	0.09	0.09
Δv_r	0.14	0.08	0.11	0.11	0.07	0.04	...	...	0.35	0.33	0.22	0.24
3585m1GC11	0.13	2.51	0.47	1.40	0.48	0.05	...	...	0.51	−0.85	0.98	0.24
$\Delta\mathcal{B}$	0.29	0.29	0.29	0.30	0.30	0.30	...	...	0.30	0.30	0.30	0.30
Δv_r	0.86	0.45	0.55	0.06	0.18	0.37	...	...	1.32	0.58	0.06	0.13
3585m1GC12	3.62	3.08	2.28	1.59	0.91	...	...	...	−1.05	−4.46	0.24	−1.37
$\Delta\mathcal{B}$	0.08	0.09	0.09	0.09	0.09	...	...	...	0.09	0.10	0.10	0.10
Δv_r	0.08	0.06	0.11	0.33	0.10	...	...	...	0.39	0.13	0.82	0.15
3585m1GC13	4.67	2.59	2.28	1.82	...	...	...	...	−3.73	−7.61	−0.80	−2.30
$\Delta\mathcal{B}$	0.20	0.21	0.21	0.21	...	...	...	...	0.23	0.23	0.24	0.24
Δv_r	0.30	0.19	0.79	0.48	...	...	...	...	1.07	0.28	0.16	0.77
3585m1GC14	3.90	1.90	0.79	1.10	0.60	0.70	...	...	−0.52	−5.13	0.99	−0.71
$\Delta\mathcal{B}$	0.22	0.22	0.22	0.23	0.23	0.23	...	...	0.24	0.25	0.25	0.26
Δv_r	1.12	0.14	0.49	0.20	0.12	0.61	...	...	0.53	0.09	0.10	0.16
3585m1GC15	0.42	0.86	0.58	0.49	0.46	−0.16	1.48	...	2.86	1.11	2.11	1.40
$\Delta\mathcal{B}$	0.15	0.15	0.16	0.16	0.16	0.16	0.16	...	0.17	0.17	0.17	0.18
Δv_r	0.17	0.24	0.66	0.29	0.39	0.08	0.67	...	0.64	0.12	0.16	0.13
3585m1GC16	3.84	2.37	1.39	1.70	...	...	...	...	−1.11	−3.44	−1.01	−0.96
$\Delta\mathcal{B}$	0.16	0.17	0.17	0.17	...	...	...	...	0.18	0.19	0.19	0.20
Δv_r	0.30	0.13	0.21	0.20	...	...	...	...	0.13	0.34	0.98	0.20
3585m1GC18	3.61	2.27	0.82	1.79	0.63	0.75	3.71	...	−0.02	−0.88	1.28	−1.06
$\Delta\mathcal{B}$	0.22	0.23	0.23	0.24	0.24	0.24	0.24	...	0.25	0.26	0.26	0.27
Δv_r	0.26	0.53	1.50	0.75	0.13	0.53	1.80	...	0.37	0.09	0.28	0.10
3585m1GC19	5.24	2.91	...	...	...	...	...	...	−2.93	−2.77	−1.45	−0.94
$\Delta\mathcal{B}$	0.19	0.20	...	...	...	...	...	...	0.22	0.22	0.23	0.23
Δv_r	0.08	0.23	...	...	...	...	...	...	1.07	0.76	0.25	0.09
3585m1GC20	4.01	2.42	2.23	1.96	1.07	0.36	4.44	0.043	−2.78	−5.31	−0.92	−1.18
$\Delta\mathcal{B}$	0.15	0.15	0.15	0.15	0.15	0.15	0.15	0.004	0.17	0.18	0.18	0.18
Δv_r	0.48	0.30	0.27	0.02	0.30	0.13	0.15	0.006	0.31	0.36	0.46	0.49
3585m1GC21	1.37	0.69	−0.51	1.38	...	...	...	...	0.85	1.14	1.31	1.04
$\Delta\mathcal{B}$	0.19	0.20	0.20	0.20	...	...	...	...	0.21	0.22	0.22	0.22
Δv_r	0.21	0.08	0.67	0.19	...	...	...	...	1.06	0.26	0.04	0.09
3585m1GC23	1.67	1.15	−1.20	1.73	−0.61	−0.42	...	...	3.47	−0.69	1.03	−0.05
$\Delta\mathcal{B}$	0.37	0.38	0.39	0.39	0.39	0.39	...	...	0.41	0.42	0.42	0.43
Δv_r	1.13	0.68	1.05	0.20	0.41	0.23	...	...	0.77	1.20	0.07	0.35
3585m1GC24	0.97	1.39	1.18	0.35	1.12	0.78	1.44	−0.030	3.08	−0.11	2.36	−0.00
$\Delta\mathcal{B}$	0.22	0.22	0.23	0.23	0.23	0.23	0.24	0.007	0.25	0.26	0.26	0.26
Δv_r	0.41	0.42	1.18	0.55	0.22	0.02	0.30	0.005	0.19	1.32	0.32	0.21
3585m1GC26	4.12	...	...	1.60	0.46	0.28	...	...	−0.97	−5.52	1.89	−2.15
$\Delta\mathcal{B}$	0.21	...	...	0.21	0.22	0.22	...	...	0.23	0.24	0.25	0.25
Δv_r	0.26	...	...	0.26	0.47	0.17	...	...	0.91	0.08	0.03	0.50
3585m1GC30	−0.09	1.88	1.32	1.07	1.20	0.34	4.67	...	2.71	0.11	1.54	0.96
$\Delta\mathcal{B}$	0.22	0.22	0.23	0.23	0.23	0.23	0.24	...	0.25	0.26	0.26	0.26
Δv_r	0.22	0.10	0.14	0.51	0.14	0.73	2.25	...	0.23	0.24	0.24	0.83
3585m1GC33	...	...	...	...	...	...	...	...	−3.46	−4.15	−1.93	−1.73
$\Delta\mathcal{B}$	...	...	...	...	...	...	...	...	0.29	0.30	0.30	0.30
Δv_r	...	...	...	...	...	...	...	...	0.59	0.88	0.48	0.58

[a] $\Delta\mathcal{B}$: Bootstraped 1σ statistical error, Δv_r: systematic uncertainty due to radial velocity errors.

Table D.8: Lick indices CN_1 – Mg_2 for **mask 1** of **NGC 5846** globular clusters.

cluster[a]	CN_1 mag	CN_2 mag	Ca4227 Å	G4300 Å	Fe4383 Å	Ca4455 Å	Fe4531 Å	Fe4668 Å	Hβ Å	Fe5015 Å	Mg_1 mag	Mg_2 mag
5846m1GC03	0.067	0.056	1.52	5.03	−1.19	1.14	2.16	−0.86	2.84	2.53	0.020	0.112
$\Delta\mathcal{B}$	0.002	0.003	0.09	0.11	0.14	0.14	0.16	0.19	0.20	0.21	0.006	0.006
Δv_r	0.003	0.032	0.18	0.73	1.51	0.08	0.38	0.39	0.35	0.34	0.005	0.006
5846m1GC04	0.230	0.269	1.28	5.98	4.91	1.55	4.06	7.49	1.71	5.52	0.159	0.353
$\Delta\mathcal{B}$	0.001	0.002	0.05	0.06	0.08	0.08	0.09	0.10	0.10	0.11	0.003	0.003
Δv_r	0.017	0.024	0.17	0.31	2.93	0.58	0.45	0.13	0.12	0.80	0.019	0.012
5846m1GC05	0.120	0.173	2.56	6.26	1.34	1.14	4.44	7.63	4.31	4.61	0.173	0.267
$\Delta\mathcal{B}$	0.003	0.004	0.13	0.14	0.18	0.19	0.20	0.24	0.24	0.25	0.007	0.008
Δv_r	0.041	0.008	0.08	1.43	0.36	0.67	0.83	0.16	0.17	1.69	0.012	0.014
5846m1GC06	0.117	0.061	1.22	3.72	−6.29	−0.15	1.29	2.83	−0.20	7.52	0.105	. . .
$\Delta\mathcal{B}$	0.003	0.005	0.15	0.18	0.22	0.23	0.24	0.28	0.29	0.31	0.008	. . .
Δv_r	0.064	0.010	0.16	1.11	1.73	0.17	1.07	2.94	0.68	1.31	0.015	. . .
5846m1GC08	0.055	0.079	1.22	5.13	0.43	1.72	2.48	2.88	1.77	5.55	0.060	0.178
$\Delta\mathcal{B}$	0.001	0.001	0.04	0.05	0.06	0.06	0.07	0.08	0.08	0.09	0.002	0.002
Δv_r	0.017	0.014	0.06	0.20	2.26	0.33	0.58	0.17	0.19	0.72	0.002	0.001
5846m1GC10	−0.005	0.057	−0.96	4.85	−5.04	−2.66	2.19	−1.53	2.84	9.82	0.069	0.024
$\Delta\mathcal{B}$	0.004	0.007	0.23	0.26	0.32	0.34	0.37	0.46	0.47	0.50	0.013	0.013
Δv_r	0.028	0.071	0.36	0.20	3.21	0.29	0.41	4.40	0.38	0.62	0.003	0.001
5846m1GC11	0.122	0.051	0.41	4.05	−1.14	2.23	3.39	1.65	1.36	5.04	0.058	0.173
$\Delta\mathcal{B}$	0.002	0.002	0.08	0.09	0.12	0.12	0.13	0.15	0.15	0.16	0.004	0.004
Δv_r	0.040	0.054	0.16	0.27	0.97	0.27	0.84	1.47	0.17	0.31	0.002	0.003
5846m1GC16	0.084	0.095	1.34	5.51	−2.68	0.16	3.56	4.56	0.38	4.60	0.063	0.190
$\Delta\mathcal{B}$	0.002	0.002	0.07	0.08	0.09	0.10	0.11	0.12	0.13	0.14	0.004	0.004
Δv_r	0.028	0.039	0.20	0.31	1.71	0.40	0.65	0.05	0.35	1.29	0.005	0.007
5846m1GC17	0.074	0.068	0.92	4.56	−0.54	1.61	4.13	2.41	1.45	3.43	0.062	0.155
$\Delta\mathcal{B}$	0.001	0.002	0.07	0.08	0.10	0.11	0.12	0.14	0.15	0.16	0.004	0.004
Δv_r	0.010	0.019	0.17	0.20	3.07	0.26	0.55	0.42	0.19	1.56	0.002	0.000
5846m1GC18	0.006	0.029	0.99	4.52	−3.42	1.47	0.84	1.15	1.87	3.81	0.033	0.103
$\Delta\mathcal{B}$	0.001	0.001	0.05	0.06	0.07	0.08	0.08	0.09	0.10	0.10	0.003	0.003
Δv_r	0.008	0.016	0.21	0.34	0.37	0.09	0.14	0.57	0.24	0.97	0.031	0.023
5846m1GC20	0.050	0.053	0.70	6.82	1.30	1.36	3.59	7.95	0.96	4.41	0.120	0.267
$\Delta\mathcal{B}$	0.001	0.001	0.04	0.05	0.06	0.07	0.07	0.10	0.10	0.11	0.003	0.003
Δv_r	0.033	0.035	0.28	0.20	0.64	1.38	0.05	0.68	0.42	1.21	0.012	0.009
5846m1GC21	0.044	0.074	0.97	4.05	0.31	1.98	4.09	2.01	1.57	3.17	0.058	0.156
$\Delta\mathcal{B}$	0.001	0.001	0.04	0.05	0.06	0.07	0.07	0.09	0.09	0.10	0.003	0.003
Δv_r	0.003	0.030	0.11	0.31	0.83	0.38	0.15	1.21	0.27	1.13	0.005	0.000
5846m1GC22	0.084	0.110	1.24	3.98	0.89	1.68	1.61	1.14	1.75	2.31	0.034	0.188
$\Delta\mathcal{B}$	0.002	0.003	0.09	0.10	0.12	0.12	0.13	0.16	0.16	0.17	0.005	0.005
Δv_r	0.058	0.020	0.19	0.58	2.33	0.61	0.52	1.20	0.82	0.63	0.002	0.002
5846m1GC23	−0.021	−0.015	0.78	3.75	1.37	0.32	1.49	−0.11	0.89	3.19	−0.004	0.088
$\Delta\mathcal{B}$	0.002	0.002	0.09	0.10	0.12	0.12	0.13	0.16	0.16	0.18	0.005	0.005
Δv_r	0.025	0.042	0.21	0.89	2.16	0.34	0.37	2.59	0.20	1.13	0.002	0.004
5846m1GC24	0.112	0.151	1.01	5.83	1.91	2.24	3.00	4.40	1.66	6.58	0.089	0.224
$\Delta\mathcal{B}$	0.001	0.001	0.04	0.05	0.06	0.06	0.07	0.08	0.08	0.09	0.002	0.002
Δv_r	0.024	0.028	0.04	0.04	1.07	0.73	1.08	0.34	0.08	1.87	0.001	0.001
5846m1GC25	0.111	0.147	1.58	5.85	−1.88	1.53	−1.16	7.01	2.67	−1.69	0.132	0.240
$\Delta\mathcal{B}$	0.004	0.007	0.21	0.23	0.28	0.29	0.31	0.38	0.38	0.40	0.011	0.011
Δv_r	0.038	0.014	0.45	0.17	0.14	0.60	1.21	1.37	1.09	1.02	0.027	0.020
5846m1GC26	0.040	0.063	0.21	5.21	−1.78	1.29	1.56	−1.52	0.94	3.28	−0.004	0.030
$\Delta\mathcal{B}$	0.002	0.003	0.10	0.12	0.15	0.15	0.17	0.23	0.24	0.25	0.006	0.006
Δv_r	0.029	0.022	0.16	0.18	2.00	0.33	1.45	0.95	0.38	0.92	0.007	0.009
5846m1GC27	0.153	0.135	1.31	5.88	2.82	1.44	3.68	5.95	1.81	5.03	0.117	0.283
$\Delta\mathcal{B}$	0.001	0.002	0.06	0.07	0.08	0.09	0.09	0.11	0.11	0.12	0.004	0.004
Δv_r	0.014	0.022	0.26	0.26	1.96	0.07	0.34	0.52	0.20	1.03	0.012	0.009
5846m1GC28	0.098	0.110	1.43	4.66	−1.22	1.56	3.54	2.86	1.89	4.38	. . .	. . .
$\Delta\mathcal{B}$	0.001	0.002	0.05	0.06	0.07	0.08	0.08	0.10	0.10	0.11	. . .	. . .
Δv_r	0.017	0.011	0.07	0.16	0.50	0.47	0.51	0.84	0.27	1.11	. . .	. . .
5846m1GC29	0.090	−0.018	1.74	2.38	1.13	4.42	3.59	3.67	3.28	0.76	0.046	0.125
$\Delta\mathcal{B}$	0.002	0.003	0.11	0.12	0.17	0.17	0.19	0.22	0.22	0.24	0.006	0.006
Δv_r	0.052	0.022	0.14	0.78	0.58	0.36	1.42	3.44	0.73	1.29	0.019	0.016
5846m1GC30	0.036	0.049	1.21	4.49	−0.89	0.98	2.89	2.58	1.68	4.12	0.042	0.167
$\Delta\mathcal{B}$	0.001	0.001	0.04	0.05	0.06	0.07	0.07	0.08	0.09	0.10	0.003	0.003
Δv_r	0.009	0.027	0.25	0.15	1.12	0.46	0.27	0.87	0.09	1.23	0.005	0.004
5846m1GC31	0.153	0.166	1.39	6.21	−1.84	1.31	4.25	4.37	1.06	6.90	0.087	0.256
$\Delta\mathcal{B}$	0.002	0.003	0.10	0.10	0.13	0.13	0.14	0.16	0.16	0.17	0.005	0.005
Δv_r	0.013	0.021	0.26	0.26	1.24	0.63	0.24	0.29	0.19	0.59	0.001	0.001
5846m1GC32	0.012	−0.025	0.76	3.40	−3.68	1.86	1.43	0.69	2.35	2.45	0.001	0.076
$\Delta\mathcal{B}$	0.001	0.001	0.05	0.06	0.08	0.08	0.09	0.11	0.11	0.12	0.003	0.003
Δv_r	0.057	0.018	0.25	0.73	0.76	0.09	0.28	0.27	0.06	0.54	0.009	0.008
5846m1GC33	−0.044	−0.107	0.10	. . .	. . .	. . .	. . .	. . .	1.70	6.86	0.043	0.138
$\Delta\mathcal{B}$	0.004	0.005	0.20	. . .	. . .	. . .	. . .	. . .	0.38	0.40	0.010	0.010
Δv_r	0.024	0.034	0.18	. . .	. . .	. . .	. . .	. . .	0.84	1.02	0.012	0.015
5846m1GC36	0.153	0.149	1.77	5.83	1.03	2.26	2.64	4.33	1.40	4.39	0.090	0.281
$\Delta\mathcal{B}$	0.002	0.002	0.07	0.08	0.09	0.10	0.10	0.13	0.13	0.14	0.004	0.004
Δv_r	0.019	0.010	0.28	0.49	1.15	0.51	0.14	0.77	0.21	0.25	0.020	0.015
5846m1GC37	0.133	0.192	0.53	7.02	−1.05	1.24	4.56	3.33	1.37	−0.18	0.091	0.256
$\Delta\mathcal{B}$	0.003	0.005	0.14	0.16	0.19	0.20	0.21	0.24	0.24	0.26	0.008	0.008
Δv_r	0.063	0.088	0.39	0.73	0.46	0.43	0.54	0.23	0.72	3.15	0.019	0.026
5846m1GC38	−0.042	−0.052	1.26	3.79	−0.36	1.51	2.42	2.89	1.93	4.53	−0.083	−0.056
$\Delta\mathcal{B}$	0.001	0.002	0.06	0.06	0.08	0.08	0.09	0.11	0.11	0.12	0.003	0.003
Δv_r	0.005	0.041	0.40	0.36	2.23	0.46	0.58	0.20	0.24	0.21	0.007	0.005
5846m1GC39	0.199	0.248	0.91	6.38	1.97	1.25	3.87	7.45	1.47	6.28	0.159	0.356
$\Delta\mathcal{B}$	0.001	0.001	0.03	0.04	0.05	0.05	0.06	0.07	0.07	0.08	0.002	0.002
Δv_r	0.003	0.019	0.34	0.35	1.34	0.96	0.80	0.19	0.12	0.54	0.005	0.003

[a] $\Delta\mathcal{B}$: Bootstraped 1σ statistical error, Δv_r: systematic uncertainty due to radial velocity errors.

Table D.8: – continued. Lick indices Mgb – Hγ_F for **mask 1** of **NGC 5846** globular clusters.

cluster[a]	Mgb Å	Fe5270 Å	Fe5335 Å	Fe5406 Å	Fe5709 Å	Fe5782 Å	NaD Å	TiO$_1$ mag	Hδ_A Å	Hγ_A Å	Hδ_F Å	Hγ_F Å
5846m1GC03	1.81	1.03	−0.01	−0.28	1.30	0.85	0.54	−0.005	−0.17	−0.87	1.57	1.49
Δ$\mathcal{B}$	0.23	0.23	0.24	0.24	0.25	0.25	0.25	0.007	0.27	0.28	0.28	0.28
Δv_r	0.61	0.21	0.58	0.72	0.15	0.59	0.72	0.002	0.18	0.27	0.21	0.63
5846m1GC04	5.66	3.06	2.21	1.92	. . .	. . .	. . .	. . .	−3.17	−5.52	−0.40	−2.16
Δ$\mathcal{B}$	0.12	0.12	0.12	0.12	. . .	. . .	. . .	. . .	0.13	0.14	0.14	0.14
Δv_r	0.27	0.46	0.21	0.18	. . .	. . .	. . .	. . .	0.65	0.91	0.24	0.32
5846m1GC05	2.29	. . .	. . .	. . .	. . .	. . .	. . .	. . .	2.37	−5.01	1.16	−1.58
Δ$\mathcal{B}$	0.27	. . .	. . .	. . .	. . .	. . .	. . .	. . .	0.30	0.31	0.32	0.32
Δv_r	0.12	. . .	. . .	. . .	. . .	. . .	. . .	. . .	0.23	0.49	0.47	0.22
5846m1GC06	. . .	4.02	3.33	1.60	−0.12	0.88	. . .	. . .	−0.75	−1.26	2.82	−0.98
Δ$\mathcal{B}$	. . .	0.33	0.33	0.34	0.34	0.34	. . .	. . .	0.36	0.37	0.38	0.38
Δv_r	. . .	0.58	0.41	0.07	0.40	0.48	. . .	. . .	0.36	2.05	0.17	0.21
5846m1GC08	3.05	1.67	1.24	1.14	1.02	0.58	. . .	. . .	−0.63	−1.39	0.68	0.05
Δ$\mathcal{B}$	0.10	0.10	0.10	0.10	0.10	0.10	. . .	. . .	0.11	0.11	0.12	0.12
Δv_r	0.38	0.63	0.04	0.05	0.20	0.01	. . .	. . .	0.03	1.83	0.10	0.40
5846m1GC10	0.45	2.89	1.16	−3.05	−1.34	. . .	. . .	. . .	−1.60	−2.67	−0.46	2.08
Δ$\mathcal{B}$	0.54	0.55	0.56	0.58	0.58	. . .	. . .	. . .	0.60	0.62	0.63	0.63
Δv_r	0.30	2.18	2.41	2.58	0.75	. . .	. . .	. . .	0.13	1.21	2.37	0.13
5846m1GC11	3.42	0.97	0.79	1.64	1.02	. . .	. . .	. . .	0.03	−1.16	1.78	0.20
Δ$\mathcal{B}$	0.17	0.18	0.18	0.18	0.18	. . .	. . .	. . .	0.19	0.20	0.20	0.20
Δv_r	0.08	0.72	0.70	0.30	0.15	. . .	. . .	. . .	0.17	2.19	0.35	0.29
5846m1GC16	1.86	1.17	1.52	0.68	. . .	. . .	. . .	. . .	−2.30	−5.93	0.14	−1.42
Δ$\mathcal{B}$	0.15	0.16	0.16	0.16	. . .	. . .	. . .	. . .	0.17	0.17	0.17	0.18
Δv_r	0.67	0.36	0.17	0.29	. . .	. . .	. . .	. . .	0.23	2.46	0.02	0.10
5846m1GC17	1.89	2.59	1.31	2.41	0.98	0.52	1.83	. . .	−2.00	−1.34	−0.00	0.40
Δ$\mathcal{B}$	0.17	0.17	0.17	0.17	0.18	0.18	0.18	. . .	0.18	0.19	0.19	0.19
Δv_r	0.48	0.46	0.23	0.32	0.49	0.14	0.13	. . .	0.09	0.93	0.31	0.09
5846m1GC18	0.99	1.14	0.31	0.72	1.03	0.30	1.36	0.002	1.05	−0.27	1.43	0.46
Δ$\mathcal{B}$	0.11	0.12	0.12	0.12	0.12	0.12	0.12	0.003	0.13	0.14	0.14	0.14
Δv_r	0.33	0.70	0.43	0.46	0.02	0.11	0.08	0.008	0.16	0.19	0.09	0.10
5846m1GC20	2.84	2.49	1.47	1.23	0.48	−0.01	. . .	. . .	−1.60	−5.70	−0.98	−2.14
Δ$\mathcal{B}$	0.11	0.12	0.12	0.12	0.12	0.12	. . .	. . .	0.13	0.13	0.13	0.14
Δv_r	0.33	0.56	0.87	0.08	0.10	0.38	. . .	. . .	0.20	1.86	0.16	0.48
5846m1GC21	1.48	2.00	1.51	1.06	0.17	0.35	. . .	. . .	−0.37	−1.02	1.64	0.60
Δ$\mathcal{B}$	0.11	0.11	0.11	0.11	0.11	0.12	. . .	. . .	0.12	0.12	0.12	0.13
Δv_r	0.63	0.39	0.10	0.16	0.39	0.11	. . .	. . .	0.39	0.32	0.68	0.48
5846m1GC22	2.33	1.96	0.66	1.20	1.05	0.12	0.92	−0.010	−1.03	−2.39	−0.19	1.54
Δ$\mathcal{B}$	0.18	0.18	0.19	0.19	0.19	0.19	0.19	0.006	0.21	0.22	0.22	0.22
Δv_r	0.24	0.28	0.10	0.18	0.24	0.45	0.32	0.006	0.70	2.17	0.28	1.78
5846m1GC23	1.46	1.82	0.50	0.56	. . .	. . .	. . .	. . .	0.74	−0.40	1.42	1.54
Δ$\mathcal{B}$	0.20	0.20	0.21	0.21	. . .	. . .	. . .	. . .	0.22	0.22	0.22	0.23
Δv_r	0.84	0.85	0.36	0.44	. . .	. . .	. . .	. . .	0.18	0.46	0.11	0.34
5846m1GC24	3.64	2.74	1.75	1.54	0.71	0.45	. . .	. . .	−1.51	−4.85	0.79	−0.95
Δ$\mathcal{B}$	0.10	0.10	0.10	0.10	0.10	0.10	. . .	. . .	0.11	0.11	0.11	0.11
Δv_r	0.16	0.11	0.07	0.33	0.07	0.16	. . .	. . .	0.02	0.38	0.38	0.42
5846m1GC25	3.84	2.05	3.25	3.34	1.18	−1.57	. . .	. . .	2.99	−1.26	4.88	1.12
Δ$\mathcal{B}$	0.43	0.44	0.44	0.45	0.45	0.45	. . .	. . .	0.47	0.49	0.49	0.50
Δv_r	0.23	0.43	0.01	0.40	0.55	0.22	. . .	. . .	0.81	0.94	0.62	0.33
5846m1GC26	−0.01	1.29	0.31	−1.28	0.43	0.73	. . .	. . .	1.28	−3.21	1.31	−0.63
Δ$\mathcal{B}$	0.28	0.29	0.29	0.30	0.30	0.30	. . .	. . .	0.31	0.32	0.32	0.32
Δv_r	0.17	0.17	0.21	0.87	0.27	0.41	. . .	. . .	1.12	1.92	0.25	0.11
5846m1GC27	4.68	2.68	1.91	1.93	. . .	. . .	. . .	. . .	−3.42	−6.75	0.36	−1.54
Δ$\mathcal{B}$	0.15	0.15	0.15	0.15	. . .	. . .	. . .	. . .	0.16	0.16	0.17	0.17
Δv_r	0.12	0.05	0.26	0.12	. . .	. . .	. . .	. . .	0.50	0.85	0.27	0.58
5846m1GC28	. . .	. . .	. . .	. . .	. . .	. . .	. . .	. . .	−2.10	−7.25	−0.36	−1.24
Δ$\mathcal{B}$	. . .	. . .	. . .	. . .	. . .	. . .	. . .	. . .	0.21	0.22	0.22	0.22
Δv_r	. . .	. . .	. . .	. . .	. . .	. . .	. . .	. . .	0.27	3.31	0.30	0.34
5846m1GC29	2.00	1.67	1.06	1.45	0.78	0.30	. . .	. . .	−0.73	2.10	1.45	1.35
Δ$\mathcal{B}$	0.26	0.26	0.26	0.27	0.27	0.27	. . .	. . .	0.28	0.29	0.30	0.30
Δv_r	0.28	0.23	1.01	0.59	0.09	0.15	. . .	. . .	0.88	0.18	0.15	0.11
5846m1GC30	3.87	1.99	1.19	1.35	0.90	0.52	. . .	. . .	0.07	−1.54	1.61	0.31
Δ$\mathcal{B}$	0.11	0.11	0.11	0.11	0.11	0.11	. . .	. . .	0.12	0.12	0.12	0.12
Δv_r	0.79	0.23	0.28	0.14	0.11	0.20	. . .	. . .	0.04	0.25	0.15	0.26
5846m1GC31	4.17	2.65	2.99	0.95	0.83	0.35	0.95	0.052	−2.02	−4.97	−0.26	−1.71
Δ$\mathcal{B}$	0.18	0.18	0.19	0.19	0.19	0.19	0.19	0.006	0.21	0.22	0.22	0.22
Δv_r	0.21	0.13	0.11	0.25	0.32	0.19	0.22	0.017	0.38	2.12	0.38	0.46
5846m1GC32	1.45	1.40	0.73	0.59	0.50	0.11	. . .	. . .	1.24	1.24	1.93	0.91
Δ$\mathcal{B}$	0.13	0.13	0.13	0.13	0.13	0.13	. . .	. . .	0.14	0.14	0.14	0.14
Δv_r	0.24	0.12	0.19	0.60	0.03	0.10	. . .	. . .	0.36	2.21	0.06	0.16
5846m1GC33	−0.49	1.66	0.88	−3.06	−1.88	0.01	0.21	. . .	2.50	. . .	0.49	. . .
Δ$\mathcal{B}$	0.44	0.45	0.46	0.47	0.47	0.48	0.48	. . .	0.49	. . .	0.51	. . .
Δv_r	1.52	0.72	1.62	2.49	1.54	0.52	9.76	. . .	0.36	. . .	0.02	. . .
5846m1GC36	4.53	3.25	2.55	1.66	0.43	0.01	. . .	. . .	−3.10	−4.76	0.22	−0.81
Δ$\mathcal{B}$	0.15	0.16	0.16	0.16	0.16	0.16	. . .	. . .	0.17	0.18	0.18	0.18
Δv_r	0.12	0.29	0.04	0.28	0.04	0.20	. . .	. . .	0.14	1.50	0.38	0.32
5846m1GC37	4.33	1.17	3.44	1.34	. . .	. . .	. . .	. . .	2.06	−4.01	0.64	−1.61
Δ$\mathcal{B}$	0.29	0.29	0.30	0.30	. . .	. . .	. . .	. . .	0.32	0.33	0.34	0.34
Δv_r	0.34	1.67	0.57	0.63	. . .	. . .	. . .	. . .	1.86	0.97	0.15	0.19
5846m1GC38	1.55	−2.70	−4.01	0.52	0.36	0.64	. . .	. . .	1.89	−1.38	2.18	0.28
Δ$\mathcal{B}$	0.13	0.13	0.13	0.13	0.13	0.14	. . .	. . .	0.14	0.14	0.14	0.15
Δv_r	0.18	0.10	0.08	0.40	0.27	0.07	. . .	. . .	0.20	0.22	0.18	0.05
5846m1GC39	5.52	2.53	2.49	1.95	1.20	0.78	. . .	. . .	−3.92	−5.76	−1.27	−1.86
Δ$\mathcal{B}$	0.08	0.08	0.09	0.09	0.09	0.09	. . .	. . .	0.09	0.10	0.10	0.10
Δv_r	0.09	0.30	0.09	0.23	0.06	0.17	. . .	. . .	0.30	0.36	0.50	0.50

[a] Δ$\mathcal{B}$: Bootstraped 1σ statistical error, Δv_r: systematic uncertainty due to radial velocity errors.

Table D.9: Lick indices CN_1 – Mg_2 for **mask 1** of **NGC 7192** globular clusters.

cluster[a]	CN_1 mag	CN_2 mag	Ca4227 Å	G4300 Å	Fe4383 Å	Ca4455 Å	Fe4531 Å	Fe4668 Å	$H\beta$ Å	Fe5015 Å	Mg_1 mag	Mg_2 mag
7192m1GC02	0.004	−0.050	−0.10	0.93	4.13	. . .	. . .	. . .	. . .	. . .	0.058	−0.048
$\Delta\mathcal{B}$	0.006	0.009	0.33	0.36	0.42	. . .	. . .	. . .	. . .	. . .	0.017	0.017
Δv_r	0.004	0.012	0.98	1.85	0.75	. . .	. . .	. . .	. . .	. . .	0.043	0.038
7192m1GC15	−0.012	0.020	1.03	4.83	−0.58	1.32	0.70	1.62	1.85	2.84	0.033	0.139
$\Delta\mathcal{B}$	0.002	0.003	0.10	0.11	0.14	0.14	0.15	0.17	0.17	0.18	0.005	0.005
Δv_r	0.024	0.061	0.13	0.71	1.48	0.33	0.33	0.62	0.33	0.71	0.000	0.002
7192m1GC16	0.028	0.050	1.06	4.51	3.36	1.39	2.56	1.97	2.02	3.32	0.080	0.175
$\Delta\mathcal{B}$	0.001	0.002	0.07	0.08	0.09	0.09	0.10	0.13	0.13	0.14	0.004	0.004
Δv_r	0.007	0.005	0.23	0.52	0.32	0.74	0.65	0.26	0.13	0.52	0.030	0.020
7192m1GC18	−0.066	−0.067	1.04	0.61	−0.68	0.57	3.97	2.83	2.42	5.01	0.085	0.163
$\Delta\mathcal{B}$	0.002	0.004	0.14	0.16	0.19	0.19	0.21	0.24	0.25	0.26	0.007	0.007
Δv_r	0.005	0.032	0.84	0.70	0.52	0.95	0.90	2.11	0.13	0.45	0.036	0.030
7192m1GC19	−0.073	−0.052	2.54	8.36	3.39	3.35	. . .	. . .	1.61	4.61	0.135	0.228
$\Delta\mathcal{B}$	0.002	0.003	0.11	0.12	0.17	0.17	. . .	. . .	0.22	0.25	0.007	0.007
Δv_r	0.036	0.015	0.17	0.28	2.18	1.38	. . .	. . .	0.69	2.17	0.004	0.003
7192m1GC20	−0.027	−0.046	0.89	5.53	3.42	1.63	1.79	3.02	2.52	4.66	0.086	0.207
$\Delta\mathcal{B}$	0.001	0.002	0.07	0.07	0.09	0.09	0.09	0.11	0.11	0.12	0.003	0.003
Δv_r	0.022	0.017	1.92	0.15	1.52	0.50	0.50	0.17	0.22	0.33	0.014	0.007
7192m1GC21	0.015	0.039	1.80	5.01	5.21	2.31	7.19	6.69	3.14	5.67	0.049	0.271
$\Delta\mathcal{B}$	0.003	0.005	0.16	0.18	0.21	0.22	0.23	0.27	0.28	0.29	0.008	0.009
Δv_r	0.094	0.093	0.45	0.87	0.54	0.49	0.21	0.74	0.54	0.56	0.022	0.020
7192m1GC22	−0.003	0.057	0.75	6.95	6.63	1.02	3.07	4.64	2.97	3.52	0.033	0.152
$\Delta\mathcal{B}$	0.003	0.004	0.15	0.17	0.22	0.23	0.25	0.28	0.29	0.32	0.009	0.009
Δv_r	0.038	0.041	0.16	0.50	0.92	0.30	0.70	0.85	0.78	2.67	0.003	0.004
7192m1GC23	−0.054	−0.076	0.45	4.49	1.15	0.62	4.81	−0.36	1.74	1.73	0.054	0.107
$\Delta\mathcal{B}$	0.002	0.003	0.10	0.11	0.14	0.15	0.15	0.19	0.19	0.21	0.005	0.005
Δv_r	0.021	0.035	0.05	0.85	1.17	0.09	0.26	0.51	0.32	0.43	0.002	0.002
7192m1GC31	−0.076	−0.086	0.63	5.23	1.54	3.43	4.40	6.25	2.73	0.53	0.020	0.113
$\Delta\mathcal{B}$	0.002	0.004	0.14	0.16	0.19	0.19	0.20	0.23	0.23	0.25	0.007	0.007
Δv_r	0.003	0.005	0.19	0.89	0.92	0.59	0.57	0.98	0.07	0.82	0.006	0.006

[a] $\Delta\mathcal{B}$: Bootstraped 1σ statistical error, Δv_r: systematic uncertainty due to radial velocity errors.

Table D.9: – continued. Lick indices Mgb – Hγ_F for **mask 1** of **NGC 7192** globular clusters.

cluster[a]	Mgb Å	Fe5270 Å	Fe5335 Å	Fe5406 Å	Fe5709 Å	Fe5782 Å	NaD Å	TiO$_1$ mag	Hδ_A Å	Hγ_A Å	Hδ_F Å	Hγ_F Å
7192m1GC02	1.43	7.00	1.18	−0.50	...	...	...	...	3.35	−4.52	1.87	−4.43
$\Delta\mathcal{B}$	0.84	0.85	0.86	0.86	...	...	...	...	0.88	0.91	0.92	0.93
Δv_r	0.10	0.96	0.34	0.37	...	...	...	...	2.05	1.14	0.47	0.92
7192m1GC15	3.23	0.78	1.71	0.63	0.65	1.06	1.09	...	3.28	2.48	3.80	−0.59
$\Delta\mathcal{B}$	0.20	0.20	0.20	0.21	0.21	0.21	0.21	...	0.22	0.23	0.23	0.24
Δv_r	0.31	0.23	0.09	0.54	0.49	0.25	0.44	...	0.07	0.46	0.36	2.12
7192m1GC16	1.73	2.58	1.83	1.88	0.11	0.15	...	...	0.19	0.18	0.85	1.12
$\Delta\mathcal{B}$	0.16	0.16	0.16	0.16	0.16	0.16	...	...	0.17	0.17	0.17	0.18
Δv_r	0.51	0.25	0.18	0.49	0.30	0.10	...	...	0.23	0.84	0.26	0.68
7192m1GC18	1.37	0.43	−0.25	2.43	2.89	...	...	...	0.89	1.29	1.07	0.19
$\Delta\mathcal{B}$	0.30	0.30	0.31	0.32	0.32	...	...	...	0.33	0.34	0.34	0.35
Δv_r	0.09	0.48	0.42	0.79	0.17	...	...	...	0.40	0.22	0.48	0.11
7192m1GC19	5.53	0.73	−1.49	...	...	...	...	...	−1.13	−0.69	0.98	1.24
$\Delta\mathcal{B}$	0.27	0.28	0.28	...	...	...	...	...	0.31	0.32	0.32	0.33
Δv_r	1.09	0.16	1.43	...	...	...	...	...	1.97	1.18	0.08	2.06
7192m1GC20	3.31	1.07	2.03	1.50	0.08	0.02	...	...	1.92	0.85	2.43	0.56
$\Delta\mathcal{B}$	0.13	0.13	0.13	0.14	0.14	0.14	...	...	0.14	0.15	0.15	0.15
Δv_r	0.46	1.45	0.05	0.09	0.20	0.12	...	...	0.06	1.32	0.02	0.72
7192m1GC21	3.64	2.44	1.86	3.33	1.57	1.65	4.86	...	−2.31	−3.32	0.10	−1.35
$\Delta\mathcal{B}$	0.31	0.31	0.32	0.32	0.32	0.32	0.33	...	0.35	0.36	0.37	0.38
Δv_r	0.25	0.52	0.58	0.39	0.23	0.46	0.29	...	3.38	0.71	0.40	0.49
7192m1GC22	1.43	8.35	−0.12	1.17	...	...	...	...	2.54	−3.79	1.64	−3.53
$\Delta\mathcal{B}$	0.35	0.36	0.37	0.38	...	...	...	...	0.39	0.41	0.42	0.42
Δv_r	0.08	0.23	1.03	0.32	...	...	...	...	2.58	0.29	0.17	3.50
7192m1GC23	1.92	1.95	0.22	0.91	−1.06	−0.17	...	...	−0.38	0.57	1.09	0.71
$\Delta\mathcal{B}$	0.22	0.23	0.23	0.23	0.24	0.24	...	...	0.25	0.25	0.26	0.26
Δv_r	0.07	0.41	0.51	0.36	0.30	0.42	...	...	0.05	0.16	0.13	1.16
7192m1GC31	1.90	0.61	1.70	0.90	0.70	1.51	2.52	0.055	−0.07	−0.62	−0.04	−0.15
$\Delta\mathcal{B}$	0.26	0.27	0.27	0.28	0.28	0.28	0.29	0.008	0.31	0.31	0.32	0.32
Δv_r	1.10	0.10	0.23	0.07	0.54	0.08	0.21	0.005	0.16	0.17	0.21	1.96

[a] $\Delta\mathcal{B}$: Bootstraped 1σ statistical error, Δv_r: systematic uncertainty due to radial velocity errors.

Appendix E

Objects #10 and #15 in the NGC 3115 Sample

In Chapter 4, for two objects no clear-cut classification could be achieved. In the following we discuss their spectra in detail.

Spectra of stars and globular clusters can partly be disentangled by means of relative line strengths of spectral features such as Balmer lines and Ca I (4227 Å) (Perelmuter et al. 1995). In globular cluster spectra the intensity of Balmer lines dominates in general the strength of the Ca I feature. This ratio approaches unity at high metallicities. On the other hand, dwarfs later than ∼G3 V show a strong Ca I feature relative to Balmer lines. This is illustrated in Figure E.1 where the spectra of objects #10 and #15 are compared with an average globular cluster spectrum (using bona-fide globular clusters in NGC 5846) and two stellar spectra of a late-type dwarf (K5 V) and a cool giant (K3 III).

The Ca I feature is not detectable in both object spectra (#10 and #15). However, judging by the relative strengths of the Mgb feature and the Balmer line Hβ both spectra are closer to the mean globular cluster spectrum than to both stellar spectra. This is less obvious for object #15 than for the spectrum of object #10.

The two objects have rather red colours: $I - K = 1.02$ and $B - K = 2.62$ for #10, and $I - K = 2.04$ and $B - K = 4.40$ for #15. The colours of object #10 are consistent with late-type G dwarfs. Object #15, on the other hand, is too red for its spectrum to be a dwarf. In this case strong molecular absorption bands would be detectable which is not the case. Its colours in combination with the type of the spectrum are rather consistent with a K giant (Cox 2000).

As an additional test we cross-correlate both object spectra with the two stellar spectra and the mean globular cluster spectrum and use the height of the cross-correlation peak (CCP) as a measure of similarity. It is important to note that the two stellar spectra and the mean globular cluster spectrum, which are considered as templates, have similarly high S/N values. For object #10, the test yields the highest CCP for the globular cluster spectrum. The spectra of object #15 and the K giant are most alike by means of this test. Both results are, however, not significantly different from the cross-correlations with the remaining template spectra.
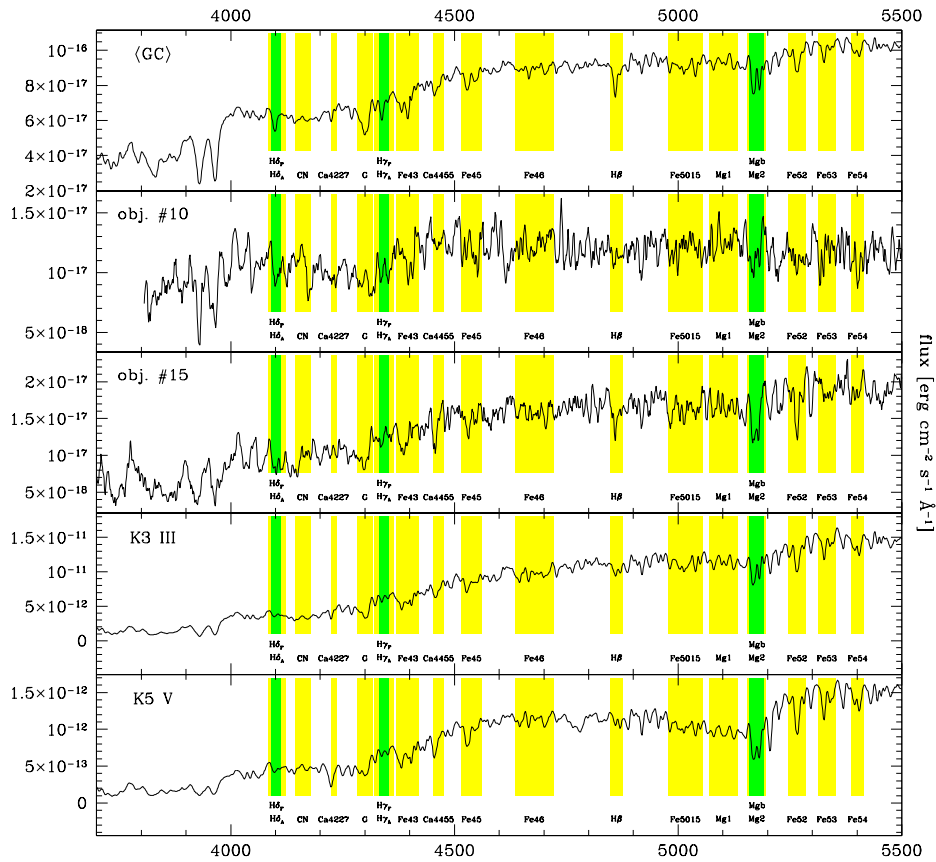
Figure E.1: Spectra from top to bottom: mean globular cluster spectrum of NGC 5846 globular clusters, object #10 and #15 in NGC 3115, a K3 giant, and a K5 dwarf spectrum. The latter two spectra were taken from our sample of Lick standard stars. All spectra are in rest frame and were smoothed to the Lick system resolution. Light shaded regions indicate feature passbands of Lick indices. Dark shaded regions indicate narrow passbands which overlap with broader passbands. The label for the narrow index is elevated.

Appendix F

Caveats

F.1 Introduction

Previous studies in the literature used a rather un-critical comparison of measurements with theoretical Lick index predictions to derive ages and metallicities of extragalactic globular clusters. Possibly due to a lack of high-quality data none of these studies troubled to discuss the relevant factors which can influence such determinations. In the following we address some caveats which can lead to biased age, metallicity, and abundance ratios predictions.

For the convenience of the reader we reproduce Figures 5.4 and 5.6 on the following pages as Figures F.1 and F.2, respectively.

F.2 Influence of the Blue Horizontal Branch at High Metallicities

The Balmer series is a measure of the mean temperature of turn-off stars. Its strength is therefore sensitive to age. However, horizontal branch (HB) stars have also strong influence on the Balmer line strength and, therefore, on spectroscopic age estimates (Rabin 1982; Buzzoni et al. 1994; Greggio 1997; de Freitas Pacheco & Barbuy 1995; Lee et al. 2000; Maraston & Thomas 2000). Depending on metallicity and mass-loss on the giant branch, the HB contributes $\sim 10 - 30\%$ to the total light of stellar populations with ages $\gtrsim 1$ Gyr (e.g. Renzini & Buzzoni 1986). Indeed, empirical evidence shows that HB stars become on average hotter as the mean cluster metallicity of Galactic globular clusters decreases. As a consequence, strong Balmer indices are expected for old and metal-poor stellar populations. This behaviour is implemented in our SSP models and is responsible for the overlapping of isochrones at old ages and very low metallicities (see Figs. F.1 and F.2). Thus, age determination are necessarily left ambiguous in this regime.

But the correlation between HB morphology and metallicity is not strict, as a yet-unknown "second parameter" can alter the HB morphology at a given metallicity (e.g. Renzini 1977; Greggio & Renzini 1990; van den Bergh 1993; Buonanno et al. 1997; Sweigart 1997; Sweigart & Catelan 1998; Soker & Hadar 2001; Rey et al. 2001). Two Milky Way globular clusters with relatively high metallicities show blue horizontal branches (NGC 6388 and NGC 6441 both at [Z/H] ~ -0.6) which cannot be explained by canonical stellar evolution models (Rich et al. 1997; Sweigart & Catelan 1998). This empirical evidence for *warm* horizontal branches at such high metallicities casts doubts on the accuracy of spectroscopic ages and metallicities of our extragalactic globular clusters. In fact, in Chapter 2 we measure a ~ 0.3 Å stronger

Figure F.1: Hγ_A vs. [MgFe]$'$ diagnostic plot for high-quality globular cluster spectra. SSP models from Chapter 3 have been overplotted for the metallicities [Z/H]=$-2.25, -1.35, -0.55, -0.33, 0.00$, 0.35, and 0.67 dex (dotted lines) and for ages 15, 10, 5, 3, 2, 1 (solid lines), and 0.8 Gyr (dashed line). The thick dotted line is an interpolated iso-metallicity track for [Z/H] $= -0.8$ and is used to split the sample between metal-poor and metal-rich globular clusters. The thick iso-age line is the 5 Gyr isochrone, and is used to split between old and formally young globular clusters.

Figure F.2: Hβ, Hδ_A, Hγ_F, and Hδ_F vs. [MgFe]$'$ diagnostic plots. Model predictions were taken from Chapter 3. As a guide to the eye the 5 Gyr isochrone and the -0.8 dex iso-metallicity track are plotted as thicker lines.

Hβ index for the photometrically determined old age of both these clusters, compared to old clusters at similar metallicities which show only red horizontal branches (Rich et al. 1997). Moreover, in Chapter 3 we find that $\sim 10\%$ of horizontal branch stars bluewards of the instability strip can explain the offset in Balmer line indices.

To estimate the effect of a varying horizontal branch morphology on Balmer indices, we parameterize the HB morphology with the HBR parameter. This parameter is defined in Lee et al. (1994) as HBR = (B$-$R)/(B+V+R), where B and R are the number of stars bluewards and redwards of the instability strip. V is the number of variable stars inside the instability strip. HBR = 1 indicates an entirely blue and HBR = -1 and entirely red horizontal branch. For Milky Way globular clusters we use data from Chapter 2 and complement them with data from Trager et al. (1998). Data for globular clusters in the Large Magellanic Cloud were taken from Beasley et al. (2002). We derive HBR parameters for globular clusters in M31 using HST data[1] (GO:6671, Rich et al. 2003). Corresponding Balmer index measurements are taken from Puzia et al. (2003b) and are complemented by data from Trager et al. (1998).

Figure F.3 shows that blue horizontal branches produce significantly stronger Balmer indices (cf. Fig. 2.9). The sequences show in each panel are basically sequences of metallicity. The scatter can be attributed to the "second parameter". We parameterise the data by metallicity: solid symbols denote globular clusters with [Z/H] > -0.6. The range in Balmer indices spanned by the entire data set is 1.9 Å for Hβ, 9.0 Å for Hγ_A, 4.1 Å for Hγ_F, 6.5 Å for Hδ_A, and 4.3 Å for Hδ_F. Note that the HBR parameter saturates for extremely red and blue horizontal branches[2] which implies that the previous variations are lower limits.

We use the globular clusters NGC 6388 and NGC 6441 and clusters at similar metallicity with an entirely red HB (e.g. NGC 6356 and NGC 6637) to derive a representative "second parameter" variation in Balmer line indices. As this approach is fully empirical and based on the largest HB morphology fluctuation which is locally observed, we have no guarantee that even more extreme HB morphologies for globular clusters at a given metallicity exist outside the Local Group. We find offsets of 0.4 Å in Hβ, 3.3 Å in Hγ_A, 1.4 Å in Hγ_F, 2.0 Å in Hδ_A, and 1.0 Å in Hδ_F between metal-rich globular clusters with entirely red HBs and NGC 6388 and NGC 6441. The HB morphology has negligible effect on the [MgFe]$'$ index. Using a 15 Gyr old stellar population as reference, these offsets correspond to age variations $\Delta t = 10$ Gyr for Hβ, 13.5 Gyr for Hγ_A and Hδ_A, and 12.5 for Hγ_F and Hδ_F. Consequently, the scatter in Figures F.1 and F.2 towards formally young ages might well be, at least partly, the result of HB morphology variations.

F.3   Influence of Satellite Lines?

Independent of model predictions, a consistency check of the data distribution in all five age/metallicity diagnostic plots in Figures F.1 and F.2 can be performed by comparing the residuals with respect to linear fits to the data. We find that residuals correlate well within index families, that is between Hγ_A and Hγ_F (Spearman correlation coefficient $R = 0.48$ with 99.9% significance), and Hδ_A and Hδ_F ($R = 0.62$, 99.9%). The correlations degrade down to $R \approx 0.3$ (with $\gtrsim 98\%$ significance), when index residuals of two different Balmer line index families are compared (e.g. Hγ_A and Hδ_A). The scatter in all these residual correlations is significant.

All plots in Figure 5.6 show a considerable fraction of data below the model grid, indicating excessively old formal ages ($\gg 15$ Gyr). This behaviour, which is most

---

[1]kindly provided by Michael Rich.

[2]Alternative non-saturating horizontal branch morphology parameter exist (e.g. Fusi Pecci et al. 1993), but are available for only a few globular clusters used here.
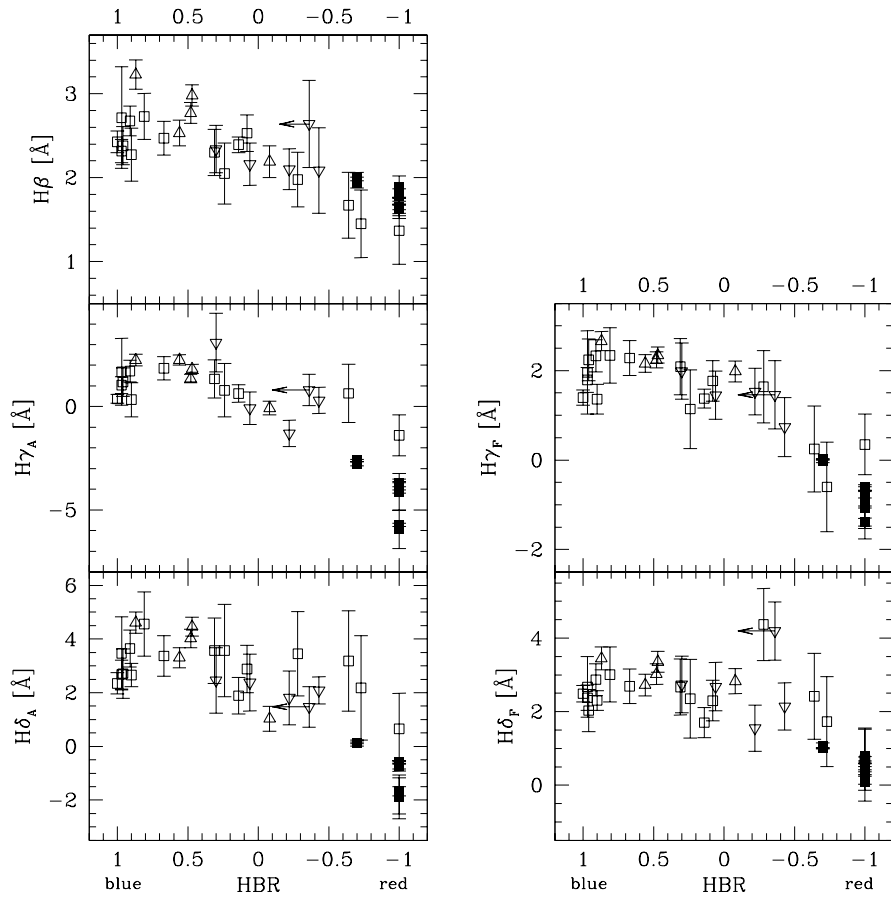
Figure F.3: The behavior of Lick Balmer indices as a function the horizontal branch morphology (HBR). Here we plot data for globular clusters in the Milky Way (*squares*: data from Chapter 2 and Trager et al. 1998), M31 (*diamonds*: Rich et al. 2003, Puzia et al. 2003b, and Trager et al. 1998), and the Large Magellanic Cloud (*triangles*: Beasley et al. 2002). Filled symbols show globular clusters with a metallicity [Z/H] > −0.6. NGC 6388 and NGC 6441 are the two filled symbols at HBR = −0.7.
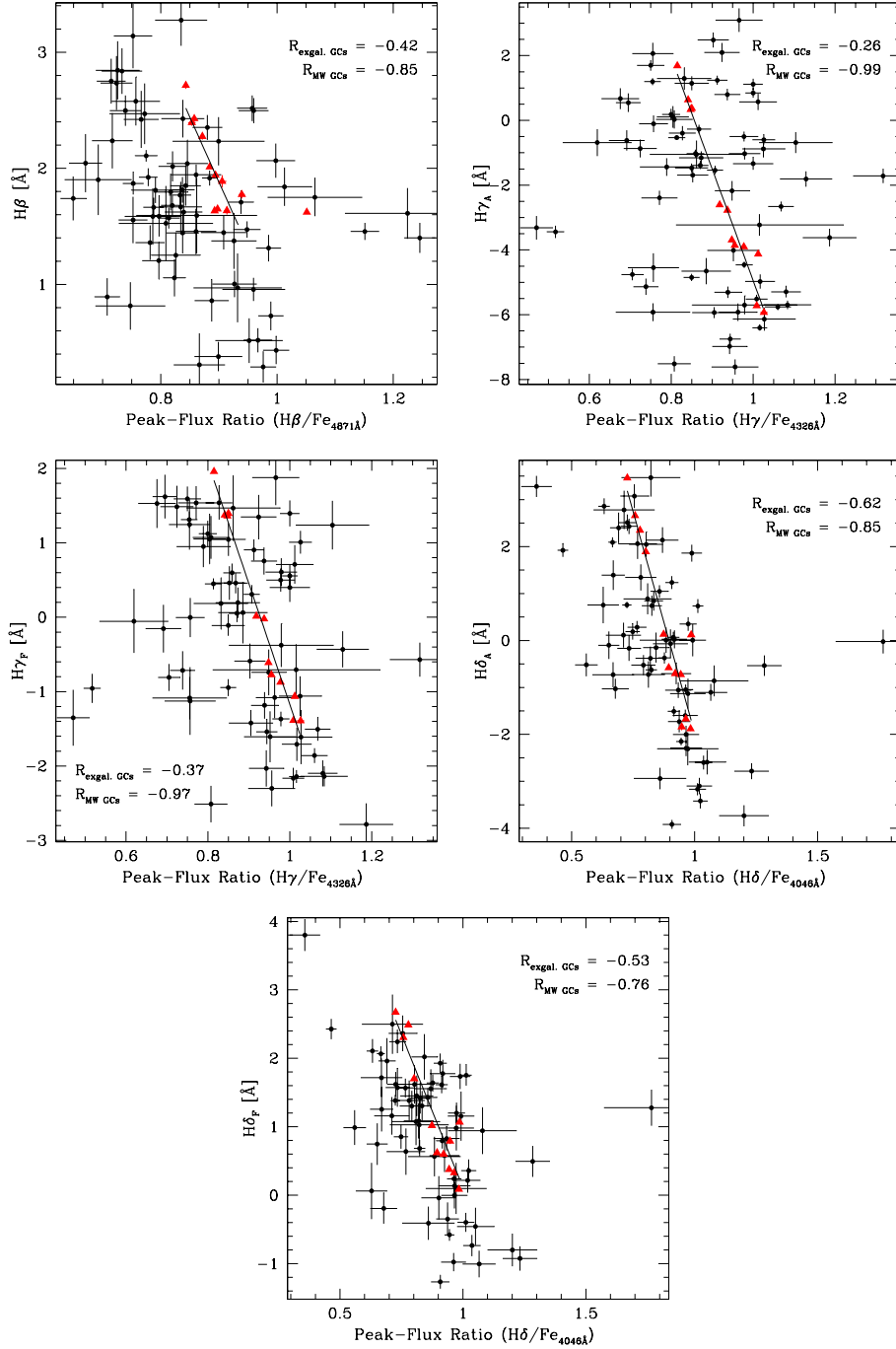
Figure F.4: Correlations of Balmer line indices with Balmer/Fe-line peak-flux ratios, measured on our unsmoothed spectra (~ 5 Å resolution). Solid dots are extragalactic globular clusters. Triangles indicate Milky Way globular clusters taken from Chapter 2. Solid lines show least-square fits to the Milky Way data. Spearman rank correlation coefficients for Galactic and extragalactic globular clusters are given in each panel. The significance of these values is always larger than 99%.

prominent in the Hβ vs. [MgFe]$'$ plot, was already reported in other studies (see references in Section 4.6) and attributed to large measurement errors. However, we find no correlation of Balmer residuals[3] with measurement errors in all five diagnostic plots.

At face value, this is consistent with the picture that Balmer-index families do indeed measure the strength of a given Balmer line *in addition to* a *similar* mix of satellite absorption features which fall inside the passband definitions (see Fig. A.1). Once indices are compared which measure the strength of different Balmer features, the *different* mix of satellite lines influences an index comparison and significantly degrades the correlation of their residuals. Although a detailed treatment of this problem would beyond the scope of this thesis, we address this problem in the following in more detail.

Figure A.1 illustrates the different satellite lines which contribute to each Lick index in addition to the main absorption feature. Iron lines predominantly contaminate feature and background passbands of all five Balmer indices. Consequently, a correlation of Balmer indices with the Iron abundance (metallicity) is observed and implemented in our SSP models (see the trend of Balmer indices as a function of metallicity in Figs. F.1 and F.2.). Since Balmer indices are more sensitive to age than metallicity, Balmer residuals (with respect to a linear fit to the data) can be expected to correlate with the Iron abundance, which might be the culprit for the increased scatter in the age/metallicity diagnostic plots in Figure F.2. However, the real Iron abundance is not accessible through the Lick system, since even Iron indices (such as Fe4383, Fe5015, Fe5270, Fe5335, etc.) are contaminated by absorption lines of various other species and therefore do no trace the Iron abundance exclusively. As expected, no correlations are found between Balmer index residuals and Fe indices.

We attempt to search for correlations between Balmer line indices and absorption line ratios, taking advantage of the full resolution (~ 5 Å) of our globular cluster spectra. We measure peak-flux ratios between Balmer lines and strong satellite Iron lines[4], such as Hβ/Fe (4871 Å), Hγ/Fe (4326 Å), and Hδ/Fe (4046 Å). All satellite Iron lines fall within the passband definitions of the corresponding Balmer index and are expected to influence their interpretation. Figure F.4 shows the correlations between all five Balmer Lick indices and the corresponding peak-flux ratios. Low numerical peak-flux ratios correspond to the inverse ratio of equivalent widths. That is, smaller peak-flux ratios indicate stronger Balmer lines with respect to the satellite Iron line. We measure the same peak-flux ratios for selected Milky Way globular clusters taken from Chapter 2 of this thesis (see also Puzia et al. (2002b)). Solid triangles mark the Galactic cluster sample which is interpolated by linear fits (solid lines in Figure F.4).

Regardless of the exact numerical values, the scatter of the correlations increases from indices which were designed to measure the strength of Hδ and Hγ towards the Hβ index. A weak dependence of a Balmer index on the Iron abundance is mirrored by a strong correlation in Figure F.4, as the Iron line flux can then be taken as a little-varying "reference continuum". Significant scatter in these correlations, on the other hand, indicates a strong effect of the satellite line flux on the line index. The increased scatter in the Hβ vs. Hβ/Fe (4871 Å) plot suggests that the age determination based on the Hβ index might be complicated by abundance variations, not only of Iron. For all Balmer indices the scatter in the extragalactic sample with respect to the solid line is $\gtrsim 3\sigma$ significant. The correlation coefficients

---

[3]Hereafter we refer to Balmer residuals as the residuals of Balmer indices with respect to the corresponding linear fit to the data in the corresponding age/metallicity diagnostic plot in Figs. F.1 and F.2.

[4]We choose only satellite lines which are nearby to the Balmer features to be maximally insensitive to reddening and flux calibration uncertainties.

for both the Galactic and extragalactic globular clusters are indicated in each panel.
In every case, the correlation for Galactic globular clusters is better than for their
extragalactic counterparts, indicating the influence of unexpected abundance ratios
which are not present in the Milky Way globular cluster system.
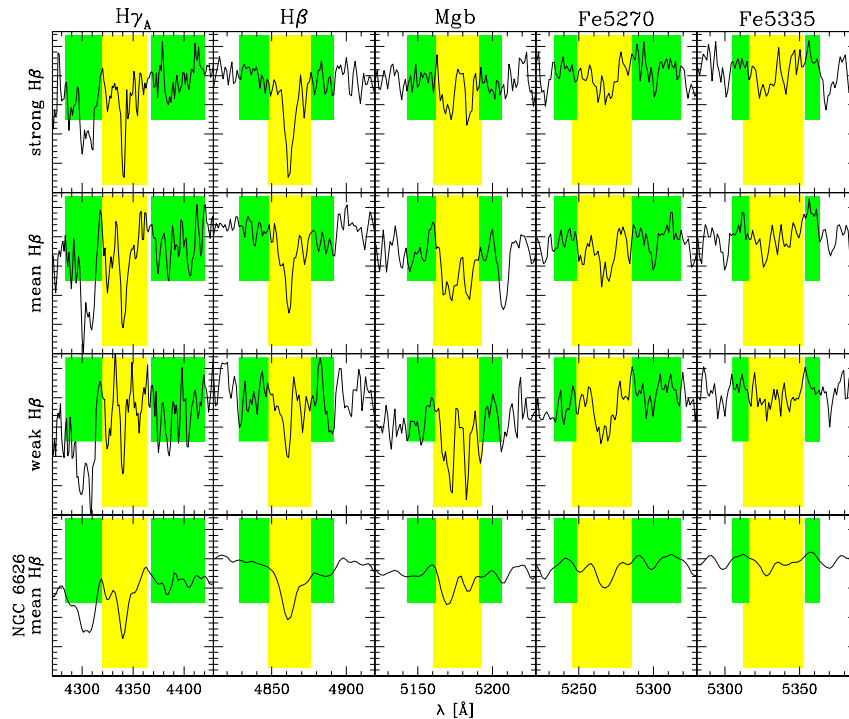
Figure F.5: Lick index passband definitions ontop of representative globular cluster
spectra with strong, mean, and weak Hβ index at a mean [MgFe]$'$ $\approx 1.2 - 1.5$ Å.
The bottom row shows for comparison the spectrum of the Galactic globular cluster
NGC 6626 (see Chapter 2) which has a similar [MgFe]$'$ and a mean Hβ strength.
Although the strength of the [MgFe]$'$ index is similar in all spectra, we find a large
variation in Hβ of about 2 Å. This variation is mainly due to the changing strength
of Mn I, Cr I, and Ti I features (cf. Fig. 5.2) inside the Hβ passband definitions.
These are indicated as light and dark shaded regions. The resolution of the Milky
Way globular cluster spectrum has roughly Lick resolution ($\sim 7 - 8$ Å), while the
resolution of the other spectra is ~ 5 Å.

The situation appears even more complicated. As found in Section 5.5, globular
clusters with relatively low Balmer indices have formally high [α/Fe]. It is well
established that varying [α/Fe] ratios are mainly driven by the Iron abundance
(Trager et al. 2000a; Thomas et al. 2003a). In other words, a comparably high
[α/Fe] ratio translates into a relatively low Iron abundance. Therefore, the found
anti-correlation of Balmer indices and [α/Fe] ratios contrasts with what would be
expected if the Iron abundance would solely drive the scatter in age/metallicity
diagnostic plots. We conclude that many other species are likely to contribute to
all Balmer indices and have the potential to blur the measurement of ages and
metallicities of individual extragalactic globular clusters.

It is intriguing that the increase of scatter in age/metallicity diagnostic plots is
closely followed by the total width of the used Balmer index. Hβ is the index with

the relatively largest scatter and it is also the most narrowly defined Balmer index (see Fig. 5.2). This shadows forth that narrowly-defined indices are likely to be more influenced by satellite absorption lines than widely-defined indices. In this respect, $H\gamma_A$ is most robust against fluctuations of satellite lines due to its relatively broad passband definitions. However, both $H\gamma$ indices include the G-band in their blue background passband (see Fig. 5.2) which introduces potential systematics locked to the abundance of CH.

To empirically illustrate that abundance ratio variations might play a significant rôle in the interpretation of Balmer line strengths, we compare selected spectral regions for globular clusters with similar $[MgFe]'$ but strongly varying $H\beta$ index. We use high-S/N spectra (S/N $\gtrsim 30$ Å^{-1}) of three different globular clusters in NGC 5846 with strong (~ 2.4 Å), average (~ 1.5 Å), and weak (~ 0.4 Å) $H\beta$ indices at similar $[MgFe]' \approx 1.3 - 1.5$ Å. Figure F.5 illustrates the influence of satellite lines on selected Lick indices, such as $H\gamma_A$, $H\beta$, Mgb, Fe5270, Fe5335. For comparison we show the same spectral features of the Milky Way globular cluster NGC 6626 (Chapter 2) which shows the same $[MgFe]'$. A comparison with Figure 5.2 shows that Mn, Cr, and Ti absorption features have the potential to significantly affect the $H\beta$ index. Higher resolution follow-up spectroscopy of "weak-$H\beta$" globular clusters in our sample would clarify this issue.

In this context a note on our stellar population models is required. Abundance ratios in theoretical models are typically locked to the solar mix or, more recently, to an arbitrarily chosen ratio of α-to-Fe-peak elements. For instance, in the models of Thomas et al. (2003a) the ratio of α elements (i.e. O, N, Mg, Ca, Na, Si, Ti) to Iron-peak elements (i.e. Cr, Fe) is varied under the constraint of constant total metallicity[5], where the carbon abundance is fixed. Other species are not included in this treatment. Changes in $[\alpha/Fe]$ are achieved by variations mainly in the abundance of Iron-peak elements (see Trager et al. 2000a; Thomas et al. 2003a, for details). It is important to note that abundance ratios within the two element groups are fixed. However, we know from higher-resolution spectroscopy of Milky Way stars, local and high-z galaxies that some of the Iron-peak elements do not change in lockstep as a function of metallicity (e.g. McWilliam 1997; Saglia et al. 2002; Pettini 2003). For instance, the $[Mn/Fe]$ and $[Cr/Fe]$ ratios are clearly not constant and behave differently as a function of metallicity (e.g. Fulbright 2002).

In summary, age-metallicity determinations of individual globular clusters are strongly dependent on the use of a specific Balmer line index. It appears very likely that the sensitivity to metal abundance variations is not negligible. This sensitivity is unique to each age/metallicity diagnostic diagram using a Lick Balmer index as age indicator. Reliable age and metallicity determinations require therefore a detailed knowledge of abundance patterns in the observed stellar population. Compared to the diffuse light of galaxies, where a global luminosity-weighted average of abundance patterns is observed, the limitations of the Lick index system are clearly reached, when globular clusters are observed. Such stellar populations can show individual and *locally* well-deviating abundance patterns from what is known for the *global* stellar population of the host. Such complex and strongly varying abundance patterns are not accounted for in our theoretical predictions, simply because, firstly, they were not expected (beacuse not observed in the local calibrators) and, secondly, we still lack response functions for some important species (e.g. Mn, S, Co, Ni, Cu, Zn, etc.). Higher resolution spectra are necessary to measure line strengths of well-resolved absorption features to derive ages, metallicities, and abundance ratios for extragalactic globular clusters which are independent of complex abundance ratio

---

[5]Note that index response functions which are used for model predictions were actually determined for solar metallicities (Tripicco & Bell 1995). Absolute index changes due to varying abundance ratios are linearly extrapolated towards lower and higher metallicities (see Thomas et al. 2003a, for details).

variations.

F.4 Contamination by Ionized Gas

It is well known that $\sim 40 - 60\%$ of early-type galaxies show indications of emission in their absorption spectra (Caldwell 1984; Phillips et al. 1986; Goudfrooij et al. 1994). However, most spectroscopic surveys focus on the very nuclear regions of galaxies. In a narrow-band imaging survey, Macchetto et al. (1996) find ionized gas in $\sim 80\%$ of early-type galaxies. This gas is located in globules with sizes between 1 and 10 kpc and distributed in a rather regular way, suggestive of a disk. Macchetto et al. find flocculent Hα+[NII] emission in NGC 3379, NGC 5846, and NGC 7192, well within $\sim 1\,R_{\rm eff}$, but no significant emission in NGC 3115. In particular, all Balmer indices would be affected, along with potential contamination of Fe5015 by [O III] ($\lambda\,5007$ Å) and of Mgb by [N I] ($\lambda\,5199$ Å) (Goudfrooij & Emsellem 1996). As a consequence, our measurements would indicate too old ages. However, this effect rapidly decreases from Hβ towards Hγ and Hδ. Osterbrook (1989) shows that the emission line ratios Hγ/Hβ and Hδ/Hβ are of the order 0.45 and 0.25, respectively, for case B recombination. In these premises, higher-order Balmer indices should be preferentially used for age determinations.

Since line emission is concentrated in the central parts of galaxies (Macchetto et al. 1996), we expect a correlation of Balmer indices with galactocentric radius if line-emission contamination is significant. We find no clear evidence that Balmer indices are correlated with galactocentric distance. A more detailed analysis of background spectra shows that most clusters are located within $\sim 2 - 3\,R_{\rm eff}$ and that the flux level of the diffuse galaxy light is well below the object flux. In particular, we find no correlation inside one effective radius, where line emission is expected to be strong. Furthermore, we find no correlations of Balmer indices with Balmer indices measured on corresponding background spectra.

Visual re-inspection of the background subtraction process for some low-Hβ outliers (see Fig. 5.6) undermine the good quality of background modeling and subtraction. However, problems with accurate background subtraction might occur in very few cases when line emission has a very filamentary structure. For instance, the worst case scenario would be when a globular cluster overlaps with a filament of ionized gas while the slit is aligned perpendicular to the filament. However, a filamentary emission pattern is not found for host galaxies included in the Macchetto et al. (1996) study. We conclude that line emission cannot explain the entire scatter in age/metallicity diagnostic plots.

F.5 Model-to-Model variations

All our results are based on one set of SSP models which were taken from Chapter 3 and Thomas et al. (2003a). These models are based on Worthey (1994) and Worthey & Ottaviani (1997) fitting functions and solar-scaled stellar evolutionary tracks from Bono et al. (1997), Cassisi et al. (1999), and Salasnich et al. (2000), and were calculated employing the principles of the fuel consumption theorem (Renzini & Buzzoni 1986). In the following we compare the age and metallicity predictions from SSP models of Vazdekis 2000 (Vazdekis et al. 1996; Vazdekis 1999; Blakeslee et al. 2001)[6] and Chapter 3. The former models are based on Worthey (1994) and Worthey & Ottaviani (1997) fitting functions and solar-scaled isochrones

---

[6]Electronic tables with model predictions were taken from
http://star-www.dur.ac.uk/~vazdekis/
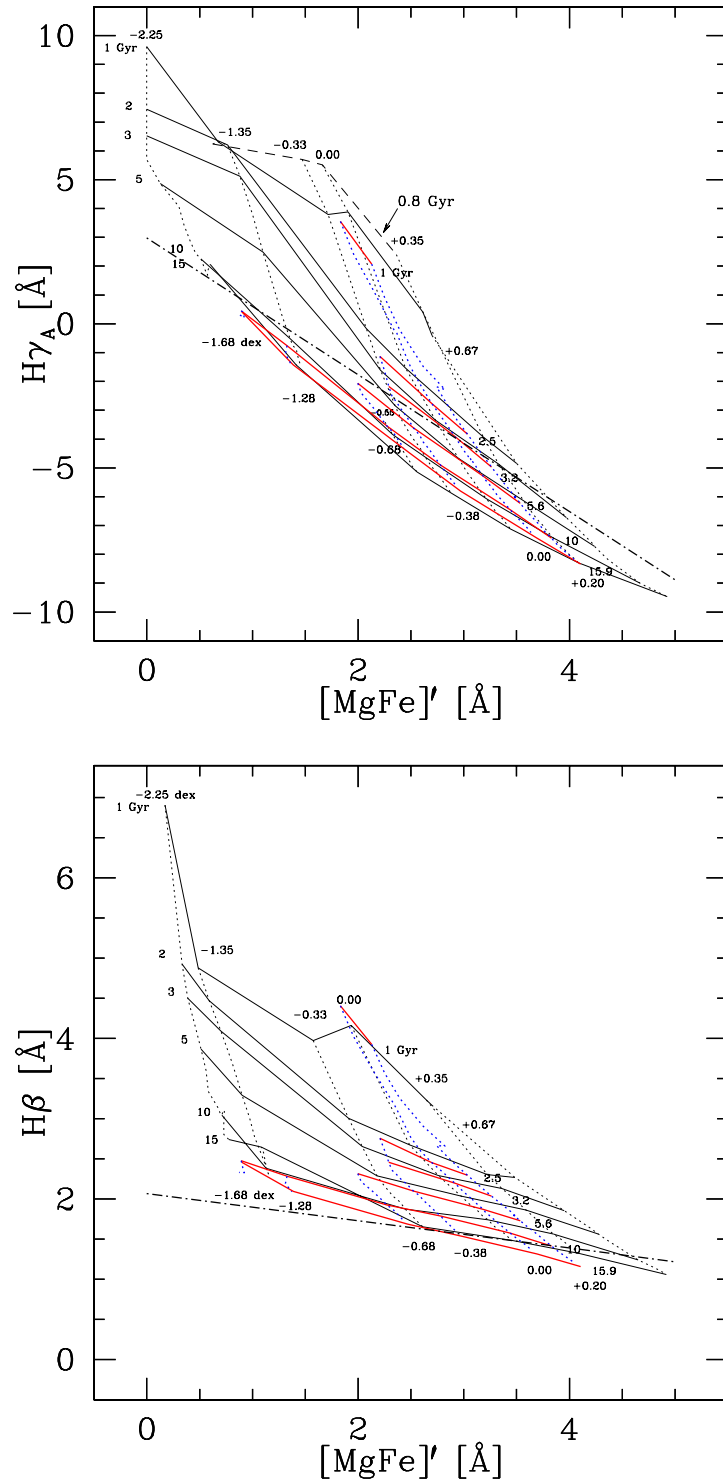
Figure F.6: Comparison of SSP model predictions of Vazdekis and Maraston. Model predictions of Maraston are plotted as *thin* lines (in particular, *solid* lines: isochrones, *dotted* lines: iso-metallicity) and are labeled accordingly above and to the left of the grid. Vazdekis predictions are plotted as thick lines and are labeled below and to the right of the grid. A ridge line of the globular cluster data is plotted as a dot-dashed line.

of Girardi et al. (2000). These models[7] were calculated with the isochrone synthesis technique (Charlot & Bruzual 1991). A comparison is given in Figure F.6 where we plot Hγ_A and Hβ vs. [MgFe]$'$.

Using a linear fit to our globular cluster data, we find a mean age-metallicity relation -1.4 ± 0.6 Gyr/dex from the Hγ_A vs. [MgFe]$'$ diagram with the predictions of Vazdekis. This is significantly flatter than the relation derived from Maraston models which is -3.5 ± 0.6 Gyr/dex. We find no significant age-metallicity relation in the Hγ_F and Hδ_F diagrams using Vazdekis' models.

Unfortunately, the Vazdekis models do not cover as large of a parameter range as the Maraston et al. models, so we cannot perform a detailed comparison. However, the two model grids tend to deviate significantly in the old metal-poor regime and in the entire metal-rich regime. At metallicities below ~ -1.4 dex, Vazdekis models predict clearly younger ages than the Maraston et al. models (at old absolute ages $\Delta t \sim 5$ Gyr). The difference increases with successively lower metallicities. Moreover, compared to Maraston et al. predictions, the metallicity scale of the Vazdekis models appears stretched. At extreme [MgFe]$'$ values, corresponding to very low and high metallicities, Maraston et al. models predict on average higher and lower metallicities, respectively. We also note that at [Z/H] ~ -0.5, isochrones older than ~ 10 Gyr deviate significantly ($\Delta t \sim 5$ Gyr), as well. The offsets in the Hγ_F, Hδ_A, and Hδ_F diagnostic plots are very similar.

In the bottom panel of Figure F.6 we compare Vazdekis' models with the predictions of Thomas et al.[8] for a Hβ vs. [MgFe]$'$. The offset at very low metallicities and old ages is comparable to other diagnostic diagrams. The 15 Gyr isochrones are significantly different in the two models, while younger isochrones diverge more and more towards the metal-rich end. Since the Vazdekis models were not calculated for constant [α/Fe], the latter deviations are the result of successively larger corrections in the metal-rich regime for constant [α/Fe]. These offsets correspond to age offsets $\lesssim 4$ Gyr. Using a much smaller metallicity range than in the Thomas et al. models (only $-0.68 \lesssim$ [Z/H] $\lesssim 0.2$), we derive a formal age-metallicity relation -5.7 ± 1.0 Gyr/dex which compares well with the value derived with the Thomas et al. models of -5.0 ± 1.0 Gyr/dex. Note, however, that the metallicity scale of the Vazdekis models in the Hβ diagram appears to be similarly skewed as in the other diagnostic diagrams.

In summary, we find largest model-to-model variations where theoretical calculations are extended towards extreme ages and metallicities. Such parameter regimes have no local calibrators and need extrapolations under assumptions of fundamental physical parameters such as mass-loss, etc. Since our models use metal-poor and metal-rich Galactic globular clusters as calibrators (see Chapter 2 and 3), with metallicities high-enough to resemble extragalactic clusters, we favour our models, but point out that age/metallicity determinations do sensitively depend on the choice of a particular SSP model.

F.6 Systematics in SSP Model Predictions

In the following we briefly address systematics hardwired into SSP models which can affect age and metallicity determinations.

---

[7] Both models use a Salpeter IMF. However, small changes can be expected for other IMF slopes since the major contribution to the integrated light of stellar populations $\gtrsim 5$ Gyr comes from stars with masses between ~ 0.1 and ~ 1 M$_\odot$. The total light is basically defined by the IMF slope in this limited mass range.

[8] for a constant [α/Fe] ratio of $+0.3$ dex

F.6.1   Mass-Loss

The effect of a changing mass-loss on isochrones is a function of metallicity and age. In our models, the mass-loss was calibrated as described in Maraston & Thomas (2000). At metallicities below [Fe/H] ≈ -0.6, older stellar populations tend to have bluer horizontal branches which produce stronger Balmer lines. This effect is reduced towards lower ages and is smaller than the mean isochrone separation $\Delta t = 1$ Gyr for ages below 8 Gyr. Consequently, old metal-poor globular clusters are mostly affected by variations of the mass-loss parameter which is illustrated in Figure F.7. Isochrones without mass-loss are plotted as solid lines, while isochrones for stellar-populations with mass-loss switched on are indicated by dashed lines. The deviations rapidly decrease towards younger ages and almost disapper for ages $\lesssim 10$ Gyr. The maximum offset for a 15 Gyr isochrone at [Fe/H] -1.4 is roughly 0.7 Å for Hβ, and 3.0, 2.4, 1.7, and 1.6 Å for Hγ_A, Hδ_A, Hγ_F, and Hδ_F, respectively. These variations correspond to formal age differences of 8.5, 11.0, 11.0, 10.0, and 11.0 Gyr for Hβ, Hγ_A, Hδ_A, Hγ_F, and Hδ_F, respectively. As the calibration of the stellar mass-loss rate is feasible only locally, a systematic difference in this parameter between the Solar neighbourhood and the dense environment of early-type galaxies cannot be ruled out.

F.6.2   Stellar Evolutionary Tracks/Isochrones

Most theoretical Lick-index predictions are based on isochrones which use solar-scaled abundance ratios. In general, α-enhanced isochrones have higher T_{eff} compared to solar-scaled isochrones at the same metallicity. This can be understood by a higher abundance of elements with high-ionization potentials which results in lower total opacities (Salaris & Weiss 1998; Salasnich et al. 2000; VandenBerg et al. 2000; Kim et al. 2002).

Our models are calculated with solar-scaled isochrones (see Sect. F.5). Recently Thomas & Maraston (2003b) studied the impact of α-enhanced isochrones on age and metallicity determinations of early-type galaxies. The authors find excessively large ages (~ 30 Gyr) for objects with had previously derived ages ~ 15 Gyr when solar-scaled isochrones are used and speculate that α-enhanced isochrones might overestimate the temperatures of stellar atmospheres at high metallicities. At this point we just note that the self-consistent use of stellar isochrones creates problems with the absolute age scale of SSP models.

F.6.3   Fitting and Response Functions

SSP models use empirical fitting functions (e.g. Worthey 1994; Worthey & Ottaviani 1997) to transform their predictions from the theoretical $\log g - T_{\text{eff}}$ plane to the observational index plane. Most fitting functions are derived from a set of nearby stars without any information on varying abundance ratios. However, varying abundance ratios in stellar atmospheres pass on the change in $\log g$ and T_{eff} to the set of fitting functions. In principle such changing abundance ratios can be accounted for by semi-theoretical response functions. Tripicco & Bell (1995) provide response functions for a sub-set of 21 Lick indices. Their calculations are restricted to a solar-metallicity 5-Gyr isochrone for a cool dwarf, a turn-off star, and a cool giant. The doubling of the abundance of 10 species (C, N, O, Mg, Fe, Ca, Na, Si, Cr, and Ti) and the doubling of all these elements at a fixed $\log g$ and T_{eff} provides the amount of variations for a given index. These variations are *linearly* extrapolated to stronger abundance changes in today's state-of-the-art SSP models (Trager et al. 2000a; Thomas et al. 2003a). For strong absorption lines though, e.g. NaD which fall in the damping regime of the curve-of-growth, such a linear extrapolation might
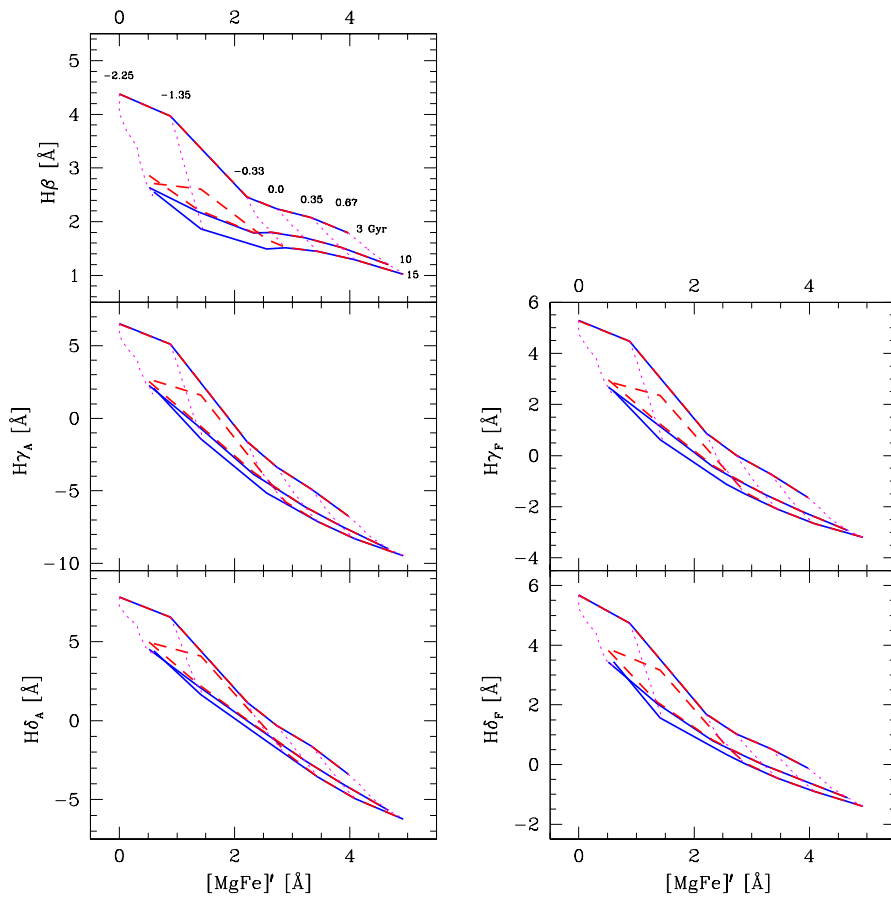
Figure F.7: Comparison of SSP model isochrones for all five Balmer indices using two different mass-loss parameter. Solid lines show isochrones for a 3, 10, and 15 Gyr old stellar population calculated without mass-loss. Dashed lines are isochrones calculated with mass-loss, which is calibrated as described in Maraston & Thomas (2000). Dotted lines indicate iso-metallicity tracks for metallicities [Fe/H] = −2.25, −1.35, −0.33, 0.0, 0.35, 0.67.

be an oversimplification.

Response functions do not provide the necessary means to model photospheric conditions in α-enhanced stellar populations in a self-consistent way. In SSP models using response function to calculate predictions for well-defined abundance patterns, abundance changes of a given element have no effect on nuclear processes, internal opacities, and the equation of state which in turn affect $\log g$, T_{eff}, and finally the index. The interplay of these effects is highly non-linear and has to be carefully modelled (Salasnich et al. 2000; Kim et al. 2002). Response functions *only* change artificially the composition of stellar atmosphere, disregarding corresponding changes in internal physics.

For instance, the abundance of oxygen, which is the most abundant α-element, is important for internal energy generation near the turn-off. This species is a bad electron donor and its contribution to the total opacity in the photosphere is not significant. However, at temperatures $\log T \gtrsim 6$ it starts to dominate the internal opacity and boost the CNO-cycle rates (VandenBerg et al. 2000). An increase of its abundance leads to an increase of the photospheric temperature and in turn to an increase of Balmer indices. Therefore, a self-consistent quantification of response functions for a variety of abundance patterns, covering a wide range of ages *and* chemical compositions needs to be performed in the future.

In general, the cure of all the above model systematics is clearly beyond the scope of this work. However, all need to be kept in mind when ages, metallicities, and abundance ratios are derived from Lick indices.

Bibliography

Ajhar, E. A., Blakeslee, J. P., & Tonry, J. L. 1994, AJ, 108, 2087

Allen, S. W. 1998, MNRAS, 296, 392

Arimoto, N. & Yoshii, Y. 1987, A&A, 173, 23

Arp, H. C. & Madore, B. 1987, Cambridge ; New York : Cambridge University Press

Ashman, K. M. & Zepf, S. E. 1992, ApJ, 384, 50

Ashman, K. A., Bird, C. M., & Zepf, S. E. 1994, AJ, 108, 2348

Ashman, K. M. & Zepf, S. E. 1998, Globular cluster systems, Cambridge University Press, 1998

Bahcall, J. N. & Tremaine, S. 1981, ApJ, 244, 805

Balcells, M. & González, A. C. 1999, ASP Conf. Ser. 182: Galaxy Dynamics - A Rutgers Symposium, 475

Baldwin J. A., & Stone R. P. S. 1984, MNRAS 206, 241

Barbuy, B., Bica, E., & Ortolani, S. 1998, A&A, 333, 117

Barbuy, B., Renzini, A., Ortolani, S., Bica, E., & Guarnieri, M. D. 1999, A&A, 341, 539

Bardeen, J. M., Bond, J. R., Kaiser, N., & Szalay, A. S. 1986, ApJ, 304, 15

Barmby, P., Huchra, J. P., Brodie, J. P., Forbes, D. A., Schroder, L. L., & Grillmair, C. J. 2000, AJ, 119, 727

Barnes, J. E. 1988, ApJ, 331, 699

Barnes, J. E. & Hernquist, L. 1992, ARA&A, 30, 705

Baugh, C. M., Cole, S., Frenk, C. S., & Lacey, C. G. 1998, ApJ, 498, 504

Baum, W. A. 1955, PASP, 67, 328

Beasley M. A., Sharples R. M., Bridges T. J., Hanes D. A., Zepf S. E., Ashman K. M. & Geisler D. 2000, MNRAS, 318, 1249

Beasley, M. A., Hoyle, F., & Sharples, R. M. 2002, MNRAS, 336, 168

Bekki, K., Forbes, D. A., Beasley, M. A., & Couch, W. J. 2002, MNRAS, 335, 1176

Bender, R. 1988, A&A, 202, L5

Bender, R. 1996, IAU Symp. 171: New Light on Galaxy Evolution, 171, 181

Bender, R., Burstein, D., & Faber, S. M. 1992, ApJ, 399, 462

Bender, R., Burstein, D., & Faber, S. M. 1993, ApJ, 411, 153

Bender, R. & Paquet, A. 1995, IAU Symp. 164: Stellar Populations, 164, 259

Bender, R., Ziegler, B., & Bruzual, G. 1996, ApJL, 463, L51

Bergbusch, P. A. & VandenBerg, D. A. 2001, ApJ, 556, 322

van den Bergh, S. 1993, AJ, 105, 971

van den Bergh, S. 1994, AJ, 107, 153

Bernstein, R. A. & McWilliam, A. 2002, IAU Symposium, 207, 739

Bertin, E., & Arnouts, S. 1996, A&AS, 117, 393

Beuing, J., Bender, R., Mendes de Oliveira, C., Thomas, D., & Maraston, C. 2002, A&A, 395, 431

Bica, E. & Alloin, D. 1986, A&A, 162, 21

Bica, E., Ortolani, S., & Barbuy, B. 1994, A&A, 106, 161

Binney, J. 1981, Structure and Evolution of Normal Galaxies, eds. D. Lynden-Bell & S.M. Fall, Cambridge University Press, Cambridge

Binney, J. & Tremaine, S. 1987, Galactic Dynamics, Princeton, NJ, Princeton University Press

Binney, J. & Merrifield, M. 1998, Galactic Astronomy, Princeton, NJ, Princeton University Press

Blakeslee, J. P. 1996, Ph.D. Thesis

Blakeslee, J. P., Tonry, J. L., & Metzger, M. R. 1997, AJ, 114, 482

Blakeslee, J. P., Vazdekis, A., & Ajhar, E. A. 2001, MNRAS, 320, 193

Bower, R. G., Ellis, R. S., Rose, J. A., & Sharples, R. M. 1990, AJ, 99, 530

Bono, G., Caputo, F., Cassisi, S., Castellani, V., & Marconi, M. 1997, ApJ, 489, 822

Borges, A. C., Idiart, T. P., de Freitas Pacheco, J. A., & Thevenin, F. 1995, AJ, 110, 2408

Bothun, G. D. & Gregg, M. D. 1990, ApJ, 350, 73

Bower, R. G., Lucey, J. R., & Ellis, R. S. 1992, MNRAS, 254, 601

Bridges, T. J., Ashman, K. M., Zepf, S. E., Carter, D., Hanes, D. A., Sharples, R. M., & Kavelaars, J. J. 1997, MNRAS, 284, 376

Brodie, J. P. & Huchra, J. P. 1991, ApJ, 379, 157

Bruzual A., G. & Charlot, S. 2000, private communication

Buonanno, R., Corsi, C., Bellazzini, M., Ferraro, F. R., & Pecci, F. F. 1997, AJ, 113, 706

Burgarella, D., Kissler-Patig, M., & Buat, V. 2001, AJ, 121, 2647

Burstein, D., Faber, S. M., Gaskell, C. M., & Krumm, N. 1984, ApJ, 287, 586

Buta, R. & Williams, K. L. 1995, AJ, 109, 543

Buzzoni, A., Gariboldi, G., & Mantegazza, L. 1992, AJ, 103, 1814

Buzzoni, A., Mantegazza, L., & Gariboldi, G. 1994, AJ, 107, 513

Caldwell, N. 1984, PASP, 96, 287

Carney, B. W. 1996, PASP, 108, 900

Carollo, C. M. & Danziger, I. J. 1994, MNRAS, 270, 523

Carretta, E. & Gratton, R. G. 1997, A&AS, 121, 95

Carretta, E. & Bragaglia, A. 1998, A&A, 329, 937

Carretta, E., Gratton, R. G., & Sneden, C. 2000, A&A, 356, 238

Carretta, E., Cohen, J. G., Gratton, R. G., & Behr, B. B. 2001, AJ, 122, 1469

de Carvalho, R. R. & Djorgovski, S. 1992, ApJL, 389, L49

Cassisi, S., Castellani, V., degl'Innocenti, S., Salaris, M., & Weiss, A. 1999, A&AS, 134, 103

Catelan, M., Bellazzini, M., Landsman, W. B., Ferraro, F. R., Fusi Pecci, F., & Galleti, S. 2001, AJ, 122, 3171

Cen, R. 2001, ApJ, 560, 592

Chandar, R., Bianchi, L., Ford, H. C., & Sarajedini, A. 2002, ApJ, 564, 712

Charlot, S. & Bruzual, A. G. 1991, ApJ, 367, 126

Cimatti, A. et al. 2002a, A&A, 381, L68

Cimatti, A. et al. 2002b, A&A, 391, L1

Coelho, P., Barbuy, B., Perrin, M.-N., Idiart, T., Schiavon, R. P., Ortolani, S., & Bica, E. 2001, A&A, 376, 136

Cohen, J. G. 2000, AJ, 119, 162

Cohen, J. G. & Sleeper, C. 1995, AJ, 109, 242

Cohen, J. G. & Ryzhov, A. 1997, ApJ, 486, 230

Cohen, J. G., Blakeslee, J. P., & Ryzhov, A. 1998, ApJ, 496, 808

Cohen, J. G., Gratton, R. G., Behr, B. B., & Carretta, E. 1999, ApJ, 523, 739

Cohen, J. G., Blakeslee, J. P., Côté, P. 2003, ApJ accepted, (astro-ph/0304333)

Cole, S., Aragon-Salamanca, A., Frenk, C. S., Navarro, J. F., & Zepf, S. E. 1994, MNRAS, 271, 781

Cole, S., Lacey, C. G., Baugh, C. M., & Frenk, C. S. 2000, MNRAS, 319, 168

Cole, S. et al. 2001, MNRAS, 326, 255

Colless, M. et al. 2001, MNRAS, 328, 1039

Copi, C. J., Schramm, D. N., & Turner, M. S. 1995, Science, 267, 192

Côté, P., Marzke, R. O., & West, M. J. 1998, ApJ, 501, 554

Côté, P. 1999, AJ, 118, 406.

Côté, P. et al. 2001, ApJ, 559, 828

Côté, P., McLaughlin, D. E., Cohen, J. G., & Blakeslee, J. P. 2003, ApJ, 591, 850

Couture, J., Harris, W. E., & Allwright, J. W. B. 1991, ApJ, 372, 97

Covino, S., Galletti, S., & Pasinetti, L. E. 1995, A&A, 303, 79

Cox, A. N. 2000, in "Allen's Astrophysical Quantities", 4th edition, ed. Arthur N. Cox, Springer

D'Antona, F., Gratton, R., & Chieffi, A. 1983, Memorie della Societa Astronomica Italiana, 54, 173

Davies, R. L., Sadler, E. M., & Peletier, R. F. 1993, MNRAS, 262, 650

Davies, R. L. et al. 2001, ApJL, 548, L33

Dawe, J. A. & Dickens, R. J. 1976, Nature, 263, 395

Durrell, P. R., Harris, W. E., Geisler, D., & Pudritz, R. E. 1996, AJ, 112, 972

Edvardsson, B., Andersen, J., Gustafsson, B., Lambert, D. L., Nissen, P. E., & Tomkin, J. 1993, A&A, 275, 101.

Eggen, O. J., Lynden-Bell, D., & Sandage, A. R. 1962, ApJ, 136, 748

Eisenstein, D. J. et al. 2003, ApJ, 585, 694

Elmegreen, B. G. & Efremov, Y. N. 1997, ApJ, 480, 235

Elson, R. A. W. 1997, MNRAS, 286, 771

Evans, N. W., Wilkinson, M. I., Perrett, K. M., & Bridges, T. J. 2003, ApJ, 583, 752

Faber, S. M. 1972, A&A, 20, 361

Faber, S. M. 1973, ApJ, 179, 731

Faber, S. M. & Jackson, R. E. 1976, ApJ, 204, 668

Faber, S. M., Friel, E. D., Burstein, D., & Gaskell, C. M. 1985, ApJS, 57, 711

Fall, S. M. & Rees, M. J. 1985, ApJ, 298, 18

Fall, S. M. & Rees, M. J. 1988, IAU Symp. 126: The Harlow-Shapley Symposium on Globular Cluster Systems in Galaxies, 126, 323

Fall, S. M. & Zhang, Q. 2001, ApJ, 561, 751

Feltzing, S. & Gilmore, G. 2000, A&A, 355, 949

Feltzing, S., Johnson, R. A., & de Cordova, A. 2002, A&A, 385, 67

Fisher, D., Franx, M., & Illingworth, G. 1995, ApJ, 448, 119

Forbes, D. A., Franx, M., Illingworth, G. D., & Carollo, C. M. 1996, ApJ, 467, 126

Forbes, D. A., Brodie, J. P., & Grillmair, C. J. 1997, AJ, 113, 1652

Forbes, D. A., Beasley, M. A., Brodie, J. P., & Kissler-Patig, M. 2001, ApJL, 563, L143

Franx, M. & Illingworth, G. D. 1988, ApJL, 327, L55

Franx, M. & Illingworth, G. 1990, ApJL, 359, L41

Freeman, K. C. & Norris, J. 1981, ARA&A, 19, 319

de Freitas Pacheco, J. A. & Barbuy, B. 1995, A&A, 302, 718

Freudenreich, H. T. 1998, ApJ, 492, 495

Frogel, J. A. 1988, ARA&A, 26, 51

Frogel, J. A., Persson, S. E., Matthews, K., & Aaronson, M. 1978, ApJ, 220, 75

Frogel, J. A., Terndrup, D. M., Blanco, V. M., & Whitford, A. E. 1990, ApJ, 353, 494

Frogel, J. A., Tiede, G. P., & Kuchinski, L. E. 1999, AJ, 117, 2296

Fuhrmann, K. 1998, A&A, 338, 161

Fuhrmann, K. 1999, Ap&SS, 265, 265

Fuhrmann, K., Axer, M., & Gehren, T. 1995, A&A, 301, 492

Fukugita, M., Hogan, C. J., & Peebles, P. J. E. 1998, ApJ, 503, 518

Fulbright, J. P. 2002, AJ, 123, 404

Fusi-Pecci, F. & Renzini, A. 1976, A&A, 46, 447

Fusi Pecci, F., Ferraro, F. R., Bellazzini, M., Djorgovski, S., Piotto, G., & Buonanno, R. 1993, AJ, 105, 1145

Gabasch et al. 2003, in preparation

Gebhardt, K. et al. 1996, AJ, 112, 105

Gebhardt, K. & Kissler-Patig, M. 1999, AJ, 118, 1526

Gebhardt, K., Pryor, C., O'Connell, R. D., Williams, T. B., & Hesser, J. E. 2000, AJ, 119, 1268

Gerhard, O., Kronawitter, A., Saglia, R. P., & Bender, R. 2001, AJ, 121, 1936

Geyer, M. P. & Burkert, A. 2001, MNRAS, 323, 988

Girardi, L., Bressan, A., Bertelli, G., & Chiosi, C. 2000, A&AS, 141, 371

Gnedin, O. Y. & Ostriker, J. P. 1997, ApJ, 474, 223

Gössl, C. A. & Riffeser, A. 2002, A&A, 381, 1095

González, J. J. 1993, Ph.D. Thesis

Gorgas, J., Efstathiou, G., & Salamanca, A. A. 1990, MNRAS, 245, 217

Gorgas, J., Faber, S. M., Burstein, D., Gonzalez, J. J., Courteau, S., & Prosser, C. 1993, ApJS, 86, 153

Goudfrooij, P., Hansen, L., Jorgensen, H. E., & Norgaard-Nielsen, H. U. 1994, A&AS, 105, 341

Goudfrooij, P. & Emsellem, E. 1996, A&A, 306, L45

Goudfrooij, P., Mack, J., Kissler-Patig, M., Meylan, G., & Minniti, D. 2001a, MN-RAS, 322, 643

Goudfrooij, P., Alonso, M. V., Maraston, C., & Minniti, D. 2001b, MNRAS, 328, 237

Gratton, R. G., Fusi Pecci, F., Carretta, E., Clementini, G., Corsi, C. E., & Lattanzi, M. 1997, ApJ, 491, 749

Gratton, R. C. 1987, A&A, 177, 177

Gratton, R. G. & Ortolani, S. 1989, A&A, 211, 41

Gregg, M. D. 1994, AJ, 108, 2164

Greggio, L. 1997, MNRAS, 285, 151

Greggio, L. & Renzini, A. 1983, A&A, 118, 217

Greggio, L. & Renzini, A. 1990, ApJ, 364, 35

Grillmair, C. J., Freeman, K. C., Bicknell, G. V., Carter, D., Couch, W. J., Sommer-Larsen, J., & Taylor, K. 1994, ApJL, 422, L9

Grundahl, F., Briley, M. M., Nissen, P. E., & Feltzing, S. 2002, A&A, 385, L14

Gunn, J. E. 1980, in Globular Clusters, ed. Hanes, D. & Madore, B., Cambridge University Press

Gunn, J. E. & Gott, J. R. I. 1972, ApJ, 176, 1

Guzman, R., Jangren, A., Koo, D. C., Bershady, M. A., & Simard, L. 1998, ApJL, 495, L13

Hanes, D. A. 1977, MmRAS, 84, 45

Harris, W. E. 1991, ARA&A, 29, 543

Harris, W. E. 1993, ASP Conf. Ser. 48: The Globular Cluster-Galaxy Connection, 472

Harris, W.E. 1996, AJ, 112, 1487, for the 1999 update see http://physun.physics.mcmaster.ca/~harris/mwgc.dat

Harris, W. E. & van den Bergh, S. 1981, AJ, 86, 1627

Harris, W.E. 2001, in Star Clusters, ed. L. Labhardt & B. Binggeli (Springer-Verlag, Berlin), p. 22

Harris, W. E. & Pudritz, R. E. 1994, ApJ, 429, 177

Harris, W. E., Pritchet, C. J., & McClure, R. D. 1995, ApJ, 441, 120

Harris, W. E., Harris, G. L. H., & McLaughlin, D. E. 1998, AJ, 115, 1801

Harris, W. E. & Harris, G. L. H. 2002, AJ, 123, 3108

Hayes, D. S. 1985, IAU Symp. 111: Calibration of Fundamental Stellar Quantities, 111, 225

Heidt, J. et al. 2003, A&A, 398, 49

Heisler, J., Tremaine, S., & Bahcall, J. N. 1985, ApJ, 298, 8

Hempel, M., Hilker, M., Kissler-Patig, M., Puzia, T. H., Minniti, D., & Goudfrooij, P. 2003, A&A, 405, 487

Hills, J. G. 1980, ApJ, 235, 986

Hogg, D. E., Roberts, M. S., & Sandage, A. 1993, AJ, 106, 907

Holtzman, J. A., Burrows, C. J., Casertano, S., Hester, J. J., Trauger, J. T., Watson, A. M., & Worthey, G. 1995a, PASP, 107, 1065

Holtzman, J. A. et al. 1995b, PASP, 107, 156

Homeier, N., Gallagher, J. S., & Pasquali, A. 2002, A&A, 391, 857

Horne, K. 1986, PASP, 98, 609

Hubble, E. P. 1926, ApJ, 64, 321

Hubble, E. 1929, Proceedings of the National Academy of Science, 15, 168

Hubble, E. 1932, ApJ, 76, 44

Huchra, J., Stauffer, J., & van Speybroeck, L. 1982, ApJL, 259, L57

Ibata, R. A., Gilmore, G., & Irwin, M. J. 1995, MNRAS, 277, 781

Jacoby, G. H. et al. 1992, PASP, 104, 599

Jedrzejewski, R. & Schechter, P. L. 1988, ApJL, 330, L87

Johnson, K. E., Vacca, W. D., Leitherer, C., Conti, P. S., & Lipscy, S. J. 1999, AJ, 117, 1708

Jones, J. E., Alloin, D. M., & Jones, B. J. T. 1984, ApJ, 283, 457

Jordán, A., Côté, P., West, M. J., & Marzke, R. O. 2002, ApJL, 576, L113

Jordán, A., West, M. J., Côté, P., & Marzke, R. O. 2003, AJ, 125, 1642

Jorgensen, I. 1997, MNRAS, 288, 161

Kauffmann, G. 1996, MNRAS, 281, 487

Kauffmann, G., White, S. D. M., & Guiderdoni, B. 1993, MNRAS, 264, 201

Kauffmann, G. & Charlot, S. 1998, MNRAS, 297, L23

Kauffmann, G. & Haehnelt, M. 2000, MNRAS, 311, 576

Kavelaars, J. J. 1998, Ph.D. Thesis

Kent, S. M., Dame, T. M., & Fazio, G. 1991, ApJ, 378, 131

Khochfar, S. & Burkert, A. 2003, ApJL submitted, (astro-ph/0303529)

Kim, Y., Demarque, P., Yi, S. K., & Alexander, D. R. 2002, ApJS, 143, 499

King, I. R. 1966, AJ, 71, 64.

Kinney, A. L., Calzetti, D., Bohlin, R. C., McQuade, K., Storchi-Bergmann, T., & Schmitt, H. R. 1996, ApJ, 467, 38

Kissler-Patig, M. 1997, PhD Thesis, Bonn University

Kissler-Patig, M. 2000, Reviews of Modern Astronomy, 13, 13

Kissler-Patig, M., Richtler, T., Storm, J., & della Valle, M. 1997, A&A, 327, 503

Kissler-Patig, M., Brodie, J. P., Schroder, L. L., Forbes, D. A., Grillmair, C. J., & Huchra, J. P. 1998a, AJ, 115, 105

Kissler-Patig, M. & Gebhardt, K. 1998, AJ, 116, 2237

Kissler-Patig, M., Grillmair, C. J., Meylan, G., Brodie, J. P., Minniti, D., & Goudfrooij, P. 1999, AJ, 117, 1206

Kissler-Patig, M., Brodie, J. P., & Minniti, D. 2002, A&A, 391, 441

Kohle, S., Kissler-Patig, M., Hilker, M., Richtler, T., Infante, L., & Quintana, H. 1996, A&A, 309, L39

Kormendy, J. & Djorgovski, S. 1989, ARAA, 27, 235

Kraft, R. P. 1994, PASP, 106, 553

Kraft, R. P., Suntzeff, N. B., Langer, G. E., Trefzger, C. F., Friel, E., Stone, R. P. S., & Carbon, D. F. 1982, PASP, 94, 55

Krauss, L. M. & Chaboyer, B. 2003, Science, 299, 65

Kundu, A. & Whitmore, B. C. 1998, AJ, 116, 2841

Kundu, A. & Whitmore, B. C. 2001a, AJ, 121, 2950

Kundu, A. & Whitmore, B. C. 2001b, AJ, 122, 1251

Kuntschner, H. 2000, MNRAS, 315, 184

Kuntschner, H. & Davies, R. L. 1998, MNRAS, 295, L29

Kuntschner, H., Smith, R. J., Colless, M., Davies, R. L., Kaldare, R., & Vazdekis, A. 2002a, MNRAS, 337, 172

Kuntschner, H., Ziegler, B. L., Sharples, R. M., Worthey, G., & Fricke, K. J. 2002b, A&A, 395, 761

Kurth, O. M., Fritze-v. Alvensleben, U., & Fricke, K. J. 1999, A&AS, 138, 19

Larsen, S. S. & Richtler, T. 2000, A&A, 354, 836

Larsen, S. S., Brodie, J. P., Huchra, J. P., Forbes, D. A., & Grillmair, C. J. 2001, AJ, 121, 2974

Larsen, S. S. & Brodie, J. P. 2002, AJ, 123, 1488

Larsen, S. S., Brodie, J. P., Beasley, M. A., & Forbes, D. A. 2002, AJ, 124, 828

Larsen, S. S., Brodie, J. P., Beasley, M. A., Forbes, D. A., Kissler-Patig, M., Kuntschner, H., & Puzia, T. H. 2003, ApJ, 585, 767

Larson, R. B. 1974, MNRAS, 169, 229

Larson, R. B. 1975, MNRAS, 173, 671

Larson, R. B. 1976, Saas-Fee Advanced Course 6: Galaxies, 69

Larson, R. B. 1996, ASP Conf. Ser. 92: Formation of the Galactic Halo...Inside and Out, 241

Lee, Y., Demarque, P., & Zinn, R. 1994, ApJ, 423, 248

Lee, H., Yoon, S., & Lee, Y. 2000, AJ, 120, 998

Lejeune, T., Cuisinier, F., & Buser, R. 1997, A&AS, 125, 229

Lejeune, T., Cuisinier, F., & Buser, R. 1998, A&AS, 130, 65

Longhetti, M., Bressan, A., Chiosi, C., & Rampazzo, R. 2000, A&A, 353, 917

Lynden-Bell, D. 1967, MNRAS, 136, 101

Macchetto, F., Pastoriza, M., Caon, N., Sparks, W. B., Giavalisco, M., Bender, R., & Capaccioli, M. 1996, A&AS, 120, 463

Mac Low, M.-M. & Kleessen, R. S. 2003, Reviews of Modern Physics, (astro-ph/0301093)

Madau, P., Ferguson, H. C., Dickinson, M. E., Giavalisco, M., Steidel, C. C., & Fruchter, A. 1996, MNRAS, 283, 1388

Majewski, S. R. 1993, ARA&A, 31, 575

Mandushev, G., Staneva, A., & Spasova, N. 1991, A&A, 252, 94

Mannucci, F., Basile, F., Poggianti, B. M., Cimatti, A., Daddi, E., Pozzetti, L., & Vanzi, L. 2001, MNRAS, 326, 745

Maraston, C. 1998, MNRAS, 300, 872

Maraston, C. 2000, The Evolution of the Milky Way: Stars versus Clusters, 275

Maraston, C. 2003, in preparation

Maraston, C. & Thomas, D. 2000, ApJ, 541, 126

Maraston, C., Kissler-Patig, M., Brodie, J. P., Barmby, P., & Huchra, J. P. 2001a, A&A, 370, 176

Maraston, C., Greggio, L., & Thomas, D. 2001b, Ap&SS, 276, 893

Maraston, C., Greggio, L., Renzini, A., Ortolani, S., Saglia, R. P., Puzia, T. H., & Kissler-Patig, M. 2003, A&A, 400, 823

de Marchi, G. & Paresce, F. 1997, ApJL, 476, L19

Marín-Franch, A. & Aparicio, A. 2003, ApJ, 585, 714

Mathieu, A., Merrifield, M. R., & Kuijken, K. 2002, MNRAS, 330, 251

Matteucci, F. 1994, A&A, 288, 57

Matteucci, F. & Greggio, L. 1986, A&A, 154, 279

McElroy, D. B. 1995, ApJS, 100, 105

McLaughlin, D. E. 1999, AJ, 117, 2398

McLaughlin, D. E., Harris, W. E., & Hanes, D. A. 1994, ApJ, 422, 486

McWilliam, A. 1997, ARA&A, 35, 503

McWilliam, A. & Rich, R. M. 1994, ApJS, 91, 749

Mehlert, D., Saglia, R. P., Bender, R., & Wegner, G. 2000, A&AS, 141, 449

Menci, N., Cavaliere, A., Fontana, A., Giallongo, E., & Poli, F. 2002, ApJ, 575, 18

Minniti, D. 1995, AJ, 109, 1663

Minniti, D., Kissler-Patig, M., Goudfrooij, P., & Meylan, G. 1998, AJ, 115, 121

Moore, S. A. W., Lucey, J. R., Kuntschner, H., & Colless, M. 2002, MNRAS, 336, 382

Murray, S. D. & Lin, D. N. C. 1992, ApJ, 400, 265

Neckel, H. 1986a, A&A, 159, 175

Neckel, H. 1986b, A&A, 167, 97

Neistein, E., Maoz, D., Rix, H., & Tonry, J. L. 1999, AJ, 117, 2666

O'Connell, R. W. 1976, ApJ, 206, 370

Origlia, L., Rich, R. M., & Castro, S. 2002, AJ, 123, 1559

Ortolani, S., Barbuy, B., & Bica, E. 1991, A&A, 249, L31

Ortolani, S., Renzini, A., Gilmozzi, R., Marconi, G., Barbuy, B., Bica, E., & Rich, R. M. 1995a, Nature, 377, 701

Ortolani, S., Bica, E., & Barbuy, B. 1995b, A&A, 296, 680

Ortolani, S., Barbuy, B., Bica, E., Renzini, A., Zoccali, M., Rich, R. M., & Cassisi, S. 2001, A&A, 376, 878

Osterbrook, D. E. 1989, Astrophysics of Gaseous Nebulae and Active Galactic Nuclei, University Science Books, Mill Valley

Pagel, B. E. J. 2001, PASP, 113, 137

Pahre, M. A. 1999, ApJS, 124, 127

Pancino, E., Ferraro, F. R., Bellazzini, M., Piotto, G., & Zoccali, M. 2000, ApJL, 534, L83

Peacock, J .A. 1999, Cosmological Physics, Cambridge University Press

Pearse, R. W. B. & Gaydon, A. G. 1976, The Identification of Molecular Spectra, Fourth Edition, Chapman and Hall, London

Peebles, P. J. E. 2003, in A New Era in Cosmology, eds. Metcalfe, N. & Shanks, T., ASP Conference Series 283, in press

Peebles, P. J. E. & Dicke, R. H. 1968, ApJ, 154, 891

Peletier, R. 1989, PhD Thesis, Rijksuniv. Groningen

Penzias, A. A. & Wilson, R. W. 1965, ApJ, 142, 419

Perelmuter, J., Brodie, J. P., & Huchra, J. P. 1995, AJ, 110, 620

Perlmutter, S. et al. 1999, ApJ, 517, 565

Peterson, R. C., Carney, B. W., Dorman, B., et al. 2003, ApJ, 588, 299, (astro-ph/0301412 and astro-ph/0303477)

Pettini, M. 2003, in Lectures of the XIII Canary Islands Winter School of Astrophysics, Cambridge University Press, (astro-ph/0303272)

Phillips, M. M., Jenkins, C. R., Dopita, M. A., Sadler, E. M., & Binette, L. 1986, AJ, 91, 1062

Pilachowski, C. A., Sneden, C., & Wallerstein, G. 1983, ApJS, 52, 241

Piotto, G. & Zoccali, M. 1999, A&A, 345, 485

Piotto, G., Bedin, L. R., Recio Blanco, A., Montalbán, J., D'Antona, F., Cassisi, S., & Heggie, D. 2002, ASP Conf. Ser. 274: Observed HR Diagrams and Stellar Evolution, 331

Poggianti, B. M. et al. 2001, ApJ, 563, 118

Press, W. H. & Schechter, P. 1974, ApJ, 187, 425

Pryor, C. & Meylan, G. 1993, ASP Conf. Ser. 50: Structure and Dynamics of Globular Clusters, 357

Puzia, T. H., Kissler-Patig, M., Brodie, J. P., & Huchra, J. P. 1999, AJ, 118, 2734

Puzia, T. H., Zepf, S. E., Kissler-Patig, M., Hilker, M., Minniti, D., & Goudfrooij, P. 2002a, A&A, 391, 453

Puzia, T. H., Saglia, R. P., Kissler-Patig, M., Maraston, C., Greggio, L., Renzini, A., & Ortolani, S. 2002b, A&A, 395, 45

Puzia, T. H., Kissler-Patig, M., Brodie, J. P., et al. 2002c, IAU Symposium 207, ed. D. Geisler, E. K. Grebel, & D. Minniti

Puzia, T. H., et al. 2003a, A&A, submitted

Puzia, T. H., Perrett, K. M., Bridges, T. J., 2003b, in preparation

Rabin, D. 1982, ApJ, 261, 85

Racine, R. 1968, JRASC, 62, 367

Ramírez, S. V. & Cohen, J. G. 2003, AJ, 125, 224

Reader J. & Corliss Ch.H. 1981, CRC Handbook of Chemistry and Physics

Renzini, A. 1977, Saas-Fee Advanced Course 7: Advanced Stages in Stellar Evolution, 151

Renzini, A. 1983, Memorie della Societa Astronomica Italiana, 54, 335

Renzini, A. 1998, AJ, 115, 2459

Renzini, A. 1999, The Formation of Galactic Bulges , 9

Renzini, A. & Voli, M. 1981, A&A, 94, 175

Renzini, A. & Buzzoni, A. 1986, ASSL Vol. 122: Spectral Evolution of Galaxies, 195

Renzini, A. & Fusi Pecci, F. 1988, ARAA, 26, 199

Rephaeli, Y. 1995, ARA&A, 33, 541

Rey, S., Yoon, S., Lee, Y., Chaboyer, B., & Sarajedini, A. 2001, AJ, 122, 3219

Rich, R. M. et al. 1997, ApJL, 484, L25

Rich, R. M. et al. 2003, in press

Richtler, T. 1995, Reviews of Modern Astronomy, 8, 163

Richtler, T. 2003, in Stellar Candles for the Extragalactic Distance Scale, Concepcion, Dec. 2002, Lecture Notes in Physics, Springer, (astro-ph/0304318)

Richtler, T. et al. 2002, IAU Symposium, 207, 263

Robin, A. C., Haywood, M., Crézé, M., Ojha, D. K., & Bienaymé, O. 1996, A&A, 305, 125

Robinson, L. B. & Wampler, E. J. 1972, PASP, 84, 161

Rose, J. A. 1984, AJ, 89, 1238

Rose, J. A. 1994, AJ, 107, 206

Rose, J. A., Bower, R. G., Caldwell, N., Ellis, R. S., Sharples, R. M., & Teague, P. 1994, AJ, 108, 2054

Saglia, R. P., Maraston, C., Thomas, D., Bender, R., & Colless, M. 2002, ApJL, 579, L13

Salaris, M., Chieffi, A., & Straniero, O. 1993, ApJ, 414, 580

Salaris, M. & Cassisi, S. 1996, A&A, 305, 858

Salaris, M. & Weiss, A. 1998, A&A, 335, 943

Salasnich, B., Girardi, L., Weiss, A., & Chiosi, C. 2000, A&A, 361, 1023

Salpeter, E. E. 1955, ApJ, 121, 161

Saviane, I., Rosenberg, A., Piotto, G., & Aparicio, A. 2000, A&A, 355, 966

Schiavon, R. P., Faber, S. M., Rose, J. A., & Castilho, B. V. 2002, ApJ, 580, 873

Schlegel, D. J., Finkbeiner, D. P., & Davis, M. 1998, ApJ, 500, 525

Schroder, L. L., Brodie, J. P., Kissler-Patig, M., Huchra, J. P., & Phillips, A. C. 2002, AJ, 123, 2473

Schweizer, F. 1982, ApJ, 252, 455

Schweizer, F. 1987, Nearly Normal Galaxies. From the Planck Time to the Present, 18

Schweizer, F. 1990, in Dynamics of Galaxies, ed. Wielen, R., Springer, Berlin

Schweizer, F. 1997, ASP Conf. Ser. 116: The Nature of Elliptical Galaxies; 2nd Stromlo Symposium, 447

Schweizer, F. 2002, IAU Symposium, 207, 630

Schweizer, F. 2003, New Horizons in Globular Cluster Astronomy, ASP Conference Series, eds. Piotto, G., Meylan, G., Djorgovski, G., & Rieke, M. 2003, in press, (astro-ph/0212243)

Schweizer, F., Miller, B. W., Whitmore, B. C., & Fall, S. M. 1996, AJ, 112, 1839

Schweizer, F. & Seitzer, P. 1998, AJ, 116, 2206

Searle, L. & Zinn, R. 1978, ApJ, 225, 357

Secker, J. & Harris, W. E. 1993, AJ, 105, 1358

Shapley, H. 1918, ApJ, 48, 154

Sharples, R. M., Zepf, S. E., Bridges, T. J., Hanes, D. A., Carter, D., Ashman, K. M., & Geisler, D. 1998, AJ, 115, 2337

Silk, J. 1977, ApJ, 214, 152

Silverman, B. W. 1986, Density Estimation for Statistics and Data Analysis, Chap and Hall/CRC Press, Inc.

Smith, M. G. & Weedmann, D. W. 1976, ApJ, 205, 709

Soifer, B. T. et al. 2001, AJ, 122, 1213

Soker, N. & Hadar, R. 2001, MNRAS, 324, 213

Somerville, R. S., Primack, J. R., & Faber, S. M. 2001, MNRAS, 320, 504

Spaenhauer, A., Jones, B. F., & Whitford, A. E. 1992, AJ, 103, 297

Spergel, D. N. et al. 2003, in press, (astro-ph/0302209)

Stanek, K. Z. 1996, ApJL, 460, L37

Stone R. P. S., & Baldwin J. A. 1983, MNRAS, 204, 347

Strader, J., Brodie, J. P., Schweizer, F., Larsen, S. S., & Seitzer, P. 2003a, AJ, 125, 626

Strader, J., Brodie, J. P., Forbes, D. A., Beasley, M. A., & Huchra, J. P. 2003b, AJ, 125, 1291

Sweigart, A. V. 1997, ApJL, 474, L23

Sweigart, A. V. & Catelan, M. 1998, ApJL, 501, L63

Tantalo, R., Chiosi, C., & Bressan, A. 1998, A&A, 333, 419

Terlevich, A. I. & Forbes, D. A. 2002, MNRAS, 330, 547

Terndrup, D. M. 1988, AJ, 96, 884

Thielemann, F.-K., Nomoto, K., & Yokoi, K. 1986, A&A, 158, 17

Thomas, D. 1999, MNRAS, 306, 655

Thomas, D., Greggio, L., & Bender, R. 1998, MNRAS, 302, 537

Thomas, D. & Kauffmann, G. 1999, ASP Conf. Ser. 192: Spectrophotometric Dating of Stars and Galaxies, 261

Thomas, D., Greggio, L., & Bender, R. 1999, MNRAS, 302, 537

Thomas, D., Maraston, C., & Bender, R. 2002, Ap&SS, 281, 371

Thomas, D., Maraston, C., & Bender, R. 2003a, MNRAS, 339, 897

Thomas, D. & Maraston, C. 2003b, A&A, 401, 429

Timmes, F. X., Woosley, S. E., & Weaver, T. A. 1995, ApJS, 98, 617

Tinsley, B. M. 1972, ApJ, 178, 319

Tinsley, B. M. 1979, ApJ, 229, 1046

Tody D., 1993, "IRAF in the Nineties" in Astronomical Data Analysis Software and Systems II, A.S.P. Conference Ser., Vol 52, eds. R.J. Hanisch, R.J.V. Brissenden, & J. Barnes, 173.

Tonry, J. L., Dressler, A., Blakeslee, J. P., Ajhar, E. A., Fletcher, A. B., Luppino, G. A., Metzger, M. R., & Moore, C. B. 2001, ApJ, 546, 681

Toomre, A. & Toomre, J. 1972, ApJ, 178, 623

Trager, S. C., King, I. R., & Djorgovski, S. 1995, AJ, 109, 218

Trager, S. C., Worthey, G., Faber, S. M., Burstein, D., & Gonzalez, J. J. 1998, ApJS, 116, 1

Trager, S. C., Faber, S. M., Worthey, G., & González, J. J. 2000a, AJ, 119, 1645

Trager, S. C., Faber, S. M., Worthey, G., & González, J. J. ;. 2000b, AJ, 120, 165

Treu, T., Stiavelli, M., Casertano, S., Møller, P., & Bertin, G. 1999, MNRAS, 308, 1037

Trinchieri, G. & Fabbiano, G. 1985, ApJ, 296, 447

Tripicco, M. J. & Bell, R. A. 1995, AJ, 110, 3035

Tsujimoto, T., Nomoto, K., Yoshii, Y., Hashimoto, M., Yanagida, S., & Thielemann, F. -K. 1995, MNRAS, 277, 945

Tully, R. B. 1988, Cambridge and New York, Cambridge University Press

van de Kamp, P. 1967, Principles of Astrometry (San Francisco: W. H. Freeman)

Unavane, M. & Gilmore, G. 1998, MNRAS, 295, 145

Unavane, M., Gilmore, G., Epchtein, N., Simon, G., Tiphene, D., & de Batz, B. 1998, MNRAS, 295, 119

VandenBerg, D. A., Swenson, F. J., Rogers, F. J., Iglesias, C. A., & Alexander, D. R. 2000, ApJ, 532, 430

van den Bergh, S., Pritchet, C., & Grillmair, C. 1985, AJ, 90, 595

van der Kruit, P. C. 1999, Ap&SS, 267, 227

de Vaucouleurs, G., de Vaucouleurs, A., Corwin, H. G. Jr., Buta, R., Paturel, G., and Fouque, P. 1991, Third Reference Catalogue of bright galaxies, Berlin: Springer

Vazdekis, A. 1999, ApJ, 513, 224

Vazdekis, A., Casuso, E., Peletier, R. F., & Beckman, J. E. 1996, ApJS, 106, 307

Vazdekis, A. & Arimoto, N. 1999, ApJ, 525, 144

Vazdekis, A., Salaris, M., Arimoto, N., & Rose, J. A. 2001, ApJ, 549, 274

Vazdekis, A., Kuntschner, H., Davies, R. L., Arimoto, N., Nakamura, O., & Peletier, R. 2001, ApJL, 551, L127

Ventura, P., D'Antona, F., Mazzitelli, I., & Gratton, R. 2001, ApJL, 550, L65

Westera, P., Lejeune, T., Buser, R., Cuisinier, F., & Bruzual, G. 2002, A&A, 381, 524

Wheeler, J. C., Sneden, C., & Truran, J. W. 1989, ARA&A, 27, 279

White, S. D. M. & Frenk, C. S. 1991, ApJ, 379, 52

White, S. D. M., Navarro, J. F., Evrard, A. E., & Frenk, C. S. 1993, Nature, 366, 429

Whitford, A. E. 1977, ApJ, 211, 527

Whitmore, B. C. & Schweizer, F. 1995, AJ, 109, 960

Whitmore, B. C., Miller, B. W., Schweizer, F., & Fall, S. M. 1997, AJ, 114, 1797

Worthey, G. 1992, Ph.D. Thesis

Worthey, G. 1994, ApJS, 95, 107

Worthey, G., Faber, S. M., & Gonzalez, J. J. 1992, ApJ, 398, 69

Worthey, G., Faber, S. M., Gonzalez, J. J., & Burstein, D. 1994, ApJS, 94, 687

Worthey, G., & Ottaviani D.L. 1997, ApJS, 111, 377

Woosley, S. E. & Weaver, T. A. 1995, ApJS, 101, 181

Wright, G. S., James, P. A., Joseph, R. D., & McLean, I. S. 1990, Nature, 344, 417

Wyse, R. F. G. & Gilmore, G. 1993, ASP Conf. Ser. 48: The Globular Cluster-Galaxy Connection, 727

Wyse, R. F. G., Gilmore, G., & Franx, M. 1997, ARA&A, 35, 637

York, D. G. et al. 2000, AJ, 120, 1579

Zepf, S. E. 1997, Nature, 390, 377

Zepf, S. E. & Ashman, K. M. 1993, MNRAS, 264, 611

Zepf, S. E., Beasley, M. A., Bridges, T. J., Hanes, D. A., Sharples, R. M., Ashman, K. M., & Geisler, D. 2000, AJ, 120, 2928

Zinn, R. 1985, ApJ, 293, 424

Zinn, R. & West, M. J. 1984, ApJS, 55, 45

Zoccali, M., Cassisi, S., Frogel, J. A., Gould, A., Ortolani, S., Renzini, A., Rich, R. M., & Stephens, A. W. 2000a, ApJ, 530, 418

Zoccali, M., Cassisi, S., Bono, G., Piotto, G., Rich, R. M., & Djorgovski, S. G. 2000b, ApJ, 538, 289

Zoccali, M., Renzini, A., Ortolani, S., Bica, E., & Barbuy, B. 2001, AJ, 121, 2638

Zoccali, M. et al. 2003, A&A, 399, 931

Danksagung

At the end of this thesis work I look on three years of exciting research, lots of experience, moments of despair and satisfaction, but most of all on three years of joy to make science. From the beginning of my personal calendar at the age of four, when my grandma showed me the twinkling of stars, the pleasure of thinking on astronomical scales never abandoned me, but rather grew throughout the years. This pleasure was constantly and is still fed by the feedback and support of many persons who I would like to thank in the following. As astronomical reasearch is a team sport, many insights would not have been possible and many projects would never have led to a fruitful completion without the help of these outstanding people.

My exemplary guide during the time of my pre-Diploma, Diploma and PhD work was **Markus Kissler-Patig**, who always loyally looked after me, not only at ESO, and fed my scientific spirit in many extended discussions. One important thing I learned from him is that there are no "20-minutes jobs" in astronomy, which most likely will enter the history of astronomy as the *Kissler-Patig quantum of action*. I have still not lost the grit to prove that this is wrong. Thank you for your motivation and support, your determination and acumen, also as a friend.

My sincere thanks go to **Roberto Saglia** for his countless suggestions, ideas, critical remarks, and his deftly handling of administrative challenges. He was always a helpful and encouraging contact at Sternwarte. I am indebted to **Ralf Bender**, my supervisor at Sternwarte, who made this project possible and was most helpful with administrative and scientific aspects of my PhD work.

For their advice and comments connected to my thesis my gratitude and respect goes to all staff members of the extragalactic group who are **Uli Hopp, Claudia Maraston, Bo Milvang-Jensen, Mark Neeser, Daniele Pierini, Mara Salvato, Stella Seitz,** and **Daniel Thomas**.

Thanks go to my fellow students who shared the spaces of Sternwarte with me, in particular **Roberto Barmina** (who untimely left our group), **Christine Botzler, Georg Feulner, Jürgen Fliri, Armin Gabasch, Yuliana Goranova, Aleksi Halkola, Maurilio Pannella, Christoph Nodes, Jan Snigula,** and **Jens Thomas**. Thank you for many nice discussions and interesting lunch and coffee breaks.

I am particularly grateful to **Claus Gössl, Tadziu Hoffmann, Andreas Korn, Harald Lesch, Joachim Puls, Tamara Repolust, Daniel Sauer, Matthias Stehle,** and **Michael Wegner** for the relaxed and mentally imbueing atmosphere at our lunch table. I shall miss our spicy indian meals which cauterized our taste buds and the poignant sarkasm that cauterized those who were meant.

Particular thanks go to my dear fellows **Philip Hultzsch, André Nickel**, and **Arno Riffeser**. *Chapeau* for running the espresso machine, dank nights in Munich nightlife, running along the Isar river, rock climbing in the Alps, saving me from falling into crevasses, discussions about god and his wife, and for becoming good friends.

My deepest gratitude goes to **Nicole Homeier**, my love, who always believes in me. Thank you for your patience, your trust, your motivation, your support, but most of all, thank you for your love.

Allen meinen Freunden sei an dieser Stelle gedankt für ihre Unterstützung in den Jahren meiner Doktorarbeit. Mein besonderer Dank geht an **Thomas Prang**, meinen teuersten Freund, der über viele Jahre hinweg immer Interesse an meiner Wissenschaft gezeigt hat. Ein ganz spezieller Dank geht an **Liliane Würstlin**, meine Zahnärztin *in spe*, die mich während des Zusammenschreibens mehrmals wöchentlich als Versuchskaninchen für ihre "Endospielchen" benutzt und mich vermutlich von um Grössenordnungen stärkeren Schmerzen in den folgenden Jahren bewahrt hat.

Der liebevollste Dank geht jedoch an meine **Eltern**, ohne deren fürsorgliche Unterstützung diese Arbeit nie möglich gewesen wäre. Ich danke Euch aus tiefstem Herzen für Eure bedingungslose Liebe. Auch meiner **Schwester** sei an dieser Stelle gedankt für unsere stundenlangen Telefongespräche und Ihre erlebnisreichen Besuche, die mich immer sehr amüsant aus dem Trott der Wissenschaft gerissen haben.

Najgłębmsze dzięki posyłam do mojej kochanej **Babci**, która jest miarodajnie odpowiedzialna za moją historie w nauce. Ona mi pokazała gwiazdy. Twój duch zawsze będzie świecił na mnie z tych ogromnych przestrzeń. Dziękuje Tobie z całego serca za Twojom miłość która była ustawicznym popędem mojej nauki.

Lebenslauf

Name:	Thomas Hyazinth Puzia
Geburtsdatum:	1. Juli 1973
Geburtsort:	Krakau
Wohnort:	Knöbelstrasse 10a, 80538 München
Staatsangehörigkeit:	deutsch
Familienstand:	ledig
Ausbildung:	• 1987 – 1993, Besuch des Otto-Hahn Gymnasiums in Gifhorn
	• 1993, Erlangung der allgemeinen Hochschulreife und des gr. Latinums
	• 1993 – 1994, Zivildienst
	• 1994 – 1999, Studium der Physik und Astronomie an der Rheinischen Friedrich-Wilhelms Universität Bonn
	• 1999, Erlangung des Diploms in Physik
	• 2000 – 2003, Promotionsstudium der Astronomie an der Ludwig-Maximilians Universität München
Forschungsaktivitäten:	• 1998, *Student fellowship* am UCO/Lick Observatory, UC Santa Cruz, Kalifornien, USA
	• 1999, Forschungsaufenthalt an der *Yale University*, New Haven, Connecticut, USA
	• 2000, *Short-term fellowship* am *European Southern Observatory*, Garching
	• 2000, Forschungsaufenthalt an der Universität São Paulo, Brasilien
	• 2001, Forschungsaufenthalt an der *Yale University*, New Haven, Connecticut, USA
	• 2001, Forschungsaufenthalt an der *University of Wisconsin*, Madison, Wisconsin, USA
	• 2001, Forschungsaufenthalt an der *McMaster University*, Hamilton, Ontario, Canada

Beobachtungserfahrung: • PI: ESO, VLT UVES, 40 hours,
High-resolution spectroscopy of globular clusters in
NGC 5128

• PI: Calar Alto, 2.2m FOCES, 3 nights,
High-resolution calibration of the Lick
Standard System

• CoI: HST, ACS, 6 orbits,
The Age and Mass Function of the Intermediate Age
globular cluster system of NGC 4365

• CoI: ESO, VLT ISAAC, 33 hours,
Understanding sub-populations of globular clusters
in early-type galaxies with near-IR photometry

• CoI: Gemini, GMOS, 18 hours,
Spectroscopy of globular clusters in dE galaxies

• CoI: ESO, VLT FORS2, 4+4 nights,
The chemistry of extragalactic globular clusters

• CoI: ESO, VLT FORS1, 3 nights,
The chemistry of extragalactic globular clusters

• CoI: Calar Alto 3.5m, MOSCA, 4 nights,
Imaging of early-type galaxies